11. EUROPEAN CONFERENCE ON RENEWABLE ENERGY SYSTEMS

ECRES 2023
18-20 May 2023
Riga / LATVIA

www.ecres.net

PROCEEDINGS

Edited by

Prof. Dr. Erol Kurt

ISBN: 978-605-70842-2-4

Organizing Institutions

University of Latvia

Electrical and Computer Engineering Research Group - ecerg.com

Projenia R&D Consultancy Service Limited Company - projenia.net

Published by
Erol Kurt
on 15th June 2023
(Ankara/Türkiye)

Book typesetted and designed by
Assoc. Prof. Dr.Yunus Uzun and Bekir Dursun

Cooperative Institutions

Supporting Institutions

Committees

CONFERENCE FOUNDER & CHAIRMAN

Prof. Dr. Erol KURT, Gazi University, Türkiye

CO-CHAIRMAN

Prof. Dr. Māris Ķļaviņš, University of Latvia, Latvia

INTERNATIONAL ORGANIZING COMMITTEE

Prof. Dr. Adnan Sozen, Gazi University, Türkiye
Prof. Dr. Alfredo Vaccaro, Sannio University, Italy
Prof. Dr. Carlos Rubio-Maya, Univ. Michoacana de San Nicolás de Hidalgo, Mexico
Assoc. Prof. Dr. Fontina Petrakopoulou-Robinson, Universidad Carlos III de Madrid, Spain
Prof. Dr. Ian Hunter, University of Leeds, UK
Prof. Dr. Jose Manuel Lopez Guede, University of Basque Country, Spain
Prof. Dr. Mehmet Tekerek, Kahramanmaras Sutcu Imam University, Türkiye
Prof. Dr. Murat Kunalbayev, Inst. of Information and Computational Technologies, Kazakhstan
Prof. Dr. Nicu Bizon, Pitesti University, Romania
Prof. Dr. Peter Childs, Imperial College London, UK
Prof. Dr. Poul Alberg Østergaard, Aalborg University, Denmark
Prof. Dr. Raoul Rashid Nigmatullin, Kazan National Research Tech. Univ., Tatarystan, Russia
Prof. Dr. Saad Mekhilef, University of Malaya, Malaysia
Prof. Dr. Saeed Badshah, Int. Islam. Uni. Islamabad, Pakistan
Prof. Dr. Sagdulla L. Lutpullaev, Uzbekistan Academy of Sciences, Uzbekistan
Prof. Dr. Serguei Martemianov, University of Poitiers, France
Prof. Dr. Shadi Shahedipour-Sandvik, University at Albany, USA
Prof. Dr. Shadia J. Ikhmayies, Al Isra University, Jordan
Prof. Dr. Waqar Mahmood, University of Engineering and Technology, Pakistan
Assoc. Prof. Dr. Yussupova Gulbakhar, Turan University, Kazakhstan

International Scientific Committee

Prof. Dr. Alessandro Zanarini, University of Bologna, Italy
Assoc. Prof. Dr. Ali Jazie, University of Al-Qadisiyah, Iraq
Dr. Angeliki Chatzidimitriou, Aristotle University of Thessaloniki, Greece
Prof. Dr. Antonio Soria Verdugo, Universidad Carlos III de Madrid, Spain
Dr. Athar Waseem, International Islamic University, Pakistan
Prof. Dr. Aybaba Hançerlioğulları, Kastamonu University, Türkiye
Prof. Dr. Ayman El-Hag, American University of Sharjah, UAE
Prof. Dr. Bernabé Marí Soucase, Polytechnical University of Valencia, Spain
Assist. Prof. Dr. Burak Akin, Yildiz Technical University, Türkiye
Assoc. Prof. Dr. Bünyamin Tamyürek, Eskisehir Osmangazi University, Türkiye
Prof. Dr. Carolina Marugan Cruz, Universidad Carlos III de Madrid, Spain

Prof. Dr. Nikolay Djagarov, Nikola Vaptsarov Naval Academy, Bulgaria
Dr. Nilufar R. Avezova, Uzbekistan Academy of Sciences, Uzbekistan
Prof. Dr. Pedro Juan Roig, Universidad Miguel Hernández, Spain
Prof. Dr. Peter Lund, Aaalto University, Finland
Prof. Dr. Poul Alberg Østergaard, Aalborg University, Denmark
Prof. Dr. Rachid Chenni, University Mentouri of Constantine, Algeria
Prof. Dr. Rafael K. Jardan, Budapest Univ. of Technology and Economics, Hungary
Prof. Dr. Rafaela Hillerbrand, RWTH Aachen University, Germany
Prof. Dr. Ramazan Bayindir, Gazi University, Türkiye
Prof. Dr. Raoul Rashid Nigmatullin, Kazan National Research Technical University,Russia
Dr. Rosaria Villari, Italian National Agency for New Technologies, Italy
Prof. Dr. Saffa Riffat, Nottingham University, UK
Assist. Prof. Dr. Sertac Bayhan, Texas A&M University at Qatar, Qatar
Prof. Dr. Shadia J. Ikhmayies, Al Isra University, Jordan
Prof. Dr. Sing Lee, Institute for Plasma Focus Studies, Australia
Prof. Dr. Sor Saw Heoh, Nilai University, Malaysia
Prof. Dr. Souad A.M. Albathi, Int. Islamic Uni. Malaysia, Malaysia
Prof. Dr. Sujit Barhate, Savitribai Phune Pune University, India
Assoc. Prof. Dr. T.Thamizhselvan, Rajalakshmi Engineering College, Chennai, India
Prof. Dr. Tae Hee Lee, Hanyang University, S. Korea
Prof. Dr. V. Jagannathan, Bhabha Atomic Research Center, India
Prof. Dr. Wail N. Al-Rifaie, Philadelphia University, Jordan
Prof. Dr. Wang Ru-Zhu, Shanghai Jiao Tong University, China
Assoc. Prof. Dr. Yong Song, Institute of Nuclear Energy Safety Technology, China
Prof. Dr. Zhiqiang Zhu, Institute of Nuclear Energy Safety Technology, China

FOREWORD

Dear Colleagues,

We are glad to see you and your contribution for the 11. European Conference on Renewable Energy Systems (ECRES 2023). The event has been organized in Riga, Latvia on 18-20 May 2023 by the local organizers University of Latvia, ECERG – Electrical and Computer Engineering Research Group and Projenia in the hybrid format. Besides, many institutions world-widely took a part as the cooperating institutions including many international refeered academic journals.

The purpose of the ECRES is to bring together researchers, engineers and natural scientists from all over the world, interested in the advances of all branches of renewable energy systems such as wind, solar, hydrogen, hydro-, geothermal, solar concentrating, fuel-cell. It aims to present and disseminate the cutting-edge results to the international community of energy in the form of research, development, applications, design and technology. It is thereby expected that it can assist researchers, scientists, manufacturers, companies, communities, agencies, associations and societies to keep abreast of new developments in their specialist fields and to find innovative solutions in their problems.

Historically, the first, second, third, fourth, fifth, sixth, seventh, eighth, ninht and tenth conferences were completed very successfully in Alanya/Antalya (2012), Antalya (2013), Kemer/Antalya (2015), Istanbul (2016), Sarajevo / Bosnia and Herzegovina (2017), Istanbul (2018), Madrid (2019), Istanbul-remote (2020), Istanbul-remote (2021), Istanbul, respectively. This serial event has been a continuous one even in the pandemic periode, worldwidely.

Many of the extended forms of selected papers were puublished in SCI, E-SCI, SCOPUS and EBSCO indexed reputable journals following the previous events. This year, 244 papers have been received world-widely. Among them, 106 papers from 50 countries have been accepted and presented. Following the physical and virtual presentations, these abstracts and papers are put into the present proceedings. We state our gratitutes to all authors, keynote speakers, special session organizers, reviewers, session chairmen and scientific board for their precisious contribution and hope to extend these cooperation for the next events, too.

This proceeedings have been delivered to the participants via the conference website link under a specific ISBN. In addition, high amount of selected and improved papers will be considered for the publication in reputable journals indexed in Science Citation Index (SCI-indexed), Emerging SCI-indexed, SCOPUS-indexed and EBSCO-indexed journals after the standard peer-review processes of the journals.

We would like to send our warmest greetings to all and looking forward to having your future contribution to the future events for a much green, pandemy-free and peaceful word. (1 June 2023, Ankara)

Prof. Dr. Erol KURT
Chairman of ECRES Series
Gazi University, Technology Faculty
Department of Electrical and Electronics Engineering
06500 Besevler ANKARA TÜRKİYE
E-mail: ekurt52tr@yahoo.com

CONTENTS

KEYNOTES

REGULAR ABSTRACTS

FULL PAPERS

KEYNOTES

RIGA 2023

Hydrogen in Electricity's Future

Ahmed F. Zobaa
Brunel University London, UK, ahmed.zobaa@brunel.ac.uk

Cite this paper as: *Zobaa, AF., Hydrogen in Electricity's Future. 11th Eur. Conf. Ren. Energy Sys. 18-20 May 2023 Riga, Latvia*

Abstract: From the current global energy map, coal leads electricity production with more than 37%, natural gas with 24%, petroleum with about 3% renewable energies with more than 26%, and nuclear energy with 10%.
Significant potential for further expansion of renewable energies combined with concerns about potential future natural gas supplies leads to a focus on hydrogen from electrolysis (green hydrogen) rather than from natural gas with carbon capture and storage ("blue" hydrogen).
As of 2020, most hydrogen (~95%) is produced from fossil fuels, but hydrogen produced from renewables has huge potential. To significantly contribute to the clean energy transition, "green hydrogen" must be produced at scale or blended into existing gas infrastructure reducing carbon emissions. Hydrogen can also be used for seasonal energy storage, industry decarbonisation and a renewable-powered future.
This talk will highlight how hydrogen will help in replacing fossil fuels in the future.

***Keywords**:* *Hydrogen, renewable energy, perspective, storage*

RIGA 2023

Building Integrated Photovoltaics: From Sufficiency to Sharing Towards Carbon Neutral Cities

Dimitrios Karamanis
University of Patras, Greece, dkaraman@upatras.gr

Cite this paper as: *Karamanis, D., Building Integrated Photovoltaics: from sufficiency to sharing towards carbon neutral cities. 11th Eur. Conf. Ren. Energy Sys. 18-20 May 2023 Riga, Latvia*

Abstract: To implement Paris agreement and keep the mean temperature increase lower than 1.5°C compared to preindustrial levels, deep decarbonization is required with the utilization of renewable energy sources. The integration of renewables in buildings is a key component in the proposed actions of WGIII and a step forward to distributed energy systems with high contribution from buildings, becoming prosumers. Since the building structure is the interface between humans and their natural environment, sustainable development requires a rethinking of the photovoltaics integration in harmony to local environmental and bioclimatic conditions. The necessity of climate crisis mitigation points towards moving beyond the self-sufficient and self-consumption concepts into positive energy sharing within local communities. In this context, the SERAS concept (sufficiency, efficiency, renewables and sharing) that we recently proposed in BIPV deployment will be presented and discussed towards carbon neutral cities.

Keywords: *Photovoltaics, environment, policy, decarbonization*

RIGA 2023

Teorical and Empirical Modeling

Jose Manuel Lopez-Guede
University of the Basque Country, Spain, jm.lopez@ehu.es

Cite this paper as: *Lopez-Guede, J.M. Teorical and Empirical Modeling. 11th Eur. Conf. Ren. Energy Sys. 18-20 May 2023 Riga, Latvia*

Abstract: Modeling complex systems is still an open issue is many fields, and among them, in the scope of energy. A good modeling provides accurate simulations that can help to pose, design and implement appropriate control algorithms, which optimize the performance of the physical elements. However, sometimes it is not clear that the first principle based modeling provides accurate enough results, and the empirical modeling becomes a promising technique to deal with complex systems. In this keynote talk a number of first principle models will be reviewed and the empirical modeling will be presented for a real case.

Keywords: *Theory, empirical model, optimization, complex*

REGULAR ABSTRACTS

RIGA 2023

Use of a Low-Cost Catalyst for the Production of Fuel Gas and Carbon Nanotubes from the Pyrolysis of Plastic Waste

Mónica Calero
University of Granada, Granada, Spain, mcaleroh@ugr.es, ORCID: 0000-0001-8029-8211

María Ángeles Martín-Lara
University of Granada, Granada, Spain, marianml@ugr.es, ORCID: 0000-0001-9515-7307

Rafael Moreno
University of Granada, Granada, Spain, rafmor@correo.ugr.es, ORCID: 0000-0003-0632-4201

Gabriel Blázquez
University of Granada, Granada, Spain, gblazque@ugr.es, ORCID: 0000-0002-0818-6300

Cite this paper as: *Calero, M, Martín-Lara, M.A., Moreno, R., Blázquez, G. Use of a low-cost catalyst for the production of fuel gas and carbon nanotubes from the pyrolysis of plastic waste. 11. Eur. Conf. Ren. Energy Sys. 18-20 May 2023, Riga, Latvia*

Abstract: Plastic waste is a problem of special interest in recent years. Reducing consumption, proper management and recycling are the options that are being considered to control plastic pollution. Chemical recycling is a very suitable alternative for plastic waste that is difficult to reuse or mechanically recycle. In this work, fuel gas and carbon nanotubes were obtained from the pyrolysis of post-consumer plastic waste using sepiolite as a low-cost catalyst. The pyrolysis has been carried out in a horizontal tubular reactor in two stages. In the first reactor, plastic waste pyrolysis is carried out at 500 ºC and the pyrolysis gases were passed through the second reactor at 800 ºC allowing the deposition of carbon on the catalyst surface while the off-gas is collected in Tedlar bags. Carbon deposition on the catalyst was analyzed using different techniques such as temperature programmed oxidation (TPO) and transmission electron microscopy (TEM). The gas is analyzed by gas chromatography. The results showed that the exhaust gas has a good calorific value, being constituted mainly by methane, ethane, carbon monoxide and in smaller quantities hydrogen or ethylene. The results of TPO allowed to determine the amount of carbon deposited while the TEM images showed the presence of carbon filaments that could be confirmed as nanotubes.

Keywords: *Carbon nanotubes, Fuel gas, Plastic waste, Pyrolysis*

RIGA 2023

Development of Sorbents for Carbon Capture to Achieve Carbon Neutrality

Maris Klavins
Department of Environmental Science, University of Latvia, Riga, Latvia, maris.klavins@lu.lv,
ORCID: 0000-0002-4088-9348
Linda Ansone-Bertina
Department of Environmental Science, University of Latvia, Riga, Latvia, linda.ansone-bertina@lu.lv;
ORCID: 0000-0001-5460-2726

Lauris Arbidans
Department of Environmental Science, University of Latvia, Riga, Latvia, lauris.arbidans@lu.lv;
ORCID: 0000-0002-5281-5485

Cite this paper as: *Klavins, M., Ansone-Bertina, L., Arbidans, L.: Development of sorbents for carbon capture to achieve carbon neutrality. 11. Eur. Conf. Ren. Energy Sys. 18-20 May 2023, Riga, Latvia*

Abstract: Climate change problems are becoming a priority issue worldwide and requiring urgent actions to reduce emissions of greenhouse gasses (GHG). However, reduction of GHG emissions alone cannot help to reach climate neutrality aims as it is stated in EU Green Deal. To reach climate neutrality aims at the same time keeping up welfare level of society, it would be important to capture carbon emitted during different technological processes, at first as a result of combustion or incineration technologies. Thus, major efforts should be put on development and implementation of carbon capture and storage (CCS) technologies. There are several approaches suggested and already implemented at pilot scale. But further testing of different approaches still is actual. One of sectors, where CCS technology application would be essential is waste processing technologies. Aim of our research is to study possibilities to develop materials for CCS and demonstrate their potential for small scale CCS, relevant for waste treatment. The application of pre-combustion carbon capture provide opportunities to reduce emissions of CO2. A number of sorbents, prospective for CCS have been elaborated and their application potential demonstrated.

Keywords: *Carbon capture, Metal organic frameworks, Hydrochar, Biochar*

Acknowledgments

Research is supported by ERDF project Nr.1.1.1.1/19/A/013 “Innovation of the waste-to-energy concept for the low-carbon economy: Development of novel carbon capture technology for thermochemical processing of municipal solid waste (Carbon Capture and Storage from Waste - CCSW)”

RIGA 2023

Investigation of Metal-Impregnated Zeolites as Catalysts in Pyrolysis of Mixed Plastic Wastes

Marco F. Paucar
University of Granada, Granada, Spain, mfpaucars@ugr.es, ORCID: 0000-0002-7804-3057

Mónica Calero
University of Granada, Granada, Spain, mcaleroh@ugr.es, ORCID: 0000-0001-8029-8211

Mario J. Muñoz-Batista
University of Granada, Granada, Spain, mariomunoz@ugr.es, ORCID: 0000-0002-1419-0592

Mª Ángeles Martín-Lara
University of Granada, Granada, Spain, marianml@ugr.es, ORCID: 0000-0001-9515-7307

Cite this paper as: *Paucar M.F., Calero M., Muñoz-Batista, M.J., Martín-Lara, M.A. Investigation of metal-impregnated zeolites as catalysts in pyrolysis of mixed plastic wastes. 11. Eur. Conf. Ren. Energy Sys. 18-20 May 2023, Riga, Latvia*

Abstract: Catalytic pyrolysis of plastic waste is an interesting option to contribute a circular economy for plastic. In this work, the performance of two known zeolites, Y and ZSM-,5, in catalytic pyrolysis of a real plastic waste mixture was investigated. The zeolites used in this work were modified by using the incipient wetness method using nitrate solutions of nickel and cobalt. First preparation of eight catalytic materials was performed (two native samples, four nickel-impregnated samples, four cobalt-impregnated samples). Second, a complete characterization of the native and metal-impregnated zeolites was carried out including textural properties as specific surface area, total pore volume and acidity. Some differences in characterization results were found as a function of type of zeolite, type of metal (Co or Ni) and amount of metal dispersed (1% and 5%). Then, catalytic pyrolysis experiments were carried out in a laboratory fixed-bed reactor at a temperature of 500 ºC. The product distribution did not change significantly, although a weak decrease in the yield of gases was observed in metal-impregnated catalysts. Also, low influence on the oil composition was detected yielding a liquid product in which a higher percentage are hydrocarbons in the gasoline range.

Keywords: *Plastic waste; Pyrolysis; Zeolites; Metal impregnation*

RIGA 2023

The Expected Dynamics of The Wind Energy in The Baltic and North Seas

Eugen Rusu
"Dunărea de Jos" University, Galaţi, Romania, erusu@ugal.ro, ORCID: 0000-0001-6899-8442

Cite this paper as: *Rusu, E, The expected dynamics of the wind energy in the Baltic and North Seas, 11. Eur. Conf. Ren. Energy Sys. 18-20 May 2023, Riga, Latvia*

Abstract: The offshore wind industry has already a spectacular development in the north of Europe. The first wind farm was installed in 1991 in the Baltic Sea and around 60 wind projects are currently operational in the Baltic and North Seas. According to the European Green Deal, a 25 times enhancement of the offshore wind power capacity is targeted in Europe by 2050 in relationship with 2021. Thus, an accelerated development of the wind farms is expected in the European nearshore. In this context, the objective of the present work is to analyze the expected dynamics of the wind power in the Baltic and North Seas until the end of the 21st century. The analysis is structured on 40-year periods. An analysis of the recent past wind data for the 40-year period 1980-2019 is first carried out based on ERA5 data. The study is continued for the future periods, near future 2021-2060, and distant future 2061-2100, considering two different RCP scenarios (4.5 and 8.5). The results indicate that moderate enhancements are expected in both seas in terms of mean wind power density. In the North Sea significant enhancements of the maximum wind speeds can be also noticed.

Keywords: *Wind power, Baltic and North Seas, RCP scenarios, near and distant future, historical data*

Acknowledgments

This work was carried out in the framework of the research project DREAM (Dynamics of the REsources and technological Advance in harvesting Marine renewable energy), supported by the Romanian Executive Agency for Higher Education, Research, Development and Innovation Funding – UEFISCDI, grant number PN-III-P4-ID-PCE-2020-0008

RIGA 2023

An Evaluation of the Future Expected Wind and Wave Power in The Black Sea

Alina Beatrice Raileanu
University Dunărea de Jos, Galaţi, Romania, alinaraileanu@univ-danubius.ro, ORCID: 0000-0001-6714-447X

Liliana Rusu
University Dunărea de Jos, Galaţi, Romania, lrusu@ugal.ro, ORCID: 0000-0002-8179-1347

Cite this paper as: *Raileanu, AB.,Rusu, L. An evaluation of the future expected wind and wave power in the Black Sea, 11. Eur. Conf. Ren. Energy Sys. 18-20 May 2023, Riga, Latvia*

Abstract: The European Green Deal assumes an accelerated implementation of the marine energy farms covering large geographical spaces in the European coastal environment, including also the Black Sea. In this context, the objective of the present work is to present a perspective of the wind and wave power dynamics in the basin of the Black Sea coming from the recent past and going until the end of the 21st century. For the historical wind data ERA5 is considered, while for the future, data from RCA4 regional climate model are processed and analysed considering various RCP scenarios. As regards the waves, a wave modelling system, SWAN based, has been implemented in the Black Sea. This system has been validated for the past period against satellite data and its outputs were found reliable. For the future, SWAN model was run using the RCM wind data. The results indicate that a slight enhancement is expected in the future both in terms of wind and wave energy and this enhancement will be higher in the western side of the sea. It was also noticed an increase of the maximum wind speeds, both in terms of frequency and intensity. On the other hand, the extreme values of the significant wave height are not expected to be higher in the future because of the cyclonic form of the extreme storms that imply variations in the wind directions, and consequently reduced fetches.

Keywords: *Wind and wave power, Black Sea, RCP scenarios, extreme events, 21st century*

RIGA 2023

A Compact Unit of Photovoltaic Solar Still Air Gap Membrane Distillation Process for Simultaneous Production of Water and Electricity

Adnan Alhathal Alanezi
Department of Chemical Engineering Technology, College of Technological Studies, The Public Authority for Applied Education and Training (PAAET), Kuwait, aa.alanezi@paaet.edu.kw , ORCID: 0000-0001-9212-3646

Cite this paper as: *Alanezi, AA., A compact unit of photovoltaic solar still air gap membrane distillation process for simultaneous production of water and electricity. 11. Eur. Conf. Ren. Energy Sys. 18-20 May 2023, Riga, Latvia*

Abstract: Remote arid and coastal areas have dry climates, limited freshwater supplies, and intense solar radiation. Solar still (SS) and photovoltaic (PV) technologies are preferred for small-scale water and power demands. However, these techniques have low thermal efficiency and thus limited water productivity. A compact hybrid system with a novel design combines a solar still air gap membrane distillation process with a photovoltaic panel. Outdoor experiments revealed daily average yields of produced water and power of 5.9 kg/m^2 and 0.68 kWh/m^2, respectively, when solar radiation intensity was 6.4 kWh/m^2. Throughout the day, the specific productivity (permeate flow) of potable water, electric power, and thermal efficiency coefficient is evaluated. The results indicate that as solar radiation increases, productivity increases. The daily yield of the hybrid system increased 1.6-fold when compared to a single-stage AGMD system and cascade solar still arrangement system, and 72% of solar energy was efficiently utilized

Keywords: *Solar still, air gap, membrane distillation, photovoltaic panel, water desalination*

RIGA 2023

Role of The Transport Sector in Hydrogen Energy System

Amela Ajanovic
Vienna University of Technology – TU WIEN, Vienna, Austria, ajanovic@eeg.tuwien.ac.at,
ORCID: 0000-0001-6840-806X

Marlene Sayer
Vienna University of Technology – TU WIEN, Vienna, Austria, sayer@eeg.tuwien.ac.at,
ORCID: 0000-0003-1593-7106

Reinhard Haas
Vienna University of Technology – TU WIEN, Vienna, Austria, haas@eeg.tuwien.ac.at,
ORCID: 0000-0001-9361-3452

Cite this paper as: *Ajanovic, A, Sayer, M, Haas, R. Role of the transport sector in hydrogen energy system. 11. Eur. Conf. Ren. Energy Sys. 18-20 May 2023, Riga, Latvia*

Abstract: Over the last decade interest in hydrogen has been rapidly rising. Hydrogen is seen as a very important energy carrier on the way to a more sustainable future. It can contribute to energy supply security, to diversification of the fuels used in the whole energy system, as well as to a better integration of electricity from variable renewable energy sources. Of special interest is its contribution to the decarbonization of the transport sector, especially of the transport modes in which electrification is too expensive or not possible. However, all benefits of hydrogen use in the transport sector are achievable only in combination with hydrogen production from renewable energy sources, so-called green hydrogen. The core objective of this paper is to investigate the perspectives for green hydrogen and fuel cell vehicles from an economic and ecological point of view in a dynamic framework till 2050. The analysis will be conducted in comparison to conventional vehicles and fossil fuels, as well as battery energetic vehicles. The method of approach is based on well-to-wheel emission analysis and dynamic economic assessment. Moreover, impact of relevant transport and energy policies will be analyzed and discussed. The major conclusion is that the future role of hydrogen is very dependent on policy framework, level of the CO_2-taxes and further technological learning, research & development of batteries and fuel cells.

Keywords: *Hydrogen economy, fuel cell vehicles, green hydrogen*

RIGA 2023

Conditions for Heading Towards Democratic and Environmentally Benign Electricity Systems

Reinhard Haas
Energy Economics Group, Vienna University of Technology, E-mail: haas@eeg.tuwien.ac.at, ORCID: 0000-0001-9361-3452

Cite this paper as: *Haas,R., Conditions for Heading Towards Democratic and Environmentally Benign Electricity Systems, 11. Eur. Conf. Ren. Energy Sys. 18-20 May 2023, Riga, Latvia*

Abstract: Today, in many countries the electricity markets are subject to comprehensive alterations. An increasing number of consumers is eager to participate in meeting the electricity they consume. This fact has been promoted by the rise of photovoltaics as a technology which can be deployed close to the user and in addition by small battery storage. The core goal of this work is to give insights on getting closer to a democratic and more environmental electricity generation system that includes larger quantities of intermittent renewable sources. Our method used relies on the basics of residual load (= this is total electricity consumption minus intermittent electricity produced) during a whole year for every hour. In addition, the intermittent renewable production from hydro, wind and photovoltaics is modeled for every hour. Our most interesting findings are: (i) most important is a pricing approach for the wholesale market in which the price signals give information to the market participants on the availability of excess electricity or scarcity in every hour of the year; (ii) to even out changes in the residual load a proper set of flexibility measures is required consisting of : (i) Demand response by means of pricing by time-of-use; (i) pumped hydro, electrochemical battery, and different other storage options; (ii) management of the demand-side by cycling; (iii) In addition, power plants with high flexibility (e.g. gas turbines) for for back-up security capacity are of relevance in both cases, without and in the case of the presence of capacity markets. The final conclusion of our investigation is, that a fundamental shift in our basic understanding of the structure of the electricity market has to take place. In this new view rather the suppliers or other coordinators of demand and supply are in the core and no longer the power plant operators. Eventually, it is of relevance that the development of such a democratic system for the integration of intermittent renewable sources in European countries will be a role model for virtually all countries world-wide.

Keywords: *Electricity markets, renewables, storage*

RIGA 2023

Development of Skutterudite-Type Thermoelectric Materials $La_xCo_4Sb_{12}$ using High-Pressure Synthesis Method

Yuttana Mona
Chiang Mai University, Chiang Mai, Thailand, yuttana.mona@eng.cmu.ac.th, ORCID: 0000-0002-1102-9242

Chatchawan Chaichana
Chiang Mai University, Chiang Mai, Thailand, c.chaichana@eng.cmu.ac.th, ORCID: 0000-0002-9392-7088

Pana Suttakul
Chiang Mai University, Chiang Mai, Thailand, pana.s@cmu.ac.th, ORCID: 0000-0002-2946-8921

Souksavath Phounsavath
National University of Laos, Laos, phounsavath@live.com, ORCID: 0000-0002-0180-1999

Yukihiro Kawamura
Muroran Institute of Technology, Hokkaido, Japan, y_kawamura@mmm.muroran-it.ac.jp, ORCID: 0000-0002-5581-0858

Chihiro Sekine
Muroran Institute of Technology, Hokkaido, Japan, sekine@mmm.muroran-it.ac.jp, ORCID: 0000-0003-1301-4690

Cite this paper as: *Mona, Y, Chaichana, C, Pana, S, Souksavath, P, Yukihiro K, Chihiro S. Development of skutterudite-type thermoelectric materials LaxCo4Sb12 using high-pressure synthesis method.. 11. Eur. Conf. Ren. Energy Sys. 18-20 May 2023, Riga, Latvia*

Abstract: Thermoelectric power generation is a promising technology for meeting the increasing global demand for energy while reducing the use of fossil fuels and their associated climate change impacts. In order to improve the efficiency of thermoelectric materials, researchers have developed various modern synthesis methods, one of which is the high-pressure synthesis method. In this study, we used the high-pressure synthesis method to synthesize the partially-filled skutterudite compound $La_xCo_4Sb_{12}$ with a La-filling ratio of up to x = 0.28, exceeding the theoretical filling limit at ambient pressure. The resulting material, $La_{0.28}Co_4Sb_{12}$, exhibited significantly lower lattice thermal conductivity of 1.3 W/mK than $CoSb_3$, suggesting that high-pressure synthesis method is a powerful tool for the development of high-performance thermoelectric materials.

Keywords: *Thermoelectric energy conversion; Thermoelectric materials; HPHT; Skutterudite*

RIGA 2023

Assessment of the Synergy Between Marine Energy Resources in the West Iberian Coast

Liliana Rusu
"Dunărea de Jos" University, Galaţi, Romania, liliana.rusu@ugal.ro, ORCID: 0000-0002-8179-1347

Cite this paper as: *Rusu, L., Assessment of The Synergy Between Marine Energy Resources in The West Iberian Coast, 11. Eur. Conf. Ren. Energy Sys. 18-20 May 2023, Riga, Latvia*

Abstract: The west Iberian coast is an area with great potential for wave and wind energy exploitation, being a location of interest for the development of wind and wave farms. Moreover, this area also seems to have great potential for solar energy exploitation, which can be extracted together with wave and wind enrgy using floating or fix structures. Taking this into consideration, the objective of the present work is to carry out a joint evaluation of the wave, wind, and solar power and the synergy between these resources along the target area. The wind and wave power assessment was made for two periods, each one covering 20 years, representing the present and near future periods. ERA5 wind data have been used for the first period, while for the second period wind data provided by the RCA4 (Rossby Centre regional atmospheric model, version 4) climate model have been considered, under RCP4.5 (Representative Concentration Pathway) scenario. Simulation results with SWAN (Simulating WAves Nearshore) model have been considered to evaluate the wave power. A good correlation between wind and wave power was found in the west Iberian nearshore, showing that this area has the potential for development of joint wind–wave projects. For 10 years in the past, solar power was estimated based on ERA5 data, and the synergy with wave and wind power was assessed with the purpose of their joint exploitation.

Keywords: *Wave energy, wind power, Iberian coast, RCP scenarios, future, historical data*

Acknowledgments

This work was carried out in the framework of the research project DREAM (Dynamics of the REsources and technological Advance in harvesting Marine renewable energy), supported by the Romanian Executive Agency for Higher Education, Research, Development and Innovation Funding – UEFISCDI, grant number PN-III-P4-ID-PCE-2020-0008.

RIGA 2023

Comparable Recovery of Metals from Waste Photovoltaic Panel using Microbial Media and Organic Acids

Mital Chakankar
Department of Power Mechanical Engineering, National Tsing Hua University, No. 101, Sec.2, Kwang Fu Rd., 30013, Hsinchu, Taiwan RoC.

Cheer Su
Department of Power Mechanical Engineering, National Tsing Hua University, No. 101, Sec.2, Kwang Fu Rd., 30013, Hsinchu, Taiwan RoC.

Hong Hocheng
Department of Power Mechanical Engineering, National Tsing Hua University, No. 101, Sec.2, Kwang Fu Rd., 30013, Hsinchu, Taiwan RoC, hocheng@pme.nthu.edu.tw

Cite this paper as: *Chakankar M., Su C., Hocheng H., Comparable Recovery of Metals from Waste Solar Electricity Panels using Microbial Media and Organic Acids, 11th Eur. Conf. Ren. Energy Sys. 18-20 May 2023, Riga, Latvia*

Abstract: Facing the huge impact of global warming, solar energy is considered as an essential alternative to the fossil fuels and a clean energy source for both industry and household. The current photovoltaic panels have a typical service life of 25-30 years, while the implementation of new photovoltaic systems is increasing continuously. The waste in one year is estimated to be about one million tons before 2050. The functioning metals in these photovoltaic panels include lead, cadmium, and bismuth which are hazardous to the human health. They also contain treasure metals such as silver, tellurium and indium. The recycling of these metals from the waste photovoltaic panels can help satisfy the materials demand as well as reduce the threat to human health. There are many studies investigating the thin-film solar panels recycling including mechanical and chemical methods. Implementing various strategies will help the transition of energy technology to be more sustainable as well as provide with the economically viable alternatives. The main purpose of the current study was to investigate and compare the use of microbial media and organic acids for reclaiming of metals from waste photovoltaic panels. Both approaches are considered valuable for developing the low-environmental impact recycling process. Among four microbes, P. chrysogenum was identified to generate 100% recovery for several metals including hazardous and valuable ones. Four organic acids, namely oxalic acid, citric acid, malic acid and gluconic acid, and their mixture were used to study the leaching performance. The experimental results suggest that oxalic acid is the most effective in reclaiming the metals. The advantages and disadvantages between two approaches are compared and elaborated.

Keywords: *Photovoltaic Panel, hazardous metal, recycling, organic acid, microbial media*

RIGA 2023

Decarbonizing a Thai Coal Power Plant: Effect of Flue Gas Loads on Carbon Capture Performance and Economics

Thananat Lungkadee
Department of Mechanical Engineering, Faculty of Engineering, Chiang Mai University, Chiang Mai, Thailand, l.thananat@gmail.com, ORCID: 0000-0002-3143-6080

Suparit Tangparitkul
Department of Mining and Petroleum Engineering, Faculty of Engineering, Chiang Mai University, Chiang Mai, Thailand, email: suparit.t@cmu.ac.th, ORCID: 0000-0003-4316-3304

Chatchawan Chaichana
Department of Mechanical Engineering, Faculty of Engineering, Chiang Mai University, Chiang Mai, Thailand, c.chaichana@eng.cmu.ac.th, ORCID: 0000-0002-9392-7088

Wongkot Wongspai
Department of Mechanical Engineering, Faculty of Engineering, Chiang Mai University, Chiang Mai, Thailand, wongkot@eng.cmu.ac.th, ORCID: 0000-0002-2273-5177

Chawannat Jaroenkhasemmeesuk
Department of Mechanical Engineering, Faculty of Engineering, Mahidol University, Nakorn Pathom, Thailand, chawannat.jar@mahidol.edu, ORCID: 0000-0002-0176-792X

Korrakot Y. Tippayawong
Department of Industrial Engineering, Faculty of Engineering, Chiang Mai University, Chiang Mai, Thailand, korrakot@eng.cmu.ac.th, ORCID: 0000-0003-4892-0079

Nakorn Tippayawong
Department of Mechanical Engineering, Faculty of Engineering, Chiang Mai University, Chiang Mai, Thailand, n.tippayawong@yahoo.com, ORCID: 0000-0002-6104-7676

Cite this paper as: *Lungkadee,T, Tangparitkul, S, Chaichana, C, Wongspai, W, Jaroenkhasemmeesuk, C, Tippayawong, KY, Tippayawong, N. Decarbonizing a Thai Coal Power Plant: Effect of Flue Gas Loads on Carbon Capture Performance and Economics, 11th Eur. Conf. Ren. Energy Sys. 18-20 May 2023, Riga, Latvia*

Abstract: To achieve net zero emission, employing CO_2 capture and storage is a must. Post-combustion separation and capture using chemical absorption is probably the most well-established carbon capture technology available to date. It can be retrofitted to existing power and industrial plants for treating full or part loads of flue gas stream. In this work, process simulation of carbon capture in a 300 MWe power unit of a Thai coal power plant was undertaken using AspenPlus software. Effect of flue gas loads on performance of a lean aqueous monoethanolamine solution capture system was considered. From the simulation study, it was found that almost 200,000 tCO2 a year could be captured by the power plant at the annualized total cost for the CCS retrofit of less than 27 million USD, operated at 10% flue gas load. This would give a total cost of the CCS plant at 135 USD/tCO2 captured. But at full load, the optimal total costs and the annualized total cost of the CCS plant were about 109 million USD and 55 USD/tCO2 captured, respectively.

Keywords: *CCS, climate mitigation, low carbon engineering, power generation, process simulation*

RIGA 2023

The Effect of Thin Strontium Titanate Films on the Raman spectrum: Ab Initio Calculations

Veera Krasnenko
Institute of Physics, University of Tartu, Tartu, Estonia,
Institute for Solid State Physics, University of Latvia, Riga, Latvia, veera.krasnenko@ut.ee,
ORCID: 0000-0001-6698-5293

Alexander Platonenko
Institute for Solid State Physics, University of Latvia, Riga, Latvia, aleksandrs.platonenko@cfi.lu.lv

Leonid L. Rusevich
Institute for Solid State Physics, University of Latvia, Riga, Latvia, leonid.rusevich@cfi.lu.lv

Yuri A. Mastrikov
Institute for Solid State Physics, University of Latvia, Riga, Latvia, yuri.mastrikov@cfi.lu.lv

Maksim Sokolov
Theoretical Inorganic Chemistry, University of Duisburg-Essen, Duisburg, Germany, maksim.sokolov@uni-due.de

Eugene A. Kotomin
Institute for Solid State Physics, University of Latvia, Riga, Latvia, kotomin@cfi.lu.lv

Cite this paper as: *Krasnenko, V, Platonenko, A, Rusevich, LL, Mastrikov, YA, Sokolov, M, Kotomin, EA, The Effect of Thin Strontium Titanate Films on the Raman spectrum: Ab Initio Calculations. 11th Eur. Conf. Ren. Energy Sys. 18-20 May 2023, Riga, Latvia*

Abstract: Thin strontium titanate (STO) films have gained attention as efficient photocatalysts for producing hydrogen fuel through photo-electrochemical water splitting. Although the bulk STO crystal characteristics are well known, the nanostructure, chemical composition, and crystallinity of ultrathin perovskites/nanoparticles and water-splitting intermediates thereon are a big challenge to understand [1]. Raman spectroscopy can be used to identify adsorbates and surfaces promising for photocatalysis [2], being an effective tool for the structural characterization of advanced materials. Interpretation of Raman spectra requires accurate assignment of peaks to specific atomic vibrations. For this purpose, the ab initio calculations can be used to reliably assign vibrational peaks of ultrathin STO films. Using ab initio DFT methods, we were able to identify the Raman frequencies that characterize the bulk STO, ultrathin films, and the change in the scattering spectra with increasing film thickness. According to our study, due to very low intensity, some peaks in the Raman spectra of thin STO films that belong to the Raman active modes of pure STO crystals are not well observed in the Raman spectra. However, as film thickness increases, their intensity also increases and Raman frequencies shift towards the characteristic modes of a pure STO bulk crystal. The results obtained make it possible to interpret the experimental data, and ab initio methods can be used to further study thin STO films with tuned catalytic properties and water-splitting intermediates

Keywords:

References

[1] M. Sokolov, Y.A. Mastrikov, G. Zvejnieks, D. Bocharov, E.A. Kotomin, V. Krasnenko. Water Splitting on Multifaceted SrTiO3 Nanocrystals: Computational Study, Catalysts 11 (2021) 1326
[2] V. Krasnenko, L.L. Rusevich, A. Platonenko, Y.A. Mastrikov, M. Sokolov, E.A. Kotomin. Water Splitting on Multifaceted SrTiO3 Nanocrystals: Calculations of Raman Vibrational Spectrum. Materials 15 (2022) 4233

RIGA 2023

Ammonia Nitrogen Removal and Recovery using Bipolar Membrane Electrodialysis with a Membrane Contactor

Kyo Sik Hwang
Korea Institute of Energy Research, Jeju, Korea, kshwang@kier.re.kr, ORCID: 0000-0003-4170-8278

Jooyoun Nam
Korea Institute of Energy Research, Jeju, Korea, jynam@kier.re.kr, ORCID: 0000-0002-5211-4857

Namjo Jeong
Korea Institute of Energy Research, Jeju, Korea, njjeong@kier.re.kr, ORCID: 0000-0003-0939-2744

Cite this paper as: *Hwang, KS, Nam, J, Jeong, N. Ammonia nitrogen removal and recovery using bipolar membrane electrodialysis with a membrane contactor. 11. Eur. Conf. Ren. Energy Sys. 18-20 May 2023, Riga/Latvia*

Abstract: Advanced post-treatment technologies are needed to improve the removal of ammonia nitrogen from wastewater through the anaerobic digestion process, in order to meet stringent discharge standards. Electrochemical systems for ammonia nitrogen removal are a promising alternative approach compared to conventional technologies. In this paper, the bipolar membrane electrodialysis with a membrane contactor (BMED-MC) process is experimentally investigated for the removal and recovery of ammonia nitrogen from synthetic wastewater. The 5-cell bipolar membrane electrodialysis stack, with a surface area of 5 x 5 cm^2, is used and each cell consists of three compartments: a base compartment, a dilute compartment, and an acid compartment, which are separated by a cation exchange membrane, a bipolar membrane, and an anion exchange membrane. A hollow fibre membrane contactor is used to recover ammonia nitrogen from the base stream to the acid stream to ammonium sulfate. The experimental results indicate that the ammonia nitrogen removal and recovery efficiency for BMED-MC are 94.8% and 93.4%, respectively, and the energy consumption is 12.8kWh/kgN at a current density of 60mA/cm^2. Also, based on the experimental results, a techno-economic evaluation of ammonia nitrogen recovery for BMED-MC is performed, comparing it with conventional technologies.

Keywords: *Bipolar membrane, electrodialysis, membrane contactor, ammonia nitrogen recovery*

RIGA 2023

Ball Mill Pretreatment for Improved Bioavailability of Biomass

Jin Hyung Lee
Korea Institute of Ceramic Engineering and Technology, Cheongju, Rep. Korea, leejinh1@kicet.re.kr,
ORCID: 0000-0002-0331-7738

Hye Sun Lee
Korea Institute of Ceramic Engineering and Technology, Cheongju, Rep. Korea, hslee@kicet.re.kr,
ORCID: 0000-0002-9910-3629

Byoung Seong Jeon
Korea Institute of Ceramic Engineering and Technology, Cheongju, Rep. Korea, a1trust@kicet.re.kr,
ORCID: 0000-0002-8769-1603

Yang Mo Gu
Korea Institute of Ceramic Engineering and Technology, Cheongju, Rep. Korea, rndidah123@kicet.re.kr,
ORCID: 0000-0001-8618-3650

Cite this paper as: *Lee, JH, Lee, HS, Jeon, BS, Gu, YM. Ball mill pretreatment for improved bioavailability of biomass. 11. Eur. Conf. Ren. Energy Sys. 18-20 May 2023, Riga, Latvia*

Abstract: Ball mill pretreatment is effective to reduce size of biomass and, subsequently, result in increased surface area and improved bioavailability. Ball mill pretreatment caused no significant change in biomass components. This study will present the improvement of the bioavailability of biomasses using ball mill pretreatment in fermentable sugar and biomethane productions. In the fermentable sugar production, the use of ball mill pretreatment eliminates the need for washing and transfer of the biomass prior to enzymatic hydrolysis while obtaining higher glucose yield than untreated sample, 84%. In the biogas production, the ball mill pretreated both food waste and rice husk to improve methane production. The ball mill improved the uniforminity of particle size and soluble chemical oxygen demand (SCOD) and, ultimately biochemical Methane Potential (BMP) of biomasses. It also induced changed in the microbial community of anaerobic digesters, which eventually led to increased methane production. Finally, the food waste and rice husk produced 490 mL CH4/g-VS and 100.4 mL CH4/g VS, respectively, in the biochemical methane potential test after the ball mill pretreatment.

Keywords: *Pretreatment, fermentable sugar, biomethane, fermentation, BMP*

RIGA 2023

Challenges and Opportunities of Enhanced Biogas Production using Anaerobic Co-Digestion with a Low Carbon Footprint

Shu-Yuan Pan
National Taiwan University, Taipei, Taiwan ROC, sypan@ntu.edu.tw, ORCID: 0000-0003-2082-4077

Chihhao Fan
National Taiwan University, Taipei, Taiwan ROC, chfan@ntu.edu.tw, ORCID: 0000-0002-9840-1835

Yo-Jin Shiau
National Taiwan University, Taipei, Taiwan ROC, yshiau@ntu.edu.tw, ORCID: 0000-0003-1368-6761

Suraj Negi
National Taiwan University, Taipei, Taiwan ROC, suraj.negi22c@gmail.com, ORCID: 0000-0002-3934-7250

Cite this paper as: *Pan, SY, Fan, C, Shiau, YJ, Negi, S. Challenges and Opportunities of Enhanced Biogas Production using Anaerobic Co-digestion with a Low Carbon Footprint. 11. Eur. Conf. Ren. Energy Sys. 18-20 May 2023, Riga, Latvia.*

Abstract: Several studies attempted to improve the biogas production from anaerobic digestion (AD) using various approaches, such as solid-state AD, an anaerobic membrane bioreactor, a coupled microbial electrolysis cell, biochar-incorporated AD, and semi-dry AD with zero valent iron and magnetite. In this study, we systematically discuss the challenges and opportunities of enhanced biogas production using anaerobic co-digestion with a low carbon footprint. We provide a few examples of AD (such as anaerobic co-digestion using swine manure and rice husk) at several synergistic scales, including mechanisms of ion transport and transformation at a molecular scale, novel unit processes at a system scale, and comprehensive evaluation methods for performance optimisation at a global scale. We also incorporate the AD processes with carbon dioxide (CO2) capture and utilization to deliver a negative CO2 emission system. We also address the environmental benefits and carbon footprints of different AD-related processes by life-cycle assessment to understand the feasibility of large-scale operations. This work should be considered as a tutorial study for enhanced biogas production using AD with a low carbon footprint, thereby moving toward a negative CO2 emission system.

Keywords: *Swine manure, rice husk, electrochemical technologies, upgrading; life cycle assessment*

RIGA 2023

Characteristics of a Small Aspect Ratio Tokamak Fusion Reactor for Nuclear Transmutation with a Molten Salt Blanket

Bong Guen Hong
Chonbuk National University, Jeonju, Republic of Korea, ORCID: 0000-0003-4459-1677

Cite this paper as: *Hong, BG, Characteristics of a small aspect ratio tokamak fusion reactor for nuclear transmutation with a molten salt blanket. 11. Eur. Conf. Ren. Energy Sys. 18-20 May 2023, Riga, Latvia*

Abstract: The optimal system parameters of the small aspect ratio tokamak fusion reactor with a fusion power less than 300 MW and molten salt transmutation blanket was found. Using a tokamak systems code coupled with a neutron transport code and a burn-up calculation code, system parameters and neutronic properties were self-consistently calculated. Advanced engineering features such as the maximum allowable magnetic field, Bmax = 23 T by adopting high temperature superconducting (HTS) magnet technology, the usage of an advanced neutron shield material like tungsten carbide (WC), a plug-bucked toroidal field (TF) magnet support structure, no central solenoid, etc., were implemented. The effects of the aspect ratio, A in the range of 1.5 to 2.0, and the fusion power on the transmutation properties were investigated with two molten salts, FLiBe and FLiNaBe were assessed, and it was found that the transmutation performance was similar. With the FLiNaBe, initial inventory of the transuranics (TRU) was smaller than the case with the FLiBe, but tritium breeding ratio (TBR) were smaller than the case with the FLiBe and additional tritium breeding blanket was required.

Keywords: *Transmutation, molten salt, TOKAMAK neutron source, low aspect ratio*

RIGA 2023

Enhancing Breakdown of Microplastics by Hydrothermal Fenton Reaction

Vikash Singh
Program in Environmental and Polymer Engineering, INHA University, 100, Inha-ro, Michuhol-gu, Incheon 22212, Republic of Korea, vikashsingh@inha.ac.kr, ORCID: 0000-0002-5131-5753

Seon Yeong Park
Institute of Environmental Research, INHA University, 100, Inha-ro, Michuhol-gu, Incheon 22212, Republic of Korea, psy7574@inha.ac.kr, ORCID: 0000-0003-2441-0488

Chang Gyun Kim
Department of Environmental Engineering, INHA University, 100, Inha-ro, Michuhol-gu, Incheon 22212, Republic of Korea, cgk@inha.ac.kr, ORCID: 0000-0002-8668-3281

Cite this paper as: *Singh, V., Park, SY., Kim, CG., Enhancing Breakdown of Microplastics By Hydrothermal Fenton Reaction. 11. Eur. Conf. Ren. Energy Sys. 18-20 May 2023, Riga, Latvia*

Abstract: Microplastics (MPs) are frequently traced in almost all environmental matrices (soil, water, air). Developing relevant technology for the detection and degradation of microplastics in them are in a very early stage.. In the present work, the oxidation of conventional microplastics (Polyethylene: PE, Polypropylene: PP, Polystyrene: PS) along with the actual plastic wastes (plastic bottles, micropipette tips, centrifuge tubes, nitrile gloves, packaging plastics) were examined by employing the coalescence of thermal-Fenton reaction carried out in a hydrothermal autoclave reactor. Typical parameters such as time, temperature, MPs dose, H_2O_2 dose, Fe^{+2} concentration, and solution pH were optimized. Medium density polyethylene showed almost ~82% weight loss at the optimum conditions (temperature = 140°C, time = 16 h, MP dose = 1 g L^{-1}, H_2O_2 dose = 200 mM, Fe^{+2} concentration = 15 mL of 1000 mg L^{-1}, solution pH = 1±0.1). The microplastic samples before and after the reactions were analyzed by SEM, FTIR, and XPS to track down the physical and chemical changes. The carbonyl indices (CI) for samples were evaluated at 0.30, 0.31, 0.51, 0.68, and 0.69 from the FTIR spectra for 4h, 8h, 12h, 16h, and 20h of reaction, respectively. In this regard, the morphological changes were observed confirming that cracks on the surface of the plastics generated have grown bigger with the reaction time.

Keywords: *Polyethylene, polypropylene, polystyrene, microplastics, Fenton-reaction, advance oxidation*

RIGA 2023

Energy Utilization of Waste for the Production of Hydrogen

Jan Najser
VSB - Technical University of Ostrava, Ostrava, Czech Republic, jan.najser@vsb.cz, ORCID: 0000-0002-0614-964

Jan Kielar
VSB - Technical University of Ostrava, Ostrava, Czech Republic, jan.kielar@vsb.cz, ORCID: 0000-0003-3770-9200

Cite this paper as: *Najser, J., Kielar J., Energy utilization of waste for the production of hydrogen. 11. Eur. Conf. Ren. Energy Sys. 18-20 May 2023, Riga, Latvia*

Abstract: The combination of plasma waste gasification and hydrogen separation technologies offers a suitable way to produce energy for fuelcells. The organic fraction of the input fuel is decomposed into permanent gases by means of plasma at very high temperatures. The inorganic fraction is melted into an inert nonleachable slag. Therefore, this process has a significant environmental advantage. The testing of the plasma gasification of municipal waste was carried out using a hybrid plasma torch with water addition as a gasification medium, because it was possible to achieve a better H_2/CO ratio in outlet gas. The test conditions were as follows: fuel dosing 25 kg/h, plasmatron power 120 kW, water addition 150 g/min and average reactor temperature 1 200 °C. After the reactor reached an operating temperature, a plasma torch with hybrid stabilization was ignited and access to the gasification medium (water) was ensured. The test results demonstrated the possibility of gasification of municipal waste. At the same time, the increased H_2/CO ratio when using H_2O as a gasification medium (compared to CO_2) has been confirmed. More detailed information on the test will be presented in the poster.

Keywords: *Hydrogen, plasma gasification, green energy, energy storage*

RIGA 2023

Performance Evaluation of Solar Aggregation Platform on the Cloud and Edge Device Integration

Panitarn Chongfuangprinya
Hitachi America, California, USA, Joseph.Chong@hal.hitachi.com, ORCID: 0000-0002-3642-6703

Bo Yang
Hitachi America, California, USA, Bo.Yang@hal.hitachi.com, ORCID: 0000-0001-5162-8840

Yanzhu Ye
Hitachi America, California, USA, Yanzhu.Ye@hal.hitachi.com, ORCID: 0000-0001-5772-5115

Natsuhiko Futamura
Hitachi America, California, USA, Natsuhiko.Futamura@hal.hitachi.com, ORCID: 0000-0003-2847-506X

Cite this paper as: *Chongfuangprinya, P, Yang, B, Ye, Y., Futamura, N, Performance Evaluation of Solar Aggregation Platform on the Cloud and Edge Device Integration. 11. Eur. Conf. Ren. Energy Sys. 18-20 May 2023, Riga, Latvia*

Abstract: In recent years, power generated from behind-the-meter or edge device has been steadily increasing. Consequently, utilities face operational challenges due to a lack of insight and control over edge devices. This paper presents (1) Behind-the-meter Solar Aggregation Platform (BSAP) on the cloud for solar situational awareness and (2) performance of BSAP and edge device integration. We developed a demo system on the cloud and interfaces to integrate the platform with edge devices. We set up a two-way data channel, with the capabilities to upload, ingest to cloud, store, and process field data in the platform. End-to-end system communication was tested. The platform received data from edge devices and sent back control signals. Examples of performance metrics of integration test include data interval, data accuracy, latency, and data throughput. We found that the platform exceeded all initial performance metrics. Based on the results, BSAP is on track to scale and operate with data from utilities in the future. The performance in this paper demonstrates how the platform and data from edge devices can help grid operators with enhanced situational awareness.

Keywords: *Solar situational awareness, distributed energy resources, DERs integration, real-time operation*

RIGA 2023

Technical Analysis of the Scale-Up and Implementation of a Membrane Contactor Plant for Biomethane Recovery in a Full-Scale Anaerobic Digestion Facility

Jesús M. Martín-Marroquín
CARTIF Technology Centre, Circular Economy Area, Boecillo, Spain, jesmar@cartif.es, ORCID: 0000-0003-2725-2067

Dolores Hidalgo
CARTIF Technology Centre, Circular Economy Area, Boecillo, Spain, dolhid@cartif.es, ORCID: 0000-0003-0846-6924

Sergio Sanz-Bedate
CARTIF Technology Centre, Circular Economy Area, Boecillo, Spain, serbed@cartif.es, ORCID: 0000-0002-2906-7706

Félix Nieto
University of Valladolid, Mechanical Engineering Department, Valladolid, Spain, felnie@idecal.es, ORCID: 0000-0001-8745-4600

Cite this paper as: *Martín-Marroquín, J.M., Hidalgo, D., Sanz-Bedate, S., Nieto, F. Technical analysis of the scale-up and implementation of a membrane contactor plant for biomethane recovery in a full-scale anaerobic digestion facility. 11. Eur. Conf. Ren. Energy Sys. 18-20 May 2023, Riga, Latvia*

Abstract: Nowadays, there are several commercially available technologies for biogas upgrading, but due to their high investment cost, high energy consumption or use of polluting chemicals, it is difficult to decide which of them to implement on an industrial scale. This study at pilot scale seeks to develop a reliable, low-risk and low-cost biogas enrichment system based on membrane contactors, capable of efficiently treating the biogas generated in different production environments. The novelties that these membrane contactors introduce with respect to the existing upgrading systems are the following: (1) Use of a gas-liquid membrane technology that allows the CO2 to be separated from the CH4 contained in the biogas at low pressure (4 bar), thus minimizing safety problems, needed investment, and the operation and maintenance costs associated with works under high pressure, commonly associated with gas-gas membranes upgrading systems (16 bar). (2) Use of low-cost technology, since the necessary infrastructure is widely spread for gasification/degassing applications in the carbonated beverage industry, thus solving the great problem of upgrading processes related to high investment costs in equipment.

Keywords: *Biogas upgrading, membrane contactors, CO_2 recovery*

RIGA 2023

Anaerobic Digestion of Kitchen Residue and its Biogas Production

Chihhao Fan
National Taiwan University, Taipei, Taiwan, chfan@ntu.edu.tw, ORCID: 0000-0002-9840-1835

Shu-Yuan Pan
National Taiwan University, Taipei, Taiwan, sypan@ntu.edu.tw, ORCID: 0000-0003-2082-4077

Cite this abstract as: *Fan, C, Pan, SY. Anaerobic Digestion of Kitchen Residue and its Biogas Production. 11. Eur. Conf. Ren. Energy Sys. 18-20 May 2023, Riga, Latvia*

Abstract: The population growth and dieting habit increase the quantity of kitchen residue over the years. Besides being used as fertilizers, most of the residues were collected and treated with incineration, which consumed energy and decreased the economic value from the perspective of the circular economy. In this study, the sludge from a domestic wastewater treatment plant was blended with kitchen residues, and the quantity of methane production by anaerobic fermentation was evaluated daily. The kitchen residue used in the study was a mixture of Chinese cabbage, beef, and fish, following the usual consumption habit in Taiwan. The result showed that the microbial activity of the sludge influenced gas production. The total gas production using the younger sludge produced 33% less than the elder one, with 46% less methane and 66% less carbon dioxide. The anaerobic treatment for well-cooked or uncooked residues also exhibited different fermentation efficiency. The gas quantity generated 16% more by the mixture of sludge and well-cooked residue, while methane generated 24% more. The elder sludge and well-cooked kitchen residue could produce more methane.

Keywords: *Reuse, kitchen residue, methanogens, anaerobic fermentation*

RIGA 2023

Anaerobic Digestion for Biogas Production using Wastewater from Polyhydroxyalkanoates Production Process

Ingyu Lee
University of Seoul, Seoul, Korea, ingyu@uos.ac.kr, ORCID: 0000-0002-9838-6428

Changgune Lee
University of Seoul, Seoul, Korea, 1119chang@uos.ac.kr, ORCID: 0000-0001-9401-665X

Jeongeun Lee
University of Seoul, Seoul, Korea, leeje1350@uos.ac.kr

Hyo Kim
University of Seoul, Seoul, Korea, hkim@uos.ac.kr, ORCID: 0000-0001-7657-4885

Hyunook Kim
University of Seoul, Seoul, Korea, h_kim@uos.ac.kr, ORCID: 0000-0003-1256-480X

Cite this paper as: *Lee, I, Lee, C, Lee, J, Kim, H, Kim, H., Anaerobic Digestion for Biogas Production using Wastewater from Polyhydroxyalkanoates Production Process. 11. Eur. Conf. Ren. Energy Sys. 18-20 May 2023, Riga, Latvia*

Abstract: Polyhydroxyalkanoate (PHA) is a high molecular substance that can be formed via bio-fermentation of a variety of food-derived ingredients and can accumulate in cells. Since it is readily biodegradable comparing to petroleum-based polymers (i.e., plastics), PHA has drawn attention as an alternative to the conventional plastics. However, a significant amount of wastewater containing a high content of organics and nutrients is generated from a process of PHA production. Since PHA-process wastewater is originated from biological process, it was assumed to be readily biodegradable, which was, in fact, verified by performing a biochemical methane potential (BMP) test. A biomethane yield of the wastewater was determined as 0.37 L CH4 gVS-1. Therefore, in this study, a two-stage anaerobic digestion (AD) system was applied for treating wastewater produced from a commercial PHA producer and eventually for producing biogas. During the continuous operation of the lab-scaled AD system, the average biomethane yield of 1.03 L CH4 gVS-1 was obtained. Through the anaerobic fermentation process, 74% of wastewater TOC (also 83% of DOC) could be transformed to biogas. In terms of conversion ratio, the current AD system based on PHA wastewater shows much higher value than an AD system based on food waste. The biomethane yield of the latter was determined as 0.46 L CH4 gVS-1 under a similar operating condition. Finally, digestrate from the two-stage AD system was evaluated for its suitability as a fertilizer; the digested material was used in a plant growth test. Comparing to the plants treated with a commercial liquid fertilizer, the plants treated with the digested sludge showed equivalent growth, indicating that the digested sludge does not exert any toxicity to plants and can be used as a fertilizer. Overall, the result of the current study clearly illustrates that AD is a promising strategy for extracting energy and nutrients from PHA-process wastewater.

Keywords: *Anaerobic digestion, biomass, PHA, biogas, toxicity of digestrate*

RIGA 2023

Estimating Energy Consumption of Battery Electric Vehicles Using in-Vehicle Sensing and Machine Learning Approaches

Pana Suttakul
Department of Mechanical Engineering, Faculty of Engineering, Chiang Mai University, Chiang Mai, Thailand, pana.s@cmu.ac.th, ORCID: 0000-0002-2946-8921

Nakorn Tippayawong
Department of Mechanical Engineering, Faculty of Engineering, Chiang Mai University, Chiang Mai, Thailand, nakorn.t@cmu.ac.th, ORCID: 0000-0002-6104-7676

Wongkot Wongsapai
Department of Mechanical Engineering, Faculty of Engineering, Chiang Mai University, Chiang Mai, Thailand, wongkot.w@cmu.ac.th, ORCID: 0000-0002-2273-5177

Kittitat Janpoom
Department of Mechanical Engineering, Faculty of Engineering, Chiang Mai University, Chiang Mai, Thailand, kittitat_j@cmu.ac.th, ORCID: 0000-0002-5805-7902

Tossapon Katongtung
Department of Mechanical Engineering, Faculty of Engineering, Chiang Mai University, Chiang Mai, Thailand, tossapon_ka@cmu.ac.th, ORCID: 0000-0001-9612-1883

Yuttana Mona
Department of Mechanical Engineering, Faculty of Engineering, Chiang Mai University, Chiang Mai, Thailand, yuttana.mona@eng.cmu.ac.th, ORCID: 0000-0002-1102-9242

Witsarut Achariyaviriya
Department of Electrical Engineering, Faculty of Engineering, Chiang Mai University, Chiang Mai, Thailand, witsarut.a@cmu.ac.th, ORCID: 0000-0002-1832-0761

Cite this paper as: *Suttakul, P, Tippayawong, N, Wongsapai, W, Janpoom, K, Katongtung, T, Mona, Y, Achariyaviriya, W. Estimating energy consumption of battery electric vehicles using in-vehicle sensing and machine learning approaches. 11. Eur. Conf. Ren. Energy Sys. 18-20 May 2023, Riga, Latvia*

Abstract: Transport electrification, which entails replacing fossil fuel-powered engines with electric drivetrains through the use of electric vehicles (EVs), has been identified as a potential strategy for reducing emissions in the transportation sector. As the adoption of EVs increases, there is a growing need to understand their performance and characteristics, particularly the factors that influence energy consumption under actual driving conditions. This study sought to investigate the actual energy consumption of commercial battery electric vehicles (BEVs) in Thailand by conducting real-world driving tests under various route conditions. Data collection was done through the use of onboard diagnostics and global positioning system devices. A machine learning approach was utilized to analyze the large dataset, predict energy consumption, and identify the key factors influencing energy consumption. The results of this study provide valuable insights into the energy consumption of BEVs and the factors affecting it, which can aid in improving energy efficiency and informing policy decisions related to transport electrification.

Keywords: *artificial intelligence; electric vehicle; clean energy; energy consumption; real-world driving*

RIGA 2023

A Potential Reduction of Energy Consumption by the Flexible Working Hour Policy: An Experimental Study in Chiangmai, Thailand

Witsarut Achariyaviriya
Department of Electrical Engineering, Faculty of Engineering, Chiang Mai University, Chiang Mai, Thailand, witsarut.a@cmu.ac.th, ORCID: 0000-0002-1832-0761

Kittitat Janpoom
Department of Mechanical Engineering, Faculty of Engineering, Chiang Mai University, Chiang Mai, Thailand, kittitat_j@cmu.ac.th, ORCID: 0000-0002-5805-7902

Pana Suttakul
Department of Mechanical Engineering, Faculty of Engineering, Chiang Mai University, Chiang Mai, Thailand, pana.s@cmu.ac.th, ORCID: 0000-0002-2946-8921

Wongkot Wongsapai
Department of Mechanical Engineering, Faculty of Engineering, Chiang Mai University, Chiang Mai, Thailand, wongkot.w@cmu.ac.th, ORCID: 0000-0002-2273-5177

Nakorn Tippayawong
Department of Mechanical Engineering, Faculty of Engineering, Chiang Mai University, Chiang Mai, Thailand, nakorn.t@cmu.ac.th, ORCID: 0000-0002-6104-7676

Yuttana Mona
Department of Mechanical Engineering, Faculty of Engineering, Chiang Mai University, Chiang Mai, Thailand, yuttana.mona@eng.cmu.ac.th, ORCID: 0000-0002-1102-9242

Cite this paper as: *Achariyaviriya, W, Janpoom, K, Suttakul, P, Wongsapai, W, Tippayawong, N, Mona, Y. Estimating energy consumption of battery electric vehicles using in-vehicle sensing and machine learning approaches. 11. Eur. Conf. Ren. Energy Sys. 18-20 May 2023, Riga, Latvia*

Abstract: Currently, electric vehicles (EVs) are being promoted worldwide due to the impact of CO_2 emissions, air pollution, and the imminent depletion of fossil energy supplies. However, EVs are still dealing with expensive battery systems and lengthy charging periods, which cause users discomfort and a high cost of ownership. Enhancing energy efficiency can alleviate these problems. Many factors affect a vehicle's energy consumption, including geography, driving behavior, and traffic conditions. Traveling during peak-hour traffic congestion causes a high variance in energy consumption. This paper gives a quantitative analysis of how travel schedules affect the energy consumption of EVs, which can be used as a guideline for creating a flexible working hour policy at the organizational level. Chiang Mai University and the surrounding area are used as the case study. The energy consumption model is developed from real-world driving test data. Based on real-time traffic information, the effects of traveling at different times of the day are examined and discussed as a guideline for flexible working hour implementation.

Keywords: *energy consumption, traffic congestion, electric vehicle, flexible working hour*

RIGA 2023

Performance of Microwave-Assisted Hydrolysis of Cattle Manure and the Effect of Food Wastewater as Chemical Catalyst

Junghyeon Kim
Pusan National University, Busan, Korea, hyeon@pusan.ac.kr, ORCID: 0000-0003-0224-9072

Imgyu Byun
Pusan National University, Busan, Korea, big815@pusan.ac.kr, ORCID: 0000-0003-4015-4437

Cite this paper as: *Kim, JH, Byun, IG. Performance of microwave-assisted hydrolysis of cattle manure and the effect of food wastewater as chemical catalyst. 11. Eur. Conf. Ren. Energy Sys. 18-20 May 2023, Riga, Latvia*

Abstract: Microwave (MW) irradiation is a promising method for the hydrolysis of cattle manure because it has lower activation energy and accelerates reaction rate. Nevertheless, it is also needed to enhance MW-assisted hydrolysis yield of organic waste because MW consumes electric energy. Thus, a series of experiments were performed to determine the solid content of cattle manure, the output power and target temperature of MW irradiation under the different MW irradiation times for each target temperature. And food wastewater (FWW), H_2SO_4 and NaCl was applied as chemical catalyst in the MW-assisted hydrolysis of cattle manure to enhance dielectric effect of MW irradiation. The solubilization efficiency of cattle manure was affected by MW power, solid content and target temperature. MW power did not significantly affect the solubilization efficiency of cattle manure, but the solid content and target temperature were optimized in the ranges of 9~12% and 40~60°C, respectively. The solubilization efficiency with MW pretreatment was 24~55% higher than that with conventional heating. The FWW-assisted MW pretreatment demonstrated higher WAS solubilization efficiency than the MW-only pretreatment due to the ions and acidic material. Therefore, FWW containing high sodium chloride could be more promising for the enhancement of cattle manure hydrolysis.

Keywords: *Cattle manure, food wastewater, hydrolysis, microwave, methane yield*

RIGA 2023

Engineering Rumen Microbiome with Megasphaera Hexanoica for Mitigating Biogas Emission

Pranav Sasidharan Nair
Hanyang University, Seoul, South Korea, psn43@hanyang.ac.kr, ORCID: 0000-0002-2306-1776

Hyunjin Kim
Hanyang University, Seoul, South Korea, hyunjinkim@hanyang.ac.kr, ORCID: 0000-0001-9689-4886

Byoung – In Sang
Hanyang University, Seoul, South Korea, biosang@gmail.com, ORCID: 0000-0001-7972-6709

Cite this paper as: *Sasidharan Nair, P, Kim, H, Sang, BI. Engineering rumen microbiome with Megasphaera hexanoica for mitigating biogas emission 11. Eur. Conf. Ren. Energy Sys. 18-20 May 2023, Riga, Latvia*

Abstract: Livestock is one of the major contributors of greenhouse gases, particularly methane (CH_4) and carbon dioxide (CO_2), due to the activity of rumen digestive pathway. Rumen digestion produces primarily, short chain carboxylic acid (SCCA), hydrogen (H_2), CO_2, and CH_4 as byproducts. SCCA, H_2, and CO_2 are further used by different classes of methanogens, leading to increased CH_4 production. The goal of this study was to add a native rumen microorganism *Megasphaera hexanoica* (MH) as a direct-fed microbial (DFM) to the invitro rumen system and see if it could help reduce biogas emissions. MH has a wide substrate coverage and also uses SCCA to produce medium chain carboxylic acid (MCCA), thus acting as both an electron sink and a potential chain elongator, thereby limiting the activity of acetoclastic and hydrogenotropic methanogenesis. In batch culture, various doses of MH were added to the media and incubated for 48 hours at 39 °C. Supplementation of MH enhanced the digestibility of substrate and decreased ruminal pH and SCCA concentration. Elevated amounts of MCCA and a sharp reduction in biogas production were observed. Results from this study suggest MH addition is a promising strategy that combines biogas mitigation with an increase in animal productivity.

Keywords: *Megasphaera hexanoica, direct fed microbial (DFM), rumen digestion, biogas mitigation*

RIGA 2023

Machine Learning Approaches for Predicting Methane Production from Anaerobic Digestion of Thermally Pretreated Slaughter Waste

Darsha Prabhaharan
Hanyang university, Seoul, South korea, darsha28@hanyang.ac.kr, ORCID: 0000-0002-6420-8957

Young Wook Go
Hanyang university, Seoul, South Korea, youngwook@hanyang.ac.kr ORCID: 0000-0002-2401-7398

Hyunjin Kim
Hanyang university, Seoul, South Korea, hyunjinkim@hanyang.ac.kr, ORCID: 0000-0001-9689-4886

Byoung-In Sang
Hanyang university, Seoul, South korea, biosang@gmail.com, ORCID: 0000-0001-7972-6709

Cite this paper as: *Prabhaharan D, Go YW, Kim H, Sang. BI. Machine learning approaches for predicting methane production from anaerobic digestion of thermally pretreated slaughter waste. 11. Eur. Conf. Ren. Energy Sys. 18-20 May 2023, Riga, Latvia.*

Abstract: Globally, slaughterhouses generate a large number of animal byproducts. In spite of being valuable energy substrates, they are always underutilized as low-value products. Biogas derived from the anaerobic digestion (AD) of thermal hydrolyzed (TH) slaughter waste can enhance energy production. AD in batch mode has been extensively assessed using the biochemical methane potential (BMP) test. However, the BMP test is quite a laborious and time-consuming process limiting its application in a large-scale AD plant. This work focused on constructing a suitable data-driven model for the efficient prediction of methane production using data from various TH-AD conditions by evaluating different machine learning (ML) methods. Based on the Pearson coefficient matrix, the high methane-specific attributes resulting from the TH pretreatment i.e., carbohydrates, protein, lipids, ammonia, and elemental composition are considered for ML model construction. The comparison of the best model with the experimental data is found to have a minimum average relative error. The proposed modeling strategy is an efficient method for determining methane yield at an extended experimental range.

Keywords: *Machine learning, anaerobic digestion, slaughter waste*

RIGA 2023

Evaluation of the Microbial Methanation Process on the Pilot Scale with Enhanced Hydrogen Mass Transfer for the High-Purity Methane Production

Young-Wook Go
Hanyang university, Seoul, South Korea, youngwook@hanyang.ac.kr ORCID: 0000-0002-2401-7398

Byoung-In Sang*
Hanyang university, Seoul, South Korea, biosang@gmail.com, ORCID: 0000-0001-7972-6709

Cite this paper as: *Go,YW, Sang, BI., Evaluation of the microbial methanation process on the pilot scale with enhanced hydrogen mass transfer for the high-purity methane production. 11. European Conference on Renewable Energy System. 18-20 May 2023, Riga, Latvia*

Abstract: Biological methanation using autotrophic methanogens could be operated at relatively low temperatures and pressure, compared with the conventional chemical methanation processes. In power-to-gas process, hydrogenotrophic methanogens use CO_2/H_2 as the sole carbon and energy source for microbial methane production. The gas-liquid mass transfer of H_2 is a crucial factor controlling the efficiency of the biological methanation process. Improving the solubility of hydrogen with a low henry's law constant is still in the-state-of-the-art for better system efficiency and requires more research. A 2400 L pilot scale reactor was used to get a high H_2 mass transfer with three pithed blade-type impellers. The reactor was operated for a microbial methanation process using a thermophilic hydrogenotrophic methanogen, *Methanothermobacter sp.* KEPCO-2. The conversion efficiencies of CO_2 and H_2 reached 97.1% and 97.9%, respectively and the maximum methane production rate was observed about 400 VVD (L/L/d). The high-purity methane from the reactor can be connected to the gas grid without additional processing stages.

Keywords: *Biological methanation, hydrogenotrophic methanogen, gas-liquid mass transfer*

RIGA 2023

Unsupervised Neural Network Optimized with Genetic Algorithm for MPPT Control of a Floating Wind Turbine

Eduardo Muñoz-Palomeque
Electromechanical Engineering Department, University of Burgos, Burgos, Spain, emp1016@alu.ubu.es,
ORCID: 0000-0001-8994-3459

Jesús Enrique Sierra-García
Electromechanical Engineering Department, University of Burgos, Burgos, Spain, jesierra@ubu.es,
ORCID: 0000-0001-6088-9954

Matilde Santos
Institute of Knowledge Technology, Complutense University of Madrid, Madrid, Spain, msantos@ucm.es,
ORCID: 0000-0003-1993-8368

Cite this paper as: *Muñoz-Palomeque, E, Sierra-García, JE., Santos, M. Unsupervised Neural Network Optimized with Genetic Algorithm for MPPT Control of a Floating Wind Turbine. 11. European Conference on Renewable Energy System. 18-20 May 2023, Riga, Latvia*

Abstract: Offshore wind turbines operate under unpredictable and changing conditions, such as turbulent wind and waves. These factors affect the turbine structure, its dynamics and influence the energy efficiency. Thus, intelligent controllers that are able to face this uncertainty, the intrinsic nonlinearity of the wind system, and complex environments are required. In this paper, an intelligent controller based on unsupervised Radial Basis Function Neural Network is designed for Maximum Power Point Tracking (MPPT) for a 1.5MW floating wind turbine. In this region, between the cut-in and rated wind speed, the goal is to produce the maximum energy, keeping the power coefficient (C_p) close to the optimum value. The control architecture uses the direct speed control (DSC) scheme to provide a reference electromagnetic torque and then regulate the speed of the turbine. The parameters of the neural controller are tuned using a genetic algorithm. The cost function defined in terms of the speed errors obtains the network weights. The implementation is carried out with Simulink and OpenFAST software. Results validate the control approach, the output power keeps the Cp near the optimum most of the time. Furthermore, it gives slightly better results than the torque control embedded in OpenFAST.

Keywords: *Floating wind turbine, MPPT, unsupervised neural networks, genetic algorithm, power coefficient*

RIGA 2023

LSTM and GRU Neural Networks for Prediction of Wind Turbine Active Power

Pablo-Andrés Buestán-Andrade
Faculty of Informatics, Complutense University of Madrid, Madrid, Spain, pbuestan@ucm.es,
ORCID: 0000-0002-9210-1591

Matilde Santos
Institute of Knowledge, Complutense University of Madrid, Madrid, Spain, msantos@ucm.es,
ORCID: 0000-0003-1993-8368

Jesús-Enrique Sierra-García
Department of Electromechanical Engineering, University of Burgos, Burgos, Spain, jesierra@ubu.es,
ORCID: 0000-0001-6088-9954

Cite this paper as: *Buestán-Andrade, PA, Santos, M, Sierra-García, JE. LSTM and GRU neural networks for prediction of wind turbine active power. 11. European Conference on Renewable Energy System. 18-20 May 2023, Riga, Latvia*

Abstract: Recurrent Neural Networks (RNN), like other machine learning (ML) techniques, are a powerful tool for forecasting the signals in renewable energy systems. This information is crucial for the operation and maintenance (O&M) of a wind turbine (WT). In this work, two of these ML techniques, long-short-term memory (LSTM) and gate recurrent units (GRU), have been used to predict the active power of a WT time series. The database corresponds to a time series of a real WT located in Yalova, Türkiye, containing 50,530 values obtained from the SCADA system. The wind speed, the wind direction, the theoretical power curve and the past values of live active power have been used as network inputs. The dataset has been normalized (preprocessing), a time window has been built, and the influence of the network parameters, such as the number of units and the number of hidden layers has been analyzed. The output is the active power produced by the WT. In this particular case, the GRUs returned a lower mean absolute error (MAE) compared to the LSTM, with a value of 0.028 and 0.040 respectively.

Keywords: *LSTM, GRU, O&M, wind turbine, LV active power, prediction*

RIGA 2023

Towards Li_2S All Solid State Batteries

Zahilia Cabán Huertas
[1]Helmholtz Institute Ulm, Helmholtzstrasse 11, Ulm, 89081, Germany
[2]Karlsruhe Institute of Technology, PO Box 3640, Karlsruhe, 76021, Germany, zahilia.huertas@kit.edu

Alberto Varzi
[1]Helmholtz Institute Ulm, Helmholtzstrasse 11, Ulm, 89081, Germany
[2]Karlsruhe Institute of Technology, PO Box 3640, Karlsruhe, 76021, Germany, alberto.varzi@kit.edu

Maider Zarrabeitia
[1]Helmholtz Institute Ulm, Helmholtzstrasse 11, Ulm, 89081, Germany
[2]Karlsruhe Institute of Technology, PO Box 3640, Karlsruhe, 76021, Germany, maider.ipina@kit.edu

Stefano Passerini
[1]Helmholtz Institute Ulm, Helmholtzstrasse 11, Ulm, 89081, Germany
[2]Karlsruhe Institute of Technology, PO Box 3640, Karlsruhe, 76021, Germany
[3]Department of Chemistry -Sapienza University of Rome, Piazzale A. Moro 5, 00185, Rome, Italy,
stefano.passerini@kit.edu

Cite this paper as: *Huertas, ZC, Varzi, A, Zarrabeitia, M, Passerini, S. Towards Li2S All Solid State Batteries. 11. European Conference on Renewable Energy System. 18-20 May 2023, Riga, Latvia*

Abstract: Consumers demand advanced electronics and sustainable industries in general. To satisfy these demands, the new generation of rechargeable batteries must provide a much higher specific energy density than the existing technology [1]. One emerging post Lithium Ion Batteries (LIBs) technology is Lithium-Sulfur Batteries (LSBs). These devices can have energy density values of 2600 $WhKg^{-1}$. However, S as an electrode suffers from a volume change of 80% [2]; this value is one of the higher registers for a positive electrode. Another issue of this batteries systems is the polysulfide shuttle effect [3]. These polysulfide chains are soluble in the electrolyte and are in contact with the positive and the negative electrode, resulting in adverse consequences. Solid State Electrolyte (SSE) and Li_2S as positive electrodes can alleviate those problems. SSE can prevent the polysulfide shuttle effect. Therefore, the sulfide cannot poison the negative electrode. Furthermore, using Li_2S as a positive electrode can avoid volume change and physical damage to the electrode. Li_2S has a specific capacity of 1166 mAh/g, four times that of the capacity in oxide/phosphate positive electrode [4]. This positive electrode material can be coupled with a lithium-free negative electrode to develop high-energy-density batteries; this can improve the safety of the devices. However, the complex synthesis method of Li_2S–carbon composites restrains large-scale productivity. We propose a method to synthesize a Li_2S-based nanocomposite cathode material. Li2S is used as the active material integrated into a conductive carbon as a matrix to enhance the conductivity using high-temperature treatment. Such cells can deliver a high specific capacity of 1000 mAhg-1 and work for 400 cycles with a fast rate response. The purpose is to incorporate this positive electrode into an all-solid-state battery to develop a safety device with high energy density and good cyclability.

Keywords: *Lithium Sulfide, solid state batteries, positive electrode*

References

[1] S. Chu, A. Majumdar, *Nature* **2012**, , 488, 294–303.
[2] P. Barrai, A. Mistry,P.P Mukherjee, Nanoscale, **2013**, 5 (6), 2186-2204
[3] Y.V. Mikhaylik, J.R. Akridge **2004** J. Electrochem. Soc. 151 A1969
[4] Y. Yang, M.T. McDowell, A. Jackson, J.J. Cha, S.S. Hong, Y. Cui, Nano Lett. **2010**, 10, 4, 1486–1491.

RIGA 2023

Design of a Shape Memory Alloy Heat Engine by Using Waste Heat

Chi Hsiang Pan
National Chin-Yi University of Technology, Taichung, Taiwan, ROC, pancs@ncut.edu.tw,
ORCID: 0000-0002-2454-3910

Cite this paper as: *Pan, CH., Design of a shape memory alloy heat engine by using waste heat. 11. Eur. Conf. Ren. Energy Sys. 18-20 May 2023, Riga, Latvia*

Abstract: In this paper, we use shape memory alloys to develop a novel heat engine mechanism, which is inspired by the mechanism of the internal combustion engine. Compared with other heat engines using shape memory alloy as actuating mechanisms in the literature, this work has the following innovative features: (1) The SMA actuating mechanism of this work has a simple structure, the cost is low, the operation stability is high, the technical threshold is not high, and it is easy to install and match with any equipment that generates waste heat. (2) The heat engine can be applied to a wide range of heat sources, including: waste heat from machinery and equipment and industrial output, or from natural heat sources (geothermal, solar thermal, etc.). (3) The heat engine can operate in high, medium or low temperature heat sources. Compared with power generation with the thermoelectric material technology, this work is more applicable to low-temperature heat sources, or heat sources with low temperature gradients. (4) The heat engine can be applied to waste heat energy recovery, which is in line with innovative energy, energy saving and efficient use of waste energy. (5) The heat engine of this work complies with net zero carbon emission, carbon neutrality and zero pollution. (6) It is easy to obtain the desired actuation performance of heat engine by adjusting some parameters of the SMA actuating mechanism.

Keywords: *Heat engine, SMA actuating mechanism, waste heat*

RIGA 2023

Comparing the Efficiency of Nano Zero Valent Iron, Activated Carbon and Hydrochar as Additives on Biohydrogen Production by Dark Fermentation

Jesús M. Martín-Marroquín
CARTIF Technology Centre, Circular Economy Area, Boecillo, Spain, jesmar@cartif.es, ORCID: 0000-0003-2725-2067

Dolores Hidalgo
CARTIF Technology Centre, Circular Economy Area, Boecillo, Spain, dolhid@cartif.es, ORCID: 0000-0003-0846-6924

Enrique Pérez-Zapatero
CARTIF Technology Centre, Circular Economy Area, Boecillo, Spain, enrper@cartif.es

Miguel Angel Sánchez-Gatón
CARTIF Technology Centre, Circular Economy Area, Boecillo, Spain, migsan@cartif.es

Cite this paper as: *Martín-Marroquín, JM, Hidalgo, D, Pérez-Zapatero, E, Sánchez-Gatón, MA, Comparing the efficiency of nano zero valent iron, activated carbon and hydrochar as additives on biohydrogen production by dark fermentation . 11. Eur. Conf. Ren. Energy Sys. 18-20 May 2023, Riga, Latvia*

Abstract: Dark fermentation is a highly promising strategy when considering biohydrogen production, since it allows the use of a wide variety of biomass substrates as feedstock. This provides an additional advantage related to waste management. However, when compared to conventional thermal processes such as reforming, dark fermentation is usually associated with low yields. In recent years, the strategy of using additives that, when added to the process, improve yields by enhancing the activity of the microorganisms has been developed with the ultimate goal of overcoming this barrier. However, the strategy of applying organic and inorganic additives in dark fermentation is not yet widely used. That is why this paper aims to shed some light on the subject by comparatively studying three types of nanoparticles: zero valent iron, activated carbon and hydrochar, analyzing their effect on the dark fermentation process and hydrogen generation.

Materials and Methods
Digestate from an anaerobic reactor operating in a municipal wastewater treatment plant and glucose were used as inoculum and carbon source, respectively in the first group of test (Tier 1). Digestate from an anaerobic reactor operating in a sugar beet factory and residual effluent from this factory were used in the second group of test (Tier 2). Zero valent iron nanoparticles (Smallops, 150±50nm diameter), activated carbon (Chiemivall, <0.5mm diameter) and hydrochar (Ingelia, <0.5mm diameter) were use as additives at a dose of 200 mg/L. Glass serum bottles of 1000 mL with working volume of 500 mL were used as batch reactors at 34±1°C. 10 g/L of glucose or sugar beet effluent and pre-incubated inoculum were taken to achieve a substrate to inoculum (S/X) ratio of 2 in the reactors. HCl was used to create acidic conditions, bringing all tests to pH 5.5.

Results and Main Conclusions
Fig. 1 shows experimental results of cumulative biogas production fitted to the modified Gompertz model for tier 1 experimentation. The additives assayed show a different degree of effectiveness on biogas production but in all the cases, the use of additives revealed to affect positively the biogas yield. Maximum biogas production is obtained by using hydrochar as an additive. In this case, 219 mL of biogas per gram of glucose are achieved. The curves corresponding to the test with activated carbon and iron nanoparticles are very similar, reaching 195 and 197 ml biogas/g glucose, respectively. Clearly, the test without the use of additive was the one that generated less biogas, with 182 ml/g glucose. Regarding the composition of the biogas, only hydrogen and carbon dioxide were detected in all cases. The non-appearance of methane reveals that no methanogenesis was generated

during the process, probably due to the acidic conditions of the test with pH starting at 5.5 and evolving to more acidic pH values until the test ended. At this time, the pH reached was around 4 in all the reactors. The maximum content of hydrogen detected in each test is shown in Table 1, highlighting the test with Fe(0) where hydrogen reached 38.4% of the biogas.

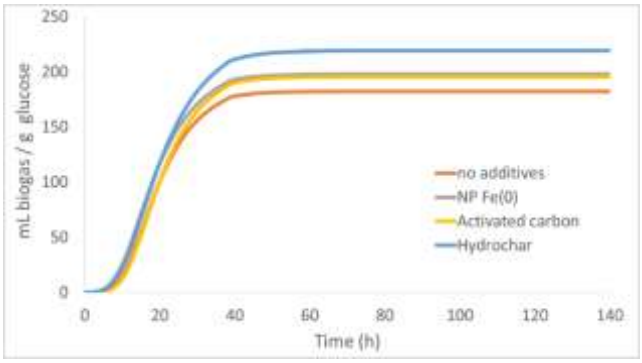

Figure 1. Effect on additives on dark fermentation. Tier 1.

Table 1. Digestate and biogas composition in Tier 1.

	No additives	NP Fe(0)	Activated carbon	Hydrochar
Biogas composition				
% H_2 max	37.4	38.4	37.7	36.5
% CH_4	0	0	0	0
Average digestate composition (SD<10% for all the measurements)				
Glucose (mg/L)	0	0	0	0
Etanol (mg/L)	16.2	12,0	10.8	5.5
Acetic acid (mg/L)	1713.7	1640.8	1650.0	1585.0
Propionic acid (mg/L)	137.8	95.5	108.1	-
Butiric acid (mg/L)	2635.6	2517.7	2704.5	2360.9
Caproic acid (mg/L)	142.2	162.3	134.5	186.5
Total VFA (mg/L)	4640.4	4416.2	4597.1	4132.3

Table 1 shows the composition of the digestate at the end of the trials in Tier 1. In all cases, it is observed how the glucose is completely consumed, generating small concentrations of ethanol and volatile fatty acids (VFA), mainly butyric, the most abundant in all trials, acetic acid and small concentrations of propionic acid in some trials. The minimum AGV concentration is observed in the test that uses hydrochar as an additive, which is consistent since it is the test in which the greatest amount of the substrate has gone to form biogas. The composition of the digestate formed opens the door for this stream to be used as a VFA source or for it to be easily degraded in a conventional anaerobic digester for biomethane production. However, if the objective of the process is to maximize hydrogen production, controlling the pH of the medium can lead to inhibiting VFA production in favor of hydrogen production. At Tier 2, where a real wastewater stream is used instead of glucose as the carbon source, preliminary studies indicate results along the same lines as those obtained at Tier 1, with increases in biogas production greater than 2 with the use of additives. Likewise, a higher hydrogen content is also observed in the biogas generated, around 2%. After confirming these promising results in a second round of tests, the next step will be to operate the reactors continuously, with pH adjustment to prevent the acidification of the medium from inhibiting the reaction, looking for maximizing hydrogen generation.

Keywords: *Green hydrogen, nanomaterials, nanoparticles, renewable gases, trace metals, waste-to-energy*

Acknowledgments

The authors gratefully acknowledge support of this work by the CDTI-Spanish Ministry of Science and Innovation in the frame of the project H24NEWAGE (Ref. CER-20211002).

RIGA 2023

The Relation Between Top-Cell Bandgap and Silicon Bottom-Cell Thickness in Double-Junction 2-Terminal Silicon-Based Tandem Solar Cells

Hesan Ziar
Delft University of Technology, Photovoltaic Materials and Devices group, Delft, the Netherlands,
e-mail address: h.ziar@tudelft.nl, ORCID No. 0000-0002-9913-2315

Cite this paper as: *Ziar H., The relation between top-cell bandgap and silicon bottom-cell thickness in double-junction 2-terminal silicon-based tandem solar cells. 11. Eur. Conf. Ren. Energy Sys. 18-20 May 2023, Riga, Latvia*

Abstract: As silicon is the basis of the photovoltaic (PV) industry, it is difficult to exclude double-junction silicon-based solar cells from future perspectives. In many cases, the top and bottom cells of the tandem solar cells are designed or even optimized separately. However, the design that guarantees the optimum performance should be done while considering both top and bottom junctions. This is more important when it comes to 2-terminal solar cells. Thus, physics-based quantified relations between the design parameters of the top and bottom cells can be helpful to designers and cell manufacturers. Two basic design parameters are the band gap of the top cell and the thickness of the silicon wafer for the bottom cell, which are related. In order to understand this relation, we developed a 1-dimensional framework based on semiconductor physics equations. We neglected the non-radiative recombination for the top cell and followed the Shockley-Queisser (SQ) approach. For the bottom silicon cell, the narrow-base assumption was used. Measured properties of silicon and free carrier absorption, incomplete ionization, photon recycling, and bandgap narrowing effects were considered. We then optimized the design at STC and quantified the relationship between the top cell band gap and silicon bottom cell thickness. Finally, a WSi -Egtop graph for the 2-terminal tandem solar cell was introduced (Fig. 1). Several interesting insights were driven from the graph including that the efficiency of 2-terminal silicon-based tandem solar cells is limited to 42.8%, which is less than reported values in the literature.

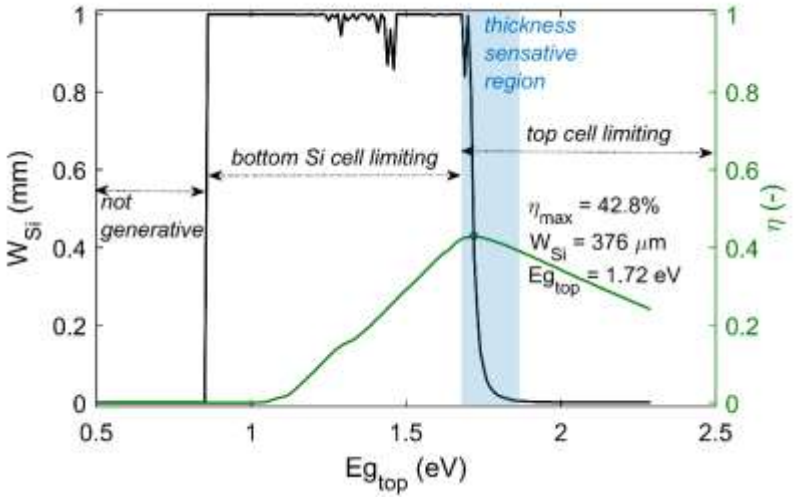

Figure 1. Silicon bottom cell bulk thickness (n-type) and tandem cell efficiency as a function of the band gap. The efficiency limit, Si thickness, and top cell band gap at maximum efficiency are also mentioned. The blue area shows the band gap range where a slight change in efficiency leads to a large change in optimum Si thickness.

Keywords: *Photovoltaics (PV), efficiency limit, silicon wafer thickness, band gap, tandem solar cell*

RIGA 2023

Characterization of Biocrude Oils from Hydrothermal Liquefaction of De-Ashed Energy Grass

Tossapon Katongtung
Department of Mechanical Engineering, Faculty of Engineering, Chiang Mai University, Chiang Mai, Thailand, email: tossapon.katongtung@gmail.com, ORCID: 0000-0001-9612-1883

Sanphawat Phromphithak
Department of Mining and Petroleum Engineering, Faculty of Engineering, Chiang Mai University, Chiang Mai, Thailand, email: s.phromphithak@gmail.com, ORCID: 0000-0001-6457-1222

Thossaporn Onsree
Department of Chemical Engineering, College of Engineering and Computing, University of South Carolina, Columbia, SC, USA, email: th.onsree@gmail.com, ORCID: 0000-0002-5685-5572

Jochen Lauterbach
Department of Chemical Engineering, College of Engineering and Computing, University of South Carolina, Columbia, SC, USA, email: lauteraj@cec.sc.edu, ORCID: 0000-0001-8303-7703

Nakorn Tippayawong
Department of Mechanical Engineering, Faculty of Engineering, Chiang Mai University, Chiang Mai, Thailand, email: n.tippayawong@yahoo.com, ORCID: 0000-0002-6104-7676

Cite this paper as: *Katongtung, T., Phromphithak, S., Onsree, T., Lauterbach, J., Tippayawong, N. Characterization of Biocrude Oils from Hydrothermal Liquefaction of De-Ashed Energy Grass. 11. Eur. Conf. Ren. Energy Sys. 18-20 May 2023, Riga, Latvia*

Abstract: Energy grass is a promising source of bioenergy. A new energy grass such as hybrid giant Juncao grass contains relatively high ash content that affects thermal conversion of the biomass material to biocrude oil. De-ashing by water washing is a simple pretreatment operation that can reduce the ash content of biomass samples. It was claimed that reducing ash could reduce the energy consumption in the hydrothermal liquefaction process since it can be performed at low temperatures. In this study, hydrothermal liquefaction of treated and raw hybrid giant Juncao grasses was carried out. Chemical composition of the biocrude oils was examined using gas chromatography-mass spectrometry, nuclear magnetic resonance and Fourier transform infrared spectroscopy techniques. De-ashing of the grass efficiently reduced its ash content from 6.34 to 4.67%. Reduction of ash affected the yield of HTL biocrude oils. It was found that higher yields were obtained, after the grass was de-ashed. The yields of bio-crude and solid residue obtained from HTL of the de-ashed grass could bring greater energy recovery (62.4%) than that of the raw biomass (49.8%). It was also found that similar HBO yields were obtained for HTL at 250, 300 and 350 °C and the biomass/water ratio of 1/5. With respect to their composition, it was shown that both raw and de-ashed grasses mainly consisted of phenols and alcohols. But in the de-ashed sample, significantly less N-containing compounds were found than in the raw biomass. This suggested that the pretreatment with partial removal of ash improved the quality of bio-crude oil.

Keywords: *Biomass, biofuels, clean energy, de-ashing, pretreatment, thermal conversion*

RIGA 2023

Conceptual Design of an Aluminum-Air Battery System to Remove Hydrogen and By-Products

Jeong-Seog Oh
Energy Network Laboratory, Korea Institute of Energy Research, Daejeon-si, Republic of Korea, jeongs5@kier.re.kr

Si-Won Yoon
Energy Network Laboratory, Korea Institute of Energy Research, Daejeon-si, Republic of Korea

Woo-Cheol Kim
Future Development Institute, Korea District Heating Corporation, Yongin-si, Republic of Korea

Cite this paper as: *Oh, J., Yoon, S., Kim, W. Conceptual design of an aluminum-air battery system to remove hydrogen and by-products. 11. Eur. Conf. Ren. Energy Sys. 18-20 May 2023, Riga, Latvia*

Abstract: In a recent year, a next generation battery system against climate change are actively under developing, as increasing interest in carbon net zero technologies in each country. The Korea Institute of Energy Research (KIER) is also conducting research and development (R&D) on the Aluminum-air batteries that is considered as new technology in a district heating sector. A conceptual design study on the aluminum-air battery system is summarized as follows (see in Fig. 1): (1) The battery system that can remove additionally generated hydrogen and by-products was conceptually designed by investigating theoretical background and previous works of aluminum-air battery systems. (2) A cyclone-type aluminum-air battery system was studied using a computational fluid dynamics (CFD) technique. (3) An aluminum-air battery unit cell capable of removing hydrogen and by-products was fabricated to find the applicability of district heating business.

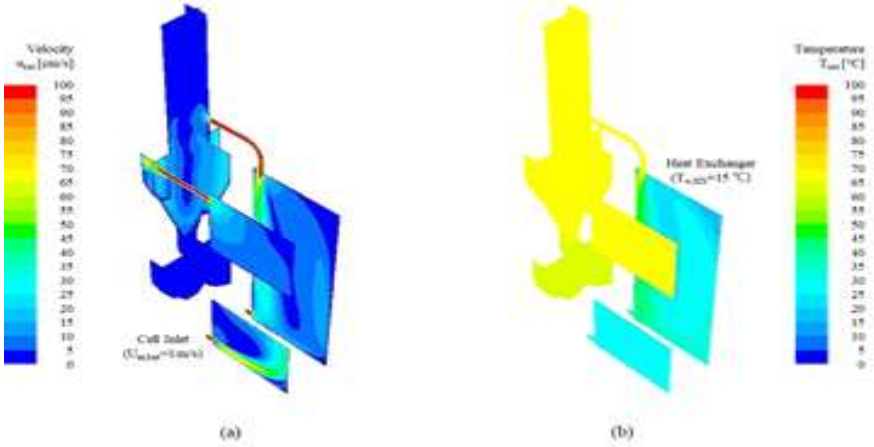

Figure 1. A cyclone-type aluminum-air battery (AAB) system: Computational fluid dynamics (CFD) analysis

Keywords: *Aluminum-air battery system, cyclone, CFD*

RIGA 2023

Iron-Chlorine Chemical Cycle for On-Demand Green Hydrogen Production Powered by Waste Heat

Matjaz Valant
University of Nova Gorica, Nova Gorica, Slovenia, matjaz.valant@ung.si, ORCID: 0000-0003-4842-5676

Uroš Luin
University of Nova Gorica, Nova Gorica, Slovenia, uros.luin@ung.si, ORCID: 0000-0001-8081-4765

Andreea Oarga-Mulec
University of Nova Gorica, Nova Gorica, Slovenia, andreea.oarga@ung.si, ORCID: 0000-0002-0885-8429

Cite this paper as: *Valant, M, Luin, U, Oarga-Mulec A., Iron-chlorine chemical cycle for on-demand green hydrogen production powered by waste heat. 11. Eur. Conf. Ren. Energy Sys. 18-20 May 2023, Riga, Latvia*

Abstract: The critical challenge for the implementation of hydrogen technology is related to the expensive and limited production of green hydrogen, which for now only accounts for a few percentages of global hydrogen production. Another challenge is the social acceptance of hydrogen technology due to safety risks related to the explosive nature of the stored hydrogen. If we can remove these hindrances the hydrogen economy can flourish. Here we are going to present an innovative technology based on the iron-chlorine chemical cycle that could use abundant sources of industrial waste heat to recharge the hydrogen carrier and produce green hydrogen on demand. Within the described material closed cycle, the heat is efficiently converted into the chemical energy of hydrogen, which is the first case of such technology. The hydrogen is released on demand within the storage unit during a reaction of diluted HCl solution with iron powder. Recharging of the used material (i. e. iron chloride solution) is carried out in a regeneration unit by a reaction with water (hydrolysis) and thermal decomposition using heat as an energy source. Also, a comparative LCA analysis will be presented to demonstrate the benefits of the cycle powered fully by sustainable energy sources.

Keywords: *Iron-chlorine chemical cycle, Hydrogen production, industrial waste heat*

RIGA 2023

Hydro-Energy Plants Modeling in Optimal Power Flow Problems

Alberto Flores
Escuela de Ingeniería Industrial y Aeroespacial de Toledo, UCLM, Toledo, Spain, alberto.flores2@alu.uclm.es,
ORCID: 0000-0002-6535-5756

Rafael Zárate-Miñano
Escuela de Ingeniería Minera e Industrial de Almadén, UCLM, Almadén, Spain, rafael.zarate@uclm.es,
ORCID: 0000-0001-5323-4909

Miguel Carrión
Escuela de Ingeniería Industrial y Aeroespacial de Toledo, UCLM, Toledo, Spain, miguel.carrion@uclm.es,
ORCID: 0000-0001-5764-3996

Cite this paper as: *Flores, A., Zárate-Miñano, R., Carrión, M. Hydro-energy plants modeling in optimal power flow problems. 11. Eur. Conf. Ren. Energy Sys. 18-20 May 2023, Riga, Latvia*

Abstract: In many optimization problems based on optimal power flow formulations, the steady-state operation characteristics of hydro-power plants are modeled in an approximate manner. The standard approach is to represent the power production limits of the plant by means of independent maximum and minimum bounds on active and reactive power outputs. Few models have been proposed based on the plant capability curve. Most of them, however, do not include the parts of the curve corresponding to stability limits or, if so, they over-simplify its representation. This work proposes a formulation for the complete capability curve of the plant, including the exact modeling of its generator stability limits. The accuracy of the proposed formulation is tested by solving a maximum loading condition problem on a one-machine isolated power system. In this optimization problem, a homotopy modeling technique is used to drive the hydro-power plant to its operating limits. In order to explore the whole operating range of the plant, the maximum loading condition problem is solved for the entire spectrum of load power factor values.

Keywords: *Salient-pole synchronous generators, capability curve, stability limits, homotopy*

RIGA 2023

Optimization of the Iron Chloride Electrochemical Cycle as a Long-Term Energy Storage Technology

Uroš Luin
University of Nova Gorica, Materials Research Laboratory, Nova Gorica, Slovenia, uros.luin@ung.si,
ORCID: 0000-0001-8081-4765

Matjaž Valant
University of Nova Gorica, Materials Research Laboratory, Nova Gorica, Slovenia, matjaz.valant@ung.si,
ORCID: 0000-0003-4333-4054

Iztok Arčon
J. Stefan Institute, Department of Low and Medium Energy Physics, Ljubljana, Slovenia, iztok.arcon@ung.si,
ORCID: 0000-0003-4842-5676

Cite this paper as: *Luin U., Valant M., Arčon I., Optimization of the Iron Chloride Electrochemical Cycle as long-term energy storage technology. 11. Eur. Conf. Ren. Energy Sys. 18-20 May 2023, Riga, Latvia*

Abstract: The growing deployment of renewable energy sources requires cost-effective energy storage (ES) technologies that can handle high-capacity and high-power demands. One potential long-term ES option via iron redox change is the Iron Chloride Electrochemical Cycle (ICEC), which uses abundant materials. This cycle technology employs electro-reducing the iron ionic species to Fe^0 in a concentrated aqueous $FeCl_2$ electrolyte solution. Energy is released on demand as H_2 (g) by a controlled hydrogen evolution reaction of Fe oxidation with HCl. Both electrolysis efficiency and electrolyte conductivity have a linear temperature dependence, but the electrolyte concentration, conductivity, and electrolysis efficiency relationship are complex. Small efficiency variations were found for $FeCl_2$ electrolyte concentrations up to the peak conductivity, followed by a rapid efficiency drop at higher concentrations. X-ray absorption spectroscopy experiments conducted at DESY in Hamburg revealed that a shift from $Fe[Cl(H_2O)_5]^+$ to $Fe[Cl_2(H_2O)_4]^0$ caused a significant decrease in solution conductivity, providing insight into the observed trends.

Keywords: *Iron chloride electrochemical cycle, energy storage, electrolyte conductivity, XAS, ionic species*

RIGA 2023

Enhancing the Performance of Human Motion Energy Harvesting through Optimal Smoothing Capacity in the Rectifier

Ilgvars Gorņevs
Riga Technical University, Riga, Latvia, Ilgvars.Gornevs@inbox.lv, ORCID: 0000-0002-8908-5332

Juris Blūms
Riga Technical University, Riga, Latvia, Juris.Blums@rtu.lv, ORCID: 0000-0002-7087-6062

Cite this paper as: *Gorņevs, I., Blūms, J. Enhancing the Performance of Human Motion Energy Harvesting through Optimal Smoothing Capacity in the Rectifier. 11. Eur. Conf. Ren. Energy Sys. 18-20 May 2023, Riga, Latvia*

Abstract: The energy harvested from human motion is often produced as irregular and low-frequency bursts of electrical power, making it difficult to efficiently convert it into a usable electrical signal. One common step in the conversion process is rectification, and to address the challenge, the current study explores the impact of the smoothing capacitor value on the full-wave rectifier output for intermittent signals. An analytical model is developed using established rectifier analysis models, revealing that a specific combination of the harvester's internal resistance, frequency, and load resistance results in an optimal smoothing capacity that provides the highest average output voltage after rectification. This hypothesis is backed up by a comprehensive computer simulation with realistic parameters, and later verified through experimental testing using both purely resistive and switching converter load configurations. The results demonstrate a 5% increase in rectified voltage RMS value and a 33% increase in converter power output by optimizing the smoothing capacity in a specific low voltage energy harvesting system. However, these findings have broad applications and can be applied to various energy harvesting purposes.

Keywords: *Low voltage rectification, smoothing capacitor, harvesting efficiency, human motion, energy harvesting*

RIGA 2023

The Influence of Recuperative Cooling Approach for Energy Harvesting on Efficiency of Thermoelectric Cooling

Vilnis Jurķāns
Riga Technical University, Riga, Latvia, Vilnis.Jurkans@rtu.lv, ORCID: 0000-0002-5736-1064

Juris Blūms
Riga Technical University, Riga, Latvia, Juris.Blums@rtu.lv, ORCID: 0000-0002-7087-6062

Cite this paper as: *Jurķāns, V., Blūms, J. The Influence of Recuperative Cooling Approach for Energy Harvesting on Efficiency of Thermoelectric Cooling. 11. Eur. Conf. Ren. Energy Sys. 18-20 May 2023, Riga, Latvia*

Abstract: Recuperative approach can be implemented into thermoelectric cooling system for harvesting excess energy by operating a thermoelectric element as a heat pump and electric generator alternately. The present work explores the influence of such approach on heat flow through thermoelectric element and change in cooling efficiency. A theoretical analysis is carried out by using thermoelectric analogy method to describe the relations between various parameters of thermoelectric element and thermoelectric effects to understand possibilities of harvesting the electrical energy and predicting the gains and drawbacks of the recuperative approach. Theoretical predictions are backed up experimentally by performing measurements with thermally isolated thermoelectric element and confirmed with measurements using realistic thermoelectric cooling system. Despite harvesting 2.1% of supplied electrical energy through recuperation, 5.8% decrease in temperature difference is observed. Such decrease in efficiency is caused by current flow during recuperation, thus creating additional heat back flow through Peltier effect. Despite the obvious drawbacks of the approach, paper discusses various conditions and applications where recuperation can be beneficial.

Keywords: *Thermoelectric element, Peltier effect, recuperation, thermoelectric cooling, energy harvesting*

RIGA 2023

Bioclimatic Strategies in Floating Houses and Quality of Life in the Lower Area of Belén, Iquitos 2022

Doris Esenarro Vargas
Universidad Ricardo Palma, Lima, Perú, doris.esenarro@urp.edu.pe, ORCID: 0000-0002-7186-9614

Vanessa Raymundo Martínez
Universidad Ricardo Palma, Lima, Perú, 202112586@urp.edu.pe, ORCID: 00000-0001-9264-0176

Nicolai Neciosup
Universidad Ricardo Palma, Lima, Perú, nicolai.neciosup@urp.edu.pe, ORCID: 0000-0000-0000-0000

Mario Gustavo Reyes Mejía
Universidad Nacional San Luis Gonzaga, Ica, Perú, mreyes@unica.edu.pe, ORCID: 0000-0002-5282-2642

Jesús Manuel Prado Meza
Universidad Ricardo Palma, Lima, Perú, jesus.prado@urp.edu.pe, ORCID: 0000-0002-8166-6044

Cite this paper as: *Vargas, DE, Martínez, VR, Neciosup, N, Reyes Mejía, MG, Prado Meza, JM, Bioclimatic strategies in floating houses and quality of life in the lower area of Belén, Iquitos 2022. 11. Eur. Conf. Ren. Energy Sys. 18-20 May 2023, Riga, Latvia*

Abstract: The objective of this research is to determine to what extent solid waste affects the quality of life and to identify the comfort of the floating houses in Belén. Due to the fact that currently, the floodable characteristics of the research area make it impossible to install an adequate conventional sewage system; to facilitate planning and rescue actions in this challenging neighborhood due to its location, type of housing and the permanent problems established in its living conditions to guarantee comfort and improve the habitability of the area. For the research methodology, information will be collected from the study area at present, information search, references that may be of support to the investigation, bioclimatic criteria through digital tools or software that help to visualize a real panorama. As a result, the precariousness of floating houses and the deficiency in terms of solid sanitary waste management were demonstrated, showing a worrying scenario of contamination to the environmental health of the inhabitants. In conclusion, the bioclimatic strategies applied in the floating house proposal will improve the quality of life.

Keywords: *Floating house, solid waste, bioclimatic, pollution, quality of life,*

RIGA 2023

Groundbreaking Materials for Retrofitting Light Water Reactor Fuels

Raul B. Rebak
GE Research, Schenectady – New York, USA, rebak@ge.com, ORCID: 0000-0002-8070-4475

Cite this paper as: *Rebak, RB. Groundbreaking Materials for Retrofitting Light Water Reactor Fuels. 11. Eur. Conf. Ren. Energy Sys. 18-20 May 2023, Riga, Latvia*

Abstract: Electricity produced by extracting the heat of a nuclear fission reaction is again gaining respect across the Globe due to the threat of climate change caused by the overuse of fossil fuels. Since the healthy construction of light water reactors in the western world in the 1970s and 1980s, few were connected to the civilian grid in the last 30 years. To extend the life of the existing reactors and avoid their premature decommissioning, revolutionary nuclear fuel materials are being considered to retrofit the aging reactors. These newer materials would be more resistant to a loss of coolant accident and make the reactors safer and more economical to operate. An overview of the corrosion performance of these revolutionary materials in the entire fuel cycle are described and ranked.

Keywords: *Nuclear Fuels, Accident Tolerant Materials, FeCrAl, Coatings*

RIGA 2023

The Reliability of the Forecast of Energy Yield: Case of Kitka Wind Farm

Bukurije Hoxha
University of Prishtina, Prishtina, Kosovo, bukuriehoxha15@gmail.com, ORCID: 0000-0002-8890-2054

Sabrije Osmanaj
University of Prishtina, Prishtina, Kosovo, sabrije.osmanaj@uni-pr.edu, ORCID: 0000-0002-4044-9879

Rexhep Selimaj
University of Prishtina, Prishtina, Kosovo, rexhep.selimaj@uni-pr.edu, ORCID: 0000-0002-4044-9878

Risto V. Filkoski
Ss. Cyril and Methodius University, Skopje, North Macedonia, risto.filkoski@mf.edu.mk,
ORCID: 0000-0002-3743-318X

Cite this paper as: *Hoxha, B, Osmanaj S, Selimaj R, Filkoski RV, The reliability of the forecast of energy yield: Case of Kitka wind farm. 11. Eur. Conf. Ren. Energy Sys. 18-20 May 2023, Riga, Latvia*

Abstract: The investments that must be made in the energy sector are high. The risk that the respective companies can face is great. The predictability of energy output in the renewable energy sector is less reliable because the energy source is unstable. Kosovo is currently facing a crisis in the energy sector, which is mostly covered by coal. Investment in the renewable energy sector is based on the private sector and the countries that are in transition have the financial aspect even more critical. The wind farm which is currently in operation is located in Kitka, 42° 39' 58.9", 21° 40' 43.2". This farm is in operation and its installed power is 32.4 MW. There are a total of 9 installed turbines with different capacities. Since this farm is in operation, then in this work a comparison is made between the energy that is predicted and the energy that is placed in the grid. The results obtained further show that often the output energy is higher than that predicted during the design of the wind farm. The results are shown in the form of a comparison showing in which part the biggest losses are realized.

Keywords: *Wind energy, energy yield, energy losses, forecast, and energy efficiency.*

RIGA 2023

Bacterial Cellulose - A Potential Biomaterial for Energy Storage and Energy Conversion Devices

Nabanita Saha
Centre of Polymer Systems, University Institute, Tomas Bata University in Zlin, Czech Republic
nabanita@utb.cz, ORCID: 0000-0002-7549-2260

Oyunchimeg Zandraa
Centre of Polymer Systems, University Institute, Tomas Bata University in Zlin, Czech Republic
zandraa@utb.cz, ORCID: 0000-0002-5330-6906

Petr Saha
Centre of Polymer Systems, University Institute, Tomas Bata University in Zlin, Czech Republic
saha@utb.cz, ORCID: 0000-0002-1873-4163

Cite this paper as: *Saha, N., Zandraa, O., Saha P. Bacterial Cellulose - A Potential Biomaterial for Energy Storage Devices. 11. Eur. Conf. Ren. Energy Sys. 18-20 May 2023, Riga, Latvia*

Abstract: In energy storage (supercapacitors, Lithium-ion, Lithium-sulfur, and Sodium-ion batteries) and energy conversion (Oxygen reduction and Hydrogen evolution reaction), even though bacterial cellulose (BC) and its composites have shown vast possible applications, still, BC is in the initial stage of research. Many appraisals (large-scale production, diversity, interface engineering, multifunctional properties, and new fabrication) are there before the execution of BC in energy storage and conversion, as a source of renewable biomaterial. Hence, in this paper focus has been given to the optimization of the 'production condition' of BC in presence of apple juice (AJ) for large-scale production. AJ was prepared from three different apple cultivars (Golden Delicious, Jonagold, and Gala) which were collected from local supermarkets in the Czech Republic. The yield of BC was evaluated (lab scale) in presence of various carbon, nitrogen sources and other factors (pH, temperature, incubation period) on BC production by *Komagataeibacter xylinus* using AJ as a fermentation medium in static mode. As the structure and properties of BC fibers are important components for the design and fabrication of 'BC-derived functional materials for electrochemical energy storage and energy conversion devices, obtained BC was characterized by FTIR, SEM, and TGA etc. 2% peptone (additional nitrogen) enhances the yield of BC. 15-30 days incubation period, 28°C temperature and 5.5 pH are the optimal condition for BC production and the yield exhibited highest in presence of AJ-Gala.

Keywords: *Bacterial cellulose, energy storage, conversion, Komagataeibacter xylinus*

Acknowledgments

The Ministry of Education, Youth and Sports of the Czech Republic – DKRVO (RP/CPS/2022/005) was supported this work.

RIGA 2023

Numerical Study on Indoor Air Purification and Heating Energy Consumption

Andrejs Sabanskis
Institute of Numerical Modelling, University of Latvia, Riga, Latvia, andrejs.sabanskis@lu.lv,
ORCID: 0000-0002-5465-7759

Dagis Daniels Vidulejs
Institute of Numerical Modelling, University of Latvia, Riga, Latvia, dagis_daniels.vidulejs@lu.lv,
ORCID: 0000-0002-7574-1052

Jānis Virbulis
Institute of Numerical Modelling, University of Latvia, Riga, Latvia, janis.virbulis@lu.lv,
ORCID: 0000-0002-5467-7864

Andris Jakovičs
Institute of Numerical Modelling, University of Latvia, Riga, Latvia, andris.jakovics@lu.lv,
ORCID: 0000-0003-3410-5081

Cite this paper as: *Sabanskis, A, Vidulejs, DD, Virbulis, J, Jakovičs, A, Numerical study on indoor air purification and heating energy consumption. 11. Eur. Conf. Ren. Energy Sys. 18-20 May 2023, Riga, Latvia*

Abstract: During the heating season, the main energy losses of indoor spaces are conductive heat fluxes through external walls as well as due to the warm air leaving through the ventilation outlets. While the walls could be additionally insulated to reduce the heat losses, a certain amount of the outside fresh air is always needed to ensure good indoor air quality for humans. The efficiency of ventilation depends on its intensity and the overall air flow pattern in the room, i.e., air mixing. In the present contribution, different heating regimes (such as air-air heat pump, capillary heating mat or radiator) are analyzed numerically by calculating the temperature and velocity distributions using OpenFOAM. A portable air cleaner capable of disinfecting airborne aerosols is also introduced by modeling the concentration field as a passive scalar transport problem. The influence of the position, orientation and flow rate of the air cleaner is investigated. Since the air cleaner alters the air flow pattern in the room, it affects the amount of pollutants which are removed through the ventilation outlet. By adjusting the air exchange rate to account for this effect, the energy consumption for the heating could be reduced.

Keywords: *Air filtering, energy efficiency, computational fluid dynamics, heat transfer, aerosol transport*

Acknowledgements

The present research has been supported by the European Regional Development Fund project “System for prediction and reduction of COVID-19 infection risk in indoor environment” No. 1.1.1.1/21/A/046.

RIGA 2023

Sustainable Energy Strategies Applied to an Experimental Aquaponic Farming Production System

Luis Mazorra Aguiar
University Institute for Intelligent Systems and Numerical Applications in Engineering,
Department of Electrical Engineering, University of Las Palmas de Gran Canaria, Spain, luis.mazorra@ulpgc.es,
ORCID: 0000-0002-9746-7461

Juan Antonio Jiménez Rodríguez
University Institute of Cybernetic Sciences and Technologies,
Department of Electronic and Automatic Engineering, University of Las Palmas de Gran Canaria, Spain,
juanantonio.jimenez@ulpgc.es, ORCID: 0000-0003-2900-3857

Priscila Velázquez Ortuño
University of Las Palmas de Gran Canaria, Spain, priscila.velazquez@ulpgc.es, ORCID: 0000-0001-5387-9723

Fabian Deniz
University Institute for Intelligent Systems and Numerical Applications in Engineering,
Department of Electrical Engineering, University of Las Palmas de Gran Canaria, Spain, fabian.deniz@ulpgc.es,
ORCID: 0000-0002-5356-4796

Lidia Esther Robaina Robaina
University Institute for Research in Sustainable Aquaculture and Marine Ecosystems, Department of Biology, Spain,
lidia.robaina@ulpgc.es, ORCID: 0000-0003-4857-6693

Joel López Suárez
University of Las Palmas de Gran Canaria, Spain, joel.lopez104@alu.ulpgc.es, ORCID: 0009-0001-5530-0698

Cite this paper as: *Aguiar, LM, , Jiménez Rodríguez, JA, Velázquez Ortuño, P, Déniz, F, Robaina Robaina, LE, López Suárez, J, Sustainable energy strategies applied to an experimental aquaponic farming production system. 11. Eur. Conf. Ren. Energy Sys. 18-20 May 2023, Riga, Latvia*

Abstract: This study develops sustainable energy strategies through the implementation of renewable technologies in experimental aquaponics production systems isolated from the electrical grid, to improve the energy efficiency of these systems. For the development of the strategies, a multi-criteria analysis is performed, considering technical and economic aspects, to identify the optimal system for the operation of the system equipment. In the study, simulations were carried out with renewable systems based on photovoltaic, wind, diesel and battery technologies. In addition, the possibilities of a better optimization of the system have been studied, achieving a better adaptation of the consumption of the aquaponic system. The study was carried out by applying the computational methodology of optimization, using as a working tool the renewable energy development software (Hybrid Optimization of Multiple Energy Resources), obtaining the first tangible results. This study will have an impact on the circular economy of experimental aquaponic farming production systems, making them more accessible in those agricultural areas with energy problems and shortages.

Keywords: *Sustainability, renewable energy, circular economy.*

RIGA 2023

Raising Awareness and Uncertainty Caused by Green Deal targets within Companies Involved in Emission Trading Scheme in Latvia

Ieva Igaune
University of Latvia, Riga, Latvia, ii12027@students.lu.lv, ORCID: 0000-0001-8285-4437

Iveta Steinberga
University of Latvia, Riga, Latvia, iveta.steinberga@lu.lv, ORCID: 0000-0002-5879-8639

Cite this paper as: *Igaune, I, Steinberga, I, Raising awareness and uncertainty caused by Green Deal targets within companies involved in emission trading scheme in Latvia. 11. Eur. Conf. Ren. Energy Sys. 18-20 May 2023, Riga, Latvia*

Abstract: More than 75% of the greenhouse gas emissions are created during production and use of energy. Therefore, decarbonization of the energy system is critical and certain goals need to be set. About 2 years ago, on 14 July 2021, the European Commission initiative on the implementation of the Green Deal initiated significant changes in all areas concerning energy production/generation. The Green Deal principles for energy sector focuses on making energy green, smart and affordable. Ambitious targets were set which can only be achieved by transforming all sectors of the economy. Achieving these targets: Reducing greenhouse gas emissions by 55% by 2030, and achieving climate neutrality by 2050, can only be achieved after a thorough inventory of the biofuel strategy. This paper describes situation for the companies involved in the emissions trading scheme in Latvia, their greenhouse gas emissions and potential risks in the future associated with the introduction of the European Green Deal actions and goals.

Keywords: *Green deal, green house gase, emission trading scheme*

RIGA 2023

Efficiency Analysis of Fixed and Axis Tracking Options of Photovoltaic Systems to be Installed in a Marina

Ali Rıza Dal
Ministry of Transport and Infrastructure, Ankara, Türkiye, ardal1969@gmail.com, ORCID: 0000-0002-3646-2288

Hiwa Najmalddin Nasraldeen
Karabük University, Karabük, Türkiye, hiwa00575877@gmail.com, ORCID: 0009-0001-0851-9380

Hacı Mehmet Şahin
Karabük University, Karabük, Türkiye, mehmetsahin@karabuk.edu.tr, ORCID: 0000-0001-7093-7673

Cite this paper as: *Dal, AR, Nasraldeen, HN. Şahin, HM, Efficiency analysis of fixed and axis tracking options of photovoltaic systems to be installed in a marina. 11. Eur. Conf. Ren. Energy Sys. 18-20 May 2023, Riga, Latvia*

Abstract: Electricity consumption is an important cost in businesses operating in the service sector such as marinas. Although the use of solar power for electricity has become widespread in various fields in Türkiye, marinas have yet to fully utilize this technology. The aim of this study is to examine the feasibility of supplying the electricity needs of a marina with a photovoltaic (PV) system. For this purpose, a marina in Muğla (Bodrum) was selected, and monthly/yearly electricity needs were determined. In this study, the PV installed capacity needed to meet the marina's electricity demand was selected. Simulations were performed for three different options using the Photovoltaic Geographical Information System (PVGIS). As a result of the calculations, a single axis tracking PV system with a capacity of 2012 kW will generate 4,469,618 kWh/year of electricity, which will be sufficient to meet the yearly electricity demand. It has been determined that the installation cost payback period is 3.91 years for the single axis tracking PV system. In addition, it was observed that both the dual-axis tracking and single-axis tracking PV systems were more efficient than the fixed options.

Keywords: *Solar energy, tracked photovoltaics, solar radiation, PVGIS*

FULL PAPERS

RIGA 2023

Capacity Factor of Wind Parks in Bosnia & Herzegovina

Elvir H. Zlomušica
Džemal Bijedić University of Mostar, Bosnia and Herzegovina, elvir.zlomusica@unmo.ba, ORCID: 0000-0003-4978-6190

Cite this paper as: *Zlomušica, EH, Capacity factor of wind parks in Bosnia and Herzegovina. 11. Eur. Conf. Ren. Energy Sys. 18-20 May 2023, Riga, Latvia*

Abstract: Of great importance during the design, and later the operation of a wind park (farm) is the capacity factor. Namely, its higher value indicates that a location or plant is of better quality (more hours of operation at nominal power) and that the return on investment is faster. Often the estimated or projected value of the capacity factor does not match that obtained from a plant. The first wind park in Bosnia and Herzegovina started operating only in 2018. This paper analyzes the capacity factor of wind parks in Bosnia and Herzegovina. The results obtained are good. The average capacity factor is 33.2%, also the average values of productivity indicators of all wind parks in Bosnia and Herzegovina are 7.6 GWh/unit, 2.9 GWh/MW, and 808.15 kWh/m2/year, which are also good values.

Keywords: *Wind energy, efficiency, capacity factor, Bosnia&Herzegovina*

1.INTRODUCTION

Between 2015 and 2022, the capacity of global wind power grew by 12%, according to [1]. The installed wind energy capacity of 236 GW (with onshore capacity of 207 GW and 28 GW offshore) was in Europe in 2021. The EU had 189 GW installed in wind energy. Onshore wind plant share was 173 GW and 16 GW offshore. In Europe, five countries account for nearly 2/3 of the total wind power capacity, with Germany leading at 64 GW, followed by Spain with 28 GW, the United Kingdom with 27 GW, France with 19 GW, and Sweden with 12 GW. To achieve the 55% target reduction in greenhouse gas emissions from 1990 levels by 2030 the EU-27 should add 32 GW in wind power each year to reach the EU's 40% renewable energy target by 2030. According to available data from 14 countries, the average power rating of new onshore wind turbines was 4 MW, while it was 8.5 MW for offshore wind plants [2,3].

In 2021, wind power plants in Europe generated 437 TWh of electricity, covering 15% of the electricity demand in the EU-27+UK, with 12.2% from onshore and 2.8% from offshore wind power plants. This was 1.4% lower than the previous year and similar to the wind energy share in 2019. The six countries with the highest wind energy share in 2021 were Denmark (44%), Ireland (31%), Portugal (26%), Spain (24%), Germany (23%), and the United Kingdom (22%) in 2021, [2,3].

Older wind energy plants have wind turbines with large generators and relatively short rotor blades, which are best suited for high wind areas. Newer wind parks are built in locations with lower wind speeds, since the best windy sites have already been occupied. Therefore, wind turbines with longer blades and smaller generators are used to improve their capacity factor. The capacity factor of new onshore wind parks is estimated to be between 30-35%, while it ranges from 42-55% for new offshore wind parks, [2].

In 2021, the average capacity factor of all wind plants in the EU and the United Kingdom was 24%, which was 3% lower than in 2020. The capacity factor for onshore plants was 23%, a 2% drop from the previous year, while for offshore plants capacity factor fell from 42% to even 35% in 2021, [2].
Most of the papers on capacity factor are actually analyses that try to choose optimal wind turbines for specific locations. Though there are many papers dealing with the issue of capacity factor calculations based on estimated

or measured wind speed at one location, this type of data is often limited by several factors, [4-7]. In his paper Boccard [4] presents some capacity factor estimates, mostly obtained by computational models.

Predictions of capacity factors ranging from 30-40% are common in evaluating wind power's potential. However, Boccard's detailed analysis [4] found that the average capacity factor for European wind parks was below 21%. According to data from the Energy Information Agency (EIA) and the Global Wind Energy Council (GWEC), Larsen & Rez determined that the average capacity factor for all wind plants between 2004-2010 was 25% in the US, 23% in the United Kingdom and Denmark, and 17% in Germany [5].

Bosnia and Herzegovina is considered to have a substantial opportunity for establishing wind farms, as evidenced by references [8-12]. The first wind farm was put into operation in 2018. After that, two more wind farms were built, so the total power of the wind farms is 135 MW. This is, of course, well below Bosnia's wind energy potential. In the energy mix, these wind plants produce a modest amount of energy of a few percent, [13]. Three wind farms in Bosnia and Herzegovina have been in operation for some time. In this paper, the capacity factor of these wind farms will be analyzed and compared with wind farms in Europe, as well as it will be analyzed the indicators of wind parks productivity: (GWh/unit), (GWh/MW), and (kWh/m^2).

2. METHOD

The capacity factor measures the efficiency of a wind turbine or wind farm in utilizing the available wind resource. It is determined as a percentage by dividing the Annual Energy Production (AEP) by the theoretical maximum energy output:

$$CF = \frac{P_{AEP}}{P_{teor}} \tag{1}$$

CF is a dimensionless quantity. For a given site's wind conditions, a wind park with higher *CF* is better designed and produces more electricity. The maximal *CF* is 1 (or 100%), but the wind is not permanent, so it is in fact not possible to reach this value. As depicted in Fig. 1, the wind parks (shown in green) in Bosnia and Herzegovina are situated in the southern region, where the Bora wind is most prevalent.

Figure 1. Wind parks in Bosnia and Herzegovina (green color)

The Bora is a strong and cold katabatic wind that typically blows from the north to northeast, starting suddenly and slowing down gradually. It can last for several days and can be either anticyclonic (dry) or cyclonic (cloudy). The conditions required for the Bora wind include mountainous terrain, varying temperatures and pressures in high and low elevations, etc. The Bora occurs along the eastern coast of the Adriatic Sea and in its hinterland. Further research on this unique wind, particularly in the hinterland, is still needed [14].

The first wind farm in Bosnia and Herzegovina was put into operation is Mesihovina in 2018. The Jelovača wind farm was put into operation in early 2019, and in 2021 the Podveležje wind farm was put into operation. [15-19]. Table 1. shows the wind parks analyzed in this paper and the wind turbines used at those wind parks.

Table 1. Wind parks characteristics in Bosnia and Herzegovina

Wind farm	Total nominal power and turbine type	WGS84
Mesihovina	50.6 MW 22 × Siemens SWT-2.3 (power 2.3 MW, diameter 108 m)	Latitude: 43° 36' 51" Longitude: 17° 13' 57.9"
Jelovača	36.0 MW 18 × Gamesa G97/2000 (power 2.0 MW, diameter 97 m)	Latitude: 43° 45' 3.4" Longitude: 17° 8' 42.8"
Podveležje	48.0 MW 15 × Siemens SWT-3.2 (power 3.2 MW, diameter 113 m)	Latitude: 43° 20' 37.1" Longitude: 17° 51' 45.5"

Data on the characteristics of wind farms were taken from companies and relevant institutions, [15-20]. Thus, a total of 55 wind turbines (units) with an average power of 2.45 MW/unit have been installed in Bosnia and Herzegovina.

3. RESULTS AND DISCUSSION

Data on the expected production was taken from the websites of wind parks (WP) owners [15,17,19]. Electricity data for all wind parks was taken from the official websites of the System Operator (NOSBiH), [21]. The electricity production of wind farms shows in Fig. 2.

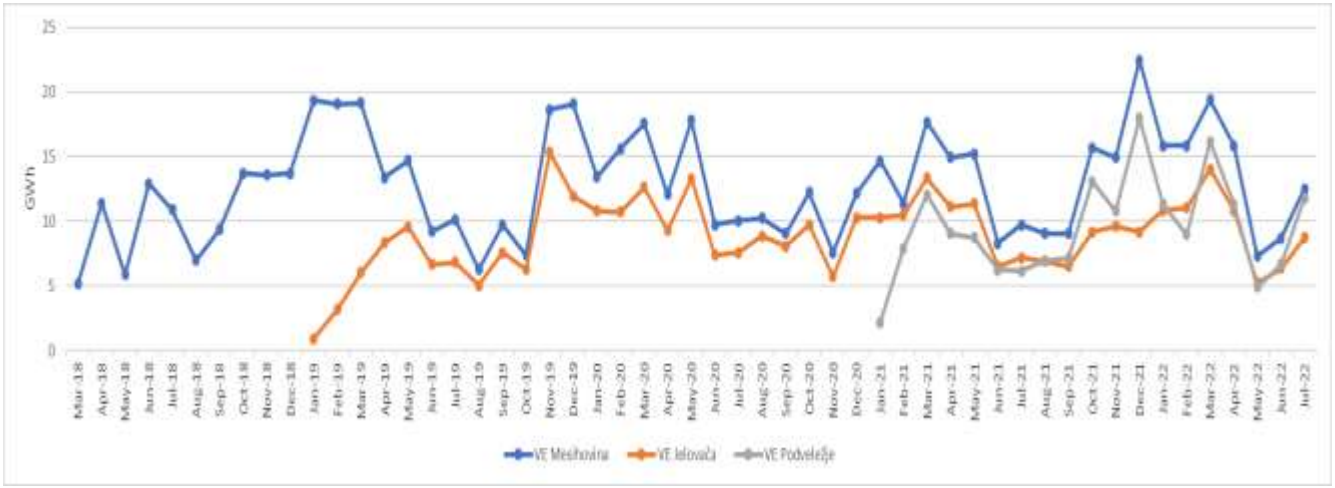

Figure 2. Electricity from wind parks in Bosnia and Herzegovina

WP Mesihovina was the first to start production in March 2018, Fig. 2. The first 6 months for all power plants is considered the trial operation of the plant, [22]. For that part of 2018 (7344 hours) *CF* was 27.8%, while for 2019 CF was 37.4%. In January 2019, WP Jelovača started working (and in the first 6 months of the trial operation); *CF* was 27.8%. In 2020, CF was 33.2% for WP Mesihovina and 36.2% for WP Jelovača. Better results were recorded in 2021, they amounted to 36.7% for WP Mesihovina and 35.4% for WP Jelovača, while for WP Podveležje, which started trial operation at the beginning of 2021, *CF* amounted to 25.7%.

If analyzing the 12-monthly period when all three wind farms were in full operation (July 2021 - Jun 2022), then *CF* is 36.9% for WP Mesihovina, 33.9% for WP Jelovača and 28.9% for WP Podveležje, as depicted in Tab. 2.

Table 2. Average capacity factors

Wind farm	Electricity from nameplate capacity (GWh)	Energy from wind farm (GWh)	Capacity factor %	Expected electricity (GWh)
Mesihovina	443.26	163.76	36.9	165.17
Jelovača	315.36	106.81	33.9	110
Podveležje	420.48	121.50	28.9	130

The capacity factor, which varies based on location and wind speed characteristics, is estimated to be between 30-35% for new onshore wind parks [2]. It is expected that the average capacity factor of all wind parks in the EU will rise to 29% in 2020 and 33% in 2030 [23]. Repowering, optimal placement, and optimized design of wind turbines are expected to enhance the overall efficiency of onshore plants. However, in 2021, the capacity factor for onshore plants in Europe decreased to 23% (from 25% in 2020) [2].

There are several indicators of the productivity of wind parks, including generation per turbine (GWh/unit), annual generation per unit of power output (GWh/MW), and specific yield, which is the generation per unit area covered by the rotor of the turbine (kWh/m2). The values of these measures are presented in Table 3 for wind parks in Bosnia and Herzegovina.

Table 3. Indicators of wind parks productivity

Wind park	Electricity per wind turbine (GWh/unit)	Electricity per MW wind turbine (GWh/MW)	Electricity per turbine rotor area in a year (kWh/m^2)
Mesihovina	7.44	3.24	812.96
Jelovača	5.93	2.97	803.42
Podveležje	8.10	2.53	808.07

If analyzing the 12-monthly period when all three wind farms were in full operation (July 2021 - Jun 2022), then the WP Mesihovina has the best indicator values with annual production of 7.44 GWh/units or 3.24 GWh/MW. Specific generation was 812.96 kWh/m^2 for WP Mesihovina. The WP Jelovača has the weakest results: 803.42 kWh/m^2 or 32.23% less than Mesihovina, see Tab. 3.

4. CONCLUSION

The EU has optimistic plans for wind energy [24]. One of the most important indicators for starting the wind project process is the capacity factor of the wind park (farm). At the EU level, a realized average capacity factor is lower than expected. In 2019, wind power plants in Bosnia & Herzegovina, with the total power of the wind parks 135 MW (55 wind turbines), produced 1.66% of total electricity, in 2020 it was 1.76% and in 2021 2.34%.

The capacity factor is the highest during winter, then during spring in Bosnia and Herzegovina. The average capacity factor for wind parks in Bosnia and Herzegovina was 33.2% (July 2021 – Jun 2022). The highest is for the Mesihovina wind park, at 36.9%, followed by Jelovača 33.9%, and the Podveležje wind park 28.9%. The average values of productivity indicators of all wind parks in Bosnia and Herzegovina are 7.6 GWh/unit, 2.9 GWh/MW, and 808.15 kWh/m^2/year, which are also good values. This is data for only one year (12 months), and in a longer period of time data will be obtained that will give a more realistic picture of the capacity factor and productivity indicators.

REFERENCES

[1] GWEC. Global wind report 2022. Global Wind Energy Council, 2022
[2] Wind Europe. Wind energy in Europe. 2021 Statistics and the outlook for 2022-2026. WindEurope Business Intelligence, 2022
[3] Wind Europe. Financing and investment trends The European wind industry in 2021. WindEurope Business Intelligence
[4] Boccard, N., Capacity factor of wind power realized values vs. estimate. *Energy Policy*, *37* (2009), 7, pp. 2679-2688
[5] Larsen, T.C. & Rez, P., Estimates of the Capacity Factor of Wind Farms in the United States. *J. Sustainable Energy Eng.*, *5* (2017), 3, pp. 194-206, https://doi.org/10.7569/jsee.2017.629514
[6] Kekana, H., & Landwehr, G., Wind capacity factor calculator, *Journal of Energy in Southern Africa, 30,* (2019), 2, pp. 118–125

[7] Diyoke, C., A new approximate capacity factor method for matching wind turbines to a site: case study of Humber region, UK, *International Journal of Energy and Environmental Engineering, 10* (2019), pp. 451–462
[8] Zlomušica, E., Wind Energy Resources in Bosnia and Herzegovina, *Thermal Science, 14* (2010), 1, pp. 255-260
[9] Ćatovic, F., Behmen, M., and Zlomušica, E., Trends in the development of the electric power systems based on wind energy in world and in Bosnia and Herzegovina, *Journal of Environmental Protection and Ecology-Official Journal of the Balkan Environmental Association (B.EN.A), 5* (2004), 4, 836-840
[10] FP6 Project: South-East Europe Wind Energy Exploitation – Research and demonstration of wind energy utilisation in complex terrain and under specific local wind systems, http://www.seewind.org
[11] Indicative Production Development Plan, 2013-2022, NOS BiH, Sarajevo, 2012
[12] Study of Energetic sector in Bosnia and Herzegovina, Energetski institut Hrvoje Pozar - Croatia, Soluziona - Spain, Ekonomski institut Banjaluka - BH, Rudarski institut Tuzla – BH, 2008
[13] Energy Statistics. Agency of Statistics of Bosnia and Herzegovina, https://bhas.gov.ba/data/Publikacije/Saopstenja/2021/ENE_03_2020_Y1_1_BS.pdf
[14] Zlomušica, E., Particular Review on SODAR and LIDAR Measurements of Bora Wind in Mostar, Bosnia and Herzegovina, *International Journal of Engineering & Technology IJET-IJENS, 13,* (2013), 6, pp. 53-61
[15] Svečano puštena u pogon prva vjetroelektrana u BiH (Ceremonially put into operation the first wind farm in B&H), https://www.ephzhb.ba/svecano-pustana-u-pogon-prva-vjetroelektrana-u-bih/?lang=en, (in Bosnian)
[16] Siemens SWT-2.3-108, https://www.thewindpower.net/turbine_en_403_siemens_swt-2.3-108.php
[17] Vjetropark Jelovača (Wind farm Jelovača), https://bih.sika.com/bs/projektne-reference/local-references/vjetropark-jelovaca.html, (in Bosnian)
[18] Gamesa G97, https://en.wind-turbine-models.com/turbines/764-gamesa-g97
[19] Završena izgradnja VE Podveležje 1 (Completed construction of VE Podveležje 1), https://www.epbih.ba/novost/32012/zavrsena-izgradnja-ve-podvelezje-1, (in Bosnian)
[20] https://en.wind-turbine-models.com/turbines/966-siemens-swt-3.2-113
[21] Independent System Operator in Bosnia and Herzegovina (NOSBiH). Reports of Electricity flows, https://www.nosbih.ba/en/trziste/izvjestaji-o-tokovima-el-energije
[22] Law on the Use of Renewable Energy Sources and Efficient Cogeneration. Official Gazette of the Federation of BiH, number 70/13 and 5/14
[23] Wind Energy - The Facts. Chapter 1: Scenarios for the EU-27, EWEA, 2008
[24] Wind energy in Europe: Scenarios for 2030, WindEurope, 2017.

RIGA 2023

Experimental Study and Modeling of Solar Drying in a Ventilated Attic

Zokagon Aristide Tieu
Université Félix Houphouet-Boigny, Abidjan, Côte d'Ivoire, tieu_aristide@yahoo.fr, 0000-0002-5155-3209

Ekoun Paul Magloire Koffi,
Institut National Polytechnique Félix Houphouet-Boigny, Yamoussoukro, Côte d'Ivoire, paumagloirel@yahoo.fr, 0000-0001-6164-537X

Kamenan Blaise Koua
Université Félix Houphouet-Boigny, Abidjan, Côte d'Ivoire, kouakb@yahoo.fr, 0000-0003-1091-1492

Prosper Gbaha
Institut National Polytechnique Félix Houphouet-Boigny, Yamoussoukro, Côte d'Ivoire, pgbaha@yahoo.fr, 0000-0001-9168-779X

Cite this paper as: *Tieu, ZA, Koffi, EPM, Koua,KB, Gbaha P. Experimental study and modeling of solar drying in a ventilated attic. 11. Eur. Conf. Ren. Energy Sys. 18-20 May 2023, Riga, Latvia*

Abstract: In most African countries, the availability of sunlight can allow drying in the attic of metal-roofed houses. A prototype ventilated attic has been constructed and tested for drying cocoa and cassava. The temperature differences between the air inside the PVC pipes used as chimneys and the air outside are close to 11° C and show that the air is circulating in the prototype. The drying of cassava and cocoa took 26 h and 27 h respectively. The semi-empirical Midilli-Kucuk and logarithmic equations best describe the drying curves of cassava and cocoa, respectively. The variation in drying air humidity is modeled by the 4th order Runge-Kutta method. The small difference between the measured and calculated values shows that the modeling describes well the variation of relative air humidity during cocoa drying. The measuring instruments used are: a Kipp and Zonen CMP 10 pyranometer (for sunshine), K-type sensors connected to Voltcraft pl-120 thermometers (for temperatures). FY-11 thermo-hygrometers (for air temperature and hygrometry)

Keywords: *Solar drying, ventilated attic, modeling, cocoa beans, cassava*

1. INTRODUCTION

In the sunny areas of the world and in particular for many African countries, the sun is available all year round, abundant and easy to capture. For these regions, mastering solar energy applications such as photovoltaics, solar heating, solar cooling and refrigeration would be a real advantage. In fact, all forms of energy in the world as we know it are of solar origin [1]. Post-harvest losses are indexed as one of the causes of rural hunger in these countries. The oldest method of food preservation is sun drying. But traditional drying has its limitations, and farmers in African countries would benefit from investing in solar dryers. Several research efforts to improve the old method are being undertaken. Roberto L. M. et al. [2] undertook an experimental and then numerical study of the drying of papaya. Different studies of food drying have been undertaken by Merlin Simo-Tagne et al. [3], [4], [5]. B. Norton [6] presented some criteria to which the dryers should be subjected depending on the type of product to be dried. Barreiro et Sandoval [7] undertook the modeling of moisture absorption of cocoa beans during storage. Attic drying is an old method still used in West Africa for the conservation of foodstuffs. The literature hardly mentions it because research work is not sufficiently directed in this direction. The products to be dried are generally spread out on bamboo racks. The heat produced by the wood smoke affects the color and taste of the dried product. Sometimes the product dries under the action of the air circulating in the loft. But the flow being very low, the drying process is very slow, which favors the formation of mold and the rotting of the products. This results in poor

quality products that are difficult to sell. The immediate corollary is the maintenance of the farmer in poverty. With modern aluminum-zinc roofs, it is possible to use them to improve this old method. Always exposed to the sun, they constitute a real source of unexploited energy. A prototype ventilated attic is built and used for solar drying of cassava and cocoa. The study of the chimney draft is carried out experimentally. The drying curves are modeled using the semi-empirical desorption equations. The evolution of the relative humidity of the drying air is also modeled.

Figure 1. Traditional drying in an attic

2. MATERIALS AND METHODS

2.1. Presentation of the Prototype

The prototype studied is a part of a roof (Fig. 2). It has three chimneys made of PVC pipes. The roof is a corrugated aluminum-zinc sheet covered with black paint in order to store enough heat and inclined 10° from the horizontal surface.

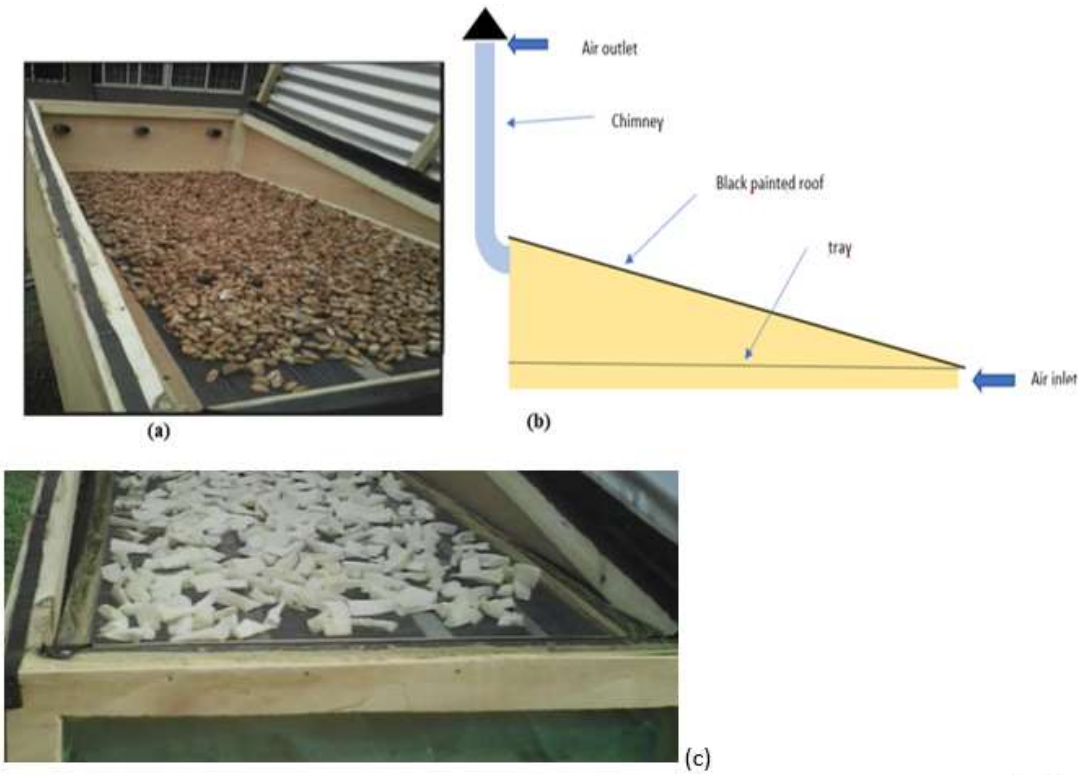

Figure 2. (a) Prototype with coca beans inside, (b) Profile view of the prototype, (c) Air inlet.

The drying rack is horizontal and made of nylon. The latter is mounted on a wooden frame. The air inlet is covered with an iron grill to prevent rodents or birds from entering. The ceiling of the prototype and the sides are made of plywood. The interior volume is about 0.24 m^3. The drying surface is 1.48 m^2. The whole thing is mounted on a 2.5 m support in order to have the height of a roof. We dried cassava and then cocoa. In this study, for cassava, we just modeled the variation of water content. The relative humidity and temperature variations were recorded during the drying of cocoa beans.

2.2. Study of the Chimneys

Ekechukwu et Norton [8] showed that the air velocity in a cylindrical, vertical chimney is related to ΔT_{ch} (rise of chimney air temperature over ambient air temperature). Indeed, in the operating temperature range of natural convection dryers (25°C - 90°C), the pressure drops inside the chimney are given by [9]:

$$\mathbf{\Delta P = 0.00308gH(T_{ch} - T_a) = 0.00308gH(\Delta T_{ch})} \quad \textbf{(1)}$$

These losses are related to the friction of the air on the wall of the chimneys by the following expression (considering a turbulent regime with a friction coefficient of 0.03):

$$\Delta P = 0.03\bar{\rho}\left(\frac{v^2 H}{2D}\right) \quad (2)$$

Combining these two equations, we obtain:

$$\mathbf{v = 0,453\left[\frac{Dg}{\bar{\rho}}.\Delta T_{ch}\right]^{1/2}} \quad (3)$$

This equation does not take into account the effect of humidity on the air speed, friction with the product and in the drying chamber, the following expression will be used:

$$\mathbf{v = f(\Delta T_{ch})^{1/2}} \quad (4)$$

2.3. Modeling of Drying Curves

Various equations give the decay, during drying, of the water content as a function of time. These equations contain constants (k, n, a, b) that are adjusted to match the experimental drying curves. For the modeling of our curves, we used 6 semi-empirical models. They are collected in the table below. The software used for this modeling is Excel solver.

Table 1. Semi-empirical models used

Models	Expression
Newton	$X = exp(- kt)$
Page	$X = exp(-kt^n)$
Henderson et Pabis	$X = a\ exp(-kt)$
Logarithmique	$X = a\ exp(-kt)+b$
Two terms	$X = a\ exp(-kt)+b\ exp(-nt)$
Midilli-Kucuk	$X = a\ exp(-kt^b)+nt$

The statistical parameters used for the choice of the best model are: a higher value of the coefficient of determination R^2 and lower values of χ^2 and root mean square error RMSE [10]:

$$\mathbf{RMSE} = \sqrt{\frac{1}{N}\sum_{i=1}^{N}\left(x_{iexp} - x_{ipre}\right)^2} \quad (5)$$

$$\chi^2 = \frac{\sum_{i=1}^{N}\left(x_{iexp} - x_{ipre}\right)^2}{N-n} \quad (6)$$

$$R^2 = 1 - \frac{\sum_{i=1}^{N}\left(x_{iexp} - x_{ipre}\right)^2}{\sum_{i=1}^{N}\left(\overline{x_{iexp}} - x_{ipre}\right)^2} \quad (7)$$

2.3. Modeling of Humidity Variation in the Prototype

Mass transfer in the prototype in the is expressed as follows [11] :

$$m_a \frac{dY_s}{dt} - \dot{m}(Y_e - Y_s) + m_0 \frac{dX}{dt} = 0 \quad (8)$$

x(t) is obtained from modeling the drying curve. The water content of the air is given by the following expression [12] where P (≃101325 Pa) est la pression ambiante, is the ambient pressure, Hr is the measured relative humidity of the air, and Ps(T) is the saturation vapor pressure obtained with the Dupré formula [13] given as a function of temperature.

$$Y_e = \frac{0.622}{\frac{P}{Hr.Ps(T)} - 1} \quad (9)$$

$$Ps(T) = e^{\left[46.784 - \frac{6435}{T+273,15} - 3.868 \ln(T+273,15)\right]} \quad (10)$$

In order to solve equation (8) by the 4th order Runge-Kutta method, we rewrite it in function form as follows (we admit that $\rho_{air} = 1.2\ kg/m^3$) :

$$f(Y_{s,n}, t_n) = \frac{\dot{m}}{m_a}(Y_e(t_n) - Y_{s,n}) - \frac{m_0}{m_a}\frac{dX(t_n)}{dt} \quad (11)$$

$Y_s(0)$ is the water content of the air in the morning at the beginning of the drying and h = 30min (1800s) is the time step. The algorithm is as follows :

$$K_1 = h\, f(Y_{s,n}, t_n)\ ;\ K_2 = h * f\left(Y_{s,n} + \frac{K_1}{2}, t_n + \frac{h}{2}\right)\ ;\ K_3 = h\, f\left(Y_{s,n} + \frac{K_2}{2}, t_n + \frac{h}{2}\right);$$
$$K_4 = h\, f(Y_{s,n} + K_3, t_n + h)\ ;\ Y_{s,n+1} = Y_{s,n} + \frac{1}{6}(K_1 + 2K_2 + 2K_3 + K_4)\ ;\ t_{n+1} = t_n + h$$

3. RESULTS AND DISCUSSIONS

Our study of the stacks is concerned with the variation of the air temperatures in the stacks in relation to the variation of the ambient temperature. Fig. 3 below shows the variations of the average temperature values in the three stacks, the temperature of the drying chamber, the ambient temperature and the ambient relative humidity with sunshine. It can be seen that the ambient temperature varies around 30° C with maximum values up to 32.6, 33.6 and 31.8 °C respectively on these three days. The internal temperatures of the stacks varied from 26.8 to 44.8 °C, from 25.9 to 43.5 °C and from 23.7 to 43.4 °C respectively on the 1st, 2nd and 3rd day. The temperature differences ΔT_{chmax} were 12.2°, 11.5°, and 11.7 °C successively on all three days. These values are close to those obtained by [8] and testify that PVC pipes are suitable as solar chimneys. The ambient relative humidity reached minimum values of 64% on the first two days and 74% on the last day. These temperature and relative humidity variations are favored by adequate sunlight, whose maximum values are close to 1000w/m².

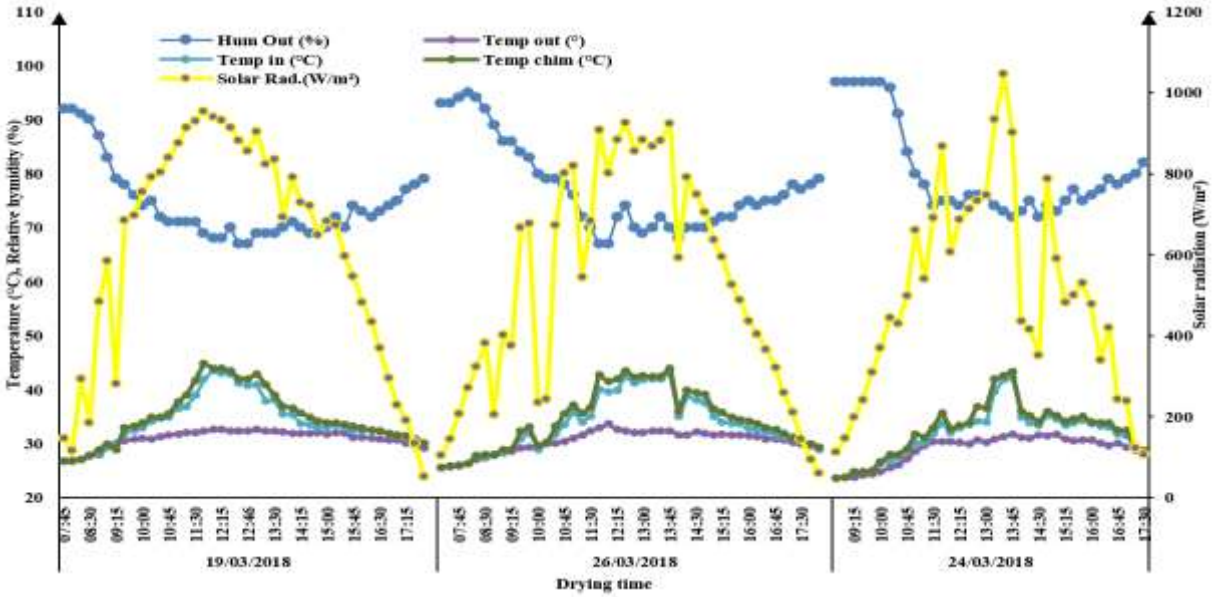

Figure 3. Humidity and temperature variations in the prototype, in the chimneys and in the ambient air with solar radiation.

Fig. 4 below shows the variations in product moisture content. During both trials, we loaded the prototype with 2.5 kg of cassava and then with 2.5 kg of cocoa beans. Mass measurements were made at various intervals, depending on how easy it was to observe the variations. We stopped measuring when no more variation in mass was observed. The initial water content of cassava is assumed to be 1.63 kg water/kg [14] and that of cocoa 1.22 kg water/kg [15] on a dry basis. At the beginning of drying, the curves decrease rapidly because of the presence of a lot of free water easy to remove. Towards the end of drying, the water remaining in the product is very much attached to it, which explains a very small variation in the curve. The results of the curve modeling are presented in Tables 2 and 3 below. For the cassava drying curve, the Midilli-Kucuk model is used. For the cocoa drying curve, the logarithmic model is appropriate.

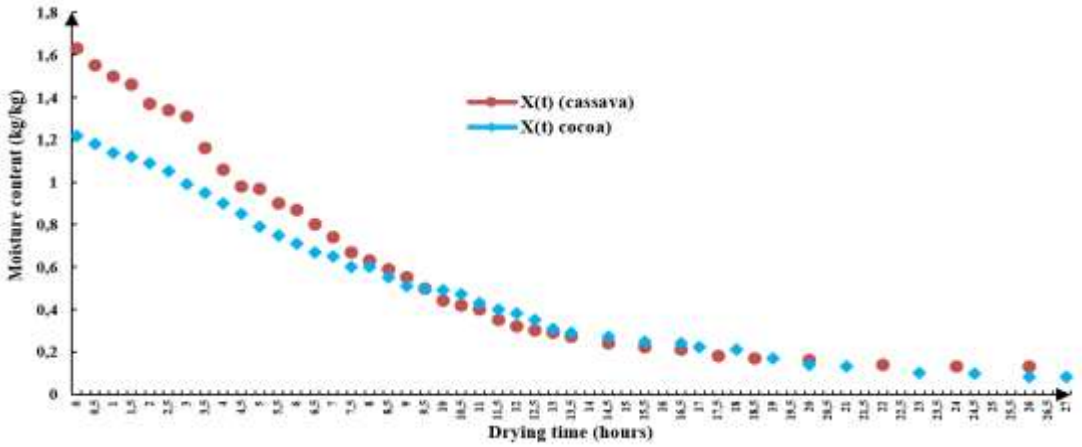

Figure 4. Experimental curve of the decrease of the water content of cassava and cocoa

Table 2. Cassava drying curve modeling results

Model	**a**	**k**	**b**	**n**	**R²**	**χ²**	**RMSE**
Newton		0.1			0.699	0.094	0.3024
Page		0,0011		2,82	0.866	0.0404	0.196
Henderson and Pabis	1.85	1.145			0.960	0.0104	0.0994
Logarithmic	1.85	1.14	0		0.960	0.0107	0.0994
Two terms	0.93	0.14	0.92	0.14	0.961	0.0107	0.098
Midilli-Kucuk	1.565	0.044	1.46	0.0005	0.977	0.0065	0.076

Table 3. Cocoa drying curve modeling results

Model	a	k	b	n	R^2	χ^2	RMSE
Newton		0.089			0.8201	0.0273	0.1631
Page		0.0088		1.939	0.937	0.00947	0.0948
Henderson and Pabis	1.395	0.122			0.932	0.01007	0.0978
Logarithmic	1.1	0.089	0		0.981	0.0028	0.0515
Two terms	0.698	0.122	0.698	0.122	0.932	0.0106	0.0978
Midilli-Kucuk	1.175	0.032	1.49	0	0.955	0.0071	0.0804

Indeed, these two models have the lowest values of χ^2 and RMSE and the highest values of coefficient of determination. The modeling of the variation in water content is done during the drying of cocoa beans. Therefore, the semi-empirical equation of x(t) is as follows:

$$x(t) = 1.1\, exp(-0.089t) \quad (12)$$

$$\frac{dx(t)}{dt} = -\mathbf{0.0979}\ \mathbf{exp}(-\mathbf{0.089t}) \quad (13)$$

Fig. 5 below shows the measured and simulated relative humidity variations of the drying air with Matlab R2014b. The statistical parameter used is the Mean Relative Error (MRE). The value of 4.67% found shows that the calculations represent well the measured values.

$$MRE = \frac{100}{N}\frac{|H_r\, exp - H_r\, theo|}{H_r\, exp} \quad (14)$$

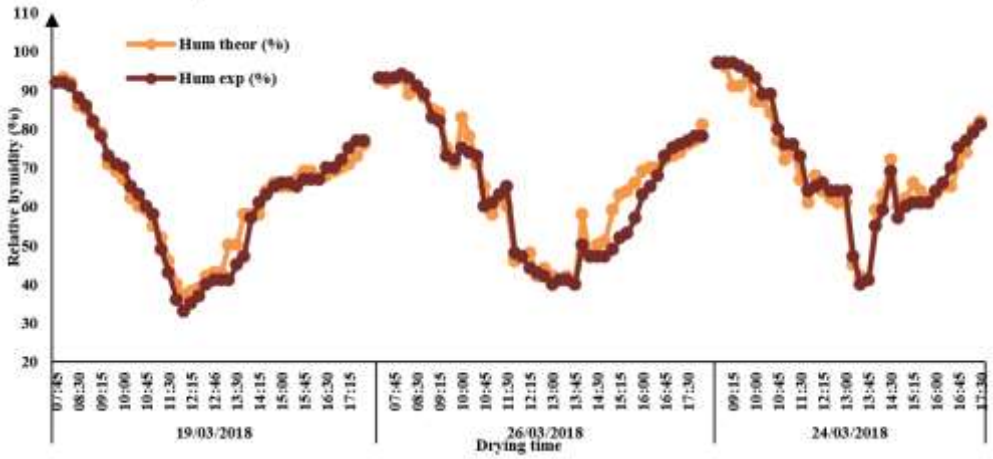

Figure 5. Variations of experimental and calculated relative humidity (MRE=4.67%)

4.CONCLUSION

The possibility of using ventilated granaries with metal roofs to improve the traditional drying of agricultural products in the granary is studied. For this purpose, a prototype of ventilated granaries equipped with PVC pipe chimneys was built and tested for drying cassava and cocoa beans. The differences between the internal temperature of the chimneys and the ambient temperature show that they are appropriate for their role. The drying of the products lasted 03 days for each sample of 2.5 Kg. The modeling of the drying curves with six semi-empirical models showed that the Midilli-Kucuk model best predicted the drying curve of cassava. As for the cocoa drying curve, the logarithmic model is suitable. The relative humidity variation in the prototype during cocoa drying is modeled with the Runge-Kutta method of order 4. The low value of the MRE (4.67%) shows that the calculated values are in agreement with the experimental values. We plan to build a prototype in real size and able to dry larger quantities and for measurements over various periods of the year.

REFERENCES

[1] Kalogirou S A. Solar Energy Engineering Processes and Systemes, Second Edition, San Diego, USA: Elsevier, 2014.

[2] Roberto A L, Carlos E Z, Antonio V G, Nelson O M. Coupled 3D heat and mass transfer model for numerical analysis of drying process in papaya slices. Journal of Food Engineering 2013; 116:109-117 <http://dx.doi.org/10.1016/j.jfoodeng.2012.10.050>

[3] Macmanus C N, Merlin S T. Study on the effect of conical and parabolic solar concentrator designs on hybrid solar dryers for apricots under variable conditions: A numerical simulation approach. International Journal of Green Energy 2021; 18:1-20 <https://doi.org/10.1080/15435075.2021.1914632>

[4] Merlin S T, Hermann T E, Ablain T T, Macmanus C N, Maryam E M. Energy, environmental and economic analyses of an indirect cocoa bean solar dryer: A comparison between natural and forced convections. Renewable Energy 2022. 187:1154-1172 <https://doi.org/10.1016/j.renene.2022.02.015>

[5] Merlin S T, Ablain T T, Macmanus C N, Lyes B, Marcel B O A, Maryam E M, Yann R. Numerical Study of the Drying of Cassava Roots Chips Using an Indirect Solar Dryer in Natural Convection. AgriEngineering 2021, 3: 138–157 <https://doi.org/10.3390/agriengineering3010009>

[6] Brian N. Characteristics of different systems for the solar Drying of Crops. Solar Drying Technology Springer 2017, 10: 978-981 <doi:10.1007/978-981-10-3833-4>

[7] Jose A B, Aleida J S. Kinetics of moisture adsorption during simulated storage of whole dry cocoa beans at various relative humidities. Journal of Food Engineering 2020, 273 <https://doi.org/10.1016/j.jfoodeng.2019.109869>

[8] Ekechukwu O V, Brian N. Design and measured performance of a solar chimney for natural-circulation solar-energy dryers. Renewable Energy 1997, 10: 81-90 < https://doi.org/10.1016/0960-1481(96)00005-5>

[9] Brenndorfer B, Kennedy L, Bateman C 0 0, Mrema G S. Solar Dryers-Their Role in Post Harvest Processing. London, UK: Commonwealth Secretariat, 1985.

[10] Pechaporn P, Morakot K, Raksuda S, Prysathryd S, Chinnathan A. Effect of temperature and shape on drying performance of cassava. Agriculture and Natural Resources 2017, 51: 402-409 <https://doi.org/10.1016/j.anres.2017.12.004>

[11] Bilal L, Abdeslam D. Thermal performance and economic analysis of an indirect solar dryer of wood integrated with packed-bed thermal energy storage system: A case study of solar thermal applications. Drying Technology 2020, 39: 1371-1388 <https://doi.org/10.1080/07373937.2020.1750025>

[12] Merlin S T, Macmanus C N, André Z, Lyes B, Fatima K S, Yann R. Numerical analysis and validation of a natural convection mix-mode solar dryer for drying red chili under variable conditions. Renewable Energy 2019, 151: 659-673 <https://doi.org/10.1016/j.renene.2019.11.055>

[13] Yves Jeannot, L'air Humide, Paris, FRANCE: CNRS, 2005.

[14] Koua B K, Fassinou W F, Gbaha P, Touré S. Etude expérimentale de la cinétique de séchage du manioc dans un séchoir solaire directe muni d'un circulateur thermique. Rev. Ivoire sci. Technol. 2007. 9:11-26

[15] Aka S K, N'Goran Y, Kouakou K, Denis B, Adama T, Diby K A, Saraka J K. A numerical model of cocoa beans drying kinetics in an indirect solar and air crossing dryer. International Journal of Inovation and Applied Studies 2018. 23:717-731

RIGA 2023

Benchmark of Electronic Controllers in a Biofuel Production Plant

Lenin Calero
Universidad Politécnica Salesiana, Ecuador, lcaleroa1@est.ups.edu.ec

Christian Castillo
Universidad Politécnica Salesiana, Ecuador, ccastilloh@est.ups.edu.ec

William Oñate
Universidad Politécnica Salesiana, Ecuador, wonate@ups.edu.ec

Sebastián Taco-Vasquez
Escuela Politécnica Nacional, Ecuador, sebastian.taco@epn.edu.ec

Gustavo Caiza
Universidad Politécnica Salesiana, Ecuador, gcaiza@ups.edu.ec

Cite this paper as: *Calero, L, Castillo, C, Oñate, W, Taco-Vasquez, S, Caiza, G, Benchmark of Electronic Controllers in a Biofuel Production Plant. 11. Eur. Conf. Ren. Energy Sys. 18-20 May 2023, Riga, Latvia*

Abstract: The availability of renewable energy sources to fulfill energy demand requires technological energy efficiency in all knowledge areas. In this context, and delving into electronic controllers through a systematic literature review, it is found a great variety of such controllers that have been implemented and simulated on industrial processes focusing on performance and robustness, but not on the energy that they consume based on the algorithm implemented and on the type of development board. On the other hand, there is a lack of studies about controllers implemented in biofuel production processes as a type of renewable energy. Thus, this study developed a heterogeneous packed bed reactor (PBR) for the production of biofuel, in which models of the behavior of the temperature in the plant are used to tune, adjust and self-tune PI, PID and self-tuning PID controllers; the performance of these controllers is further compared. Results show that it was possible to produce biofuel, and besides it was achieved a reduction in energy consumption of the controllers corresponding to 6.88% for phase 2 and 20% for phase 3, with improved temperature settling times of 2s for phase 2 and 47s for phase 3.

Keywords: *Renewable energy, technological energy efficiency, biofuel production process, electronic controllers*

1. INTRODUCTION

Several years ago, the idea that renewable energies would become capable of fulfilling future worldwide energy needs was a utopia. Despite this, a Regional Energy Deployment Simulation (ReEDS) model developed in the National Renewable Energy Laboratory (NREL), indicated that 80% of the global energy supply for 2050 will come from renewable energies [1], i.e., net zero emissions (NZE). Nevertheless, to achieve these objectives, the International Energy Agency (IEA) [2] and [3] state that energy efficiency is one of the most important issues to obtain energy sustainability; in other words, each energy unit must contribute more than it does today for NZE [4].

Based on the above, there are different fields of study and subsystems that contribute to energy improvement of renewable energy systems. This is the case of [5], which simulates a plant that produces biofuel from recycled cooking oil, and analyzes the efficiency of the production costs through the study of the reversible and irreversible exergy. From the point of view food security, [6] establishes that biodiesel and bio gasoline do not use food crops, and thus do not affect such security; hence, its economically favorable sustainability would be guaranteed [7]. On the other hand, the use bioethanol as a biocomponent has decreased because it is extracted from corn [8]; this has led to technological setbacks, and lack of techno-economic analyses (TEA) and data for R&D [9]. Now, the following works can be found when tracing a path of electronic control systems that contribute to energy sustainability for the production of biofuels. A comparison is carried out in [10] between Fuzzy and PID controllers applied at the evaporation stage to improve the production of bioethanol; in addition, after a systematic review the authors state that there is a lack of comparative studies of the performance of traditional and robust controllers, and of commercial equipment. On the other hand, the review in [11] specifies that traditional methods for mass production of biofuels are no longer feasible and, thus, it is required intelligent machines with energy efficiency and energy saving features in their processes. Nevertheless, since this is a recent technology, [12] states that barely 10% of the academic papers are aimed at the industrial area, of which only 24% are implemented in different production branches and there is a lack regarding the production of biofuels.

Based on the literature review, a deficit is found regarding the implementation of electronic control systems in biofuel production processes, for the analysis of the performance and consumption variables of such controllers. Thus, this paper designed a PBR with laboratory features to obtain biofuel from the injection of ethanol, to further implement different classical PI and PID temperature control systems in the preheater and reactor stages. Afterwards, the performance variables are compared with respect to a commercial industrial system for digital control of temperature (self-tuning PID), evaluating settling times, power absorbed and energy consumed. Finally, the elements that constitute the obtained condensable hydrocarbon are identified through a mass percentage analysis.

The document is structured as follows. Section 1 presents the introduction, section 2 describes the methodology, section 3 analyzes the results, and finally section 4 states the conclusions.

2. MATERIALS AND METHODS

To obtain biofuel as the process output and to implement a control system for a chemical reaction plant that produces hydrocarbons, the following general aspects were taken into account: performance equation, contact model and kinetics. Considering that the input may be continuous or discontinuous, the contact depends on the type and number of phases, and it may be homogeneous or heterogeneous.

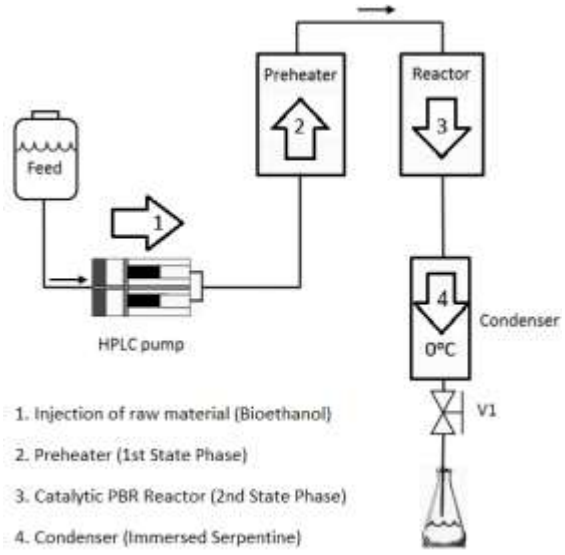

Figure 1. Stages of a packed bed catalytic reactor (PBR) (Adapted from [13]).

At last, it was analyzed the kinetics of the variables involved in the process, namely, volume, flow, temperature, spatial velocity, etc. This information is relevant for the development of a biofuel production plant for experimental use in an academic environment. Consequently, and based on the above, the design of the Packed Bed Catalytic Reactor (PBR) is extracted from, and Fig. 1 shows its schematic diagram.

2.1.Oligomerization process to hydrocarbon:

Using an HPLC peristaltic pump (phase 1), ethanol is injected as reactant fluid, which is then passed through the preheater (phase 2) to be dehydrated for obtaining a gaseous fluid with a spatial velocity (Weight hourly space velocity, WSHV) related to the mass flow and to the mass of catalyst (Zeolite HZSM-5 (280)) contained in the reactor (phase 3), as indicated by Eq. [1].

$$WHSV = \frac{m_{reactant}}{m_{catalyst}} \quad (1)$$

A $WHSV = 0.9468\ [h^{-1}]$ was obtained experimentally, injecting ethanol to an inlet mass flow of 2 $[ml/min]$. The catalyst used in phase 3 was the commercial HZM5, due to its features in industrial and environmental applications, and its synthesis activity persistence even when reutilized after various experiments [14].

In order to reach a laminar behavior of the fluid and based on the reactor design parameters, the calculated Reynolds number was 18.75, with a mass flow of $0.00043833\ [kg/s\ m]$, a pipeline diameter of $0.025\ [m]$ and a fluid dynamic viscosity [μ] of $0.00119\ [kg/s\ m]$. The oligomerization process to hydrocarbon was carried out in the city of Quito at $2977\ m.a.s.l.$; at atmospheric pressure and with temperatures of 300°C in phase 2 and 350°C for phase 3, it was guaranteed that the reactive boils without degrading, obtaining condensable hydrocarbons as products. At last, with an approximate temperature of 0°C in the condenser (phase 4), the liquid and gaseous phases separate to obtain a final product (gasoline).

2.2.Model of the PBR

For the process to obtain the biofuel it is necessary to have stable temperatures, both in the preheater and in the reactor; consequently, it is required to control this variable. The models of these systems were determined applying as input a step signal at the desired temperature, and obtaining output signals that represent the behavior during heating and cooling periods for the second and third state phases, as it is shown in Fig. 2.

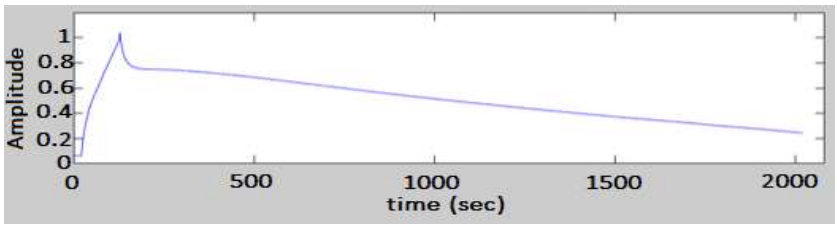

(a)

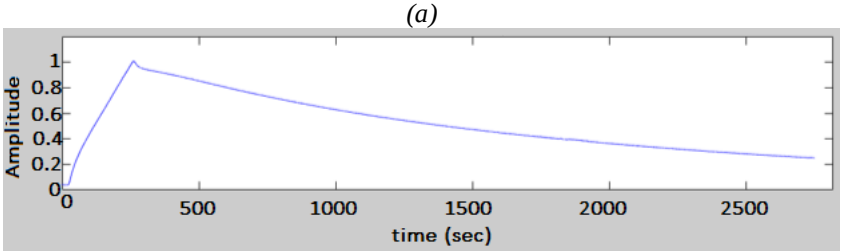

(b)

Figure 2. Models of the system behavior for phases 2 (a) and 3 (b).

Table 1 shows the continuous-time transfer functions of the PBR, obtained with the Matlab identification toolbox.

Table 1. Control Parameters of the PBR.

System parameters	Phase 2	Phase 3
Manipulated variable	PTO	PTO
Control variable	Temperature	Temperature
Disturbance	External temperature	External temperature
First–Order Approximation s-domain	$G(S) = \frac{0.006107}{s + 0.0006123}$	$G(S) = \frac{0.006107}{s + 0.0006123}$
Modeling accuracy	78,67%	94%

3. ANALYSIS OF RESULTS

Two classical control systems, namely PI and PID, were tuned. These control systems were considered with the purpose of analyzing information about performance and robustness in phases 2 and 3 of the PBR. Afterwards, the controller with the best performance will be compared with a commercial temperature controller.

3.1. PI and PID Controllers in Phases 2 and 3

For the step signal, the PI controller exhibits no overshoot in both heater and reactor; however, the settling times of its responses are 623 s and 840 s, respectively. On the other hand, the PID controller exhibits overshoots of 11.3% and 12.7% in the two phases, with settling times of 239 s and 291 s, respectively. Due to the control process and the results obtained, the PID controllers are considered for further comparison with the commercial self-tuning PID controllers. Table 2 shows the tuned parameters.

Table 2. Tuning parameters of the PID controllers in Phases 2 and 3 of the PBR

Control	P	I	Td
Phase 1	8.107	90.7151	1.565
Phase 2	12.37	77.8	1.71

3.2. PID and self-tuning PID Controllers in Phases 2 and 3

According to the datasheet, the digital temperature controller of the brand BERM REX-C100 exhibits features such a fast temperature control, fast response and low overshoot. In this context, a field test was conducted establishing independent set-points for each phase of the PBR, to obtain the settling times of the system and the energy consumption. Fig. 3 shows the results of energy consumption for the controllers subject to test, under equal external conditions as disturbance, same flow of ethanol injected to the preheater and same set-point.

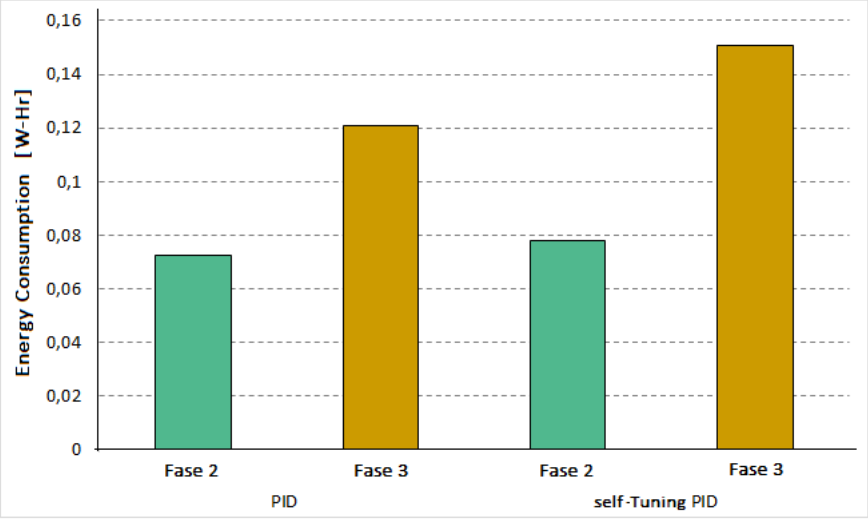

Figure 3. Energy Consumption of the PID and self-tuning PID controllers in phases 2 and 3.

According to the parametric conditions for obtaining biofuel in the PBR, a set-point of 300°C is established in phase 2, achieving settling times of 158s and 160s for the commercial self-tuning PID controller and the PID controller of the case study, respectively, and absorbing a mean power P_o of 1.75[W] and 1.65[W], respectively, which indicates, according to Fig. 3, that the PID controller reduces its energy consumption 6.88% with respect to the commercial controller. For the case of phase 3, the self-tuning PID and PID controllers settle at a temperature of 350°C in 263s and 310s, respectively, and the mean powers P_o absorbed were 1.50[W] and 1.75[W], respectively, indicating, according to Fig. 3, that the PID controller of the case study reduces energy consumption 20% with respect to the self-tuning PID controller.

3.3. Chemical Compounds in the Biofuel

Using a gas chromatograph, a test was conducted to determine the main organic compounds that constitute the samples given by the packed bed reactor. Taking into account that the main hydrocarbons present in the fuels are paraffins, isoparaffins, naphthenes, aromatic compounds, sulfur compounds and oxygenates, the concentration of each element that constitute the sample obtained is observed in Fig. 4.

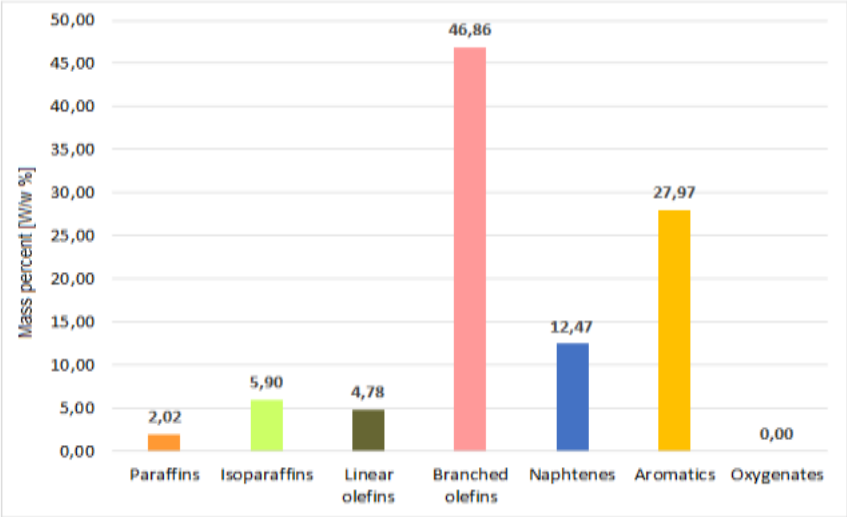

Figure 4. Concentration of the elements that constitute the sample obtained.

According to the compounds and the amount of area constituted in the resulting samples, in general terms the results correspond to a noncommercial biofuel, due to the low concentrations of paraffins.

4. CONCLUSIONS

Two After the experimental tests of the controllers in the biofuel PBR (preheater and reactor), it was observed that the availability of appropriate models of the behavior of the plant improve the responses of the performance variables, since during the comparison with the performance variables of the commercial controller it was evidenced a reduction in energy consumption of the controllers of 6.88% for phase 2 and 20% for phase 3, with a settling time of the temperature that is improved 2 s in phase 2 and 47 s in phase 3. On the other hand, the biofuel obtained shows noncommercial features, since it only has 16.83% of paraffins with respect to the base. For further studies, in addition to the temperature control systems for phases 2 and 3, it is recommended to also control pressure and flow to achieve a better production efficiency and different types of biofuels.

REFERENCES

[1] NREL-ReEDS, "| Regional Energy Deployment System Model (ReEDS) NREL." https://www.nrel.gov/analysis/reeds/index.html (accessed Jul. 21, 2022).
[2] AIE, "Net Zero by 2050 Scenario," 2021. https://www.iea.org/data-and-statistics/data-product/net-zero-by-2050-scenario.
[3] A. Fernández Pálid, S. Bouckaert, T. Abergel, and T. Goodson, "Net zero by 2050 hinges on a global push to increase energy efficiency," IEA París, 2021, [Online]. Available: https://www.iea.org/articles/net-zero-by-2050-hinges-on-a-global-push-to-increase-energy-efficiency.

[4] D. Crow, I. Handschuch, G. Saive, and L. Staas, “Do we need to change our behaviour to reach net zero by 2050?,” IEA Paris, 2021, [Online]. Available: https://www.iea.org/articles/do-we-need-to-change-our-behaviour-to-reach-net-zero-by-2050.

[5] H.-W. Hsu, E. Binyet, Y.-H. Chang, and W.-C. Wang, “Energy, economic and environmental (3E) analysis for the renewable jet fuel production process,” Sustain. Prod. Consum., vol. 33, pp. 146–157, 2022, doi: 10.1016/J.SPC.2022.06.026.

[6] A. S. Mohamed Boly, “Biofuels and food security: evidence from Indonesia and Mexico,” Energy Policy, vol. 163, p. 112834, 2022, doi: 10.1016/J.ENPOL.2022.112834.

[7] J. V. Tirkey, A. Kumar, and D. K. Singh, “Energy consumption, greenhouse gas emissions and economic feasibility studies of biodiesel production from Mahua (Madhuca longifolia) in India,” Energy, vol. 249, p. 123690, 2022, doi: 10.1016/j.energy.2022.123690.

[8] A. Piwowar and M. Dzikuć, “Bioethanol Production in Poland in the Context of Sustainable Development-Current Status and Future Prospects,” Energies, vol. 15, no. 7, pp. 1–13, 2022, doi: 10.3390/en15072582.

[9] P. Kumar, M. Latha, N. Prem, and P. Pabbathi, “Second-generation bioethanol production from corncob – A comprehensive review on pretreatment and bioconversion strategies , including techno-economic and lifecycle perspective,” Ind. Crop. Prod., vol. 186, no. June, p. 115245, 2022, doi: 10.1016/j.indcrop.2022.115245.

[10] E. Y. Emori, M. A. S. S. Ravagnani, and C. B. B. Costa, “Application of fuzzy control in the evaporation stage of a first- and second-generation sugarcane ethanol biorefinery,” Chem. Eng. Commun., pp. 1–18, Jun. 2022, doi: 10.1080/00986445.2022.2084393.

[11] S. Hansen and A. Mirkouei, “Past Infrastructures and Future Machine Intelligence (MI) for Biofuel Production: A Review and MI-Based Framework,” no. December, 2018, doi: 10.1115/detc2018-86150.

[12] P. Asghari, A. M. Rahmani, and H. H. S. Javadi, “Internet of Things applications: A systematic review,” Comput. Networks, vol. 148, pp. 241–261, 2019, doi: 10.1016/j.comnet.2018.12.008.

[13] Taco-Vasquez, S., Salinas, M., Murillo, H., and Oñate, W., “Ethanol to high-octane hydrocarbons using HZSM-5 as catalyst”, in IOP Conference Series: Earth and Environmental Science, 2022, vol. 1094, no. 1. doi:10.1088/1755-1315/1094/1/012005.

[14] Chen, J., Li, C., Zhou, Y., Sun, C., & Sun, T. (2019). An efficient, scalable and eco-friendly synthesis of 4,5-substituted pyrrole-3-carbonitriles by intramolecular annulation on Pd/C and HZSM-5. ChemCatChem. doi:10.1002/cctc.201900154.

RIGA 2023

Forecasting Electricity Consumption for Covid-19 Pandemic Period and Beyond

Gabriel Nasser Doyle de Doile
Federal University of Itajubá – Unifei, Itajubá – MG, Brazil, d2021103246@unifei.edu.br, ORCID: 0000-0001-7700-5481

Mirelli de Castro Cesário
Federal University of Itajubá – Unifei, Itajubá – MG, Brazil, d2022100374@unifei.edu.br, ORCID: 0000-0003-3351-5548

Pedro Paulo Balestrassi
Federal University of Itajubá – Unifei, Itajubá – MG, Brazil, pedro@unifei.edu.br, ORCID: 0000-0003-2772-0043

Miguel Castilla Fernandez
Polytechnic University of Catalonia – UPC, Spain, miquel.castilla@upc.edu, ORCID: 0000-0002-3284-860X

Cite this paper as: *De Doile, GND, Cesário, MC, Balestrassi, PP. Castilla M. Forecasting Electricity Consumption for Covid-19 Pandemic Period and Beyond. 11. Eur. Conf. Ren. Energy Sys. 18-20 May 2023, Riga, Latvia*

Abstract: Covid-19 pandemic lockdowns have significantly changed the energy consumption patterns. Therefore, well known energy forecast tools must be adapted for the new scenarios. Sometime, it is need only a fast, reliable, and easy-to-implement tool, not a complex computational tool as presented in the majority of scientific papers. The aim of this article is to propose an easy tool to forecast electricity consumption during and after the pandemic lockdown in order to decision makers can taking confident decision in the return of presential activities. Such a tool should be easily implemented in a spreadsheet without the need of sophisticated computer software. The model widely used for trended, seasonal, and non-stationary time series, as presented in an electricity consumption time series, is the ARIMA. However, in this study the Holt-Winters method is compared with the former one. Results pointed that the second method is equally accurate and effortless to implement, being the recommended one in this work.

Keywords: *Demand prediction, coronavirus, Unifei, ARIMA, Holt-Winters*

Nomenclature	
ACF	Autocorrelation Function
ANN	Artificial Neural Networks
AR	Autoregressive model
ARIMA	Autoregressive Integrated Moving Average
ARIMAX	Autoregressive Integrated Moving Average with Exogenous
ARMA	Mixed Autoregressive-Moving Average model
HW	Holt-Winters
LSTM	Long Short-Term Memory
MA	Moving Average model
MAPE	Mean Absolute Percentage Error
NARX	Nonlinear Autoregressive
OLS	Ordinary Least Squares
PACF	Partial Autocorrelation Function
PV	Photovoltaic
SVR	Support Vector Regression
Unifei	Federal University of Itajubá
UKCeMGA	UK Centre for the Measurement of Government Activity

XGBoost	Extreme Gradient Boosting

1. INTRODUCTION

"It is difficult to make predictions, especially about the future", a statement attributed to Neils Bohr and to many other prominent people, suggests that should be easy to predict the past [1]. However, sometime an unexpected event, as the covid-19 pandemic, changes the normal behaviour of a variable that should be predicted in the future. In such a case, it will be needed to predict the normal behaviour during the pandemic period, i.e., it will be needed to predict the past without the real data.

The coronavirus pandemic and government restrictions have significantly influenced on the environment and energy profiles behaviours. Electricity consumption was quite affected by such a pandemic, as many activities were done remotely growing residential consumption and decreasing electricity consumption in other segments. Public and commercial services were the main affected kind of business, but no one escaped of electricity consumption changes effects [2]. Services affected by lockdowns and/or remote activities, as Universities, have had their electricity consumption dropped and the consumption growth in the return of normal activities is still unknown. To predict this new post-pandemic consumption, make necessary to predict how would be the consumption if there was not the pandemic.

The campus of Federal University of Itajubá (Unifei) can be seen as a microgrid, as it has clear electrical boundary, a single grid connection, own generation, battery banks, and several kinds of loads [3], as laboratories, classrooms, and many other activities, Fig. 1. Almost all of these activities were affected by the change to remote mode during the pandemic period of two and half years, from March of 2020 up to July of 2022. As the Unifei is supplied in part by the public grid and in part by own solar photovoltaic generation, the post-pandemic consumption should be predicted to planning activities and reinforce such a generation.

Figure 1. Unifei campus schematic. Adapted from https://unifei.edu.br/institucional/mapa-do-campus-Itajubá/

In this study it is proposed an easy-to-implement model to forecast electricity consumption during the pandemic period and for next years. The tool should be easily implemented in a spreadsheet, without the need of sophisticated computer software, to help decision makers taking confident decision related to electricity consumption after the return of presential activities. It was considered not only the grid consumption but also the own generation and, for a next step, campus occupation. The last one is need as some activities will be permanently in remote mode after pandemic. It was considered the two main models used to predict time series, the autoregressive integrated moving average (ARIMA), also known as Box-Jenkins model, and the Holt-Winters (HW) exponential smoothing model. Both are adequate to forecast future values based on trended and seasonal non-stationary time series [4].

Results had shown that both models are similar in accuracy with mean absolute percentage error (MAPE) less than 4%. However, the HW model is the easiest to implement in spreadsheets, as it has less equations to be implemented.

HW was the recommended method by this study, nevertheless, if it is needed more accuracy, deep studies should be carried out including other variables and more sophisticated tools, as artificial neural networks (ANN).

This paper is organized in four sections. In section 2 a literature background is presented, while in section 3 methodology and previous data are presented. Results and discussion are shown in section 4 and, finally, section 5 is dedicated to conclusions and recommendations for future works.

2. THEORETICAL BACKGROUND

Farrokhabadi et al. [5] have assessed the IEEE demand forecasting competition facing the pos-covid-19 paradigm. They received several studies from all over the world. The winners have used multi-model ensembles to predict day-ahead demand. Nevertheless, authors observed that many competitors have used data from the pandemic period to training models making less robust such models. In addition, large model ensembles are staff and computational costly, to aggregate a little improvement in results.

Rayash and Dincer [6] has analysed the electricity demand trends amidst the coronavirus pandemic in Canada. The work used the smart cities concepts to conclude that all of them should be rethought after the post-pandemic behaviour changes, including energy demand prediction. Similar study done in three US states presents the same worries. Even with a little change in demand post-pandemic, several other factors where affected, as power grid stress indicators [7].

The behaviour changes after pandemic period will have long-term effects and not only the energy consumption was affected, but also the power grid reliability, as stated by Alasali et al. [8] The authors have used ARIMAX and ANN to develop a stochastic model to generate scenarios in the post-pandemic period. In the beginning of Brazilian mobility constraining, Carvalho et al. [9] have analysed the electricity consumption behaviour. In general, all Brazilian regions have presented a reduction in electricity consumption, even with the residential demand growth presented by other authors [10].

One of the main antecedents in the literature for time series analyses and forecasting, the main support for this work, is the book wrote by Montgomery, Jennings, and Kulahci [4]. Such a book starts with a review of statistics fundamentals, presents the regression analysis and forecasting for general data. Then, the authors focus on time series, and present Smoothing methods for general time series. For trended and seasonal time series, the work presents the methods autoregressive (AR), moving average (MA), mixed autoregressive-moving average (ARMA) and, finally, the most used, autoregressive integrated moving average (ARIMA). Nevertheless, many authors have been studying time series analysis before Montgomery as Daves and Flores [11] that presented a confident sequence of tests to identify seasonality in time series. Holt-Winters (HW) exponential smoothing method is an adequate tool to forecast small time series with trend and seasonality, according to comparative studies carried out by Jiang et al. [12] that stated the HW exponential smoothing can accurately forecast time series with relatively few data, and Makatjane and Moroke [13] that concluded HW is more adequate to forecast car sales than ARIMA, even both presenting good performance based on same metrics. Winters [14], the father of HW method, suggested two types of adjustment, additive and multiplicative methods. The first one is applied when the time series presents trend and seasonality, however, the seasonality amplitude remains constant, whereas the multiplicative case is applied when the seasonality is time dependent, i.e., as the time growth, the seasonality amplitude increase or decrease. The model widely used for trended, seasonal, and non-stationary time series is the ARIMA, also known as Box-Jenkins model, that is compound of the two basic models AR and MA linked by an integrating component I. However, in several examples HW and the ensemble of both methods usually provide more accurate results [15]. Even for simple implementation in a spreadsheet, in some cases, the HW shows itself as more accurate than ARIMA model, as recommended by UK Centre for the Measurement of Government Activity (UKCeMGA) [16].

There are many tools for more accurate predictions, as nonlinear autoregressive (NARX) and long short-term memory (LSTM) ANN presented by Ozbay and Dalcali [17], and extreme gradient boosting (XGBoost) or support vector regression (SVR) used by Wasesa et al. [18] in their work. However, these tools are costly both in personnel and computational effort.

3. METHODOLOGY

Electricity consumption and solar photovoltaic (PV) generation data have a time series behaviour, as they are a chronological sequence of observation. Therefore, it is necessary to define the pattern of a time series in order to choose the best model to fit and forecasting. Time series can be random, trended, seasonal etc, and its pattern can be revealed by a time series plot, among other tools.

Since June of 2016 Unifei has in operation a solar photovoltaic (PV) micro-plant of 28.5 kW installed power. Even been a small production when compared with energy consumption, such a production should be added to make a more confident prediction for the future. The energy production of Unifei PV plant is presented in Tab. 1 (source: https://www.solarweb.com).

Table 1. Electricity production of Unifei PV plant in MWh[1].

Month	2016	2017	2018	2019
January		3.12	3.05	*0.58*
February		3.19	3.11	*0.89*
March		3.94	3.85	3.46
April		3.83	3.74	3.46
May		3.77	3.69	2.96
June	*1.55*[2]	2.88	2.75	
July	3.84	3.61	3.52	
August	3.41	3.21	3.13	
September	3.87	3.63	3.55	
October	3.43	3.22	3.15	
November	3.21	3.01	2.94	
December	2.94	2.76	2.70	

[1] *Measurement was stopped in 2019 and not returned until the end of this work.*
[2] *Values in italic were considered outliers*.

Due to the lack of measurement, data should be predicted from June 2019. The first step for a prediction is to identify the time series pattern. The time series plot, Fig. 2 (a), reveals three outliers. The first month in operation was not a complete month and June and July of 2019 present probable data transcription errors. In Fig. 2 (b) the time series without outliers is shown.

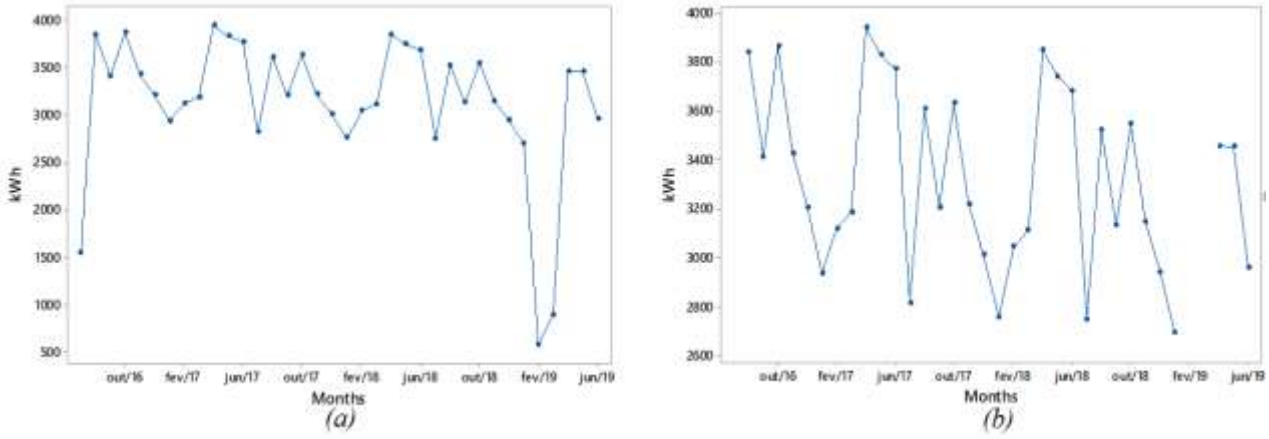

Figure 2. Time series plot of Unifei PV generation (a) including outliers, and (b) without outliers.

Another important task is to identify trend and seasonality, that can be done with the help of Minitab® software. In Fig. 3 it is possible to identify a negative trend slightly higher than the average nominal yield of solar panels marketed in 2022. However, such a trend is compatible as the PV panels' actual yield follows similar exponential decay curve, i.e., the more time, the less is the absolute loss of efficiency.

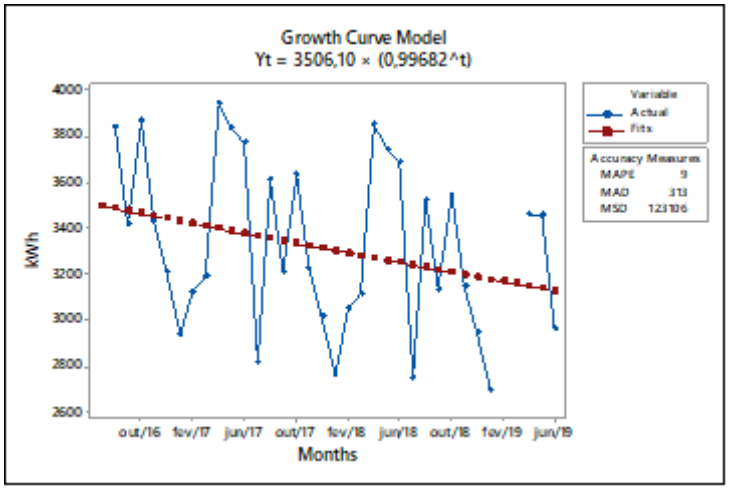

Figure 3. Trend analysis for Unifei PV generation.

If there is no a clear seasonal pattern, the seasonality can be identified firstly by autocorrelation plot, Fig. 4, and then, confirmed by the significance of Box-Pierce and ANOVA tests [11]. Both tests resulted significant indexes for a 12-month seasonality and all multiples of three, clearly denoting the four seasons of the region, where PV power plants produce more in clear winters and summers and, less in clouded autumns and springs.

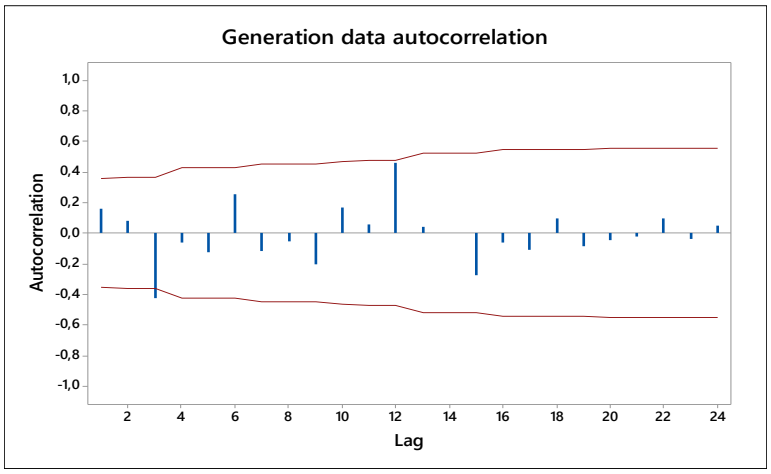

Figure 4. Autocorrelation function for Unifei PV generation.

As the time series has a few data, the HW method will be used in this case. The author assume that time series can be represented by Eq. 1 in the additive type of adjustment and by Eq. 2 in the multiplicative one.

$$Y_t = L_t + T_t + S_t + \varepsilon_t \quad (1)$$

$$Y_t = (L_t + T_t)S_t + \varepsilon_t \quad (2)$$

where L_t represents the linear component, T_t is the trend component, S_t is the seasonal component, and ε_t is a standard error.

To forecast future values using the method of Eq. 1 can be reach by the following set of Eqs. 3-6, whereas when using the multiplicative method, the forecast should follow the set of Eqs. 7-10, as taught by the UKCeMGA [16].

$$L_t = \alpha(Y_t - S_{t-p}) + (1-\alpha)(L_{t-1} + T_{t-1}) \quad (3)$$

$$T_t = \beta(L_t - L_{t-1}) + (1-\beta)T_{t-1} \quad (4)$$

$$S_t = \delta(Y_t - L_t) + (1-\delta)S_{t-p} \quad (5)$$

$$\hat{Y}_t = L_{t-1} + T_{t-1} + S_{t-p} \quad (6)$$

$\hat{Y}_t$ are future values to be predicted, p is the seasonality lag and α, β, and δ are estimated coefficients that should be adjusted for better forecast.

$$L_t = \alpha(Y_t/S_{t-p}) + (1-\alpha)(L_{t-1} + T_{t-1}) \quad (7)$$

$$T_t = \beta(L_t - L_{t-1}) + (1-\beta)T_{t-1} \quad (8)$$

$$S_t = \delta(Y_t/L_t) + (1-\delta)S_{t-p} \quad (9)$$

$$\hat{Y}_t = (L_{t-1} + T_{t-1})S_{t-p} \quad (10)$$

The 10 previous equations can be easily implemented in a spreadsheet available in several office computer package. Therefore, they were used in this case of solar PV generation. Results are in the next section.

Our purpose is to propose an easy implementing tool, in a spreadsheet, to forecast what would be the Unifei energy consumption during the pandemic lockdown if there was not such a lockdown. Data of Unifei grid consumption from 2015 up to 2022 is presented in Tab. 2 (source: electricity bills provided by distribution company).

Table 2. Electricity grid consumption of Unifei in MWh.*

Month	2015	2016	2017	2018	2019	2020	2021	2022
January	170.1	179.9	189.7	186.9	189.7	200.2	146.3	133.7
February	170.0	165.2	151.2	182.0	202.3	175.0	133.7	151.2
March	161.0	184.1	177.8	181.3	193.2	163.8	142.1	196.0
April	203.0	236.6	228.9	234.5	210.7	173.6	114.8	184.1
May	189.0	224.7	204.4	247.8	224.0	119.0	119.7	167.3
June	174.3	202.3	208.6	200.2	205.8	115.5	112.7	147.0
July	163.8	200.9	200.9	191.1	177.1	119.0	113.4	154.0
August	156.1	168.7	168.7	170.8	168.7	121.8	120.4	149.1
September	182.0	198.1	205.1	205.8	185.5	121.8	135.8	167.3
October	196.7	205.1	214.9	207.9	209.3	142.1	135.1	186.2
November	215.6	220.5	237.3	238.7	238.7	138.6	137.9	
December	214.9	210.0	211.4	217.7	219.1	140.7	157.5	

**Data represent the sum of peak and out-of-peak consumption.*

The total consumption is the sum of grid consumption plus the consumption supplied by own generation, as shown in Fig. 5. As can be seen in the figure, there is a significative electricity consumption droop from March 2020 when the covid-19 lockdown started.

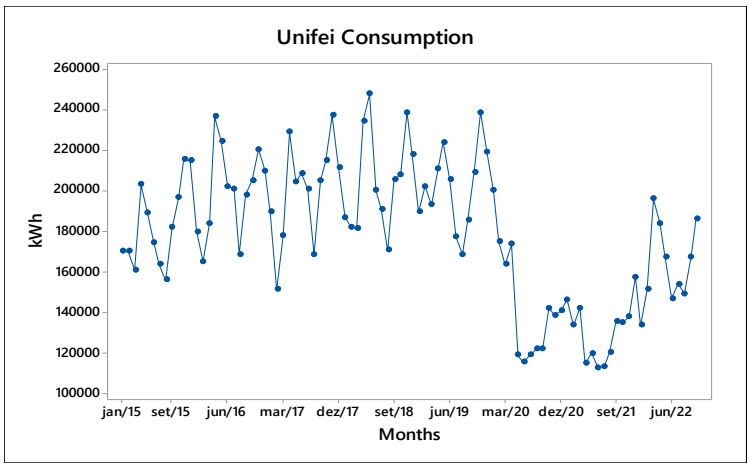

Figure 5. Unifei total electric energy consumption.

The same steps that have been done before to identify trend and seasonality in the energy production time series was done here for consumption time series. Data used to adjust the model was from 2015 up to 2018. 2019 data was used for model test and validation. Then a forecast to 2020 up to 2022 was carried out. Fig. 6 (a) allow to identify an upward trend and, in (d) a 12-month seasonality for adjustment data as well as a non-stationary behaviour of the time series. In Fig. 6 (b) each component of adjustment data time series is presented, and finally in (c) residual plots are shown. The residues behaviour demonstrates a good model for the decomposed time series as well as the accuracy metric MAPE equal to 4%.

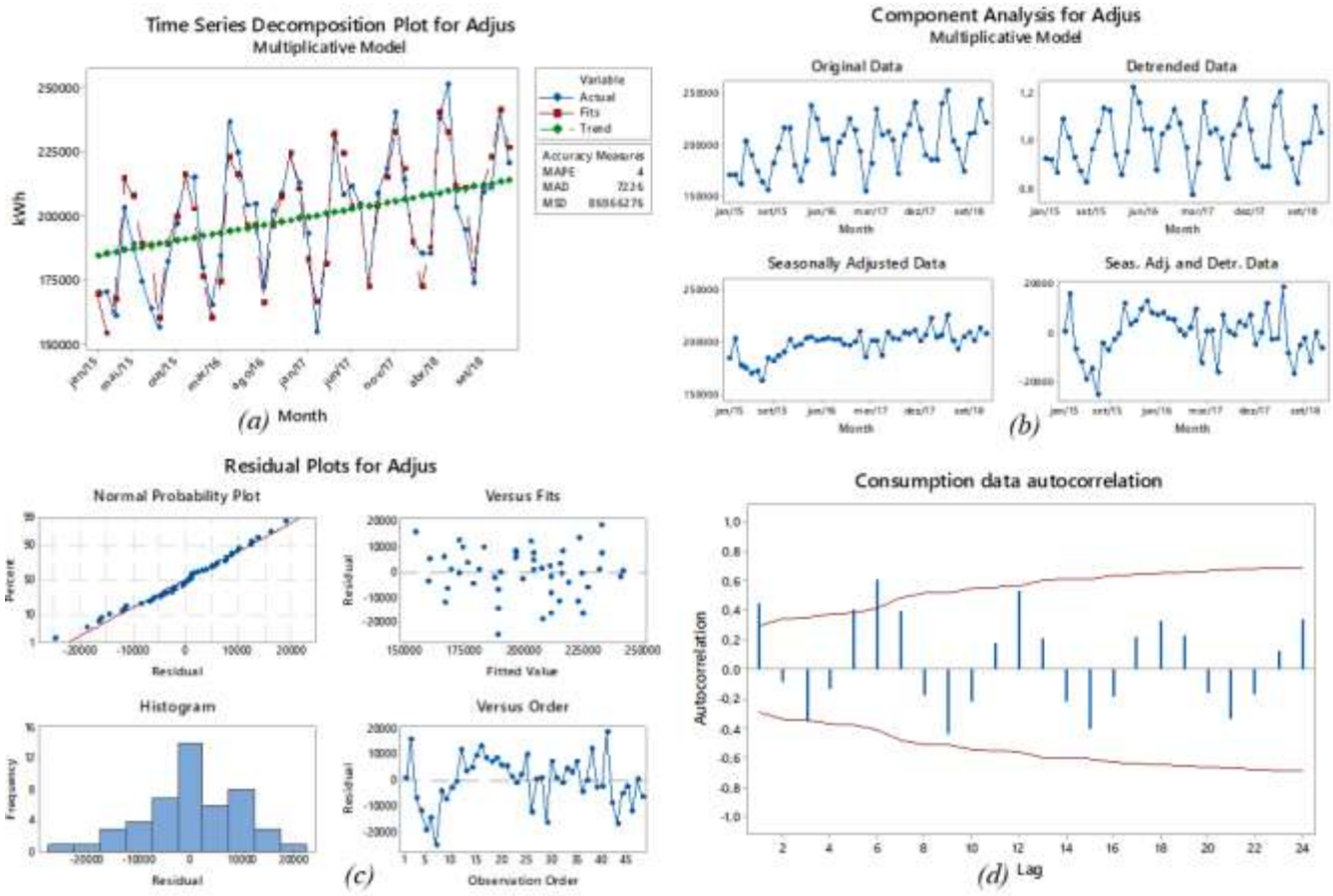

Figure 6. Pattern identification of adjustment (Adjus) data time series.

ARIMA model can be defined by two basic models. The autoregressive (AR) general model defined by Eq. 11 and the moving average (MA) general model given by Eq. 12 [16].

$$Y_t = \emptyset_0 + \emptyset_1 Y_{t-1} + \emptyset_2 Y_{t-2} + \cdots + \emptyset_p Y_{t-p} + \varepsilon_t \quad (11)$$

$$Y_t = \mu + \varepsilon_t - \omega_1 \varepsilon_{t-1} - \omega_2 \varepsilon_{t-2} - \cdots - \omega_q \varepsilon_{t-q} \quad (12)$$

where ϕ_p and ω_q are coefficients to be calculated by ordinary least squares (OLS), p is the AR lag, and q is the MA lag. A useful way is to use the delay operator B to rewrite the models as in Eqs. 13 and 14.

$$\emptyset(B) Y_t = \varepsilon_t \quad (13)$$

$$Y_t = \theta(B) \varepsilon_t \quad (14)$$

where $BY_t = Y_{t-1}$, $B^2 Y_t = Y_{t-2}$, … $B^d Y_t = Y_{t-d}$. The I in the acronym ARIMA refers to model integration term given by middle term in Eq. 15.

$$\emptyset(B)(1 - B)^d Y_t = \theta(B) \varepsilon_t \quad (15)$$

where $(1 - B)^d Y_t$ is the difference operator equal to $(Y_t - Y_{t-1}) - (Y_{t-1} - Y_{t-2}) - \ldots - (Y_{t-d-1} - Y_{t-d})$, and d is the order of such a difference. Thus, the complete model is called the seasonal non-stationary ARIMA (p, d, q). It is recommended to include a second ARIMA to analyse seasonal time series. The seasonal stationary ARIMA (P, D, Q)s, where s represents the main seasonality, is calculated by Eq. 16. The combined model is known as SARIMA (p, d, q) × (P, D, Q)s [19], given by Eq. 17.

$$\Phi(B_s)(1 - B_s)^D Y_t = \Theta(B_s)\varepsilon_t \quad (16)$$

$$\emptyset(B)(1 - B)^d \Phi(B_s)(1 - B_s)^D Y_t = \theta(B_s)\,\Theta(B_s)\varepsilon_t \quad (17)$$

Montgomery, Jennings, and Kulahci [4] summarize the model to be chosen by the autocorrelation function (ACF) and partial autocorrelation function (PACF) as presented in Tab. 3.

Table 3. Behaviour of ACF and PACF for stationary time series [4].*

Model/Function	ACF	PACF
MA (q)	Cuts of after lag q	Exponential decay and/or damped sinusoidal
AR (p)	Exponential decay and/or damped sinusoidal	Cuts of after lag q
ARMA (p, q)	Exponential decay and/or damped sinusoidal	Exponential decay and/or damped sinusoidal

** For non-stationary time series, the term I of ARIMA should be used.*

Based on Montgomery teachings, the ACF, Fig. 6 (d) suggests a MA (3) model and, the PACF in Fig. 7 clearly reveals an AR (2) model. As the time series is non-stationary, the ARIMA (p, d, q) model will be ARIMA (2, 1, 3) or even the SARIMA $(2, 1, 0) \times (0, 1, 3)_{12}$.

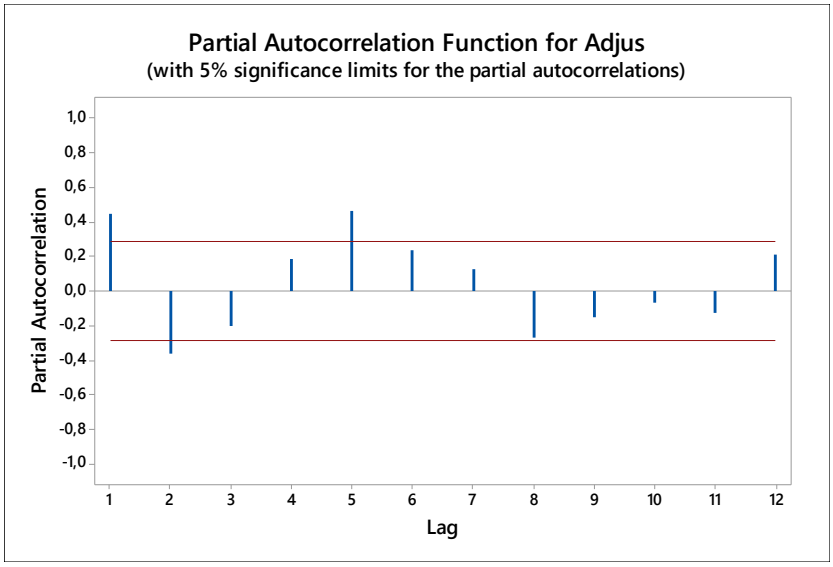

Figure 7. Partial autocorrelation of adjustment data time series (2015 up to 2018 data).

The ARIMA (2, 1, 3) was applied in this case of energy consumption forecasting. The second most used method is the Holt-Winters (HW), already used in this paper to predict Unifei energy production. The HW model for adjustment time series was implemented firstly in Excel®, to adjust the coefficients, and then in Minitab® that produced the results. Both results are in the following section.

4. RESULTS AND DISCUSSION

Eqs. 1-10 were implemented in an Excel® spreadsheet and, then for the case of solar PV generation, it was used the HW exponential smoothing in the Minitab® software, adjusting coefficients in the Excel® using the Solver tool. The

results are presented in Fig. 8 and Table 4. From June 2019 up to October 2022 are forecasted values. The mean absolute percentage error (MAPE), the widely used accuracy measurement tool, applied to a control group of variables, was 1,3% indicating that forecasted values are very close to actual ones. Values from Table 4 were added to energy bill data to forecast what would be the Unifei energy consumption if there was not the pandemic period.

Table 4. Electricity production of Unifei PV plant including forecasted values (in italic) in MWh.

Month	2016	2017	2018	2019	2020	2021	2022
January		3.12	3.05	0.58	*2.91*	*2.87*	*2.85*
February		3.19	3.11	0.89	*2.97*	*2.94*	*2.92*
March		3.94	3.85	3.46	*3.68*	*3.64*	*3.65*
April		3.83	3.74	3.46	*3.57*	*3.54*	*3.53*
May		3.77	3.69	2.96	*3.52*	*3.49*	*3.44*
June	1.55	2.88	2.75	*2.66*	*2.63*	*2.60*	*2.58*
July	3.84	3.61	3.52	*3.48*	*3.43*	*3.40*	*3.41*
August	3.41	3.21	3.13	*3.09*	*3.05*	*3.04*	*3.00*
September	3.87	3.63	3.55	*3.50*	*3.45*	*3.46*	*3.41*
October	3.43	3.22	3.15	*3.10*	*3.06*	*3.07*	*2,98*
November	3.21	3.01	2.94	*2.90*	*2.86*	*2.87*	
December	2.94	2.76	2.70	*2.66*	*2.62*	*2.62*	

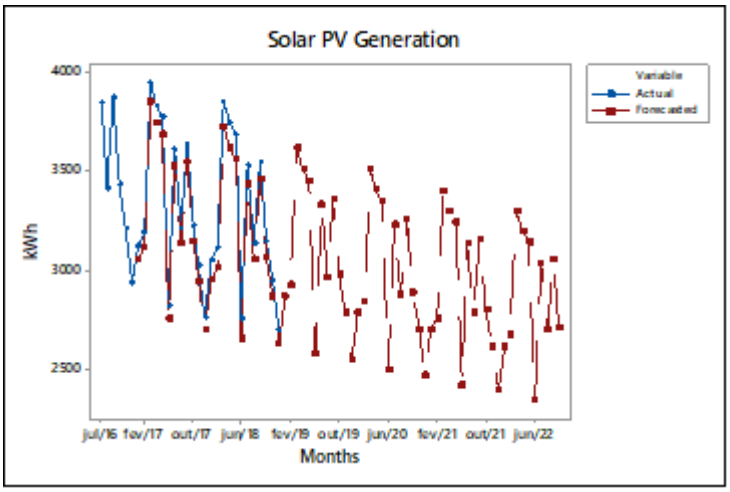

Figure 8. Unifei PV generation including predicted values.

Firstly, the year of 2019 was forecasted to validate the model. The results, using ARIMA (2, 1, 3), are presented in Table 5 and Fig. 9. Errors present only two values greater than 10 MWh in February and March, as just these two months followed an unusual behaviour in 2019 compared with previous years. The residual plots, Fig. 9 (b) show that residues are close to a white noise that represents a perfect fitting of the model, as well as the calculated MAPE of 3.85%. It is worth mention that residual analyses compare fitted values with the actual ones, whereas the calculated MAPE compare the forecasted values with the validation sample, in this case, the year 2019's Unifei consumption data.

Table 5. Unifei energy consumption including the year 2019 forecasted using ARIMA model.

Month	2015	2016	2017	2018	2019	*2019**	*Abs. error*
January	170.1	179.9	189.7	186.9	192.7	*191.9*	*0.80*
February	170.1	165.2	151.2	182.0	205.3	*184.6*	*20.7*
March	161.0	184.1	177.8	181.3	196.9	*179.0*	*17.9*
April	203.0	236.6	228.9	234.5	214.3	*222.1*	*7.80*
May	189.0	224.7	204.4	247.8	227.6	*217.7*	*9.90*
June	174.3	202.3	208.6	200.2	208.5	*196.4*	*12.1*
July	163.8	200.9	200.9	191.1	180.6	*180.7*	*0.10*
August	156.1	168.7	168.7	170.8	171.8	*172.3*	*0.50*
September	182.0	198.1	205.1	205.8	189.0	*203.9*	*14.9*
October	196.7	205.1	214.9	207.9	212.4	*214.5*	*2.10*
November	215.6	220.5	237.3	238.7	241.6	*246.5*	*4.90*

December	214.9	210.0	211.4	217.7	221.8	*225.4*	*3.60*

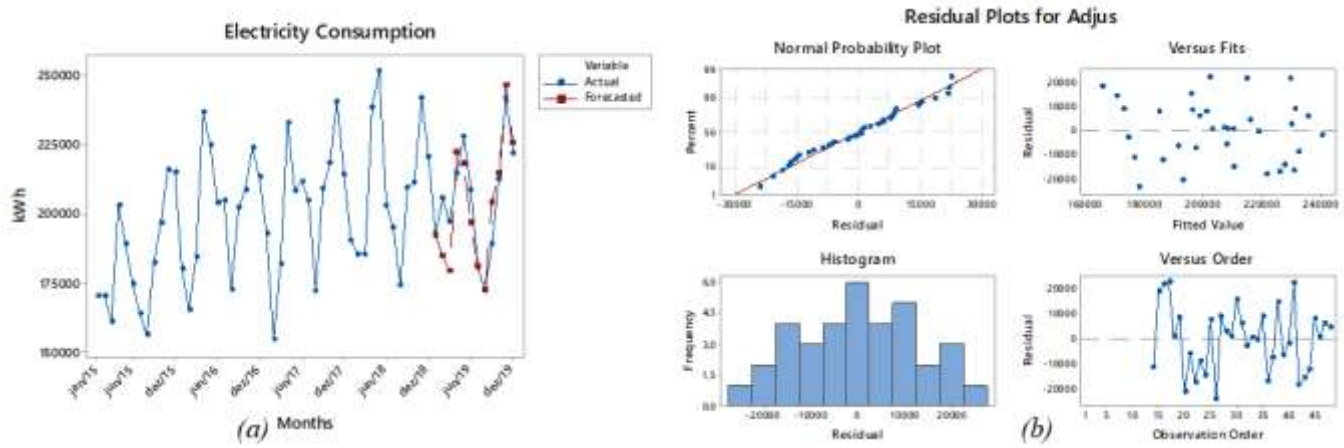

Figure 9. Results of ARIMA forecasting to 2019 (a) time series actual x forecasted, (b) residual analyses.

The results using Holt-Winters method are shown in Fig. 10 and Table 6. Once again residues are close to a white noise with calculated MAPE of forecasted results being 3.64%, a little lower than that one from ARIMA model.

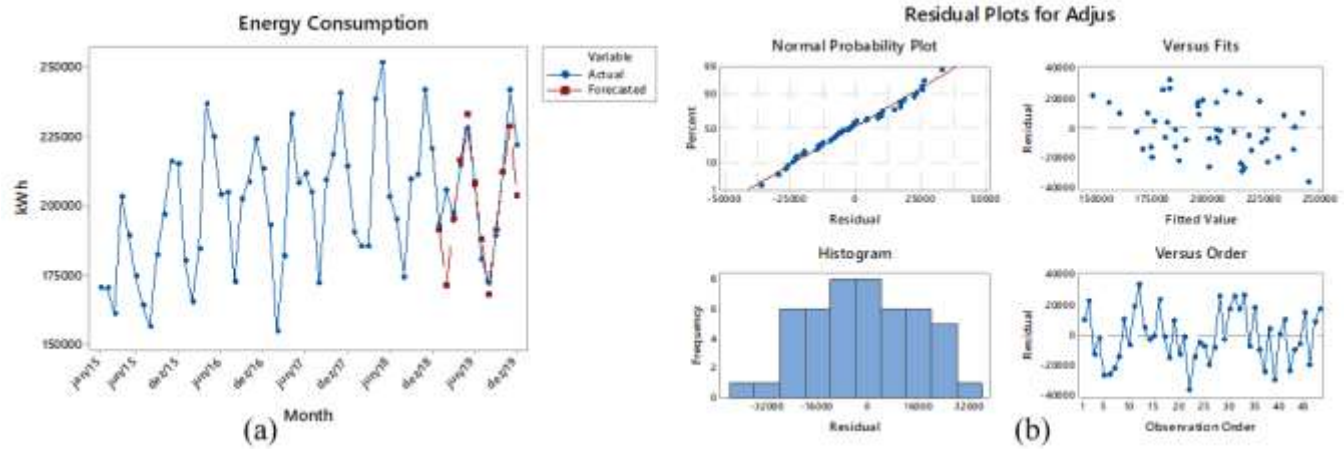

Figure 10. Results of HW method forecasting to 2019 (a) time series actual x forecasted, (b) residual analyses.

Table 6. Unifei energy consumption including the year 2019 forecasted using HW model.

Month	2015	2016	2017	2018	2019	*2019**	*Abs. error*
January	170.1	179.9	189.7	186.9	192.7	*191.1*	*1.58*
February	170.1	165.2	151.2	182.0	205.3	*170.9*	*34.5*
March	161.0	184.1	177.8	181.3	196.9	*194.8*	*2.08*
April	203.0	236.6	228.9	234.5	214.3	*215.9*	*1.57*
May	189.0	224.7	204.4	247.8	227.6	*232.8*	*5.25*
June	174.3	202.3	208.6	200.2	208.5	*207.5*	*1.00*
July	163.8	200.9	200.9	191.1	180.6	*187.4*	*6.82*
August	156.1	168.7	168.7	170.8	171.8	*167.5*	*4.23*
September	182.0	198.1	205.1	205.8	189.0	*191.1*	*2.07*
October	196.7	205.1	214.9	207.9	212.4	*211.7*	*0.71*
November	215.6	220.5	237.3	238.7	241.6	*228.3*	*13.3*
December	214.9	210.0	211.4	217.7	221.8	*203.4*	*18.4*

From above results, it can be stated that Holt-Winters model have had a better performance than ARIMA model in this case of study. Therefore, the forecast for 2020 up to 2022 was carried out using HW method. In Fig. 11 a comparison between forecasted and measured values is presented, including the pandemic period. As it can be seen, the consumption curve from March 2020 does not follow the normal behaviour as predicted anymore. Even with the presential activities returns in the 2022 second semester, the actual curve did not reach the forecasted one.

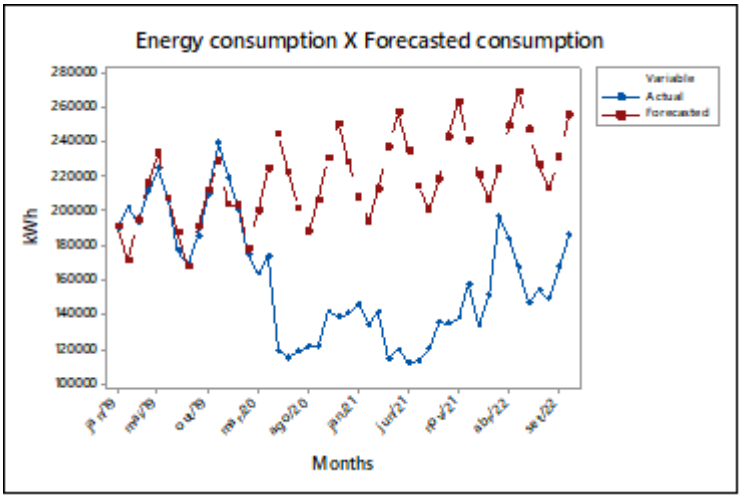

Figure 11. Final results of 2019 up to 2022 forecast using HW method.

As expected in some kind of business the new-normal after pandemic period will be different than before covid-19. Maybe the electricity consumption will never reach the old pattern, as many activities successfully done remotely will continues in this work mode. Therefore, a deeper study should be done, taking into account several variables as the own generation, the use of campus installations, and the number of people working presential, among others. Future research will consider such variables using artificial neural networks (ANN) to find variables dependence and, then make a more accurate prediction.

5. CONCLUSION

Forecast the past would be an easy task if the past had followed a well-known pattern. However, when an exception happens, as the covid-19 pandemic, it becomes equal to predict the future. It is necessary to know the expected behaviour of electricity consumption during the pandemic period, as if did not happen such a lockdown, to planning the future after the pandemic period.

In this study, it was assessed the two main forecasting tools to predict the energy consumption of a microgrid formed by Unifei campus in Itajubá – MG, Brazil. Firstly, it was predicted the own solar photovoltaic generation and, then expected consumption during the pandemic period. As expected, the forecasted consumption was higher than the actual one, even for 2022 when almost all activities returned to presential mode. Planning and budget workers should take in account such an electricity consumption reduction for next years. According to the results, it is recommended the use of Holt-Winters (HW) exponential smoothing method to forecast energy consumption, as the results is similar to ARIMA model that is a more complex model. HW can be easily implemented in a spreadsheet and can be found in several statistical software. Some application could need a more accurate prediction. In this case, it is recommended the use of more sophisticated computational tool, as artificial neural networks (ANN), at a cost of expert staff need and more computational time. The extended version of this article should include a comprehensive assessment of other variables, such as campus occupancy, type of activities, among others that may influence energy consumption, through ANN resources.

Acknowledgment

The authors thank the Federal University of Itajubá (Unifei), the Polytechnic University of Catalonia (UPC), Minas Gerais State Research Support Foundation (FAPEMIG), Higher Education Personnel Improvement Coordination – Brazil (CAPES) Financial Code 001, National Research and Development Council (CNPq) and National Electric Energy Institute (INERGE) for all support.

References

[1] Dickstein DP. Editorial: It's Difficult To Make Predictions, Especially About the Future: Risk Calculators Come of Age in Child Psychiatry. *J Am Acad Child Adolesc Psychiatry*. 2021;60(8):950-951. DOI:10.1016/j.jaac.2020.12.029

[2] Ceylan Z. The impact of COVID-19 on the electricity demand: a case study for Türkiye. *Int J Energy Res*. 2021;45(9):13022-13039. DOI:https://doi.org/10.1002/er.6631
[3] U.S. Department of Energy (DOE). *Combined Heat and Power Technology*.; 2016. Available at: https://www.energy.gov/sites/prod/files/2017/12/f46/CHP Overview-120817_compliant_0.pdf Accessed on Nov. 2022.
[4] Montgomery DC, Jennings CL, Kulahci M. *Introduction to Time Series Analysis and Forecast*. 1st ed. New York, USA, John Wiley & Sons. Inc; 2008.
[5] Farrokhabadi M, Browell J, Wang Y, Makonin S, Su W, Zareipour H. Day-Ahead Electricity Demand Forecasting Competition: Post-COVID Paradigm. *IEEE Open Access J Power Energy*. 2022;9(March):185-191. DOI:10.1109/OAJPE.2022.3161101
[6] Abu-Rayash A, Dincer I. Analysis of the electricity demand trends amidst the COVID-19 coronavirus pandemic. *Energy Res Soc Sci*. 2020;68(July):101682. DOI:10.1016/j.erss.2020.101682
[7] Agdas D, Barooah P. Impact of the COVID-19 Pandemic on the U.S. Electricity Demand and Supply: An Early View from Data. *IEEE Access*. 2020;8:151523-151534. DOI:10.1109/ACCESS.2020.3016912
[8] Alasali F, Nusair K, Alhmoud L, Zarour E. Impact of the covid-19 pandemic on electricity demand and load forecasting. *Sustain*. 2021;13(3):1-22. DOI:10.3390/su13031435
[9] Carvalho M, Bandeira de Mello Delgado D, Lima KM, Camargo Cancela M, Siqueira CA, Souza DLB. Effects of the COVID-19 pandemic on the Brazilian electricity consumption patterns. *Int J energy Res*. 2021;45(2):3358-3364. DOI:10.1002/er.5877
[10] Abdeen A, Kharvari F, O'Brien W, Gunay B. The impact of the COVID-19 on households' hourly electricity consumption in Canada. *Energy Build*. 2021;250:111280. DOI:10.1016/j.enbuild.2021.111280
[11] Davey AM, Flores BE. Identification of seasonality in time series: A note. *Math Comput Model*. 1993;18(6):73-81. DOI:10.1016/0895-7177(93)90126-J
[12] Jiang W, Wu X, Gong Y, Yu W, Zhong X. Holt–Winters smoothing enhanced by fruit fly optimization algorithm to forecast monthly electricity consumption. *Energy*. 2020;193:116779. DOI:10.1016/j.energy.2019.116779
[13] Makatjane KD, Moroke ND. Comparative study of holt-winters triple exponential smoothing and seasonal Arima: forecasting short term seasonal car sales in South Africa. Risk Governance & Control: Financial Markets & Institutions, Vol. 6, Issue 1, Winter, 2016, Available at SSRN: https://ssrn.com/abstract=2742481 Accessed on Nov. 2022.
[14] Winters PR. Forecasting sales by exponentially weighted moving averages. *Manage Sci*. 1960;6(3):324-342. DOI: 10.1287/mnsc.6.3.324
[15] de Oliveira EM, Cyrino Oliveira FL. Forecasting mid-long term electric energy consumption through bagging ARIMA and exponential smoothing methods. *Energy*. 2018;144:776-788. DOI:10.1016/j.energy.2017.12.049
[16] UK Centre for the Measurement of Government Activity. From Holt-Winters to ARIMA Modelling: Measuring the Impact on Forecasting Errors for Components of Quarterly Estimates of Public Service Output. Office of national Statistics, August 2008,1149-1165. Available at https://www.ons.gov.uk/, accessed on Nov. 2022.
[17] Özbay H, Dalcali A. Effects of COVID-19 on electric energy consumption in Türkiye and ANN-based short-term forecasting. *Turkish J Electr Eng Comput Sci*. 2021;29(1):78-97. DOI:10.3906/ELK-2006-29
[18] Wasesa M, Andariesta DT, Afrianto MA, et al. Predicting Electricity Consumption in Microgrid-Based Educational Building Using Google Trends, Google Mobility, and COVID-19 Data in the Context of COVID-19 Pandemic. *IEEE Access*. 2022;10:32255-32270. DOI:10.1109/ACCESS.2022.3161654
[19] Tsui WHK, Balli HO, Gilbey A, Gow H. Forecasting of Hong Kong airport's passenger throughput. Tour Manag. 2014;42:62-76, DOI: 10.1016/j.tourman.2013.10.008

RIGA 2023

Energy Efficiency in the Last Mile: From Conventional to Renewable Energy Transport

Olga Levkovych
University of Maastricht, Maastricht, The Netherlands, o.levkovych@alumni.maastrichtuniversity.nl

Adriana Saraceni
University of Maastricht, Maastricht, The Netherlands, a.saraceni@maastrichtuniversity.nl

Cite this paper as: *Levkovych,O., Saraceni, A. Energy Efficiency in The Last Mile: From Conventional to Renewable Energy Transport. 11. Eur. Conf. Ren. Energy Sys. 18-20 May 2023, Riga, Latvia*

Abstract: Logistics providers are gradually considering innovative transportation alternatives for last mile delivery that can address energy efficiency needs. This research aims to compare autonomous ground vehicles with conventional and electric vans, based on associated vehicle costs and benefits, taking into account their engines and combustion features. Cost per vehicle kilometre is derived using the total cost of ownership method, adjusted with the inclusion of labour costs, while travel time-related and capacity occupations and reliability benefits serve as a basis for the total possible number of parcels delivered. The novelty of our paper lies in the incorporation of solar panels on top of vehicles to assess their impact on energy efficiency. The results show that, under the current structural and infrastructural conditions of urban delivery, the experimental model can be potentially successful in terms of cost per kilometre, but not as effective in terms of the total possible number of parcels delivered. This study defines autonomous ground vehicles with lockers as an innovative last mile solution and contributes to the academic literature by investigating the potential of renewable energy systems adoption in the last mile delivery.

Keywords: *Renewable energy, autonomous ground vehicles, last mile delivery, electric cars, solar panels*

Nomenclature	
APK	Algemene Periodieke Keuring
IM	Autonomous Ground Vehicle
km	Kilometers
L	Liter
LMD	Last Mile Delivery
LML	Last Mile Logistics
LSP	Logistics Service Provider
SOT	Solar On Top
TCO	Total Cost of Ownership

1. INTRODUCTION

The collocation “last mile” indicates the final leg of technology that connects an end-user to the rest of the internet network in telecommunications. In the logistics sector, the term refers to direct end-customer interaction [1] while last mile logistics (LML) is experiencing enhanced attention from the scientific community [2]. This interest is related to trends in purchasing behaviour and demographics, as well as increasing challenges that practitioners face while trying to keep up with the basic LML principle: minimizing the freight movement required to satisfy demand, while minimizing costs and negative impact [3, 4].

Existing research on the topic offers either narrow targeted improvements of the last mile delivery (LMD) process, such as a routing optimization [5] or focus on a unidimensional analysis of alternatives within a thematic class, for instance transport mode or delivery system's externalities [6, 7]. In relation to autonomous ground vehicles (AGVs), studies are mostly devoted on adoption acceptance [8, 9] environmental [10, 11] or efficiency assessments [10, 12] neglecting supplementary beneficial or counterbalancing factors that could provide a more holistic picture and fuller understanding of the context. This research seeks to answer: *What are the cost-benefit segments of last mile delivery using renewable energy transport in urban areas?* A monetary comparison will be conducted, between an AGV, a conventional and an electric van, by analysing the main cost and benefit vehicle related segments. The outcomes can assist third party logistics service providers (LSPs) as a structural example for multifaceted comparative analysis among a separate class of future robotic solutions, namely an AGV, and other conventional transportation alternatives.

2. TOTAL COST OF OWNERSHIP ANALYSIS AND COST-RELATED BENEFITS

Fleet electrification is the main short-term challenge for many leading LSPs, based on the current technology maturity. As the penetration rate of any technology highly depends on associated costs, the increasing supply of affordable electric energy [13, 14] and decreasing battery costs, the most expensive component of electric vehicles (EV) [15, 16], became the main drivers of fuel transition. While many articles highlight the environmental advantages of electric transport compared to fossil fuel emissions, this paper is primarily interested in the economic performance and cost-related benefits evaluation of certain vehicles, hence in quantitative methodologies allowing for results in monetary units [17].

Several papers advocate the advantages of using electric vehicles and their cost competitiveness in all mobility categories i.e. 2-wheelers, cars, buses, heavy and light vehicles [18]. Among those reviewed, total cost of ownership (TCO) is a widely used method for understanding potential benefits of a new technology [18, 19, 20]. Based on a TCO analysis, the most advantageous technology in terms of cost can be chosen, while the most problematic cost areas in need of improvement can be identified. The method summarizes all costs related to ownership of a given subject, during a certain period of ownership. There are usually four types of input information needed to conduct a TCO on a transport vehicle, namely ownership period, travel data, vehicle data and cost data (for a detailed overview see Appendix A).

Concurrently to costs, innovative technology adoption should foster optimization along with sustainability and effectiveness benefits, related to fuel efficiency, travel time-related, capacity occupation & reliability improvements of costs [21]. Benefits also depend on specific vehicle characteristics and dimensions, but can be further stimulated by ancillary mechanisms and methods, for instance congestion mitigation, de-emphasized performance, vehicle right-sizing and light-weighting, eco-driving and eco-routing, and higher speed limits. Other possible benefits can be related to the factors mentioned under the cost data of TCO analysis [21]. Similar discounts could be implemented for AGVs, as they eliminate the human error and thereby increase safety and reduce the chances of an accident. Figure 1 (Appendix A) presents the selected framework for the input data and TCO assessment algorithm.

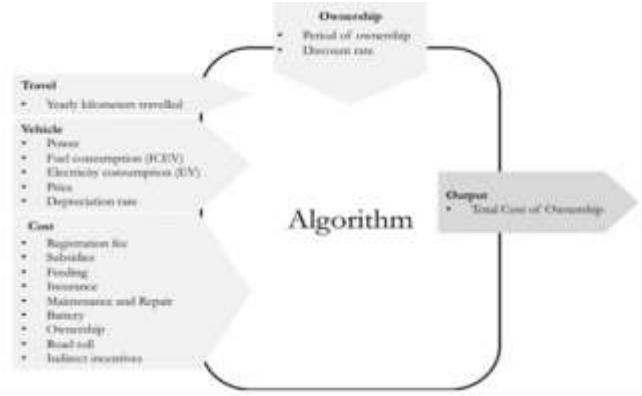

Figure 1. TCO assessment algorithm. Source: [18]

3. METHODOLOGY

The TCO method will be used for three different types of transport. As a baseline, a conventional van with an internal combustion engine representing the current state of LMD will be used; an electric van as a common solutions of the near future; and an autonomous ground vehicle as a further future potential solution. Additionally, each of the options will be assessed with the use of solar panels as an auxiliary tool for cost savings. The data were collected taking into account the specifics of urban delivery, based on resources and institutions operating in the Netherlands, and therefore reflects the context of the Dutch LMD market.

The data collection mechanisms for each of the variables needed to calculate the total actual costs and kilometers (km) driven during the full ownership period. The algorithm in Eqs. (1, 2), Appendix A, is taken as a TCO input framework and includes variables such as ownership period, travel data, vehicle characteristics, and associated capital and operational costs. The results of the TCO assessment will be obtained using the Formula (1) (see Appendix A) proposed by [18], and adjusted to include solar panels costs and labour costs for a delivery van driver, a substantial part of the LMD cost [22] which in AGVs will be eliminated. Costs will be adjusted annually according to the discount rate of the present discounted value shown in Formula (2) (see Appendix A) [23]. The total possible parcels delivered, together with the total cost per km gained from TCO, are two representative metrics of delivery performance. This research will examine solar panels fuel-saving capabilities and their effect on cost per km for each vehicle, and the effect on the total possible parcels delivered due to operational time increase. Subsequently, a sensitivity analysis of cost and benefit segments will follow, allowing for deeper analysis and robustness check.

TCO Calculation: Coming back to the TCO calculation algorithm, the following main blocks of data are to be considered: vehicle characteristics, ownership period, travel data and labour costs. Then, the Benefits Calculation of Capacity Occupation & Reliability, Fuel Efficiency and Travel Time: Total Operational Time Increase.

***Vehicle Characteristics**:* Vehicle type largely affects the remaining variables, and therefore, requires a primary outline. PostNL, the main parcel delivery service provider in the Netherlands, made a deal with Renault group on the purchase of light commercial electric vehicles - Master Z.E (L3H2) [24], as a part of its plan on emission-free LMD by 2030 [41].

Solar panels: Current technology maturity does not allow for commercial vehicles running entirely on solar power, yet there are few examples of solar panels providing fuel savings and extending a vehicle's battery life. Dutch company IM Efficiency has developed the SolarOnTop (SOT) product, providing trucks with clean electricity generated by solar panels otherwise generated by the alternator [25], reducing the load on the engine and hence fuel consumption, thus preventing the costly idling hours. All SOT related information used was obtained during an informal interview with a company representative. The SOT price is determined separately for each vehicle.

Depreciation rate: According to Dutch law, the depreciation rate for delivery vans is 100% after five years. Due to the lack of similar information concerning the AGVs, the same depreciation rule will be applied to the AGV with lockers, considering the residual value of €0 in all cases (see Table 4, Appendix A).

Vehicle related costs - Fees and taxes: Upon purchase, a vehicle owner is automatically responsible for registration, insurance, APK (Algemene Periodieke Keuring), and motor vehicle tax (see Appendix A).

Vehicle related costs - Subsidies and Indirect initiatives: According to Netherlands Enterprise Agency, there is a list of financial support for business driving electric with a minimum reliability level 2+ with 'RVO services' authorization is assumed in order to receive these subsidies. Allowances are applied to corresponding purchase costs, and can be combined except the MIA and EIA combination. Among those able to be applied to this research are presented in detail in Appendix A.

***Ownership Period**:* The transport industry in general operates on low margins, therefore tends to exploit its assets on the maximum to minimize operational costs distributed over the asset's lifespan [26]. According to Topsector Logistics, transport industry standards, limit the recommended period of usage for a commercial van to 8 years.

The same amount of years is proposed by the European Environment Agency. The real discount rate was set on the level of 0,05%, to eliminate the complexity of inflation consideration within the present value calculations.

Travel Data: Information on the specific annual mileage numbers for vans used by the PostNL parcel delivery subdivision is confidential. However, the approximate annual mileage value for the parcel transporters like PostNL, DHL, and UPS can be retrieved from the Central Bureau of Statistics of the Netherlands (CBS) and RDW [27]. In the Netherlands, third party LSPs are registered under the SBI code "53: Postal and courier activities" [28]. The average annual mileage for these sectors is 38,753 km that matches the annual mileage (39.082 km) that can be calculated using the case study within the outlook of the 'Package market and home deliveries' city logistics segment in the MRDH region [29]. Accordingly, an annual mileage amount of 39,000 km was chosen.

Labour Costs: The average hourly salary for parcel delivery employee in PostNL is €10.79 according to the last update on May 25, 2021, by Indeed, [30], which is in line with wage information under parcel deliverer vacancy at PostNL - €1,973 gross per month assuming 23 working days, 8 hours per shift.

Benefits Calculation

Capacity Occupation & Reliability: LSPs are also concerned about the maximum possible number of items delivered. In November 2020 Topsector Logistiek conducted an analysis on parcel and home delivery at MRDH area, and noted 75000 parcels delivered daily by 340 vans, that equals to 220 parcels per car [31]. The study also found that the capacity of one van is 300 parcels and it usually has an average load factor of 73%, which corroborates the 220 parcels value per van. Neolix offers three different configurations of lockers, namely: Big locker dimensions: 420 x 280 x 510 mm (59L); Medium locker dimentions: 420 x 245 x 125 mm (15L); Small locker dimensions: 420 x 280 x 83.3 mm (9.7 L); Total lockers volume: 471.5 L.

For items less than 2 kg and with a maximum size of 380 x 265 x 32 mm, PostNL and Bol.com use Letterbox Packets+, an intermediate package between letter and a parcel. Solely from the parcels perspective, according to the study of [39] exploring the last mile parcel delivery market in Groningen, parcel sizes of 8, 13, and 18 litres were among the most frequently used, with the volume distribution of 40%, 40% and 20% respectively. Thus, taking into account the average parcel volume of 12 litres and the Neolix Express total volume of 471.5 litres, the maximum capacity of 39 packages per one delivery cycle was obtained.

Fuel Efficiency: Energy obtained through solar panels can substitute part of the electricity needed for all vehicle types, and even affect fuel consumption for vehicles with internal combustion engines (ICEV), therefore, reduce feeding costs. According to the company's representative [25], $1m^2$ of SOT can produce about 250 kWh per year, which in the case of electric cars increases the maximum power reserve of the vehicle at a previous rate of electricity consumption. For conventional vehicles, an additional supply of electricity, along with keeping the battery charged, also lower the load on the engine, resulting in less fuel needed to produce Tank-to-Wheel energy [32]. The SOT simulation application developed by IM Efficiency used to calculate the total fuel savings for a vehicle with a diesel engine is confidential and restricted for external disclosure.

Travel Time: Total Operational Time Increase: According to the service information and vacancy description at PostNL, the working activities related to the parcels' delivery are taking place between 7:00 and 23:00 (two shifts/day), six days a week excluding Sundays and holidays (302 working days in 2021), while deliveries can be expected between 8:00 and 21:30 [33]. In this study, the assumption on the expansion of delivery hours using Neolix to 7:00 -1:00 range is made, to calculate the total operational time increase benefit. Nonetheless, the suggestion is a presumption that requires scientific evaluation.

4. SENSITIVITY ANALYSIS

The TCO analysis conducted in this paper for the period 2021 to 2028, contains several assumptions that imply varying degrees of uncertainty (see Appendix C, Tables 5, 6, 7, 8). Therefore, sensitivity analysis is performed for the vehicles without SOT, to test the robustness of either cost segments that have a significant variability potential, or segments whose change vector is known, but the degree of influence itself represents a focus of interest.

Sensitivity analysis on parcel size and density is also be performed, to assess the competitiveness position of AGVs with lockers.

Costs of Ownership (+APK) will increase by 40% the next eight years due to termination of current tax discounts for electric vehicles. Yet, it is unclear how strong government support for renewable and green energy investments will be, or whether ownership taxes for internal combustion engines vehicles will be increased. A change in the cost per km as a result of a 20%, 30% and 40% increase in +APK, and a change of 10%, 20% and 30% in the Purchasing cost of the vehicle itself, will be considered as main components of the TCO per km. A similar sensitivity analysis will be performed for Feeding, M&R, Insurance and Labour costs (see Table 4, Appendix A). Insurance costs for Neolix is the most unpredictable cost segment in terms of direction and amplitude of change. It may decrease, following the assumption that driverless vehicles will reduce the claim frequency [34], or increase, considering high costs of sensors needed for autonomy and for repair, at least on an early adoption stage. Based on the assumption of 50% premium reduction, the change by 50%, 100% and 150% in Insurance cost will be considered. Changes in cost segments are assessed uni-dimensionally.

Table 1. Sensitivity analysis for cost per km: cost segments change variation

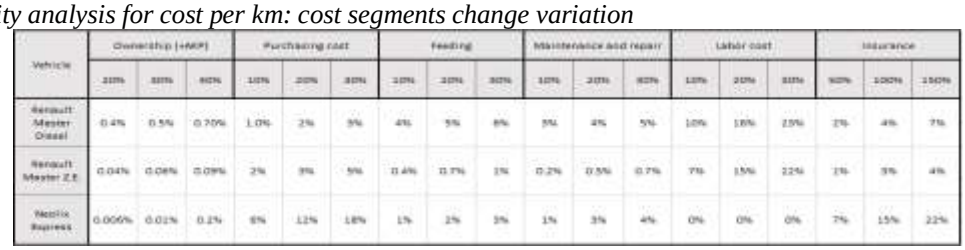

Sensitivity analysis on cost per km confirms the finding of TCO analysis, in which labour cost plays a vital role in total cost formation for non-autonomous vehicles, increasing the cost of km by as much as 23% for Renault Master Diesel and 32% for Renault Master Z.E., in case of 30% increase of the courier salary.

For autonomous vehicles, the purchasing cost itself represents the cost segment significantly affecting cost per km, giving an 18% increase of total costs with a 30% purchasing cost increase. As for insurance costs, although the percentage change in TCO per km appears large (7% to 22%), it should be noted that it almost coincides with one caused by Purchasing cost variation, while initial change percentages of Purchasing cost segment is five times smaller than in case of Insurance cost segment. Also, in absolute terms, even 150% of Insurance cost variation induced by autonomy is far away from the 10% Labour cost variation effect on the TCO per km for the rest of non-autonomous vehicles, which confirms, from an efficiency perspective, the advantageousness of the next technological transition, even at a potentially high insurance cost.

Since the conditions for using Neolix were equated to cargo bicycles, usually used for express and small parcels delivery, the shift to smaller than 12L parcels can give results that are more prominent. Especially since, according to DHL, bicycle couriers can be more productive, delivering up to 25% more parcels than vans in particularly busy and difficult to access urban areas [35]. In addition, although the small size parcels are prevailing in B2C deliveries, inefficiency in packaging methods remains a big concern, currently allowing for a 20% reduction in average parcel size [36]. At the same time, Bol.com plans to ship products with their own sturdy packaging, without outer additional cardboard boxes, encouraging their third party merchants to follow [37]. Retail order consolidation is another practice gaining popularity in e-commerce, which on opposite aims on combining multiple orders into one single package, potentially resulting in fewer shipments of fuller cartons [38].

The existing variability in relation to the size and number of packages prompts to conduct the sensitivity analysis on percentage distributions of 8L, 13L, and 18L parcel dimensions towards the total deliverable capacity of Neolix. Two scenarios are considered: the 1st puts emphasis on smaller parcels with a percentage distribution of 70%, 20%, 10%; the second includes Letterbox Parcel + size having a maximum of 3.2 L, instead of big 18L, with a percentage distribution of 40%, 40%, 20% from the smallest to the biggest parcel size. In the second scenario, the income per parcel delivered is changed according to the Letterbox Parcel + size distributional inclusion and its domestic tariffs (assuming equal distribution among online/offline franking) resulting in a new value of €5.94. Table 2 gives an

overview of both average parcel size scenarios, in comparison to the baseline for Neolix, Renault Master Diesel and the electric Z.E. version.

Table 2. Sensitivity analysis: average parcel size

Sensitivity Analysis: average parcel size

Master Diesel	Master Z.E.	Neolix	Neolix scenario 1	Neolix scenario 2	
132,880	132,880	124,254	149,742	210,276	Delivery volume per year (units)
78,000	78,000	103,131	103,131	103,131	Delivery likometre per year (km)
1.70	1.70	1.20	1.45	2.04	Parcels per kilometre delivered (units)
7.00	7.00	7.00	7.00	5.94	Income per parcel delivered (€)
11.93	11.93	8.43	10.16	12.11	Income benefit per kilometre (€)
0.90	0.96	0.13	0.13	0.13	Cost per kilometre (€)
11.03	10.96	8.30	10.03	11.98	Revenue/Loss per kilometre (€)

Scenario 1: The average parcel size in this case is 10L, resulting in maximum of 47 parcels that can fit in Neolix (471.5L). With nine daily delivery cycles, the maximum of 423 daily and 149,742 annual deliveries can be achieved respectively. Break-even point: 52 parcels of 9,06L size.

Scenario 2: The average parcel size in this case is 7.08L, resulting in maximum of 66 parcels that can fit in Neolix (471.5L). With nine daily delivery cycles, the maximum of 594 daily and 210,276 annual deliveries can be achieved respectively. Break-even point: 61 parcels of 7,73L size.

As expected, with a decrease in the average parcel's size and an increase in Neolix's total capacity, its overall profitability increases. Experimentally, the break-even points in relation to Renault Master Diesel in revenue per km for both scenarios were determined. Another way to improve profitability without changing vehicle capacity is to increase parcel density of the delivery area, meaning the change in the performance indicator of 0.83 km per parcel delivered, as determined for Neolix. Taking the initial Neolix calculations with 39 parcels capacity and 124,254 annual delivery volume as a baseline, increases of parcel density by 20% in scenario 1 and 30% in scenario 2 were considered. Parcel density directly affects annual millage, meaning that with the higher density, the total km needed to cover this area, therefore total costs, decrease. Density, on the other hand, can be improved by reducing the overall distance travelled in a single delivery cycle, based on better delivery route planning or deployment of inner-city micro-hubs reducing the longest plot (depot-1st delivery address) of entire delivery cycle steps.

Table 3. Sensitivity analysis: parcel density

Sensitivity Analysis: parcel density

Master Diesel	Master Z.E.	Neolix	Neolix scenario 1	Neolix scenario 2	
132,880	132,880	124,254	124,254	124,254	Delivery volume per year (units)
78,000	78,000	103,131	85,942	79,331	Delivery likometre per year (km)
1.70	1.70	1.20	1.45	1.57	Parcels per kilometre delivered (units)
7.00	7.00	7.00	7.00	7.00	Income per parcel delivered (€)
11.93	11.93	8.43	10.12	10.96	Income benefit per kilometre (€)
0.90	0.96	0.13	0.13	0.13	Cost per kilometre (€)
11.03	10.96	8.30	9.99	10.83	Revenue/Loss per kilometre (€)

Table 3 gives an overview of parcel density scenarios in comparison to Neolix's baseline, as well as Renault Master in diesel and electric version. In the first scenario, the increase of 20% gives the new density of 0.69 km per parcel and delivery cycle millage of 26.98 km. The second scenario with a density increase of 30% gives new performance indicators of 0.64 km and 24.90 km respectively. Improvement of 33% gives a new density of 0.62 and delivery cycle millage of 24.34 km, representing the break-even point from which Neolix brings more revenue per km than both Renault Master vans. As parcel density from the Parcel Market and Home Deliveries analysis was 0.6 km per parcel [31], with additional infrastructure like micro-hubs, Neolix has the potential to be fully competitive. The TCO cost segments for each vehicle is presented in Figure 2.

Figure 2. TCO per km comparison

Some segments were grouped together for comprehensive purposes. For instance, Subsidies and Indirect initiatives is combined with Purchasing cost, under "Purchasing cost", and Registration fee, BPM tax, Road tax, and APK inspection are gathered under "Ownership (+ APK)". The presented TCO analysis demonstrates a scientific breakthrough of energy efficiency competitiveness using renewable energy transport for last mile delivery. Based on the results, it is possible to argue on the adoption potential of autonomous ground vehicles with lockers as an innovative last mile solution.

5. CONCLUSIONS

The aim of this study was to explore the cost-benefit segments of LMD operations, using renewable energy transport in urban areas. Based on the TCO analysis, the biggest cost segment for non-autonomous vehicles is labour cost of delivery van drivers, simultaneously representing the potential savings in case of AGVs. Purchasing cost was another significant element, proving that technological deployment highly relies on economic feasibility and practicality. Thus, electric vehicles, while still being more expensive than diesel ones, even with governmental subsidies (€26,520.95 versus €44,318.75), over an ownership period of eight years will be cheaper to retain (€25,5894.2 versus €28,0501.96), encouraging an ongoing shift towards electrification. Contrary, AGVs with lockers, Neolix in this study, despite the lowest Purchasing and TCO costs (€24,910.75 and €41,574.82), make autonomy an expensive option, questioning its practicality, as the AGV's load capacity is times times smaller than a delivery van. Therefore, supplementary beneficial factors such as fuel efficiency, total operational time increase, capacity occupation and reliability were evaluated, opposed to the one-dimensional analysis based solely on costs. Regarding fuel efficiency, the effect of the auxiliary tool – SOT on vehicles' feeding costs was considered, discovering a significant difference in savings capabilities for diesel versus electric vehicles. Lastly, cumulative savings over eight years were not enough even to overcome the initial technology investment, while resulted in €1,518.07 of annual savings when applied to diesel engine vehicles. Summing up, the conclusion upon results indicates that autonomous ground vehicles with lockers are an innovative potential solution and more competitive when adopting renewable energy. In addition, for the branch of science of renewable energy systems, this research contributes with a scientific breakthrough about energy efficiency competitiveness using renewable energy transport for last mile delivery.

ACKNOWLEDGEMENTS

The authors would like to thank the OP Zuid program awarded funding. The project is made possible, in part, by financial support from the European Union (European Fund for Regional Development), OP-Zuid, the Province of North Brabant, the Province of Limburg and the Ministry of Economic Affairs and Climate.

REFERENCES

[1] Macharis, C., & Melo, S. 'City Distribution and Urban Freight'. (2011*). Transport*, 45-60. DOI: 10.4337/9780857932754
[2] Olsson, J., Hellström, D., & Pålsson, H. 'Framework of Last Mile Logistics Research: A Systematic Review of the Literature'. (2019). *Sustainability, 11*(24). DOI: 10.3390/su11247131
[3] Letnik, T., Peruš, I., Božičnik, S., & Mencinger, M. 'On fundamental principles of the optimal number and location of loading bays in urban areas'. (2019). *Transport, 34*(6), 722–740. https://doi.org/10.3846/transport.2019.11779
[4] Savelsbergh, M., & Van Woensel, T. '50th Anniversary Invited Article—City Logistics: Challenges and Opportunities'. (2016). *Transportation* Science, 50(2), 579-590. DOI: 10.1287/trsc.2016.0675
[5] Maestro, J., Rodriguez, S., Casado, R., Prieto, J., & Corchado, J. 'Comparison of Efficient Planning and Optimization Methods of Last Mile Delivery Resources'. (2021). *Lecture Notes Of The Institute For Computer Sciences, Social Informatics And Telecommunications Engineering*, 163-173. DOI: 10.1007/978-3-030-68737-3_11
[6] Ongel, A., Loewer, E., Roemer, F., Sethuraman, G., Chang, F., & Lienkamp, M. 'Economic Assessment of Autonomous Electric Microtransit Vehicles'. (2019). *Sustainability, 11*(3), 648. DOI: 10.3390/su11030648
[7] Ranieri, L., Digiesi, S., Silvestri, B., & Roccotelli, M. 'A Review of Last Mile Logistics Innovations in an Externalities Cost Reduction Vision'. (2018). *Sustainability, 10*(3), 782. DOI: 10.3390/su10030782
[8] Hamadneh, J., Szabolcs Duleba, S. & Esztergár-Kiss, D. 'Stakeholder viewpoints analysis of the autonomous vehicle industry by using multi-actors multi-criteria analysis'. (2022). *Transport Policy, 126,*65-84. DOI: https://doi.org/10.1016/j.tranpol.2022.07.005
[9] Pani, A., Mishra, S., Golias, M., & Figliozzi] Pani, A., Mishra, S., Golias, M., & Figliozzi, M. 'Evaluating public acceptance of autonomous delivery robots during COVID-19 pandemic'. (2020). *Transportation Research Part D: Transport And Environment*, *89*, 102600. DOI: 10.1016/j.trd.2020.102600
[10] Figliozzi, M. 'Carbon emissions reductions in last mile and grocery deliveries utilizing air and ground autonomous vehicles'. (2020). *Transportation Research Part D: Transport And Environment*, *85*, 102443. DOI: 10.1016/j.trd.2020.102443
[11] Li, D., Huang, Y. & Qian, L. 'Potential adoption of robotaxi service: The roles of perceived benefits to multiple stakeholders and environmental awareness'. (2022). *Transport Policy, 126,*120-135. DOI: https://doi.org/10.1016/j.tranpol.2022.07.004
[12] Reed, S., Campbell, A. M. & Thomas, B. W. 'Impact of Autonomous Vehicle Assisted Last-Mile Delivery in Urban to Rural Settings'. (2022). *Transportation Science,* Articles in Advance, 1–19. DOI: https://doi-org.mu.idm.oclc.org/10.1287/trsc.2022.1142
[13] Dobbins, A., Nerini, F. F., Deane, P., & Pye, S. 'Strengthening the EU response to energy poverty'. (2019). *Nature Energy*, *4*(1), 2-5.
[14] Shivakumar, A., Dobbins, A., Fahl, U., & Singh, A. 'Drivers of renewable energy deployment in the EU: An analysis of past trends and projections'. (2019). *Energy Strategy Reviews, 26,* 100-402. DOI: 10.1016/j.esr.2019.100402
[15] Lebeau, P. Towards the electrification of city logistics. (2016). Vrije Universiteit Brussel, Brussel. DOI: 10.13140/RG.2.1.3527.9768
[16] Richter, F. *Infographic: Can Falling Battery Prices Power EV Breakthrough?*. (2020). Retrieved 10 May 2021, from https://www.statista.com/chart/7713/electric-car-battery-prices/
[17] de Rus, G., Socorro, M.P., Valido, J. & Campos, J. 'Cost-benefit analysis of transport projects: Theoretical framework and practical rules'. (2022). *Transport Policy, 123,* 25-39. DOI: https://doi.org/10.1016/j.tranpol.2022.04.008
[18] Siragusa, C., Tumino, A., Mangiaracina, R., & Perego, A. 'Electric vehicles performing last-mile delivery in B2C e-commerce: An economic and environmental assessment'. (2020). *International Journal Of Sustainable Transportation*, 1-16. DOI: 10.1080/15568318.2020.1847367
[19] Desreveaux, A., Hittinger, E., Bouscayrol, A., Castex, E., & Sirbu, G. M. 'Techno-Economic Comparison of Total Cost of Ownership of Electric and Diesel Vehicles'. (2020). IEEE Access, 8, 195752-195762.
[20] Glitman, K., Farnsworth, D., & Hildermeier, J. 'The role of electric vehicles in a decarbonized economy: Supporting a reliable, affordable and efficient electric system'. (2019). *The Electricity Journal*, *32*(7), 106623. DOI:10.1016/j.tej.2019.106623
[21] Wadud, Z. 'Fully automated vehicles: A cost of ownership analysis to inform early adoption'. (2017). *Transportation Research Part A: Policy And Practice, 101,* 163-176. DOI: 10.1016/j.tra.2017.05.005
[22] Schröder, J., Heid, B., Neuhaus, F., Kässer, M., Klink, C., & Tatomir, S. *Fast forwarding last-mile delivery – implications for the ecosystem*. McKinsey & Company. (2018). Retrieved 10 May 2021, from https://www.mckinsey.com/
[23] Mearig, T., Coffee, N. and Morgan, M. Life Cycle Cost Analysis Handbook. (1999). *State of Alaska, Department of Education & Early Development.*
[24] Renault Case Elektrisch Rijden: PostNL. Renault.nl. (2018). Retrieved 31 May 2021, from https://electric.renault.nl/nl/case-postnl
[25] SolarOnTop - the future is on the roof | IM Efficiency. (2021). Retrieved 31 May 2021, from https://imefficiency.com/solarontop
[26] Dablanc, L. Goods transport in large European cities: Difficult to organize, difficult to modernize. (2007)
Transportation Research Part A: Policy and Practice, 41(3), 280-285. DOI: https://doi.org/10.1016/j.tra.2006.05.005
[27] Kenteken auto overschrijven | RDW. (2021). Retrieved 31 May 2021, from https://www.rdw.nl/particulier/voertuigen/auto/kopen-en-verkopen/kenteken-overschrijven

[28] Standaard Bedrijfsindeling - English [Ebook]. CBS. (2017). Retrieved 31 May 2021, from https://www.cbs.nl/-/media/_pdf/2017/31/sbi%202008%20versie%202017%20engels.pdf
[29] Kin, B., Quak, H., Hopman, M., Nesterova, N., & de Vries, J. Outlook Pakketmarkt En Thuisleveringen. (2020). Retrieved 31 May 2021, from https://topsectorlogistiek.nl/wptop/wp-content/uploads/2021/02/Outlook-Pakketmarkt-en-Thuisleveringen.pdf
[30] Salaris voor Bezorger (m/v) in Nederland. Indeed. (2021). Retrieved 31 May 2021, from https://nl.indeed.com/career/bezorger/salaries
[31] Outlook-Pakketmarkt-en-Thuisleveringen. Topsector Logistiek. (2020). Retrieved 11 August 2021, from https://topsectorlogistiek.nl/
[32] Bradfield, M. Improving Alternator Efficiency Measurably Reduces Fuel Costs. (2008). Retrieved 20 June 2021, from https://www.delcoremy.com/documents/high-efficiency-white-paper.aspx
[33] Postnl.be. (2021). Retrieved 6 July 2021, from https://www.postnl.be/en/contact/receiving-your-parcel/delivery-time/. [PostNL] Vacatures in de postbezorging & sortering. PostNL. (2021b). Retrieved 31 May 2021, from https://www.postnl.nl/over-postnl/
[34] Analyse van de Nederlandse verzekeringsmarkt 2019. KPMG. (2020). Retrieved 31 May 2021, from https://assets.kpmg/content/dam/kpmg/nl/pdf/2021/sectoren/analyse-nederlandse-verzekeringsmarkt-2019.pdf
[35] Rates for mail and parcels. PostNL. (2021d). Retrieved 31 May 2021, from https://www.postnl.nl/Images/tarievenfolder-2021-en-web_tcm10-194354.pdf?version=1
[36] Jonker, D., & Zschocke, K. The average parcel size in e-commerce shipments – a variable in coping with congestion in carrier networks? (2018). Retrieved 11 July 2021, from https://www.kennisdclogistiek.nl/
[37] Sword, A. *Bol.com removes parcel packaging from 7 million items*. (2020). Retrieved 11 July 2021, from https://internetretailing.net/operations-and-logistics/operations-and-logistics/bolcom-removes-parcel-packaging-from-7-million-items-21553
[38] Apparel and General Merchandise Guideline – Order Consolidation Best Practices. GS1 US. (2019). Retrieved 11 July 2021, from https://www.gs1us.org/
[39] Louter, T. A simulation study on standardized containers and the interplay between routing efficiency and material handling. (2019). Retrieved 6 July 2021, from https://feb.studenttheses.ub.rug.nl/24273/1/Msc_Thesis_S2520559.pdf
[40] Subsidies and programmes. RVO. (n.d.)Retrieved 31 May 2021, from https://english.rvo.nl/subsidies-programmes
[41] van Wees, I. *Operational Deep-dive Parcels.* (2019). Retrieved 31 May 2021, from https://www.postnl.nl/Images/parcels-operational-deep-dive_tcm10-149463.pdf
[42] VAT tariffs. Belastingdienst. (2021). Retrieved 31 May 2021, from https://www.belastingdienst.nl/

APPENDIX

Appendix A

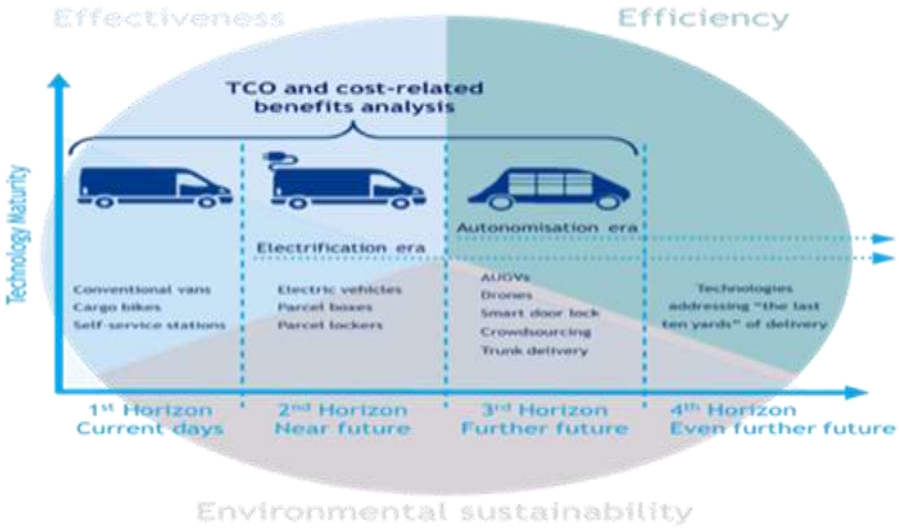

Figure 6. Boysen and Schröder Conceptual framework

$$TCO_T = PP_0 - RV_T + RFC_0 - S_0 + \sum_{t=0}^{T} \frac{FC_t + IC_t + MRC_t + BC_t + OC_t + RT_t - II_t}{(1+i)^t} \quad (1)$$

TCO assessment formula proposed by [18]

$$PV = A_t \times \frac{1}{(1+I)^t}$$

Where:

PV = Present value

A_t = Amount of one-time cost at a time t

I = Real discount rate (2)

t = Time (expressed as number of years)

Table 4. Vehicles overview

Vehicle name	Motor type	Payload m^3	Curb Weight (kg)	Max. Speed (km/h)	Purchase price (€, excl. VAT)	Max. Range (km)	Fuel consumption (l/100km or kWh/100km)
Renault Master Diesel	2.3L diesel engine	13.0	2066	148	31,940	1,200	6.7
Renault Master Z.E.	57kW BEV with 33kWh battery	13.0	2050	100	58,700	120	27.5
Neolix Express	BEV with swappable 12.9kWh battery	2.4	371	50	30,000	100	12.9

Input information needed for a TCO on a transport vehicle [18]

1) Ownership period – predefined time interval parameter that defines the estimation scope (year, life span);

2) Travel data – travel statistics or kilometers that a vehicle is predicted to travel during ownership, usually depending on the industry and purpose the vehicle is used for;

3) Vehicle data – cover the cost of the vehicle unit and summarize its main model characteristics affecting unit price and operational costs. It is the most important and predetermining data set of a TCO, as the vehicle's features and fuel type heavily correlate with vehicle structure and associated costs. For example, to ensure the required level of autonomy, additional equipment is needed, like sensors and cameras to perceive the environment and their own movement, onboard computer hardware and special actuators for vehicle control, while a driver's presence is usually required in order not to miss some conventional parts. For the same reasons, personnel costs are later included or excluded in operational costs. Fuel type can also entail changes in a form of battery, solar panels, hydrogen tanks or adjusted engine and affect the depreciation rates changing the residual end value of the vehicle [*15.*].

4) Cost data - traditionally include all operational costs involved, i.e. registration fees, subsidies, feeding (fuel costs), insurance, maintenance and repair, taxes, road toll, indirect incentives that might deviate depending on the economic situation, governmental policies and vehicle usage related factors [*18*].

VEHICLE RELATED COSTS - FEES AND TAXES

Registration fee – any vehicle over 750 Kg must be registered at RDW. The price for that is €10.75 [*27*].

BPM charge (Bijzondere Verbruiksbelasting van Personenautos) - tax payable by the first person to register a newly purchased vehicle in the Netherlands [42]. However, there is an option to avoid BPM by obtaining the grey license plate that also allows for a reduction benefit on road tax. Both diesel and electric Renault Master delivery vans meet the conditions for the grey license plate when used for business purposes that make them eligible for exemption from the BPM. Under Dutch law, Neolix is not recognized as a delivery van, therefore cannot claim for grey license plate and, from this point in this study, will be equated to a passenger car used for business purposes [42]. For passenger cars, BPM is determined by the CO2 emissions in grams/km, therefore for electric Neolix, BPM is not charged [42].

APK – is a general periodic inspection in Europe. Delivery vans up to 3500 kg obey the same inspection rules as passenger cars [27]. The only difference is the frequency of inspection that depends on the fuel type. Vehicles with electric or gasoline engines need to be first checked when they are four years old, then twice every two years and then every other year (the 4-2-2-1 schedule). For diesel, gas or other engines, the schedule is 3-1-1. The price of

APK varies per service provider and, on average, accounts for €45 for an electric van, €52 for a conventional van and €35 for passenger cars.

Road (motor vehicle) tax – annual fee on the use of a vehicle that depends on weight, fuel type, level of pollution caused by a vehicle, and province. According to [42], the conventional diesel vehicles for business use with "Empty vehicle mass" of 2051-2150 kg should pay €142 every three months, while electric vehicles are exempt from this tax until 2024. Then in 2025, there will be a 75% tax discount, and from 2026 the full rate of tax should be paid again. The road tax for an electric van with "Empty vehicle mass" of 1951-2050 kg is €135, and for Neolix type of vehicle (1-550 kg), it is €30 respectively.

VAT- value added consumption tax on goods and services. The general VAT in the Netherlands is 21%. However, if vehicle is fully count as a business asset, which is the case for this study, the VAT can be deducted [42].

VEHICLE RELATED COSTS - SUBSIDIES AND INDIRECT INITIATIVES

Subsidy Scheme for Emission-Free Company Cars (SEBA) – subsidy functioning from 15/03/2021 to 31/12/2025 and gives 10% refund up to maximum €5000 on the net list price for a completely emission-free company vehicle under category N1 [40] . All vehicles under consideration in this research meet the requirement of the N1 category and are therefore eligible for SEBA (Transportpolicy.net, 2021).

Environmental Investment Allowance (MIA) – tax benefit for investment in environmentally friendly assets approved and mentioned in so-called "positive lists" [40]. Renault Master Z.E. with asset case G3101, is eligible for an allowance for a maximum of €75,000 of the investment amount with a total MIA benefit of 36% and condition of the previous deduction from the purchasing price of any subsidies receives like SEBA [40].

Small-scale investment allowance (KIA) – business investments in assets in the range of €2,401 to €59,170 are eligible for 28% of the investment amount [42]. There is no evidence of Neolix cannot be qualify for this investment allowance, the same can be applicable to Renault Master Z.E. and one with a diesel engine and even to SolarOnTop [42].

Energy investment allowance (EIA) – allowance for CO2 reduction, energy-efficient techniques and sustainable energy-related investments. It gives an average advantage of 11% and lowers energy bills, allowing for subtraction of the electricity generated with EIA investment [40] . Solar panels used in this research comply with the description under asset code 251115 of Energy List - Solar panels or foil for electricity generation on means of transport [40].

C) Feeding - Energy or fuel costs, specifically electricity and diesel fuel. Electricity price exc. VAT is 0,11€/kWh as per Eurostat 2021, and diesel price is €1,520/L according to Average National Recommended Price as per Unitedconsumers.com,

D) Insurance - Auto insurances vary depending the service provider, and are usually more expensive for business than for private vehicles because of higher annual mileage and risks related. Therefore the insurance premiums from Achmea, the leader of the insurance Dutch market [34], were taken. During calculations, the price of Full WA+ Casco was considered based on a 33-year-old driver with no accidents in the last 10 years. Accordingly, for diesel vans the premium is €128.03 per month, while for electric vans it is only around €69.84. Nowadays, nobody can predict the premium amount on autonomous vehicles, especially for delivery robots like Neolix. In this study, an estimation of 50% premium reduction comparing to the conventional van was chosen. It leads to €64 of the insurance premium for Neolix delivery vehicle.

E) Maintenance and repair - Maintenance costs for electric vehicles are lower than for a conventional van with an internal combustion engine, because they have fewer moving components and don not need oil and filter replacements. [15] in their TCO comparison study on electric vehicles, retrieved the cost of maintenance of 0.019c€/km and 0.052c€/km for electric and diesel vehicles respectively. Their estimations are in line with, claiming that the MR costs of the electric vehicle's battery are half of the conventional cars.

F) Battery - the battery lifespan is typically determined by a number of full charging cycles performed before the battery reach a certain level of initial capacity or so-called state of health (SoH). For Renault Master Z.E. 33 kW/h battery the minimum SoH after which it cannot be used in the automotive industry anymore is 66% [24]. After eight years, average battery degradation will reach around 12.8 - 18.4 % (Argue, 2020), still being far from the critical 66% SoH. Battery longevity can vary depending on many factors, for instance usage, climate, and charging frequency, thus is hard to predict, but according to the Groupe Renault [24] it was estimated around ten years for its electric vehicle product line. No information was found on the lifespan of the Neolix battery. Therefore, no battery cost will be considered in this research.

E) Road toll - Currently, there are no toll roads in the Netherlands for vehicles less than 12 tons (UTA, 2021). However, there are zero-emission zones in 13 municipalities restricting entry of diesel vehicles with emission class 3 and lower. Renault Master with a diesel engine has an emission class of 6.

Appendix B

Vehicles' Descriptive Information

Neolix specifications and details. Sources: Design Intelligence Award (2021); Dérobert (2020)

Technical details

Model:	SLV11
Drive system:	electric (battery)
Range per battery charge:	100 kilometres
Speed in the trial:	6 km/h
Range in hours:	around 8 hours
Unladen weight:	371 kg
Maximum load:	350 kg
Length x width x height:	2.69 x 1 x 1.87 metres
Number of compartments:	22 (2x11)
Compartment dimensions:	large compartments: 510 x 280 x 420 mm / small compartments: 125 x 245 x 420 mm
Turning radius:	6.90 metres
Braking distance:	around 1 metre at 10 km/h (depends on speed)

Battery

Charging time: zero hours	(battery can be replaced)
Capacity:	12.9 kwh
Voltage:	72 volts
Maximum power:	8 kilowatts

Safety/navigation systems

4 LiDAR systems, 6 cameras and 14 sensors

Renault Master specifications and details. Sources: [24]

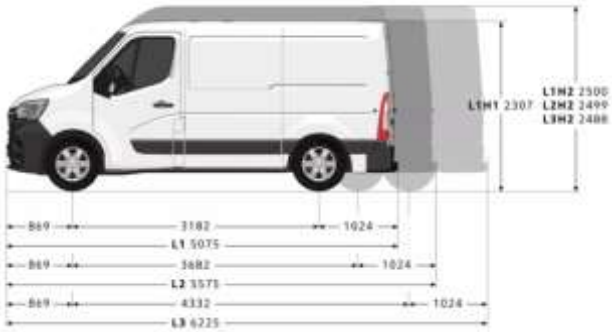

Appendix C

Table 5. SolarOnTop savings performance

Vehicle name	Area suitable for SOT installment (m2)	Annual energy generated (kWh)	Annual fuel savings (L)
Renault Master Diesel	6.88	-	998.73
Renault Master Z.E.	6.88	692.50	-
Neolix Express	3.25	346.25	-

Table 6. Summary of the TCO cost segment

Cost segments / Vehicle	Master Diesel	Master Diesel + SolarOnTop	Master Z.E.	Master Z.E. + SolarOnTop	Neolix	Neolix + SolarOnTop
Purchasing cost (€)						
Purchasing cost (€)	31,940.00	37,290.00	58,700.00	64,050.00	30,000.00	352,500.00
Subsidies and Indirect initiatives (€)	5,429.80	6,412.86	14,392.00	14,766.50	5,100.00	6,064.69
Ownership (+AKP) (€)						
Registration fee (€)	10.75	10.75	10.75	10.75	10.75	10.75
BPM tax (€)	-	-	-	-	-	-
Road tax (€) (for 3 months)	142	142	135 (from 2026)	135 (from 2026)	30 (from 2026)	20 (from 2026)
APK inspection (€) (schedule pattern)	52 (3-1-1)	52 (3-1-1)	45 (4-2-2-1)	45 (4-2-2-1)	35 (4-2-2-1)	35 (4-2-2-1)
Feeding cost (€/L , €/kWh)	1.52	1.52	0.11	0.11	0.11	0.11
Insurance cost (€/month)	128.03	128.03	69.84	69.84	64.00	64.00
Maintenance and repair (€/km)	0.052	0.052	0.019	0.019	0.019	0.019
Battery cost (€)	-	-	-	-	-	-
Road toll (€)	-	-	-	-	-	-
Labour cost (€/month)	1,973.00	1,973.00	1,973.00	1,973.00	-	-
TCO for 8 years (€)	280,501.96	266,450.62	255,894.20	260,261.67	41,574.82	45,566.12

Table 7. Maximum delivery volume calculation per vehicle

Renault Master	Neolix		Neolix delivery perfomance	
220	39	Load capacity in units	16	Vehicle speed in km/h
08:00-21:30	07:00-01:00	Working hours	0.83	Vehicle km per unit
13.5	18		39	Load capacity in units
6	7	Working days per week	32.37	Delivey cycle millage
302	354	Working days per year	2	Delivery cycle duration in hours
440	351	Maximum delivery volume per day	9	Number of cycles per day
2,640	2,457	Maximum delivery volume per week	351	Maximum delivery volume per day
132,880	124,254	Maximum delivery volume per year		

Table 8. Cost-benefit summary of last mile delivery vehicles

Master Diesel	Master Z.E.	Neolix	
132,880	132,880	124,254	Delivery volume per year (units)
78,000	78,000	103,131	Delivery likometre per year (km)
1.70	1.70	1.20	Parcels per kilometre delivered (units
7.00	7.00	7.00	Income per parcel delivered (€)
11.93	11.93	8.43	Income benefit per kilometre (€)
0.90	0.96	0.13	Cost per kilometre (€)
11.03	10.96	8.30	Revenue/Loss per kilometre (€)

Purchasing and annual Ownership (+APK) costs calculations

Purchasing price calculation

	Master Diesel	Master Diesel + SolarOnTop	Master Z.E.	Master Z.E. + SolarOnTop	Neolix	Neolix + SolarOnTop
Price of vehicle excl. VAT/BPM	31,940.00	31,940.00	58,700.00	58,700.00	30,000.00	30,000.00
Price of SolarOnTop		5,350.00		5,350.00		5,250.00
Vehicle related capital costs						
Registration fee	10.75	10.75	10.75	10.75	10.75	10.75
BPM 37.7% (+273)	-	-	-	-	-	-
Total	31,950.75	37,300.75	58,710.75	64,060.75	30,010.75	35,260.75
Subsidies and Indirect initiatives						
MIA 36% (9%)	-	-	21,132.00	21,132.00	-	-
KIA 28% (5.5%)	8,943.20	10,441.20	16,436.00	17,934.00	8,400.00	9,870.00
EIA 45.5% (11%)	-	2,434.25	-	-		2,388.75
Net benefit at 25% nominal tax	2,235.80	3,218.86	9,392.00	9,766.50	2,100.00	3,064.69
SEBA	3,194.00	3,194.00	5,000.00	5,000.00	3,000.00	3,000.00
Total subsidies	5,429.80	6,412.86	14,392.00	14,766.50	5,100.00	6,064.69
Total purchasing price	**26,520.95**	**30,887.89**	**44,318.75**	**49,294.25**	**24,910.75**	**29,196.06**

Annual Ownership (+APK) costs

Year		Master Diesel	Master Diesel + SolarOnTop	Master ZE	Master ZE + SolarOnTop	Neolix	Neolix + SolarOnTop
2021	1	567.72	567.72				
2022	2	567.43	567.43				
2023	3	619.07	619.07				
2024	4	618.76	618.76	44.91	44.91	34.93	34.93
2025	5	618.45	618.45	33.67	33.67	7.48	7.48
2026	6	618.14	618.14	179.46	179.46	64.81	64.81
2027	7	617.83	617.83	134.53	134.53	29.90	29.90
2028	8	617.53	617.53	179.28	179.28	64.74	64.74
Total 8 years		4844.94	4844.94	571.85	571.85	201.85	201.85

RIGA 2023

The Analysis of Energy Efficiency Measures in Multiapartment Buildings in Latvia

Aleksandra Cimbale
College of Law, Riga, Latvia, a.cimbale@inbox.lv, ORCID: 0000-0002-9994-2764

Iveta Amoliņa
Riga Technical University, Riga, Latvia, iveta.amolina@rtu.lv, ORCID: 0000-0003-2500-0501

Cite this paper as: *Cimbale A., Amoliņa A., The Analysis of Energy Efficiency Measures in Multiapartment Buildings in Latvia 11. Eur. Conf. Ren. Energy Sys. 18-20 May 2023, Riga, Latvia*

Abstract: Much research and many articles have been done on energy efficiency matters and particular instruments to monitor, determine and reduce consumption of different types of energy. The most consumed energy form by multiapartment buildings is still heat power presented either by heating of the rooms, or both by heating and hot water preparation. Observing the household bills of all apartment owners in Riga and Latvia during past 5-10 winters or heating seasons can be concluded that this type of energy forms 50% and more of all dwelling maintenance costs. Many communities of apartment owners due to different financial and psychological reasons are not ready to participate in co-funding programs of complex renovation. A big part of society is ready to invest money they have already saved up in maintenance and repairments of the apartment buildings. The authors of this research have chosen a methodology which in relation with types and series of buildings is able to show reduction of heat power consumption after performing the most popular repairments. Thus, giving a roadmap to the apartment owners and maintenance companies on different ways how to save up money and reduce the negative ecological impact by reducing energy consumption and heat losses.

Keywords: *Energy efficiency, sustainability, multiapartment buildings, heat loses, repairments*

1. INTRODUCTION

Every product or service has a lifecycle consisting of particular and definable phases. This cycle can be reduced to three main stages for any unit – production, transportation, and consumption. Heat power and electricity are not an exception. Manufactured in a powerplant, provision to households, industrial objects and public venues via pipelines and grids, further consumption by individuals and processes makes both energy types relevant to the previously described formula. Without doubt heat power and electricity make any building attractive and useable during every time of the year, but already a while uncontrolled and highly likely unmeasured consumption becomes a financial burden for owners and users of any kind of immovable property. Definitely, the climate of the Baltic States and generally of Northern Europe does not allow to provide comfort for inhabitants of dwellings without proper and almost constant heating, but measuring, accounting and energy efficiency increasing procedures are a must have both for owners and maintenance companies in these countries, as well as in Latvia in particular.

Due to uneven level of wealth of persons forming the communities of apartment owners in every apartment building, and because of many other reasons and circumstances defined by the authors of the article and determined analyzing the results of a questionnaire developed for this research, the performing of the full renovation of buildings does not happen as fast as needed and forecasted. The results of the questionnaire will be published in a different article because of the ongoing collection of data and respondents. The research performed by the authors

tries to find technical solutions that can be performed cheaper, faster, with lesser administrative costs, still showing appropriate results in the field or reduction energy losses.

Energy efficiency has gained a lot of prominence in housing policy due to its potential consequences for climate change. There are numerous local, national and also international initiatives to promote energy savings and the use of renewable energy to reduce the environmental burden. The residential built environment is a significant factor in the use of fossil energy sources and, therefore, has a substantial potential in the reduction of this energy use efficiency in housing [1].

The amount of literature, especially articles in peer-reviewed journals, on the topic of energy efficiency in multiapartment buildings is wide and multifaceted. The authors of this research attempted to create a review of literature that might help define the most important difference in the situation in comparison with other countries. Even Lithuania and Estonia, representing the same region, show a different approach, policy, technological problems and solutions. Around 67% of population of Latvia are living in multiapartment buildings constructed between 1945 and 1991. The construction principles in the Soviet Union were common for all the fifteen member countries, but still a variety of types and series of multiapartment buildings was allowed to be designed and used locally, never leaving the territory of the particular country. That makes the multiapartment buildings generally like the ones created around the whole union but having their own remarkable features which however are not always positive. Not many authors before this research have evaluated the panel, block and brick residential constructions presented in Latvia in the context of energy efficiency and performed repairments.

The first recognizable publication on mass construction in Latvia is the research “Soviet housing: who built what and when? The case of Daugavpils, Latvia.” made by Gentile M. and Sjoberg O. in 2010. However, the authors have put the emphasis on social and economic aspects of mass housing both in general and primarily in one of the biggest cities of Latvia, the idea that “the built environment and, concomitantly, the socialist spatial structures inherited by today's post-socialist cities have by no means been squeezed out by the market” [2]. It means that the preservation of these buildings, its overall renovation and reduction of heat power losses might ensure not only a well-deserved place for these objects in the landscape of the modern cities, but also provide wealth and comfort to its current inhabitants. Appropriate maintenance, timely refurbishment works, careful and thoughtful exploitation makes the society less energy import dependent and more sophisticated. In accordance with Davor Mikulić’s, Sunčana Slijepčević’s, Goran Buturac’s article “Energy renovation of multi apartment buildings: Contributions to economy and climate changes” - renovations induce 32 jobs in Croatian economy per 1 million EUR of investments [3]. Thus, stimulating the well-being of the society, which is also important aim for Latvia.

Of course, local scientists have also addressed the question of mass construction, its appropriate maintenance and energy efficiency matters. The group of authors consisting of Kristaps Zvaigznitis, Claudio Rochas, Gatis Zogla, Agris Kamenders in their research “Energy efficiency in multi-family residential buildings in Latvia. Cost benefit analysis comparing different business models.” have not considered the technical aspects of renovation, but the financial matters of energy efficiency projects. Still the paper shows not only economic advantages of renovated buildings but provides the comparison of energy consumption in dwellings that have participated in the ESCO project [4]. The authors of the current research have determined that the society in general avoids participating in ESCO projects, loans, EU co-financing of renovation. Similar questions were asked by the authors of this paper. The questionnaire released in summer of 2022. 224 respondents have replied to several questions on housing, energy efficiency and repairs in multiapartment buildings. 67% of respondents agree that the dwellings have to be renovated as a preauction for further living. The evaluation of the readiness of neighbors forming the community of the apartment owners was estimated as very poor – only 17.9% are sure that the community of a particular house is capable to make the decision on renovation matters.

There are many two most popular recipes to reach the main goal - to reduce energy consumption and heat losses, to increase energy efficiency and the lifespan of the multiapartment buildings - performing complex renovation works at once, but receiving a debt, or complete stage by stage repairs in accordance with the amount of money saved up by the community of apartment owners. Of course, the second scenario might have both positive and negative effects on the house. While completing the exchange of the roof surface material and insulating the attic, the foundation and plinth might be breaking down, lead water through damaging the foundation and the whole construction. Different elements of the house lose stability and solidity gradually and emergency state can be

reached on different terms, but the mass construction was performed from concrete prefabricated elements which are similar in many aspects, also in the durability and lifespan. The deterioration of these elements might be reached almost simultaneously thus making for the community of owners hard to provide the necessary amount of money for repairs without a loan or co-funding program. Still, single repairs are popular among the apartment owners, so it is important to determine the output in terms of saved energy after completion of different kinds of works. Therefore the general aim of the research of the authors is to determine the impact of energy efficiency increasing measures on heat consumption in multiapartment buildings. This aim can be reached by completing a list of tasks, such as creating or developing an existing methodology of calculation of heat losses for single repairment works, collecting as much as possible data on typical dwellings, completed repairment works and heat consumption before and after interfering, experimenting on an algorithm that might become a roadmap for apartment owners willing to go different roads to increase energy efficiency and the lifespan of their homes. The presented article shows the start of a big research including the search for methods and instruments to calculate the reduction of energy consumption by every single work performed in the house; the determination of social, economic and psychological aspects preventing communities of owners from global important steps towards putting in order their homes; defining an algorithm and roadmap that might help apartment owners and maintenance companies to make the correct decisions on preservation of dwellings based on research, economy and sustainability factors.

2. METHODOLOGY

The authors of the research tried to find different criteria to divide in groups the repairments needed by an apartment building. Grouping and classifying mostly depends on local legislative acts, which means that the offered system might not be appropriate for any other country except Latvia but might show the basic principles useful for other scientists working in this field. Conceptually the massive of the repairs can be related to:

1. Expenses and the source of them.
2. Confirmation, approving, and technical documentation needed beforehand the construction works.
3. Result in form of reduction of heat loses and increase of energy efficiency parameters of the building.

The expenses parameter is not only variable but depends on many social and economic aspects – the wealth level of the apartment owners, possible and available co-funding programs, amount and type of repairs needed, the novelty, originality and complications of the chosen repairment methods impacting both the price and availability on the market. The process of confirmation of a repairments also might be an additional complication before fast and effective implementation, and, of course, also a classification parameter. Most of the repairs performed in multiapartment buildings do not require any kind of agreement received from the Riga City Council Department of City Development in case of Riga or similar organizations in case of other cities of Latvia, but if more complex repairs are chosen, many different alterations are going to be done, the more detailed documentation must be prepared. In the context of this research, the parameter of energy efficiency is the determining and crucial, due to the policy of the country, European Union, and the whole world. The forecasted shortage of resources determines the necessity to evaluate repairs not only as an instrument to prolong the lifespan of an object, but as a tool to allow the building to serve society as long as possible, consuming many less energies in comparison to present times.

The authors of the presented research have made several attempts to find a universal methodology to calculate mostly precise the reduction of energy consumption following different repairs completed in multiapartment buildings. The most logical way to find the efficiency degree of any repair is to compare the heat consumption of a building during the winter before the works and during the winter after them. However, this “easy” method has many important drawbacks. The most important variable parameter is the duration of the real, not the calendar winter. The real winter or namely the heating season duration alters every year. Also, the air temperatures are very different during this season. During a very long heating season the temperatures might drop only till -5°…+5°C, but a rather short winter might bring temperatures lower than -10°C on a constant basis. The combination of temperatures and duration has a significant impact of the overall energy consumption of the building.

The most appropriate for this occasion calculation attempt was made by two Ukrainian engineers Aleksandr Gut and Aleksej Zhdanov in 2016 [5]. They offer to calculate a correction coefficient that gives the required precision to an ordinary comparison of heat consumption during any period. The coefficient is determined using the following formula:

$$K = \frac{GDD_{year+1}}{GDD_{year}} \quad (1)$$

K – correction coefficient of heat power consumption;
GDD_{year+1} – degree day amount in the year / winter / single winter month after the repairments;
GDD_{year} – degree day amount in the year / winter / single winter month before the repairments [5].

The degree day amount in Riga is determined by the local district heating company JSC "Rīgas siltums" and their collected data has been used to perform calculations for the capital of Latvia. All multiapartment houses whose data has been used in this research are located in Riga and receive heat power from JSC "Rīgas siltums".

The heat power consumption reduction is calculated in the following way:

$$I = \frac{Q_{2015} - Q_{2016}}{Q_{2016}} 100\% \quad (2)$$

I – the economy or reduction of heat power, %;
Q_{year} – heat power consumption in the year / winter / single winter month before the repairments, J;
Q_{year+1} – heat power consumption in the year / winter / single winter month after the repairments, J.
Therefor the corrected economy or reduction of heat power is equal to:

$$I_{corrected} = IK \quad (3)$$

$I_{corrected}$ – the corrected economy or reduction of heat power, %;
I – the economy or reduction of heat power, %;
K – correction coefficient of heat power consumption [5].

To show the readers the usage of this method and its reliance to any kind of repairs performed in multiapartment buildings let please the authors show a humble example. The research is based on most typical repairments completed in typical, concrete panel houses build in accordance with a particular series. The repairments in the field of interest of the corresponding research theoretically might positively affect energy efficiency of an object and reduce heat losses. Such works are insultation of the envelope of the building, exchange of doors and windows, hermitization of junctures between panels, renovation of foundation and plinth. These works are not only important to minimize energy consumption, but also very popular among maintenance companies and apartment owners' communities as they prolong the lifespan of the corresponding object. In the year 2016, in October one house in Riga has undergone the insulation works of both end walls or being more precise - firewalls. The house corresponds to 602nd series, which is widely distributed not only in Riga, but overall, in Latvia.

First, the correction coefficient of heat power consumption has been calculated:

$$GDD_{2016\ january} = 218 \times (20 - -2.7) = 4948.6 \quad (4)$$
$$GDD_{2017\ january} = 204 \times (20 - -1.6) = 4406.4 \quad (5)$$
$$K_{2016\ january}/_{2017\ january} = \frac{4406,4}{4948,6} = 0.89 \quad (6)$$

The economy or reduction of heat power comparing two Januarys equals to.

$$I = \frac{132.95 - 121.8}{121.8} \times 100\% = 9.15\% \quad (7)$$

Using the correction coefficient, the actual reduction is equal to:

$$I_{2016\ january}/_{2017\ january} = 9.15 \times 0.89 = 8.14\% \quad (8)$$

In this case after completing the repairments – the insulation of both firewalls has allowed to achieve 8,14% reduction of heat consumption. Performing analogical calculations, positive results were received for other types of refurbishments.

3. TYPES OF REPAIRMENTS ANALYZED

The multiapartment buildings in Latvia are maintained by different bodies. There are state and municipal companies providing the obligate variety of services, private companies acting upon a contract, cooperatives and partnerships of apartment owners. Analyzing the most common repairments chosen by these maintenance bodies the authors have come to one main conclusion – the choice of the type of the repairment does not depend on the person providing maintenance, but it depends on the type, lifespan, construction features and other technical aspects of the building. Still, the most widespread multiapartment buildings were constructed in accordance with types or series, replicating not only the facades and internal utilities, but also making mistakes and disadvantages common and repeated. Thus, the mostly performed repairments are following:

1. Replacement of windows and doors;
2. Replacement of the surface of the rooftop;
3. Insulation of the overlap between the basement and the first floor or the attic and the last floor.
4. Hermitization of junctures between panels;
5. Exchange of the horizontal and vertical pipelines of cold, hot water and sewage;
6. Renovation and modernization of the heating system;
7. Modernization of the lighting and electricity supply systems;
8. Repairs of the balconies and loggia;
9. Insulation of the façade.

The methods and principles of construction works performed in the multiapartment buildings to complete the mentioned above repairments are not the topic of this research. The authors are more interested in the actual reduction of heat losses and the optimization of use of the heat power provided to any dwelling house in the country. Deepening in the analysis of the existing apartment buildings in Riga and Latvia makes clear that the impact of performed repairs on different types of concrete, block and brick constructions varies, which is only natural and logical. One of the further aims of the authors of the presented paper is to go in details for every possible type or series of building to be capable of giving advice – which repairments might bring the most positive effect on prolonging the lifespan of the dwelling house while reducing the energy consumption needed to provide maximal comfort for the inhabitants. During the first stage researchers have acquired data on numerous houses that have undergone different repairs during the last 10 years, as well as created a database where every entry consists not only of the year and type of works done, but also of energy consumption before and after the works, type or series of the dwelling house. By collecting more data on different buildings in Riga and other cities of Latvia will be enabled the possibility to calculate the average reduction of energy consumption for the most common series of brick and concrete panel buildings after the completion of the most popular repairments.

For example, in Fig. 1 is presented one of the most widespread type of dwelling house corresponding to the 602nd series. Such houses form complete micro districts in Riga, Jelgava, Jūrmala and other cities. The problems of this series of houses are important for a large group of customers of maintenance companies. Apartment owners who are not ready to invest in overall renovation are willing to acquire a checklist of works crucial to their homes. Before such list can be created, calculations as presented in section 2 must be performed.

Figure 1. Multiapartment building of the 602 series.

The researchers have determined that at least 13 houses in Riga during just 2 years have completed hermitization of junctures between panels in 602 series dwelling houses. Collected data and calculated values are presented table 1.

Table 1. The comparison of heat power consumption reduction in 602 series dwelling houses that have completed hermitization of junctures between panels

№	Multiapartment building	Year of the works	Series	Heat power consumption in January of the year before the repairments, Q_{before}, MWh	Heat power consumption in January of the year after the repairments, Q_{after}, MWh	The economy or reduction of heat power, I, %	The corrected economy or reduction of heat power, $I_{corrected.}$, %
(1)	(2)	(3)	(4)	(5)	(6)	(7)	(8)
1	House 602 1	2016	602	125.15	108.33	15.53	13.83
2	House 602 2	2016	602	188.8	169.82	11.18	9.95
3	House 602 3	2017	602	227.29	215.97	5.24	5.77
4	House 602 4	2017	602	103.76	98.22	5.64	6.21
5	House 602 5	2017	602	118.3	113.31	4.40	4.85
6	House 602 6	2017	602	249.16	248.58	0.23	0.26
7	House 602 7	2017	602	239.42	228.74	4.67	5.14
8	House 602 8	2017	602	199.77	190.35	4.95	5.44
9	House 602 9	2017	602	146.38	139.37	5.03	5.53
10	House 602 10	2017	602	172.41	170.51	1.11	1.23
11	House 602 11	2017	602	114.35	108.75	5.15	5.67
12	House 602 12	2017	602	169.15	158.3	6.85	7.54
13	House 602 13	2017	602	156.15	156.82	-0.43	-0.47

The best result or the most perceptible economy is shown by House 602 1, but House 602 13 shows a negative result, even a rise of heat power consumption after the hermitization of junctures between panels. Taking in account all 13 results, the researchers receive an average heat power consumption reduction equal to 5.45%, which might make this type of work more attractive for the communities of apartment owners in comparison with other works. Thus, the hermitization of junctures not only helps preserve the panels of the façade, but reduces heat loses leading to accountable economy of money. Also, this result might become better in case the heating system of these houses would be regulated and balanced taking in account the performed works. Among the analyzed multiapartment houses were other series – for example 119th, 464th, 467thA, 467th, 103rd, 104th and 101st. Still, the other series gave the researchers a smaller number of objects where the junctures have been hermitized. With the thirteen houses of the 602nd series, the total number of dwelling houses with this king of repairments done was 27. The total average reduction of heat power consumption was equal to 8.73%.

4. CONCLUSIONS

The current main aim of the researchers and authors of this paper is to collect more real data on multiapartment buildings not only in Riga, but also in other cities of Latvia, as well as to create an algorithm answering the most common questions of apartment owners and maintenance companies – what king of positive impact might have different repairments and modernization works offered by the construction market, communities capable to pay for, offered by the maintenance companies, and not only reducing heat power consumption, but also prolonging the service time of the house. After the completion of the first stage of this study is already clear that the complex renovation of any object is the fastest and easiest way to receive a high-standard dwelling in a single approach. Still, the income of many apartment owners makes them feel frightened of bank loans. Many people, especially elderly ones, are not ready to live being in debt. Their worries on leaving a financial burden for the next generations overwhelms the will to understand this kind financial instruments, which actually is not that dangerous. The maintenance companies, project managers working in the field of renovation of apartment buildings must find a method to lead the dialogue with those unsure and anxious. Many calculi on the economy of heat power and reduction of corresponding payments exist in different literature sources, but none have been made for particular repairments and house types / series. Such approach might lead to two possible and successful scenarios – single repairments will be chosen wisely on many existing criteria and of course on the reduction of heat power consumption as well or the calculations might lead the society to the conclusion that complex renovation is the only method to preserve the existing real estate fund. Also, the next step of the research must observe and determine the strict necessity of balancing of the heating system after any kind of repairments. Currently many dwelling houses do not feel the reduction of heat losses after, for example, insulation of the overlap between the basement and the first floor or the attic and the last floor. The loss of effect occurs due to the neglection of the regulation of the heating system or even the technical drawbacks of the system no allowing to perform any kind of regulation. Persons inhabiting the apartments of the first and last floor control the internal temperature of the rooms by opening the windows. Thus, the persons are investing money both in repairments and the heating of the atmosphere, of course unable to notice any positive changes in everyday life and expenses. Undoubtedly, it must be remembered that performing any activities to preserve the dwellings depends on the acceptance of the idea by the apartment owners. Many functions have been transferred to maintenance companies, but global changes can be performed only after positive evaluation and decision making of the owners of the object. Crucial is to speak to all members of the community, finding the biggest worries and frights, addressing them with a corresponding solution. True and checked results, experience, previous projects can make a positive impact on the communities in general, and single owners of apartments. Every such research and the continuing of the work of the authors of this paper in the field of energy efficiency allows the society to make a secure step towards economy of resources, preservation of apartment buildings and saving up money – everything for a better, sustainable future.

REFERENCES

[1] Nieboer, N., Gruis, V., Van Hal, A., Tsenkova, S. Energy efficiency in housing management – conclusions from an international study. Enhr Conference 2011 – 5-8 July, Toulouse, 2021, <https://surfsharekit.nl/public/926f206e-aa51-42cd-a5a9-b9eefaae3112>

[2] Gentile, M., Sjöberg, Ö. Soviet housing: who built what and when? The case of Daugavpils, Latvia. Journal of Historical Geography 2010, 36: 453-465 <https://doi.org/10.1016/j.jhg.2010.01.001

[3] Mikulić, D., Slijepčević, S., Buturac, G. Energy renovation of multi apartment buildings: Contributions to economy and climate changes. Energy and Buildings, 2022, 224. <https://doi.org/10.1016/j.enbuild.2020.110247>

[4] Zvaigznitis, K., Rochas, C., Zogla, G., Kamenders, A. Energy Efficiency in Multi-Family Residential Buildings in Latvia. Cost Benefit Analysis Comparing Different Business Models. Energy Procedia, 2015, 72: 245-249 <https://doi.org/10.1016/j.egypro.2015.06.035>

[5] The Regulation of the heating System of an Office Building / Регулирование системы отопления офисного здания. https://aw-therm.com.ua/regulirovanie-sistemy-otopleniya-ofisnogo-zdaniya/

RIGA 2023

PV based DC-DC Converter for Hybrid Storage System using Deadbeat Controller

Mohamed Junaid K A
R.M.K. Engineering College, Thiruvallur, India, kam.ece@rmkec.ac.in, ORCID: 0000-0002-2019-8339

Sukhi Y
R.M.K. Engineering College, Thiruvallur, India, ysi.eee@rmkec.ac.in, ORCID: 0000-0002-9478-4306

Jeyashree Y
SRM Institute of Science and Technology, Kattankulathur, India, jeyashy@srmist.edu.in, ORCID: 0000-0001-8395-8502

Anita S
R.M.K. Engineering College, Thiruvallur, India, saa.eee@rmkec.ac.in, ORCID: 0000-0003-3336-732X

Cite this paper as: *Mohamed Junaid, K A, Sukhi, Y, Jeyashree, Y, Anita, S. PV based DC-DC Converter for Hybrid Storage System using Deadbeat Controller. 11. Eur. Conf. Ren. Energy Sys. 18-20 May 2023, Riga, Latvia.*

Abstract: In this paper, an effective and simple deadbeat controller is used for the energy storage in supercapacitor and battery. The stored energy is supplied to the load which is connected to the DC bus. This deadbeat controller has an inheriting control strategy of generating triggering waveforms in one control cycle with optimal duty ratio. This nature provides a faster response during disturbance as compared to the widely used proportional integral method. The supercapacitor used as storage element provides high power density which in turn reduces the burden of battery and improves the life span of the battery. This system provides bidirectional power flow for electric vehicle battery charging. Due to the application of PV panels for supplying power, this system can provide a longer driving range. The mismatch between the power generation using photo voltaic panel and power demand by the load are solved effectively due to the integration of storage system. The size of the components is reduced with a flexible control. The design of the deadbeat controller is analyzed for the prototype developed. The proto type is developed to show the experimental results and its effectiveness.

Keywords: *Dc-dc converter, hybrid energy storage, battery, supercapacitor, deadbeat controller, photo voltaic*

1. INTRODUCTION

In the present electric vehicle system, the storage devices like batteries, supercapacitors, etc., are used. The different storage elements have their own characteristic feature to store the electrical charges. In this aspect, the supercapacitors have the capacity to a high value of power density and the bearing capacity of battery is related to high value of energy density. The high-power density devices need not be high energy devices. The power density is related to the energy discharging capacity of the device. Now a days PV powered electric vehicles are used for transportation. In this PV panels are used for charging the batteries. In addition, this method of charging improves the average distance travelling by the vehicle. There are researches in the electric vehicle field for sustainable development In this system, proportional integral (PI) controller is used for controlling the power flow. There is spikes in the system output during the variations in intensity of the solar panel output with this method of control [1]. When the energy sources are supercapacitor and fuel cell, parallel converters are used to boost the voltage level. In this system, nonlinear control method [2] implemented to control the system output voltage produces large variations in the DC bus voltage. Also, the PI controller implemented for such system produces a sluggish behavior [3]. Figure1. sows the general block diagram of solar assisted electric vehicle. When battery and super capacitor is

used for storing the energy, there is a large variation in battery current. The high amount of current flow in batteries reduces the life of the battery [4]. The use of super capacitor is not able to reduce the stress developed on battery. Most of the control methods use PI controllers [5-10] in parallelly connected converters. Since the load and the PV produces disturbances, there is spikes in system output.

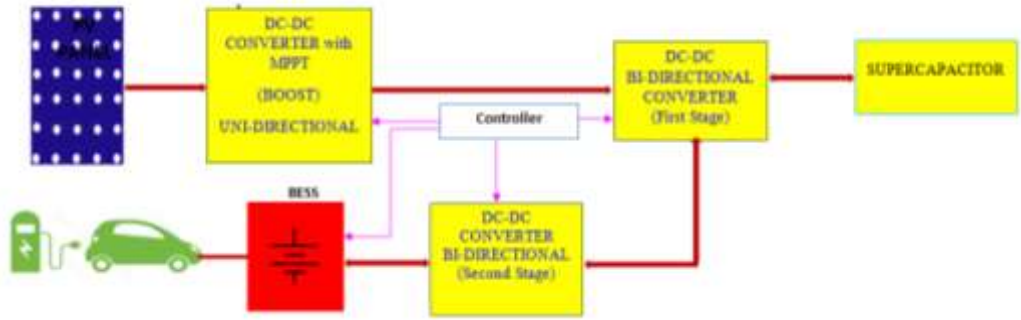

Figure 1. General Block diagram of solar based EV.

This method produces large super capacitor and battery current. But this method can be implemented for hybrid energy management system [11]. The implementation of quasi-Z-source for the storage system provide coupling between super capacitor and the battery. The coupling between the storage devices produces high ripples in the battery current [12]. This increases stress on the supercapacitor and reduces the lifetime of battery. This can be overcome with the help of bidirectional cascaded converter [13] in case of PV based EVs. The three-level configuration of cascaded converter is used for systems using supercapacitor. The power management between the between the supercapacitor and the battery is regulated using deadbeat control method. This method is one of the simple methods and responding fast with high accuracy. This method is able to produce the optimum value of duty cycle in one control cycle. This is implemented to remove quickly the errors due to state variable. The bidirectional converter topology and its operation is dealt in section II. The proposed deadbeat controller is discussed in section III. The hardware prototype and its results are discussed in section IV. The conclusion of the proposed paper is given in section V.

2. BIDIRECTIONAL BOOST CONVERTER

The proposed system uses PV based hybrid energy storage system using bidirectional boost converter. The converter is developed to have bi-directional power flow is shown in Fig. 2. The storage elements are connected in the proposed system which consists of solar PV panel, supercapacitor, battery, proposed bidirectional boost converter and load.

2.1. Converter configuration

Maximum power point tracking is done using P&O algorithm. The proposed bidirectional boost converter consists of four switches M_A, M_B, M_C and M_D and two capacitors C_A and C_B. For simplification purpose, the values of capacitors are considered to be equal of value. There are two stages to connect the energy storage devices. At the output of the converter, an inductor LA is used to connect the supercapacitor which is the first stage of the output. At the output of first stage, two switches M_E and M_F and an inductor L_B are used to connect the battery which is the stage 2 of the output.

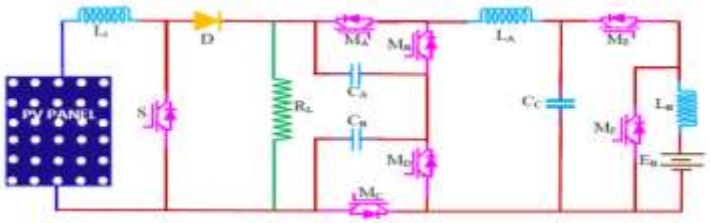

Figure 2. Proposed converter.

In the circuit diagram, v_{PV}, i_{PV} represents the PV panel current and PV panel voltage, i_B, v_B represents the battery current and battery voltage, S is the switch in the PV side, DPV is the diode in the PV side i_S, v_S represents the supercapacitor current and battery voltage, i_{LA} represents the current through inductor L_A, i_{LB} current through inductor L_B, i_{CA} represents the current through capacitor C_A, i_{CB} represents the current through capacitor C_B, R is the load resistance, i_L is the current through load resistance. The duty ratio of the switches is made to turn ON/OFF of the switched on a complementary basis. The complementary pairs are for operation of the converter are (M_A, M_B), (M_C, M_D) and (M_E, M_F). The complementary switches are (M_A, M_B) contributes to the duty cycle D_1, the complementary switches are (MC, M_D) contributes to the duty cycle D2, and the complementary switches are (M_E, M_F) contributes to the duty cycle D_3. Due the complementary action, when one switch is ON, the other switch is in OFF condition. In this the battery voltage is less than the supercapacitor voltage. The DC bus voltage may be more than supercapacitor voltage. The power rating of the switches in the proposed converter is less than the conventional converters. This reduces the cost of the converter. The stress developed in the switches in terms of voltage is less. The difference in voltage between the battery and the supercapacitor is very less. This makes the inductor of low value of inductance required between the battery and the supercapacitor. This method of indirect method of integration of energy sources to the load leads to a reduced rating of components and switching devices.

2.2. Converter Analysis

The proposed converter and its operation are explained. The boost converter is used to increase the gain of the photo voltaic energy is simple and widely used solar energy system. The converter configuration and the analysis explained in the following section.

Based on the power generation and power consumption, the battery used to supply power to the load can operate in either charging mode or discharging mode. The independent regulation can be implemented for both the stages. In this the second stage of circuit is similar to a conventional converter. Figure 3. shows the typical waveforms of the converter elements and switches during the bidirectional power flow.

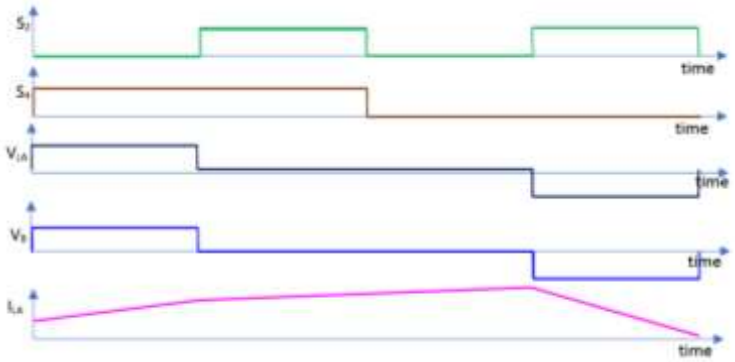

Figure 3. Typical waveforms of the converter.

3. CONTROL METHOD

In this paper deadbeat control is used for changing the voltage level. Since the switches are used in complementary mode, duty ratios (D_1, D_2, D_3) for the pair of switches is considered. The bidirectional current flow in the first stage is controlled using switches M_A, M_B, M_C, M_D. For the operation of the converter in the first stage average duty cycle is calculated. Supercapacitor, inductor L_A, and the switches M_A, M_B, M_C, M_D forms the first stage of the proposed converter. The two pair of switches having duty ratios DA and DB form the average duty cycle as below.

$$D_{avg(t)} = \frac{D_A(t)+D_B(t)}{2} \qquad (1)$$

Maximum power point tracking is done using P&O algorithm. The proposed bidirectional boost converter consists of four switches M_A, M_B, M_C and M_D and two capacitors C_A and C_B. For simplification purpose, the values of capacitors are considered to be equal of value. There are two stages to connect the energy storage devices. At the output of the converter, an inductor LA is used to connect the supercapacitor which is the first stage of the output.

At the output of first stage, two switches M_E and M_F and an inductor L_B are used to connect the battery which is the second stage of the output.

A small variation in duty cycle is calculated as given below

$$\Delta D = \frac{D_B(t) - D_A(t)}{2} \tag{2}$$

Using equation (1) and equation (2), the duty ratio $D_A(t)$ and $D_B(t)$ are derived as below.

$$D_A(t) = D_{avg}(t) - \Delta D(t) \tag{3}$$

$$D_B(t) = D_{avg}(t) + \Delta D(t) \tag{4}$$

The expression for the current through the supercapacitor is expressed as below

$$L_A \frac{di_A(t)}{dt} = v_A(t) - v_{CA}(t)\, D_A - v_{CB}(t) - \Delta D(t)\,[v_{CB}(t) - v_{CA}(t)] - v_B(t) D_{avg}(t) \tag{5}$$

Where $v_B(t) = v_{CB}(t) + v_{CA}(t)$. The product of the terms $\Delta D(t)$ and $\Delta v(t) = v_{CB}(t) - v_{CA}(t)$ is negligible when the voltages $v_{CA}(t)$ and $v_{CB}(t)$ are balanced. This leads a conclusion that the duty ratio variation is independent of the balancing of the capacitor voltage. The duty ratio variation is calculated using the difference of capacitor voltages. This is used to calculate duty ratio D_A and D_B.

The average value for duty ratio for the i-th instant in terms of sampling time (t_r) can be written as below in equation (6)

$$D_{avg}(i) = \frac{v_A(i)\, t_r - \left(i_{LA}(i+1) - i_{LA}(i)\right) L_A}{v_B(t) t_r} \tag{6}$$

Using the above equation, the duty ratio is calculated to maintain the battery current. Many algorithms are developed to have closed loop control. Dual PI control using voltage outer loop and inner current provides simple and highly reliable control. But it is difficult to have ideal tracking using this method. The deadbeat controller provides better sensitivity even under dynamic conditions. It also provides a robust system control. The deadbeat controller used for the generation of gate pulse is shown in figure 4. with its block diagram. Based on this reference current, the duty ratio is found out for the bidirectional converter using equation (6).

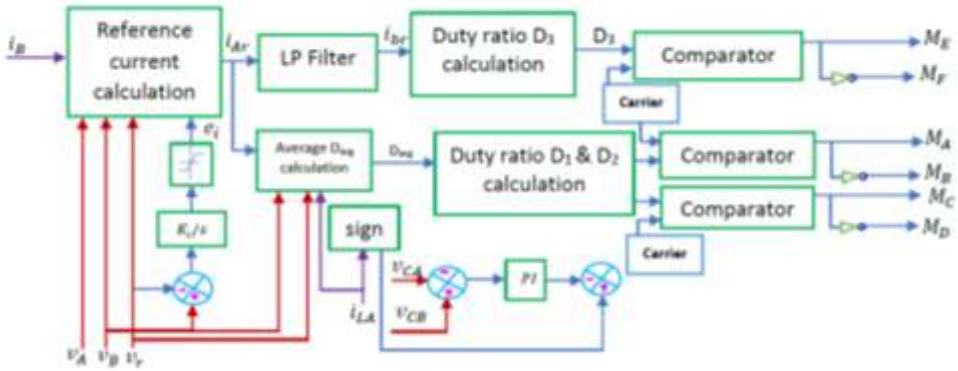

Figure 4. Block diagram of controller.

As shown in the block diagram, battery reference current is required to find out the duty ratio for the second stage converter. This battery reference current is obtained from the low-pass filter. The supercapacitor reference current is fed as input of the filter. The average value of duty cycle is calculated using the input values given to the average

duty ratio calculator. Similarly, the small variation in the duty ratio is derived from capacitor voltage difference and the direction of supercapacitor current is used to calculate the duty ratio increment. The reference signal is generated based on these values. The carrier wave for duty ratios D_1 and D_2 are complement each other. These values are used to calculate the duty ratio for the complementary switches. The carrier waveform is generated to compare with the reference signal and to set the duty ratio for the switches.

4. EXPERIMENTAL RESULTS

The validation for the proposed converter with the deadbeat controller is done using the results obtained from the prototype developed. The filter cut-off frequency is selected as 50rad/sec. The development of two stage configuration makes the value of battery inductor less than the supercapacitor inductor. This is done for variations in the input power generation. Initially, the input current is 0.5A, then changed to 1A, then to 1.5A and then decreased to 1A, then to 0.5A, then to 0A. Due the shading on the PV panel, there is a decrease in the power generation. During the variations in the power generation, there is a change in the mode of operation of the converter. This produces a transition from continuous mode to discontinuous mode. In order to have smooth control of operation, the power imbalance is supplied by the battery and the supercapacitor.

The bus voltage is controlled to be maintained at 24V. The variations in the input power produces a small variation in bus voltage of 0.5V. Figure 5. shows the current through the supercapacitor inductor current and the battery current. Figure 6. shows the load current and the load voltage.

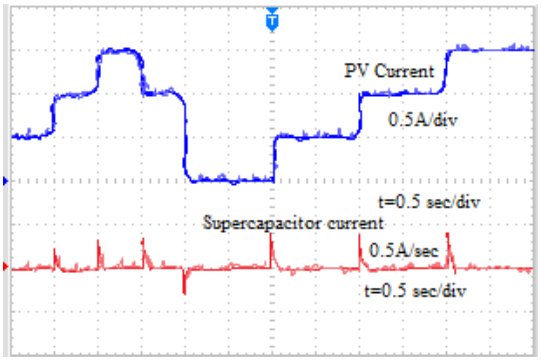

Figure 5. PV current and supercapacitor current.

When the load is varied for constant input power, the mode of operation changes. The input current is maintained at a constant value of 1A. The load current varies in a step manner between o.5A and 1A. When the continuous mode of operation is prolonging for a long time, the load variation is not changing the mode of operation. The average power required by load is supplied by the battery and the power demand due to the sudden variations in the load is supplied by the supercapacitor. The variations in the bus voltage is maintained within 1V by the deadbeat controller.

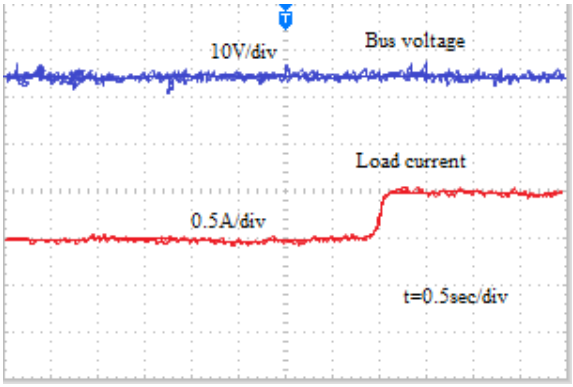

Figure 6. DC Bus voltage and load current.

The ripples produced in the bus voltage is more during discontinuous mode of operation. The ripples created in the bus voltage is due to the DC bus filter current. It can be noted that the both PV and battery supply power during discontinuous mode of operation and the PV supply power during continuous mode of operation.

5. CONCLUSION

This paper presents a deadbeat control method for the regulation of the output voltage. This method provides fast response having high accuracy with a simple circuit. The optimum duty ratio is generated using one control cycle for the storage elements. This simplifies the control of transient power demand. The load voltage is regulated in a simple manner. This method relives the stress on the battery and improves the life span of the battery. The bidirectional power flow in the storage and the load uses two stage structure. Prototype is developed to validate the performance of the proposed converter.

REFERENCES

[1] B. Wang, U. Manandhar, X. Zhang, H. B. Gooi and A. Ukil, "Deadbeat Control for Hybrid Energy Storage Systems in DC Microgrids," in IEEE Transactions on Sustainable Energy (2019) vol. 10, no. 4, pages. 1867-1877. Doi:<https://ieeexplore.ieee.org/document/8481368>

[2] B. Wang, X. Zhang, U. Manandhar, H. B. Gooi, Y. Liu and X. Tan, "Bidirectional Three-Level Cascaded Converter With Deadbeat Control for HESS in Solar-Assisted Electric Vehicles," in IEEE Transactions on Transportation Electrification (2019), vol. 5, no. 4, pages. 1190-1201, Dec. 2019. <https://ieeexplore.ieee.org/document/8826447>

[3] M. O. Badawy, T. Husain, Y. Sozer and J. A. De Abreu-Garcia, "Integrated Control of an IPM Motor Drive and a Novel Hybrid Energy Storage System for Electric Vehicles," in IEEE Transactions on Industry Applications, vol. 53, no. 6, pp. 5810-5819, Nov.-Dec. 2017, doi:< https://ieeexplore.ieee.org/document/8012534>.

[4] J. -F. Stumper, V. Hagenmeyer, S. Kuehl and R. Kennel, "Deadbeat Control for Electrical Drives: A Robust and Performant Design Based on Differential Flatness," in IEEE Transactions on Power Electronics (2015), vol. 30, no. 8, pages. 4585-4596. doi:< https://ieeexplore.ieee.org/document/6908002>.

[5] Ahmed Al-Qallaf and Kamal El-Sankary, "Design of Time-Mode PI Controller for Switched-Capacitor DC/DC Converter Using Differential Evolution Algorithm—A Design Methodology", IEEE Transactions on Computer-Aided Design of Integrated Circuits and Systems (2022) vol. 41, No. 12. doi:< https://ieeexplore.ieee.org/document/9707489>.

[6] A. G. Perry, G. Feng, Y. -F. Liu and P. C. Sen, "A Design Method for PI-like Fuzzy Logic Controllers for DC–DC Converter," in IEEE Transactions on Industrial Electronics (2007) vol. 54, no. 5, pp. 2688-2696. doi:< https://ieeexplore.ieee.org/document/4292357>.

[7] H. Shayeghi, A. Rahnama, N. Takorabet, P. Thounthong, N. Bizon, "Designing a multi-stage PD(1+PI) controller for DC–DC buck converter", Energy Reports (2022), Volume 8, Supplement 16, Pages 765-773. doi:< https://doi.org/10.1016/j.egyr.2022.10.448>.

[8] Madisa V.G. Varaprasad, N.S.S. Ramakrishna, Innocent Kamwa, M. Venkatesan, Dasari Manikanta Swamy, S.M. Muyeen, Sk. A. Shezan, Md. Fatin Ishraque, "Design and analysis of PV fed high-voltage gain DC-DC converter using PI and NN controllers", Ain Shams Engineering Journal (2022), 102061. doi:< https://doi.org/10.1016/j.asej.2022.102061>.

[9] Mizraim Martinez-Lopez, Javier Moreno-Valenzuela, Wei He, "A robust nonlinear PI-type controller for the DC–DC buck–boost power converter", ISA Transactions (2022) Volume 129, Part A, Pages 687-700. doi:< https://doi.org/10.1016/j.isatra.2022.01.016>.

[10] Amir Sharifian, Samaneh Fathi Sasansara, Alireza Agah Balgori, "A new control method based on type-2 fuzzy neural PI controller to improve dynamic performance of a half-bridge DC–DC converter", Neurocomputing, Volume 214, 2016, Pages 718-728. doi:< https://doi.org/10.1016/j.neucom.2016.07.001>.

[11] R. R. Ahrabi, H. Ardi, M. Elmi, and A. Ajami, "A novel step-up multiinput dc–dc converter for hybrid electric vehicles application," IEEE Trans. Power Electronics (2017) vol. 32, no. 5, pages. 3549-3561. doi:< https://ieeexplore.ieee.org/document/7499872>.

[12] H. Aljarajreh, D. D. -C. Lu, Y. P. Siwakoti and C. K. Tse, "A Nonisolated Three-Port DC–DC Converter With Two Bidirectional Ports and Fewer Components," in IEEE Transactions on Power Electronics (2022), vol. 37, no. 7, pages. 8207-8216. doi:< https://ieeexplore.ieee.org/document/9695335>.

[13] K. Suresh et al., "A Multifunctional Non-Isolated Dual Input-Dual Output Converter for Electric Vehicle Applications," in IEEE Access, (2021) vol. 9, pp. 64445-64460. doi:< https://ieeexplore.ieee.org/document/9410234>.

RIGA 2023

Characterization of Bifacial Technology PV Systems

Luis Pulido López
University of Jaén, Jaén, Spain, lplopez@ujaen.es, ORCID: 0000-0003-2836-2110

Sergio Manuel Moreno Buesa
University of Jaén, Jaén, Spain, smmoreno@ujaen.es, ORCID: 0000-0002-0049-7382

Gustavo Nofuentes Garrido
University of Jaén, Jaén, Spain, gnofuen@ujaen.es, ORCID: 0000-0002-5305-3830

Slawomir Gulkowski
Lublin University of Technology, Lublin, Poland, s.gulkowski@pollub.pl, ORCID: 0000-0003-4082-1391

Emilio Muñoz Cerón
University of Jaén, Jaén, Spain, emunoz@ujaen.es, ORCID: 0000-0003-1499-3376

Juan de la Casa Higueras
University of Jaén, Jaén, Spain, delacasa@ujaen.es, ORCID: 0000-0002-1781-3417

Jorge Aguilera Tejero
University of Jaén, Jaén, Spain, aguilera@ujaen.es, ORCID: 0000-0001-9684-4635

Cite this paper as: *Pulido-López, L, Moreno-Buesa, SM, Nofuentes, G, Gulkowski, S, Muñoz, E, de la Casa Higueras, J, Aguilera Tejero, J, Characterization of bifacial technology PV systems. 11. Eur. Conf. Ren. Energy Sys. 18-20 May 2023, Riga, Latvia*

Abstract: Nowadays, bifacial PV technology is rapidly overtaking the market share of monofacial PV technologies. However, this emerging technology is affected by new parameters that have to be determined for its proper characterization such as rear irradiance reflected by albedo. The objective of this research is to analyze the performance of a 3.3 kW bifacial technology photovoltaic system located at the University of Jaén, Spain. To address this challenge, specially designed structures have been installed to avoid possible shading and easy albedo modification. The aforementioned generator is made up of eight bifacial PV modules divided into two strings, both connected to an inverter with two independent MPPTs. To characterize the PV system, a monitoring system has been designed following the IEC 61724-1:2022 standard. Consequently, sensor data is collected to measure variables such as frontal irradiance, operating temperature, wind speed, individual voltages and currents of each module, as well as system power. Additionally, rear irradiance sensors built from modules of the same technology have been integrated in order to characterize this new technology. Based on the foregoing, the most relevant analyses of the system performance are shown: rear irradiance maps, GNU, PR at STC with temperature compensation, among others.

Keywords: *Photovoltaic systems, bifacial, rear irradiance, performance analysis, solar energy*

1. INTRODUCTION

In contrast to monofacial solar cells, bifacial technology cells simultaneously receive photons from incident radiation and albedo impinging on both the front and rear side of the module. This technology has been investigated since the 1960s and was initially described in the scientific literature by Spanish researchers [1] as a new concept to improve the energy production of photovoltaic systems.

Nowadays, bifacial technology is considered as one of the most promising approaches and its market is expected to expand dramatically [2]. Based on various tests carried out in real south-facing sunlight at an installation angle of 30° and an albedo of about 50% using bifacial technology, a bifacial gain in terms of annual energy delivered exceeding 20% has been determined compared to monofacial technology [3]. This gain can be decisive when purchasing bifacial technology PV modules, since although they incur a larger cost compared to monofacial technology, the energy production is higher. Thus, replacing conventional monofacial silicon PV modules with bifacial silicon PV modules can increase plant capacity or, alternatively, reduce the number of modules required for energy production systems and the total cost of installation, including land area, materials, labor costs and construction time. This will require optimizing the installation conditions to obtain such an improvement in energy production. Nevertheless, very few publications related to bifacial technology are currently available. Unlike the consolidated single-facial technology, there is a lack of information on how to proceed in the optimization of bifacial silicon photovoltaic systems, which further complicates the study. Aware of this lack, this research is responsible for analyzing a bifacial photovoltaic system connected to the grid, including new parameters that influence the behavior of this technology which are not present in the already known monofacial photovoltaic systems. In Sec. 2, the bifacial PV system designed and installed for this purpose will be presented. It will show both the generation system and the monitoring system in charge of measuring the new parameters mentioned above. On the other hand, section 3 will show the results extracted from the analysis of the installation, with special emphasis on the analysis of the PR in DC under STC with temperature compensation. Given that it is a bifacial PV system, the rear irradiance should be considered. Nevertheless, a discrepancy arises when it comes to selecting the sensor that represents the rear irradiance received by the modules. Finally, in section 4 the conclusions drawn from this research will be outlined.

2. EXPERIMENTAL SETUP

2.1. Measuring System

A 3.3 kW bifacial PV system has been installed on one of the roof terraces located on the university campus of the University of Jaén (Jaén, Spain, latitude 37°47'16"-N, longitude 3°46'40"-W). This PV system is divided into two strings each consisting of four 410-W LG Neon 2 BiFacial LG410N2T-L5 modules [4]. Each string is independently connected to one of the two MPPTs of the inverter installed. Due to the site layout constraints, string 1 is placed in one structure while string 2 is divided into two (Figs. 1(a,b)). These structures have been designed exclusively for the module model mentioned, in order to reduce the shading losses on the rear side of the module.

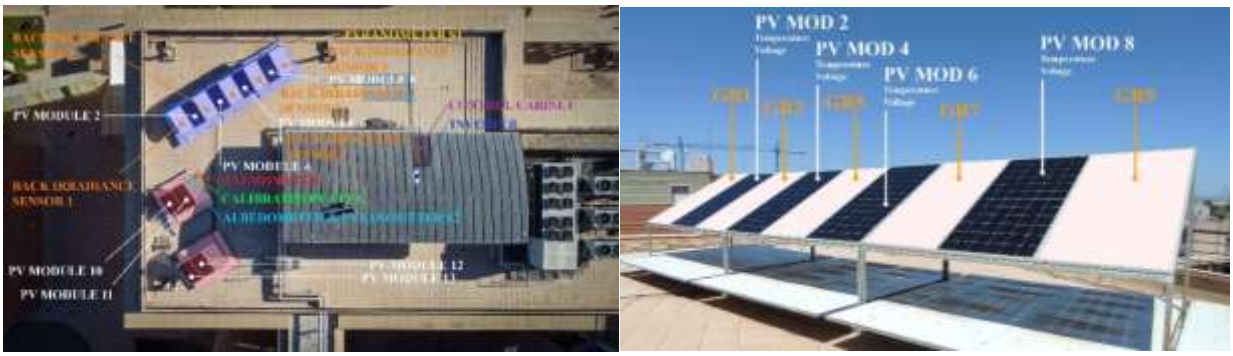

(a) (b)

Figure 1. (a) Aerial view of the monitoring system with the elements highlighted. Shaded in blue the modules belonging to string 1 and in red the modules belonging *to string 2. (b) Detailed view of string 1. The modules acting as rear irradiance sensors labelled as GRi, with i=1,3,5,7,9 as well as the generation modules labelled as PV MODj, with j= 2,4,6,8 are shown in the picture.*

(b)

Figure 1 shows the monitoring system designed [7] according to IEC 61724-1 [5]. This system comprises the following sensors: six type K thermocouples pasted on the rear side of four modules of the first string and in two modules of string 2. Additionally, a suitably shaded type K thermocouple intended to measure ambient temperature

has been installed. A SR20-T2 Hukseflux pyranometer in conjunction with a SMP6 Kipp&Zonen pyranometer coplanar with every string record the irradiance received by the front faces of the bifacial modules. An albedometer has been placed in string 2 that corresponds to the same SMP6 pyranometer model mentioned above, but its orientation is arranged opposite to the latter. A PCE-WS V anemometer has also been installed. Five rear irradiance sensors located at the ends of the structure of string 1, as well as intercalated between the generation modules and devised from calibrated modules of the same technology have also been deployed. The latter sensors have been obtained in the following way: the front side of each calibrated module has been covered by a piece of white vinyl canvas in order to prevent the sun irradiance from impinging on that side. Every calibrated module has been short-circuited by using 5 A calibrated shunt resistors. The current generated by each string is collected as per two 15 A calibrated shunt resistors.

The sensor outputs have been connected to a high-precision Graphtec GLT400 data logger. The measurement campaign is ranged from November 2022 to February 2023. Both electrical and environment data were taken at one-minute intervals

2.2. Characterization of Bifacial Modules

In order to guarantee the correct measurement of the monitoring system, an experimental campaign has been established to characterize both sides of each of the modules. To this end, calibration certificates in which the main electrical parameters measured at STC are provided issued for two modules by CIEMAT (Madrid), an accredited independent laboratory. Then, the characteristics of both sides of each module of the two strings were determined separately under STC using the Entec Solar E1000 I-V curve tracer. For this purpose, comparative and simultaneous measurements of a calibrated module and the module under test were carried out. Since both modules are under the same irradiance and temperature conditions, the characteristic data of the calibrated module can be extrapolated [6] to the module to be measured. This is achieved by means of:

$$\frac{{P_{eval}}^{STC}}{P_{eval}} = \frac{{P_{CIEMAT}}^{STC}}{P_{CIEMAT}} \qquad (1),$$

where: ${P_{eval}}^{STC}$ is the power at STC to be obtained for the module under test (W), P_{eval} is the power measured at that instant for the module under test (W), ${P_{CIEMAT}}^{STC}$ is power at STC of the calibrated module according to CIEMAT calibration certificate (W) and P_{CIEMAT} is the power measured at that instant for the calibrated module (W). The above procedure together with Eq.[1] was applied to both the front and the rear side of every module under study.

Table 1. Front and rear side power at STC of the PV modules under study.

Name	Reference	Front side power at STC (W)			Rear side power at STC (W)
		P_{eval}^{STC}	According to manufacturer flash list	Percentage deviation of P_{eval}^{STC} from manufacturer flash list	P_{eval}^{STC}
CIEMAT	**008K5MH212EE**	407.70	414.71	-1.69%	287.90
Module 1	008K5CY212E5	414.08	414.79	-0.17%	298.39
Module 2	008K5UR21598	401.44	410.74	-2.26%	289.65
Module 3	008K5FS2158H	404.16	412.40	-2.00%	283.53
Module 4	008K5EB2130X	405.68	411.07	-1.31%	286.33
Module 5	008K5KG2159A	407.93	411.21	-0.80%	280.50
Module 6	008K5VZ212E1	402.46	414.97	-3.01%	290.97
Module 7	008K5EB21596	400.49	411.19	-2.60%	287.55
Module 8	008K5MH21595	405.79	412.67	-1.67%	283.19
Module 9	008K5DW215A0	402.44	411.02	-2.09%	284.88
Module 10	008K5NA215A5	401.23	411.95	-2.60%	262.68
Module 11	008K5EB2159C	404.96	411.43	-1.57%	285.06
Module 12	008K5RT2159F	413.33	411.25	0.51%	288.08
Module 13	008K5UR2159G	406.44	411.71	-1.28%	294.99

Table 1 shows the Front and rear side power at STC of the PV modules under study. By comparing each of the modules, it was determined which modules would be used as generators and which ones would be used as rear irradiance sensors of the same technology. These modules were selected for either purpose depending on whether they had defects on their front side, thus becoming apparent by delivering less power or lower short-circuit current. String 1 consisted of modules 1,4,12,13 with a total front surface power of 1640 W. String 2 was composed of modules 5,8,9,11 and its total front surface power is 1621 W. Modules 2,3,6,7,10 were selected to operate as rear irradiance sensors.

3. RESULTS

3.1. Analysis of the PV System Yield at 25ºC

The DC output energy of each of the strings corrected at 25 ºC (Fig. 2(b)) following IEC 61724-1 [5] has been obtained as follows:

$$E_A = \sum_k \frac{P_{out,k}\tau_k}{C_{k,25ºC}} \quad (2),$$

where $P_{out,k}$ is the *k*-th value of the power delivered by the string under scrutiny (W) and τ_k is the sampling interval (s).
$C_{k,25ºC}$ is given by:

$$C_{k,25ºC} = 1 + \gamma(T_{mod,k} - 25ºC) \quad (3),$$

where γ is the relative maximum-power temperature coefficient (°C^{-1}), and $T_{mod,k}$ is the *k*-th value of the module temperature averaged on τ_k (in ºC).

The energy production of string 1 was found to be 493.66 kWh over the course of the measurement campaign, which is equivalent to an average of 6.86 kWh/day. On the other hand, string 2 generated 474.95 kWh, equivalent to 6.60 kWh/day over the same period. These small differences are attributed to the discrepancies between the values of PV modules power shown in Table 1.

.

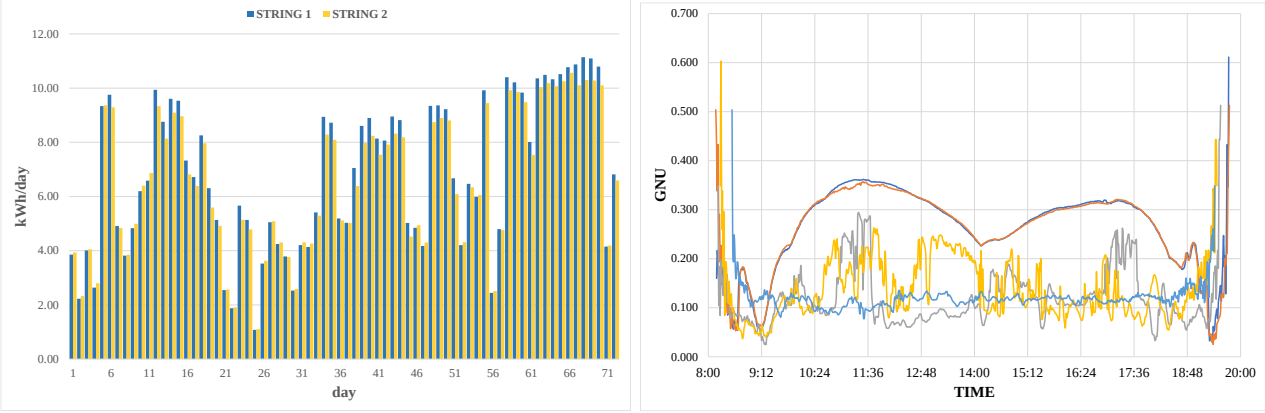

(a) *(b)*

Figure 2. (a) DC energy analysis in STC of string 1 and 2 over the measurement campaign. (b) GNU of different days (cloudy and sunny) over sunshine hours.

3.2. PR_{DC} at 25 ºC Analysis of the PV Generator

The PR has been calculated for string 1 and 2 following the IEC 61724-1 [5]. The 25 °C performance ratio, $PR'_{25ºC}$ is calculated by adjusting the power rating at each recording interval to compensate for differences between the actual PV module temperature and the STC reference temperature of 25 °C. $PR'_{25ºC}$ is calculated by introducing factor $C_{k,25ºC}$ as follows:

$$PR'_{25ºC} = \left(\sum_k P_{out,k}\tau_k\right) \Big/ \left(\sum_k \frac{(C_{k,25ºC}P_0)G_{i,k}\tau_k}{G_{i,ref}}\right) \quad (4)$$

The string DC power rating, P_0, is the sum of the DC power output of the PV modules of the string at the power rating STC. $G_{i,ref}$ is the reference irradiance (1000 W/m^2) and $G_{i,k}$ is the irradiance received by front side of the module (W/m^2).

Eq. [4] is addressed to evaluate the value of $PR'_{25ºC}$ of monofacial modules, so only the irradiance received by the front surface of the module is considered. Following the above, the results obtained for the analysis of both strings yield a PR greater than the unit (Fig. 4(b)). In order to perform a correct analysis of the $PR'_{25ºC}$, the monofacial performance ratio formulas presented above must be transformed to bifacial performance ratio formulas by introducing the bifacial irradiance factor (BIF) to correct the measured irradiance terms, according to IEC 61724-1 standard [5].

$$PR'_{25ºC,bi} = \left(\sum_k P_{out,k}\tau_k\right) \Big/ \left(\sum_k \frac{(C_{k,25ºC}P_0)G_{i,k}BIF_k\tau_k}{G_{i,ref}}\right) \quad (5),$$

where:

$$BIFk = 1 + \varphi_{Pmax}\,\rho_{i,k} \quad (6),$$

where: φ_{Pmax} is the ratio between maximum output DC power of the rear side and the front side of a bifacial string under STC (Table 1) and $\rho_{i,k}$ is the *k*-th value of the ratio of the irradiance incident on the rear side of the modules in the PV string to the irradiance incident on the front side.

As shown in Eqs.[5,6], it is essential to determine the ratio between the rear and front irradiance received by the string. However, there are discrepancies in selecting the sensor that determines the values of the former irradiance. Figure 3 shows two rear irradiance maps differentiating a cloudy day from a sunny day. If analyzing the incident irradiance on the rear side of the modules, there is a lack of homogeneity in sunny days. The modules at both ends of every array receive more irradiance than those in the center of the string, especially during the first and last hours of the day. The difficulty of choosing the right sensor to determine the rear irradiance received by the modules becomes noticeable when performing this analysis.

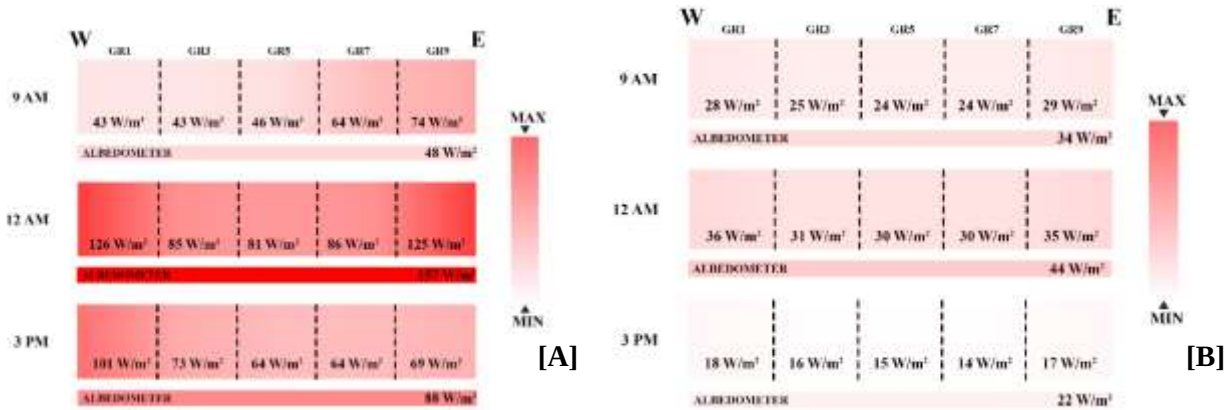

Figure 3. Rear irradiance map made from the same technology modules (GR1, GR3, GR5, GR7 and GR9) and the albedometer. On the left (a) representation of a sunny day. On the right (b) a cloudy day.

Another analysis has been carried out to quantify the extent of non-uniformity of the irradiance impinging on the rear side of the modules by means of the GNU index, defined as follows,

$$GNU = \frac{max(GR_{sensor\ module}) - min(GR_{sensor\ module})}{max(GR_{sensor\ module}) + min(GR_{sensor\ module})} \quad (7)$$

where $max(GR_{sensor\ module})$ (W/m^2) and $min(GR_{sensor\ module})$ (W/m^2) are the maximum and minimum rear irradiance values from rear irradiance sensors 1,3,5,7,9, respectively. (b)

Figure 1(b) represents the GNU during different days (cloudy and sunny). Note the low uniformity of irradiance in cloudy days.

Table 2. Value of PR of each string using only the frontal irradiance, as well as the frontal and rear irradiance computed over the experimental campaign.

	G_F	$G_F + G_{ALB}$	$G_F + G_{R1}$	$G_F + G_{R3}$	$G_F + G_{R5}$	$G_F + G_{R7}$	$G_F + G_{R9}$
String 1	1.07	0.94	0.96	0.98	0.98	0.97	0.95
String 2	1.05	0.92	0.95	0.96	0.97	0.96	0.94

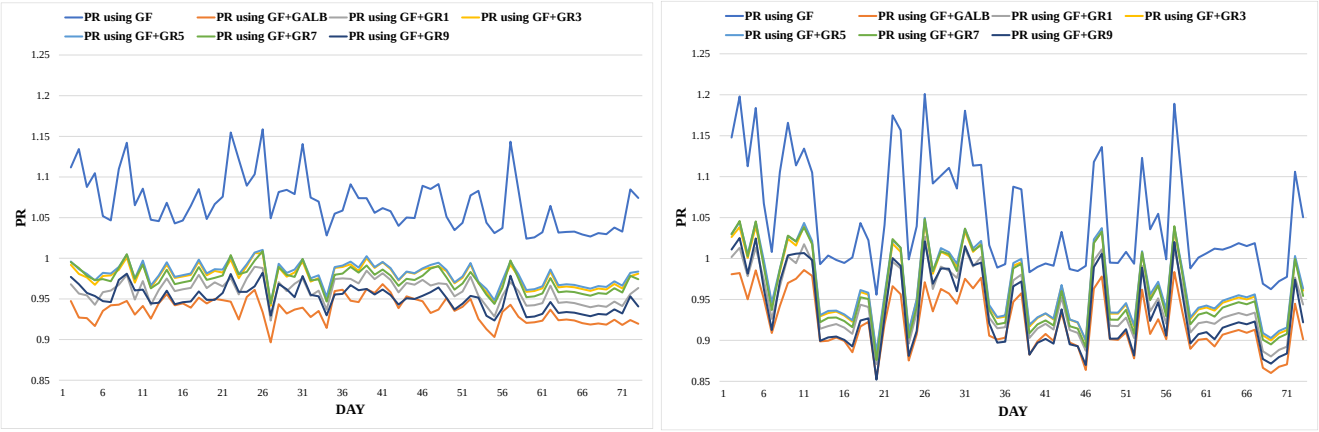

(a) *(b)*

Figure 4. Analysis of the PR of each string throughout the experimental campaign using the frontal irradiance (GF) and adding the rear irradiances of the albedometer (GR_{ALB}) and rear irradiance sensors (GR_1, GR_3, GR_5, GR_7, GR_9). Plot (a) corresponds to string 1, while plot (b) represents string 2.

(b)

Figure 4(a,b) shows the differences of the PR at 25ºC analysis performed on both strings during the measurement campaign. For this purpose, the following cases have been considered: PR analysis using only front irradiance Eq.[4] and PR analysis using front and rear irradiance data obtained by the different sensors (albedometer and sensors of the same technology as the PV modules) as per Eq. 6 shows the average PR obtained during the experimental campaign. Given the complexity of choosing the most appropriate sensor to measure rear irradiance, an additional analysis has been performed. (b)

Figure 5(b) represents the PR given by Eq. 4 versus the front irradiance measured by pyranometers of each string during the experimental campaign.

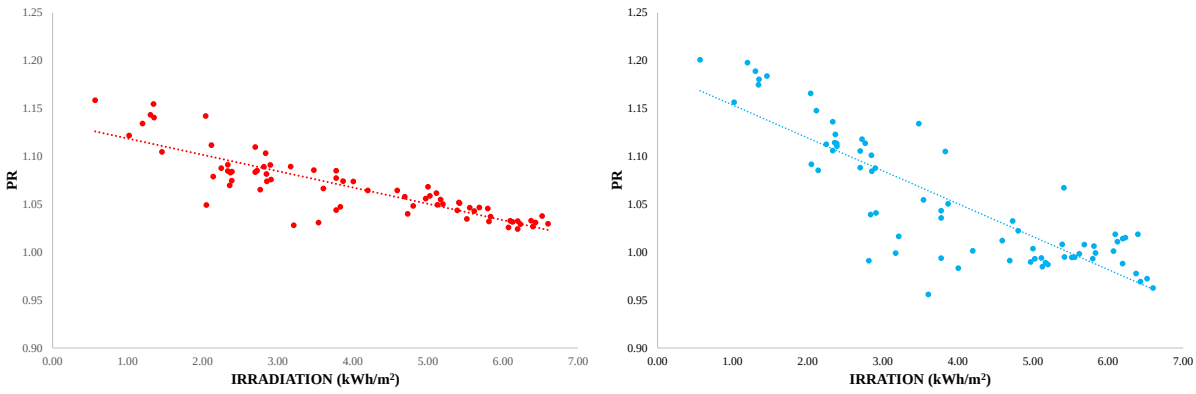

(a) *(b)*

Figure 5. Analysis of the PR of each string versus irradiance. The left plot (a) represents string 1, while the right plot (b) corresponds to string 2.

4. CONCLUSIONS

To evaluate the performance of a bifacial installation properly, it is essential to determine the parameters of the module on both the front and the rear side. The rear irradiance plays a crucial role, but determining its value is not easy. The results shown here prove the influence of the location of the rear irradiance sensor in the installation. Sensors located in the center or at the ends of the string give different values depending on the time of day. By analyzing the values of PR of the installation, differences of 18% are observed if studied as a monofacial generator. This difference is reduced to 5% when we analyze the PR with different sensors considering the generator composed of bifacial modules. In addition, the use of rear irradiance sensors of the same technology is more suitable than the use of albedometers, since the differences are lower. Finally, it is noticeable that during days where the recorded irradiance is lower, the PR is higher and vice versa. This is due to the fact that on days with lower irradiance, the irradiance has a significant diffuse component. An experimental campaign of longer duration has been established in order to collect more data to validate the results shown. In this way, with the analyses carried out and following the current IEC standards, it would be possible to predict the performance of PV plants using the emerging bifacial technology.

Acknowledgments

The authors thank the financial support granted by the Research Project: "Optimized models for the energy characterization of grid-connected photovoltaic systems with bifacial technology" (Ref. 1380734) financed with ERDF funds from the European Union.

References

[1] Luque, A, Cuevas, A, Ruiz, J.M. Double-sided n plus/p/n plus solar cell for bifacial concentration. Solar Cells, vol. 2, Oct. 1980, p. 151-166.
[2] Rodríguez-Gallegos, C. D., Bieri, M., Gandhi, O., Singh, J. P., Reindl, T., & Panda, S. K. Monofacial vs bifacial Si-based PV modules: Which one is more cost-effective? Solar Energy 2018, 176. https://doi.org/10.1016/j.solener.2018.10.012
[3] L. Kreinin, N. Bordin, A. Karsenty, A. Drori and N. Eisenberg. Outdoor evaluation of power output improvement of the bifacial module. 37th IEEE Photovoltaic Specialists Conference, Seattle, WA, USA, 2011, pp. 001827-001831.
[4] LG Electronics Inc. LG Neon 2 BiFacial LG410N2T-L5 datasheet. www.lg-solar.com 2020.
[5] International Electrotechnical Commission. Photovoltaic system performance - Part 1: Monitoring. IEC 61724-1:2022. URL: https://webstore.iec.ch/publication/65561
[6] Caamaño, E., E. Lorenzo, R. Zilles. Quality control of wide collections of PV modules: lessons learned from the IES experience. Progress in Photovoltaics 7 (1999): 137-149
[7] Pulido-López, Luis. Design and Implementation of Monitoring Systems for the Characterization of Bifacial FV Technology. MSc, University of Jaén, Jaén, Spain, 2022.
[8] Nofuentes, G., Aguilera, J., Santiago, R.L., de la Casa, J. and Hontoria, L. A reference-module-based procedure for outdoor estimation of crystalline silicon PV module peak power. Prog. Photovolt: Res. Appl., 2006, 14: 77-87. https://doi.org/10.1

RIGA 2023

Prediction of the Variability of Wave Energy Potential in an Offshore Point

Deivis Avila
Higher Polytechnic School of Engineering (EPSI), University of La Laguna, 38001, Tenerife, Spain.
davilapr@ull.edu.es, ORCID: 0000-0001-6460-7571

Graciliano N. Marichal
Higher Polytechnic School of Engineering (EPSI), University of La Laguna, 38001, Tenerife, Spain.
nicomar@ull.edu.es, ORCID: 0000-0002-6490-0556

Yanelys Cuba Arana
Centre for Advanced and Sustainable Manufacturing Studies, University of Matanzas, 44740, Matanzas, Cuba.
yanelys.cuba@umcc.cu. ORCID: 0000-0002-9535-8253

Ramón Quiza
Centre for Advanced and Sustainable Manufacturing Studies, University of Matanzas, 44740, Matanzas, Cuba.
ramon.quiza@umcc.cu. ORCID: 0000-0003-1293-6044

Cite this paper as: *Avila D, Graciliano NM, Cuba YC, Quiza R. Predicting the variability of wave energy conversion in an offshore point. 11. Eur. Conf. Ren. Energy Sys. 18-20 May 2023, Riga, Latvia.*

Abstract: In this paper, a polynomial regression is used to forecast the probable power energy produced from diverse Waves Energy Converters (WECs) in Tenerife. The WEC systems analyzed in the study were, Oyster, Aqua Buoy, Pelamis, SSG and Wave Dragoon. The model was applied and validated, with the dataset of Tenerife Sur (2446) deep water buoy, that belong to Spanish Port System and cover a historical time of 19 years. Once the study is finished, it is possible to confirm that the model based on polynomial regression is a robust tool to calculate the energy transformation that is carried out for different WECs

Keywords: *wave energy; polynomial regression, WEC; Tenerife, Canary Islands*

1.INTRODUCTION

Spain is one country of the European Union with outermost regions and is really interested in developing renewable energies on its Atlantic islands. Despite all the efforts made, renewable energies supply less than 12% of the electricity mix in their outermost islands in this case Canary Islands [1], and work is ongoing to develop new and more advanced renewable energy projects, being so important due to the inexistent electricity interconnection with any continent and its dependence on fuel for electricity generation [2]. To achieve these goals, it will be necessary to address promising new renewable energy sources involving the ocean, especially with the new energetic scenery for the Europe, gas restrictions and fuels price increase. Taking into account the good wave potential in many regions of the Canary Islands [3], it is feasible to develop the wave energy industry in the marine water around the islands.

As exposed in [3,4], the wave energy industry has not yet established a commercial prototype and has only conducted demonstration prototypes of wave energy converters (WECs) to date. But many researchers, governments, and investors around the world are working tirelessly to produce a competitive commercial prototype.

To predict the power conversion capabilities that can be obtained from different WECs, dissimilar authors have developed many mathematical models, such as Avila et al. [2,3,5]; Ahn et al. [6,7]; Swan Team [8] and Sandvik et al. [9].

Many studies from different researches are based on the power matrices of WECs to predict their behavior in different conditions, for that reason, the main purpose of this study will be to determine the wave energy convection considering several devices, through an arrangement of bivariate Weibull distributions and polynomial regressions.

This paper is organized into eight different sections. Following this introduction, the other parts of the study is organized as follows. Sections 2 and 3 expose the geographic location of the buoy used in the research and the features of the five WECs considered in the study. The modelling of the bivariate Weibull distribution is set in Section 4. Section 5 detailed the polynomial regression and their evaluation. The wave energy transformation capacity of the five WECs, in study at the Tenerife Sur buoy is provided in Section 6. The suggested model is validated in Section 7, and the conclusions are delivered at the end, in Section 8.

2.DATA SOURCE

Fig. 1 show the position of the buoy Tenerife Sur (2446) from were collected the data for this study, whose location is longitude 16.58° W and latitude 27.99° N, the buoy is placed a depth of 710 m. The buoy model is a SeaWatch with an Oce-Met directional sensor.

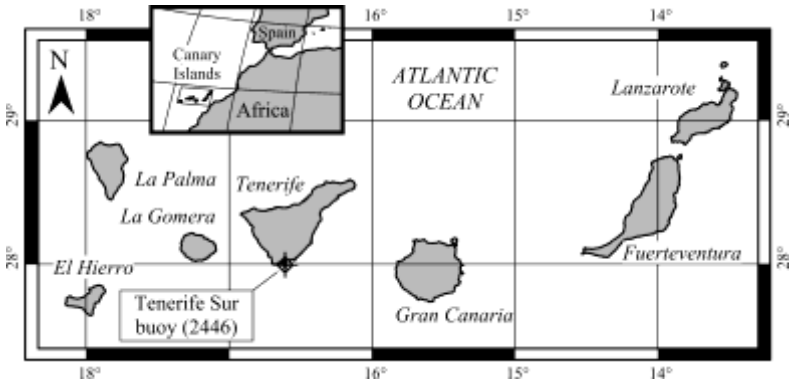

Figure 1. Geographic location of the studied buoy

For describing the wave behaviour, mean peak period (*T*) and, significant spectral height (*H*), were recorded each hour, computed on a period of 24 min, from 1998 to 2017. The measurement accuracy was ±0.05 m for *H* and ±0.05 s for *T*.

3. WEC SYSTEMS

In this study five WECs whit different power take-off (PTO) was take in consideration. The WECs are, Pelamis, Oyster, SSG, Aqua Buoy, and Wave Dragon. Taken in consideration the mean peak period (*T*), the spectral significant wave height (*H*) and the power matrices of each WEC is possible calculated the power output of the five WECs in dissimilar sea states. The characteristic of the WECs used in the research are show in Table 1. The five power matrices considered in the study ware taken from Avila et al [2].

Table 1. Characteristic of the WECs [2].

WEC	***Nominal Power [kW]***	***Power Matrix Resolution [m × s]***
Aqua Buoy	250	0.5 ×1.0
Oyster Converters	290	0.5 × 1.0
Wave Dragon	7,000	1.0 × 1.0

SSG	20,000	0.5 × 0.5
Pelamis	750	1.0 × 0.5

4.BIVARIATE WEIBULL DISTRIBUTION

For fitting the bivariate Weibull distribution, which describe the wave characteristics, data was grouped in periods of five days, counted from the beginning of the year. Data from year 1998 to 2014 were used for obtaining the distribution equations, in the form:

$$f(H,T)=\frac{k_1k_2\left(\frac{H}{c_1}\right)^{k_1-1}\left(\frac{T}{c_2}\right)^{k_2-1}}{c_1c_2(1-c_{12}^2)}\exp\left[-\frac{\left(\frac{H}{c_1}\right)^{k_1}+\left(\frac{T}{c_2}\right)^{k_2}}{1-c_{12}^2}\right]B_0\left[-\frac{2c_{12}\left(\frac{H}{c_1}\right)^{k_1}\left(\frac{T}{c_2}\right)^{k_2}}{1-c_{12}^2}\right];\ (1)$$

where the coefficients c_1, k_1, c_2, k_2 and c_{12} were computed with the Simultaneous Maximum Likelihood Estimate method [2,3,10].

As can be noted (see Fig. 2), coefficients c_1 and c_2, which describes the values of H and T where the maximum probability is reached, display a slight but visible seasonal behaviour. This can be also noted in coefficient k_1, but not for k_2 and c_{12}.

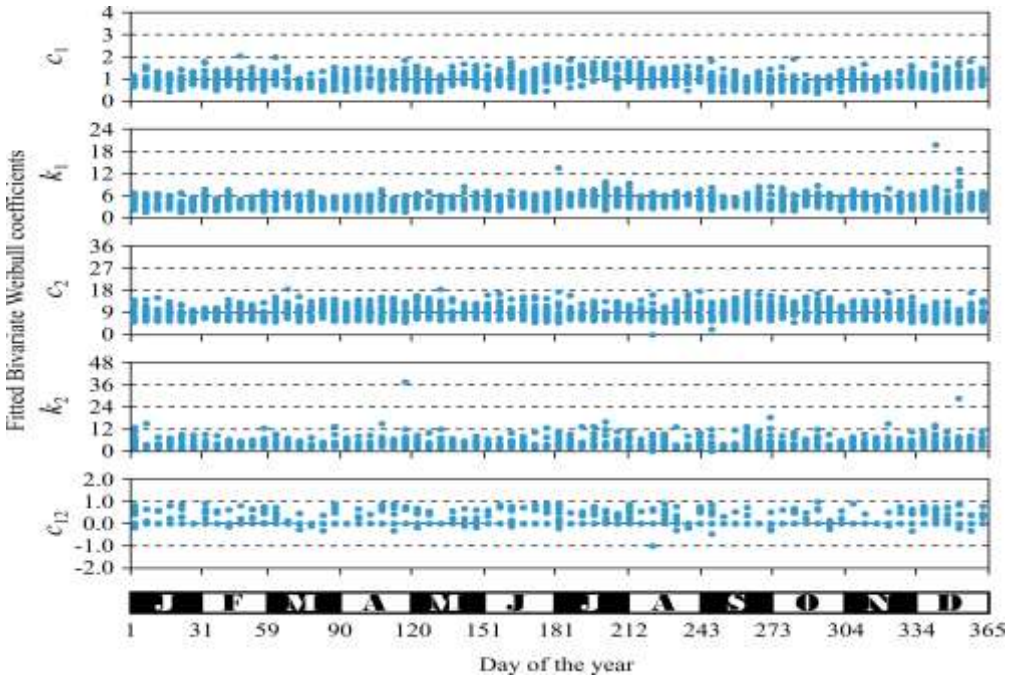

Figure 2. Bivariate Weibull distributions coefficients

5.POLYNOMIAL MODELS

In order to predict the value of the bivariate Weibull distribution coefficients, fourth order polynomial regression, as follows [3]:

$$\hat{c}(d)=\mathbf{b}^{\mathrm{T}}\mathbf{d};\qquad (2)$$

were fitted, by using the least squares method, where the coefficients $\mathbf{b} = \{b_0, \ldots, b_4\}^T$ were computed through the expression:

$$\mathbf{b} = \left(\mathbf{X}^T\mathbf{X}\right)\mathbf{X}^T\mathbf{y}\,; \tag{3}$$

where:

$$\mathbf{X} = \begin{bmatrix} 1 & d_1 & d_1^2 & d_1^3 & d_1^4 \\ \vdots & \vdots & \vdots & \vdots & \vdots \\ 1 & d_n & d_n^2 & d_n^3 & d_n^4 \end{bmatrix}; \tag{4}$$

is the matrix of powers of the independent variable (i.e., the day of the year), and:

$$\mathbf{y} = \begin{bmatrix} c_1, & \ldots, & c_n \end{bmatrix}^T; \tag{5}$$

is the vector of values of the dependent variable (i.e., each of the coefficients of the bivariate Weibull regression)

On the other hand, the standard deviation of the predictions, *s*, can be computed by the expression:

$$s = \sigma\sqrt{\mathrm{diag}\left(\mathbf{x}\left(\mathbf{X}^T\mathbf{X}\right)^{-1}\mathbf{x}^T\right)}; \tag{6}$$

Where σ is the standard deviation of the residuals and **x** is the vector of dependent variable powers. The obtained regressions took the form:

$$c_1 = 8.8859\cdot10^{-10}d^4 - 6.3767\cdot10^{-7}d^3 + 1.4189\cdot10^{-4}d^2 - 0.0100d + 1.0975\,; \tag{7a}$$

$$k_1 = 1.6576\cdot10^{-9}d^4 - 1.2603\cdot10^{-6}d^3 + 3.0007\cdot10^{-4}d^2 - 0.0215d + 4.3733\,; \tag{7b}$$

$$c_2 = -3.3380\cdot10^{-9}d^4 + 2.4448\cdot10^{-6}d^3 - 6.0046\cdot10^{-4}d^2 + 0.0558d + 7.5741 \tag{7c}$$

$$k_2 = 2.7334\cdot10^{-10}d^4 - 8.8533\cdot10^{-8}d^3 + 3.9757\,; \tag{7d}$$

$$c_{12} = 2.4368\cdot10^{-10}d^4 - 1.7201\cdot10^{-7}d^3 + 3.9237\cdot10^{-5}d^2 - 0.0032d + 0.1613\,. \tag{7e}$$

Note that second and first order coefficients were removed from regression of k_2 as they were not statistically significant.

Fig. 3 shows the polynomial models, represented by the expected value and the 90% confidence limits. Also, 100 points, randomly generated from the normal distribution given by the obtained mean and standard deviation, were plotted for each day of the year.

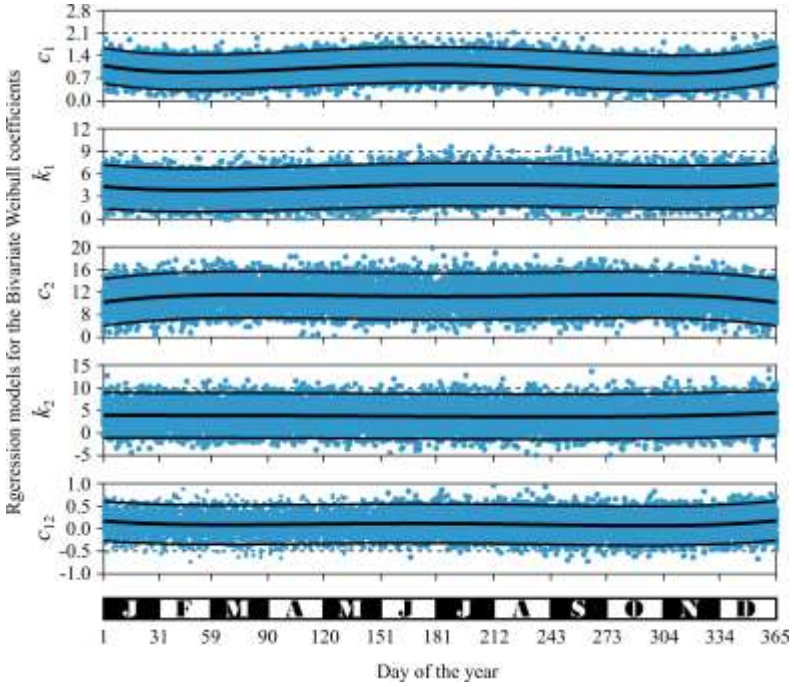

Figure 3. Polynomial models for coefficients

As in the original data, the seasonal behaviour can be noted in regressions for c_1, k_1 and c_2, but not for k_2 and c_{12}.

6.POWER CONVERTING PREDICTIONS

Power conversion was analysed through five different converters: Aqua Buoy, Oyster, Pelamis, SSG and Wave Dragoon, whose conversion matrix are shown in the appendices. For a given wave bivariate Weibull distribution, $f(H,T)$, the converted energy, P_D, can be computed by the expression:

$$P_D = \sum_{i=1}^{R}\sum_{j=1}^{C} \mathrm{cdf}_{i,j}\varepsilon_{i,j}\,; \tag{8}$$

where R and C are number of rows and columns in the conversion matrix; $\varepsilon_{i,j}$ is the conversion factor for the i-th row and j-th column, and $\mathrm{cdf}_{i,j}$ is the cumulative density of the probability corresponding to the interval given by the i-th row and j-th column $(H_i^{\mathrm{L}} \le H \le H_i^{U}, T_j^{\mathrm{L}} \le T \le T_j^{\mathrm{U}})$, which can be computed by the expression:

$$\mathrm{cdf}_{i,j} = \int_{H_i^{\mathrm{L}}}^{H_i^{U}}\int_{T_j^{\mathrm{L}}}^{T_j^{\mathrm{U}}} f(H,T)\,\mathrm{d}H\mathrm{d}T\,; \tag{9}$$

and numerically approximated by using the fifth order Gauss-Legendre quadrature for double integrals:

$$\mathrm{cdf}_{i,j} \approx \frac{(H_i^{U}-H_i^{\mathrm{L}})(T_j^{\mathrm{U}}-T_j^{\mathrm{L}})}{4}\sum_{p=1}^{5}\sum_{q=1}^{5} w_p w_q f(H_i,T_j)\,; \tag{10}$$

where:

$$H_i = \frac{(H_i^{U}+H_i^{\mathrm{L}})}{2} + \xi_i\frac{(H_i^{U}-H_i^{\mathrm{L}})}{2}\,; \tag{11a}$$

$$T_j = \frac{(T_j^{\mathrm{U}} + T_j^{\mathrm{L}})}{2} + \xi_j \frac{(T_j^{\mathrm{U}} - T_j^{\mathrm{L}})}{2}; \qquad (11b)$$

and w_n and ξ_n are the corresponding weights and evaluation points of the interpolation polynomial [11].

Fig. 4 shows the converted energy computed for each evaluated converter, considering the 100 random values of coefficients computed obtained in the previous section. As can be sees, also the seasonal behaviour is not excessively pronounced, it can be noted in the form of higher values in the periods of June-July and December-January.

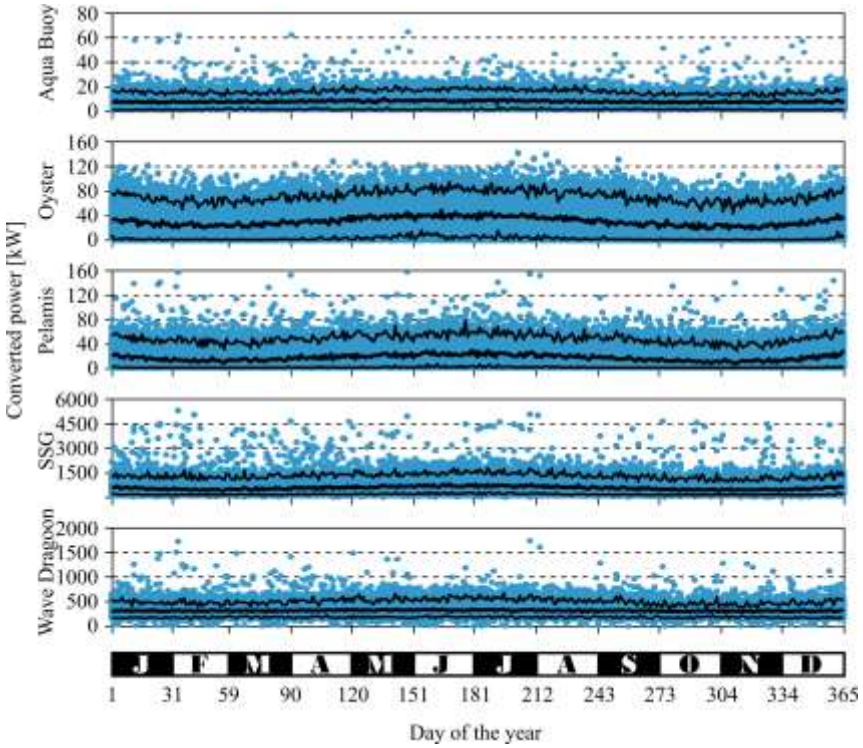

Figure 4. Converted power predictions

7.VALIDATION

For validating the proposed approach, the monthly power confidence intervals were computed for each converter (see Fig. 5) and compared with real values gotten for the years from 2015 to 2017, which were not used for fitting the models. It must be remarked that all the observed values fall within the predicted intervals, which validates the proposed approach for predicting converted wave power in offshore points.

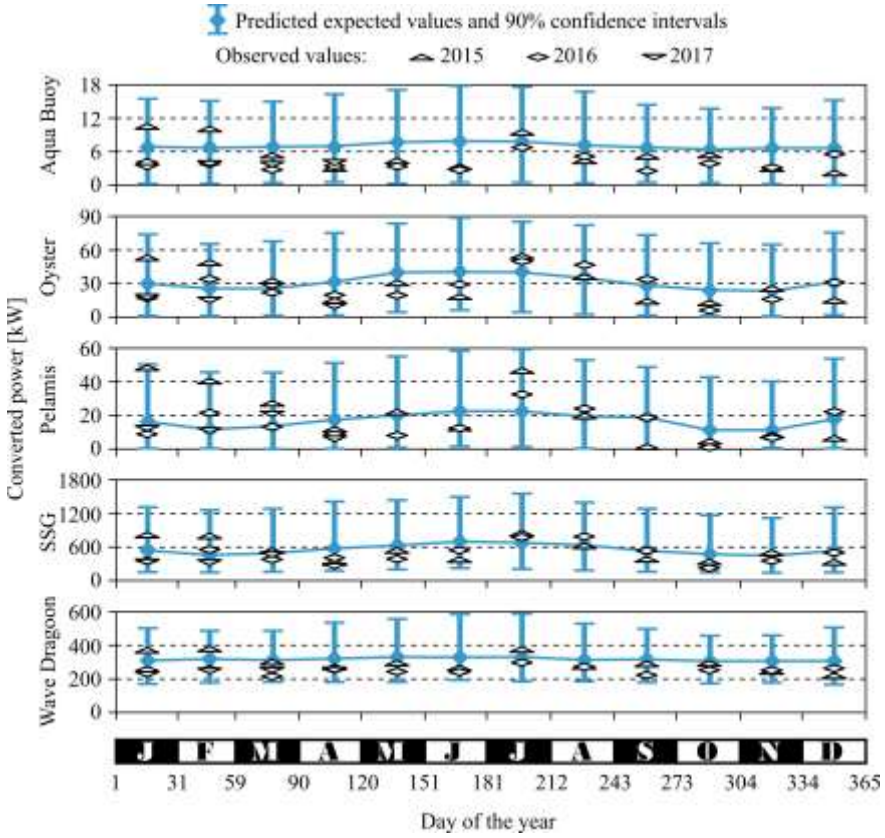

Figure 5. Monthly converter *power*

8.CONCLUSIONS

The implemented method combines the use of bivariate Weibull probability distributions and polynomial regressions for predicting the converted wave power in an offshore point. The models were fitted from measured data and they were capable of predicting not only the expected value but also the confidence intervals of those predictions. Validation of the model, carried out by using data excluded from the model fitting, shows an excellent prediction capability, as all the observed values fall within the predicted intervals. The predicted wave energy conversion values for the various converters show the usefulness of the proposed approach and its effectiveness, when they match the power data used for validation.

ACKNOWLEDGEMENTS

This research has been co-funded by FEDER funds, INTERREGMAC 2014-2020 Programme of the European Union, as part of the E5DES project (MAC2/1.1a/309).

REFERENCES

[1]. Canary Government, "Energetic yearbook of the Canary Islands", 2019. [Online]. Available http://www.gobiernodecanarias.org/istac/jaxi-istac/menu.do?uripub=urn:uuid:131cf873-66a9-408d-8cfa537d6be0506 [Accessed: 3-september-2022].

[2]. Avila D, Quiza R, Marichal GN. An approach for evaluating the stochastic behaviour of wave energy Converters. *Applied Ocean Research* 2022; 129: 103372 <https://doi.org/10.1016/j.apor.2022.103372>

[3]. Avila D, Marichal G N, Quiza R, San Luis F. Prediction of Wave Energy Transformation Capability in Isolated Islands by Using the Monte Carlo Method. *Journal of Marine Science and Engineering* 2021; 9: 980. <https://doi.org/10.3390/jmse9090980>

[4]. Padrón I, García MD, Marichal GN, Avila D. Wave Energy Potential of the Coast of El Hierro Island for the Exploitation of a Wave Energy Converter (WEC) *Sustainability* 2022; 14: 12139. <https://doi.org/10.3390/su141912139>

[5]. Avila D, Marichal G N, Padrón I, Quiza R, Hernández A. Forecasting of wave energy in Canary Islands based on artificial intelligence. *Applied Ocean Research* 2020; 101: 102–189. https://doi.org/10.1016/j.apor.2020.102189

[6]. Ahn S, Haas KA, Neary VS. Wave energy resource characterization and assessment for coastal waters of the United States. *Applied Energy* 2020; 267: 114922. <http://dx.doi.org/10.1016/j.apenergy.2020.114922>
[7]. Ahn S, Neary VS, Allahdadi MN, He R. Nearshore wave energy resource characterization along the East Coast of the United States. *Renewable Energy* 2021; 172: 1212–1224. <http://dx.doi.org/10.1016/j.renene.2021.03.037>
[8]. Swan Team. "SWAN scientific and technical documentation". 2020. [Online]. Available <http://swanmodel.sourceforge.net/download/zip/swantech.pdfAccessed:2022.09.05> [Accessed: 15-september-2022].
[9]. Sandvik E, Lonnum OJJ, Asbjornslett BE. Stochastic bivariate time series models of waves in the North Sea and their application in simulation-based design. Applied Ocean Research 2019; 82: 283–295. <http://dx.doi.org/10.1016/j.apor.2018.11.010>
[10]. Desouky MA, Abdelkhalik O. Wave prediction using wave rider position measurements and NARX network in wave energy conversion *Applied Ocean Research* 2019; 82: 10–21. <http://dx.doi.org/10.1016/j.apor.2018.10.016>
[11]. Kiusalaas J. Numerical Methods in Engineering with MATLAB. Cambridge University Press, Cambridge, 2005.

RIGA 2023

Comparative Study of Cylindrical and Triple Concentric Tube Models for PCM-based Thermal Energy Storage

Abhinav Rajan
Heat Transfer and Thermal Power Laboratory, Indian Institute of Technology Madras, Chennai, India,
rajan.abhinav9@gmail.com, ORCID: 0000-0003-3404-2228

K. S. Reddy
Heat Transfer and Thermal Power Laboratory, Indian Institute of Technology Madras, Chennai, India,
ksreddy@iitm.ac.in, ORCID: 0000-0003-0562-4042

Cite this paper as: *Rajan, A, Reddy, KS. Comparative study of cylindrical and triple concentric tube models for PCM-based thermal energy storage. 11th Eur. Conf. Ren. Energy Sys. 18-20 May 2023, Riga, Latvia*

Abstract: Thermal energy storage (TES) using phase change materials (PCMs) is a promising technology for improving the efficiency and dispatchability of solar power plants. PCMs have a high energy storage density and can absorb or release large amounts of heat with PCM phase transitions. This makes them well-suited for storing thermal energy from solar power plants and releasing it on demand to generate electricity or process heating applications. In this work, the cylindrical and triple concentric tube models are considered for TES. The study of TES is performed using a numerical model in the ANSYS® Fluent 2020 R1. The enthalpy porosity model is used to simulate the melting of PCM. The developed model for simulating the PCM is verified with reported experimental and numerically estimated results. The PCM in the cylindrical model melted completely in 7.89 hours while using the triple concentric tube model, the melting time decreased by 82.38 %. Moreover, variation in outer diameter for the triple concentric tube model is made and found that a diameter of 0.1 m is best performing among all the configurations.

Keywords: *Integrated solar energy system, thermal energy storage, phase change material*

1. INTRODUCTION

Thermal energy storage (TES) refers to a promising technology that allows excess heat or cold to be stored for later use. It is an important component of integrated solar energy systems because it enables excess solar energy to be collected and used when needed, rather than being wasted. There are several types of TES systems, including sensible heat [1], latent heat [2], and thermochemical storage [3]. Sensible heat storage involves storing heat in a material that has a high heat capacity, such as water or concrete. Latent heat storage systems store heat in a material that changes phase, such as ice or a phase change material. Thermochemical storage uses to store heat produced from a chemical reaction that can be reversed, such as the reaction between hydroxide ions and protons to form water.

Phase change materials (PCMs) are materials that enable the storing and releasing of thermal energy by changing between solid and liquid states. PCM-based TES systems use PCMs to regulate the temperature of a space or system. It is possible to use a triple concentric tube model to design a PCM-based TES system, in which the PCM is contained within the innermost tube, with working fluid circulating in the tubes to transfer heat to or from the PCM [4]. The outer tubes could be used to insulate the system and reduce heat loss. PCM-based TES systems could potentially have a higher energy density and be more efficient than other types of TES systems, due to the high heat capacity of PCMs [2,5]. However, the design and performance of such a system would depend on the specific properties of the PCM and heat transfer fluid used, as well as the temperature range and heat transfer rates required [5,6].

PCM-based TES systems can be used in conjunction with building heating and cooling [7], industrial processes [8,9], and renewable energy systems [10,11]. In renewable energy systems, a PCM-based TES system can be used to store excess energy from renewable energy sources, such as solar or wind power, for use during periods when the energy source is unavailable, or the energy demand is high. This can help to improve the reliability and stability of the renewable energy system [12].

It's worth noting that while PCM-based TES systems can be an effective means of storing and releasing heat, they may not be suitable for all applications. Factors such as cost, maintenance requirements, and the temperature range and heat transfer rates required will all need to be considered when deciding whether a PCM-based TES system is the best option for a particular application [2]. The PCM-based heat exchanger as TES can be classified as [4]: (a) cylindrical; (b) pipe, (c) multiple-tube, and (d) triple concentric tube models. Out of the first three models, the cylindrical model is the most common type of TES [13]. However, in recent times, the triple concentric tube model is gaining attention due to the advantage of its ease of use in simultaneous charging and discharging as well as dual charging or discharging [4,14].

In this work, a comprehensive analysis is conducted for a PCM-based TES system integrated with a concentrated solar power system for process heating applications. This study reports cylindrical and triple concentric tube models as single tube analysis. In the annulus between tubes, the PCM is filled which stores the energy while melting. The comparison between both said models is conducted using ANSYS® Fluent 2020 R1. The numerical model is established for accomplishing the simulation and it is verified with reported work in the literature. The enthalpy porosity technique is adopted to simulate the PCM phase transition. Further, the study is conducted by changing the outer diameter of the triple concentric tube model to obtain the best-performing configuration.

2. PHYSICAL MODEL

Figure1 illustrates the integrated solar energy system for process heating applications, which includes the parabolic dish collector and TES. In this work, the PCM-based TES is used to regulate the energy from the parabolic dish collector to the end user for process heating applications. The incoming energy from the sun is collected by the receiver of a 40 m^2 parabolic dish collector [15], here receiver may be of any shape such as cylindrical [16], conical [17], spherical [18], etc. For just sake of representation, the cylindrical receiver in the dish-receiver system is used in Figure1. The receiver is then supplied the collected amount of energy to a PCM-based TES system, where PCM materials are heated above their melting point to store up a significant amount of thermal energy in the form of latent heat. This stored energy can then be released by allowing the PCM to solidify again.

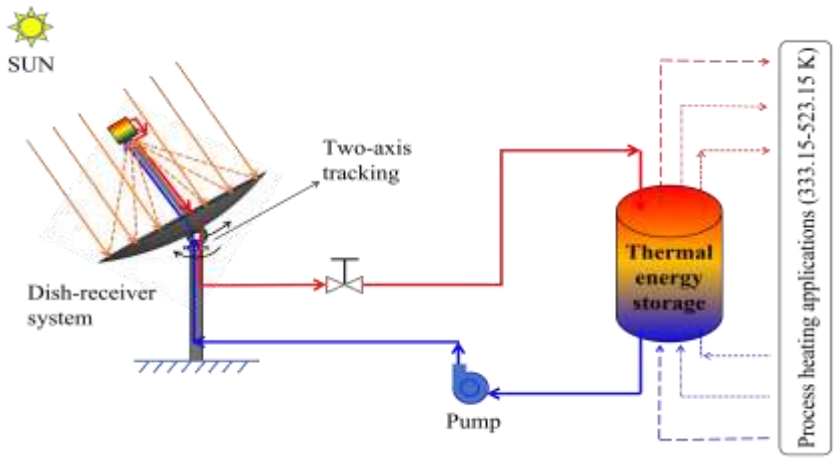

Figure 1. Integrated solar energy system with PCM-based TES.

The present TES system consists of multiple tube arrangements in the shell as shown in Figure 22. The cylindrical and triple concentric tube models are chosen to investigate and are illustrated in Figure 22(a-b). In this study, the single tube analysis for said models is conducted using a validated numerical model. The tubes of 1 m in length and 0.0025 m in thickness are used for cylindrical and triple concentric tube models. The complete details of geometrical

parameters are given in Table 1. For grid generation in the present study, the default tool of ANSYS® Workbench is used. The generated grid for TES is displayed in Figure 22(c).

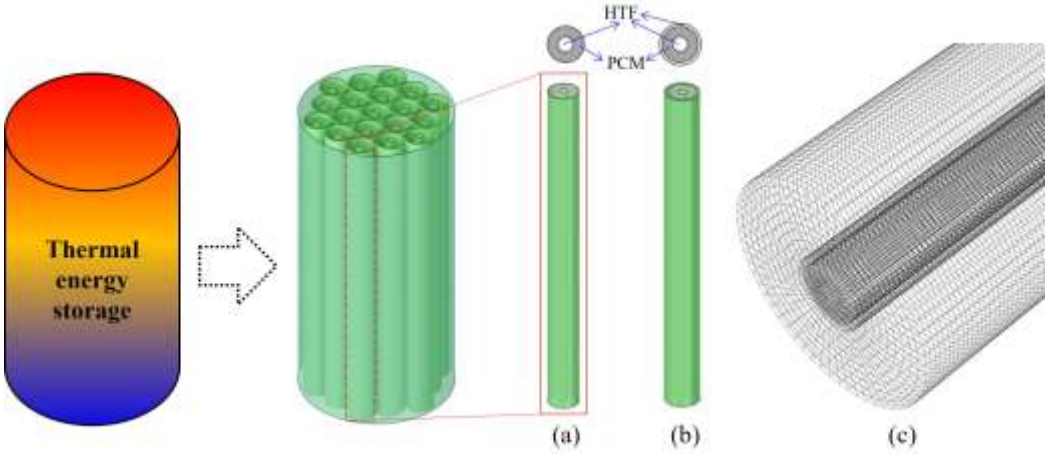

Figure 2. Shell and tube arrangements (a) cylindrical model, (b) triple concentric tube model, and (c) meshing.

Table 1. Geometrical parameters for TES in this study.

Parameter	Cylindrical model	Triple concentric tube
Length	1 m	1 m
Diameter of inner tube	0.022 m	0.022 m
Diameter of middle tube	-	0.085 m
Diameter of outer tube	0.085 m	0.1-0.13 m
Tube thickness	0.0025 m	0.0025 m

The considered PCM here is Paraffin Wax (RT 50). This PCM is preferred for low-temperature applications, for instance, drying, and space heating. The properties for RT 50 are listed in Table 2. The tube annulus is packed with 4 kg of RT 50. The water at 343.15 K as heat transfer fluid (HTF) is used to melt the PCM. In the cylindrical model, HTF is set to go in the inner tube while the triple concentric tube has HTF in the inner as well as outer tubes. The energy starts storing in PCM once it melts. The energy stored with melting PCM is called charging.

Table 2. Thermophysical properties of Paraffin Wax as PCM in TES.

Property	Value	Unit
ρ	820	kg/m^3
c_p	2000	J/kgK
k	0.2	W/mK
μ	$5\times10^{-7}T^2 - 0.0004T + 0.0859$	kg/ms

3. NUMERICAL MODELING

To simulate the solid-to-liquid phase transition and vice versa, the enthalpy porosity method with Boussinesq approximation is used in ANSYS® Fluent 2020 R1. The natural convection is considered within the liquid PCM by enabling Boussinesq approximation. The pertinent assumptions made to work the investigation are: (a) the flow is assumed to be 3-D transient, incompressible, and laminar for the liquid PCM; (b) viscous dissipation is negligible; (c) radiation effect is not considered; (d) the entire system is initially at 296.15 K; and (e) adiabatic condition is assumed at the lateral surface of the outer tube. The boundary conditions are defined as a mass flow of 0.0167 kg/s at the inlet and an outflow condition at the outlet of the inner tube. The SIMPLE algorithm is incorporated for pressure-velocity coupling. The QUICK scheme is used for momentum and energy equations, while the pressure term is discretized using the PRESTO! scheme. The governing equations (Eqs. 1-8) include continuity, momentum, and energy equations that are solved sequentially. The residuals of 10^{-3}, $10^{-6,}$ and 10^{-8} are set for continuity, momentum, and energy equations, respectively, as convergence criteria. The symbols used in Eqs. (1-8) are defined in Table 3.

Continuity equation:

$$\nabla.\vec{V} = 0 \tag{1}$$

Momentum equation:

$$\frac{\partial \vec{V}}{\partial t} + \vec{V}.\nabla\vec{V} = \frac{1}{\rho}\{-\nabla P + \mu\nabla^2\vec{V} + \rho\beta\vec{g}(T - T_{ref})\} + \vec{S} \tag{2}$$

where, $\vec{S}$ is source known as Darcy's law damping term. This additional source term in the momentum equation includes phase change effects on the heat transfer owned by convection. The source term, $\vec{S}$, is described as:

$$\vec{S} = \frac{(1-\lambda)^2}{\lambda^3} A_m \vec{V} \tag{3}$$

where, A_m is a mushy zone constant. The value for this constant is usually 10^4-10^7. In the present context, a value of 10^5 is assumed for A_m. λ is the melt fraction and is expressed as:

$$\lambda = \begin{cases} \frac{\Delta H}{L} = 0 & if\ T < T_s \\ \frac{\Delta H}{L} = 1 & if\ T > T_l \\ \frac{\Delta H}{L} = \frac{T - T_s}{T_l - T_s} & if\ T_s < T < T_l \end{cases} \tag{4}$$

Thermal energy:

$$\frac{\partial h}{\partial t} + \frac{\partial(\Delta H)}{\partial t} + \nabla.(\vec{V}h) = \nabla.\left(\frac{k}{c_p}\nabla h\right) \tag{5}$$

The summation of sensible enthalpy and latent heat is estimated as the total enthalpy of the material.

$$H = h + \Delta H \tag{6}$$

where,

$$h = h_{ref} + \int_{T_{ref}}^{T} c_p \Delta T \tag{7}$$

The latent heat content can be defined as:

$$\Delta H = \sum_{i=1}^{n} \lambda L \tag{8}$$

where ΔH varies from 0 (solid) to L (liquid).

Table 3. Symbols used in the governing equations.

A_{mush}	Mushy zone constant	$\vec{S}$	Source term
c_p	Specific heat	T	Temperature
λ	Melt fraction	T_s	Solidus temperature
H	Total enthalpy	T_l	Liquidus temperature
h	Sensible enthalpy	ρ	Density
h_{ref}	Reference enthalpy	β	Thermal expansion coefficient
ΔH	Latent heat	μ	Dynamic viscosity
$\vec{V}$	Velocity	L	Latent heat of material

4. RESULTS AND DISCUSSION

To verify the reliability of the developed model in the ANSYS® CFD package, the practice is made to replicate the geometrical model [19] to solve. The mesh elements of 5.5×10^5 is chosen for TES analysis. The time step of 1 s is adopted as the variations for 0.5 s and 1 s are almost marginal. All the simulations are performed using the AQUA Super Cluster of High Performance Computing Environment (HPCE) at IIT Madras. On completing the simulation, the volume-average temperature of liquid PCM is evaluated and equated with Hosseini et al. [19]. As seen in Figure 33, the trends of the temperature profile are found to be congruent with the data of reported methods. The discrepancies among the models are within the acceptable range and this present model is assumed to be accurate in the present context.

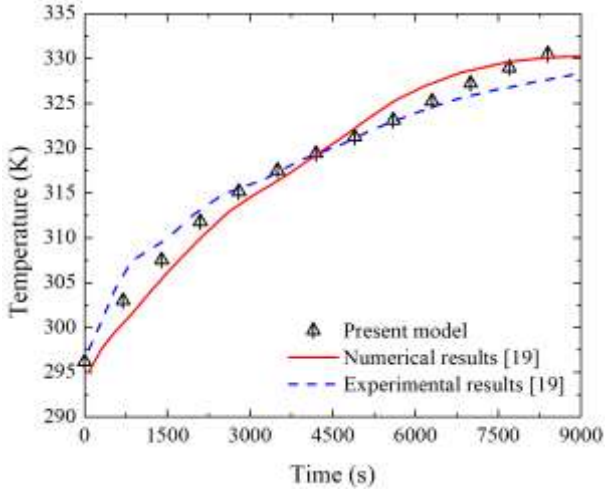

Figure 3. Validation of the present model with well-established models.

Figure 44 illustrates the thermal response (average temperature) and melting fraction for cylindrical and triple concentric tube models. The HTF inlet temperature was 343.15 K. In the cylindrical model, the PCM melts completely in 7.89 hours while it is just 1.39 hours for the triple concentric tube model. One can notice that the melting time reduces by 82.38 % by using the triple concentric model.

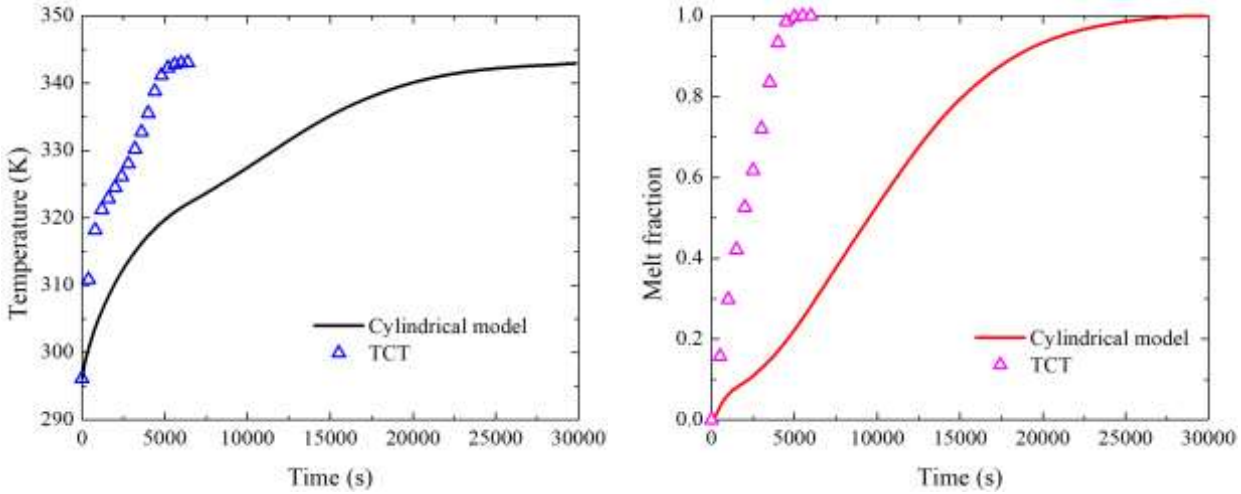

(a) (b)

Figure 4. Comparison of cylindrical and triple concentric tube (TCT) model (a) temperature, and (b) melt fraction.

Figure 55 demonstrates the variation of outer diameter (D) of the triple concentric tube model for thermal response and melting fraction during the charging process. The outer tube diameter from 0.1 m to 0.13 m is considered. As seen in Figure 5, the diameter of 0.1 m achieves the maximum temperature compared to others in less time. The melting time of 0.1 m is also less than that of other values of diameter. Melting time increases by 26 % to 60 % for other diameters compared to 0.1 m.

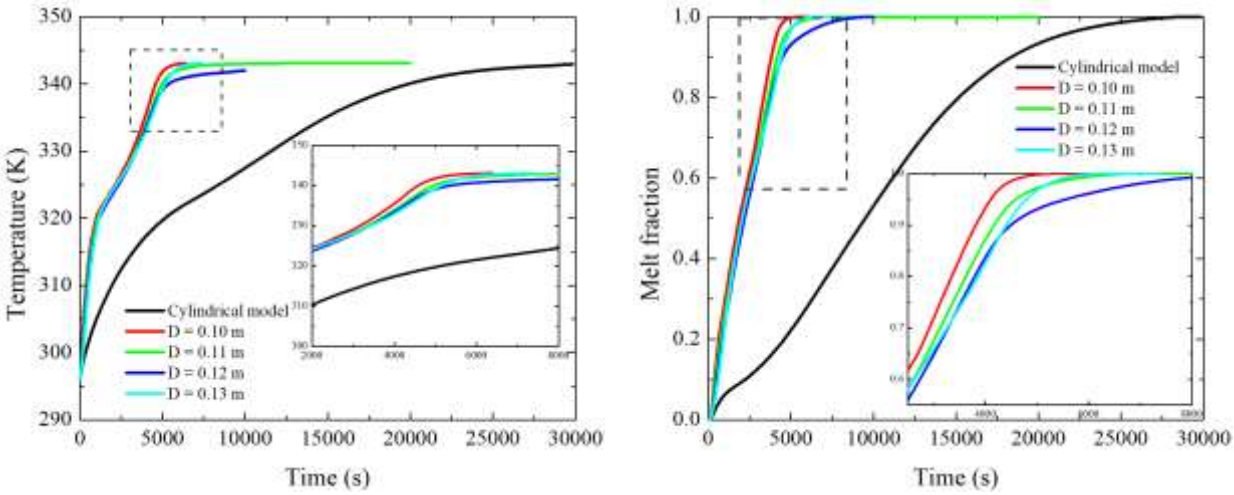

(a) (b)

Figure 5. Variation of outer tube diameter of the triple concentric tube.

5. CONCLUSION

So far, the analysis was performed for PCM-based TES of cylindrical and triple concentric tube models using finite volume software, ANSYS® Fluent 2020 R1. The single tube analysis of both models was reported for average temperature and melting time in the 3-D transient, incompressible, and laminar flow model. The Paraffin Wax (RT 50) as PCM is used in the TES for storing energy. The present numerical model was validated with well-established reported experimental as well as numerical data. In the present work, the comparison was made between cylindrical and triple concentric models, and additionally, the optimum outer diameter of the triple concentric tube model was found by varying the dimensions. From this comprehensive study, out of both models, the triple concentric tube model was more efficient. The melting time was decreased by 82.38 % for the triple concentric tube model compared to the cylindrical one. Further, in the triple concentric tube model, the outer diameter was varied to obtain the best optimum for the thermal storage system. The diameter of 0.1 m was found to be the best configuration, while others increased the melting time of PCM by 26 % to 60 %. The present numerical model could be expected to be valuable in the design and optimization of various PCM-based TES systems for process heating applications.

Acknowledgments

We acknowledge the funding provided by the Department of Science & Technology, India, through Grant ID: DST/TMD/CERI/RES/2020/14(C). We also acknowledge the use of the computing resources at HPCE, IIT Madras.

References

[1] Elouali A, Kousksou T, El Rhafiki T, Hamdaoui S, Mahdaoui M, Allouhi A, et al. Physical models for packed bed: Sensible heat storage systems. *J Energy Storage* 2019;23:69–78. https://doi.org/10.1016/J.EST.2019.03.004
[2] Sharma SD, Sagara K. Latent Heat Storage Materials and Systems: A Review. *Int J Green Energy* 2005;2:1–56. https://doi.org/10.1081/GE-200051299
[3] Aydin D, Casey SP, Riffat S. The latest advancements on thermochemical heat storage systems. *Renew Sustain Energy Rev* 2015;41:356–67. https://doi.org/10.1016/J.RSER.2014.08.054
[4] Kalapala L, Devanuri JK. Influence of operational and design parameters on the performance of a PCM based heat exchanger for thermal energy storage – A review. *J Energy Storage* 2018;20:497–519. https://doi.org/10.1016/J.EST.2018.10.024
[5] Samykano M. Role of phase change materials in thermal energy storage: Potential, recent progress and technical challenges. *Sustain Energy Technol Assessments* 2022;52:102234. https://doi.org/10.1016/J.SETA.2022.102234
[6] Dinker A, Agarwal M, Agarwal GD. Heat storage materials, geometry and applications: A review. *J Energy Inst* 2017;90:1–11. https://doi.org/10.1016/j.joei.2015.10.002
[7] Soares N, Costa JJ, Gaspar AR, Santos P. Review of passive PCM latent heat thermal energy storage systems towards buildings' energy efficiency. *Energy Build* 2013;59:82–103. https://doi.org/10.1016/J.ENBUILD.2012.12.042
[8] Crespo A, Barreneche C, Ibarra M, Platzer W. Latent thermal energy storage for solar process heat applications at medium-high temperatures – A review. *Sol Energy* 2019;192:3–34. https://doi.org/10.1016/J.SOLENER.2018.06.101

[9] Reddy KS, Pradeep N. Stability analysis of the thermocline thermal energy storage system during high flow rates for solar process heating applications. *Sol Energy* 2021;226:40–53. https://doi.org/10.1016/J.SOLENER.2021.08.026
[10] Yang X, Sun L, Yuan Y, Zhao X, Cao X. Experimental investigation on performance comparison of PV/T-PCM system and PV/T system. *Renew Energy* 2018;119:152–9. https://doi.org/10.1016/J.RENENE.2017.11.094
[11] Stropnik R, Stritih U. Increasing the efficiency of PV panel with the use of PCM. *Renew Energy* 2016;97:671–9. https://doi.org/10.1016/J.RENENE.2016.06.011
[12] Zhang S, Pu L, Mancin S, Dai M, Xu L. Role of partial and gradient filling strategies of copper foam on latent thermal energy storage: An experimental study. *Energy* 2022;255:124517. https://doi.org/10.1016/j.energy.2022.124517
[13] Agyenim F, Hewitt N, Eames P, Smyth M. A review of materials, heat transfer and phase change problem formulation for latent heat thermal energy storage systems (LHTESS). *Renew Sustain Energy Rev* 2010;14:615–28. https://doi.org/10.1016/J.RSER.2009.10.015
[14] Elbahjaoui R. Improvement of the thermal performance of a solar triple concentric-tube thermal energy storage unit using cascaded phase change materials. *J Energy Storage* 2021;42. https://doi.org/10.1016/J.EST.2021.103047
[15] Rajan A, Reddy KS. Optical modeling of solar parabolic dish collector coupled with conical cavity receiver. In: 6th Sustain. Energy Environ. Challenges, SEEC2021-074, 27-29 Dec 2021, Lucknow, India. https://doi.org/10.13140/RG.2.2.23847.42402
[16] Xiao L, Guo F-W, Wu S-Y, Chen Z-L. A comprehensive simulation on optical and thermal performance of a cylindrical cavity receiver in a parabolic dish collector system. *Renew Energy* 2020;145:878–92. https://doi.org/10.1016/J.RENENE.2019.06.068
[17] Rajan A, Reddy KS. Convective heat loss prediction from conical cavity receiver of solar parabolic dish collector using numerical method and artificial neural network. *Numer Heat Transf Part A Appl* 2022;0:1–24. https://doi.org/10.1080/10407782.2022.2102338
[18] Reddy KS, Sendhil Kumar N. Combined laminar natural convection and surface radiation heat transfer in a modified cavity receiver of solar parabolic dish. *Int J Therm Sci* 2008;47:1647–57. https://doi.org/10.1016/j.ijthermalsci.2007.12.001
[19] Hosseini MJ, Rahimi M, Bahrampoury R. Experimental and computational evolution of a shell and tube heat exchanger as a PCM thermal storage system. *Int Commun Heat Mass Transf* 2014;50:128–36. https://doi.org/10.1016/j.icheatmasstransfer.2013.11.008

RIGA 2023

Design and Implementation of DC-DC Converter for PV based EV Battery Storage System

Jeyashree Y
SRM Institute of Science and Technology, Kattankulathur, India, jeyashy@srmist.edu.in, ORCID: 0000-0001-8395-8502

Sukhi Y
R.M.K. Engineering College, Thiruvallur, India, kam.ece@rmkec.ac.in, ORCID: 0000-0002-9478-4306

Jenifer A
R.M.K. Engineering College, Thiruvallur, India, ajr.eee@rmkec.ac.in, ORCID: 0000-0003-3336-732X

Fayaz Ahamed A
R.M.K. Engineering College, Thiruvallur, India, afd.eee@rmkec.ac.in, ORCID: 0000-0003-2994-6337

Cite this paper as: *Jeyashree Y, Sukhi, Y, Jenifer, A, Fayaz Ahamed, A. Design and Implementation of DC-DC Converter for PV based EV Battery Storage System. 11. Eur. Conf. Ren. Energy Sys. 18-20 May 2023, Riga, Latvia.*

Abstract: In this paper, a novel DC-DC converter for PV based applications is developed. The converter configuration is designed to provide voltage gain over a wide range. This converter switching devices are subjected to less stress and is designed with less number of components. This makes the system applicable electric vehicles with battery storage system. The switches operating in complementary basis with synchronous rectification provides improved efficiency. The analysis of the converter is done to derive equations for the design of the converter components. The designed converter is simulated to find out its features.

Keywords: *dc-dc converter; battery storage system; photo voltaic; wide voltage gain; renewable energy*

1. INTRODUCTION

In the present scenario, there is a great demand for renewable energy conversion due to the green gas emission. The diminishing rate of fossil fuel also have led to use of renewable energy sources. The power generation using the renewable sources are fed to the microgrid[1]. The intermittent supply of power to the microgrid may cause disturbance in the microgrid. Therefore, it is necessary to reduce the variations in the supply of power [2]. This require storage devices to store the extra power and to supply the stored power in demand. The block diagram of the solar power with energy storage battery is shown in fig.1. Generally, the power generated due to the PV panel is connected charge controller to change the voltage level as per the requirement of the load [3]. The power source uses a unidirectional converter and the power in the battery is transferred using bi-directional converter [4]. The use of bidirectional converter is to store energy during excess power generation and to supply power during demand [5]. In case of electric vehicle, there is motoring mode in which power is received from the source and regenerative mode in which power is supplied by the vehicle [6]. Therefore, it is necessary to develop different configurations of bi-directional converter. These converters are operating in buck mode during one mode and in boost mode in the other mode. It will be better if the converter is operating in buck boost configuration for both the modes of operation. This require voltage gain of the converter to be wide range [7]. Conventional buck boost converters are subjected to high voltage stress with reduced voltage [8]. The rating of the devices used these bidirectional converters are high [9]. This leads to poor efficiency of the converter. The design of converter to achieve high voltage ratio provide more amount of losses due the resistance present in the reactive elements []. It is difficult to achieve wide range of voltage gain due to the limitation in duty cycle due to loss component [11]. The cascaded buck boost converter uses one inductor or one capacitor in the middle between two half bridges which has two switches in each can provide

high voltage gain [12]. One bridge is designed to provide step down voltage and the other bridge is designed to provide step up voltage. The inductor in the middle converter provide discontinuous current which results in high range capacitors in both the ports. The capacitor in the middle converter provides continuous current but it requires three inductors and two capacitors [13]. The Cuk converter used for battery energy storage provide continuous current in input and output ports but it requires capacitance in both the ports. The paper structure is organized as follows. The configuration of the converter and its working are explained in section II. The circuit modelling is explained in section III. The design of the controller is discussed in section IV. The simulation results are given in section V. The conclusion of the paper is done in section VI.

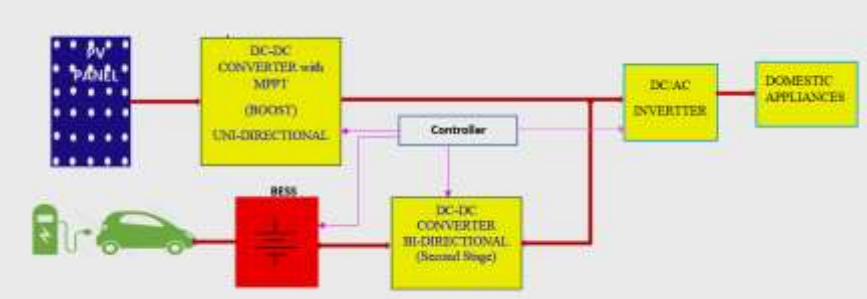

Figure 1. General Block diagram of solar based EV.

2. DC-DC CONVERTER

The proposed system is based on battery energy storage system using bidirectional buck boost converter is given in figure 2. The elements which are connected in the proposed system are solar PV panel, battery, proposed bidirectional buck boost converter and load.

2.1 Proposed Converter

The structure of the DC-DC converter configuration for high voltage gain is given in figure 2. It has two ports (input port P_I, output port P_O), four capacitors (C_A, C_B, C_C, C_D), two inductors (L_A, L_B), three switches (M_A, M_B, M_C). The power can flow input port to output port and vice versa. The triggering pulses applied to the switches are represented as G_A, G_B, G_C for the switches M_A, M_B, M_C respectively. Gating signals G_B, G_C are identical and are complementary to the gating signal of switch A, G_A.

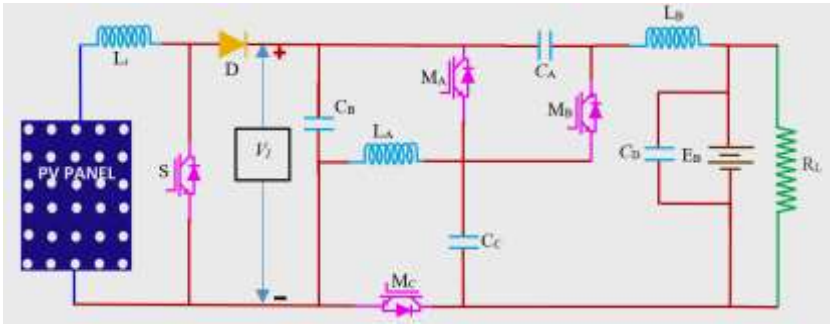

Figure 2. Proposed converter.

This configuration provides synchronous rectification. In order to make analysis simple, the following points are assumed.

1) The components of the converter are assumed to be ideal

2) The switches, resistances, inductances, capacitances are considered to be ideal

3) The small ripple approximation can be made to capacitance and inductance due to its large value.

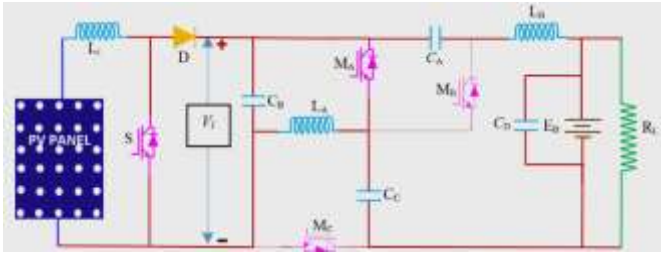

Figure 3. Circuit for power flow from source to load in buck mode.

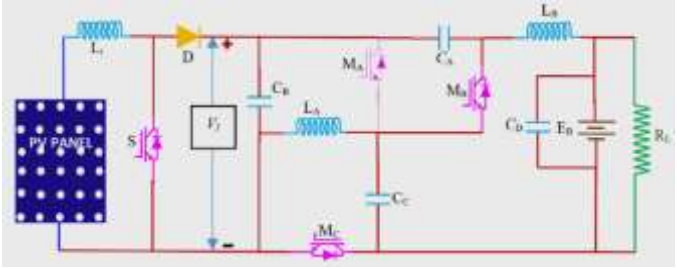

Figure 4. Circuit for power flow from source to load in boost mode.

The structure of converter for the buck mode and boost mode are given in figure 3 and figure 4 respectively. In this structure, power is allowed to flow from input to output and from output to input. In both the directions buck boost operation is possible. The typical waveform is shown in figure 5.

The typical waveform of the converter for power flow from load to source is given in figure 7. In the triggering pulses, there are two states (0 and 1). There is one main switch M_A and two complementary switches which form synchronous rectifier. When the switches are changing its state, there is dead time between the rising and falling edges. This occurs for the gating pulses of switches between M_B and M_A.

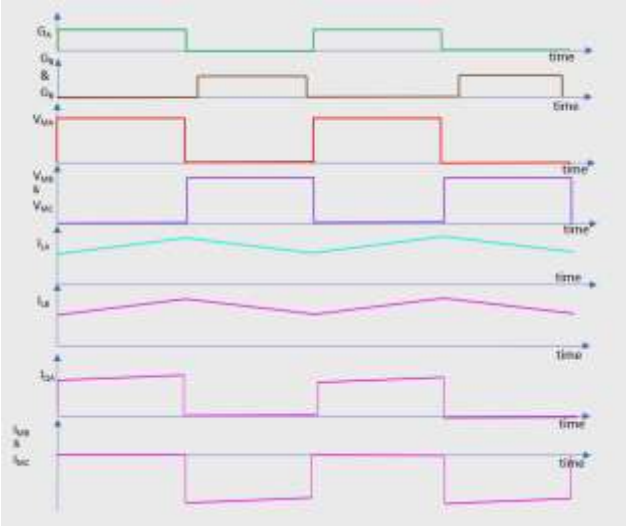

Figure 5. Key waveforms.

Similarly, the deadtime occurs between the gating pulses of switches M_C and M_A. When the deadtime occurs, the diodes parallel to the switches carry the current. In this condition, the switch voltage becomes zero. This results in zero voltage switching for the switches which are turned ON and OFF. In the input to output power flow, the two states are 0 and 1 which are explained as follows. During the state 0, the main switch M_A is turned ON and the switches M_B and M_C are in OFF condition. During this period $D_A T$, current flow path is shown in figure 3. and figure 4. for the switch M_A in ON and OFF condition respectively. The current and voltage equations related to this mode is derived as below.

$$V_{LA} = V_I \qquad (1)$$

$$V_{LB} = V_{CA} - V_O + V_{CC} \quad (2)$$

$$i_{CA} = i_{CC} = -i_{LB} \quad (3)$$

$$i_{CD} = i_{LB} - \frac{v_O}{R_L} \quad (4)$$

Similarly, during the state 0, the main switchM_A is turned OFF and the switches M_B and M_C are in ON condition. During this period $(1 - D_A T)$, current flow path is shown in figure 5. and figure 6. for the switch M_A in OFF and ON condition respectively.

$$V_{LA} = -V_{CC} = V_I - V_{CA} \quad (5)$$

$$V_{LB} = V_{CC} - V_O \quad (6)$$

$$i_{CA} = i_{CC} = \frac{I_{LA} - I_{LB}}{2} \quad (7)$$

$$i_{CD} = i_{LB} - \frac{v_O}{R_L} \quad (8)$$

The converter voltage gain for the operation of power flow from input to output is given by the equation (9).

$$G_{IO} = \frac{V_O}{V_I} = \frac{2D_A}{1 - D_A} \quad (9)$$

2.2 Efficiency Calculation and Analysis

The proposed converter efficiency is calculated after calculating the losses. The various losses occurring in the converter are switching loss (P_{MS}) in the switches, conduction loss (P_{MC}) during the ON condition of the switches, losses due to inductance resistance (P_{RL}) component and losses due to capacitance resistance (P_{RC}) component in the circuit constitute the total losses in the converter. These losses are expressed by the equation shown below.

$$P_T = P_{MC} + P_{MS} + P_{RC} + P_{RL} \quad (10)$$

The converter efficiency for the power flow from input to output is given by the expression (11)

$$Efficiency\ \eta = \frac{V_I \times I_{LB} \times G_{IO} - P_{TL}}{V_I \times I_{LB} \times G_{IO}} \quad (12)$$

3. MODELLING OF THE CONVERTER

In this paper the transfer function of the converter is derived using small signal analysis. This is used for the design of controller and to analyze the converter under transient conditions. For the flow of power from input to output, modelling is done using small signal analysis. In this, the input and the state variables are applied with a small ac perturbation. The variables for the small signal modelling are inductor currents I_{LA} , I_{LB} , capacitor voltage V_{CA}, duty ratio of the main switch A, D_A and the perturbations of these variables are represented as $\widehat{\imath_{LA}}$, $\widehat{\imath_{LB}}$, $\widehat{v_{CA}}$, $\widehat{D_A}$ and the output voltage $\widehat{v_O}$. The small signal model is given by the equations (13)-(17)

$$L_A \frac{d\widehat{\imath_{LA}}}{dt} = -D_A \widehat{v_{CA}} + V_{C1} \widehat{D_A} \quad (13)$$

$$L_B \frac{d\widehat{\imath_{LB}}}{dt} = V_{C1} \widehat{D_A} + \left(D_A + \frac{C_A}{C_C}\right) \widehat{v_{CA}} - \widehat{v_o} \quad (14)$$

$$\widehat{v_{CC}} = \frac{C_A}{C_C}\widehat{v_{CA}} \tag{15}$$

$$C_D \frac{d\widehat{v_O}}{dt} = \widehat{i_{LB}} - \frac{\widehat{v_O}}{R_L} \tag{16}$$

$$2C_A \frac{d\widehat{v_{CA}}}{dt} = D_A\widehat{i_{LA}} - (I_{LA} + I_{LB})\widehat{D_A} - (1 + D_A)\widehat{i_{LB}} \tag{17}$$

3. DESIGN OF CONTROLLER

The converter is controlled using PI controller to maintain the voltage level in the output. The approximate value of K_p and K_i is calculated using the expressions given below.

$$K_p = \frac{0.04 f_c}{R_S f_s} \tag{18}$$

$$K_i = \frac{0.04 f_c}{R_S f_s^2} \tag{19}$$

where f_c is the clock frequency, R_S resistance connected for feedback sensing and f_s represents switching frequency. The exact value of the K_p and K_i is calculated after fine tuning using MATLAB.

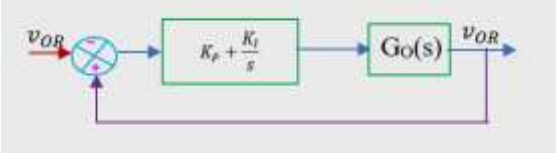

Figure 6. Feedback Controller.

The block diagram of the PI controller used in the feedback of the converter is shown in figure 6. After the implementation of feedback in the converter, the transfer function of the converter under feedback is given by the equation (20). The component values are given in the Table I.

$$G_C(s) = K_p + \frac{K_i}{s} G_O(s) = \frac{a_0 + a_1 s + a_2 s^2 + a_3 s^3}{s(b_o + b_1 s + b_2 s^2 + b_3 s^3 + b_4 s^4)} \tag{20}$$

5. SIMULATION RESULTS

The results obtained after simulation are given below. The results are taken for boost operation for an input of 50V Figure 7. and the output Figure 8. obtained is 400V. Similarly, the results are taken for buck operation for an input of 400V Figure 9. and the output obtained is 50V Figure 10.

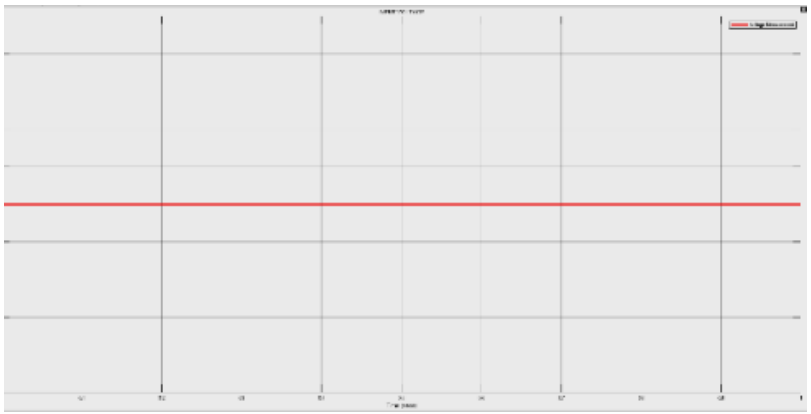

Figure 7. Input applied voltage for boost operation

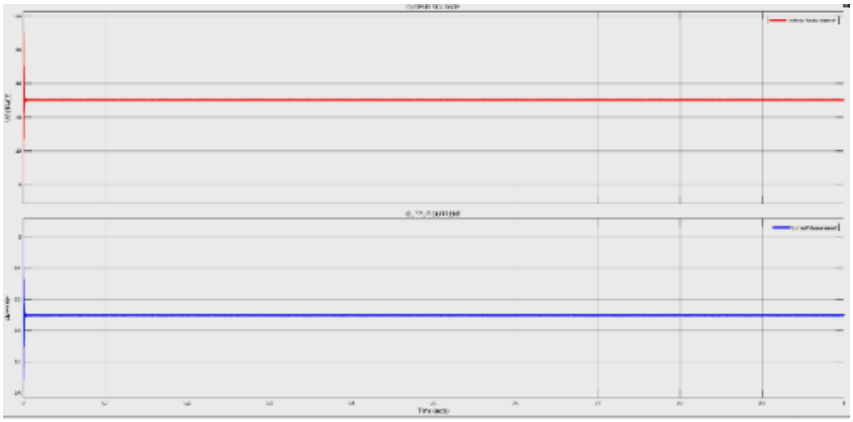

Figure 8. Output voltage of boost operation.

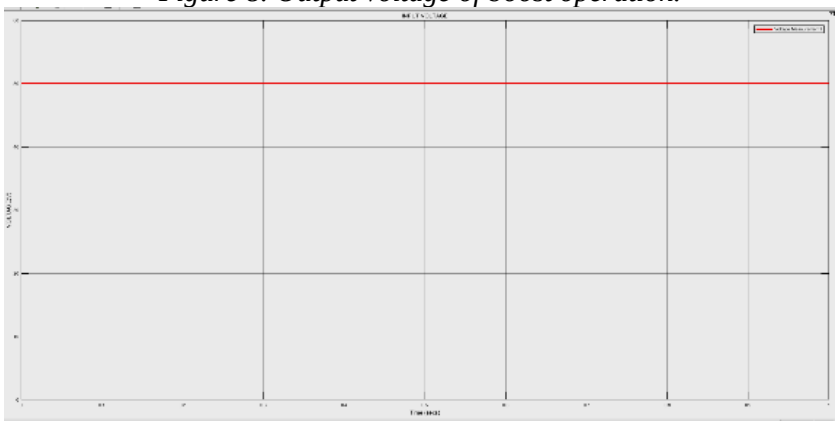

Figure 9. Input applied voltage for buck operation

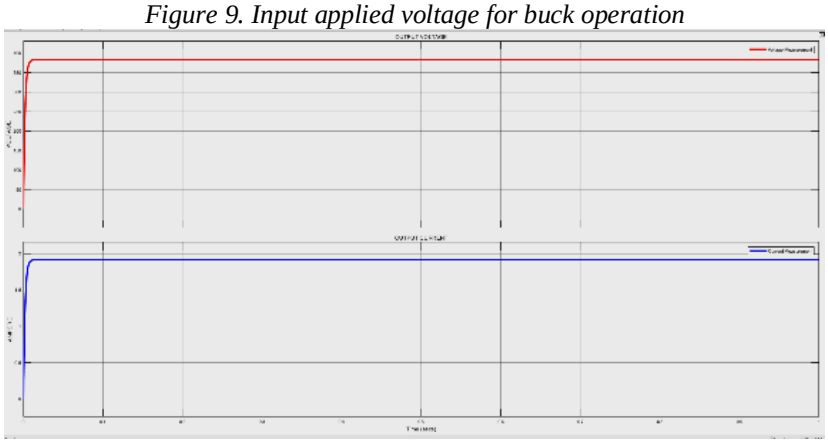

Figure 8. Output voltage of buck operation.

6. CONCLUSION

This paper presents a novel DC-DC converter for solar PV applications to buck and boost the input voltage as well as output voltage. In the converter configuration, synchronous rectification is implemented to have better efficiency. The method of synchronous rectification results in ZVS during the turn-ON as well as turn-OFF of the switches. This results in less stress on the switches. Also, the structure is very simple with less number of components. The results of the converter show that it is able to perform better during steady state conditions as well as dynamic conditions.

REFERENCES

[1] B N. Elsayad, H. Moradisizkoohi and O. A. Mohammed, "Design and Implementation of a New Transformerless Bidirectional DC–DC Converter With Wide Conversion Ratios," in IEEE Transactions on Industrial Electronics, vol. 66, no. 9, pp. 7067-7077, Sept. 2019,. Doi:< https://ieeexplore.ieee.org/document/8517159 >

[2] Vasiliki Gogolou, Konstantinos Kozalakis, Thomas Noulis, Stylianos Siskos,Integrated DC - DC converter design

methodology for design cycle speed up, Integration, Volume 88, 2023,Pages 80-90. < https://doi.org/10.1016/j.vlsi.2022.09.003>

[3] Jiulong Wang, Bingquan Wang, Lei Zhang, Jianjun Wang, N.I. Shchurov, B.V. Malozyomov,Review of bidirectional DC–DC converter topologies for hybrid energy storage system of new energy vehicles, Green Energy and Intelligent Transportation,Volume 1, Issue 2,2022,100010. doi:< https://doi.org/10.1016/j.geits.2022.100010>.

[4] Alireza Rajabi, Farzad Mohammadzadeh Shahir, Reza Sedaghati,New unidirectional step-up DC-DC converter for fuel-cell vehicle: Design and implementation,Electric Power Systems Research, Volume 212,2022,108653,.doi:< https://doi.org/10.1016/j.epsr.2022.108653>.

[5] Y. Sukhi, S. Kirthiga and N. Sujitha: Implementation and Analysis of Low Stress PWM DC-DC Converter for Battery Charger, Indian Journal of Science and Technology, Vol 8(28), pages 1-6, October 2015.doi:< 10.17485/ijst/2015/v8i28/71686>.

[6] T. Jarin, Stephy Akkara, S.S. Sreeja Mole, Arthi Manivannan, A. Immanuel Selvakumar,Fuel vehicle improvement using high voltage gain in DC-DC boost converter,Renewable Energy Focus, Volume 43,2022,Pages 228-238. doi:< https://doi.org/10.1016/j.ref.2022.09.008>.

[7] H. Shayeghi, A. Rahnama, N. Takorabet, P. Thounthong, N. Bizon, “Designing a multi-stage PD(1+PI) controller for DC–DC buck converter”, Energy Reports (2022), Volume 8, Supplement 16, Pages 765-773. doi:< https://doi.org/10.1016/j.egyr.2022.10.448>.

[8] Anagha E B, Bos Mathew Jos, Kiran Boby, Meenu Gibi, Multiple output high gain DC-DC converter, Materials Today: Proceedings, Volume 58, Part 1,2022,Pages 540-546. doi:< https://doi.org/10.1016/j.matpr.2022.03.060>.

[9] Murad Ali, Yu Haitao, Zhiyuan Che, Zakiud Din, Control of Free Piston Stirling Linear Generator system connected with dc/dc converter for energy storage applications based on SVPWM Rectification Method, Energy Reports, Volume 8, 2022, Pages 15421-15435. doi:< https://doi.org/10.1016/j.egyr.2022.11.095>.

[10] K.A. Mohamed Junaid, Y. Sukhi, Y. Jeyashree, A. Jenifer, A. Fayaz Ahamed,PV based electric vehicle battery charger using resonant converter,Renewable Energy Focus,Volume 42, 2022,Pages 24-32. doi:< https://doi.org/10.1016/j.ref.2022.05.005>.

[11] David Palomeque-Mangut, Ángel Rodríguez-Vázquez, Manuel Delgado-Restituto, A 4.2–13.2 V, on-chip, regulated, DC-DC converter in a standard 1.8V/3.3V CMOS process, AEU - International Journal of Electronics and Communications,2023,154527. doi:< https://doi.org/10.1016/j.aeue.2023.154527>.

[12] H. Aljarajreh, D. D. -C. Lu, Y. P. Siwakoti and C. K. Tse, "A Nonisolated Three-Port DC–DC Converter With Two Bidirectional Ports and Fewer Components," in IEEE Transactions on Power Electronics (2022), vol. 37, no. 7, pages. 8207-8216. doi:< https://ieeexplore.ieee.org/document/9695335>.

[13] Sukhi Yesuraj, Jeyashree Yesuraj, Perarasi Muthaiah& Sarojini Balaraman : Standalone PV-fed LED Street Lighting Using Resonant Converter, Electric Power Components and Systems, Vol. 45, issue 5, Feb 2017.pp. 548-559. doi:< https://doi.org/10.1080/15325008.2016.1271063>.

RIGA 2023

CO_2 Capture by Mineralization and Utilization: Primary Assessment of Thai Ultramafic Rock Resource

Waranya Thepsaskul
Program in Energy Engineering, Department of Mechanical Engineering, Faculty of Engineering, Chiang Mai University, 50200, Thailand, waranya@eng.cmu.ac.th, ORCID: 0000-0003-0288-261X

Wongkot Wongsapai
Science and Technology Research Institute, Chiang Mai University, Chiang Mai, 50200, Thailand, wongkot@eng.cmu.ac.th, ORCID: 0000-0002-2273-5177

Tadsuda Taksavasu
Department of Mining and Petroleum Engineering, Faculty of Engineering, Chiang Mai University, Chiang Mai, 50200, Thailand, ORCID: 0000-0003-4112-5603

Cite this paper as: *Thepsaskul, W, Wongsapai, W, Taksavasu, T. CO_2 Capture by Mineralization and Utilization: Primary Assessment of Thai Ultramafic Rock Resource. 11. Eur. Conf. Ren. Energy Sys. 18-20 May 2023, Riga, Latvia*

Abstract: Vertical ground-coupled heat pump systems have shown good potential to improve energy efficiency of HVAC system, especially for commercial applications due to the relatively high cost involved. Although well proven in temperate climates, vertical ground-coupled systems have been less tested in tropical climates. However, with the need to find means to reduce the carbon footprint of buildings, especially with the temperature extremes observed due to climate change in the previous decade, the combination of passive design principles with efficient controls can lead to significant energy savings, and further savings can be achieved by using a ground-coupled heat exchanger. This paper presents the preliminary test and simulation results obtained with a vertical borehole drilled to a depth of 20m, together with the thermal conductivity results. The experimental results on the borehole have been used to develop the CFD model, allowing to predict the performance of the system and carry out parametric analysis.

Keywords: *Vertical ground-coupled heat pump, CFD analysis, Building energy performance*

1. CO_2 EMISSION SITUATION IN THE WORLD AND THAILAND

In 2022, the average global temperature is approximately 1.15 ◦C (1.02 - 1.28 ◦C), which is higher than the pre-industrial average temperatures recorded during 1850-1900 [1]. The Paris Agreement on climate change is a legally binding international treaty aiming to limit the global warming to well below 2 ◦C, preferably 1.5 ◦C [2]. Currently, the greenhouse gases (GHG) emission of global rises constantly. By 2021, the carbon-dioxide or CO_2 emissions from fossil fuels and from industries will be in a total of 37.12 billion tCO_2. However, the land-use modification has been excluded [3]. According to such vital data, Thailand is one of the World's ninth countries affected by the climate change [4]. The Prime Minister of Thailand clearly stated that Thailand must be achieved a carbon neutrality by 2050 and gains a net zero greenhouse gas emissions no later than 2065, in the 26th United Nations Climate Change Conference in Glasgow, Scotland [5,6]. In 2021, CO_2 emission of Thailand is of 278.50 $MtCO_2$, which is accounted for 0.75% of the global CO_2 emission. This CO_2 amount is equal to the per-capita CO_2 emission of 3.89 tCO_2.

The major sources for Thai CO_2 emission are come from energy-generating sectors, largely by oils (108.75 $MtCO_2$), natural gases (77.39 $MtCO_2$), and coals (70.65 $MtCO_2$). In addition, other CO_2 emission sources include industrial activities and material production, e.g., cements (21.15 $MtCO_2$) and flaring (0.55 $MtCO_2$) [7].

2. CARBON CAPTURE UTILIZATION AND STORAGE

Reduction of the GHG emission by tried-and-true methods seems to be a common knowledge and necessity, the uses of renewable and clean energy. Enhancing energy efficiency or even reforestation may not sufficiently reduce the GHG emission as fast as they need. Hence, the Carbon-dioxide Capture, Utilization, and Storage or "CCUS" provides technological, engineering, and scientific concepts to solve or reduce these problems [8,9]. The CCUS has significantly provided a potential of substantially CO_2 reduction [10,11].

The CCUS is unlike to a novel concept, and various CO_2 capture technologies, including commercially available technologies, have been developed [8]. According to the Technology Readiness Level or TRL of the CCUS technologies, there are various types of the CO_2 capturing, utilizing, and storing methods occurred in different stages and many of them are currently in commercial operations, such as the CO_2-EOR or CO_2 storage in deep saline formations (see in Fig. 1). In 2022, there are a hundred and ninety-six commercial-Carbon Capture & Storage (CCS) and thirty operational CCS facilities are run globally with a total capture-capacity of 243.90 Mtpa [12].

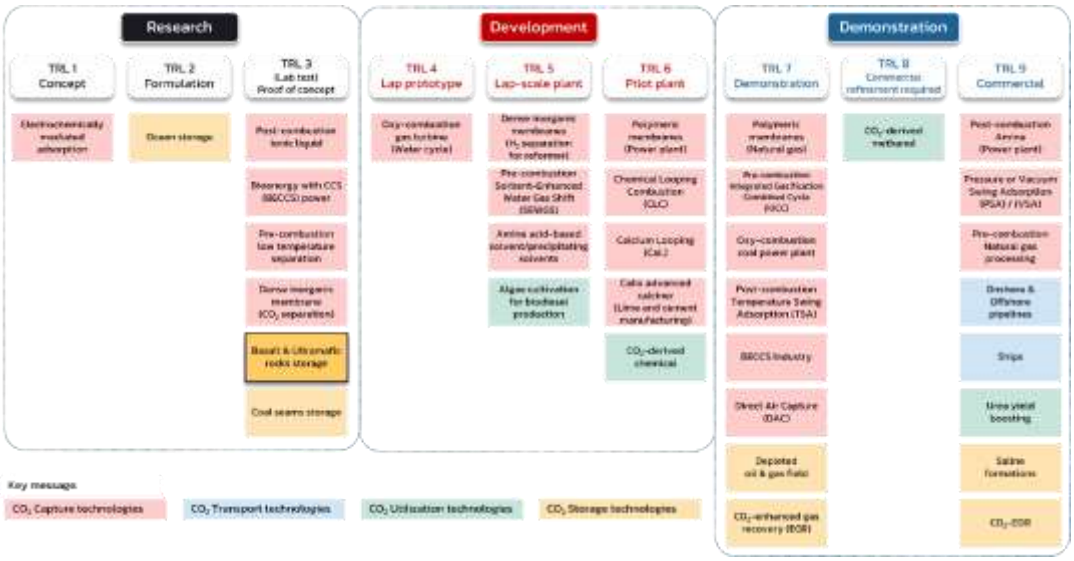

Figure 1. Technology Readiness Level (TRL) of certain CCUS technologies, modified from [13-15].

However, some of the CCUS technologies have a highly potential for CO_2 capturing and reuses it in upstream industries. These include a process of CO_2 capturing in a solid mineral through a carbon mineralization and a formation of a new mineral, which could be a by-product for other purposes [16]. Ultramafic igneous rocks contain CO_2 reactive minerals that allow the reactions between CO_2 gas and rock-forming minerals to naturally occur. The results of the chemical reaction are related to the occurrence of carbonate minerals that can be further considered for cement industries. This rock type is apparently an unique geo-resource with the CO_2 capturing potential.

3. CARBON MINERALIZATION

Carbon mineralization naturally occurs when the high-Mg, high-Ca, high-Fe, and high-alkali rocks have been exposed to atmospheric surface, where the CO_2 is suspended (see in Fig. 2). The mineralizing process changes original silicate minerals to "new carbonate minerals" such as magnesite, calcite, and siderite. The CO_2 captured by carbonate minerals is stable in solid and non-toxic forms and is permanently removed from the atmosphere [17, 18]. Natural carbon mineralization is also responsible for the annual CO_2 removal of approximately 0.3 $GtCO_2$ [19].

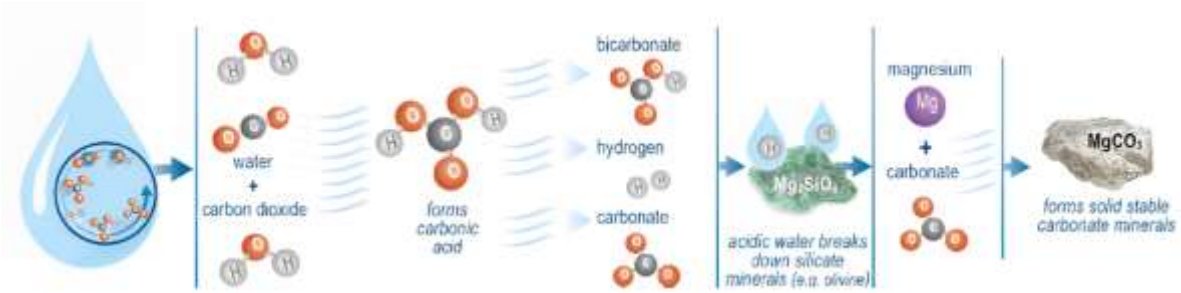

Figure 2. Carbon molecules along through action of mineralization [17].

Since the 1990's, the carbon mineralization has been discussed as a new potential replacement method for the CO_2 capture. One of the essential factors is an availability of Ca- and Mg-bearing mineral resources [20]. If we focus only the Mg- and Ca-rich rocks including ultramafic rocks, basalts, and anorthites, these rocks can potentially store 10,000-1,000,000 Gt of the CO_2 [16,21]. The areas of the specific CO_2 capture rocks are represented in Fig. 3. Focusing of Thailand's areas, there are few target areas determined that have a potential for the occurrence of Mg-rich ultramafic rocks. The potential areas are located in the northern and northeastern parts of Thailand.

Figure 3. Accessibility of minerals on a global scale, modified from [8,22].

3.1 Chemical Reaction of Carbon Mineralization

Carbon mineralization technologies are linked to the concept of the CCUS, and they are completely reliant on the mineralization-chemical reaction, which can be seen occurring in nature [23]. Mafic and ultramafic rocks certainly contain the most effective rock-forming minerals at reacting to the CO_2 gas. The mineral assemblages are changed from silicate compounds to carbonate when react with the CO_2, however, the process is quite slow [24]. In another word, this reaction shows that the CO_2 gases are absorbed by the rocks and the rocks change in their mineral compositions.

In general, igneous rocks can be classified into 4 subtypes based on their colors ranging from dark to light. Each type exhibits specific features, mineral assemblages, and chemical composition (Table 1). The ultramafic rocks have a relative high content of dark-colored minerals such as olivine, pyroxene, and serpentine. These minerals are importantly composed of magnesium and calcium, which are reactive elements to the CO_2 reaction. Based on

previous studies, the ultramafic rock samples collected from the Naga Hills Ophiolites contain 26.51-44.40 wt.% MgO [25]. More previous geochemical data indicates that the ultramafic rocks can also contain MgO as high as 48 wt.% [26].

Table 1. Classified igneous rocks, modified from [19,26,27].

Characteristics	Ultramafic	Mafic	Intermediate	Felsic
				
Color	Dark			Light
SiO_2	40%	50%	60%	70%
MgO	48%	15%	2.5%	0.95%
Example rocks	Peridotite, Pyroxenite, Dunite	Basalt, Gabbro	Andesite, Diorite	Rhyolite, Granite
Major minerals	Olivine, Serpentine, Pyroxene	Plagioclase feldspar	Amphibole	Potassium feldspar, Quartz

The CO_2 in gaseous phases are favored to react with Mg-silicate minerals in the mafic and ultramafic rocks. After the reaction has been achieved, the new phases of materials occur including magnesite ($MgCO_3$) and silica or silicon dioxide (SiO_2), which are both in solid phases. Ideal chemical reaction of olivine, serpentine and pyroxene are as followed equations (1-3):

Olivine: $\mathbf{Mg_2SiO_4} + 2CO_2 \rightarrow 2MgCO_3 + SiO_2$ (1)

Serpentine: $\mathbf{Mg_3Si_2O_5(OH)_4} + 3CO_2 \rightarrow 3MgCO_3 + 2SiO_2 + 2H_2O$ (2)

Pyroxene: $\mathbf{MgSiO_3} + CO_2 \rightarrow MgCO_3 + SiO_2$ (3)

3.2 Methods for Carbon Mineralization

In the carbon mineralization processes, the sources of CO_2 can either come from a direct air capture or an extraction from the pollutant-waste industrial sites. There are 3 approaches to accomplish reliable storage [28] as shown in Fig..4.

- In-situ carbon mineralization involves the circulation of CO_2-bearing fluids through appropriate rock formations located at deep.
- Surficial carbon mineralization occurs when a fluid or gas containing CO_2 reacts with mine tailings, alkaline industrial wastes, or sedimentary formations rich in reactive rock fragments. All of these materials have a high fraction of reactive surface area.
- Ex-situ carbon mineralization involves the transportation of solid reactants to a location for CO_2 capture, followed by a reaction with a CO_2-rich fluid or gas.

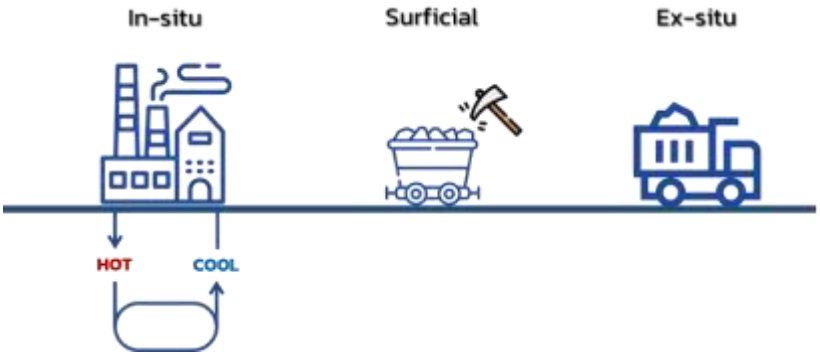

Figure 4. Methods for Carbon mineralization, modified from [29].

Using the ultramafic rocks for CO_2 capturing is one potential way of the surficial carbon mineralization processes. Before the calculation and interpretation of reactive CO_2 minerals and relative volumes of carbonate by-products have been approached, the potential rock deposits have been identified, as a study case of Thailand.

3.3 Ultramafic rock resource in Thailand

As shown in the geologic map of Thailand with a scale of 1:1,000,000 [30], the ultramafic rocks have been divided into three types: (i) peridotites, (ii) pyroxenites and (iii) serpentinites with the total area of 878,504,413.33 m^2 at 1.5-meter depth. The rocks are located in two regions covering by four provinces. Based on specific gravities of these types of rocks, a total weight of these rocks is around 3,972.45 million tons. According to a mole calculation of chemical reactions, one mole of the CO_2 gas, which reacted with a silicate mineral, likely produces a two-time amount of carbonate minerals. If the carbon mineralization phenomenon can be successfully occurred, a primary estimated amount of the CO_2 permanently captured by minerals is approximately 3,220.65 Mt or 3.22 Gt. The detail has been shown in the Table 2.

Table 2. Detail of the ultramafic rocks and their estimates in Thailand

Region	Northern of Thailand		Northeast of Thailand		Total
Province	Chiang Rai	Nan-Uttaradit	Loei	Sa-Kaeo	
Area (m^2)	54,986,580.97	446,398,005.00	5,093,418.23	372,026,409.13	878,504,413.33
Volume (m^3) (1.5-meter depth)	82,479,871.46	669,597,007.50	7,640,127.35	558,039,613.70	1,317,756,620.01
Rocks	peridotites, pyroxenites, serpentinites	peridotites, pyroxenites, serpentinites	serpentinites	pyroxenites, serpentinites	
Total weight (Mt of rocks)	252.94	2,053.43	19.86	1,646.22	3,972.45
Calculated reactive CO_2 ($MtCO_2$)	190.22 - 199.39	1,544.22 - 1,618.69	28.39	1,457.82 - 1,507.81	3,220.65 - 3,325.89

Note: Ultramafic rocks, including peridotite and pyroxene, have a specific gravity of 3,300 kg/m^3, while serpentinite has a specific gravity of 2,600 kg/m^3.

The geologic map representing the ultramafic rock resources in Thailand is shown in Fig. 5. The map includes enlarged mapping images of four provinces that consists of (1) Chiang Rai, (2) Nan-Uttaradit, (3) Loei, and (4) Sa-Kaeo.

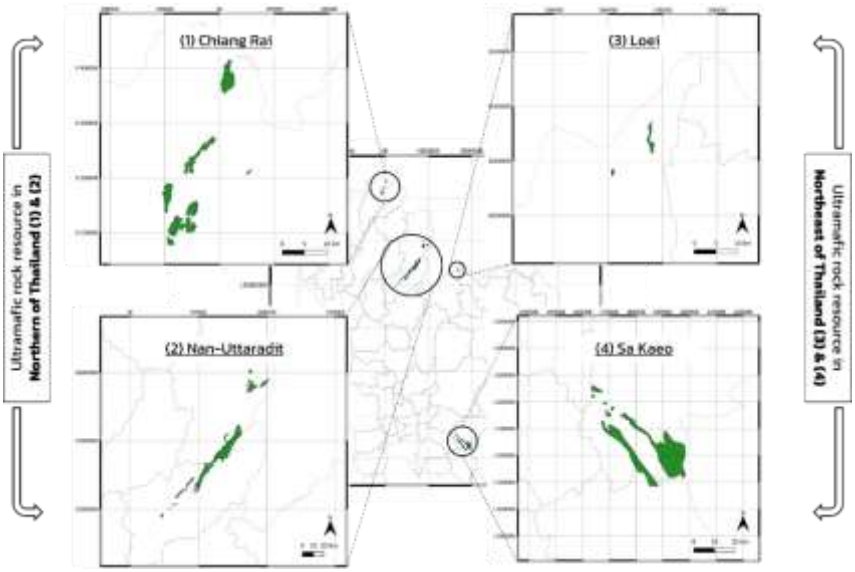

Figure 5. Ultramafic rock resource in Thailand [30].

4. APPLICATION OF CARBON MINERALIZATION FOR POTENTIAL INDUSTRY

As results of the minerals and CO_2 reactions, the products of CO_2 mineralization seem to have a potential to replace a conventional product in multiple industries. These facts apparently increase economic and environmental possibilities of the CCUS by substituting the conventional production [31]. While the carbon mineralization has been extensively explored for carbon capture and storage [32], the possible use of mineralization products has recently attracted considerable interest [21]. This shift leads to mineralization based CCU. CCU by mineralization keeps CCS's benefits and adds value. Value-added products boost CCU's economic potential through additional earnings and environmental benefit through substitution of conventional production [31]. Techno-economic carbon mineralization is possible in a variety of connected industries, including cement, concrete, steel, and construction.

4.1 **Cement Industry**

Limestone ($CaCO_3$) is a significant feedstock utilized in the cement production process for the creation of clinker. It was traditionally required for limestone mining. According to the model shown in Fig. 6, it was determined that CO_2 emissions from cement plants may be captured by installing a mineralization facility. Through chemical reactions, CO_2 combines with oxides of alkaline or alkaline-earth metals such as calcium oxide (CaO) and magnesium oxide (MgO) to generate carbonates through the following reaction: equation (4) [33]. The minerals in the rocks are then transformed into carbonate by-products that are recycled back into the cement industry. In addition to lowering CO_2, it is eco-friendly and can be included into a circular economy.

$$(Ca,Mg)SiO_3\ (s) + CO_2\ (g) \rightarrow (Ca,Mg)CO_3\ (s) + SiO_2\ (s) \quad (4)$$

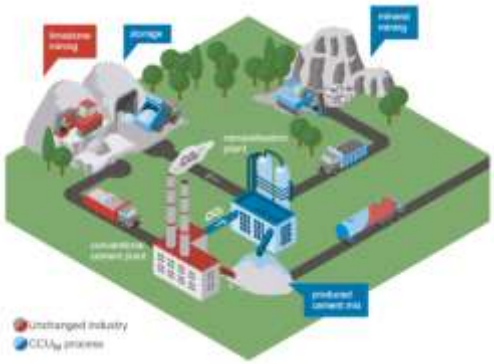

Figure 6. Integrating CO_2 mineralization into the cement production process [34].

4.2 Concrete & Construction Industry

In the procedures under consideration, CO_2 reacts with either selected minerals or the industrial wastes depicted in Fig. 7(Left: A) and Fig. 7(Right: B) demonstrates the application or curing (i.e., hardening) of standard concrete (CO_2 curing of concrete) to produce a solid carbonate that retains CO_2 permanently [35]. These procedures can provide cement additives (supplementary cementitious materials, SCM) [34] that are commercially viable for the building industry, synthetic aggregates and cement treated by CO_2 [36].

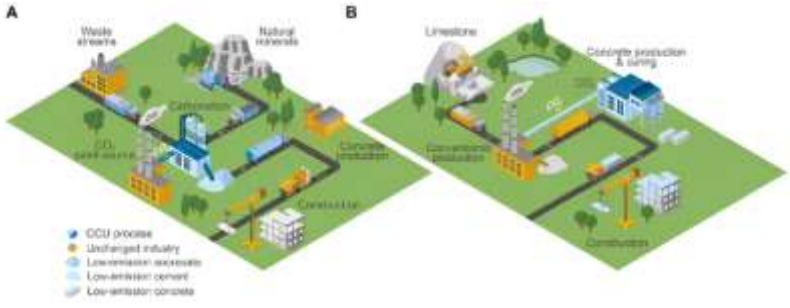

Figure 7. Concrete and construction industry CO_2 mineralization concepts [37].

5. CONCLUSION

This study preliminary examine and basically review specific uses of ultramafic rocks for the CO_2 permanent capture by the surficial carbon mineralization method in combination with the calculation and estimation of CO_2 reactive minerals and volume of carbonate by-products. Based on Thai ultramafic rocks, there are three main types including peridotites, pyroxenites, and serpentinites located in two regions covering by four provinces including (1) Chiang Rai, (2) Nan-Uttaradit, (3) Loei, and (4) Sa-Kaeo. The estimated amount of the CO_2 trapped in the carbonate minerals apparently ranges from 3,220.65 to 3,325.89 Mt. This study provides a preliminary potential assessment based on the geologic map analysis and the mole-based calculation. Further steps are to test the real CO_2 reaction with those reactive minerals of the ultramafic rocks.

Declaration of Competing Interest

The authors declare that they have no known competing financial interests or personal relationships that could have appeared to influence the work reported in this paper.

References

[1] World Meteorological Organization (WMO) [Internet]. Eight warmest years on record witness upsurge in climate change impacts [Published 2022 November 6; cited 2022 December 16]. Available from: https://public.wmo.int/en/media/press-release/eight-warmest-years-record-witness-upsurge-climate-change-impacts
[2] United Nations Framework Convention on Climate Change (UNFCCC) [Internet]. The Paris Agreement [cited 2022 December 16]. Available from: https://unfccc.int/process-and-meetings/the-paris-agreement/the-paris-agreement
[3] Our World in Data based on the Global Carbon Project (2022) [Internet]. Annual CO_2 emissions [cited 2022 December 16]. Available from: https://ourworldindata.org/grapher/annual-co2-emissions-per-country?country=~OWID_WRL
[4] Eckstein D., Künzel V., and Schäfer L. Global Climate Risk Index 2021. Germanwatch [Internet]. [Published 2021 January; cited 2022 December 16]. Available from: https://www.germanwatch.org/en/19777
[5] Bangprapa M. News: Bangkok Post Public Company Limited [Internet]. There's no Planet-B,' PM warns [Published 2021 November 3; cited 2022 December 16]. Available from: https://www.bangkokpost.com/thailand/general/2208459/theres-no-planet-b-pm-warns
[6] Royal Thai Embassy, Washington D.C. [Internet]. Thai Prime Minister pledges more electric vehicles at COP26 [cited 2022 December 16]. Available from: https://thaiembdc.org/2021/11/10/thai-prime-minister-pledges-more-electric-vehicles-at-cop26/
[7] Ritchie H. and Roser M. Our World in Data based on the Global Carbon Project (2022) [Internet]. Thailand: CO2 Country Profile [cited 2022 December 16]. Available from: https://ourworldindata.org/co2/country/thailand
[8] Sanna A., Uibu M., Caramanna G., Kuusik R., and Maroto-Valer M. M. A review of mineral carbonation technologies to sequester CO2. Chem.Soc.Rev.,2014, 43, 8049-8080. Available from: https://doi.org/10.1039/C4CS00035H
[9] Pacala S. and Socolow R. Stabilization Wedges: Solving the Climate Problem for the Next 50 Years with Current Technologies. Science, 2004, 305, 968–972. Available from: https://www.science.org/doi/10.1126/science.1100103
[10] Thailand Greenhouse Gas Management Organization (TGO) [Internet]. Carbon Capture, Utilisation and Storage (CCUS) [cited 2022 December 16]. Available from: http://www.tgo.or.th/2020/index.php/en/post/carbon-capture-utilisation-and-storage-ccus
[11] IEA (2021) [Internet]. About CCUS, IEA, Paris Available from: https://www.iea.org/reports/about-ccus, License: CC BY 4.0
[12] Steyn M., Oglesby J., Turan G., Zapantis A., Gebremedhin R., Zapantis A. et al., Global Status of CCS 2022. Global CCS Institute. Available from: https://status22.globalccsinstitute.com/
[13] Hong W. Y. A techno-economic review on carbon capture, utilisation and storage systems for achieving a net-zero CO2 emissions future. Carbon Capture Science & Technology 3 (2022) 10004. Available from: https://doi.org/10.1016/j.ccst.2022.100044
[14] Bui M., Adjiman C. S., Bardow A., Anthony E. J., Boston A., Brown S. et al., Carbon capture and storage (CCS): the way forward. Energy Environ. Sci., 2018, 11, 1062-1176. Available from: https://doi.org/10.1039/C7EE02342A
[15] Kearns D., Liu H., and Consoli C. Technology Readiness and Costs of CCS (2021) [Published 2021 March 29]. Global CCS Institute. Available from: https://www.globalccsinstitute.com/resources/publications-reports-research/technology-readiness-and-costs-of-ccs/
[16] Gadikota G. Carbon mineralization pathways for carbon capture, storage, and utilization. Commun Chem 4, 23 (2021). Available from: https://doi.org/10.1038/s42004-021-00461-x
[17] Sandalow D., Aines R., Friedmann J., Kelemen P., McCormick C., Power I. et al., ICEF 2021 Roadmap: Carbon Mineralization (2021). Innovation for Cool Earth Forum (ICEF). Available from: https://www.icef.go.jp/roadmap/
[18] Seifritz W. CO2 disposal by means of silicates. Nature 345, 486 (1990). Available from: https://doi.org/10.1038/345486b0

[19] Ciais P., Sabine C., Bala G., and Peters W. (2013). Carbon and Other Biogeochemical Cycles. Climate Change 2013: The Physical Science Basis. Contribution of Working Group I to the Fifth Assessment Report of the Intergovernmental Panel on Climate Change (pp. 465-570). Cambridge University Press. Available from: https://doi.org/10.1017/CBO9781107415324.015
[20] Styles M. T., Sanna A., Lacinska A. M., Naden J., and Maroto-Valer M. The variation in composition of ultramafic rocks and the effect on their suitability for carbon dioxide sequestration by mineralization following acid leaching. 2013, Greenhouse Gas Sci Technol. 4:440–451 (2014). Available from: https://doi.org/10.1002/ghg.1405
[21] Sanna A., Hall M. R., and Maroto-Valer M. Post-processing pathways in carbon capture and storage by mineral carbonation (CCSM) towards the introduction of carbon neutral materials. Energy Environ. Sci., 2012, 5, 7781-7796. Available from: http://pubs.rsc.org | doi:10.1039/C2EE03455G
[22] Matter J., Kelemen P., Park Ah-hyung A., and Greeshma G. Geo-Chemo-Mechanical Studies for Permanent Storage of CO2 in Geologic Formations DE-FE0002386. Columbia University, New York, U.S. Department of Energy National Energy Technology Laboratory Carbon Storage R&D Project Review Meeting, August 21–23, 2012, Available from: http://www.netl.doe.gov/.
[23] Thonemann N., Zacharopoulos L., Fromme F., and Nühlen J. Environmental impacts of carbon capture and utilization by mineral carbonation: A systematic literature review and meta life cycle assessment. Journal of Cleaner Production 332 (2022) 130067. Available from: https://doi.org/10.1016/j.jclepro.2021.130067
[24] Hills C.D., Tripathi N., and Carey P.J. (2020). Mineralization Technology for Carbon Capture, Utilization, and Storage. Front. Energy Res. 8:142. Available from: https://doi.org/10.3389/fenrg.2020.00142
[25] Dey A., Hussain M. F., and Barman M. N. Geochemical characteristics of mafic and ultramafic rocks from the Naga Hills Ophiolite, India: Implications for petrogenesis. Geoscience Frontiers 9 (2018) 517-529. Available from: http://dx.doi.org/10.1016/j.gsf.2017.05.006
[26] Geology In [Internet]. How to Classify Igneous Rocks Into (Ultramafic, Mafic, Intermediate and Felsic). Available from: https://www.geologyin.com/2014/12/how-to-classify-igneous-rocks-into.html
[27] Geology.com [Internet]. Rocks: Igneous, Metamorphic and Sedimentary. Available from: https://geology.com/rocks/
[28] National Academies of Sciences, Engineering, and Medicine. 2019. Negative Emissions Technologies and Reliable Sequestration: A Research Agenda. Washington, DC: The National Academies Press. Available from: https://doi.org/10.17226/25259.
[29] Dipple G., Kelemen P., and Woodall C.M. Carbon Dioxide Removal Primer, 2021, Available: https://cdrprimer.org/read/chapter-2
[30] Geologic Map of Thailand; scale of 1:1,000,000, Department of Mineral Resources of Thailand, 1999
[31] Ostovari H., Sternberg A. and Bardow A. Rock 'n' use of CO2: carbon footprint of carbon capture and utilization by mineralization. Sustain. Energy Fuels (2020). 4, 4482-4496. Available from: DOI: 10.1039/d0se00190b
[32] Romanov V., Soong Y., Carney C., Rush G.E, Nielsen B., and O'Connor W. Mineralization of Carbon Dioxide: A Literature Review. ChemBioEng Rev 2015, 2, No. 4, 231–256. Available from: https://doi.org/10.1002/cben.201500002
[33] Meng J., Liao W., and Zhang G. Emerging CO2-Mineralization Technologies for Co-Utilization of Industrial Solid Waste and Carbon Resources in China. Minerals 2021, 11, 274. Available from: https://doi.org/10.3390/min11030274
[34] Strunge T., Renforth P., and Van der Spek M. Towards a business case for CO2 mineralisation in the cement industry. Communication Earth & Environment (2022), vol. 3, 59. Available from: https://doi.org/10.1038/s43247-022-00390-0
[35] SCOT project (2016). EU_ETS to Incentivise CO2 Utilisation? SCOT Project Briefing Paper.
[36] Hendriks C., Paul N., Paul Z., and Cook G. Implications of the Reuse of Captured CO2 for European Climate Action Policies (2013). Utrecht: ECOFYS Netherlands B.V. Available from: doi:10.2790/11560
[37] Olfe-Kräutlein B., Strunge T., and Chanin A. Push or Pull? Policy Barriers and Incentives to the Development and Deployment of CO2 Utilization, in Particular CO2 Mineralization. Front. Energy Res (2021). 9:742709. Available from: doi: 10.3389/fenrg.2021.742709

RIGA 2023

Educational Study on Performance Comparison of PID, Fuzzy Logic-PID, and Bode Editor Techniques for Series Wound DC Motor Speed Control

Gonca Çam
Marmara University, Istanbul, Türkiye, gonca-cam@hotmail.com, ORCID: 0000-0002-6160-9309

Necibe Fusun Oyman Serteller
Marmara University, Istanbul, Türkiye, fserteller@marmara.edu.tr, ORCID: 0000-0003-3147-2740

Cite this paper as: *Çam, G, Serteller, NFO. Educational Study on Performance Comparison of PID, Fuzzy Logic-PID, and Bode Editor Techniques for Series Wound DC Motor Speed Control. 11. Eur. Conf. Ren. Energy Sys. 18-20 May 2023, Riga, Latvia*

Abstract: DC motor speed is controlled using various control methods. PID control is widely preferred in control systems. In this paper, the speed of the series wound DC motor is controlled by the PID control system. The system has been modeled and simulated in Matlab/ Simulink environment. In order to analyze Series Wound DC Motor (SWDCM) speed control, P, I, and D parameters should be selected according to the system. PID tune and Bode editor techniques are designed for educational purposes and used to determine parameters suitable for system control. In addition, the PID controller and Fuzzy Logic controller have been added to the system together. It is aimed to teach how to operate and use these methods by showing them step by step in the Matlab environment. The simulation results generated using these techniques are given in comparison

Keywords: *Bode Editor, Education, Fuzzy Logic, PID controller, SWDCM*

1. INTRODUCTION

DCM (Direct Current Motor) is quite used in industrial control applications, robotics, and electricity. Many situations can cause the speed of the DCM to change. Therefore, DC motor speed control is substantial for all projects and applications in research areas and accurate and effective methods must be established for the speed control of DCM [1,2]. Series Wound DC (SWDC) motors operate with quite high torque at the beginning and these motors can work properly even under heavy loads. With these properties, SWDCMs are used in a great variety of industrial applications. They can also be used in electric vehicles, mobile electrical equipment, small electrical appliances, cranes, and hoists. The speeds of SWDCMs vary with changes in load. Changing the speed of the motor also makes them usable in vehicles such as vacuum cleaners, sewing machines, and elevators [2,4]. Hence, speed control of SWDC motors is very important. PID control is frequently mentioned in industrial control systems and is very preferred. It has higher characteristics such as simple mathematical modeling, good reliability, high reliability, stability and ease of use, and steady-state error correction[5]. Although the PID and Fuzzy-PID controllers have been examined in recent years[6,7], in this paper, the effect of the Bode technique which is a classical control technique, on the system has also been discussed beside them. PID control parameters are set to the best value for the desired control response using the PID tune techniques [4,5] of MATLAB. System control is improved by changing the PID controller parameters. The parameters of the PID controller are set with Bode editor. In addition, a fuzzy logic controller(FLC) has been added to the PID controller to improve PID control coefficients. The purpose of the study is to teach how to make all these applications using MATLAB. System control is provided by using PID/PID (using Bode editor technique)/PID-Fuzzy Logic, respectively, and the productivities of these techniques are compared at the same transition levels. The remainder of the article includes: Section II includes the model of the SWDC motor and explains briefly the PID controller, Fuzzy Logic, and Bode Editor, section III presents the system block Diagram and results of the simulations, and lastly, section IV put forwards the conclusion.

2. SERIES WOUND DC MOTOR MODELING-PID, FUZZY LOGIC CONTROLLER, AND BODE EDITOR TECHNIQUE

Series Wound DC Motor

The working principle of an SWDC motor is based on the electromagnetic principle. It converts electrical energy into mechanical energy according to the electromagnetic principle. These types of DC motors contain a power supply terminal at one end of the armature and field coils. When voltage is applied to terminals, current passes both through the armature and field windings. Because the conductors in these windings are connected in series, a huge current starts to flow in the field coils. With the flow of this current, a powerful magnetic field is generated which originates a large torque at the shafts. This high torque turns the armature and generates the purpose of mechanical energy. The armature current of an SWDCM is at the same time as its field current. This means that the speed of SWDCMs increases as the load decreases [1]. A circuit model of an SWDC motor is shown in Figure 1 below.

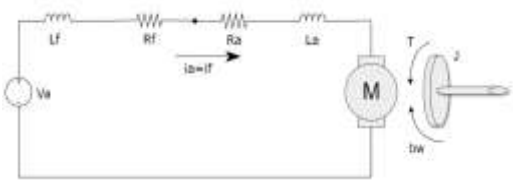

Figure 1. SWDC Motor equivalent diagram

Table 1. Parameters of SWDC Motors

Parameter	Description	Value	Unit
$\mathcal{J}$	Moment of inertia	0.1352	$kg\,m^2/s^2$
$\mathcal{K}_t$	Torque constant	0.6	Nm/Amp
b	Coefficient of viscous friction	0	Nms
$\mathcal{R}_a$	Armature resistance	1.2	Ω
$\mathcal{R}_f$	Field resistance	0.026	Ω
$\mathcal{L}_a$	Armature inductance	0.05	H
$\mathcal{L}_f$	Field inductance	0.167	H
$\mathcal{K}_b$	Back emf constant	0.6	$V\,s/rad$

Where, $\mathcal{T}$ is the electromagnetic torque (Nm), w is the angular velocity (rad/sec), i_a is the armature current (Amp), $\mathcal{V}_a$ is armature voltage (V), and $\mathcal{E}_b$is back emf (V). The parameter values of the SWDC motor used in this study are given in Table 1.

Speed control is one of the important components in DC motor operation. Controlling the speed of the DCM is essential in such applications. The following dynamic equations describe the behavior of the SWDCM.

$$\mathcal{T}(t) = \mathcal{J}\frac{dw(t)}{dt} + bw(t) \quad (1)$$

$$\mathcal{T}(t) = \mathcal{K}_t i_a(t) \quad (2)$$

$$\mathcal{V}_a(t) - \mathcal{E}_b(t) = (\mathcal{R}_a + \mathcal{R}_f) i_a(t) + \mathcal{L}_a \frac{di_a(t)}{dt} + \mathcal{L}_f \frac{di_a(t)}{dt} \quad (3)$$

$$\mathcal{E}_b(t) = \mathcal{K}_b w(t) \quad (4)$$

The transfer function is obtained by using DC motor equations.

$$\frac{w(s)}{\mathcal{V}(s)} = \frac{\mathcal{K}_t}{((\mathcal{L}_a+\mathcal{L}_f)s+\mathcal{R}_a+\mathcal{R}_f)(\mathcal{J}s+b)+\mathcal{K}_t\mathcal{K}_b} \quad (5)$$

The block diagram of equation (5) is simulated in Figure 2. Where wr is the reference speed and is given to the system as the step input, wo is the output speed.

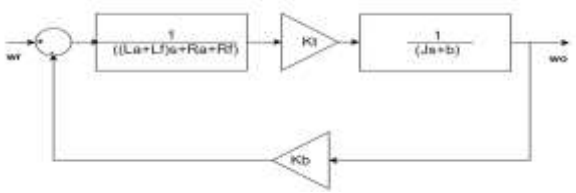

Figure 2. Block diagram of SWDC motor

The transfer function is written using the parameters in Table 1. (6).

$$\frac{\omega(s)}{v(s)} = \frac{1}{0.05s^2 + 0.28s + 0.6} \qquad (6)$$

Proportional(P)- Integral(I)- Derivative(D) Controller

PID (Proportional/Integral/Derivative) controller is frequently used as a controller in motor applications and industrial control systems. [4,5]. In addition, PID controllers have a very simple control structure, which provides ease of use and is also cheaper[2]. The purpose of the PID controller is to minimize error and maximize the system efficiency by adjusting the control inputs. The proportional mode reduces error and accelerates dynamic response by adjusting the manipulated variable. Integral mode reaches zero offsets. Derivative mode improves the system with a quick fix based on the rate of change of the variable being controlled. The block schematic of the PID is given in Fig.3.

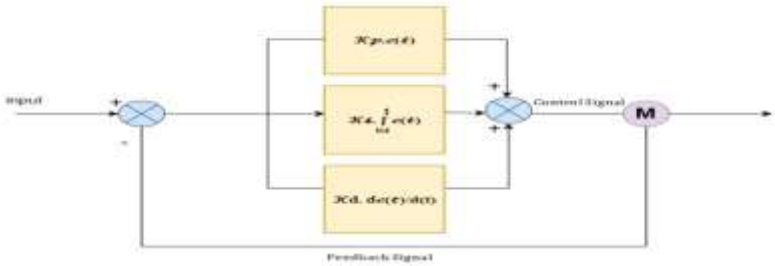

Figure 3. Block diagram of PID controller

Fuzzy Logic Controller

Fuzzy logic(FL) is created using human language. [8,13]. The working logic of the fuzzy controller is that the output of the controller is obtained by fuzzing both the inputs and the outputs using the associated membership functions. In the FL methodology, a linguistic control strategy is transformed into an automatic control strategy by a fuzzy controller, and FL rules are created using specialist experience or database knowledge [9]. The $e(t)$ (error) and the $ce(t)$ (change of the error) of the angular speed are the variable inputs. The $u(t)$ (control voltage) is the variable output of the fuzzy logic controller.

$$\left.\begin{aligned} e(t) &= r(t) - u(t) \\ ce(t) &= e(t) - e(t-1) \end{aligned}\right\} \qquad (7)$$

Bode Editor and Root Locus Techniques

To demonstrate the frequency response of the system, the frequency versus the time-invariant system of a transfer function graph can be given which is defined as the Bode diagram of the system. The main idea of a frequency-based system is to use Bode diagrams(editor) to understand and predict open-loop transfer functions and closed-loop responses and compare these functions. In this context, it is very vital to solve the axis language and the effect of graphs on dynamic behavior. [14]. A Bode editor is an interactive graphical method of modifying a compensator to achieve a specific open-loop response (loop shaping). In the Bode editor, the open-loop bandwidth and design can be adjusted according to the gain and phase margin specifications. In this study, the compensator gain value has been changed using the bode diagram and improved system response.

3. SYSTEM BLOCK DIAGRAM AND RESULTS OF THE SIMULATIONS

System Model Using PID Controller

In this section, the PID model is explained. A PID controller has been added to the system for SWDC motor speed control and the system output speed has been observed as a result of the simulation. PID parameters (P, I, D) have been determined using MATLAB's tune technique.

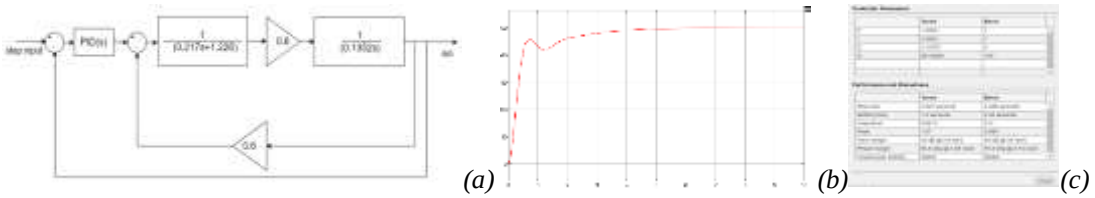

(a) (b) (c)

Figure 4. Series DC motor speed control using PID Controller(a) Step Response(b) Performance value table for the System using PID Controller (c)

The closed-loop control system is given in Figure 4(a). In this closed-loop, PID parameters is found using the MATLAB Tune technique are given in Figure 4(b),(c).

The simulation result of the response of the system to the step input is shown in Figure 4(b). In this system using PID control, an overshoot has occurred as seen in Figure 4(b) but the system soon settled down. The performance values of the graph in Figure 4(b), which is the system response, can be seen in the table in Figure 4(c).

System Model Using Fuzzy Logic - PID Controller

The reaction of the system using only the PID controller is shown in Fig.5. In this section, a Fuzzy Logic controller is added to a system using a PID controller to improve system response. The model of this system generated in Matlab Simulink is shown in Figure 5(a). In this system, PID parameters are set using Fuzzy logic. The PID controller block diagram of the system is indicated in Figure 5(b).

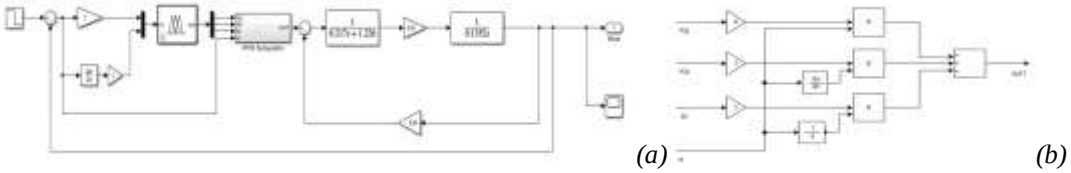

(a) (b)

Figure 5. Fuzzy and PID Controller block diagram(a) Fuzzy PID (FPID) Controller Subsystem(b) The following parameters are used for the system generated in Figure 5(a, b)

Table 2. The rules in the PID controller for Kp, Ki, Kd

e\ce	NL	NS	ZE	PS	PL
NL	PVL	PVL	PVL	PVL	PVL
NS	PML	PML	PML	PL	PVL
ZE	PVS	PVS	PS	PMS	PMS
PS	PML	PML	PML	PL	PVL
PL	PVL	PVL	PVL	PVL	PVL

e\ce	NL	NS	ZE	PS	PL
NL	PM	PM	PM	PM	PM
NS	PMS	PMS	PMS	PMS	PMS
ZE	PS	PS	PVS	PS	PS
PS	PMS	PMS	PMS	PMS	PMS
PL	PM	PM	PM	PM	PM

e\ce	NL	NS	ZE	PS	PL
NL	PVS	PMS	PM	PL	PVL
NS	PMS	PML	PL	PVL	PVL
ZE	PM	PL	PL	PVL	PVL
PS	PML	PVL	PVL	PVL	PVL
PL	PVL	PVL	PVL	PVL	PVL

The inference of Fuzzy consists of two methods. These are Mamdani and Sugano. In this study, the Mamdani method has been used, which can be seen in Figure 6. The control error(e) and the change of the control error(ce) are the inputs of the system which are shown in Figure 6. The setting of the PID controller is based on Fuzzy Logic relationship between the error(e) and error(ce) and the PID parameters. As shown in the figure below, Fuzzy Logic membership functions are set to step by step. The degree of membership of change kp, ki, kd is indicated in detail in Figures 6 and 7. According to the rules in Table 2, when e is equal to 5 and ce is equal to 2.5, kp, ki, kd is presented as follows.

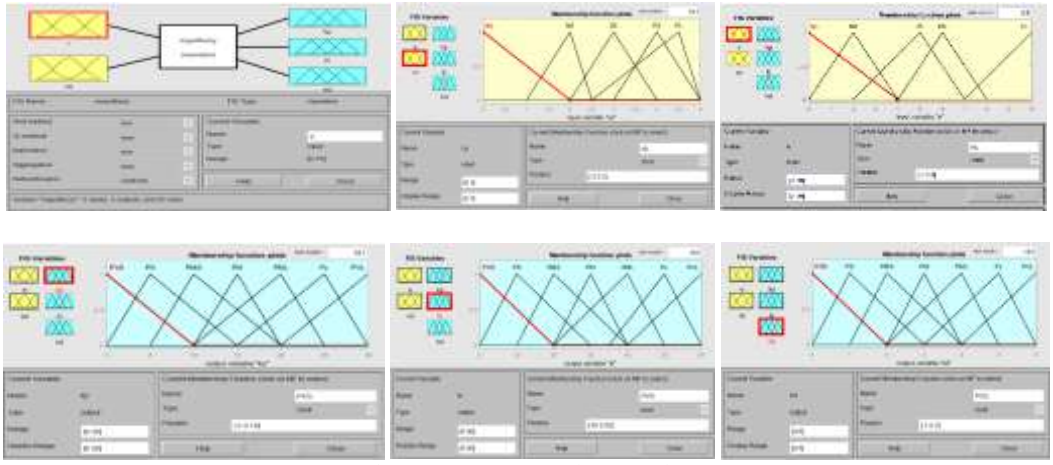

Figure 6. Fuzzy Logic Function

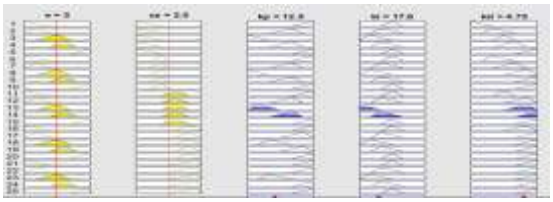

Figure 7. Fuzzy Rule Viewer

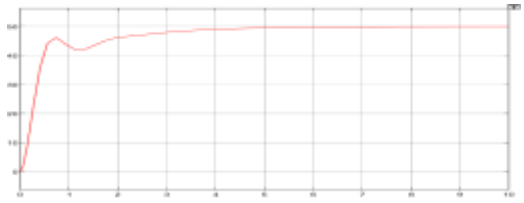

Figure 8. Step Response for the System using FPID

System Model Using PID Controller with Bode Editor Technique

Compensator parameters have been adjusted with the PID tune technique using the control system designer, which is a MATLAB application. The poles and zeros in design diagrams such as bode, which are classical control techniques, are graphically generated. The magnitude response has been dragged up in the Bode Editor to increase the compensator gain to generate a faster response. The used techniques are presented in steps from figures 9-10. The system step response has been improved by using Bode editor techniques. The following steps have been tracked to design the system.

Figure 9: Creating new plot, input-output signals, PID Tuning, and obtaining step response graph.

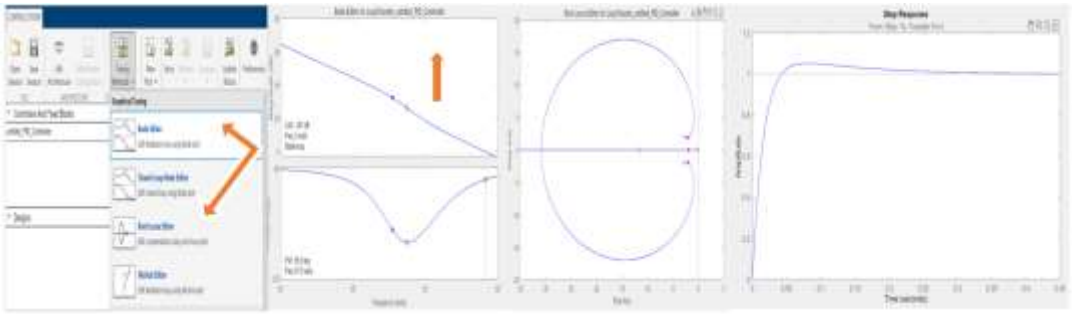

Figure 10: Using Graphical Tuning (Bode- Editor), Bode and Root Locus graph and Step Response.

Size response drags up in Bode Editor, the compensator gain is increased and a faster response is created. Overall, the comparative representation is given in Table 3.

Table 3. Comparison Between the Output Responses

Controller	Rise Time(s)	Settling Time (s)	Overshoot (%)	Peak
PID(using Matlab Tune)	**0,327**	**1,400**	**6,96**	**1,070**
Fuzzy Logic and PID	**1,036**	**0,020**	**0,468**	**1,000**
PID(using Bode Technique)	**0,027**	**0,198**	**5,080**	**1,050**

4. CONCLUSION

This paper discusses the speed control analysis of SWDC motors at the educational level. A commonly used PID controller and different techniques for tuning PID parameters have been implemented in steps. In a system using a PID controller, an over-shoot may occur and if this overshoot damages the system, it would be correct to add Fuzzy Logic to the system. When the system response needs to be faster in speed control made with a PID controller, the response of the system to the parameters set with the PID tune can be accelerated by using the Bode Editor Technique. When the gain is increased with the Bode Editor technique, the system results in a faster response. As a result, we can say that each method can be used successfully in system control with knowledge and experience. We think that this educational study will light the young researchers and engineers who study in this field.

REFERENCES

1. O.I. Okoro, Ph.D., C.U. Ogbuka, B.Eng., M.U. Agu, Ph.D. Simulation of D.C. Machines Transient Behaviors: Teaching and Research. The Pacific Journal of Sci. and Technology, 2008; 9: 142-148.
2. R. K. Munje, P. P. Shinde and S. S. Kale. Performance Comparison of PI/PID Controllers for DC Motor. In: 2014 Annual IEEE India Conference (INDICON); 2014: pp.1-3.
3. I. Liebgott. Integration of the Model Based Design – Industrial Approach – for Teaching Engineering Science. (EDUCON); 10-13 April 2016, pp. 697-701.
4. S. D. Sahputro, F. Fadilah,N. A. Wicaksono,F. Yusivar. Design and Implementation of Adaptive PID Controller for Speed Control of DC Motor. In: IEEE 2017 15th Intl. Conf.2017: pp. 179-183.
5. S. Anatoli, Y. Naung, H. L. Oo, Z. M. Khaing, K. Zaw Ye. The Comparative Analysis of Modelling of Simscape Physical Plant System Design and Armature Controlled System Design of DC Motor. In: IEEE, *EIConRus*; 2017: pp. 998-1002.
6. M. S. Mohiuddin. Comparative study of PID and Fuzzy tuned PID controller for speed control of DC motor. International Journal of Innovations in Engineering and Technology (IJIET); 2: 291-301.
7. D. Somwanshia, M. Bundeleb, G. Kumar, G. Parashard. Comparison of Fuzzy-PID and PID Controller for Speed Control of DC Motor using LabVIEW. In: PerCAA 2019 International Conference on Pervasive Computing Advances and Applications; 2019: pp.252-260.
8. H. Ahmed, Dr. G. Singh, V. Bhardwaj, S. Saurav, S. Agarwal. Controlling of D.C. Motor using Fuzzy Logic Controller. Conf. on Advances in Communication and Cont. Systs; 2013, pp.666-670.
9. I. H. Usoro, U. T. Itaketo, and M. A. Umoren. Control Of a DC Motor Using Fuzzy Logic Control Algorithm. Nigerian Journal of Technology(NIJOTECH) 2017; 36: 594 –602.
10. I. Kandilli. Real-time speed controlling of a DC motor using fuzzy logic controller. Pamukkale University Journal of Engineering Sciences 2017; 23(5): 543-549.
11. N. L. Ismail, K. A. Zakaria, N. S. Moh Nazar. DC motor speed control using fuzzy logic controller. In: AIP Conference Proceedings, 2018,pp. 020026-1-020026-6.
12. A. K. Rajagiri, S. R. MN, S. S. Nawaz,S. Kumar T. Speed Control of DC Motor using Fuzzy Logic Controller by PCI 6221 with MATLAB. In: E3S Web of Conferences; 2019: pp.1-6.
13. F. Kose, K. Kaplan, H. M. Ertunc:STM32F407 Based Speed Control of DC Motor in Real Time with PID and Fuzzy Logic. In: TOK2013,Malatya,Türkiye; 2013: pp.1178-1183.
14. N. F. O. Serteller. Study the Control Analysis Methods on a Direct Current Motor. In: 2020 IEEE 29th Inter. Symposium on Ind. Electronics (ISIE); 2020: pp. 436-439.

N. Messaadi, A. Amroun. Speed Control of DC Motor Using Fuzzy PID Controller. In: Elsevier; 11 August 2021: pp.1-14

RIGA 2023

Design, Performance Testing and Optimization of a Forced Convection Indirect Solar Dryer

Yves Narcisse Droguy
Unités Mixtes de Recherche et d'Innovations Mécanique et Sciences des Matériaux (UMRI 18), Institut National Polytechnique Félix HOUPHOUËT-BOIGNY de Yamoussoukro, BP 1093 Yamoussoukro, Côte d'Ivoire, yves.droguy@inphb.ci , ORCID : 0000-0003-4132-4127

Paul Magloire Ekoun Koffi
Unités Mixtes de Recherche et d'Innovations Mécanique et Sciences des Matériaux (UMRI 18), Institute National Polytechnique Félix HOUPHOUËT-BOIGNY de Yamoussoukro, BP 1093 Yamoussoukro, Côte d'Ivoire, ekoun.koffi@inphb.ci, ORCID: 0000-0001-6164-537X

Amara Sissoko
Unités Mixtes de Recherche et d'Innovations Mécanique et Sciences des Matériaux (UMRI 18), Institute National Polytechnique Félix HOUPHOUËT-BOIGNY de Yamoussoukro, BP 1093 Yamoussoukro, Côte d'Ivoire, amara.sissoko@inphb.ci, ORCID: 0000-0003-2900-4526

Prosper Gbaha
Unités Mixtes de Recherche et d'Innovations Mécanique et Sciences des Matériaux (UMRI 18) , Institute National Polytechnique Félix HOUPHOUËT-BOIGNY de Yamoussoukro, BP 1093 Yamoussoukro, Côte d'Ivoire, prosper.gbaha@inphb.ci, ORCID: 0000-0001-9168-779X

Yaya Soro
Laboratoire des Procédés Industriels de Synthèse, de l'Environnement et des Energies Nouvelles (LAPISEN), Institut National Polytechnique Félix HOUPHOUËT-BOIGNY de Yamoussoukro, BP 1093 Yamoussoukro, Côte d'Ivoire, yaya.soro@inphb.ci

Cite this paper as: *Droguy, YN, Koffi, PME, Sissoko A, Gbaha P, Soro, Y. Design, performance testing and optimization of a forced convection indirect solar dryer. 11. Eur. Conf. Ren. Energy Sys. 18-20 May 2023, Riga, Latvia*

Abstract: A forced convection solar dryer with two air inlets has been developed under three configurations. Three parameters that are the evolution of temperatures, efficiency and global losses have been studied. Thus, the average value of the drying chamber temperature is 40°C for configuration 1, 51°C for conf iguration 2 and 52°C for configuration 3. As for the efficiency, the average is 58% for configuration 1, 47% for configuration 2 and 27% for configuration 3. The losses were evaluated at 103W for configuration 1 and 82W for configurations 2 and 3. Three conclusions emerge from this study. The hot air recovery system for configurations 2 and 3 behaves as a back-up energy that feeds the dryer during a decrease in sunlight. The recovery system decreases the airflow and therefore the efficiency inside the dryer when the lower collector orifice is closed as defined for configuration 3. Closing the lower collector orifice stores heat in the lower part of the collector, which heats up the absorber during a drop in sunlight.
To conclude, configuration 2 is the best configuration without any load.

Keywords: *Flat sensor, efficiency, recovery system;*

1. INTRODUCTION

The drying of agricultural products has been of great importance to humanity since ancient times and is essential for increasing the shelf life of foodstuffs [1,2]. Indeed, a wide variety of products in dried form are used in cooking due to their convenience and permanent availability (e.g. turmeric, peppers, fenugreek leaves, etc.). [1]. This drying is achieved either by using fossil fuels in an artificial mechanical drying process or by using solar energy. The first method is costly and it should be noted that the crisis currently shaking the energy sector in the world and the tension experienced by fossil fuels have made the development of alternative and renewable energies essential [3]. As a result, developing countries have favoured solar drying.

However, the efficiency of outdoor drying processes is low given the many hazards (meteorology, constituents of the product sensitive to ultraviolet radiation, insects, rodents, etc.). To overcome these drawbacks, solar dryers have been designed [3]. These solar dryers are the subject of many works, particularly in Africa and Asia. The objective of these researchers is to optimize dryer technologies in order to obtain better quality drying under adverse metrological conditions. This work is therefore a contribution to the development of solar dryer technologies.

2. MATERIALS AND METHOD

The experimental device is an indirect solar dryer with forced convection designed and manufactured in the workshop of the Mechanical Engineering of the INP-HB. Its innovation lies in having two air intake ports at the flat sensor and a hot air recovery system that can be reassembled at the exit of the drying chamber.

In order to optimize and obtain better quality drying, three (3) different configurations were adopted. The purpose of this study is to determine the best no-load configuration.

Configuration 1

Figure 1. Experimental solar dryer conf.1

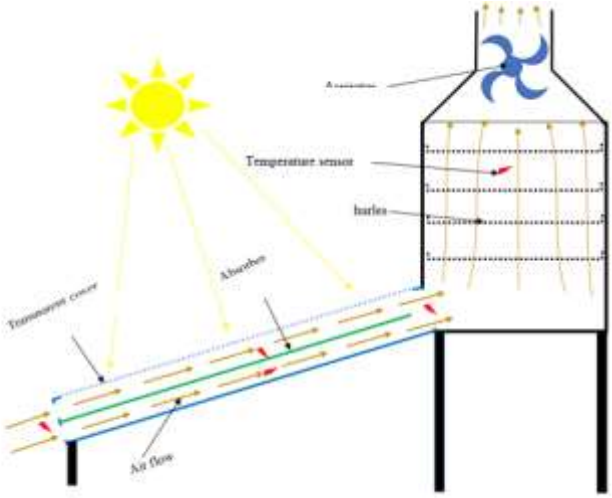

Figure 2. Operating principle conf.1

Figure 3. Inlet ports

The air enters through the two holes of the flat sensor and is heated. This air is then driven inside the drying chamber by the action of a vacuum cleaner that creates forced convection. Finally, the hot air is rejected to the outside.

Configuration 2

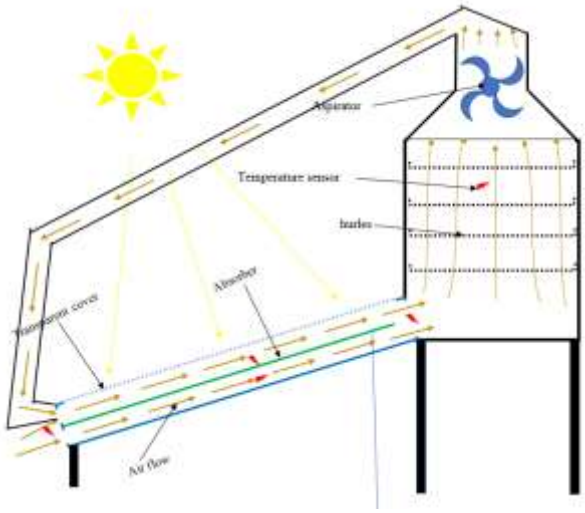

Figure 4. Principle of operation conf. 2

Figure 5. Experimental solar dryer conf.2

The air enters through the two holes of the flat sensor and is heated. This air is then driven inside the drying chamber by the action of a vacuum cleaner that creates forced convection. Finally, the hot air is recovered, dehumidified and rerouted to the upper port of the sensor.

Configuration 3

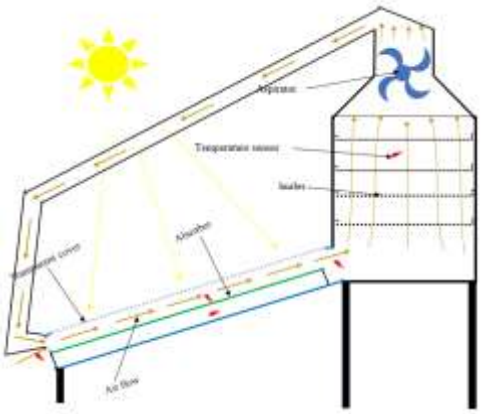

Figure 6. Operating principle conf.3

The air enters through the Upper Hole of the flat panel sensor and is heated. This air is then driven inside the drying chamber by the action of a vacuum cleaner that creates forced convection. Finally, the hot air is recovered, dehumidified and rerouted to the upper sensor port. The lower part of the flat sensor will remain closed on either side.

The dryer was also equipped with five (5) temperature sensors presented as follows:

Table 1. List of temperature sensors

Item No.	Item Description
T_{amb}	Sensor Inlet Temperature (Ambient Temperature)
T_{abs}	Absorber temperature
T_{dow}	Loss temperature
T_{out}	Temperature sensor output
T_{dry}	Temperature drying chamber

Equations

Useful flow transmitted to heat transfer fluid (W) [4]. *(1)*

$$\varphi_u = q_{cf}\left(T_{fs} - T_{fe}\right)$$

q_{cf} : Heat flow rate of heat transfer fluid *(W.°C-1)*
T_{fe} : Temperature of the heat transfer fluid at the inlet of the absorber *(°C)*
T_{fs} : Temperature of the heat transfer fluid at the outlet of the absorber *(°C)*

Yield global instantaneous (%) [4,5].

$$\eta = \frac{\varphi_u}{G^*_{(i,\gamma)} \times S} \quad (2)$$

$G^*_{(i,\gamma)}$: Solar illuminance (flux density) incident on the collector (W.m-2)
S: Flat sensor area (m^2)

Total heat losses [4.5,].

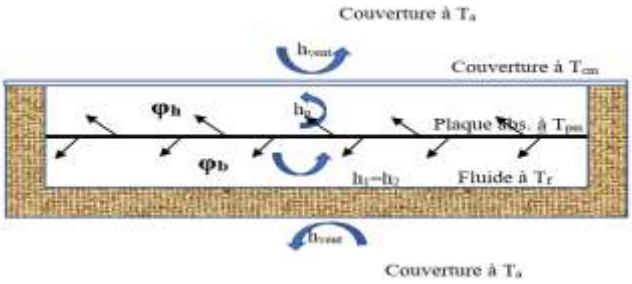

$$\varphi_{pt} = \varphi_h + \varphi_b \quad (3)$$

$$\varphi_p = h_p\left(T_{pm} - T_a\right)S \quad (4)$$

$$h_p = \frac{1}{\frac{1}{h_{c,p-c} + h_{r,p-c}} + \frac{1}{h_{vent} + h_{r,a-c}}} + \frac{1}{\frac{1}{h_{c,p-b} + h_{r,p-b}} + \frac{e_j}{\lambda_i S} + \frac{1}{h_{vent}}} \quad (5)$$

$$N_u = \frac{hl}{\lambda} \quad (6)$$

$$P_r = \frac{v}{a} \quad (7)$$

$$R_e = \frac{Ud}{v} \quad (8)$$

$$N_{u_x} = 0{,}332.R_{e_x}^{1/2}.P_r^{1/3} \quad (9)$$

φ_{pt}: Total heat losses *(W);* φ_h: Upward heat losses *(W);* φ_b: Downward heat losses *(W)*

T_{pm}: Average absorber temperature (°C); T_a: Ambient air temperature (°C);

e_j , λ_i : Thickness and thermal conductivity of the insulation ; h_p : Coefficient of overall convection (W.m-2.°C-1)

N_u : Nusselt number; P_r : Prandtl number; Re: Reynolds number

3. RESULTS AND DISCUSSIONS

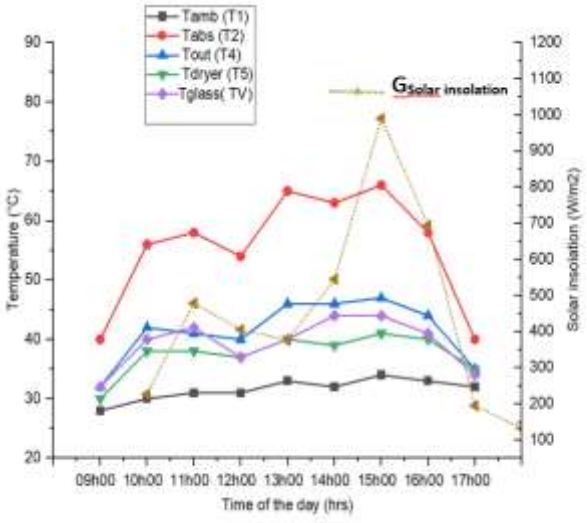

Figure 7. Evolution of dryer temperatures during the day conf.1

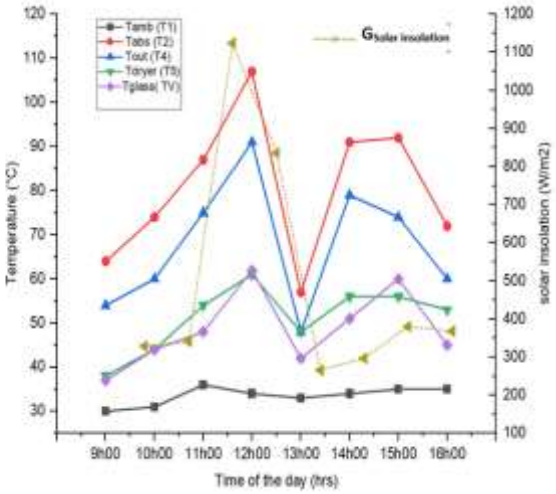

Figure 8. Evolution of dryer temperatures during the day Conf. 2

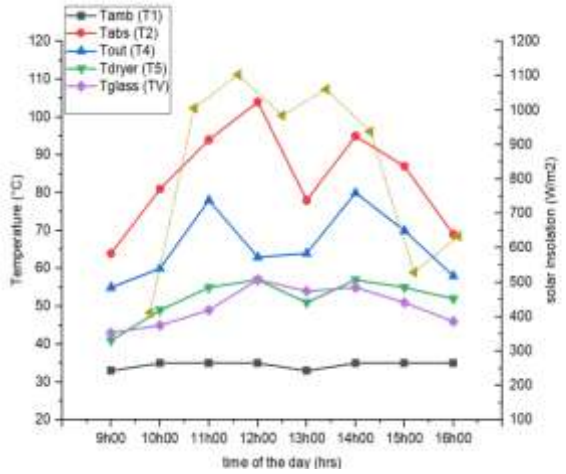

Figure 9. Evolution of dryer temperatures for conf. 3

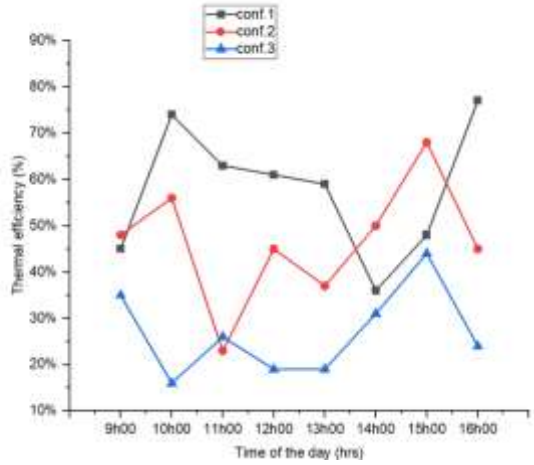

Figure 10. Performance evolution for each configuration

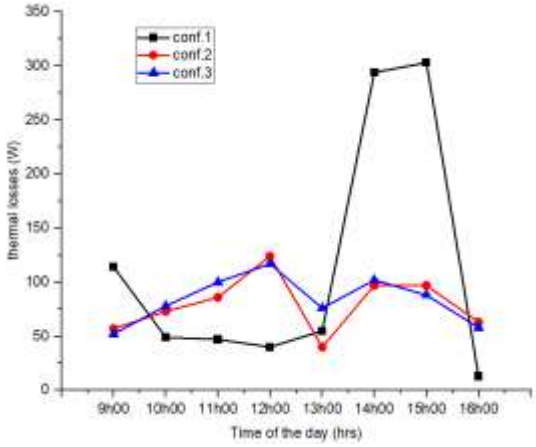

Figure 11. Evolution of losses for each configuration

With an average Sunshine Value of 450 W/m^2, 492 W/m^2 and 833 W/m^2 for configuration 1, 2 and 3, the absorber temperature (T_{abs}) for configuration 1 reaches 55°C (fig.7) , çùçvcconfiguration 2 reaches 80 ° C (fig.8) and that

of configuration 3 is 84 ° C (fig.9). This rise in the temperature of the absorber to the last two configurations is explained by the fact that the air recovery system acts as a backup energy. Thus, the heat coming out of the dryer is no longer lost but reintroduced into the flat sensor.

As regards the temperature inside the drying chamber T_{dry}, it reaches an average value of 40 ° C (fig.7) for conf.1, 51 ° C (fig.8) for conf.2 and 52 ° C (fig.9) for conf.3. This demonstrates that the return of air has a beneficial effect on the drying temperature of the product. Also, note that the temperature of the drying chamber T_{dry} of conf.2 varies abruptly (fig.8) with the sunshine while that of conf.3 is more stable (conf.9). This divergence is due to the fact that at the level of conf.3, the lower part behaves like a heat accumulator which restores it when the sunshine decreases.

As for the yield, it reaches on average for conf.1 58% (fig.10), 47% for conf.2 (fig.10) and 27% for (fig.10) for conf.3. This difference is justified by the fact that the return air reduces the air flow inside the sensor. The efficiency being a function of the air flow (eq.1, eq2), the air conf.2 and conf.3 will therefore have a relatively low efficiency compared to that of configuration 1.

On the other hand, Figure 11 shows the evolution of the sensor's heat losses for each configuration. Thus, for configuration 1, the average loss is 103 W and 82 W for configurations 2 and 3. This low level of loss for the last two configurations shows that the return air reduces heat losses at the sensor.

It should also be noted that these results are similar to the research carried out by *Yunfeng Wang.and al.2019* who also used the secondary heat recovery system for drying mangoes. The latter obtained an average temperature inside the drying chamber of 45 ° C and a yield of 33.4% [6] . Also, *Mortezapour and al.2019* have developed a solar dryer with heat recovery system for drying onions. An average yield of 45% and a drying chamber temperature of 55 ° C were obtained by the latter [7]. What is formed to the values found for configuration 2.

5. CONCLUSION AND OUTLOOK

At the end of the first part of this study, the solar dryer was evaluated empty in three different configurations. It was first found that regarding the temperature of the drying chamber, configurations 2 and 3 give better results thanks to the hot air recovery system that behaves as a make-up energy. Then, for yields, this air recovery system will reduce the air flow, which will result in a drop in the efficiency of configurations 2 and 3. Finally, for heat loss, heat storage in the lower part of the collector will reduce heat loss for configuration 3.

Given its three criteria, configuration 2 is the best for these empty tests. However, there will be a need to increase the fan power in order to increase the airflow inside the sensor for configuration 2. This would increase yield.

The rest of this study will consist in testing this dryer under load under the three configurations.

REFERENCES

[1] Belessiotis V, Delyannis E. Solar drying. *Sol Energy*. 2011;85(8):1665-1691. doi:10.1016/j.solener.2009.10.001
[2] Ertekin C, Firat MZ. A comprehensive review of thin-layer drying models used in agricultural products. *Crit Rev Food Sci Nutr*. 2017;57(4):701-717. doi:10.1080/10408398.2014.910493
[3]Amraoui-Mohammed-Aminepdf.pdf. Accessed January 15, 2023. http://dspace.univ-tlemcen.dz/bitstream/112/1977/1/Amraoui-Mohammed-Aminepdf.pdf
[4] Design and study of a sensor.pdf. Accessed January 15, 2023. https://dspace.univ-adrar.edu.dz/jspui/bitstream/123456789/4803/1/Conception%20et%20%C3%A9tude%20d%E2%80%99un%20capteur.pdf
[5] pfe.gm.0066.pdf. Accessed January 15, 2023. https://beep.ird.fr/collect/thies/index/assoc/HASHb20d.dir/pfe.gm.0066.pdf
[6] Wang Y, Li M, Qiu Y, et al. Performance analysis of a secondary heat recovery solar-assisted heat pump drying system for mango. *Energy Explor Exploit*. 2019;37(4):1377-1387. doi:10.1177/0144598718823937
[7] Mortezapour H, Rashedi SJ, Akhavan HR, Maghsoudi H. Experimental Analysis of a Solar Dryer Equipped with a Novel Heat Recovery System for Onion Drying.

RIGA 2023

Design and Control of Switched Reluctance Motors with Different Stator and Rotor Pole Numbers by Co-simulation: Comparatively Performance Analysis

Bekir Gecer
Atasehir Adiguzel Vocational School, Istanbul, Türkiye, bekirgecer@adiguzel.edu.tr, ORCID: 0000-0002-7803-3844

N. Fusun Oyman Serteller
Marmara University, Istanbul, Türkiye, fserteller@marmara.edu.tr, ORCID: 0000-0003-3147-2740

Alper Nabi Akpolat
Marmara University, Istanbul, Türkiye, alper.nabi@marmara.edu.tr, ORCID: 0000-0002-6972-2509

Cite this paper as: *Gecer, B., Serteller, N.F., Akpolat, A.N. Design and Control of Switched Reluctance Motors with Different Stator and Rotor Pole Numbers by Co-simulation: Comparatively Performance Analysis. 11. Eur. Conf. Ren. Energy Sys. 18-20 May 2023, Riga, Latvia*

Abstract: This study presents the design, control, and performance analysis of Switched Reluctance Motors (SRMs) with, 6/4, 8/6, and 10/8 stator and rotor ratio pole numbers for many applications such as electric vehicles and proportion systems. The whole system design has been implemented in Ansys/Maxwell and MATLAB/Simulink jointly to take advantages of their strong features and to provide more precise information for real-time applications such as e-mobility. To perform this study, Ansys has been utilized for motor design and magnetic analysis, and also MATLAB has been used for the mentioned system's drive and control. Tuning and Fuzzy-PI Tune control methods have been applied to the system for optimal control. Critical parameters pertaining to the system such as efficiency, magnetic flux, magnetic flux density, magnetic materials, current and torque behaviors of the motors have been analyzed individually. Furthermore, motors have been compared with each other about speed and torque ripples. The abstract should be prepared via Times New Roman (Font) and 10 pts, single spaced with 2 cm margins on all sides and align full. The length of Abstract should be between 150 and 200 words. The abstract should be informative by referring study aims, the methodology, the instruments, the major findings and implications of the study.

Keywords: *Switched reluctance motor, design, control, simulation, performance analysis.*

1. INTRODUCTION

Switched Reluctance Motor (SRM) is an electric motor that runs by reluctance torque (SRM) has many inherent advantages such as their simple structure, lack of any coil or permanent magnet on the rotor, on the other hand, high torque ripple can be assumed as prime disadvantage of SRMs due to their double salient pole structure [1]. In the industry, various designs of SRM especially with different numbers of poles such as 4/2, 6/4, 8/6, 10/8, and 12/8 (stator poles numbers/rotor poles numbers) have been launched recently. Magnetic field knowledge is quite essential for the motor design process, as it directly affects the flux and torque characteristics of machines [2]. Torque, speed, magnetic flux, current, and other parameters of the motor depend on the number of stator and rotor poles. The change of the poles numbers effects on the motor performances and characteristics are analysed using engineering software programs such as MATLAB/Simulink and Ansys/Maxwell [3-5]. Especially, the magnetic analysis tools of Ansys are very useful for the studies of the magnetic field [4]. Moreover, the MATLAB simulation program can study SRM control techniques, driver systems, and performance analysis [5]. In [14] a co-simulation method based on Ansys software (Maxwell and Twin Builder) and MATLAB/Simulink for Permanent Magnet Synchronous Motor (PMSM) model is presented. Most of the SRM works in the literature are on torque ripple minimizing e.g. in [6], [7]. Besides torque ripple studies, there are also many SRM applications such as electric

vehicles in industry and academic fields. In [9], active discharge process of SRM's drive has been simulated for electric vehicle application using the MATLAB program. Vector control of high-speed SRM is presented to handle the difficulty of torque controller design for electric vehicles in [10]. Also, there are several studies on the efficiency and core losses of SRM using the improved analytical techniques for optimum motor performance [11], [12]. In [13], which techniques are applied to optimize the geometries and topologies of SRMs to enhance machine performance is discussed.

In this paper, the overview of dynamic behaviours of SRMs is given in section 2. The models of three motors with the same power density/ volume are designed and analysed in section 3. Section 4 presents SRMs driver and control system with the PI Tune and Fuzzy-PI Tune methods in MATLAB, results of the co-simulation systems analysis and discussion of the programs are evaluated comprehensively in 5. The concluding remarks are discussed in section 6.

2. DYNAMIC MODEL OF SRM

The analysis presented in this section is based on the dynamic equivalent circuit mathematical equation of the SRM which is given as follows:

$$v = R_s\, i + e \quad , \; e = \frac{d(\phi)}{dt} = \frac{d(Li)}{dt} \qquad (1)$$

The ω_r $(rad/s)$is mechanical angular velocity. Where $R_s\,(\Omega)$ is stator resistance, i(A) is phase current, $L(H)$ is the phase inductance and $\theta\,(rad)$is the rotor position. The phase voltage is also written in terms of magnetic flux $\lambda(Wb)$.

$$\lambda = L(\theta, i)i \;, \qquad v = R_s i + \frac{d\lambda(\theta,i)}{dt} \qquad (2)$$

The mechanical equations that depend on the rotor position of SRM are written in (3)

$$J\frac{d\omega_r}{dt} = T_e - T_L - b\,\omega_r \qquad (3)$$

Where, J is the inertia moment, b is the friction coefficient, T_e is induced torque, and T_L is the load torque [1].

3. ANSYS MODEL OF SRMs

ANSYS software magnetic and transient analysis has been used to design and improve the motor structure parameters [3, 8]. In this part, models of three motors with the same power density/ volume are designed and analysed in Ansys/RMxprt and Ansys 2D.

Design of SRMs in Ansys 2D

The 6/4, 8/6, and 10/8 types are designed according to motor design parameter values which are given in Table I. They have been optimized considering the high efficiency and the low torque ripples. To obtain close identical values, the steel type of material, stacking factors embraces, yoke thickness, air gap, reference speed values, and power density (power /volume, volume= $\pi\,(\frac{D_{stator\ outer}}{2})^2 L_{axial\ length}$) are taken the same of all motors during the design procedure.

Table 1. Motor design parameters in Ansys

Parameters	6/4 SRM	6/4 SRM	10/8 SRM
Steel Type	M19_24G	M19_24G	M19_24G
Stator Resistance	2.04 Ω	2.04 Ω	0.12 Ω
Aligned Inductance	205e-3 H	205e-3 H	26.2e-3 H
Unaligned Inductance	15e-3 H	15e-3 H	2.8e-3 H

Stator outer diameter	182.31 mm	182.31 mm	194 mm
Stator inner diameter	91.17 mm	91.17 mm	99 mm
Rotor outer diameter	90.17 mm	90.17 mm	98 mm
Rotor inner diameter	40.32 mm	40.32 mm	36.2 mm
Power	570 W	570 W	2200 W
Axial Length	26.9 mm	26.9 mm	92 mm
Power Density Per Volume	0.812 W/cm3	0.812 W/cm3	0.812 W/cm3
Reference Speed	1500 RPM	1500 RPM	1500 RPM

2D transient model structure schemes of the 6/4(3 phases), 8/6(4 phases), and 10/8(5 phases) are given in Fig. 1 respectively.

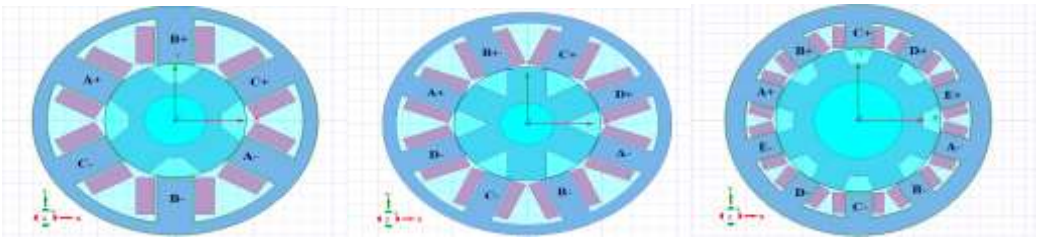

(a) *(b)* *(c)*

Figure 1. a) 6/4 2D Transient Model, b) 8/6 2D Transient Model, c) 10/8 2D Transient Model.

To optimize and obtain the most efficient operation of the SRM parameters, the core materials are primarily discussed and studied. Here, same design and optimization procedures have been realized for 3 types of motors. B-H graph of M19_24G is given in Fig. 6 (d) to detect the magnetic flux density saturation points of the motors.

4. DRIVER and CONTROL SYSTEMS OF SRMs IN MATLAB/Simulink

In literature, the most favoured driver circuit for the SRM is the Asymmetric Bridge Converter (ABC) due to its advantages such as cost and easy to be used in the SRM [3], [11]. ABC has been controlled by the PI Control system. It creates a gate signal according to its input values; position sensor, I(A), and ω_r . Especially, the position sensor information is crucial for learning the inductance profile of SRM.

Driver System of SRM

The 8/6 SRM driver circuit (ABC) and control system model are seen in Fig. 2 and Fig. 3 respectively. In Fig. 2, switching circuit of SRM is created with developed semiconductors such as MOSFETs and diodes. Here, switching frequencies are very important as they affect the motor behaviour. In Fig. 3, the model has four main blocks: SRM, converter, position sensor, and controller. The controller block with its user-friendly features is the advantage of MATLAB over ANSYS.

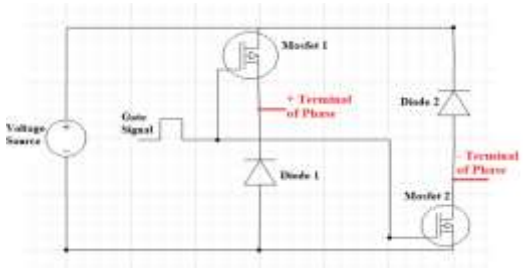

Figure 2. 8/6 SRM Driver for per phase (ABC).

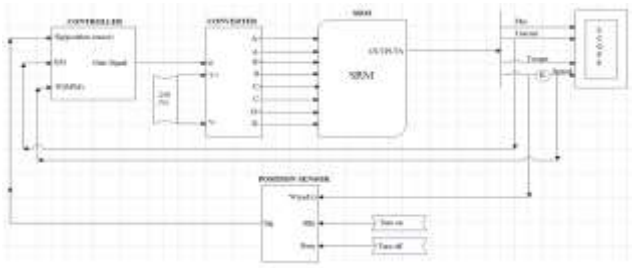

Figure 3. Control System Model of 8/6 SRM in Simulink

The inputs of phase windings of the motor are controlled by MATLAB/Simulink and output parameters such as flux, torque and speed are transmitted to Simulink to observe the behaviour of operation parameters.

Control System of SRM

PI controllers are preferred to control SRM because of its fast and easy applicability. The PI Tuning and Fuzzy-Tuned PI methods have been applied. Optimal PI gains are seen in Table IV, and the speed performances of SRMs are shown in Fig. 8. The gains have been obtained by the Fuzzy-Tuned PI method to find optimum values for the control of SRMs in MATLAB. SRMs operate at full loads which are transferred from Ansys. The operation load values are 2.75 Nm for 6/4, 13.6 Nm for 8/6, and 3.22 Nm for 10/8. To ensure used optimal PI coefficients, they are automatically adjusted online according to the error and its change of rate of speed in the transient period. It is the Fuzzy-Tuned PI method and its Simulink model is seen in Fig. 4. Membership functions and rules of Fuzzy Logic have been found as a result of experiences based on analysis.

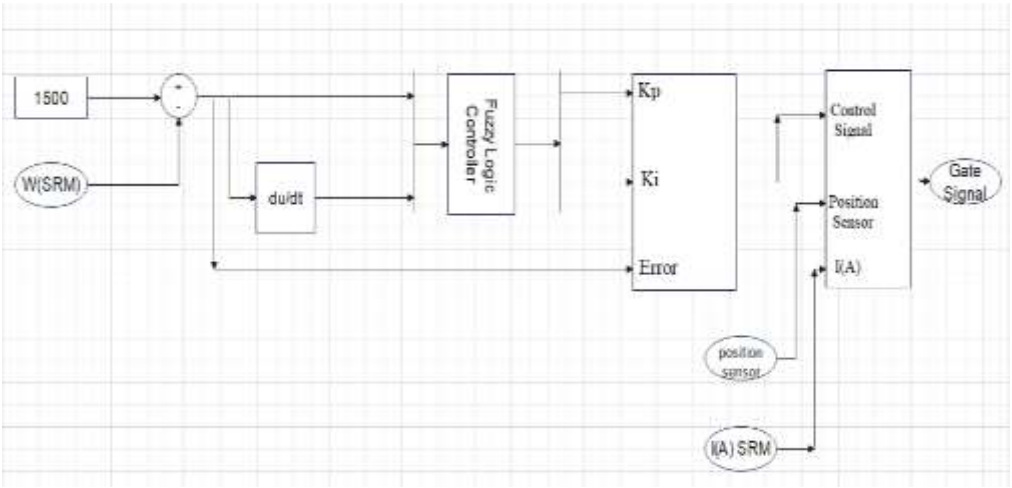

Figure 4. Fuzzy-Tuned PI Model.

The characteristics of both types of controllers are obtained from graphs and their values are given in Table II.

Table 2. Time response characteristics of PI Tuning and Fuzzy Tuned PI for 8/6

Type of Controller	PI Tuning	FUZZY-PI
Rise Time	0.0015	0.0010
Steady-state error(rpm)	12	4
Settling Time	0.17	0.12
Oscillations	More	Less

5. ANALYSIS RESULTS OF ANSYS AND MATLAB/SIMULINK

SRM Ansys designs and control circuit of MATLAB have been assembled to see the results of the co-simulated system. Variations of inductance (L) depending on current (i) and position (θ) are given in Fig. 5 for all SRMs. The color bar is about electrical degree with 0-720 gap. The magnetic flux density distributions of three motors are presented in Fig. 6 (a), (b), and (c) which are performed in the ANSYS. The torque performances of SRMs are compared to average torque and torque ripple in Fig. 7 and Table III respectively. The speed performance comparisons are presented in Fig. 8.

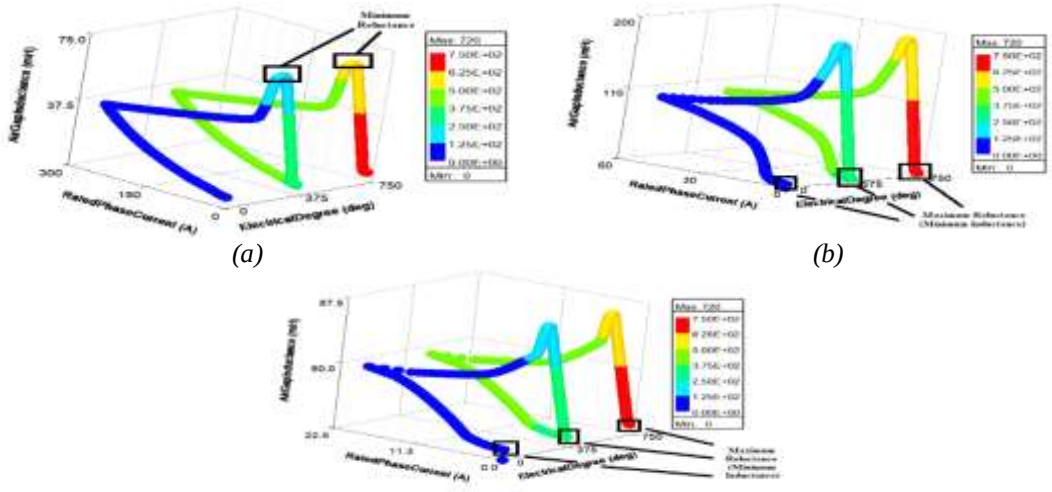

(a) *(b)*

(c)

Figure 5. (a) Inductance value of 6/4, (b) 8/6, and (c) 10/8 related phase current and electrical degree.

The energized phase poles are seen in green or close to green whereas non-energized is blue on the magnetic flux density distribution in Fig. 6. The maximum magnetic flux density value of 8/6 is higher than 6/4 and 10/8, with 1.54 T. It is as it should be because the magnetic flux is proportional to the current and has the highest current value of 8/6. Their flux distributions are seen in Fig. 6 (a), (b), and (c).

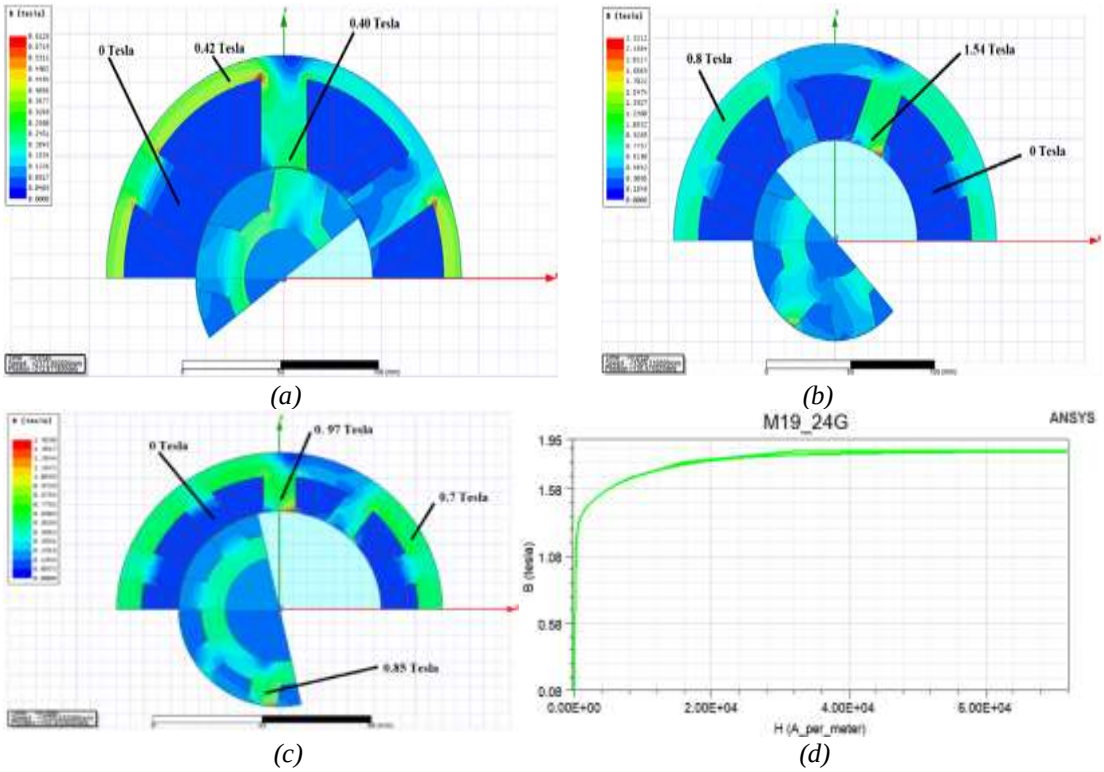

(a) *(b)*

(c) *(d)*

Figure 6. (a)Magnetic Flux Density Distribution (B) of 6/4, (b) 8/6, (c) 10/8, (d) B-H Characteristic of M19_24G.

The 8/6 has a maximum average torque value in SRMs according to Table III because of its high-power value. The torque performances of the 6/4, 8/6, and 10/8 are seen in Fig. 7. While 6/4 has maximum torque ripples with 50%, 8/6 has a minimum value of 16.6%. The torque ripple percentage formula can be given as follows:

$$T_{ripples} = \frac{T_{max} - T_{avg}}{T_{max}} \times 100 \qquad (6)$$

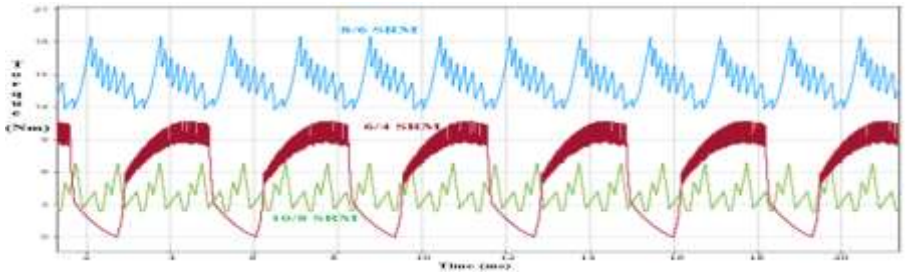

Figure 7. Comparison Torque Results of 6/4, 8/6, and 10/8 SRM in MATLAB/Simulink

Table 3. Comparison of SRMs

SRMs	Average Torque of Matlab	Volume (cm^3)	Efficiencies of Ansys	Maximum Flux Density	Torque Ripples (%)	Total Weight (kg)
6/4	4.7 Nm	701.77	83.36 %	0.42 T	50	4.39 kg
8/6	15 Nm	2662.3	86.21 %	1.54 T	16.6	18.49
10/8	4.5 Nm	734	84.52 %	0.97 T	27.42	21.51

The analysis results of Ansys and MATLAB are like in Table III. According to PI control gains, seen in Table IV, speed performances of SRMs are illustrated in Fig. 8. The 8/6 reaches the reference speed value the fastest, while the steady-state error is smallest in 10/8. The gains are obtained by the PI Tuning method. The motors, which are transferred their data from ANSYS, operate at their nominal loads. The load values are 2.75 Nm for 6/4, 13.6 Nm for 8/6, and 3.22 Nm for 10/8. The optimal results are obtained in 8/6 for the torque performance, efficiency, and torque ripples.

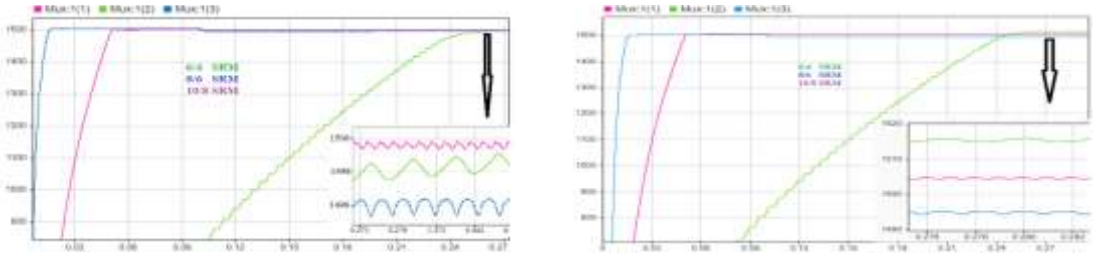

(a) *(b)*

Figure 8. Comparison Speed Results of 6/4, 8/6, and 10/8 SRM in MATLAB/Simulink: (a) Fuzzy-PI, (b) PI Tuning.

Table IV. PI Tuning control coefficients

SRMs	Proportional(P)	(I)Integral
6/4	1.18	0.28
8/6	1.2	0.08
10/8	1.04	0.04

The 8/6 has maximum flux density and 6/4 has maximum torque ripple. 10/8 performed closest to the reference speed.

6. CONCLUSION

In this paper, design, control, and performance analysis of SRMs over the examples of 6/4, 8/6, and 10/8 are comprehensively studied. Ansys/Maxwell and MATLAB/Simulink software programs are run together to have more powerful analyses and to present more detailed information for real-time applications. The SRMs are designed with the same power density in Ansys while their controls are performed in MATLAB. SRM models and control circuits are integrated for co-simulated system. Co-simulation is performed to analysis the motor operation performances for all states, from transient to steady state in detail. PI Tuning and Fuzzy-Tuned PI methods are applied to realize the optimal controls. Additionally, the motors are compared to each other in magnetic flux density distribution, efficiency, speed, and torque ripple. Using the co-simulation model, the optimal performance characteristic is achieved in the 8/6 with Fuzzy-Tuned PI methods. For future works, the structure design and control system of SRM can be updated.

REFERENCES

[1]- Miller, T. J., Switched Reluctance Motors and Their Control. Oxford: Hillsboro, OH, 1993.
[2]- Krishnan R., Switched reluctance motor drives: modelling, simulation, analysis, design, and applications. CRC Press, Boca Raton, p 432, 2001.
[3]- Gecer, B., Serteller, N.F., Investigation of Effect of Pole Number Change on Operating Parameters in Switched Reluctance Motors, MSc Thesis of Marmara University Electrical and Electronic Engineering, Istanbul, Türkiye, 2019.
[4]- Gecer, B., Serteller, N.F., Understanding Switched Reluctance Motor Analysis Using Ansys/Maxwell, In: IEEE International Symposium on Industrial Electronics (ISIE), 2020.
[5]- Anyalebechi, A.E., Simulation of Speed Control Techniques of Switched Reluctance Motors (SRM), In: International Research Journal of Engineering and Technology (IRJET), 2018.
[6]- Naein, V., A detailed magnetic equivalent circuit modelling for torque ripples minimizing of a switched reluctance motor, International Transaction on the electrical energy system, 220, Vol.30, Issue 1, pp.1-14.
[7]- Hui C., Hui W., Mengqiu L., Torque Ripple Reduction for Switched Reluctance Motor with Optimized PWM Control Strategy, College of Electrical and Information Engineering, Hunan University, Changsha 410082, China, 20 November 2018.
[8]- Gecer, B., Serteller, N.F., Understanding a Switched Reluctance Motor Control and Analysis Methods Using MATLAB/Simulink, In: IEEE World Conference on Engineering Education, Guatemala, 2021, Doi: 10.1109/edunine51952.2021.9429155.
[9]- Deepak, G., Das, C., Active Discharge of Dc Link Capacitor in SRM Drive for Electric Vehicle Application, International Journal of Engineering Applied Sciences and Technology (IJEAST), 2020, Vol.5, Issue 3, pp.568-571.
[10]- Aiso, K., Takahashi, M., "Study of High-Speed SRM Using Vector Control for Electric Vehicle", In: 10^{th} International Conference on Power Electronics- ECCE Asia, 2019.
[11]- Afjei, E., Siadatan, A., Construction Of A Low-Cost Asymmetric Bridge Converter For switched Reluctance Motor Drive, In: Iranian Conference on Electrical Engineering (ICEE), 2013, DOI: 10.1109/IranianCEE.2013.6599797.
[12]- Parsapour, A., Moallem, M., Predicting core losses and efficiency of SRM in the continuous current mode of operation using the improved analytical technique, In: Journal of Magnetism and Magnetic Materials, 2015, Vol. 378, pp. 118-127.
[13]- Sahin, F., Ertan, H. B., Optimum Geometry for Torque Ripple Minimization of Switched Reluctance Motors, IEEE Transactions on Energy Conversion, 2020, vol. 15, no. 1.
[14]- Mersha, T., Changqing D., Co-Simulation and Modelling of PMSM Based on Ansys Software and Simulink for EVs, World Electric Vehicle Journal, 2022.

RIGA 2023

Activation to Elasticity in Electricity and Heat Consumption

Merja Mäkelä
South-Eastern Finland University of Applied Sc., Kotka, Finland, merja.makela@xamk.fi, ORCID:0000-0002-6464-1902

Turo Laine
South-Eastern Finland University of Applied Sc., Kotka, Finland, turo.laine@xamk.fi, ORCID: 0000-0002-4373-8844

Paulus Kiviranta
South-Eastern Finland University of Applied Sc., Kotka, Finland, paulus.kiviranta@xamk.fi, ORCID: 0000-0002-9485-6971

Erja Tuliniemi
South-Eastern Finland University of Applied Sc., Kotka, Finland, erja.tuliniemi@xamk.fi, ORCID: 0000-0002-6324-5481

Cite this paper as: *Mäkelä, M., Laine, T., Kiviranta, P., Tuliniemi, E. Activation to elasticity in electricity and heat consumption. 11. Eur. Conf. Ren. Energy Sys. 18-20 May 2023, Riga, Latvia*

Abstract: Consumption elasticity implies saving energy during high consumption peaks. Principally, total energy consumption could be reduced during the high peaks and thus less energy capacity would be needed. If the high energy consumption peaks could be avoided, this would lead permanently to less energy capacity needs. The high consumption peaks could also be covered using special pre-planned energy reserves but energy savings would not be achieved. In this article the elasticity in electricity consumption, as well as in heat consumption, is discussed. It is possible to get energy savings from different sources. Since 2021 in Finland possible electricity communities are expected to increase savings, and their feasibility is analyzed in this article. Also, the optimizing of electrical and thermal loads using smart control technology decreases consumption. Some results of case studies in district heating communities are given. The awareness of consumers using online monitoring of their electricity and heat consumption helps to save energy, and practical examples are presented. In 2022, less electricity was used in Finland, although the industrial and business activities were high.

Keywords: *Community, consumption, elasticity, electricity, heat*

Nomenclature	
CHP	Combined Heat and Power
DSO	Distribution Supplier Organization
IEA	International Energy Agency
PHEV	Plug-in Hybrid Electric Vehicle
PV	Photo-Voltaic
TSO	Transmission System Operator
VPP	Virtual Power Plant

1. INTRODUCTION

Energy production and consumption are today market-driven in many countries. Due to the continuous global warming of climate, changes in energy-related political decision-making and people's minds are needed. The use of energy is expected to increase. According to IEA scenarios a green transition from fossil sources to renewable ones will accelerate [1]. Natural resources and readiness to commission renewable sources vary from country to country. Recent political changes in Eastern Europe imply new energy source arrangements in most European countries. Some ways to ease this too slow green transition are the promotion of distributed, small-scale production and the increase of energy consumption elasticity. The consumption elasticity mostly stands for transferring the energy usage from high consumption peaks to low consumption periods.

People are encouraged to consumption elasticity both in homes and in energy communities. According to Finnish laws it has been possible to establish energy communities since 2021 [2]. Virtual energy communities work for the sharing of their participants' energy resources in a sustainable way. By making investments in common, it is possible to get some economic advantages, as well. These virtual energy communities may have power and heat production, and storage capacity, and they are participating in the consumption elasticity by optimizing their loads in a profitable way. The energy communities may have virtual power plants (VPP) which are digital platforms. The VPPs are aiming at the controlling of energy consumption, especially in different kinds of residential, public and business properties.

2. ACTIVATION TO ELECTRICITY CONSUMPTION ELASTICITY

Generally, power transmission is regarded as a monopoly business. High voltage networks of Transmission System Operators (TSO) deliver electricity from centralized, large-scale power production to the networks of Distribution Supplier Organizations (DSO) and directly to large consumers. Finland has one TSO called Fingrid. The DSOs transfer electricity further to low voltage networks where small consumers are connected. Distributed, weather-dependent renewable power production to low voltage networks increases from wind turbines and solar photo-voltaic (PV) systems. More elasticity is needed in the management of networks, and in the consumption behavior.

In their energy usage consumers are encouraged to participate in market-based consumption elasticity. In principle there are three different mechanisms for consumption elasticity to choose:

- The power consumption is reduced in high consumption periods, and missing production will not be compensated. Consumers are asked for energy savings.
- The power consumption of high consumption peaks is changed over to lower consumption periods. This mechanism is often desired.
- In very high consumption peaks different kinds of reserves are commissioned in order to cover needed energy consumption. TSOs have reserve mechanisms.

A virtual electricity community stands for a body that produces, delivers, aggregates and stores energy, or offers energy efficiency services and recharging services of vehicles to its shareholders. Instead of getting pure financial profits, the virtual electricity communities are aiming at economic, environmental and social benefits for their shareholders. The virtual electricity communities utilize local low and medium voltage networks of DSOs, and high voltage transmission lines. Local energy communities can operate inside single properties or be extended outside properties using separate connection lines, while distributed energy communities are geographically distributed.

Local electricity community inside a property

An electricity community inside a property consists of power consumers located in the same property or property group. The costs and profits of solar PV systems, for example, are shared by the community participants, and in a longer term, electricity costs can be reduced. There is no taxation for the consumed electricity which has been produced by the community itself. The Finnish Electricity Market Act 4§ states that a microgrid can be built inside a property or property group without a permission from Finnish Energy Authority [2]. The energy community inside a property can utilize two cost distribution methods: compensation calculation or post-measuring [3]. The ownership of buildings determines if an energy community can operate inside a single property line. The property group is not defined in the Electricity Market Act but based on the inquiry made by a local energy company, Finnish Energy Authority stated that a property group can only be established between the buildings with a same owner [4].

The investment costs of large PV systems are shared by the community participants, for example based on their housing area. In a compensation calculation, the electricity production from the PV system is distributed to the participants based on their share of the investment. There is no taxation for the consumed electricity which has been produced by the community itself if the yearly production amount is less than 800 000 kWh [5]. The compensation calculation is a good option for completed buildings because it utilizes the existing electricity meters of properties.

In a post-measuring method, the consumption of every participant is measured with a separate electricity meter. With the utilization of accurate measuring of electricity consumption and production inside the community, there is no need to divide the solar PV system into segments. This increases the flexibility between participants and helps further investments such as electric vehicle recharging facilities. The post-measuring model needs an operator to control the electricity usage and the property will be operated using a single electricity contract. This method implies that participants cannot manage and bid their own contracts. The post-measuring method suits best to novel buildings [3].

Electricity communities of several properties

An electricity community extending outside a property has electricity consumption and production in separated, neighboring properties. This community network is connected to the low and medium voltage networks over one single connection point. This community model is feasible in villages where solar PV power production could take place on one neighbor's field, and the participating neighbors would share the costs and production. Neighboring properties with different owners have been able to share a large solar PV system in Finland since 1.8.2021. Larger solar PV systems utilized by many participants decrease investment costs for single consumers compared to their own small systems. In this energy community model, the production plant must be divided into smaller segments. Thus, the solution is limited in terms of flexibility between the consumers.

A geographically distributed electricity community comprises a bigger unit of power consumers and producers which are in any location in Finland. Distributed communities aim at utilizing own power production as effectively as possible. Those communities utilize low, medium and high voltage networks, and thus pay taxes, and pay for power transmission. The distributed energy communities virtually utilize self-produced electricity from different locations. The production that cannot be consumed on own property is sold to the grid and some other participant of the community can utilize that overproduction for own consumption. This kind of community working is profitable if buying from the national grid is more expensive than selling to the grid. Co-operation with local DSOs is needed.

Smart measurement and control technology

Since about 30 years electricity retailers have guided consumers to rough consumption elasticity by offering inexpensive night tariffs in low-peak electricity consumption periods. It has been common to heat floors and warm water boilers, for example, using this inexpensive, time-dependent tariff. These night tariffs have been fixed agreements, adapting night tariff charging, for example from 22 to 7. In old houses the heating control of floors and boilers have been implemented using simple hard-wired technology. The floors and boilers are heated at night when needed, and room radiators are switched off when sauna heating is switched on.

Electric residential and office heating, as well as the heating of warm water boilers, are regarded as potential objects for electricity consumption elasticity. It is estimated that there is a large, about 1000-1800 MW heating load, in the electric heating of Finnish residential houses and warm water boilers [6]. The national TSO would like to give up the stiff, time-dependent day and night tariff arrangements organized by DSOs. Due to green transition, there is pressure to come over to more market-based heating optimization than before. The electricity market prices should affect the heating control. Thus, advanced heating control optimization methods are called for.

In Finland the first-generation smart electricity meters were commissioned mostly in 2008-2013 by DSOs, and the coverage is almost 100 % [7]. These first meters have allowed the remote monitoring of electricity consumption data by DSOs and retailers in order to charge up-to-date. The meters have been able to compute incoming and outgoing electricity. The consumers are able to get information online. Unfortunately, the life-cycle of this first-generation metering technology has been only about 15 years. The first meters should be replaced in coming years 2022-2028 mainly due to the commissioning of 15-minute imbalance settlement time. The next generation meters are expected to fulfil also other requirements such as load control [8]. Besides electricity metering, these smart meters should have control capacity to optimize the heating load of homes and offices. Some Finnish DSOs have already announced coming next generation metering [8].

Role of private consumers in electricity elasticity

Private consumers are encouraged to electricity savings and load optimization. DSOs offer their customers online services with monitoring the consumption of electricity. The hourly consumption of electricity in a home is presented as trend curves (Fig. 1). The total electricity consumption has been 22 kWh during one day. A high consumption peak at night appears as PHEV recharging, while another peak in the evening stands for Saturday sauna heating.

Figure 1. Authentic view of electricity consumption in a home on Saturday, Aug. 20th, 2022 (blue: hourly electricity consumption, green: outside temperature, black: previous day).

Principally, the control logic for optimizing electricity consumption load can be either in DSOs' smart electricity meters or in consumers' own devices. Smart vehicle recharging units can be programmed to work for less busy times. The recharging periods could be chosen based on market prices in the future. With increasing rechargeable electric vehicles, batteries of vehicles could serve as short-term electricity storages in the future. These vehicle battery storages, or other local battery storages could be used to cover occasional high consumption peaks. The incentives of private consumers to electricity consumption elasticity are needed. It is suggested that DSOs could, for example, give reduction to basic electricity fees if consumers offer some elasticity from their properties to network needs. This kind of a working principle would be easy for customers but requires new business behaviour and services from DSOs.

3. ACTIVATION TO HEAT CONSUMPTION ELASTICITY

In Finland, 25 % of final energy consumption is used for space heating, while industries need 48 %, transport and others 27 % [9]. District heating is widely used for space heating in Northern and Eastern Europe. These effective production facilities are called Combined Heat and Power (CHP) plants, and their total efficiency lies in 80-85 %. Two thirds of district heating come from CHPs and one third comes from separate heating plants. District heating as a heating method covers 46 % of residential, commercial and public buildings in Finland. In 2019, the CHPs for district heating and electricity used 41 % renewable fuels and 10 % heat recovery and heat pump sources [10]. Unfortunately, 49 % of CHP fuels were fossil. There is plenty of potential in the development of district heating. More waste heat of industries and data centres can be utilized. Surplus PV and wind power can be utilized in district heating networks. The use of different kinds of heat recovery and heat pump systems can be increased. Both short-term and long-term heat storage capacities can be developed. Sector coupling in district heating networks is increasing. The heat consumption elasticity of participants in district heating networks could be strengthened.

Industrial power and heat communities

Since a long time, heat and electricity production and consumption have been optimized in pulp and paper industries, and this development work is still going on. Recovery boilers are needed as a part of recovery processes of cooking chemicals. Black liquor, a waste mixture of cooking chemicals and remaining wood components without fibres, is combusted in the recovery boilers producing heat and electricity. Also, renewable bark, sludges and product wastes are combusted in pulp mills. The produced heat as steam is used in evaporation stations belonging to the chemical recovery, in pulp drying and some other fibre line processes. If there are paper or board machine lines in the same mills, heat is also needed in web drying sections. The produced steam is mostly used as low pressure components of 10-12 bar and 3-5 bar, for example. The steam turbines of modern pulp mills produce the needed electricity in the mills. In many pulp and paper mill communities the mills provide also local residential buildings with district heating].

Heat elasticity methods in apartment house communities

The attitudes and awareness of district heating consumers towards heat consumption elasticity in apartment house communities were studied based on an inquiry in South-Eastern Finland, in 2021-2022. Based on the 148 inquiry responses, over 90 % of consumers generally pay attention to their heat consumption significantly, while the heat consumption elasticity is not a very well identified concept among consumers. The heat consumption elasticity mostly refers to the optimization of heat consumption. Momentary high heat consumption peaks should be avoided or transferred to low consumption periods. Almost all consumers would accept optimizing control actions in heating systems if they would take place automatically, and if the consumers would get financial profits.

The inquiry concerning heat consumption elasticity was followed by a pilot project using automatic control technology in the adaptation of heat consumption. In an apartment house pilot, the heating of apartments was chosen as a control object for heat consumption elasticity. The temperature of the incoming water to apartment heating circulations was reduced during the high total heat consumption peaks of the community. There was also a control action to decrease the temperature slightly at night. The high total heat consumption peaks in the apartment house community come mostly from plentiful warm water usage in showers and household activities mornings and evenings. The control actions in the apartment heating water circulations didn't influence on the household warm water flow or temperature. The pilot project was carried out together with a local energy company, a local apartment house company and a technology provider company using smart control technology [12].

Heat elasticity in private homes

The heating of spaces and warm water boilers needs plenty of energy. The warm water boilers equipped with solar thermal systems help to reduce the electricity consumption needed for warm water heating. The heating takes place at the daytime when warm water is also needed. The solar thermal systems also work as short-term heat accumulators. Solar thermal systems are provided with digital control systems to maximize their heat transfer according to conditions.

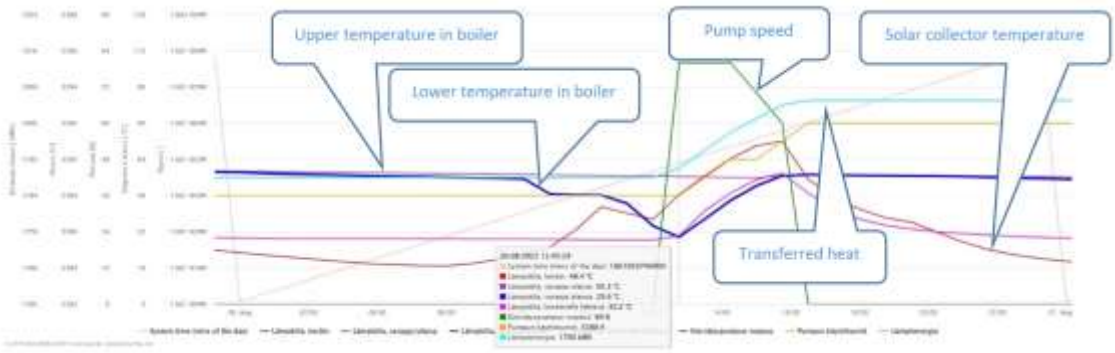

Figure 2. Authentic trend curves of heat transfer from a solar thermal collector to a warm water boiler in a home on Saturday, Aug. 20th, 2022 (red: upper temperature in boiler, blue: lower temperature in boiler, orange red: solar collector temperature, magenta: circulation fluid temperature before collector, turquoise: cumulative heat energy in kWh, green: pump speed).

The heat transfer of solar thermal systems can be monitored in online services of suppliers. The status of a solar heating system is presented as trend curves (Fig. 2). The pumped circulation fluid transfers heat from the solar collector to the lower part of the warm water boiler. In the case of August, 20th, 2022, the solar heating increased the enthalpy of the boiler water 4,5 kWh taking the temperature of the water to its setpoint 62 °C, and no electric heating was needed.

4. CONCLUSIONS

More renewable, emission-free energy and consumption elasticity are needed to avoid very high energy prices. Already in the fall 2021 exceptional high electricity prices were faced in the Nordic electricity market. Finland has not been self-sufficient with electricity during the last decennials. Now wind energy capacity has been increasing significantly. One novel nuclear reactor is expected to start in full production in February 2023.

District heating is a widely used, efficient heating method of residential, commercial and public buildings. Two thirds of district heating in Finland come from CHP production sources. Both renewable fuels, like black liquor and other wood-based materials, and fossil fuels, such as oil and some natural gas, are used. There are interests in small modular nuclear reactors for district heating.

Private people and companies are encouraged to more energy savings and consumption elasticity with electricity and heat communities. This requires some new technology, new generation electricity meters and control systems for optimizing electricity and heating loads, but it also gives additional business opportunities. The significantly rising energy prices increase the awareness and needs of electricity and heat consumption elasticity but the incentives should become more visible to energy consumers. Finland has been able to reduce the electricity consumption in 2022.

References

[1] Outlook for enegy demand, World Energy Outlook 2022, IEA. Available 22.1.2023 in: https://www.iea.org/reports/world-energy-outlook-2022/outlook-for-energy-demand.
[2] Sähkömarkkinalaki (Electricity Market Act) 9.8.2013/588. Modification decree 15.7.2021/730.
[3] Auvinen, K., Honkapuro, S., Ruggiero, S., Juntunen, J. Aurinkosähköä taloyhtiön asukkaille – Mittaushaasteista kohti digitaalisia energiayhteisöpalveluja (Solar power to property inhabitants – From measurement challenges to digital energy community services). Unigrafia Oy, Helsinki, 2020. Series Trade and Economy 3/2020 of Aalto University. ISBN: 978-952-60-8988-1.
[4] Lempäälän lämpö Oy:n lausuntopyyntö (Statement request on property group), Energy Authority Finland, 2020. Available 15.10.2022 in: https://Energiavirasto-Lempaalan-Lampo-Oy-lausunto-1468_403_2020.pdf (eehanke.fi).
[5] Laki sähkön ja eräiden polttoaineiden valmisteverosta (Act on excise duty on electricity and certain fuels) 13.12.1996/1260.
[6] Pahkala, T., Uimonen, H., Väre, V. Joustava ja asiakaskeskeinen sähköjärjestelmä (Flexible and customer-centred electricity system) – Älyverkkotyöryhmän loppuraportti (Final report of the Smart Grid Working Group), Report 33. Helsinki: Työ- ja elinkeinoministeriö (Ministry of Economic Affairs and Employment), 2018. ISBN 978-952-327-346-1. p. 29.
[7] Liite Älyverkkotyöryhmän ehdotukset ja niiden perustelut (Attachment Proposals and arguments of Smart Grid Working Group). Työ- ja elinkeinoministeriö (Ministry of Economic Affairs and Employment), 2018. pp. 58-61.
[8] Asennamme älykästä huomista Elenian kanssa (We install smart future with Elenia). Elenia, 2021. Available 15.10.2022 in: https://www.voimatel.fi/asennamme-alykasta-huomista-elenian-kanssa/.
[9] Source: Official Statistics of Finland (OSF): Energy supply and consumption [e-publication]. ISSN=1799-7976. 4th Quarter 2018, Appendix figure 14. Final energy consumption by sector 2018. Helsinki: Statistics Finland [referred: 7.2.2020]. Access method: http://www.stat.fi/til/ehk/2018/04/ehk_2018_04_2019-03-28_kuv_014_en.html.
[10] Official Statistics of Finland (OSF): Production of electricity and heat [e-publication]. ISSN=1798-5099. 2020, Appendix figure 3. Electricity generation by production mode 2000-2020. Helsinki: Statistics Finland [referred: 1.4.2022]. Access method: http://www.stat.fi/til/salatuo/2020/salatuo_2020_2021-11-02_kuv_003_en.html.
[11] Our self-learning AI engine and cloud service. Kiona, 2023. Available 22.1.2023 in: https://kiona.com/fi/tuotteet/edge.

RIGA 2023

Investigation of the Latest Developments in Battery Technology for Enhanced Performance and Increased Range in Electric Vehicles.

El Fakkak Omar
EMISys Research Team, Engineering 3S Research Center Mohammadia School of Engineers, Mohammed V University in Rabat, Morocco e-mail: omarfakkak@gmail.com

Mounir Hamid
EMISys Research Team, Engineering 3S Research Center Mohammadia School of Engineers, Mohammed V University in Rabat, Morocco e-mail: mounir@emi.ac.ma

Cite this paper as: *Omar, EF, Hamid, M. Investigation of the latest developments in battery technology for enhanced performance and increased range in electric vehicles. 11. Eur. Conf. Ren. Energy Sys. 18-20 May 2023, Riga, Latvia*

Abstract: This article presents an in-depth examination of electric vehicle (EV) battery technologies, including their technological evolution, and future prospects. The study delves into the various component materials utilized in battery systems, including active electrode materials, supplementary component materials, refining and purification processes, and battery management systems. Furthermore, the principles of battery design and optimization in EVs are discussed, including the mechanism and reaction of lithium ion migration, self-discharge performance of different battery types, and capacity fade rate. Theoretical models for electrochemical modeling of lithium batteries, performance evaluation through cycling tests, and calculations of system capacity, C-rate, and capacity are also covered. The article also explores the phenomenon of hysteresis and irreversible capacity effects, as well as the use of in situ diagnostic methods for real-time monitoring of battery performance. Finally, the study projects future developments in EV battery technologies through analysis of radar graphs and market trends

Keywords: *Electric vehicle batteries, Operational traits, Theoretical models, Performance.*

1.INTRODUCTION

The construction of battery gigafactories, which produce large quantities of batteries, has increased to meet the growing demand for EVs. China has the most battery gigafactories in operation or under construction, with Europe also having a significant number. These facilities require significant investment and the trend is expected to continue as companies seek to meet demand and take advantage of economies of scale. The goal of these efforts is to increase the energy density of batteries, which allows EVs to have longer ranges and appeals to consumers. Advanced battery cells for EVs should have energy densities of at least 350 Wh/kg by 2020[1]. Predictions for future lithium batteries forecast energy densities will increase to around 200 Wh/kg after 2020 and 300 Wh/kg toward 2030[2].

Researchers are working to improve the performance and reduce the cost of batteries in various ways to accelerate the widespread adoption of EVs. The HORIZON 2020 program of the European Commission is focused on the development of nanotechnologies, advanced materials, and post-lithium-ion batteries for use in EVs [3]. Other efforts include research on new cell chemistries and the development of recycling technologies. Additionally, researchers are focused on improving the thermal stability, charging speed, safety, and environmental impact of batteries, as well as better understanding the aging mechanisms of batteries to improve their lifetimes and reduce the need for frequent replacement. Overall, the development of advanced batteries is critical for the widespread adoption of EVs.

2.EV BATTERY TECHNOLOGIES AND COMPONENT MATERIALS

International standards and future developments in EV battery technology

There are several international standards that pertain to EV batteries, such as ISO 12405, ISO 16750, ISO 26262, and IEC 62133, which provide guidelines for the design, performance, testing, and safety of EV batteries [4]. These standards help ensure that EV batteries meet certain minimum requirements. Future battery development includes technologies such as solid-state electrolytes, lithium-sulfur batteries, and lithium-air batteries which offer better energy density, longer lifespan, and improved safety. Other technologies such as supercapacitors, flow batteries, and thermophotovoltaic batteries are also being researched for energy storage solutions [5,6].

Electrode active materials

EV batteries use a variety of electrode active materials, including lithium cobalt oxide (LiCoO2), lithium manganese oxide (LiMn2O4), and lithium iron phosphate (LiFePO4). These materials determine the energy density and stability of the battery. LiCoO2 offers the highest energy density, but lower thermal stability, LiMn2O4 has a lower energy density, but higher thermal stability, and LiFePO4 has a moderate energy density, but high thermal stability and longer cycle life [7,9]. The stability of a battery is also determined by the active materials used in the electrodes. Impurities in the materials can greatly impact the performance and stability of the battery. For example, LiCoO2 can develop impurities and defects during processing, which can cause the battery to degrade over time and even lead to safety issues [8]. LiMn2O4 can suffer from transition metal impurities, leading to poor cycle life and capacity fading. LiFePO4 is considered purer and stable than other materials, but can still suffer from impurities like FeO or Fe2O3.

Other component materials

The electrolyte, current collectors, and separators are important components of an EV battery system. The electrolyte is a chemical solution that allows for ion movement during charging and discharging, while current collectors transport electrical current in and out of the battery. Separators are thin, porous sheets that prevent direct electrical contact between electrodes. Impurities in these materials can negatively impact battery stability, resistance, conductivity and overall performance, leading to issues such as dendrite formation and short-circuiting.

Table 1. Common types of batteries and the materials used in their anodes, cathodes, and electrolytes[12]

Battery Type	Anode Material	Cathode Material	Electrolyte Material
Lead-acid	Lead	Lead oxide	Sulfuric acid
Nickel-cadmium (Ni-Cd)	Cadmium	Nickel oxide	Alkaline solution
Nickel-metal hydride (NiMH)	Metal hydride	Nickel oxide	Alkaline solution
Lithium-ion (Li-ion)	Graphite	Lithium cobalt oxide or lithium iron phosphate	Lithium salt solution
Lithium-polymer(Li-poly)	Graphite	Lithium cobalt oxide or lithium iron phosphate	Polymer electrolyte
Zinc-carbon	Zinc	Carbon	Zinc chloride
Alkaline	Zinc	Manganese dioxide	Potassium hydroxide

Refining and purification process

The purity of the materials used in the construction of EV batteries plays a crucial role in determining their performance and key characteristics. Studies have shown that impurities in the active materials, such as lithium iron phosphate and lithium cobalt oxide, can decrease the capacity and stability of the battery, and that purifying these materials can improve their performance [10]. Researchers are also developing new and more efficient methods for purifying these materials, such as acid washing, centrifugation, electrodeposition, chemical-mechanical polishing, solid-state synthesis, co-precipitation, sol-gel methods, etc. each one with specific advantages and disadvantages. It is important for researchers to consider all factors when choosing the best method for a specific material [10].

The purity of other components in the battery, such as the electrolyte, current collectors, and separators, is also important for the overall performance of the battery [11]. Overall, it's a field of active research to improve the material purity of EV batteries to achieve high-performance and stable batteries to use in the electric vehicles.

Battery management systems

BMS monitor and control various parameters, including state of charge (SOC), current, and temperature, to prevent overcharge, overdischarge, overcurrent, and overheating. Key functions of BMS include SOC estimation, current estimation, temperature monitoring, and safety control. Algorithms such as Kalman filtering, model predictive control, and artificial intelligence techniques are used to perform these functions. BMS can improve EV battery performance, safety, and lifespan, but can also present challenges in practical applications due to complexity, scalability, cost, and lack of standardization.

3.PRINCIPLES OF BATTERIES IN EVS: DESIGN AND OPTIMIZATION OF BATTERY SYSTEMS.

Mechanism and reaction in Lithium battery migration

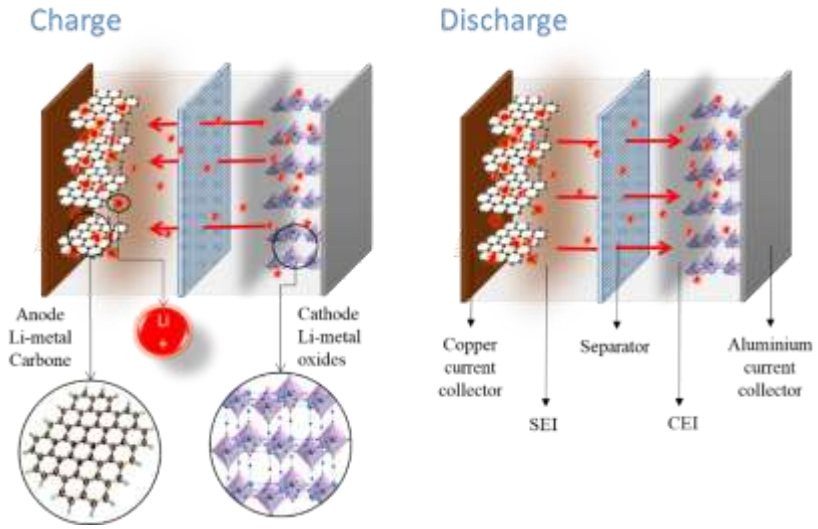

Figure 7. Cross-sectional view of a lithium battery cell, showing the anode made of graphite, the cathode made of lithium metal oxide ,the separator made of polyethylene, the electrolyte made of lithium hexafluorophosphate (LiPF6) in an organic carbon

In a lithium-ion battery, the movement of lithium ions between the cathode and anode is driven by a redox reaction, where electrons are transferred between the electrodes and lithium ions are transferred between the electrolyte and electrodes. The efficiency of this redox reaction is crucial for the overall performance and lifespan of the battery [13]. The type and purity of the materials used, the design of the electrodes and electrolyte, and the temperature of the battery all play a role in determining the efficiency of the redox reaction. Additionally, there are various types of batteries used for different applications such as lead-acid, nickel-cadmium, nickel-metal hydride, lithium-ion, and lithium-polymer batteries. Each type has its own unique combination of anode, cathode, and electrolyte materials as well as specific characteristics such as capacity, voltage, current, and lifespan.

Table2. General comparison of the technical characteristics of different commercial batteries for EV's [12].

Battery Type	Energy Density (Wh/kg)	Voltage (V)	Lifespan (cycles)	Operating Temperature Range (°C)
Lead-acid	30-50	2	500-1,000	-20 to 50
Nickel-metal hydride (NiMH)	60-100	1.2	500-1,000	-20 to 60
Lithium-ion (Li-ion)	100-250	3.7	1,000-5,000	-20 to 60
Lithium-polymer (Li-poly)	100-250	3.7	1,000-5,000	-20 to 60

Self-discharge performance of different batteries in EVs

The self-discharge rate of a battery is a measure of how much the battery's capacity is reduced over time when it is not in use. The self-discharge rate is an important metric in evaluating the performance of a battery, as it indicates the battery's ability to maintain its charge over time. The self-discharge rate is typically expressed as a percentage per month.

Table 3 Self-Discharge Rate: The percentage of the battery's capacity that is lost per month when not in use[12].

Battery Type	Self-discharge rate (per month)
Lead-acid	20-30%
NiMH	10-20%
Li-ion	1-5%
Li-polymer	<1%

Lithium-ion and lithium-polymer batteries have significantly lower self-discharge rate compared to other types of batteries, making them suitable for applications where the battery is not frequently used or required to be available on demand [14]. This makes them ideal for standby power applications where the battery is required to provide power during power outages. Additionally, the self-discharge rate of lithium-ion batteries is not affected by temperature, making them suitable for use in a wide range of temperatures and environments. Overall, self-discharge rate is an important metric in evaluating the performance of a battery, and lithium-ion and lithium-polymer batteries are favorable in this aspect [15].

Capacity fade rate

The capacity fade rate is a measure of how much the capacity of a battery decreases over time as a result of charging and discharging cycles. It is typically expressed as a percentage of the initial capacity per cycle. It is an important metric to consider when evaluating the performance and lifespan of a battery, as it can impact the battery's availability and overall lifespan. The capacity fade rate can vary depending on the specific battery design and application, but is generally lower for lithium-ion and lithium-polymer batteries than for lead-acid and nickel-metal hydride batteries. The capacity fade rate can be reduced by minimizing deep discharges, overcharging, and by using high-quality materials and optimizing the manufacturing process [16]. Additionally, using a battery management system (BMS) and optimal charging and discharging algorithms can also help to minimize capacity fade.

4.THEORETICAL MODELS

Electrochemical Modeling of Lithium Batteries:

There are several theoretical models that have been developed to predict and analyze the performance of EV batteries. These models take into account various factors such as the electrochemical reactions within the battery, the transport of charge carriers through the electrodes and electrolyte, and the temperature and state of charge of the battery.

Table 4. Main theoretical models that have been developed for EV batteries

Model	Description
Single Particle Model [17].	This model describes the transport of a single lithium ion through the electrodes and electrolyte of an EV battery. It is a simple model that is useful for understanding the basic mechanisms of lithium ion transport.
Diffusion Model [18].	This model describes the transport of multiple lithium ions through the electrodes and electrolyte of an EV battery. It takes into account the concentration gradients of lithium ions within the battery and the effects of diffusion on the transport of ions.
Electrochemical Model [19].	This model describes the electrochemical reactions that occur within an EV battery, including the reactions at the electrodes and the transport of charge carriers through the electrodes and electrolyte. It is a more detailed and complex model than the single particle or diffusion models and is useful for predicting and analyzing the performance of an EV battery under different operating conditions.

Thermal Model [20].	This model describes the temperature changes that occur within an EV battery during charging and discharging. It takes into account the heat generated by the electrochemical reactions within the battery, as well as the heat transfer between the battery and its surroundings. The thermal model is useful for predicting and analyzing the temperature profile of an EV battery and for designing temperature control measures.

Electrochemical modeling is an important tool for understanding the behavior of EV batteries and informing the design of EV battery systems. Different models such as single particle model (SPM), phase field model (PFM), porous electrode model (PEM), and equivalent circuit model (ECM) can be used to understand the fundamental physics of lithium-ion transport, and to predict the behavior of the battery under different operating conditions. Each model has its advantages and limitations, and the choice of which model to use will depend on the specific application and the level of detail required. For example, SPM can provide detailed insight into the physics of lithium-ion transport, but PEM or ECM are more suitable for system-level design and optimization. Equivalent circuit models (ECM) are based on circuit theory and can be used to identify causes of performance issues. One of the main advantages of ECM is the simple and fast simulation which is suitable for system design, but a disadvantage is that it lacks the ability to predict detailed physical phenomena.

Cycling tests for performance evaluation of Li-ion batteries

Cycling tests are used to evaluate the performance of lithium-ion batteries. These tests involve repeatedly charging and discharging the battery to simulate real-world usage. The data obtained from cycling tests is used to determine the battery's capacity, energy efficiency, and longevity. Common cycling tests include: Constant current discharge (CCD) cycling, Constant power discharge (CPD) cycling, Constant current charge (CCC) cycling, Constant voltage charge (CVC) cycling, and Hybrid cycling. These tests measure the battery's ability to store and release energy, maintain a consistent power output, charge efficiently, handle different charging and discharging conditions, and simulate real-world usage. Overall, cycling tests provide a comprehensive evaluation of a battery's performance and help identify potential issues that may arise in real-world usage [21].

Calculation of system capacity, C-rate, and capacity

In evaluating the performance of a positive electrode material in a lithium-ion battery, it is important to consider key metrics such as discharge capacity, capacity retention, and C-rate. Discharge capacity is a measure of the material's energy performance and can be determined by analyzing charge/discharge curves. Capacity retention over time is a measure of cycling stability. The C-rate, which quantifies the rate of charge or discharge relative to the battery's capacity, can greatly impact the battery's performance and longevity. High C-rates can lead to reduced battery life, diminished performance and an increased risk of thermal runaway [22]. It's crucial to consider the appropriate C-rate for the given application and to use a battery management system to regulate it. In addition, factors such as safety, cost and environmental impact of the materials should be considered when selecting the appropriate positive electrode material for a specific application.

Study of hysteresis and irreversible capacity effects

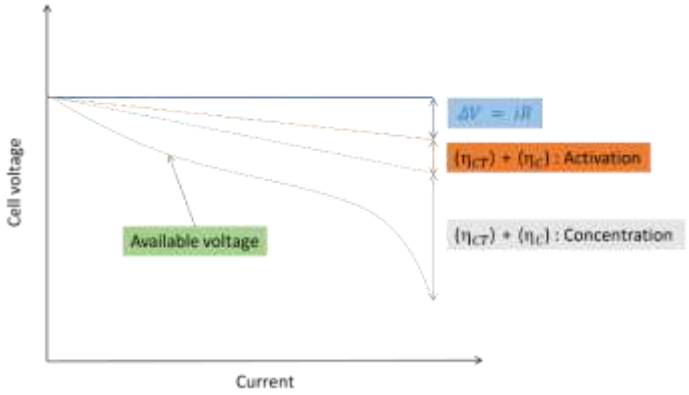

Figure 2. Ohmic drop,polarisation and overvoltage in a cell

Hysteresis is a phenomenon that occurs in lithium-ion batteries, which refers to the difference in potential between the charging and discharging processes. It can affect the performance and longevity of the battery. The irreversible capacity, which represents the energy lost during the charge-discharge cycle, is another metric that can be affected by hysteresis. The Ohmic drop, caused by the internal resistance of the battery, can also lead to a voltage drop across the electrodes and affect the performance of the battery. Additionally, the overvoltage caused by transfer polarizations can also negatively impact the battery's energy density and overall performance [23]. To minimize these effects, researchers and manufacturers use materials with lower resistance, design electrodes with higher surface area, and use electrolytes with higher conductivity. These factors can help improve the performance and longevity of the battery. However, it is worth noting that hysteresis and these other factors are complex phenomena that can be affected by temperature, aging, and mechanical stress, and further research is needed to fully understand and mitigate these effects.

Diagnosis operando to monitor battery performance in real-time

Characterizing lithium-ion battery materials at the nanoscale is crucial for understanding the mechanisms of operation and degradation of these materials(Fig3). Transmission Electron Microscopy (TEM) is a commonly used technique that allows for the imaging of the internal structure of the materials, including the morphology and composition of the active materials, electrolyte, and interfaces. High-resolution TEM (HRTEM) can be used to visualize the atomic structure of the materials and identify defects. Scanning Transmission Electron Microscopy (STEM) is another important technique that allows for the elemental mapping of the materials at the nanoscale, and can be used to study the formation of lithium dendrites and other degradation mechanisms. Scanning Probe Microscopy (SPM) techniques such as Atomic Force Microscopy (AFM) and Electrochemical Force Microscopy (EFM) can be used to study the surface and interfacial properties of the materials and can provide important information on the formation of lithium dendrites. These techniques provide important insights into the mechanisms of operation and degradation of lithium battery materials [24,25].

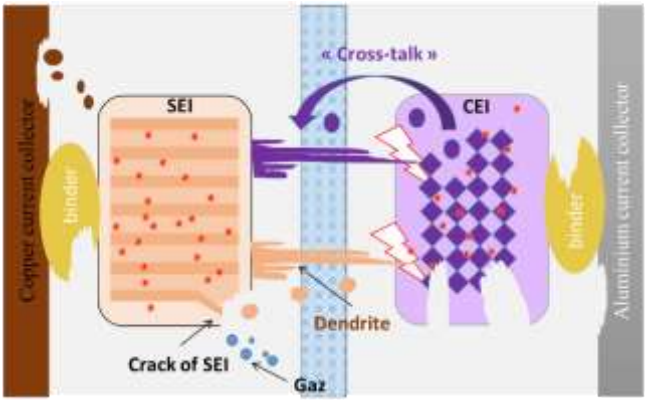

Figure 3. Chemical degradation: The electrodes, electrolyte, and separator can degrade chemically over time, leading to a loss of active material and a decrease in overall capacity.

5.FORECASTING THE DEVELOPMENT TREND OF EV BATTERY TECHNOLOGIES

Radar Graphs:

A radar chart can be used to compare the characteristics of different rechargeable batteries, including lithium-ion, nickel-cadmium, nickel-metal hydride, and lead-acid batteries. This can be useful for quickly visualizing the strengths and weaknesses of different battery types. It can also help to compare the potential performance, safety, and cost benefits of advanced lithium-ion battery technologies such as solid-state, lithium-sulfur, and lithium-air when compared to traditional lithium-ion batteries.

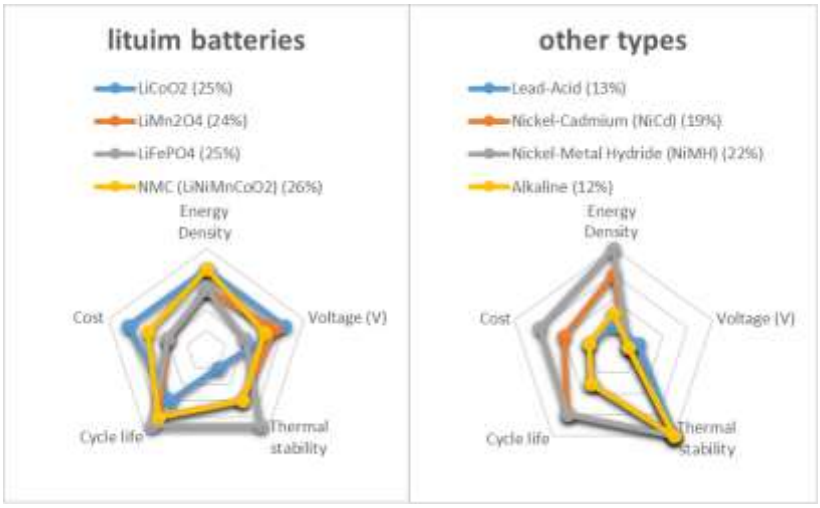

Figure 4. Comparison of energy density, thermal stability and cost of various lithium batteries and others

Market Analysis and Future Predictions:

The EV battery market is projected to grow significantly in the next few years, driven by increasing demand for electric vehicles. According to a report by MarketsandMarkets, the EV battery market is projected to grow from USD 29.5 billion in 2020 to USD 93.1 billion by 2025, at a CAGR of 25.3% during the forecast period (2020-2025) [26]. Furthermore, in recent years, leading players such as Tesla, Panasonic, and CATL have been increasing their market share and investment in EV battery technology.

Advanced lithium-ion battery technologies, such as solid-state batteries, lithium-sulfur batteries, and lithium-air batteries, have the potential to improve the performance, safety, and cost of EV batteries. The analysis of graphs can also be used to identify the areas where current technologies fall short and predict the potential future development trends of EV battery technologies. For example, graphs have been used to compare the performance of different EV battery technologies in terms of energy density, power density, cost, safety, and lifespan. According to radar graph analysis by Navigant Research, lithium iron phosphate batteries currently have a lower energy density than other lithium-ion batteries, but they have a longer lifespan and are more cost-effective and safer [27]

6.CONCLUSION

comparing the potential performance, safety, and cost benefits of these advanced technologies to traditional Li-ion batteries, it is clear that they have the potential to significantly improve the performance of EV batteries. However, these technologies are still in the early stages of development, and significant challenges must still be overcome before they can be commercialized for EV applications. Additionally, solid-state batteries are considered closer to commercialization than lithium-sulfur and lithium-air batteries, but still require improvements in cost and scalability before they can be adopted on a large scale.

In conclusion, the EV battery market is expected to grow significantly in the next few years and advanced lithium-ion battery technologies have the potential to significantly improve the performance, safety, and cost of EV batteries. However, these technologies are still facing significant challenges and further research and development is needed before they can be widely adopted

REFERENCES

[1] Benchmark Mineral Intelligence: global battery gigafactory pipeline tops 300; China dominates , *Green Car Congress*. https://www.greencarcongress.com/2022/05/20220521-benchmark.html.

[2] « Q&A: The European Battery Alliance », *European Commission - European Commission*. https://ec.europa.eu/commission/presscorner/detail/en/QANDA_22_1257

[3] E. Cready, J. Lippert, J. Pihl, I. Weinstock, et P. Symons, « Technical and Economic Feasibility of Applying Used EV Batteries in Stationary Applications », Sandia National Lab. (SNL-NM), Albuquerque, NM (United States); Sandia National Lab. (SNL-CA), Livermore, CA (United States), SAND2002-4084, mars 2003. DOI: 10.2172/809607.
[4] ISO 12405-4:2018(en), Electrically propelled road vehicles — Test specification for lithium-ion traction battery packs and systems — Part 4: Performance testing» https://www.iso.org/obp/ui/#iso:std:iso:12405:-4:ed-1:v1:en
[5] M. M. A. Gamel *et al.*, « A Review on Thermophotovoltaic Cell and Its Applications in Energy Conversion: Issues and Recommendations », *Materials (Basel)*, vol. 14, no 17, p. 4944, août 2021, DOI: 10.3390/ma14174944.
[6] Zhong, D. Yida, W. Hu, J. Qiao, L. Zhang, et J. Zhang, « A review of electrolyte materials and compositions for electrochemical supercapacitors », *Chemical Society Reviews*, vol. 44, p. 7431-7920, June 2015, DOI: 10.1039/c5cs00303b
[7] X. Chen, Y. Li, et J. Wang, « Enhanced Electrochemical Performance of LiFePO4 Originating from the Synergistic Effect of ZnO and C Co-Modification », *Nanomaterials*, vol. 11, no 1, Art. no 1, January. 2021, DOI: 10.3390/nano11010012.
[8] Z. Chang *et al.*, « A lithium-ion battery using an aqueous electrolyte solution », *Sci Rep*, vol. 6, no 1, Art. no 1, June 2016, DOI: 10.1038/srep28421
[9] F. Schipper *et al.*, « Study of Cathode Materials for Lithium-Ion Batteries: Recent Progress and New Challenges », *Inorganics*, vol. 5, no 2, Art. no 2, June 2017, DOI: 10.3390/inorganics5020032
[10] Y. Miao, P. Hynan, A. von Jouanne, et A. Yokochi, « Current Li-Ion Battery Technologies in Electric Vehicles and Opportunities for Advancements », *Energies*, vol. 12, no 6, Art. no 6, janv. 2019, DOI: 10.3390/en12061074.
[11] J. B. Goodenough et Y. Kim, « Challenges for Rechargeable Li Batteries », *Chem. Mater.*, vol. 22, no 3, p. 587-603, févr. 2010, DOI: 10.1021/cm901452z.
[12] « Battery University », *Battery University*, 13 September 2019. https://batteryuniversity.com/
[13] J. S. Gnanaraj, M. D. Levi, Y. Gofer, D. Aurbach, et M. Schmidt, « LiPF3 (CF 2 CF 3) 3 : A Salt for Rechargeable Lithium Ion Batteries », *J. Electrochem. Soc.*, vol. 150, no 4, p. A445, févr. 2003, DOI: 10.1149/1.1557965.
[14] M. S. Ramkumar *et al.*, 'Review on Li-Ion Battery with Battery Management System in Electrical Vehicle', *Advances in Materials Science and Engineering*, vol. 2022, p. e3379574, May 2022, DOI: 10.1155/2022/3379574.
[15] Y. Xing, E. W. M. Ma, K. L. Tsui, et M. Pecht, « Battery Management Systems in Electric and Hybrid Vehicles », *Energies*, vol. 4, no 11, Art. no 11, nov. 2011, DOI: 10.3390/en4111840.
[16] T. Mesbahi, R. B. Sugrañes, R. Bakri, et P. Bartholomeüs, « Coupled electro-thermal modeling of lithium-ion batteries for electric vehicle application », *Journal of Energy Storage*, vol. 35, p. 102260, mars 2021, DOI: 10.1016/j.est.2021.102260.
[17] W. Zhou, Y. Zheng, Z. Pan, et Q. Lu, « Review on the Battery Model and SOC Estimation Method », *Processes*, vol. 9, no 9, Art. no 9, sept. 2021, DOI: 10.3390/pr9091685.
[18] F. B. Planella *et al.*, « A continuum of physics-based lithium-ion battery models reviewed », *Prog. Energy*, vol. 4, no 4, p. 042003, juill. 2022, DOI: 10.1088/2516-1083/ac7d31.
[19] R. Kempaiah, G. Vasudevamurthy, et A. Subramanian, « Scanning probe microscopy based characterization of battery materials, interfaces, and processes », *Nano Energy*, vol. 65, p. 103925, nov. 2019, doi: 10.1016/j.nanoen.2019.103925.
[20] S. Basak *et al.*, « Characterizing battery materials and electrodes via in situ/operando transmission electron microscopy », *Chem. Phys. Rev.*, vol. 3, no 3, p. 031303, sept. 2022, DOI: 10.1063/5.0075430
[21] H. Li, 'Practical Evaluation of Li-Ion Batteries', *Joule*, vol. 3, no. 4, pp. 911–914, Apr. 2019, DOI: 10.1016/j.joule.2019.03.028.
[22] Z. Ahmed, A. J. Roberts, and T. Amietszajew, 'Operando Thermo-Electrochemical Diagnostics with Au, TiO2, and LiFePO4 as Reference Electrodes in Li-Ion Pouch Cells', *Energy Technology*, vol. 10, no. 10, p. 2200248, 2022, DOI: 10.1002/ente.202200248.
[23] E. Zhao *et al.*, 'Quantifying the Anomalous Local and Nanostructure Evolutions Induced by Lattice Oxygen Redox in Lithium-Rich Cathodes', *Small Methods*, vol. 6, no. 11, p. 2200740, 2022, DOI: 10.1002/smtd.202200740.
[24] Z. Gao, H. Xie, X. Yang, W. Niu, S. Li, and S. Chen, 'The Dilemma of C-Rate and Cycle Life for Lithium-Ion Batteries under Low Temperature Fast Charging', *Batteries*, vol. 8, no. 11, Art. no. 11, Nov. 2022, DOI: 10.3390/batteries8110234.
[25] B. Ma, S. Agrawal, R. Gopal, and P. Bai, 'Operando Microscopy Diagnosis of the Onset of Lithium Plating in Transparent Lithium-Ion Full Cells', *ACS Appl. Mater. Interfaces*, vol. 14, no. 49, pp. 54708–54715, Dec. 2022, DOI: 10.1021/acsami.2c16090.
[26] Y. Miao, P. Hynan, A. von Jouanne, et A. Yokochi, « Current Li-Ion Battery Technologies in Electric Vehicles and Opportunities for Advancements », *Energies*, vol. 12, no 6, Art. no 6, janv. 2019, DOI: 10.3390/en12061074.
[27] Electric Vehicle Battery Market Size, Share and Outlook 2027 », *MarketsandMarkets*. https://www.marketsandmarkets.com/Market-Reports/electric-vehicle-battery-market-100188347.html .

RIGA 2023

Saving Energy By Changing Lighting in A 24-Hour Store

Artur Rusowicz
Institute of Heat Engineering, Faculty of Power and Aeronautical Engineering, Warsaw University of Technology, Nowowiejska 21/25, 00-665 Warsaw Poland, artur.rusowicz@pw.edu.pl
:0000-0001-7949-6907

Cite this paper as: *Rusowicz A.. Saving energy by changing lighting in a 24-hour store. 11. Eur. Conf. Ren. Energy Sys. 18-20 May 2023, Riga, Latvia*

Abstract: The paper presents the balance of electricity and fuel oil consumption of a medium-sized 24-hour store. Measurements of electricity consumption of individual components of the balance were made. Their shares over the 12 months of measurements were determined. Opportunities to reduce electricity consumption by changing the type of lighting of the facility were identified. . lighting replacement reduced electricity consumption by 38535.8 kWh, a total reduction of 21.2% in the store's annual electricity consumption.

Keywords: *Energy efficiency, electricity consumption, lighting*

1. INTRODUCTION

Energy generation in Poland has been a matter of course for many years, the vast reserves of coal and lignite used as fuel in our power plants meant that for decades people were relatively unconcerned about energy consumption in their daily lives. Electricity was cheap, and at one point also readily available to almost every resident. In our daily lives, we use electricity to power virtually every goto household appliance. A similar situation occurred with heat generation. Heating with coal was a well-known and easy-to-use technique, and the availability of the fuel was high and at a good price. Therefore, in the vast majority of entrepreneurs and owners of domestic farms, wishing to avoid wrong decisions and high initial costs, chose traditional coal or, at a later stage, electric heating as the heat source in their facility. Only changes in the EU's 3x20 package forced a change in approach to reduce CO2 emissions, increase energy efficiency and increase the share of renewable energy sources. Electricity in Poland is produced primarily in utility thermal power plants. In 2020, the volume of production at these facilities amounted to 120.5 TWh, which accounted for 76.3% of total production. The share of thermal utility power plants in production has decreased by 11.6 percentage points since 2014. The efficiency of public thermal power plants has remained at a similar level for years, and amounted in 2020. 42,6%. Industrial power plants generated in 2020. 16.8 TWh, which accounted for 10.7% of total generation. In this case, a significant increase in production and efficiency can be observed, which reached 57.5% in 2020. The remaining production of electricity is the result of independent power plants, mainly wind power. In 2020, the structure of energy generation in Poland, unfortunately, was still largely based on hard coal and lignite. The most important fuel for electricity generation in 2020 was hard coal, with a share of 44.1%, and lignite with a share of 24,1%. The share of these fuels in production decreased by 13.2 percentage points since 2014. Production from renewable energy sources accounted for 17.9% and increased by 5.4% since 2014 [1]. The most important carriers in this group were wind energy and biomass and biogas. Solar energy has the smallest share, but has the highest growth rate. Increasing energy efficiency is related to performing energy audits. An energy audit of various types of facilities is now a mandatory activity for various types of facilities. Conclusions of the energy consumption analysis are presented to users with proposals to reduce energy intensity for the facility within the framework of reasonable economic solutions [2],[3],[4],[5],[6]. IT systems are also proposed to optimize the energy consumption of facilities [7].

The study analyzed the electricity consumption of a 24-hour store that also provides fast food sales services. Energy consumption was metered over a 12-month period (July 2019-June 2020). The studied facility is representative of

a large chain of medium-sized stores, amounting to almost 1,100 facilities in Poland. The analysis of consumption makes it possible to isolate the components of electricity consumption and propose to increase their energy efficiency.

2. ANALYZED OBJECT

The medium-sized store open 24 hours a day, also offering café services in the Warsaw area, was analyzed. The heated area of the store is 313 m^2, while the area available to customers is 120 m^2. There is an illuminated parking lot in front of the store. Heating and cooling of the facility is provided by compressor air-conditioning units with a heat pump. Domestic hot water and supplementary heating are provided by an oil furnace.

Electricity and fuel oil consumption were measured from July 2019 to June 2020. During this period, the number of customers visiting the store was 33,500 people, or an average of about 2,800 people per month. Electricity consumption was measured for indoor and outdoor lighting, air conditioning, refrigeration equipment, equipment for the cafeteria (fast food). Nonmetered equipment represents the difference between total electricity consumption and that of metered equipment.

The outdoor lighting was sodium lamps, while the indoor lighting was fluorescent lamps in open fixtures. The measured electricity consumption for the lighting is presented in Fig.1.

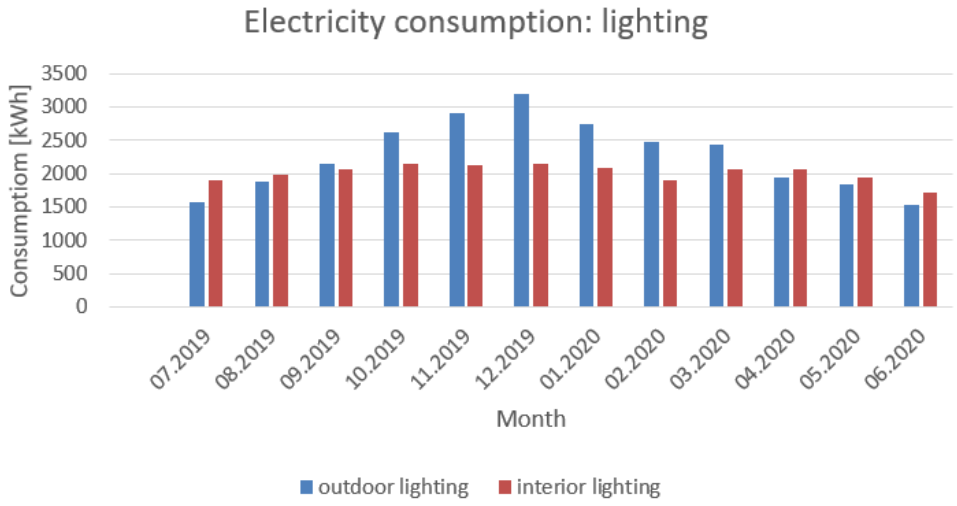

Figure 1.Electricity consumption of lighting during the study period

Electricity consumption presents a stabilized consumption throughout the year with an average value of about 2,000 kWh/month. Interior lighting is practically not correlated with the length of the day, while exterior lighting is clearly correlated with the length of the day [8],[9].

As for the electricity consumption of refrigeration equipment, which are 3 refrigeration counters, an open front refrigerator, an ice maker and a freezer, there is a stabilized consumption throughout the year, with an average of 2844 kWh/month. The situation is similar for cafe equipment (oven, coffee maker, microwave oven). The average monthly consumption of electricity is 443 kWh/month. Nonmetered appliances are mainly electrical outlets to which various current consumers (e.g. vacuum cleaners, hand dryers) are connected periodically. A summary of the electricity consumption of groups of appliances during the year is shown in Fig.2.

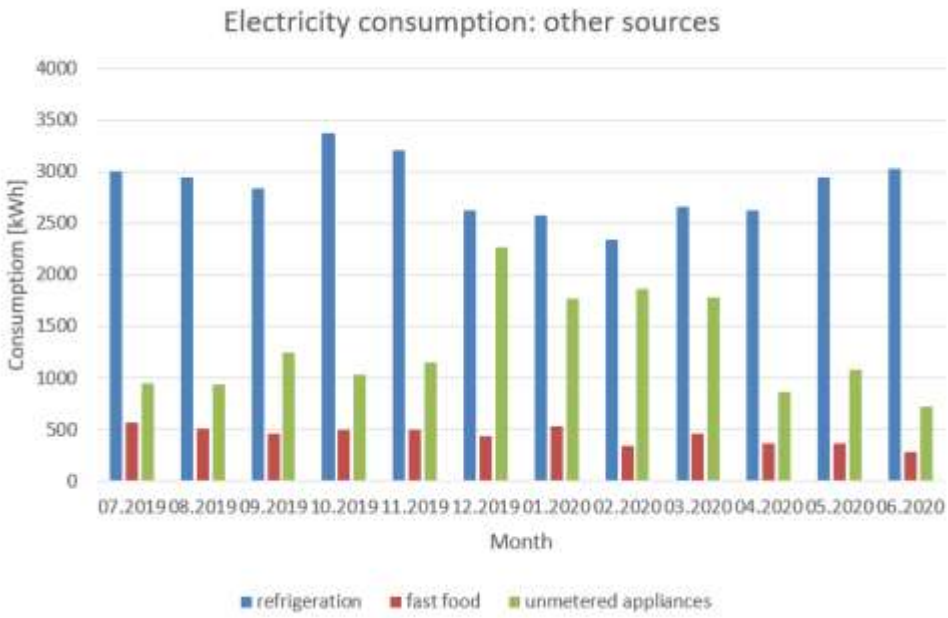

Figure 2. Electricity consumption by various sources during the study period

In the case of air conditioning in the store, compressor air-conditioning units with heat pump function were used. Electricity consumption of air-conditioning is presented in Fig.3. It can be seen that electricity consumption is clearly higher in the summer months. In the other months, consumption is at an average level of 1500 kWh/month.

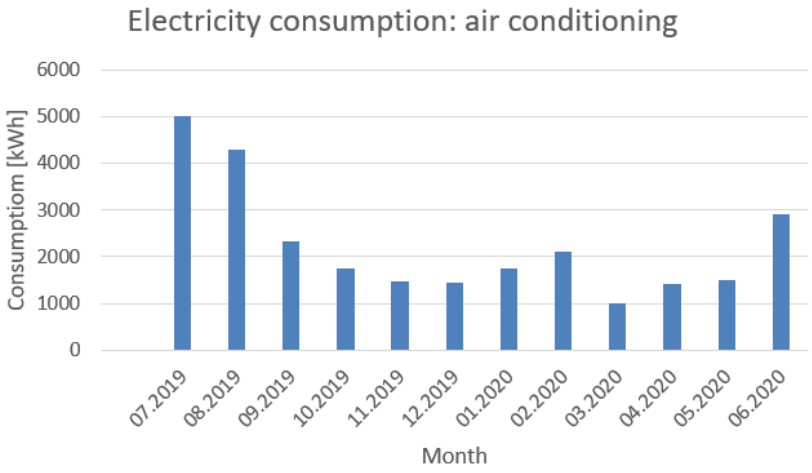

Figure 3. Electricity consumption of air conditioning during the study period

Domestic hot water and main heating in winter is provided by an oil furnace. Figure 4 shows oil consumption throughout the year. The highest consumption is in the winter months (December-April)

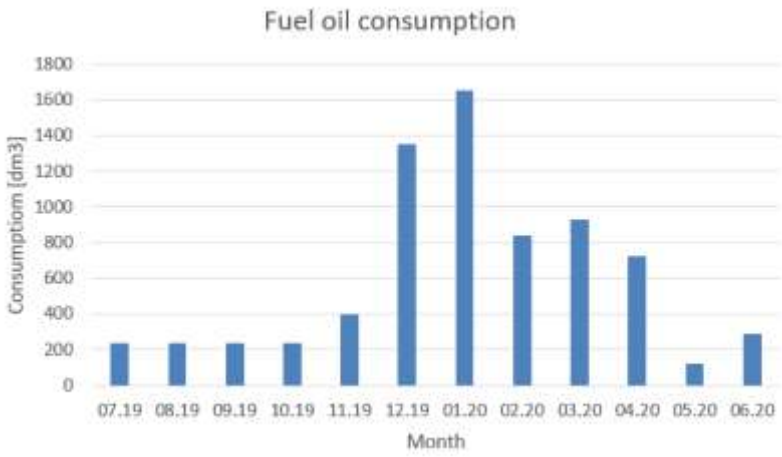

Figure 4. Fuel oil consumption during the study period

The share of electricity consumption by source is presented in Fig. 5. Interior and exterior lighting consumes 28.3% of the electricity needed for this store. The same level of consumption is for air-conditioning equipment - 28.3%. In the case of the analyzed store, the air-conditioning and refrigeration equipment and for fast food are relatively new equipment.

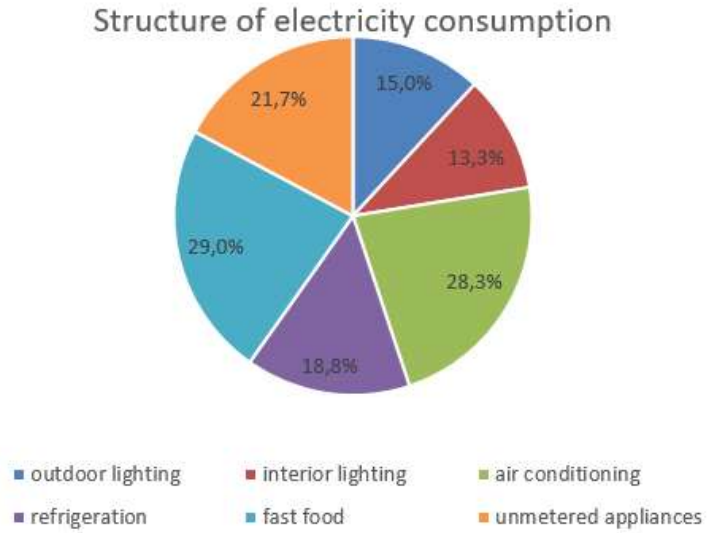

Figure 5. Structure of electricity consumption in the study period

Based on a preliminary analysis, it can be concluded that improving energy efficiency can focus primarily on lighting replacement. Based on the literature on road lighting [[10],[11],[12]], there is an existing potential to reduce the electricity consumption of outdoor parking lot lighting. According to [[10]], replacing the installation of high-pressure sodium lamps with high-efficiency LED lighting results in electricity consumption savings of 31%, while maintaining uniform luminance levels. Similar values of 21.9% reduction in electricity consumption are presented by [13]. The use of an additional multi-stage dimming system reduces electricity consumption by a further 20% over the year. Similar values for savings from the use of dimming systems are presented by [14], noting an increase in installation costs by a similar 30%. In the case of road lighting, sodium lamps are preferred due to their lighting quality [11], the use of LED lamps does not always result in savings in electricity consumption when high lighting standards are needed. The use of LED lighting generates reactive power consumption. The occurrence of reactive power causes an increase in current, which increases electricity losses in AC power generation and transmission equipment (generators, transmission lines and transformers). The use of electronic dimming systems in LED lighting additionally, further increases the generation of reactive power [[13],[14]]. The analysis of increasing the energy efficiency of the store assumes a 25% reduction in electricity consumption for lighting. In a year, 38535.8 kWh is consumed for lighting. At an electricity price of 0.15Euro/kWh, savings of 5780 Euro/year were obtained. In the current year, electricity prices in Poland for entrepreneurs are four times higher than in the analyzed 2020.

3. RESULTS AND DISCUSSIONS

The paper presents the balance of electricity consumption of a 24-hour store. Measurements were taken from July 2019 to June 2020. Various components of electricity consumption were analyzed in conjunction with the existing state of the equipment. In order to improve the energy efficiency of the facility, it was proposed to replace the lighting from fluorescent lamps inside the store and sodium lamps in the parking lot. In the case of the parking lot, dimming systems were not used, due to the cost of replacement and the increased generation of additional reactive power. As a result of the lighting replacement, electricity consumption was reduced by 38535.8 kWh, a total reduction of 21.2% in the store's annual electricity consumption. In 2020, savings of 5780 euros/year were obtained. In the current year, electricity prices in Poland for entrepreneurs are four times higher than in the analyzed 2020.

References

[1] Energy statistics in 2019 and 2020, Statistics Poland, Warsaw 2021

[2] Rusowicz, A., Grzebielec, A. Refrigeration equipment as essential elements of a heat recovery system in public buildings. *Rynek Energii, 2014, 113, 125–129.*

[3] Rusowicz, A., Grzebielec, A., Ruciński, A. Energy conservation in buildings using refrigeration units. W D. Čygas & T. Tollazzi (Red.), 9th International Conference on Environmental Engineering (s. 6). 2014, Vilnius Gediminas Technical University Press Technika. https://doi.org/10.3846/enviro.2014.281

[4] Grudzień, A. M., Rusowicz, A., Leszczyński, M. Analysis of air conditioning systems for different types of hotels. Rynek Energii, 2019, 47–52.

[5] Rusowicz, A., Ruciński, A., Laskowski, R. The Analysis of Modifications in Cooling Systems for High-Performance Data Centers. A Case Study. W D. Čygas & R. Vaiskunaite (Red.), Proceedings of the 10th International Conference Environmental Engineering (s. 1–6). 2017 Vilnius Gediminas Technical University. https://doi.org/10.3846/enviro.2017.273

[6] Rusowicz, A., Grzebielec, A., Laskowski, R. Modification in cooling systems for high-performance data centers -A case study. *Rynek Energii, 2017, 128, 67–72.*

[7] Ziąbka, T., Grzebielec, A., Rusowicz, A. ISEE - Intelligent System of Energy Efficiency. *Modern Engineering, 2020, 6–10.*

[8] Doulos, L.T., Kontadakis, A, Madias, E.N., Sinou, M., Tsangrassoulis A. Minimizing energy consumption for artificial lighting in a typical classroom of a Hellenic public school aiming for near Zero Energy Building using LED DC luminaires and daylight harvesting systems. *Energy & Buildings 2019 194, 201–217.* https://doi.org/10.1016/j.enbuild.2019.04.033

[9] Jakubowsky, M., de Boer, J., Façade elements for room illumination with integrated microstructures for daylight redirection and LED lighting. *Energy & Buildings 2022, 266, 112106*. https://doi.org/10.1016/j.enbuild.2022.112106

[10] Djuretic, A., Kostic, M. Actual energy savings when replacing high-pressure sodium with LED luminaires in street lighting. *Energy 2018 157 (2018) 367-378.* https://doi.org/10.1016/j.energy.2018.05.179

[11] Suntiti Yoomak, Atthapol Ngaopitakkul. Optimisation of lighting quality and energy efficiency of LED luminaires in roadway lighting systems on different road surfaces. *Sustainable Cities and Society 2018, 38, 333–347.* https://doi.org/10.1016/j.scs.2018.01.005

[12] Polzin, F., von Flotow, P., Nolden, C. Modes of governance for municipal energy efficiency services e The case of LED street lighting in Germany. *Journal of Cleaner Production 2016, 139, 133-145.* http://dx.doi.org/10.1016/j.jclepro.2016.07.100

[13] Byun J., Hong, I., Lee B., Park, S. Intelligent Household LED Lighting System Considering Energy Efficiency and User Satisfaction. *IEEE Transactions on Consumer Electronics, 2013 Vol. 59, No. 1, 70-76*

[14] Farahat, A., Florea, A., Lastra, J.L.M., Brañas, Ch., Sánchez, F., J., A. Energy Efficiency Considerations for LED-Based Lighting of Multipurpose Outdoor Environments. *IEEE Journal of Emerging and Selected Topics in Power Electronics, 2015, Vol. 3, No. 3, 599-608*

RIGA 2023

State of Charge Estimation by Online OCV Evaluation using an Auxiliary Controlled Load

Abdelaziz Zermout
Signals and Systems Laboratory, Institute of Electrical and Electronic Engineering, University M'Hamed BOUGARA of Boumerdes, Boumerdes, Algeria, az.zermout@univ-boumerdes.dz, ORCID: 0000-0003-4219-1901

Hadjira Belaidi
Signals and Systems Laboratory, Institute of Electrical and Electronic Engineering, University M'Hamed BOUGARA of Boumerdes, Boumerdes, Algeria, hadjira983@yahoo.fr, ha.belaidi@univ-boumerdes.dz, ORCID: 0000-0003-2424-626X

Ahmed Maache
Signals and Systems Laboratory, Institute of Electrical and Electronic Engineering, University M'Hamed BOUGARA of Boumerdes, Boumerdes, Algeria, a.maache@univ-boumerdes.dz, ORCID: 0000-0001-5069-6972

Cite this paper as: *Zermout, A, Belaidi, H, Maache, A. State of charge estimation by online OCV evaluation using an auxiliary controlled load. 11. Eur. Conf. Ren. Energy Sys. 18-20 May 2023, Riga, Latvia*

Abstract: Several methods and strategies were established for online Lithium-ion batteries' State-of-Charge (SoC) estimation; however, the load consumption of batteries fluctuates in real-time as a result of supplied device actions. Therefore getting an accurate online (while the load is supplied) SoC estimation is still a challenge.
This paper suggests a new technique for online Open-Circuit-Voltage (OCV) evaluation for online battery's SoC estimation. The developed strategy proposes to add an auxiliary controlled load that can be used to force certain predefined shapes of the battery's current curve temporarily under some conditions which help to enhance, and facilitate the online OCV calculations. The proposed method is described in details in this work, and a number of tests were performed to validate its effectiveness. The obtained results prove its efficiency with acceptable online OCV estimation accuracy, generally the error is less than 8.5mV, and in some tests close to 0 mV.

Keywords: *SoC, OCV, Auxiliary controlled load, Lithium-ion battery, Dynamic load*

1. INTRODUCTION

SoC can be one of the most important parameters of lithium-ion batteries for efficient and secure use in different fields such as control of photovoltaic–wind–battery systems [1], Electrical vehicle [2–4], microgrid energy management [5, 6], and numerous other applications. There exist many methods for SoC estimation such as Coulomb counting [7, 8], open circuit voltage (OCV) [9, 10], Model-based method [11], impedance spectroscopy [11,12], Kalman filter [13, 14], data-driven models [15, 16], etc.… Each of these methods has advantages and disadvantages, and still, more investigation is required.

Coulomb counting is one of the simplest and most effective ways to estimate SoC; however, it might suffer from drift caused by errors in current measurement and must be recalibrated from time to time. One of the calibration methods is Open Circuit Voltage (OCV); yet, this method requires the battery to be at rest (offline) for a long duration, which is not a favored option for many applications. Online OCV estimation is possible, and some online OCV estimate algorithms by adopting a certain Equivalent Circuit Model (ECM) were proposed for SoC estimation in the literature, which processes the real-time current and voltage of the load using Kalman Filter (KF), Extended Kalman Filter (EKF), Recursive Least Squares (RLS) [17–19].

However, the online OCV estimation is computational complex, and can be challenging with the existing methods because, in most applications, the load current, and voltage cannot be easily predicted or tracked effectively due to its drastic variations to be used for evaluating the OCV online. The proposed method in this paper is to add an auxiliary controlled load, which can be employed to get a known predefined shape of the current curve under some conditions (for instance, during the test, the dynamic load current cannot exceed a certain level) that will help to facilitate the online OCV calculations. The proposed technique is explained in the paper's context. A test bench is used, and a number of tests were performed as real typical scenarios to validate the approach's accuracy.

The proposed approach, the performed tests, the calculations, results and discussion, and finally the conclusion and future work are described next in this work.

2. THE PROPOSED OCV ESTIMATION TECHNIQUE

The proposed configuration is shown in Fig. 1(a). The main load of the system is a dynamic load like home, microgrid, as well as other systems, and its current cannot be predicted; hence, an auxiliary-controlled load is added. Therefore the battery current can be controlled, so, it will be the sum of the current consumed by both loads:

$$I_{battery} = I_{dynamic} + I_{controlled} \quad (1)$$

Test Setting:

Our method relies on the first order RC equivalent circuit of the lithium-ion [4] illustrated in Fig. 1(b), and the time constant is assumed to be less than *100s* according to Table 1 [4].

Table 1. Lithium-ion 1-RC model time constant in different states of charges [4]

SoC	τ_1/s	R_1/Ω	$C_1/10^3$ F
0	56.2430	0.0382	1.4743
0.05	42.8082	0.0263	1.6265
0.1	51.3875	0.0226	2.2758
0.15	47.5964	0.0244	1.9491
0.2	55.9597	0.0237	2.3622
0.3	34.7826	0.0203	1.7126
0.4	35.8938	0.0204	1.7612
0.5	41.9287	0.0211	1.9919
0.6	37.5657	0.0267	1.4049
0.7	40.6504	0.0242	1.6798
0.8	38.5654	0.0272	1.4178
0.9	37.3134	0.0235	1.5878
1	46.2321	0.0240	1.9287

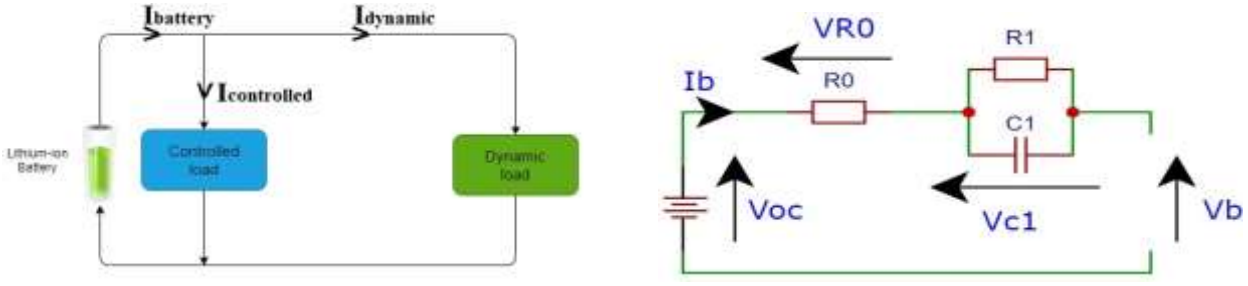

(a) *(b)*

Figure 1. The used circuits. (a) Dynamic load with auxiliary controlled load. (b) First order RC equivalent circuit model.

Illustration tests scenario were conducted as shown in Fig. 2 where from *0* to *500s*, the current was random and less than *500mA* similar to the dynamic load's current. After that, from *500s* to *1000s*, the current is fixed to *500mA* in order to simulate the controlled load intervention. Then, the current pulse of *300mA* was created at *1000s.* At *1030s*

the current was forced to *500mA* again for *30s*. Finally, at *1060s*, the battery current is *0A*, in real scenario after the OCV is estimated, the controlled load current becomes *0A*, and the battery current will be equal to the dynamic load current, however in the preformed tests scenario the battery was disconnected for around *1 hour* to get the open circuit voltage and compare it to the estimated OCV using the proposed method. Fig. 3(a) illustrates the points used for OCV calculation method.

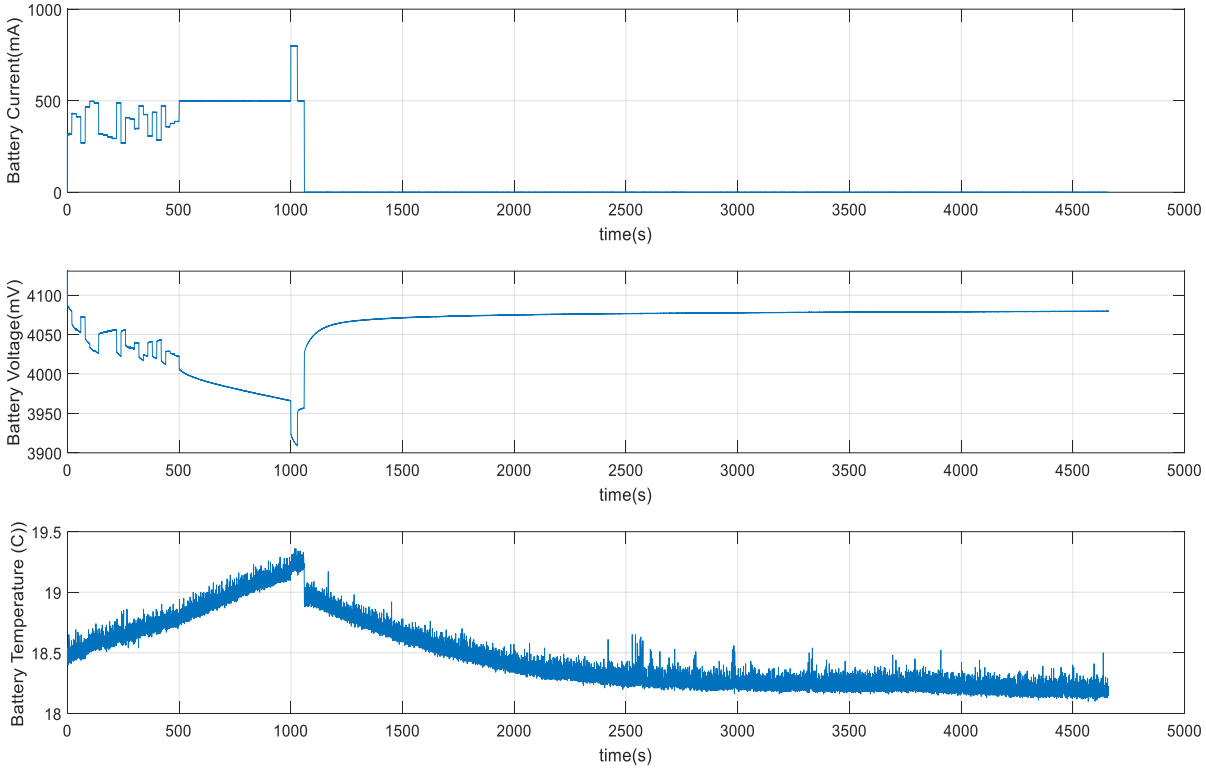

Figure 2. Conducted test illustration.

OCV Calculation:

First, the OCV drop per *30s* at *500mA* must be calculated. Since the current was *500mA* for *500s* the capacitor C1 can be assumed to be at its steady state and the voltage drop from *970s* to *1000s* can be expressed by Eq. [2]:

$$OCV_{\text{drop/30s@500mA}} = P1 - P2 \qquad (2)$$

Then, the OCV drop per *30s* at *800mA* must be calculated from *1000s* to *1030s*. Assuming that the OCV drop rate per current is constant during the test, so:

$$OCV_{\text{drop/30s@800mA}} = OCV_{\text{drop/30s@500mA}} * (800/500) \qquad (3)$$

When the pulse of *300mA* is applied from *500mA* to *800mA* the capacitor can be considered in the charging phase, as shown in Fig. 3(b). The charged voltage can be found using Eq. [4]:

$$Vcharged = P3 - P4 - OCV_{\text{drop/30s@800mA}} \qquad (4)$$

Whereas, the discharged voltage is calculated using Eq. [5] (see Fig. 3(b)):

$$Vdischarged = Vcharged - (P6 - P5 + OCV_{\text{drop/30s@500mA}}) \qquad (5)$$

The circuit charging equation can be expressed by Eq. [6] as follow:

$$0.3 * R1 * \left(1 - e^{-\frac{30}{T}}\right) = Vcharged \quad (6)$$

Whereas, the discharging equation can be written as follow:

$$Vdischarged = Vcharged * e^{-\frac{30}{T}} \quad (7)$$

Therefore, from Eq. [7] the time constant T can be extracted by Eq. [8]:

$$T = -30/\ln\left(\frac{Vdischarged}{Vcharged}\right) \quad (8)$$

Then, T can be substituted in Eq. [6] to calculate R1 as explained in Eq. [9]

$$R1 = \frac{Vcharged}{0.3\left(1 - e^{-\frac{30}{T}}\right)} \quad (9)$$

And

$$R0 = \frac{P2 - P3}{0.3} \quad (10)$$

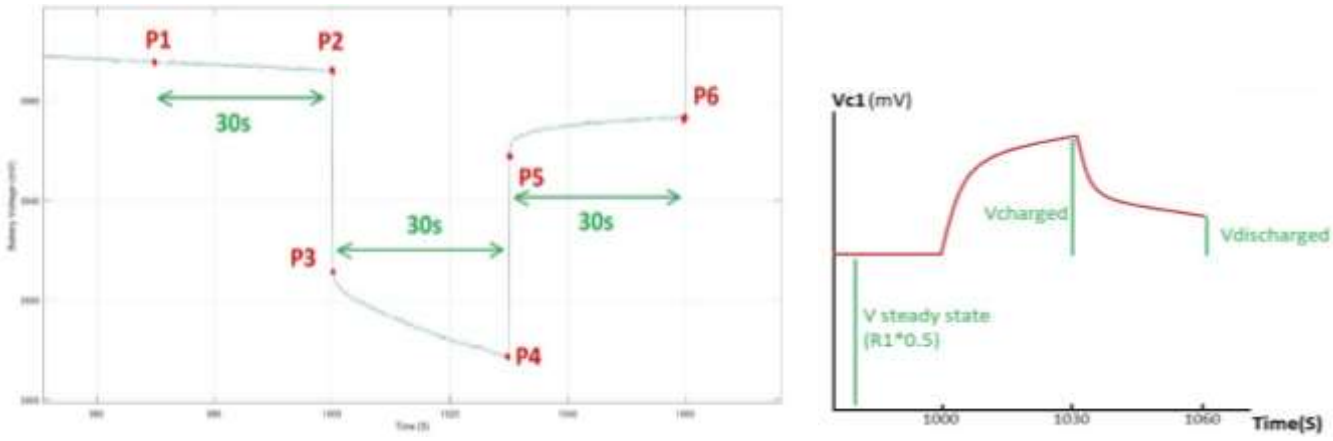

(a) *(b)*

Figure 3. Zoomed-in voltage of the test. (a)Illustration of the pointes used for the OCV calculation. (b) Illustration of voltage charging and discharging curve shape of C1 during the test.

Finally, the estimated OCV can be calculated based on the model shown in Fig.2 where Voc=Vb+VR0+Vc1; assuming that Vc1 is in its steady state.

$$OCV@P2 = P2 + (R0 + R1) * 0.5 \quad (11)$$

Hence, the OCV in this test is calculated at P6; hereafter, it will be compared with the one-hour OCV.

$$OCV@P6 = OCV@P2 - OCV_{\text{drop/30s@800mA}} - OCV_{\text{drop/30s@500mA}} \quad (12)$$

C1 is not used to calculate the OCV; on the other hand, if needed it can be calculated using Eq. [13]:

$$C1 = \frac{T}{R1} \quad (13)$$

3. RESULTS AND DISCUSSION

The tests were performed on an aged lithium-ion cell that has the characteristics shown in Table 2.

Table 2. Characteristics of the used Lithium-ion battery cell

Manufacturer	Model	Rated capacity	Maximum voltage	Minimum voltage
LG	LGABD18650	3000 mAh	4.35V	3.0V

The used test bench diagram is shown in Fig. 4, it has already been used in previous work for battery characterization (the temperature-controlled chamber was not used) [20]. Where the ESP32 is the main control unit that controls the Relay1, Relay2, charging and discharging load for different battery tests. The ADS1115 is a 16bit 2's compliment ADC that reads the battery voltage and also the shunt resistor voltage to get the current. It measures also the temperatures and then sends the data to the ESP32; then, the ESP32 sends the data to the computer to be stored and processed. The test bench characteristics and the system performance are summarized in Table 3.

Table 3. The test bench performances

Voltage resolution	Current resolution	Configured sampling rate	Maximum voltage	Maximum current	Load hysteresis at *1A*	Voltage error	current error
0.187mA	0.153mA	10 Samples/S	5V	5A	<3.5mA	0.6mV	<1.5%

Table 4 (given as an appendix) summarized the results obtained from the tests as illustrated in Fig. 2. These tests are performed in a complete discharge cycle with room temperature around *16 °C* to *19 °C*. The error of the estimated OCV compared to the 1h-OCV (one-hour OCV) is consistent; on another side, some of it can be justified by the drift in the current sensor (see Table 3). The resulting error can be minimized by adding an offset of *13.90 mV* (the average error) to the estimated OCV, as shown in Table 4, the *1 hour* OCV, the estimated OCV, and the estimated OCV with the offset. When comparing the *1 hour* OCV with the (estimated OCV with offset), the error is very low, especially in the range where SoC is between *0.2* and *0.4* the plots almost identical, the error is less than *3.3 mV* (as illustrated in Fig. 5). The error in general does not exceed *8.5 mV* except for one error spike of *15.7 mV* where the SoC is around *0.63*, and also where the SoC is very low the error is high.

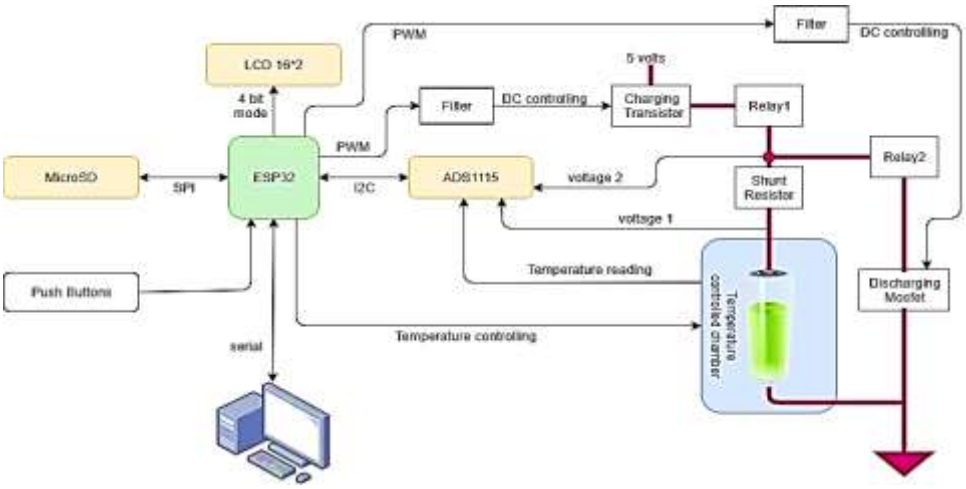

Figure 4. Battery test diagram used in this work [20].

As it can be noticed in the last tests where SoC is less than *0.2*, the error is not consistent, and that can be due to the rapid drop rate change of the Battery OCV. Hence, this method is not recommended at low SoC.

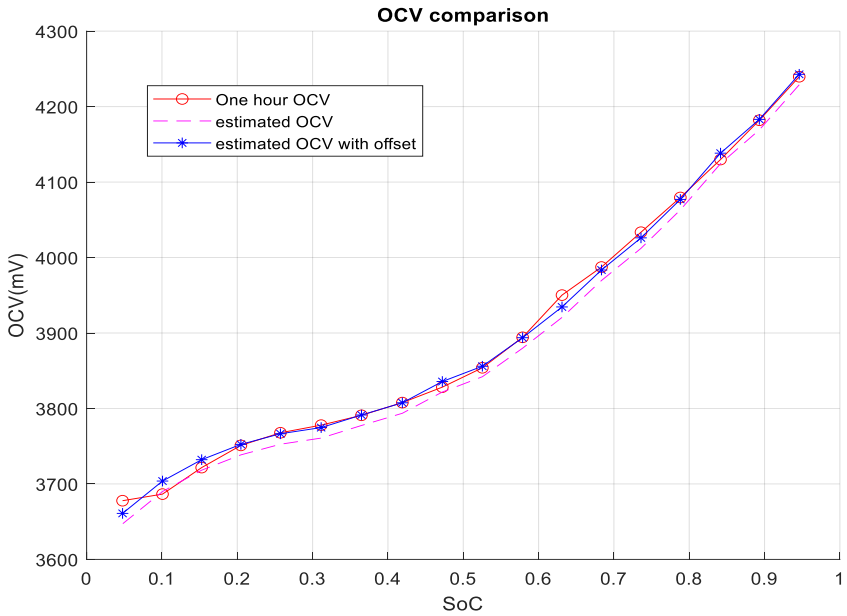

Figure 5. Comparison between the 1-hour OCV, the estimated OCV and the estimated OCV after adding the offset.

Fig. 6 (given as an appendix) summarizes the working principle of this proposed method. For example, this method can be used with coulomb counting method to calibrate its SoC that can happened from time to time to omit the drift that occurs. First, it reads the actual SoC that was tracked by coulomb counting; then, if the SoC is very low or the battery current is high, the recalibration should not be performed. Otherwise, the dynamic load maximum current during the estimation time should be assumed to be less than certain value X. After that, predefined current shape is applied by using the controlled load where the battery current should be equal or superior to the assumed current X. However, if the dynamic load current suddenly raised more than the assumed current X, the wanted current shape for calculating the OCV will be distorted. Therefore, the OCV estimation process will stop and the controlled load current will become zero, and start the process from the beginning.

On the other hand, if the estimation process completed successfully during the estimation time; then, the controlled load will become zero, and the online OCV can be calculated using the proposed method as described above. Thus, the SoC can mapped using the OCV-SoC lookup table and finally the coulomb counting SoC can be recalibrated. This process can be repeated periodically once recalibration is required.

4. CONCLUSION AND PERSPECTIVES

This paper described the working progress of an online OCV estimation method which is based on forcing a predefined current curve using an auxiliary controlled load, this novel technique can be ideal for coulomb counting calibration. The obtained results were acceptable according to the used battery test system which is not of high performance. Thus, some drift in the current sensor showed up. The potential advantages of this proposed method is that it is simple and has low computational complexity; moreover, it obtains the equivalent circuit model parameters online which enhance the accuracy, and reliability, thus it can be not affected by temperature and aging. Concerning our future work vision, our objective is to repeat these tests with a sophisticated shunt resistor, and with using calibrated and high-performance battery test bench system. In addition, the work can be tested under variable temperatures and also estimating the OCV with 2-RC equivalent circuit model or other models. Furthermore, more tests can be carried out for better forced current curves' shapes to get optimal performances.

Acknowledgment

We would like to thank DGRSDT (The Directorate-General for Scientific Research and Technological Development) for its financial help.

References

[1] M. Azaroual, M. Ouassaid, and M. Maaroufi, 'Model predictive control-based energy management strategy for grid-connected residential photovoltaic–wind–battery system', in *Renewable Energy Systems*, Elsevier, 2021, pp. 89–109. doi: 10.1016/B978-0-12-820004-9.00014-0.

[2] K. Wang, W. Wang, L. Wang, and L. Li, 'An Improved SOC Control Strategy for Electric Vehicle Hybrid Energy Storage Systems', *Energies*, vol. 13, no. 20, p. 5297, Oct. 2020, doi: 10.3390/en13205297.

[3] R. Zhang *et al.*, 'State of the Art of Lithium-Ion Battery SOC Estimation for Electrical Vehicles', *Energies*, vol. 11, no. 7, p. 1820, Jul. 2018, doi: 10.3390/en11071820.

[4] L. Zhang, H. Peng, Z. Ning, Z. Mu, and C. Sun, 'Comparative Research on RC Equivalent Circuit Models for Lithium-Ion Batteries of Electric Vehicles', *Appl. Sci.*, vol. 7, no. 10, p. 1002, Sep. 2017, doi: 10.3390/app7101002.

[5] H. Belaidi, H. Bentarzi, Z. Rabiai, and A. Abdelmoumene, 'Multi-agent System for Voltage Regulation in Smart Grid', in *Artificial Intelligence and Renewables Towards an Energy Transition*, vol. 174, M. Hatti, Ed. Cham: Springer International Publishing, 2021, pp. 487–499. doi: 10.1007/978-3-030-63846-7_46.

[6] H. Belaidi and Z. Rabiai, 'Decentralized Energy Management System Enhancement for Smart Grid':, in *Research Anthology on Smart Grid and Microgrid Development*, I. R. Management Association, Ed. IGI Global, 2022, pp. 77–90. doi: 10.4018/978-1-6684-3666-0.ch004.

[7] K. S. Ng, C.-S. Moo, Y.-P. Chen, and Y.-C. Hsieh, 'Enhanced coulomb counting method for estimating state-of-charge and state-of-health of lithium-ion batteries', *Appl. Energy*, vol. 86, no. 9, pp. 1506–1511, Sep. 2009, doi: 10.1016/j.apenergy.2008.11.021.

[8] W.-Y. Chang, 'The State of Charge Estimating Methods for Battery: A Review', *ISRN Appl. Math.*, vol. 2013, pp. 1–7, Jul. 2013, doi: 10.1155/2013/953792.

[9] G. Dong, J. Wei, C. Zhang, and Z. Chen, 'Online state of charge estimation and open circuit voltage hysteresis modeling of LiFePO4 battery using invariant imbedding method', *Appl. Energy*, vol. 162, pp. 163–171, Jan. 2016, doi: 10.1016/j.apenergy.2015.10.092.

[10] F. Zheng, Y. Xing, J. Jiang, B. Sun, J. Kim, and M. Pecht, 'Influence of different open circuit voltage tests on state of charge online estimation for lithium-ion batteries', *Appl. Energy*, vol. 183, pp. 513–525, Dec. 2016, doi: 10.1016/j.apenergy.2016.09.010.

[11] J. Meng *et al.*, 'An Overview and Comparison of Online Implementable SOC Estimation Methods for Lithium-Ion Battery', *IEEE Trans. Ind. Appl.*, vol. 54, no. 2, pp. 1583–1591, Mar. 2018, doi: 10.1109/TIA.2017.2775179.

[12] X. Wang, X. Wei, H. Dai, and Q. Wu, 'State Estimation of Lithium Ion Battery Based on Electrochemical Impedance Spectroscopy with On-Board Impedance Measurement System', in *2015 IEEE Vehicle Power and Propulsion Conference (VPPC)*, Montreal, QC, Oct. 2015, pp. 1–5. doi: 10.1109/VPPC.2015.7353021.

[13] P. Spagnol, S. Rossi, and S. M. Savaresi, 'Kalman Filter SoC estimation for Li-Ion batteries', in *2011 IEEE International Conference on Control Applications (CCA)*, Denver, CO, USA, Sep. 2011, pp. 587–592. doi: 10.1109/CCA.2011.6044480.

[14] B. Rzepka, S. Bischof, and T. Blank, 'Implementing an Extended Kalman Filter for SoC Estimation of a Li-Ion Battery with Hysteresis: A Step-by-Step Guide', *Energies*, vol. 14, no. 13, p. 3733, Jun. 2021, doi: 10.3390/en14133733.

[15] M. Ali *et al.*, 'An Online Data-Driven Model Identification and Adaptive State of Charge Estimation Approach for Lithium-ion-Batteries Using the Lagrange Multiplier Method', *Energies*, vol. 11, no. 11, p. 2940, Oct. 2018, doi: 10.3390/en11112940.

[16] Y. Wang, D. Yang, X. Zhang, and Z. Chen, 'Probability based remaining capacity estimation using data-driven and neural network model', *J. Power Sources*, vol. 315, pp. 199–208, May 2016, doi: 10.1016/j.jpowsour.2016.03.054.

[17] R. Xiong, Q. Yu, and L. Y. Wang, 'Open circuit voltage and state of charge online estimation for lithium ion batteries', *Energy Procedia*, vol. 142, pp. 1902–1907, Dec. 2017, doi: 10.1016/j.egypro.2017.12.388.

[18] Y. Song, M. Park, M. Seo, and S. W. Kim, 'Online State-of-Charge Estimation for Lithium-Ion Batteries Considering Model Inaccuracies Under Time-Varying Current Conditions', *IEEE Access*, vol. 8, pp. 192419–192434, 2020, doi: 10.1109/ACCESS.2020.3032752.

[19] J. Meng, M. Boukhnifer, and D. Diallo, 'Comparative study of lithium-ion battery open-circuit-voltage online estimation methods', *IET Electr. Syst. Transp.*, vol. 10, no. 2, pp. 162–169, Jun. 2020, doi: 10.1049/iet-est.2019.0026.

[20] A. Zermout, H. Belaidi, and A. Maache, 'Implementation of Battery Characterization System', in *ICCEIS 2022*, Jan. 2023, p. 12. doi: 10.3390/engproc2023029012.

APPENDICES

Table 4. The results table of the performed tests.

test-ref	P1 (mV)	P2 (mV)	P3 (mV)	P4 (mV)	P5 (mV)	P6 (mV)	R0 (mOhm)	R1 (mOhm)	τ (s)	estimated OCV (mV)	1H-OCV (mV)	error (mV)	error with offset (mV)
1.1	4129.89	4127.68	4087.19	4066.97	4108.22	4117.14	134.950	83.243	27.229	4228.91	4239.6	-10.69	3.21
1.2	4069.64	4067.61	4027.75	4007.88	4048.60	4057.60	132.850	83.497	27.538	4169.18	4181.94	-12.76	1.14
1.3	4018.71	4017.29	3978.43	3959.50	3998.92	4007.64	129.533	91.155	31.940	4124.39	4129.88	-5.49	8.41
1.4	3967.86	3966.05	3927.44	3908.80	3947.54	3956.60	128.683	75.962	25.563	4063.13	4079.59	-16.46	-2.56
1.5	3917.51	3915.51	3877.00	3857.93	3896.73	3905.54	128.367	77.722	26.273	4012.17	4033.56	-21.39	-7.49
1.6	3867.70	3866.23	3827.49	3808.34	3847.23	3856.89	129.123	84.525	27.623	3969.58	3987.41	-17.83	-3.93
1.7	3810.66	3809.22	3766.75	3745.24	3787.41	3799.98	141.567	87.839	22.981	3920.62	3950.22	-29.60	-15.70
1.8	3773.13	3771.94	3731.69	3711.96	3753.66	3764.75	134.160	86.232	25.689	3879.86	3894.28	-14.42	-0.52
1.9	3742.03	3740.83	3700.57	3682.27	3723.09	3734.16	134.193	72.875	21.684	3842.05	3853.9	-11.85	2.05
1.10	3717.95	3717.26	3676.75	3659.20	3699.66	3710.91	135.027	75.559	23.190	3821.80	3828.25	-6.45	7.45
1.11	3694.44	3693.61	3652.77	3635.29	3675.48	3687.79	136.117	66.144	17.852	3793.63	3807.77	-14.14	-0.24
1.12	3674.23	3673.75	3632.18	3614.95	3655.78	3668.31	138.567	69.527	19.245	3777.44	3790.93	-13.49	0.41
1.13	3657.15	3656.50	3615.25	3596.70	3637.79	3651.28	137.507	72.339	18.237	3760.75	3777.9	-17.15	-3.25
1.14	3643.78	3643.28	3602.30	3582.58	3624.09	3638.00	136.600	82.823	20.927	3752.59	3767.8	-15.21	-1.31
1.15	3626.32	3625.38	3583.18	3559.86	3601.97	3619.00	140.667	88.373	17.315	3738.50	3751.05	-12.55	1.35
1.16	3594.19	3592.40	3549.42	3518.17	3561.84	3582.72	143.267	118.570	18.743	3718.22	3721.64	-3.42	10.48
1.17	3538.91	3536.94	3490.54	3444.61	3491.52	3526.81	154.667	163.711	14.648	3689.92	3686.52	3.40	17.30
1.18	3491.06	3486.12	3436.53	3366.39	3415.78	3465.86	165.300	234.661	13.923	3647.05	3677.77	-30.72	-16.82

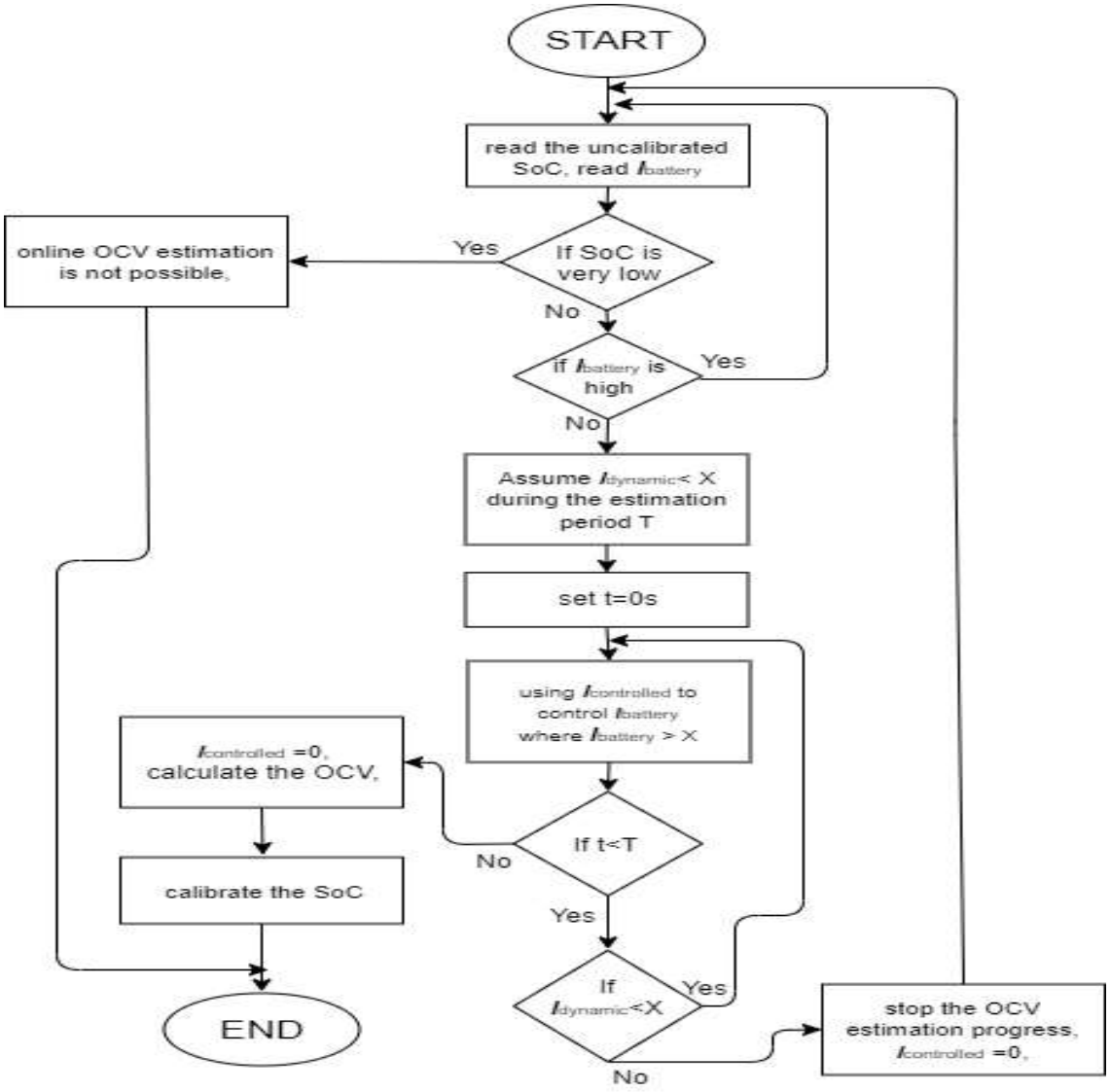

Figure 6. The flowchart representing the described method.

RIGA 2023

Experimental Investigation of PCM Based Thermal Energy Storage Unit with Finned Tubes

Maciej Jaworski
Warsaw University of Technology, Warsaw, Poland, maciej.jaworski@pw.edu.pl, ORCID: 0000-0001-8506-3534

Artur Rusowicz
Warsaw University of Technology, Warsaw, Poland, artur.rusowicz@pw.edu.pl, ORCID: 0000-0001-7949-6907

Andrzej Grzebielec
Warsaw University of Technology, Warsaw, Poland, andrzej.grzebielec@pw.edu.pl, ORCID: 0000-0003-3320-5929

Adam Szelągowski
Warsaw University of Technology, Warsaw, Poland, adam.szelagowski@pw.edu.pl, ORCID: 0000-0003-1017-1949

Cite this paper as: *Jaworski, M, Rusowicz, A, Grzebiele, A, Szelągowski A. Experimental investigation of PCM based thermal energy storage unit with finned tubes. 11. Eur. Conf. Ren. Energy Sys. 18-20 May 2023, Riga, Latvia*

Abstract: The paper presents the results of an experimental investigation of the thermal energy storage unit with phase change material (PCM) and finned tubes for heat transfer fluid (HTF). The research was focused on the discharge of the storage unit, mainly on the temperature variations of HTF at the outlet of the unit during this process. This temperature shows the quality of heat released from the storage unit and the exergy efficiency of the thermal energy storage process. In the research reported in this paper, the influence of HTF temperature at the inlet to the unit and HTF flow rate were analyzed. The experimental tests were performed at a specially developed stand allowing also for visualization of the process of PCM solidification. The results showed that the removal of heat from the storage unit is of relatively low intensity, even with the finned surface area on the PCM side, resulting in substantial losses of the quality (exergy) of accumulated heat. To reduce these losses temperature of HTF should be very close to the melting point of PCM or relatively small flow rates should be applied.

Keywords: *Phase change materials, thermal energy storage, experimental investigation*

1. INTRODUCTION

Latent heat thermal energy storge (LHTES), the technique based on the use of phase change materials (PCM) as a medium accumulating heat, is still the most promising technology of thermal energy storage. PCMs, thanks to their high thermal capacity in the temperature range around melting point, are able to absorb (during charging) and subsequently release (during discharging) large amount of heat with relatively small changes of temperature of the medium transferring heat to and from TES unit. Although, heat storage techniques utilizing enthalpy of chemical reactions or heat of sorption processes are characterized by much higher thermal capacity, but they are not yet as mature as those with PCMs [1, 2, 3].

Although LHTES is a mature technology, it is still the subject of many scientific studies, also of a basic nature, because there is still potential to increase the efficiency of heat storage. The most important problems that require special attention include the stability of the thermophysical properties of PCM materials (especially the inorganic ones), supercooling occurring during solidification of some kinds PCMs, as well as the low intensity of heat transport resulting from relatively low thermal conductivity of PCMs [4]. To improve heat transfer to/from the PCM, thus increasing the rate of charging/discharging of the storage unit, different configurations of heat exchangers (storage unit is in fact a kind of a heat exchanger) are considered. The most often used configuration is based on the shell and tube HEx, where heat transfer fluid flows inside tubes that have finned external surface

(embedded in PCM zone) [5, 6, 7]. Other storage units use capsulated PCM, in the capsules of different shapes, embedded in the tank filled with e.g. water [8, 9]. There are also concepts with PCM inside tubes [10].

Thermal performance characteristics of PCM based storage unit are defined in a different way, e.g.: time of charging/discharging, rate of these processes, power per unit mass of PCM during discharging, also detailed characteristic of melting process [5, 6, 10, 11, 12]. Specific research goals are: optimization of fin configuration [5, 6, 13], variation of PCM and heat transfer fluid temperatures during charging and discharging [8, 12, 14].

Reviewing literature it can be seen that the majority of studies, related to the performance of storage units, are focused on detailed analysis of heat transfer process during charging and discharging, especially on melting and solidification of PCM. The research is conducted both experimentally and/or using mathematical modelling and numerical techniques. It is very important issue for cognitive reasons, however from the point of view of the user of heat which is accumulated, the most important is the quality of heat delivered to him during discharge of the store. In other words the user is rather interested in the temperature of heat transfer fluid during discharging. Taking the above into consideration an experimental study was proposed, which is basically focused on the investigation of the influence of different parameters on the performance characteristics of the discharge phase on the storage, with particular emphasis on heat transfer fluid temperature variations with time. The storage unit with finned pipes (external fins) was selected. An experimental stand was designed in such a way that pipes with different fins could be investigated.

2. EXPERIMENTAL SET-UP AND METHODOLOGY

Experimental tests were conducted in a specially prepared model of TES unit in a form of a rectangular box of dimensions consistent with dimensions of the heat exchanger. The heat exchanger, the duct for heat transfer fluid, was made of stainless steel pipes with a rounded fines. External dimension of the pipe is 10 mm, thickness of the wall 1 mm. The thickness of the fin is 1 mm, the height 10 mm, the distance between the fins is 10 mm (9 mm gap). In this paper the results for the above finned configuration are presented. The complex research includes the study of fins with of different heights and made of different materials (copper and aluminum). The heat exchanger is made of 6 pipes, each of 1 m length, so the total (effective, finned) length of HEx is equal to 6 m. Individual pipes are connected with a plastic pipes, in some of them (the connectors) temperature sensors are inserted. The photo of the heat exchanger/package of the finned pipes is shown in Fig. 1. This package is located in the rectangular box which is then filled with PCM. The box is made of PMMA (plates of 10 mm thickness) thus allowing visualization of the process of PCM solidification. For the external diameter of finned pipe equal to 30 mm the with of the box is equal to 34 mm – the distance between fins of neighboring pipes and the pipe and the wall of the box is equal to 2 mm. During the tests the whole box was thermally insulated with the plates, 30 mm thickness, made of a foam.

Figure 1. Finned tubes based heat exchanger.

During charging of the unit hot water flows from the top (upper pipe) to the bottom. During discharging the flow is reversed. This allows that the melting starts in the upper part of the box, while during solidification solid phase starts to create in the lower part.

In the study discussed hear phase change material RT62HC (Rubitherm, Germany) was used. The melting point is around 62°C. Heat storage capacity in the temperature range from 55 to 70°C is estimated to 230 kJ/kg, however the majority of thermal energy, nearly 200 kJ/kg, is absorbed/released in a narrow temperature range 61-63°C [15].

Thermal conductivity 0.2 W/(m·K), density of solid and liquid 0.85 and 0.84 kg/dm^3 (thermophysical data provided by manufacturer). The provider of this PCM declares its corrosive effect on metals, this was a reason for the selection of stainless steel pipes in the initial part of the research [16].

The box, TES unit, was filled with melt PCM just above the edge of the fins in the upper pipe.

Heat transfer fluid (water) temperature was controlled in the thermal bath (DD-900F, Julabo, Germany), with a volume capacity equal to 25 litres. The thermal bath also provided control of flow rate of water. More precise setting of the flow was done by means of a valve in the water path.

The main aim of the research was determination of performance characteristics of the storage unit during its discharge, especially the variations of heat transfer fluid temperature at the outlet of the unit during the time of this process. Based on this measurements also output heat power can be determined.

For this purpose four temperature sensors were located along the path of water flow. The thermocouples (type K, diameter 0.5 mm, manufacturer Omega, USA) were inserted inside the plastic pipes at the inlet and outlet of the heat exchanger and inside connectors (red pies visible in Fig. 1). Temperature was measured at the inlet after 2 and 4 meters from the inlet and at the outlet. Temperatures were recorded using an ADDA converter (National Instrument, PCI-6281 with module SCB-68) [17, 18, 19]. After connection to the signal convertor all thermocouples were calibrated in the temperature range from 20 to 80°C using mentioned above thermal bath. In the water path there was a three-way valve allowing a precise control of the flow through the heat exchanger inside TES unit. The actual value of the flow rate was controlled by means of a rotameter (Dwyer, USA).

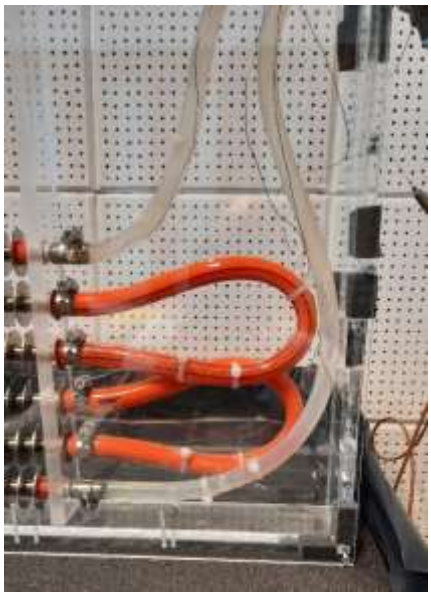

Figure 2. Heat exchanger inside the box (TES unit), thermocouples inserted in the water pipes.

Before the main test the TES unit was charged with a hot water – temperature 70°C, set in the thermal bath – until PCM inside he box completely melted. In the charged state temperature of the PCM was around 69°C (temperatures indicated by the sensors inside the box).

The tests were performed in different operational condition, the influence of two parameters on the process of discharging was investigated:

- water flow rate – three values were selected: 0.5, 1.0 and 1.5 l/min; these correspond to water velocities in the pipes: 0.165, 0.33 and 0.49 m/s;
- cooling water temperature at the inlet to the TES unit: 25°C, 35°C and 45°C.
-

3. RESULTS AND DISCUSSIONS

Figure 3 shows the set of results obtained for the case with inlet water temperature equal to 35°C and for different flow rates. In each figure temperature variations of water in different points of heat exchanger are shown – at the inlet (T_in), after passing two first pipes (T_2), two meters from the inlet, after passing four pipes (T_4), four meters from the inlet and at the outlet (T_out). The time of each test is different since with increasing flow rate the intensity of cooling also increases. The test was finished when water temperature increase in the TES unit dropped to about 5 K (which can be seen in the following charts). These tests show also that the experimental set-up requires improvement since in this configuration it gives no possibility to stabilize inlet temperature of water during the process – although water capacity of thermal bath is rather high, its cooling capacity is insufficient for heat power rates of discharging (this problem was not observed during heating/charging of TES unit).

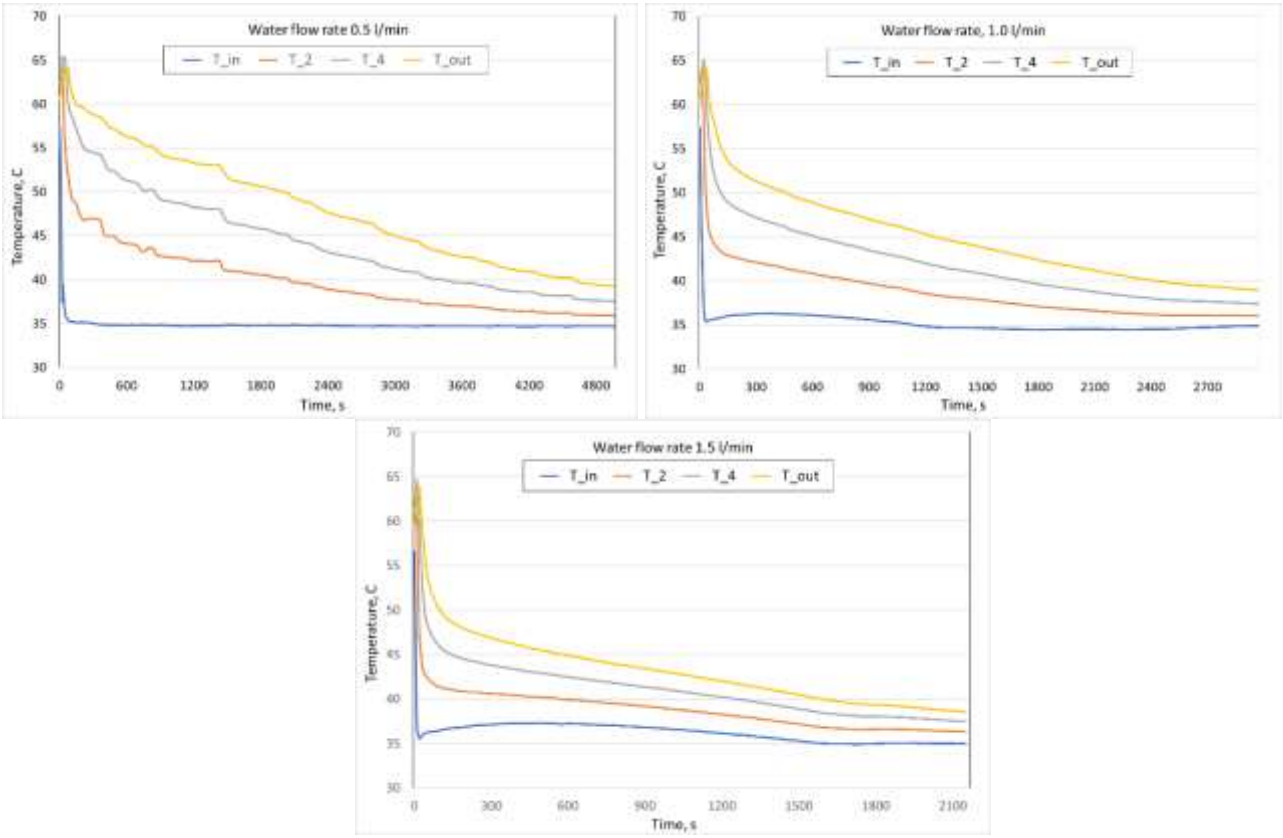

Figure 3. Water temperature variations in time of discharging for different flow rates and for inlet temperature equal to 35 ℃.

Figure 4. A photo of a heat exchanger with the shape of solidification front after 14 minutes from the beginning of discharging; water flow rate 1.0 l/min, water inlet temperature 45 ℃.

Similar tests were performed for other values of inlet water temperature, i.e. for 25°C and 45°C. For these tests only cumulative measurement results are discussed later.

In Fig. 4 one can see a photo of the part of the finned heat exchanger during solidification. The creation of solid phase of PCM on the surface of the pipe is visible. The thickness of the solid PCM is clearly greater on the surface of the pipe, much lower on the surface of the fins – this is due to the fact, that stainless steel has rather poor thermal conductivity and heat transfer along fins is not so intense. Also, much larger amount of solidified PCM can be observer on the first pipe in the package, i.e. at the bottom. This is the pipe into which the cool water flows directly from the thermal bath. The water heats and its temperature is higher in the subsequent pipes. However, it looks like the intensity of solidification on the other pipes was on the same level.

In the following charts – Figures 5 to 7 – cumulative results for all tests are presented. For each value of inlet water temperature under consideration the following results are shown: increase of heat transfer fluid temperature during heat removal (discharge of the TES unit) as a function of the time of the process (left charts) and temporal variations of heat output power during the discharge of the unit (right charts).

What seems to be obvious, temperature increase of the cooling water is much higher when its flow rate is lower. And the temperature rise decreases much slower with the time of the process, and the process of discharging (with the criterions of its end mentioned earlier) lasts longer – blue lines in the charts. Left charts show also a distinct difference between curves for flow rates 0.5 l/min and 1.0 l/min, but the difference between curves for 1.0 and 1.5 l/min is not so significant. This suggest that the change of the flow rate form 0.5 to 1.0 l/min (change of water velocity form 0.16 to 0.33 m/s) is associated with the substantial change of the intensity of heat transfer on the water side.

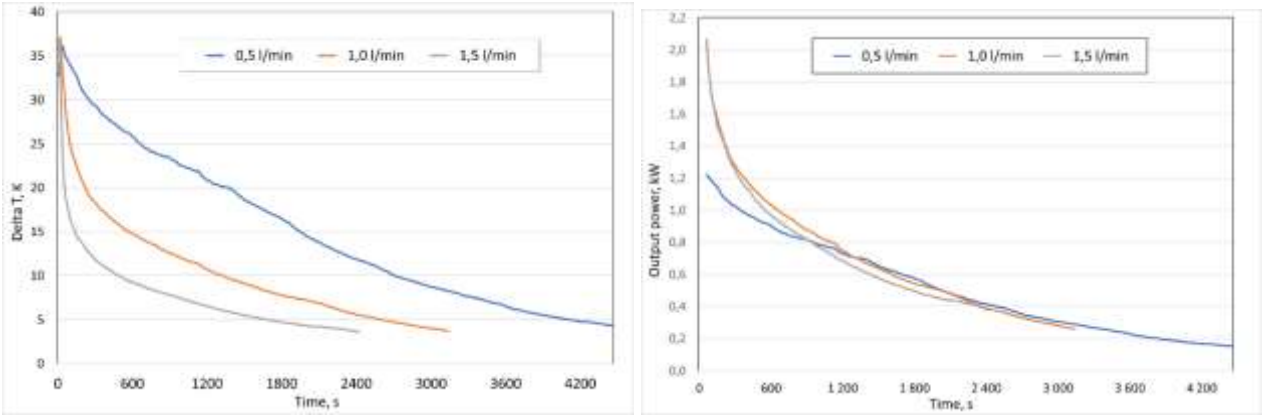

Figure 5. Water temperature increase (left) and output power (right) during time of discharging for inlet temperature equal to 25 ℃.

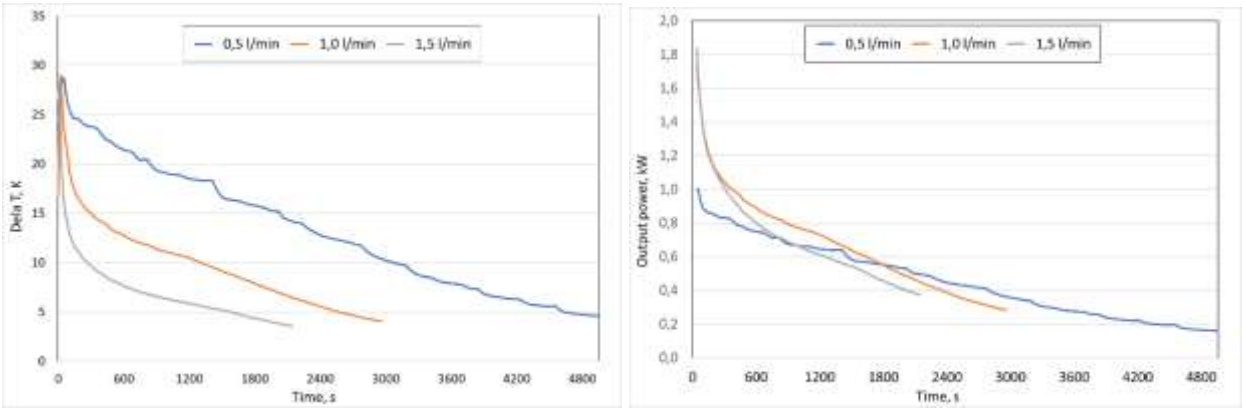

Figure 6. Water temperature increase (left) and output power (right) during time of discharging for inlet temperature equal to 35 ℃.

In right charts one can see temporal variations of heat output power for TES unit for different inlet water temperatures. What is interesting, output power seems to be independent from the water flow rate. Significant differences are observed in the initial phase of the process, but this could be the result of inaccuracy of the measurement , instability of the flow rate (which was noticed during the tests) and the differences in the initial state of the unit (PCM temperature distribution in the box). After rather short time all curves of heat output power have a close track. From these charts it can also be seen that heat output power ate the end of the discharging process decreases to the level of. 0.2 kW, in each case of inlet water temperature. But in the beginning the values are substantially different – about 1.2 kW for 25°C, about 1.0 kW for 35°C and about 0.7 kW for 45°C. That means that with the inlet water temperature closer to the melting point of phase change material (the level of temperature at which the majority of heat is accumulated) the characteristics of discharge, here characterised by the output power, are more stable in time.

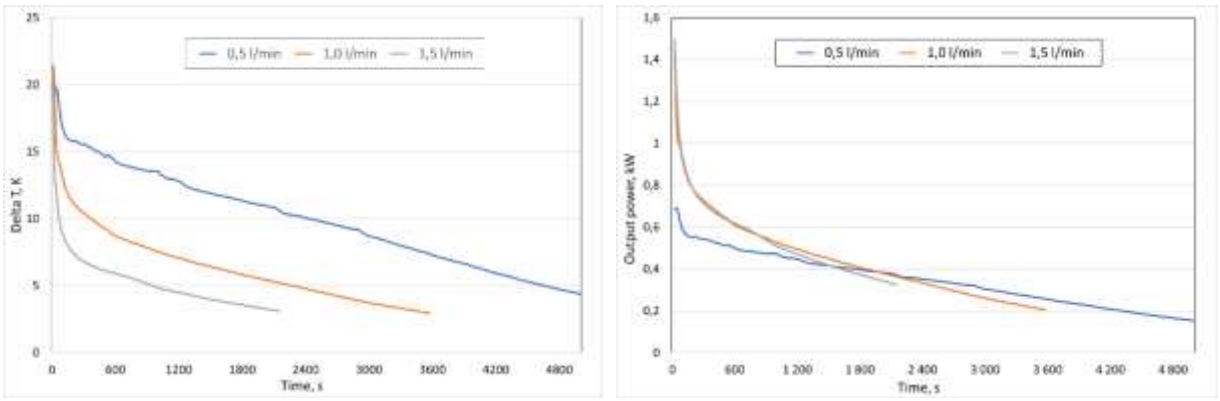

Figure 7. Water temperature increase (left) and output power (right) during time of discharging for inlet temperature equal to 45 ℃.

4. CONCLUSIONS

The paper present the results of the preliminary experimental study focused on the thermal behavior characteristics of latent heat thermal energy storage unit with heat exchanger made of pipes with finned external surface. One configuration of the unit was tested, i.e. the unit with fins of 10 mm height, but different parameters of operation (charging/ discharging) were taken into account. The study was focused on the discharging of the TES unit.

Based on the tests performed, a few conclusions/observations can be formulated:

- Although the length of the heat exchanger (heat transfer fluid path) was rather long (6 meters), and the PCM side was finned, outlet water temperature rapidly decreased during discharging process. With the assumption that the process finished when water temperature rise in TES unit decreased to 5 K, the duration of the process was from about 35 minutes for flow rate 1.5 l/min to about 80 minutes for flow rate 0.5 l/min.
- It is much better to use heat transfer fluid of an inlet temperature closer to the melting point of PCM. In such a case outlet water temperature during discharging is higher, that also means that exergy losses in the process of heat storage ale lower. With higher inlet water temperature also heat output power temporal variations are more smooth than in other cases (lower inlet temperatures).

Acknowledgment

The study was financed by the National Centre for Research and Development (Poland) in the framework of the grant No POIR.04.01.04-00-0100/17.

References

[1] Rocha, T.T.M, Martins T.T, Trevizoli P.V, de Oliveira R.N. A timeline of the phase-change problem for latent thermal energy storage systems: A review of theoretical approaches from the 1970′s to 2022, Solar Energy 2023, 250, 248-284, https://doi.org/10.1016/j.solener.2022.12.035.
[2] Delgado-Diaz, W, Stamatiou, A, Maranda, S, Waser, R, Worlitschek, J. Comparison of Heat Transfer Enhancement Techniques in Latent Heat Storage, Applied Sciences 2020, 10, 5519; doi:10.3390/app10165519
[3] Maldonado, J.M, de Gracia, A, Cabeza, L.F. Systematic review on the use of heat pipes in latent heat thermal energy storage tanks, Journal of Energy Storage 2020, 32, 101733, https://doi.org/10.1016/j.est.2020.101733
[4] Khademi, A, Shank, K, Mehrjardi, S.A.A, Tiari, S, Sorrentino, G, Said, Z, Chamkha, A.J, Ushak, S. A brief review on different hybrid methods of enhancement within latent heat storage systems, Journal of Energy Storage 2022, 54, 105362, https://doi.org/10.1016/j.est.2022.105362
[5] Mahdi, M.S, Mahood, H.B, Alammar, A.A, Khadom, A.A. Numerical investigation of PCM melting using different tube configurations in a shell and tube latent heat thermal storage unit, Thermal Science and Engineering Progress 2021, 25, 101030, https://doi.org/10.1016/j.tsep.2021.101030
[6] Deng, S, Nie, Ch, Jiang, H, Ye, W-B. Evaluation and optimization of thermal performance for a finned double tube latent heat thermal energy storage, International Journal of Heat and Mass Transfer 2019, 130, 532-544, https://doi.org/10.1016/j.ijheatmasstransfer.2018.10.126
[7] Koukou, M.K, Vrachopoulos, M.Gr, Tachos, N.S, Dogkas, G, Lymperis, K, Stathopoulos, V. Experimental and computational investigation of a latent heat energy storage system with a staggered heat exchanger for various phase change materials, Thermal Science and Engineering Progress 2018, 7, 87-98, https://doi.org/10.1016/ j.tsep.2018.05.004
[8] Afshan, M.E, Selvakumar, A.S, Velraj, R, Rajaraman, R. Effect of aspect ratio and dispersed PCM balls on the charging performance of a latent heat thermal storage unit for solar thermal applications, Renewable Energy 2020, 148, 876-888, https://doi.org/10.1016/j.renene.2019.10.172
[9] Koželj, R, Mlakar, U, Zavrl, E, Stritih, U, Stropnik, R. An experimental and numerical analysis of an improved thermal storage tank with encapsulated PCM for use in retrofitted buildings for heating, Energy and Buildings 2021, 248, 111196, https://doi.org/10.1016/j.enbuild.2021.111196
[10] Chen, G, Sun, G, Jiang, D, Su, Y. Experimental and numerical investigation of the latent heat thermal storage unit with PCM packing at the inner side of a tube, International Journal of Heat and Mass Transfer 2020, 152, 119480, https://doi.org/10.1016/j.ijheatmasstransfer.2020.119480
[11] Bentivoglio, F, Rouge, S, Soriano, O, Tempass de Sousa, A. Design and operation of a 180 kWh PCM heat storage at the Flaubert substation of the Grenoble urban heating network, Applied Thermal Engineering 2021, 185, 116402, https://doi.org/10.1016/j.applthermaleng.2020.116402
[12] Agarwal, A, Sarviya, R.M. An experimental investigation of shell and tube latent heat storage for solar dryer using paraffin wax as heat storage material, Engineering Science and Technology, an International Journal 2016, 19, 1, 619-631,

https://doi.org/10.1016/j.jestch.2015.09.014
[13] Yang, X, Guo, J, Yang, B, Cheng, H, Wei, P, He, Y-L. Design of non-uniformly distributed annular fins for a shell-and-tube thermal energy storage unit, Applied Energy 2020, 279, 115772, https://doi.org/10.1016/j.apenergy. 2020.115772
[14] Youssef, W, Ge, Y.T, Tassou, S.A. CFD modelling development and experimental validation of a phase change material (PCM) heat exchanger with spiral-wired tubes, Energy Conversion and Management 2018, 157, 498-510, https://doi.org/10.1016/j.enconman.2017.12.036
[15] www.rubitherm.com
[16] Rolka, P, Karwacki, J, Jaworski, M. Compatibility Tests between Three Commercially Available Organic PCMs and Metals Typically Used in Fin-and-Tube Heat Exchangers. Materials 2021, 14, 5172. https://doi.org/ 10.3390/ma14185172
[17] Rusowicz, A, Laskowski, R, Grzebielec, A. The numerical and experimental study of two passes power plant condenser, Therma Science 2017, 21, 1, 353-362, https://doi.org/10.2298/TSCI150917011R
[18] Jaworski, M, Bednarczyk, M, Czachor, M. Experimental investigation of thermoelectric generator (TEG) with PCM module, Applied Thermal Engineering 2016, 96, 527-533, doi: 10.1016/j.applthermaleng.2015.12.005
[19] Jaworski, M. Thermal performance of building element containing phase change material (PCM) integrated with ventilation system – An experimental study, Applied Thermal Engineering 2014, 70, 665-674, doi:10.1016/ j.applthermaleng.2014.05.093

RIGA 2023

Study of Thermodynamic Processes of Hydraulic Compression of Hydrogen by Numerical Simulation

Bezrukovs V
ERI VIRAC of Ventspils University of Applied Sciences, Ventspils, Latvia, elmag@inbox.lv, ORCID: 0000-0002-1755-497X

Bezrukovs Vl.*
Ventspils University of Applied Sciences Development Fund, Ventspils, Latvia, vladislavsb@venta.lv, ORCID: 0000-0003-3655-2280

Konuhova M.
ERI VIRAC of Ventspils University of Applied Sciences, Ventspils, Latvia, marina.konuhova@venta.lv, ORCID: 0000-0003-0743-5915

Bezrukovs D.
ERI VIRAC of Ventspils University of Applied Sciences, Ventspils, Latvia, dbezrukovs@gmail.com, ORCID: 0000-0002-7898-9870

Kaldre I.
Faculty of Physics, Mathematics and Optometry, University of Latvia, Riga, Latvia, imants.kaldre@lu.lv, ORCID: 0000-0003-1536-4539

Cite this paper as: *Bezrukovs V., Bezrukovs Vl., Konuhova M., Bezrukovs D., Kaldre I. Study of thermodynamic processes of hydraulic compression of hydrogen by numerical simulation. 11. Eur. Conf. Ren. Energy Sys. 18-20 May 2023, Riga, Latvia*

Abstract: The paper presents the results of numerical simulation of thermodynamic processes in a hydraulic hydrogen compression system applicable as a booster compressor in hydrogen refuelling stations. The modelling has been performed using COMSOL Multiphysics® 6.0 software with the CFD and Heat Transfer modules. To keep calculations relatively simple, the superposition method is used to simulate the hydraulic compression of hydrogen. In this case, the properties of working fluid and hydrogen are uniformly distributed and their volumes do not mix during the compression process. The calculations are carried out for several volumes of stainless-steel compression chamber having height of 145, 290, 435 and 725 *mm*, inner diameter 100 *mm* and wall thickness 5 *mm*. The simulations for inlet hydrogen pressures P_1 = 3.0 *MPa* and 20.0 *MPa* at a temperature of 300 *K* are evaluated. The authors consider thermodynamic processes performed during a single stroke t_s, with durations in the range of 0.5 to 20.0 *s*, with a compression factor K_c =5.0. The purpose of these simulations is to investigate the temperature change limits of hydrogen and working fluid. The results are given in the form of curves of temperature change for hydrogen and working fluid, allowing to estimate temperature conditions in the compression chamber and to estimate the energy consumption during the compression process. The results of the study can be used to enhance the efficiency of devices using the principle of hydraulic gas compression

Keywords: *Hydrogen, refuelling stations, hydraulic compressors, numerical simulations, CFD modelling.*

1.INTRODUCTION

In recent years, the use of hydrogen energy in transport and the concept of a hydrogen economy has benefited from another wave of strong political support. At the same time, rapidly evolving technologies have raised the possibility of using hydrogen as a driver for future carbon-neutral energy systems. At the heart of this initiative is the need for

energy security and independence. At the same time, the European Union has set an ambitious goal to become the first climate neutral continent by 2050, which is in line with the guidelines of the European Commission [1].

The conversion of hydrogen energy into electric current without burning it allows this attractive energy source to be used to power electric cars. Currently, there are already examples of successful implementation of hydrogen technology for cars and truck [2, 3]. However, when deploying hydrogen infrastructure for vehicle refuelling, it is essential to take advantage of simple and affordable devices for hydrogen compression tasks. The earliest known gas hydraulic compression application dates back to 1906. This solution was used in an internal combustion engine for pumping water, known as the Humphrey pump [4]. The Humphrey pump followed the Atkinson cycle and demonstrated efficiencies of between 5% and 10% [5]. The use of a liquid as a piston allows a significant increase in the efficiency of gas compression. Using a simplified model, it has been demonstrated that this concept can increase the compression efficiency from 70% to over 83% [6]. Several new technical solutions proposed by the authors [7 - 10] can also be used to solve this problem.

The results of the study of thermodynamic processes carried out by the means of numerical simulations presented in this paper allow to examine the temperature patterns of hydrogen and working fluid in the compression chamber and to estimate the energy consumption required for the hydraulic compression process of hydrogen. These findings can be used to improve the efficiency of devices using the principle of hydraulic gas compression.

2.THE NUMERICAL MODEL OF HYDROGEN HYDRAULIC COMPRESSION

The thermodynamic processes associated with hydrogen compression have been investigated using COMSOL Multiphysics® 6.0 software with CFD and Heat Transfer modules. As a reference computational model, a semi-symmetric stainless-steel cylinder with 145 *mm* height, 100 *mm* inner diameter and 5 *mm* wall thickness, with a volume of 1.14 *l*, shown in Fig. 1, was used. Initial parameters and physical properties of hydrogen, liquid piston and cylinder used in the model described in [11]. In the numerical simulations in the beginning of the compression process the inner space of the cylinder is filled with hydrogen with pressures P_1 = 3.0 *MPa* and 20.0 *MPa* at a temperature of 300 *K*. The thermodynamic compression process, takes into account heat exchange between gas, working fluid and cylinder walls, as well as the process of convective heat transfer to the surrounding space.

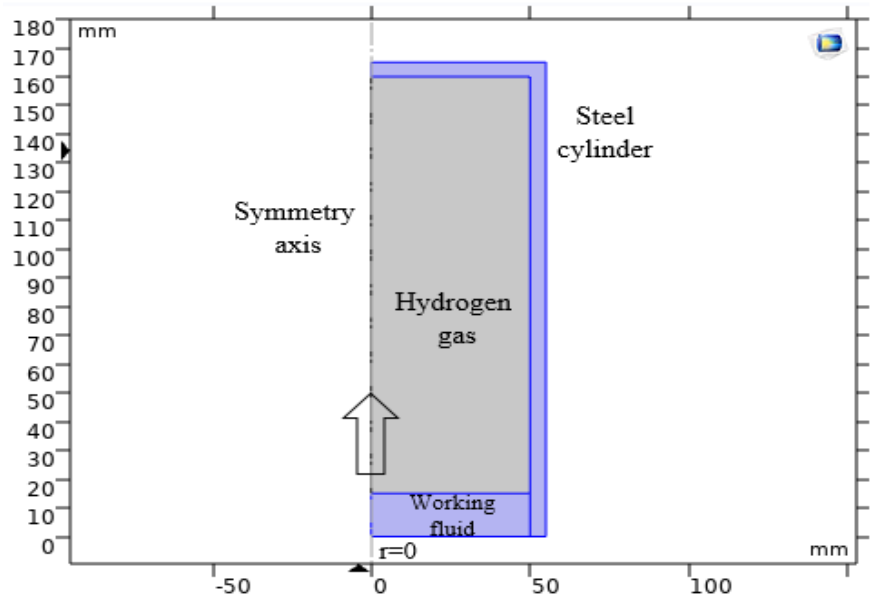

Figure 1. A basic model of a stainless-steel cylinder-shaped chamber where hydrogen is compressed by the working fluid coming from below in the direction of the arrow.

It should be noted that the gas compression process is accompanied by high heat generation and the high temperature of the compressed gas has an immediate effect on the working fluid. In fact, the fluid and the gas are compressed together, but since the fluid has a higher density and a higher heat capacity, the heat generated during compression is effectively absorbed by the fluid and the surrounding walls of the compression chamber.

The analysis of the results of these numerical simulations makes it possible to investigate the effect of different compression chamber geometries on the final gas temperature during the compression. Consequently, this allows to estimate the energy consumption required to raise the pressure at a given compression ratio K_c, depending on the speed of the compression process.

An example of temperature field distribution patterns derived from the numerical simulation for the hydrogen confined inside the cylinder body can be seen in Fig. 2. This figure shows changes in the gas temperature during a single 20-second stroke for time intervals: 0, 10, 15 and 20 *s*. The colour palette with a scale corresponds to the temperature limits of 300 – 550 *K*.

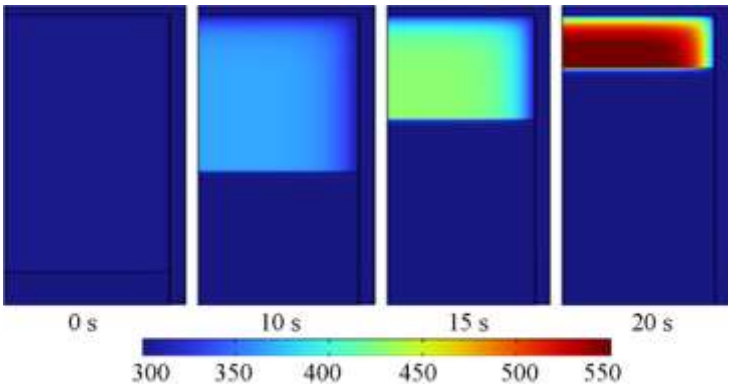

Figure 2. Distribution of the temperature of hydrogen in the compression cylinder during a single 20-second compression stroke. The hydrogen average temperature rises from 300 K to 488.6 K, at the initial pressure of P_1 = 3.0 MPa and compression ratio K_c = 5.0.

To keep calculations relatively straightforward, the superposition method is used to describe the process originating in the compression chamber. The process of increasing pressure in the cylinder chamber is a result of discrete changes of volume, which is filled with hydrogen and working fluid, taking into account the increase of gas temperature. The time of the discrete change of working fluid volume used in the calculations is constant and is set equal to Δt_s = 0.01 *s*. Each step of the discrete change increases the height of the fluid by a certain amount, determined by a given stroke time t_s. In this case, we assume that at each time step of the hydraulic compression of hydrogen in the model, the properties of working fluid and gas are uniformly distributed and their volumes do not mix. Heat transfer between hydrogen, working fluid and the walls of stainless-steel cylinder occurs only due to thermal conductivity of these materials.

The paper considers the processes occurring during a single compression stroke, the time t_s of which ranges from 0.5 to 20.0 *s*. Initial temperature of hydrogen and working fluid is 300 *K*, compression coefficient K_c = 5.0. Calculations are made for two scenarios, at the initial gas pressure of P_1 = 3.0 *MPa* and 20.0 *MPa*.

3.THE RESULTS OF THERMODYNAMIC MODELLING OF THE HYDROGEN COMPRESSION PROCESS

The purpose of the simulation is to investigate the temperature change limits of hydrogen, cylinder walls and working fluid during pressure increase by shrinking the gas volume in the compression chamber. Calculations have been carried out for several volumes of compression chamber, which have heights of 145, 290, 435 and 725 *mm* with wall thickness of 5 *mm* and a constant inner diameter of 100 *mm*.

The use of the superposition method makes it possible to consider the rise in temperature in each medium separately. The model specifies that the only heat source is compressible hydrogen. The presented results show the maximum temperature of the hydrogen, under the assumption that the mediums do not mix. In a real compression process, if the gas and fluid are intensively mixed, the gas will transfer heat to the fluid much more rapidly.

The energy consumed in the process of hydraulic compression of hydrogen depends on the rate of filling the compression chamber with fluid to achieve a certain compression ratio K_c. As a result, the structure of distribution of this thermal energy is shown in Fig. 3. The distribution of total energy Q_T between working fluid Q_F, hydrogen

Q_H and stainless-steel cylinder body Q_S is shown for different durations of the compression stroke t_s. The initial hydrogen pressures are P_1 = 3.0 *MPa* and 20.0 *MPa*, compression ratio set to K_c= 5.0. It can be noted that with raising inlet pressure up to 20.0 *MPa* most of the energy is concentrated in hydrogen as its mass increases with increasing pressure.

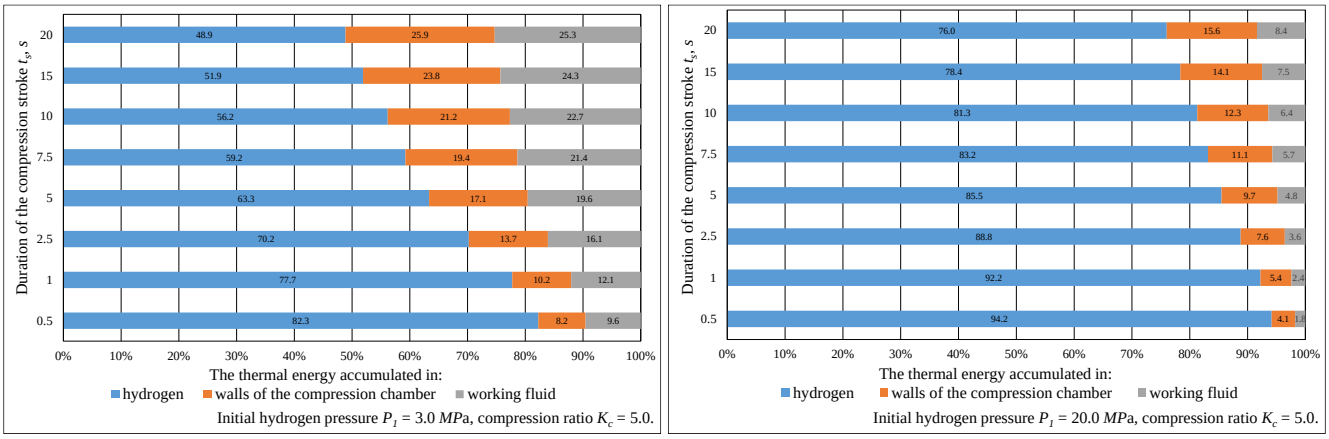

Figure 3. Diagram of total thermal energy distribution Q_T between energies accumulated in hydrogen Q_H, working fluid Q_F and compression cylinder body Q_s for different durations of the compression stroke t_s at initial pressures P_1 = 3.0 MPa (left) and 20.0 MPa (right).

As can be seen from Fig. 4, the increase in hydrogen temperature ΔT_H during the compression process significantly depends on the duration of the compression stroke and tends to increase slightly with increasing compression chamber volume and initial hydrogen pressure. By reducing the compression speed, the final gas temperature can be lowered considerably, resulting in lower energy consumption.

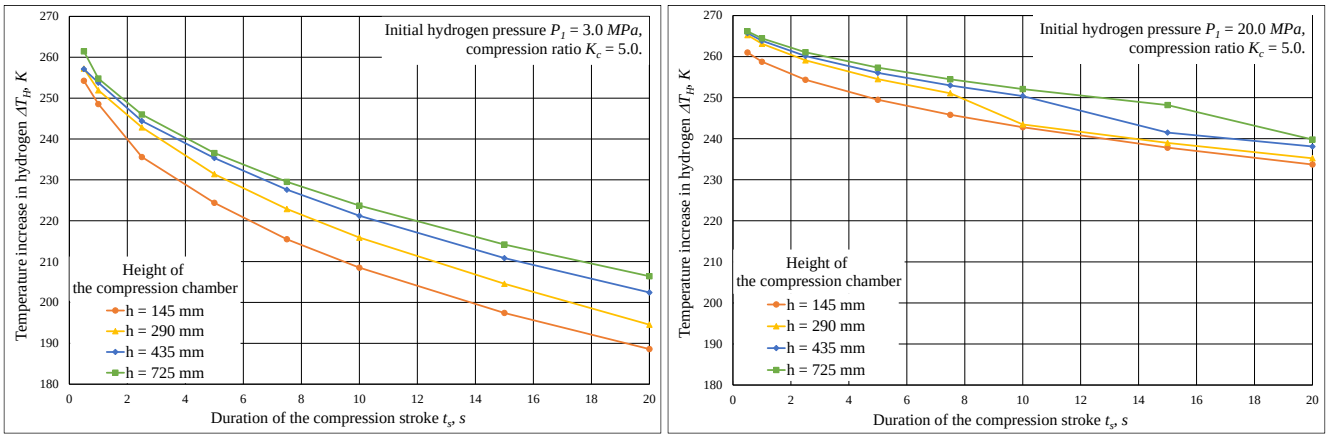

Figure 4. The curves of temperature increase in hydrogen ΔT_H for different durations of the compression stroke t_s at initial pressures P_1 = 3.0 (left) and 20.0 MPa (right). The compression chamber height varies from 145 mm to 725 mm.

The change in temperature of the working fluid ΔT_F, shown in Fig. 5, grows slowly as the compression stroke time extends. The volume occupied by the fluid and its high heat capacity generally determine the overall temperature inside the compression chamber.

The study of thermal processes taking place in the compression chamber shows that cooling the working fluid in an external heatsink can also effectively reduce the temperature of the compressed hydrogen and hence reduce the undesirable gas pressure resulting from the high gas temperature.

In real applications, hydrogen compression process takes place under the conditions of intensive gas and fluid stirring, leading to thermal energy transfer from hydrogen to the working fluid and subsequent pass through the walls of the cylinder. For the acceleration of heat transfer from gas to working fluid, it is suggested to use cylinder design with tangential fluid feed into the compression chamber [12].

To compare different compression scenarios, including stroke duration, initial pressure and cylinder geometry, overall temperature of the system ΔT_O, equivalent to the energy consumed for hydrogen compression, is employed. The changes of the ΔT_O for the different durations of compression stroke t_s are shown in Fig. 6. As the pressure in the compression chamber increases, the ΔT_O increases proportionally, as can be seen by comparing the curves for an initial pressure of 3.0 *MPa* and 20.0 *MPa*.

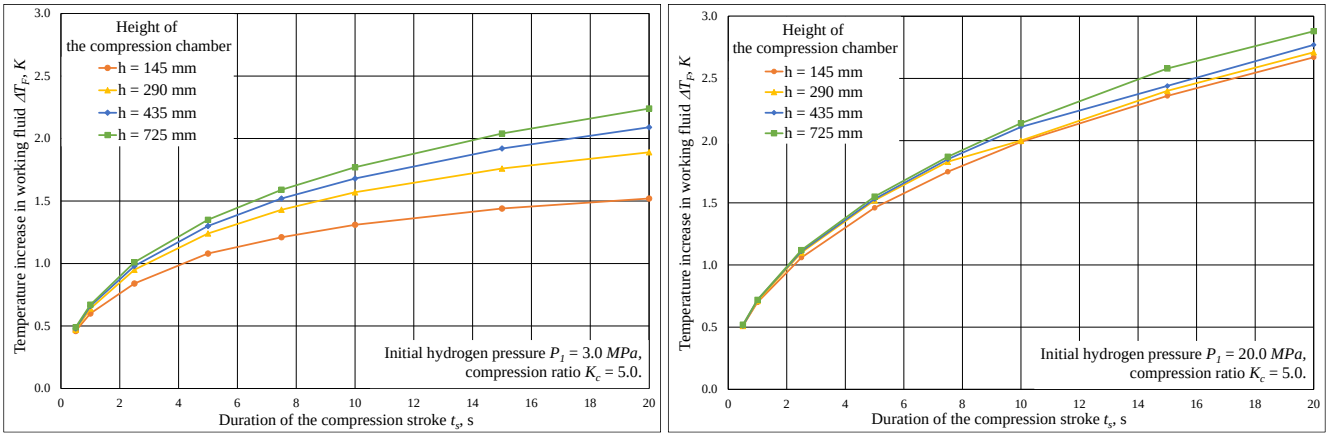

Figure 5. The curves of temperature increase in working fluid ΔT_F for different durations of the compression stroke t_s at initial pressures P_1 = 3.0 (left) and 20.0 MPa (right). The compression chamber height varies from 145 mm to 725 mm.

The results obtained with the considered numerical model allow to calculate the energy consumption and to estimate the power *W*, corresponding to the power of the motor that drives the liquid pump. Fig. 7 shows curves of power consumption for hydrogen compression for different durations of the compression stroke t_s for initial pressures P_1 = 3.0 *MPa* and 20.0 *MPa*.

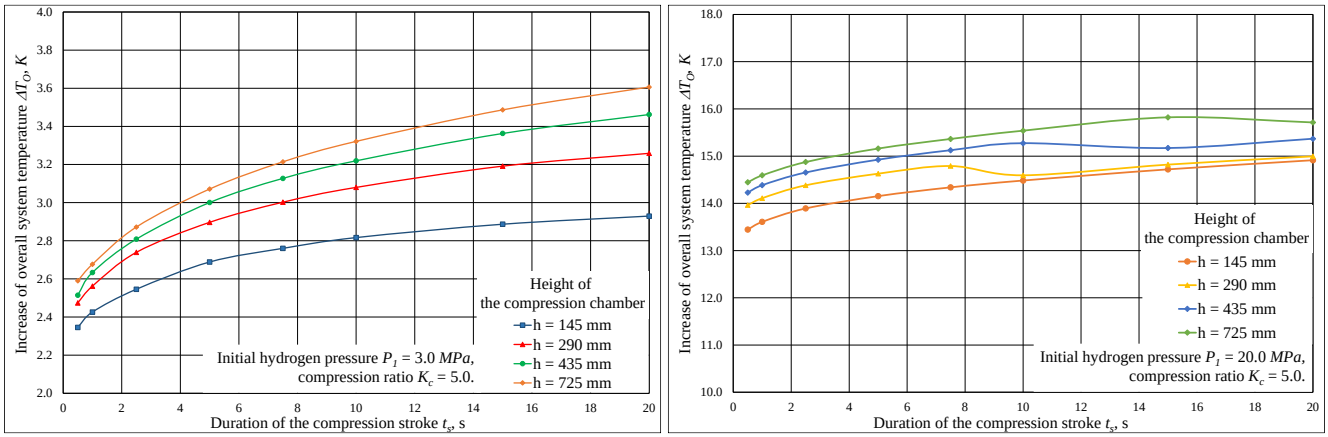

Figure 6. Increase of overall system temperature ΔT_O for different durations of the compression stroke t_s at initial pressures P_1 = 3.0 MPa (left) and 20.0 MPa (right). The compression chamber height varies from 145 mm to 725 mm.

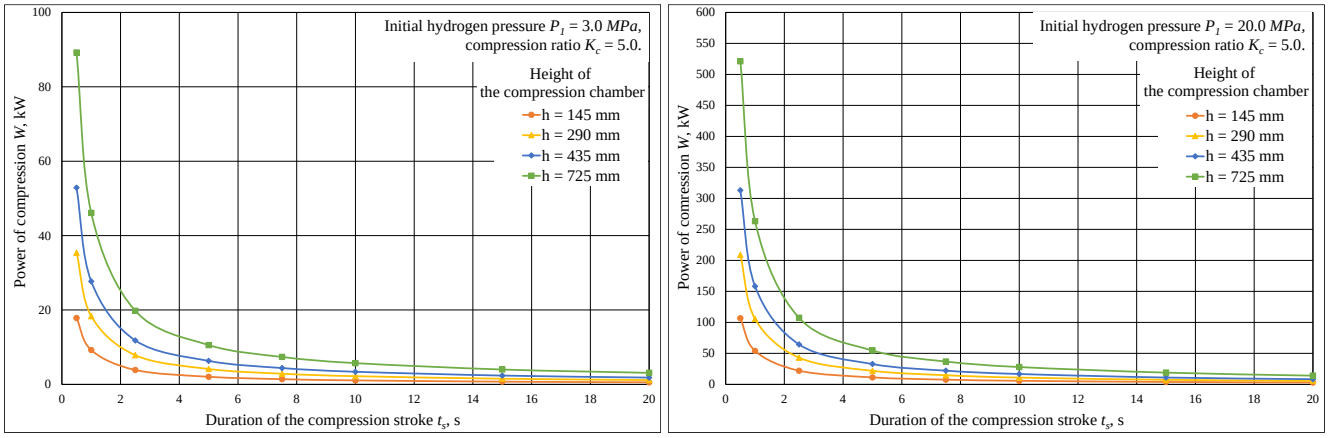

Figure 7. Curves of the power W required for hydrogen compression for different durations of the compression stroke t_s at initial pressures P_1 = 3.0 MPa (left) and 20.0 MPa (right). The compression chamber height varies from 145 mm to 725 mm.

4.DISCUSSION

The study of thermodynamic processes during hydraulic compression of hydrogen makes it possible to assess the heating limits of the gas, working fluid and walls, thus providing for a methodology to determine the optimum size of the compression chamber.

The results of simulations allow to estimate energy consumption and determine the setup conditions leading to the increase of efficiency of operation of the hydrogen compression system under consideration. This, in turn, makes it possible to determine the most suitable power rating for the motor that drives the liquid pump.

The analysis of the simulation results for a compression chamber with heights of 145, 290, 435 and 725 *mm* with a constant radius shows that the power required for compression increases in proportion to the initial hydrogen pressure and the mass of hydrogen in the chamber volume. It should be noted that the power required to drive the liquid pump decreases with increasing compression stroke duration.

Acknowledgments

This work is financed by ERDF project “Experimental studies and development of technology on hydraulic compression of hydrogen” No 1.1.1.1/20/A/185, being implemented in Ventspils University of Applied Sciences. We are grateful to the "Process Analysis and Research Centre (PAIC) Ltd” for support in the numerical modeling.

References

1. European Commission (2020): Communication from the Commission to the European Parliament, the Council, the European economic and social committee and the committee of the regions. A hydrogen strategy for a climate-neutral Europe. Brussels, 8.7.2020. COM (2020) 301 final.
2. Sdanghi G., Maranzana G., Celzard A., Fierro V. (2019): Review of the current technologies and performances of hydrogen compression for stationary and automotive applications, *Renewable and Sustainable Energy Reviews*, Volume 102, 2019, p. 150-170.
3. Fuel Cell Electric Vehicles. https://afdc.energy.gov/vehicles/fuel_cell.html. Available 10.01.2023.
4. Humphrey HA. (1909): An internal-combustion pump and other applications of a new principle. *Proc. Inst. Mech. Eng.* 1123.
5. Joyce NG. (1984). The Humphrey pump – an internal combustion pump. In: Proceedings of the conference on small engines and their fuels in developing countries, Reading, Berkshire, England. p. 31–44.
6. James D. Van de Ven, Perry Y. Li (2009): Liquid piston gas compression. *Applied Energy*. Volume 86. Issue 10. p. 2183–2191. doi:10.1016/ j.apenergy.2008.12.001
7. Bezrukovs V., Bezrukovs Vl., Bezrukovs D., Orlova S., Konuhova M., Berzins A., Kadakovskis J., Pranskus P. (2021): Hydrogen hydraulic compression device. PCT/IB2021/058102, 13.08.2021.
8. Bezrukovs V., Bezrukovs Vl., Bezrukovs D., Konuhova M., Berzins A. (2022): Hydrogen hydraulic compression device. LVP2022000071, 31.08.2022.

9. Bezrukovs V., Bezrukovs Vl., Bezrukovs D., Konuhova M., Berzins A. (2022): Hydrogen hydraulic compression device. PCT/IB2022/058904, 21.09.2022.
10. Bezrukovs V., Bezrukovs Vl., Konuhova M., Bezrukovs D., Berzins A. (2022): Hydrogen hydraulic compression system for refuelling stations, Latvian Journal of Physics and Technical Sciences 2022, N3, (Vol. 59), pp. 96-105. DOI: 10.2478/lpts-2022-0028.
11. Bezrukovs V., Bezrukovs Vl., Bezrukovs D., Konuhova M., Kaldre I, Berzins A (2023): R&D of a hydraulic hydrogen compression system for refuelling stations. Latvian Journal of Physics and Technical Sciences 2023, in print.
12. Bezrukovs V., Bezrukovs Vl., Bezrukovs D., Konuhova M., Berzins A. (2022): Cylinder for hydraulic compression of hydrogen with limited foam formation in the working fluid. LVP2022000090, 21.11.2022.

RIGA 2023

Grid-Connected and Grid-Islanded Energy Consumption Management

Djillali Kaddour
Signals and Systems Laboratory, Institute of Electrical and Electronic Engineering, University M'Hamed BOUGARA of Boumerdes, Boumerdes, Algeria, djillali.kaddour@yahoo.fr, d.kaddour@univ-boumerdes.dz, ORCID: 0000-0002-3287-6563

Hadjira Belaidi
Signals and Systems Laboratory, Institute of Electrical and Electronic Engineering, University M'Hamed BOUGARA of Boumerdes, Boumerdes, Algeria, hadjira983@yahoo.fr, ha.belaidi@univ-boumerdes.dz, ORCID: 0000-0003-2424-626X

Dehia Belaidi
Signals and Systems Laboratory, Institute of Electrical and Electronic Engineering, University M'Hamed BOUGARA of Boumerdes, Boumerdes, bdehia@hotmail.fr, ORCID: 0000-0001-7017-0804

Cite this paper as: *Kaddour, D, Belaidi, H, Belaidi D. Grid-connected and grid-islanded energy consumption management. 11. Eur. Conf. Ren. Energy Sys. 18-20 May 2023, Riga, Latvia.*

Abstract: Ensuring microgrid continuity and improving system reliability in grid-connected and islanded modes is crucial for a reliable and sustainable power system. With intelligent EMS (Energy Management System), appropriate sizing, and resource optimization, the microgrid can handle the peak demand even under challenging weather conditions, in both (Connected/Islanded) modes without consuming any extra power from the grid facility or any external resources yet maintaining a reliable power supply. In this paper, a case study of load profile and power consumption estimation of some buildings in our institution IGEE (Institute of Electrical and Electronic Engineering) is used to test and illustrate our EMS performance via MATLAB Simulink. The DG-PV (Diesel Generator-Photovoltaic panel) synchronization technique is adopted to overcome the grid-tied PV system limitation and make it functional in off-grid mode. We used The same DERs (Distributed Energy Resources) sizing for (PV and BESS (Battery Energy Storage System)) in both modes, with advanced control algorithms and monitoring to ensure that our microgrid can have the ability to operate in both modes with a smooth transition from one to another. Hence, by improving the overall system reliability and continuity, we can benefit from all the microgrid mode's advantages to make our system work more efficiently and sustainably.

Keywords: *Grid connected/Islanded mode, microgrid, supply continuity, grid-tied PVs, Diesel Generator, Battery System*

1. INTRODUCTION

Regarding power supply continuity, grid-connected and islanded-mode microgrids offer unique advantages and challenges. Grid-connected mode allows for seamless integration with the main power grid, providing a stable and reliable power supply and the opportunity to sell excess energy back to the grid (net metering). However, it can also leave the microgrid (MG) vulnerable to power outages caused by issues on the main grid. On the other hand, the islanded mode offers greater autonomy and control by relying on the microgrid's DERs (Distributed Energy Resources), such as solar panels, wind turbines, and ESS (Energy Storage Systems) [1, 2].

This mode is particularly useful in remote or off-grid locations where the main power grid is unavailable. However, it can be challenging to ensure a stable and reliable power supply without the backup of the main grid.

When it comes to renewable energy, one of the most popular options is the grid-tied PV solar system. This solar power system is connected to the main power grid and generates electricity using photovoltaic (PV) panels. The generated energy is used to power the buildings, and the excess energy is sent back to the grid. One of the most significant advantages of the grid-tied PV solar system is that it can help reduce electricity costs by decreasing the reliance on traditional fossil fuels. It also helps reduce carbon emissions, making it a more environmentally friendly option. Another advantage is that it allows for net metering, which means that the excess energy generated by the PV system can be sent back to the grid. The homeowner can receive credits on their utility bill for the extra energy generated. However, the grid-tied PV solar system also has its disadvantages. One of the main disadvantages is that it can only generate electricity when the main grid is available, and during power outages, the system cannot generate energy. It can also be affected by shading, which can decrease the system's efficiency [3].

Incorporating the DG (Diesel Generator) is a powerful and dependable solution to overcome the most significant disadvantages of a PV grid-tied system when the main grid is unavailable, by providing power references (voltage amplitude, frequency, and phase) for the grid-tied solar inverter to be synchronized and functional. One of the essential factors for DG-PV synchronization is the MLF (Minimum Load Factor). It is set as 30-40% of the DG maximum capacity. This will ensure that the engine is working in the best conditions. It also helps to save maintenance costs and maximize engine life. The MLF guarantees that the engine runs optimally, reducing fuel consumption and emissions [4–7].

Nowadays, MG faces the formidable challenge of maintaining a consistent and reliable power supply while operating in both connected and islanded modes. The current infrastructure of all MGs relies on a mix of different DERs technology with varying sizes, which makes it challenging to optimize energy generation and storage capacity and handle the power demands in various weather conditions. This results in an unreliable power supply and higher maintenance and energy consumption costs.

This paper aims to propose a solution to this problem by implementing a new approach that incorporates using the same DERs technology with the exact sizing for the (ESS and PVs) in both modes. Additionally, developing an intelligent EMS that can adapt to the changing power demands, ensuring a consistent and reliable power supply for both connected and islanded modes. A case study of some buildings our IGEE load profile and power conception is used to lustrate our proposed approach and algorithms to maintain a continuous and reliable power supply during the peak demand period, in the two MGs' different modes under challenging weather conditions.

2. SYSTEM DESCRIPTION AND SIZING

In this paper, two microgrid modes are addressed: the Grid-connected mode, where our microgrid is supposed to be connected to the main conventional grid, and the Grid-Islanded mode, where the microgrid is considered totally disconnected from the conventional grid, therefore it has to use its resources to satisfy the load needs. The system is built on ESS (Energy Storage System), PV (Photovoltaic Generator), and DG (Diesel Generator) in addition to the conventional grid (in case of grid-connected mode). The system sizing is given in Table 1 in the appendices section., then the system functionality and our obtained results are given after.

3. THE PROPOSED CONTROL STRATEGY

Fig. 1 describes the load profile and power consumption estimation of some buildings in our Institute of Electrical & Electronic Engineering (IGEE). The peak demand period typically occurs during the late morning and early afternoon hours when classes and research activities are in session. During this time, lights, heating, cooling systems, and various electrical machines and electronic devices such as computers, servers, and lab equipment are in use, resulting in high power demand. The peak demand period lasts almost 2 hours, from 11 am to 1 pm.

Based on the power consumption estimation, the electronic faculty buildings in the IGEE consume around 250-300 KW during the peak demand period [6h to 8h].

As the day progresses and classes end, the Students leave the buildings, and lights and other electronic devices are turned off. Thus, the power demand begins to decrease. However, some research activities may continue in the labs

during the evening hours, which could result in moderate power consumption. The power consumption estimation during evening hours [8h to 16h] is around 100-200 KW.

When most buildings are unoccupied at night, power consumption decreases significantly. Due to the lights being turned off, heating and cooling systems are set to a lower energy-saving mode. Additionally, many electronic devices such as computers, servers, and lab equipment are turned off as well. The power consumption estimation at night period [16h to 24h] is around 80-100 KW.

Grid-Connected Mode System Functionality Discerption:

The grid-tied PV solar power is connected to the utility grid creating a bidirectional MG, allowing energy to flow in both directions between the customer and the grid. The clients will be able to use power from the grid when needed and also sell power back to the grid when there is excess. This allows for more efficient energy use and can also help reduce customer costs (net metering).

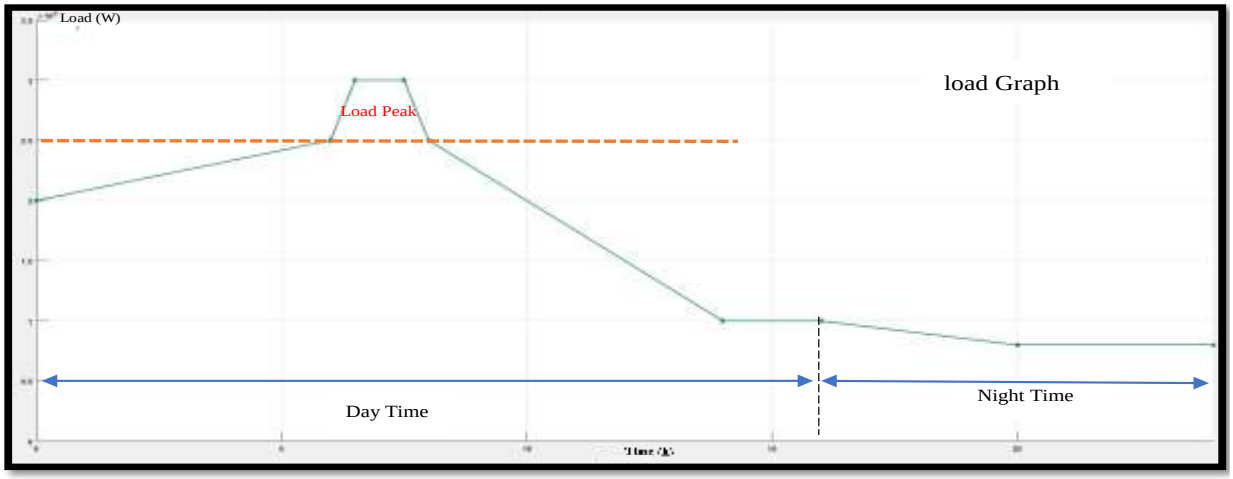

Figure 1. Daytime And Nighttime Load Profiles.

The grid-tied PV system has a three-phase grid-tie inverter with a PID control that helps to synchronize the power generated by the solar panels with the power that comes from the grid. Ensuring the PV power is in phase with the grid power and can be easily integrated into the system. The PV system is connected to a Maximum Power Point Tracking (MPPT) Controller that uses the "Incremental Conductance + Integral Regulator" technique to optimize the energy extraction from the PV panels.

When the solar panels generate more power than is needed by the system, the excess energy goes to the battery System, which has an advanced three-phase inverter containing a PID controller for power flow synchronization and control. The Battery stored energy can be used later when the solar panels are not generating enough power, such as at night or on cloudy days. Additionally and most importantly, we can use it for peak shaving to reduce the peak demand on the grid. Using the PV system's stored power during the daytime will help reduce the grid's strain and lower the customer's electricity costs. The algorithm summarizing this approach is given in Appendix A. The abbreviations used to refer to the constants and the variables used in the flowcharts of EMS for both modes are given in Table 2 in the appendices section.

Grid-Islanded Mode System Functionality Discerption:

Our islanded MG system contains a DG, PV system, and BESS to provide continuity of supply and handle the peak demand with the peak shaving strategy and utilizing the different characteristics of each energy source in a coordinated and optimized way.

The DG is a traditional power source that provides a reliable and consistent power source for the MG. It can be used as the primary power source during times of high demand or when the PV system is not producing enough

power due to weather conditions. The DG can also be used as a backup power source in case of an unexpected outage or failure of the PV system or the battery system.

The main objective of the suggested control algorithm is to minimize the DG system's consumption and maximize the PV power output while considering The minimum load factor of the diesel generators (MLF), which is set to guarantee that the engine works in the best conditions to save maintenance costs and maximize engine life. MLF is often between 30% and 40% of the DG-rated capacity. The diesel generator operates optimally by adjusting its power according to the MG's demand [4]–[7].

The PV system, on the other hand, provides a renewable and clean source of power. It can be used as the primary source when weather conditions are favorable. The PV system can also be used to charge the battery system, which will be used to store excess energy and provide power to the MG during periods of high demand or when the PV system is not producing enough power. The PV system is connected to MPPT Controller uses to optimize the energy extraction from the PV panels.

The battery system, through an advanced three-phase inverter, contains a PID controller. It can be used for both supply continuity and peak shaving. It stores the excess energy generated by the PV system during periods of low demand, which can then be used to provide power to the MG during periods of high demand or when the PV system is not producing enough power. The battery system can also provide backup power to the MG in case of an unexpected outage or failure of the PV system or the DG. The algorithm summarizing this approach is given in Appendix B.

4. RESULTS AND DISCUSSION

Grid-Connected Mode (GCM):

From [0 – 6.5] hours (Battery charging):

With the correct sizing and optimization for our PV system, we can provide enough power to satisfy the load and charge the Battery system simultaneously with high stability and efficiency. The battery charge power in Fig. 2 (Graph 5) represents the extra energy the PV system provides, which can reach a maximum value of 130KW (the negative values of the Battery charge power indicate the opposite direction of the current flowing to the battery). During the 6.5 hours of charging time, the battery SOC (see Fig. 2 Graph 6) increases from 29% to 57%, and it can go even higher with better weather conditions.

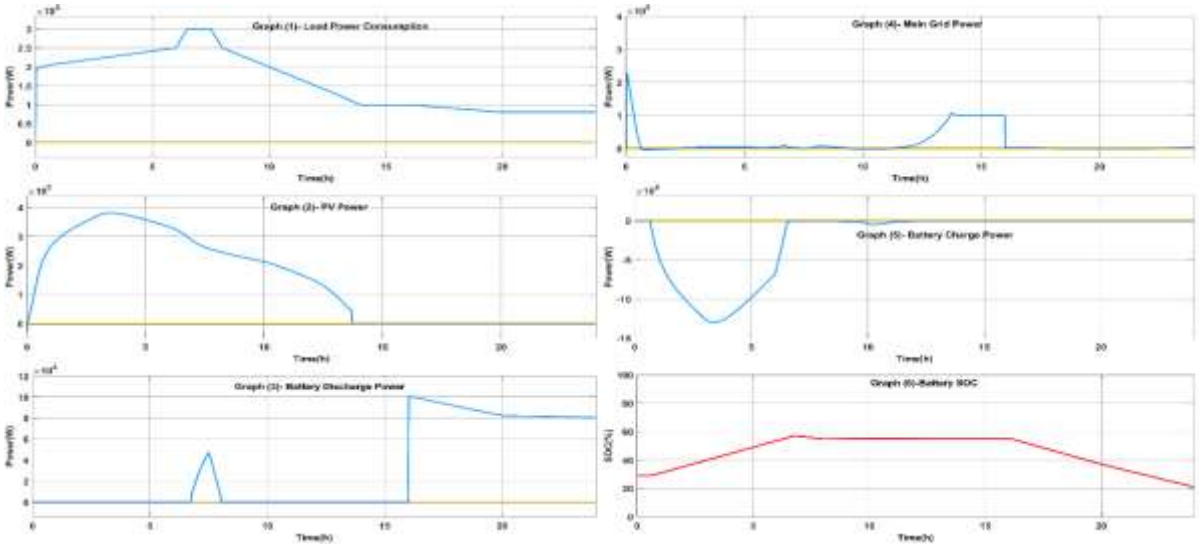

Figure 2. Grid-Connected Mode's Simulation Results.

From [6.5 - 8] hours (peak-shaving):

The graphs demonstrate that we handled the peak demand when load power consumption surpassed 250KW and reached 300kw for 1.5 hours (Fig. 2 Graph 1), even with challenging weather circumstances, without consuming any power from the grid facility. When the PV system power dropped under 300KW (Fig. 2 graph 2) due to unforeseen weather conditions. As a result, the peak shaving technique is used by reinforcing the PV system power with a maximum power of 46KW from the Battery (Fig. 2 Graph 3) to provide a reliable and continuous power supply to the load, which decreases the Battery SOC (Fig.2 Graph 6) from 57% to 55%.

From [8 – 12.3] hours (Battery charging or injecting power into the grid):

As the graphs show, during the daytime, with good weather conditions, our PV system was successfully able to satisfy the load (Fig.2 Graph 1) and deliver the extra power to charge the Battery (Fig.2 Graph 5) with a maximum power of 5KW for 4 hours. That increased the Battery SOC (Fig.2 Graph 6) from 55% to 56%. Additionally, with the bidirectional power flow, the extra power can be injected from PV and sell it to the grid facility if our Battery system is fully charged with SOCmax equal to or more than 90%.

From [12.3 - 16] hours (Grid-Tied PV System's performance):

To demonstrate the performance of the Grid-Tied PV System during the daytime, where the PV solar radiation decreased due to various reasons such as weather conditions, evening time, or just a cloud passing. We can see that the PV power is reduced (Fig.2 Graph 2). As a result, the grid power (Fig.2 Graph 4) starts increasing to satisfy the 100KW load with a stable and continuous power flow.

From [16 - 24] hours (Night time):

The last 8 hours of the (load graph shown in Fig. 2 Graph 1) represents the nighttime, where the load reaches its lowest value (100KW to 80KW). The Battery system is connected to deliver stable and continuous power through the night using the stored energy from the PV system during the daytime. As a result, the Battery SOC (Fig. 2 Graph 6) decreased from 56% to 20% during the 8 hours of nighttime.

Grid-Islanded Mode (IGM):

From [0 – 6.3] hours (Battery charging):

The output in Fig. 3 Graph 4 shows that DG operates at a minimum load MLF (30% to 40%) of its rated power 400KVA to provide stable frequency and voltage references for our grid-tied PV solar system for power synchronization. During the 6.3 hours, the PV system (Fig. 3 Graph 2) produces enough power to simultaneously meet the load power consumption and charge the battery (Fig. 3 Graph 5) with high stability and efficiency. The *Battery charge Power* represents the extra energy of the PV system produced throughout the day, which can go up to a maximum of 252KW (Fig. 3 Graph 5) or even higher to increase the battery SOC from 29% to 89% (Fig. 3 Graph 6) During the 6.3 hours.

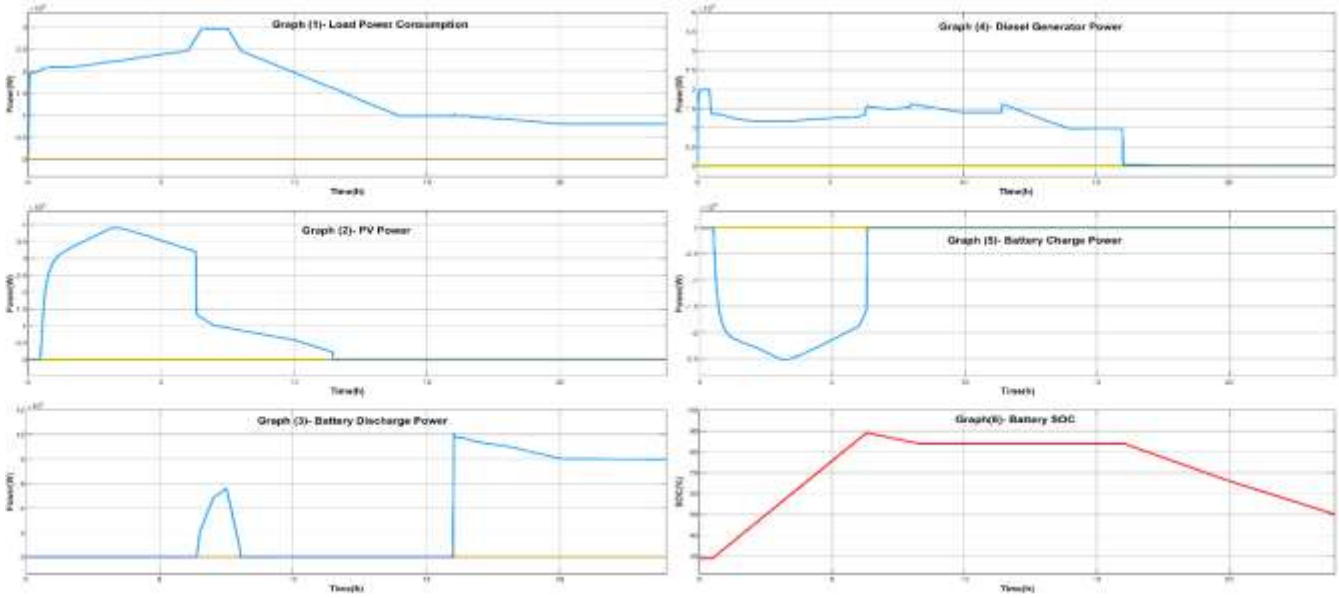

Figure 3. Grid-Islanded Mode Simulation Results.

From [6.3 - 8] hours (peak-shaving):

During the peak demand period, where the load power consumption can go from 250KW to 300KW for 1.7 hours, the PV system power shown in Fig. 3 Graph 2 drops due to unforeseen weather conditions. The battery charging process stops (Fig. 3 Graph 5). So, the Battery system power, can be incorporated to support the PV (peak shaving technique) to provide a maximum power of 56KW (Fig. 3 Graph 3) during 1.7 hours, which reduces the Battery SOC from 89% to 84% (Fig. 3 Graph 6) without drawing additional power from the DG.

From [8 - 16] hours (PV-DG synchronization performance):

The PV system power (Fig.3 Graph 2) starts decreasing, referring to a rainy day, evening time, or just a cloud passing during the daytime because, as we can see, the system load is still relatively higher than 100KW. As a result, the DG (Fig. 3 Graph 4) will respond quickly to the PV power fluctuation and keep providing continuous energy for the system requirements.

From [16 - 24] hours (Night time):

The last part of the graph represents the 8 hours of nighttime, where the load power consumption reaches its lowest value (100KW to 80KW). Thus, the DG (Fig. 3 Graph 4) is disconnected and the Battery system is connected (Fig. 3 Graph 3) to deliver stable and continuous power with a maximum value of 100KW through the 8 hours of night using the stored energy from the PV system during the daytime, which reduces the battery Soc from 84% to 50%.

The Two Modes Comparison:

Based on the simulation results and the two system comparisons presented in Table 3, it can be concluded that both systems can maintain and ensure the continuity of the supply. Moreover, both systems have advantages and disadvantages considering the five comparison factors given in Table 3, where the most considerable advantages for GIM are the battery charge time and the reliability control and supervision. On the other hand, GCM has better PVs exploitation and bidirectional power flow which can reduce the cost with the net metering by selling excess power to the grid facility. However, in this study, the most crucial factor to be considered is the reliability and supply continuity of our system which make the GIM more efficient and suitable choice due to the relative ease of supervision and control management to eliminate unexpected interruption from the main grid regarding the cost and the bidirectional power flow. This last, can be improved by implementing more advanced technology and resource optimization technics.

Table 3. Grid-Connected and Grid-Islanded Mode comparison.

Comparison factors	Connected mode (GCM)	Islanded mode (GIM)
Battery charge time	During the daytime, the battery charge power relies on the PV's excess power, which means that the load power consumption will determine the battery charging power.	During the daytime, the DG will constantly supply the load with 30% to 40% (MLF) of its rated capacity. Thus, the PVs can provide more power to charge the battery even faster.
PV exploitation	100% of PV power can be used all the time, the PVs extra energy will be used to charge the battery, or it can be sell back to the grid facility.	Only 100 % of PVs power can be used to charge the battery; otherwise, PV power should be reduced. Lp >= 30% Pdg + Ppv
Bidirectional power flow	In GCM, the system can take power when needed or inject it and sell it to the grid facility when the battery system is fully charged.	In GIM, the MG is disconnected from the grid. Hence, no power can be sell to the main grid. The extra power can only be used to charge the battery. Otherwise, the system's power must be reduced.
Reliability	In GCM, our system reliability will be directly linked to the main grid reliability, which makes the system supervision very challenging and vulnerable to unexpected power interceptions from the grid facility.	In GIM, the system reliability only depends on our DER's reliability; thus, giving us more control and supervision of our system performance and reliability.
Daily cost	In GCM, we are only charged for our power consumption from the grid. Additionally, Any excess power generated by our solar panels can be fed into the grid and credited to our account (net metering).	The DG power production dilly cost can vary depending on many factors such as the cost of diesel fuel, the generator's size, and the maintenance cost. However, running the DG with 30% to 40% all day to provide synchronization reference factors to the PV and the battery will increase the bills.

5. CONCLUSION

A case study of the load profile and power consumption estimation of some buildings in our institution (IGEE) was used to test and illustrate our EMS algorithm's performance under MATLAB Simulink. Handling peak demand while maintaining a reliable and continuous power supply in both modes was the primary goal of our study. The obtained simulation results showed that both systems can maintain and ensure supply continuity with comparable advantages and disadvantages for each, which makes favoring one system over another vary depending on the usage criteria. In our case study, supply continuity was prioritized over all the other criteria, despite the cost and net metering limitations. Hence, the relative ease of control and supervision in the GIM makes it a more suitable and reliable choice based on our usage benchmarks.

Acknowledgment

We would like to thank DGRSDT (The Directorate-General for Scientific Research and Technological Development) for its financial help.

References

[1] H. Belaidi and Z. Rabiai, 'Decentralized Energy Management System Enhancement for Smart Grid':, in Research Anthology on Smart Grid and Microgrid Development, I. R. Management Association, Ed. IGI Global, 2022, pp. 77–90. doi: 10.4018/978-1-6684-3666-0.ch004.

[2] H. Belaidi, H. Bentarzi, Z. Rabiai, and A. Abdelmoumene, 'Multi-agent System for Voltage Regulation in Smart Grid', in Artificial Intelligence and Renewables Towards an Energy Transition, vol. 174, M. Hatti, Ed. Cham: Springer International Publishing, 2021, pp. 487–499. doi: 10.1007/978-3-030-63846-7_46.

[3] A. Awasthi et al., 'Review on sun tracking technology in solar PV system', Energy Rep., vol. 6, pp. 392–405, Nov. 2020, doi: 10.1016/j.egyr.2020.02.004.

[4] A. Khirennas, A. Kaabeche, A. Talha, and Y. Bakelli, 'A new optimal sizing methodology of storage-less PV system for retrofitting existing diesel-based power generation system within mini-grids', Energy Convers. Manag., vol. 250, p. 114854, Dec. 2021, doi: 10.1016/j.enconman.2021.114854.

[5] I. Ali, G. Shafiullah, and T. Urmee, 'A preliminary feasibility of roof-mounted solar PV systems in the Maldives', Renew. Sustain. Energy Rev., vol. 83, pp. 18–32, Mar. 2018, doi: 10.1016/j.rser.2017.10.019.
[6] W. K. Yap and V. Karri, 'An off-grid hybrid PV/diesel model as a planning and design tool, incorporating dynamic and ANN modelling techniques', Renew. Energy, vol. 78, pp. 42–50, Jun. 2015, doi: 10.1016/j.renene.2014.12.065.
[7] D. Tsuanyo, Y. Azoumah, D. Aussel, and P. Neveu, 'Modeling and optimization of batteryless hybrid PV (photovoltaic)/Diesel systems for off-grid applications', Energy, vol. 86, pp. 152–163, Jun. 2015, doi: 10.1016/j.energy.2015.03.128.
[8] https://energetechsolar.com/30mwh-large-energy-storage-module-lithium-batteries.
[9] J. Xiao, L. Bai, F. Li, H. Liang, and C. Wang, 'Sizing of Energy Storage and Diesel Generators in an Isolated Microgrid Using Discrete Fourier Transform (DFT)', IEEE Trans. Sustain. Energy, vol. 5, no. 3, pp. 907–916, Jul. 2014, doi: 10.1109/TSTE.2014.2312328.

RIGA 2023

Floating DC Nano Grid for Solar Charging of Recreational Boats

T. Akca
The Hague University of Applied Sciences, Delft, Netherlands, T.Akca@student.hhs.nl

K. Kontas
The Hague University of Applied Sciences, Delft, Netherlands, K.Kontas@student.hhs.nl,

S. Onderwater
The Hague University of Applied Sciences, Delft, Netherlands, S.C.S.E.Onderwater@student.hhs.nl

D. Termoshuizen
The Hague University of Applied Sciences, Delft, Netherlands, D.L.J.Termoshuizen@student.hhs.nl

D.C. Zuidervliet
The Hague University of Appl. Sc., Delft, Netherlands, D.C.Zuidervliet@hhs.nl, ORCID: 0000-0003-0833-5975

P.J. van Duijsen
The Hague University of Appl. Sc., Delft, Netherlands, P.J.vanDuijsen@ hhs.nl, ORCID: 0000-0001-5717-4333

Cite this paper as: Akca, T., Kontas, K., Onderwater, S., Termoshuizen, D., Zuidervliet, D.C., van Duijsen, P.J., DC Nano Grid for Solar Charging of Recreational Boats. 11. Eur. Conf. Ren. Energy Sys. 18-20 May 2023, Riga, Latvia

Abstract: In this paper we're going to discuss the application DC nano grid in a harbor, to charge small electric recreational boats and exchange solar energy between the boats. The main problem is the fact that the harbor is quite large, and the charging power at the end of the line could be comparatively high, causing a large voltage drop across the line. Furthermore there should be the possibility to exchange solar energy between the boats. Therefore we looked for a DC nano grid solution where we can lower the voltage drop across the line. The DC nano grid allows us to charge the boats, and also allows us, to exchange energy between the boats. The control of this DC nano grid is based on a voltage based droop control. This allows us to exchange energy between the boats and to control the level of charging depending on the amount of available energy available in the DC grid. Solar power is available on most of the boats and is also used to charge the boats and via the DC nano grid also used to charge the surrounding boats.

Keywords: *AC grid, DC grid, DC-Nano grid, Caspoc, corrosion, Self-sustainable*

Nomenclature	
AC	Alternating Current
DC	Direct Current
PV	Photovoltaic
MPP	Maximum Power Point
SoC	State of Charge

1. INTRODUCTION

To make small recreation boats more energy efficient and environmentally friendly, users install solar panels on their boats. But often enough nothing happens with the excess energy that is generated by the solar panels. It would be useful if the boats could utilize all this energy or return the excess energy to the grid.

Currently the boats are charged from an AC grid wall connection, but because of the long lines , there is a sincere voltage drop along the line, making it impossible to charge the boats at the end of the harbor.

At the dock in Vlietstreek at Laakhaven in The Hague[1], Netherlands, there is space for a maximum of 150 boats, which are currently charged from the public AC grid. Most of these boats have solar panels for charging their onboard battery. However, when the battery is fully loaded, there is excess of potential solar energy, not being utilized.

A DC-Nanogrid could be useful in this situation, as it allows bidirectional power exchange[2]. The excess solar energy will be used and redirected to the grid by using this DC-Nanogrid. The main idea is to create a sustainable DC-Nanogrid on every boat moored in the Laakhaven. This system can operate independently of the main power grid. Furthermore, the boats can charge each other if needed and deliver the surplus power back to the main grid. so a larger extended DC-Nanogrid will be created.

In section 2 we discuss the problem of voltage drop in the current AC grid, for which we introduce an alternative system architecture in section 3. In section 4 the concept of the DC grid is explained, which is first simulated in section 5. In section 6 the demonstrative setup is shown, which is build inside each boat.

2. CURRENT SITUATION

Currently the Vlietstreek has a dock with a total of 150 docking places shown in Figure 1. All of those docking spots have available wall sockets for each boat to plug into. At the start of the dock there is a main breaker unit which carry's all the power from one wall socket to the next, to a total of 315 meters at the end of the dock. In Figure 1 the path of the dock is shown by the white line drawn on the photograph taken from above.

Figure 8. Docking of the Vlietstreek (Google maps), main grid (white), 15m(blue), 115m(red), 215m(light blue), 315m (green).

Currently at the Vlietstreek there are three main issues with the system:

1. Voltage drops from 230 Volts at the beginning of the distribution line to 175 Volts at the end of the line.
2. No power congestion management in the system, and no exchange of energy.
3. Charging more than two batteries, will trip the main breaker.
4.

A. Voltage drop

In Figure 2, a graph with corresponding colors and distances is displayed, these are 15 meters (blue), 115 meters (red), 215 meters (light blue), 315 meters (green). The graph shows 4 different measurement points at different distances from the main breaker unit. In this simulation instance 3 boats where plugged in at 15 meters, 215 meters and 315 meters to simulate a real life scenario of people coming to the Vlietstreek and charging their boats[3].

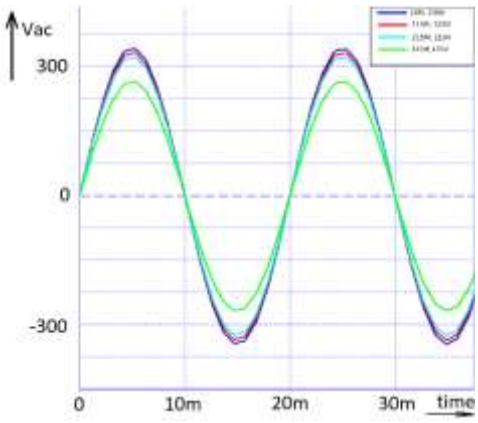

Figure 2. AC voltage drop.

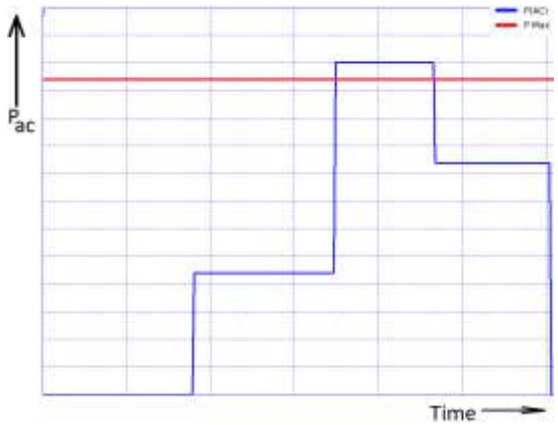

Figure 3. Charge power depends on the number of loads connected.

Assuming that at the start of the dock there is a 230V RMS value. In Figure 2 (light blue) there is a noticeable voltage drop at 215 meter. The voltage at this measurement point is 210V RMS which is 10 percent lower. Furthermore at 315 meter a voltage level of 175V RMS is shown. This is dangerously low and is not allowed only a 10 percent deviation is allowed according to NEN-1010 norm[4].

A too low of a voltage is not safe for the battery, as for the same power level the current level increases. This will create excess heat on the battery which is dangerous. The main reasons for the big voltage drop is, when boats are docked and plugged in a wall socket, the battery wants to instantaneously fully charge and draw full power. When multiple larger loads are connected, the impedance's of the cables to the loads are connected in series. This long line, with high current demand, develops a large voltage drop across the line.

B. Power congestion

At the Vlietstreek the flow of energy is not regulated, This means that the PV solar energy generated by all the boats cannot be stored or fed back to the grid. In practice this means a lot of wasted energy. Currently the Vlietstreek has a 3 phase 230V voltage 16A line coming out of the main breaker unit this equates to 11kW of maximum power rating for the breaker. It is assumed all the charging poles are equally divided over the 3 phases which means each pole can't handle more than 2 boats at a time. In Figure 3 the maximum allowed power, per charging pole, is shown(red) and the power delivered to the boats is shown (blue). Looking at Figure 3, 1 Boat is plugged in at 38 minutes so in the graph it shows a peak to 2.3kW (blue) plugged in, the value 2.3kW was taken from the survey we took at the Vlietstreek. The red line in the graph shows the maximum allowed power of the circuit breaker which is a 3 phase 16A fuse, which is a total of 5.7kW. At 70 minutes 2 other boats are connected to the system so a total of 3 boats are plugged in to the system. Looking at the blue line it shows crossing the red line, meaning the circuit breaker trips leaving the system powerless. The circuit breaker trips because the power goes above the allowed 5.7kW, to a total of 6kW. This is because the power is not regulated in the system.

3. SYSTEM ARCHITECTURE

The DC Nano grid at the Laakhaven, The Hague is divided in to three main parts as shown in Figure 4:

1. The main distribution line will be converted from 230V Alternating Current to a new 48V Direct Current grid.
2. Boat to boat power distribution in the 48Vdc line through the charging stations.
3. Creating boat setups which can bidirectionally charge boats or feed it back in to the grid using only available off the shelve products.

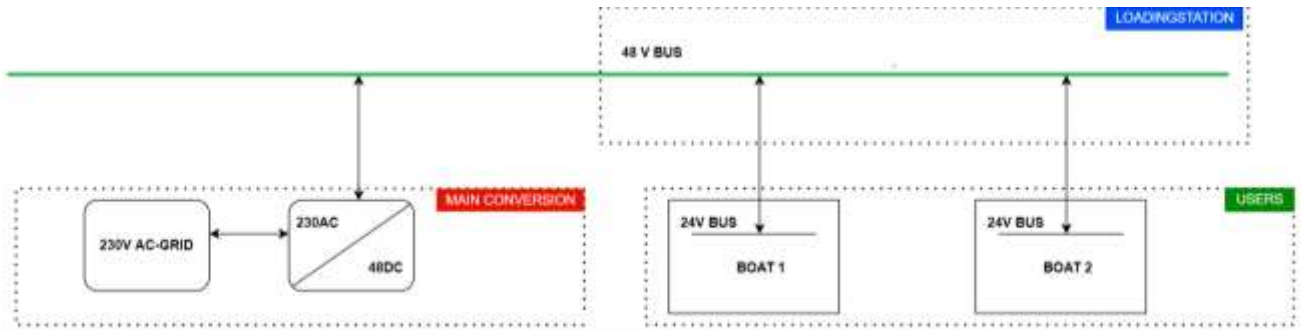

Figure 4. System overview, the green line includes the 350 volt DC grid with bidirectional conversion to the 48 volt DC grid.

4. DC GRID

To overcome the voltage drop problem and to be able to exchange energy among the boats, a DC grid is employed[5]. A DC grid with a nominal voltage of 350Volt was installed for the power distribution in the harbor, see Figure 5. Inside each boat a DC nano grid of 48 volt is designed and coupled to the 350volt grid via a commercial available Buck or Boost converter with contactor, see Figure 6.

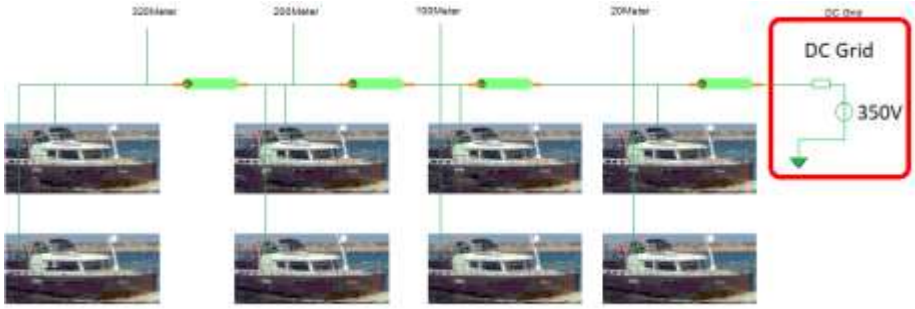

Figure5. 350 Volt DC grid.

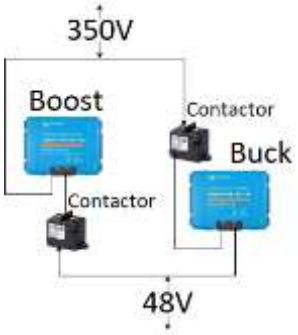

Figure 6. Coupling DC grids.

The 350 volt DC grid is continuously powered from the wall power connected to the AC grid. This unidirectional connection provides power to the 350 volt DC grid, whenever there is power demand on the DC grid. The ACDC converter[6] is simply maintaining the 350 volt on the DC grid by simple voltage control. No further droop control[7] is implemented here. The 48 volt DC nanogrids inside the boats are simply powered from the 350 volt grid or from the onboard battery. Depending on the state of charge [SOC] of the battery and the amount of available solar power as well as the power demand on the boat itself, there is bidirectional power flow between the 350 volt and 48 volt grid.

If the battery is not fully charged and there is no solar power, the 350 volt DC grid powers the 48 volt grid via the Buck converter, from which the battery is charged and the onboard loads are powered. If the battery is charged and there is excess solar power, this energy is returned from the 48 volt grid into the 350 volt grid using the Boost converter. The two contactors in Figure 6 control the power transfer.

The final droop control is implemented in the battery charger, see Figure 7. Depending on the amount of solar power, energy from the 48 volt DC grid is used for charging the battery according to the droop characteristic in Figure 7. If the battery is fully charged and there is still excessive power, it is transferred into the 350 volt DC grid via the contactor and Boost converter in Figure 6.

Nearby boats, still charging their batteries from the 350 volt DC grid are then using the energy from the boat which is feeding back into the 350 volt DC grid. This amount of power does not have to be delivered from the wall AC grid, giving two main advantages

1. Less power from the main AC grid is required and solar power is shared among the other boats
2. Less voltage drop, as the power is no also coming from the nearby boats.

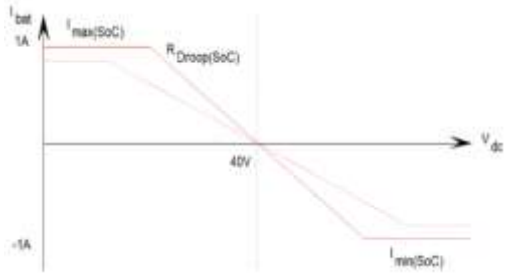

Figure 7. Droop control for battery charging.

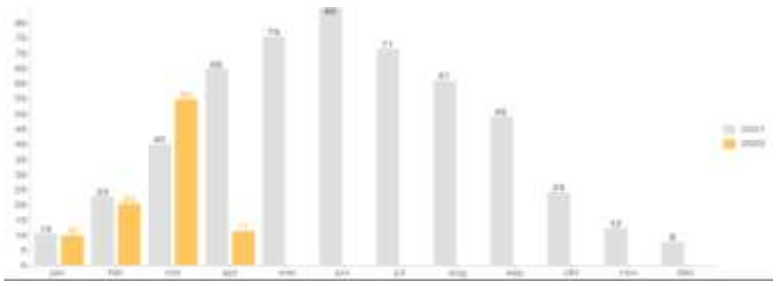

Figure 8. Solar panel power at the harbor during 2021 and 2022 until April.

5. DC-SIMULATION

The DC simulation[3] gives an indication of what the new system should look like and the solution for the Laakhaven. With the simulations made, the values of the components can be chosen, for a realistic use for the boats in the Laakhaven and for the demonstrative test.

A. Droop control

The simulation of the DC part is done using the droop control of the DC/DC converter of 350V/48V or 350V/24V. A droop control should adjust the voltage output so that the system stabilizes, whatever the input voltage is[8, 9]. A DC voltage above the nominal value causes it to feed back to the DC-grid and a DC voltage below the nominal voltage of the battery causes the voltage to be compensated with the DC-Grid grid

B. Solar energy Laakhaven

The solar panels cannot provide constant energy, this can be due to the placement of the solar panels on the boat, shadows and location. A research has been done on the generated energy at the location laakhaven. In Figure 8 it can be seen that in 2021 in there is about 497kWh of solar energy generated at the location Laakhaven. This result is used during simulation to give an indication for the new boats.

C. Simulation design

The simulation schematic shown below in Figure 9, is a design of simulated operation of DC Droop control. The simulation is divided into 5 parts. The red part is the DC grid of 350VDC. The blue part is the DC-DC converter of 350/48 or 350/24 with droop control. The yellow area is the battery. With the battery, there is no DC-DC converter placed of for example 24/24 VDC for a stable power supply, because the droop control must receive voltage at both ends to work in the simulation. Otherwise the simulation will not work. The green part is solar panel with the MPP. The solar panel is set with the data from Figure 7. The DC-DC converter at the load provides a stable power supply so that the equipment is not damaged or does not get enough voltage.

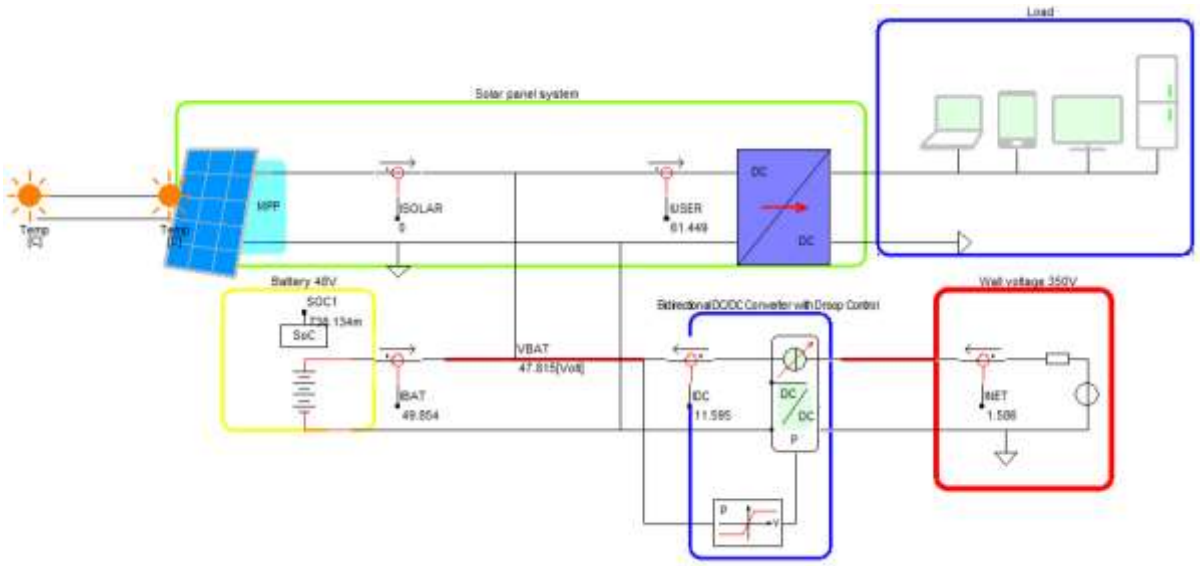

Figure 9. DC simulation of the Droop Control.

6. DEMONSTRATION SETUP

A test set up in the laboratory was build, see Figure 10 and Figure 11, according to the simulation schematic from Figure 9. Figure 10 shows the 3D rendering of the setup which represents the a installed installation on a boat, while the final implementation is shown in Figure 11 on the right.

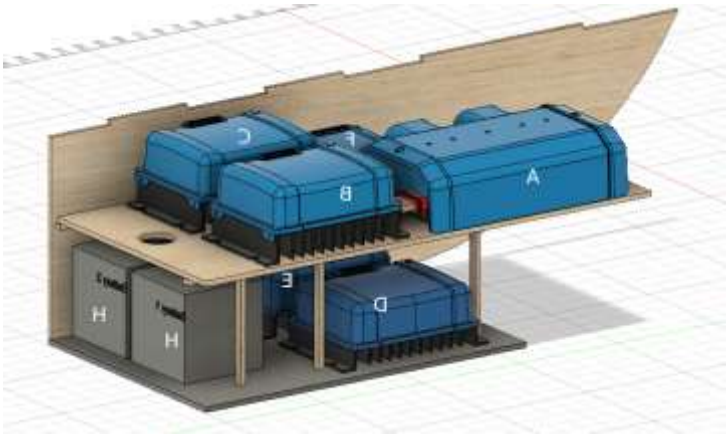

Figure 10. Solar inverters, chargers and batteries

Figure 11. Test set up (left) and final application (right)

The final schematic for the setup is shown in Figure 12. Here contactors are used to connect the commercial available inverters and chargers to the DC grid. With the four states in witch the contactors can be switched from a microcontroller, charge mode (grid and PV), return to grid mode (PV only), return to grid mode (Battery and PV) and fully charged mode (stand-alone).

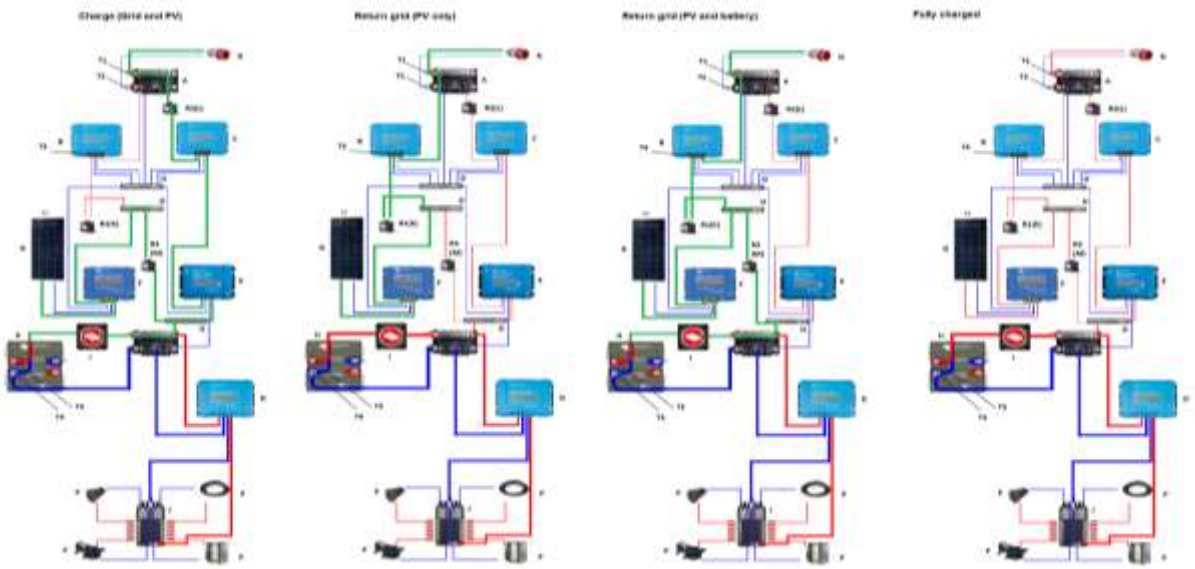

Figure 12. The four connection diagrams with contactors to control the DC grid operation.

7.CONCLUSION

Using commercial available solar converters and battery chargers, a DC Nano Grid was build, to charge recreational electric boats. In the harbor is a 350 volt DC grid where the boats connect to. Each boat has an internal 48 volt DC grid. Using the contactors, power management was implemented, although droop control was not possible using the commercially available chargers. The droop control was implemented in the onboard 48 volt DC grid for the battery charger and the onboard-loads. Excess solar power can be delivered into the 350 volt grid to charge batteries on other boats, and thus saving energy from the main AC grid wall connection. Using commercial available components it is possible to build power management systems with a minimum droop control functionality. This enabled two of the main goals, firstly, power congestion management to avoid congestion on the wall connection and secondly, energy exchange between the boats.

Acknowledgment

The authors would like thank initiator Nico Persoon and the The Hague Government for their generous support to enable DC applications and accelerating the transition to renewable energy.

References

[1] Floating DC Nano Grid (Energiehaven) project page, Available: https://www.linkedin.com/groups/12697654/
[2] Y. Ito, Y. Zhongqing and H. Akagi, "DC microgrid based distribution power generation system," The 4th International Power Electronics and Motion Control Conference, 2004. IPEMC 2004., Xi'an, China, 2004, pp. 1740-1745 Vol.3.
[3] Caspoc , Simulation Research. [Online]. Available: https://www.caspoc.com. (Accessed) January 22, 2023.
[4] Wetten.overheid.nl. 2022. wetten.nl - Regeling - Netcode elektriciteit - BWBR0037940. [online] Available at: https://wetten.overheid.nl/BWBR0037940/2022-05-18 [Accessed May 4th, 2022].
[5] J. M. Guerrero, J. C. Vásquez and R. Teodorescu, "Hierarchical control of droop-controlled DC and AC microgrids — a general approach towards standardization," 2009 35th Annual Conference of IEEE Industrial Electronics, Porto, Portugal, 2009, pp. 4305-4310, doi: 10.1109/IECON.2009.5414926.
[6] P. van Duijsen and D. Zuidervliet, "Grid-tied AC DC Converters and Protection in the DC Grid," PCIM Europe 2022; International Exhibition and Conference for Power Electronics, Intelligent Motion, Renewable Energy and Energy Management, Nuremberg, Germany, 2022, pp. 1-6, doi: 10.30420/565822205.
[7] L. Ott et al., "An advanced voltage droop control concept for grid-tied and autonomous DC microgrids," 2015 IEEE International Telecommunications Energy Conference (INTELEC), Osaka, Japan, 2015, pp. 1-6, doi: 10.1109/INTLEC.2015.7572406.
[8] P. J. van Duijsen and D. C. Zuidervliet, "Structuring, Controlling and Protecting the DC Grid," 2020 International Symposium on Electronics and Telecommunications (ISETC), Timisoara, Romania, 2020, pp. 1-4, doi: 10.1109/ISETC50328.2020.9301065.
[9] A. Spaans, D. Zuidervliet and P. van Duijsen, "Droop Control in DC Grids for Kitchen Appliances to avoid Power Congestion," 2022 8th International Conference on Control, Decision and Information Technologies (CoDIT), Istanbul, Türkiye, 2022, pp. 791-796, doi: 10.1109/CoDIT55151.2022.9804126.
[10] DC-Lab. (2021). "Dc lab, research dedicated to direct current and power electronics," [Online]. Available: http://dc-lab.org. (Accessed) January 22, 2023.

RIGA 2023

Experimental Study of the ORC System with Isobutane (R600a) as a Working Fluid

Andrzej Grzebielec
Warsaw University of Technology, Warsaw, Poland, andrzej.grzebielec@pw.edu.pl, ORCID: 0000-0003-3320-5929

Adam Szelągowski
Warsaw University of Technology, Warsaw, Poland, adam.szelagowski@pw.edu.pl, ORCID: 0000-0003-1017-1949

Łukasz Cieślikiewicz
Warsaw University of Technology, Warsaw, Poland, lukasz.cieslikiewicz@pw.edu.pl, ORCID: 0000-0002-5905-990X

Piotr Łapka
Warsaw University of Technology, Warsaw, Poland, piotr.lapka@pw.edu.pl, ORCID: 0000-0003-3039-9588

Mirosław Seredyński
Warsaw University of Technology, Warsaw, Poland, miroslaw.seredynski@pw.edu.pl, ORCID: 0000-0002-0341-6250

Cite this paper as: *Grzebielec, A, Szelągowski A, Cieślikiewicz, Ł, Łapka, P, Seredyński, M. Experimental study of the ORC system with isobutane (R600a) as a working fluid. 11. Eur. Conf. Ren. Energy Sys. 18-20 May 2023, Riga, Latvia*

Abstract: In ORC systems, refrigerants are commonly used as working fluids. However, due to the fact that the European Parliament is increasingly restrictive towards f-gases, new solutions should be sought. One of the ideas is to use hydrocarbons as working fluids in ORC systems. This paper presents the results of experimental studies of a small ORC system using propane - R600a as a working medium. The results show that isobutane is well suited to work in ORC systems, and the efficiencies obtained in heat exchangers can be even higher than with typical f-gases. The device was filled with 2.6 kg of isobutane and generated electricity up to 0.8 kW. During the experiment, the boiling point was maintained at a very low level of 60-75ºC and still quite good results were obtained. The efficiency of the ORC system was 4.5%. It is worth noting that compared to the Carnot cycle for the same temperatures, efficiency is 40%.

Keywords: *ORC, isobutane, R600a, energy efficiency, waste heat recovery*

1. INTRODUCTION

Organic Rankine Cycles (ORC) implement the basic Rankin cycle. However, instead of water, they use other working media. This is due to the fact that they work with a much lower temperature of the upper heat source than in a traditional power plant or combined heat and power plant [1]. The most popular refrigerants in ORC systems are: R245fa, R236fa, R227ea [2,3,4]. Unfortunately, all these factors have high GWP - global warming potential [2,3]. As a result, some of them are already banned in new installations, and others will be banned in the coming years. For this reason, device manufacturers are looking for a new solution. It becomes natural to use refrigerants from the hydrocarbons (HC) group. While previously used refrigerants were safe for people, non-flammable and non-explosive, hydrocarbons are flammable and explosive [5,6]. For this reason, for years they have not been treated as good refrigerants or as a medium in ORC systems. Nowadays, however, the use of HC is becoming more and more common, in refrigeration (R290, R1270), air conditioning and heat pumps (R290) [7,8,9]. Therefore, as part of this project, it was decided to check the possibility of using isobutane in low-temperature ORC systems.

ORC systems are used to utilize waste heat with temperatures ranging from 70 to 300 ºC. This temperatures can be also utilized and stored by systems with PCM and TEG [10,11,12], but for ORC system efficiency is an higher level.

Such low temperature range, especially the lower range, would cause steam to work in under pressure even in the evaporator. For this reason, low-boiling fluids are used in ORC.

Figure 1 shows a typical ORC system. The device consists of an evaporator, an expander, a regenerative heat exchanger, a condenser and a refrigerant pump.

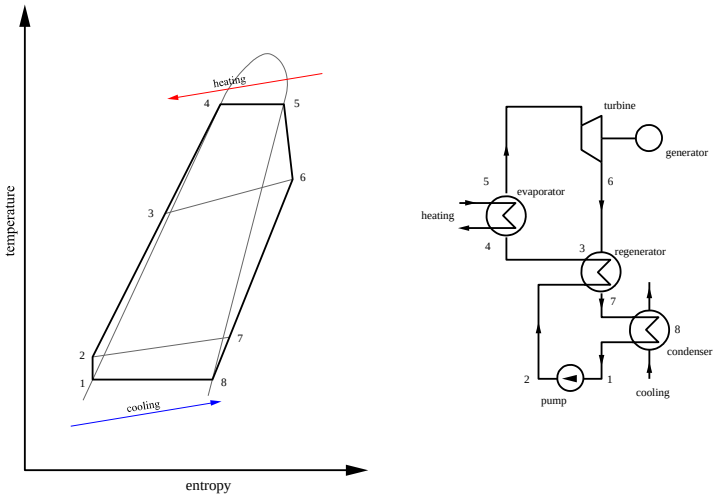

Figure 1. Typical ORC device.

This what should be remembered during using flammable fluids in sealed devices - and this is the case in ORC systems, it does not mean that the entire environment, automation must meet the EX requirements. The device must first of all meet the tightness requirements. But this is the principle of both refrigeration equipment and ORC with non-flammable refrigerants too. The only legal restriction for such machines is the location of the device. Therefore, a device in which the working medium is, for example, isobutane is an amount exceeding 150 grams must be placed outside the building. It should be reminded that in almost 100% of European refrigerators the working medium is isobutane, and these devices are located inside buildings (because there is less than 150 grams).

2. EXPERIMENTAL SET-UP

The device was built from commercial components. Plate heat exchangers have been used as evaporator, condenser and regenerator. A diaphragm pump with the ability to work up to 200 bar was used, driven by an asynchronous motor. The speed of which can be changed using an inverter. A screw expander (Fig. 2) was used in the tests, which allowed the output of the generated power outside. Where, by means of a belt transmission, the energy was transferred to a DC generator. Figure 3 shows a diagram of the measuring apparatus. It consists of three sub-systems: the proper ORC system, the system simulating the upper heat source and the system simulating the lower heat source. In the proper ORC system, pressures and temperatures are measured between all elements of the device. On the other hand, in heat source systems, temperatures and streams of the flowing medium are measured.

Figure 2. Screw expander example.

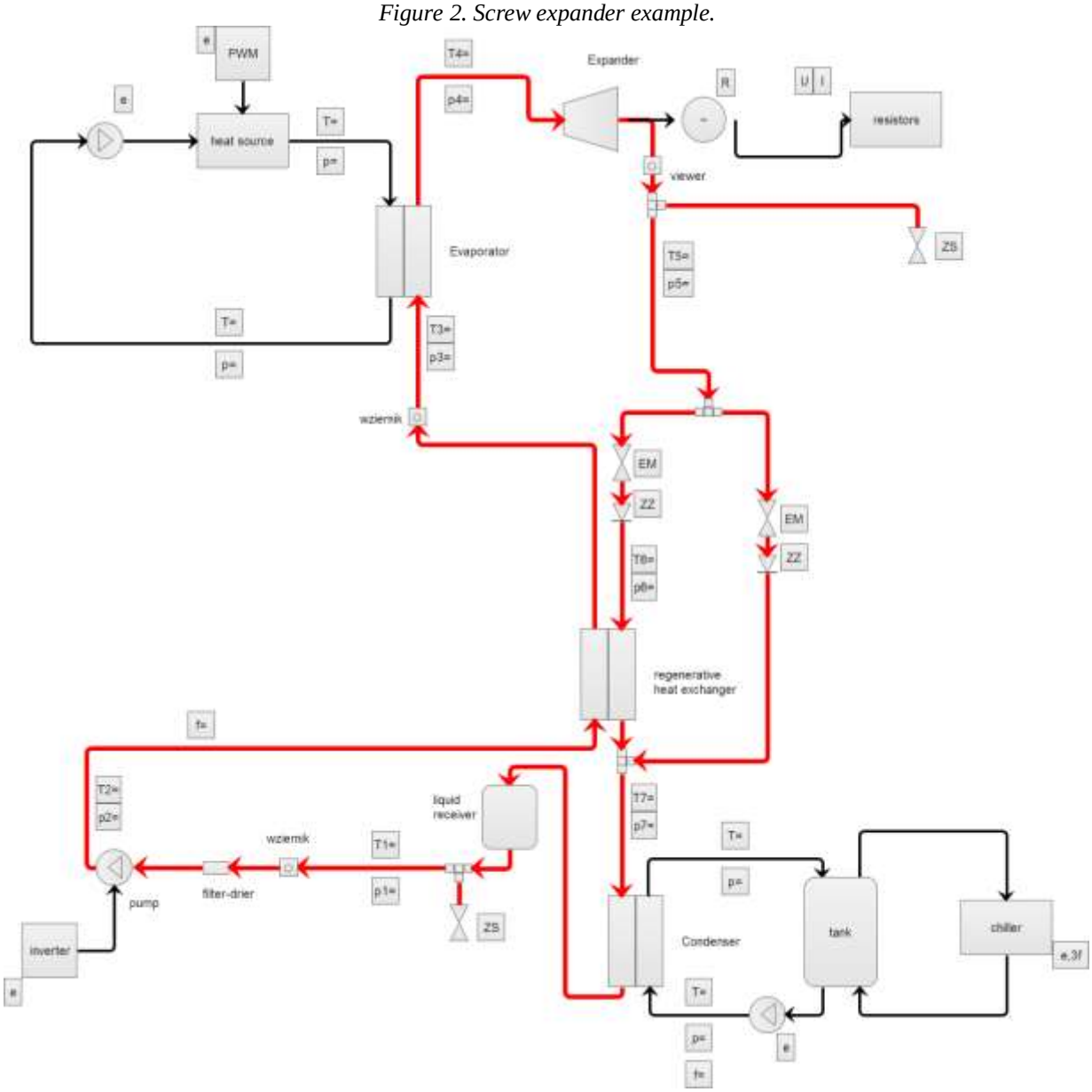

Figure 3. Experimental setup schema
(T-temperature measurement, P-pressure measurement, f-flow meter, e-electric power meter
EM-electromagnetic valve, ZZ - check valve, ZS – service valve)

Figure 4. Experimental set-up

The test stand allowed to:

- Work with or without regenerator;
- Changing the temperature of the upper heat source;
- Changing the temperature of the lower heat source;
- Changing the stream of the medium flowing through the upper heat source;
- Changing the stream flowing through the lower heat source;
- Adjusting the speed of the refrigerant pump in the ORC.

3. RESULTS

In previous publications, it was estimated that for a finite heat flux on the side of the upper heat source, the goal is not to achieve the highest system efficiency values, but to achieve the maximum generated electric power [6]. For this reason, it was checked how the system would behave for various operating parameters of the upper heat source. The system was tested in the mode of operation with the regenerator and operation without the regenerator.

The operation of the system without a regenerator is the simplest possible cycle implemented in ORC systems. On the other hand, the use of a regenerator enables the transfer of part of the energy from the line before the condenser to the line before the evaporator.

Figure 5 presents the temperatures measured in the upper heat source for both cases. Figure 6 shows the power that was obtained in the upper heat source.

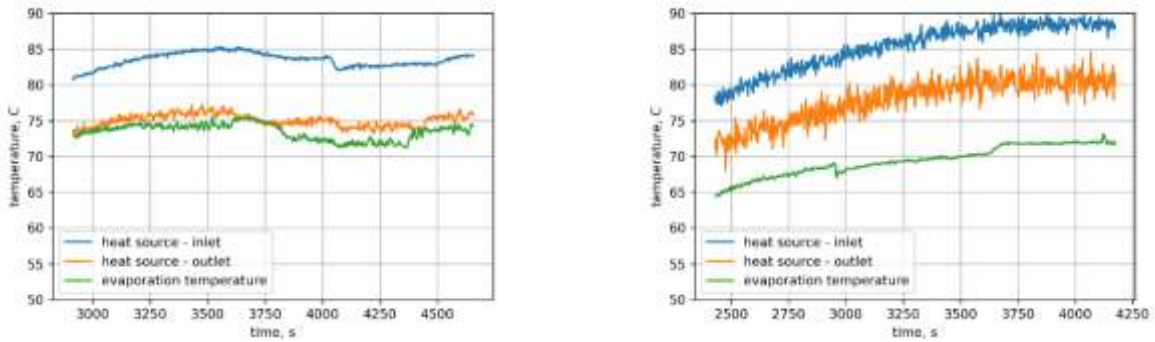

Figure 5. Temperature change in evaporator
(without regenerator – left side, with regenerator – right side)

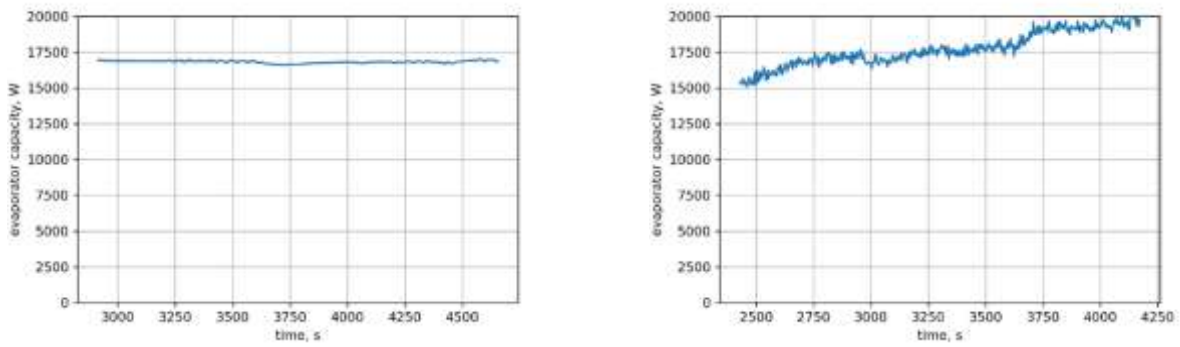

Figure 6. Evaporator capacity
(without regenerator – left side, with regenerator – right side)

Figure 7 shows the measured isentropic efficiency of the expander. The obtained value is around 40% for the system without regenerator and 45% for the system with regenerator. Figure 8, in turn, shows the results obtained for the power obtained in the expander - the obtained values oscillated between 500 and 600 W for the system without the regenerator and reached almost 800 W for the system with the regenerator.

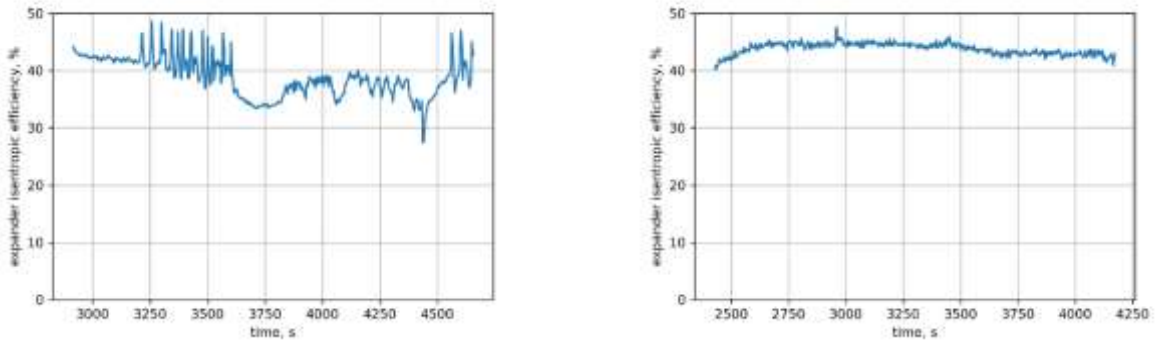

Figure 7. Expander efficiency
(without regenerator – left side, with regenerator – right side)

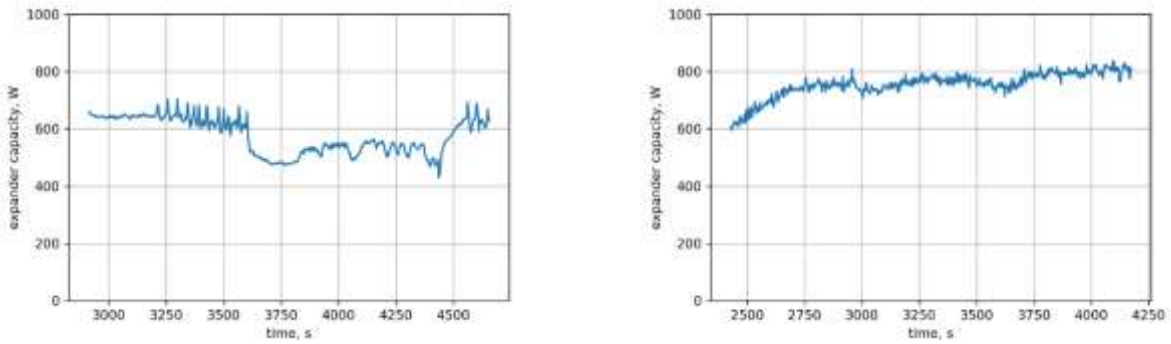

Figure 8. ORC Capacity
(without regenerator – left side, with regenerator – right side)

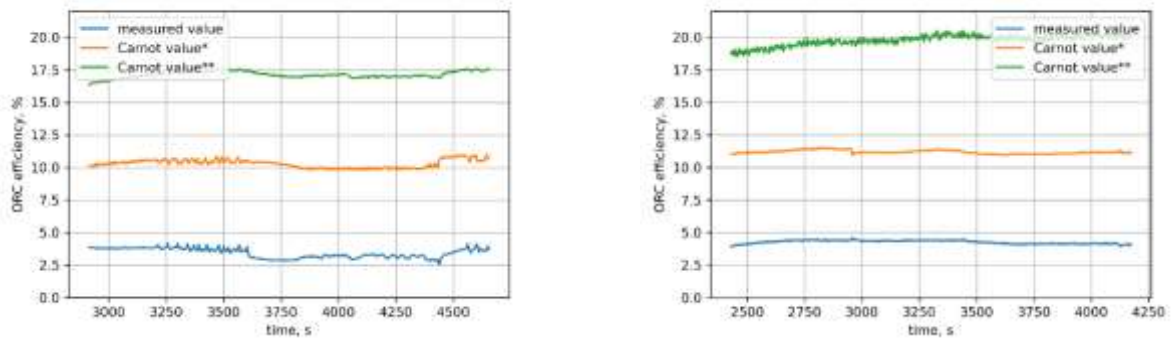

Figure 9. ORC Efficiency
(without regenerator – left side, with regenerator – right side)
** according to evaporation/condensing temperature*
*** according to heat sources temperatures*

Figure 9 presents the obtained efficiency values of the entire ORC system. The measured value for the system without regenerator oscillated between 3 and 4%, while for the system with regenerator this value was stable at 4.5%. The graphs also show the Carnot efficiencies in order to illustrate the limits of the system's capabilities for such low temperature heat sources. Since the evaporation temperature was deliberately kept low in the system, the Carnot efficiency was shown in two ways. The first is related to the vaporization/condensation temperature of isobutane. The second is related to the temperature of the upper and lower source at the inlet to the heat exchangers.

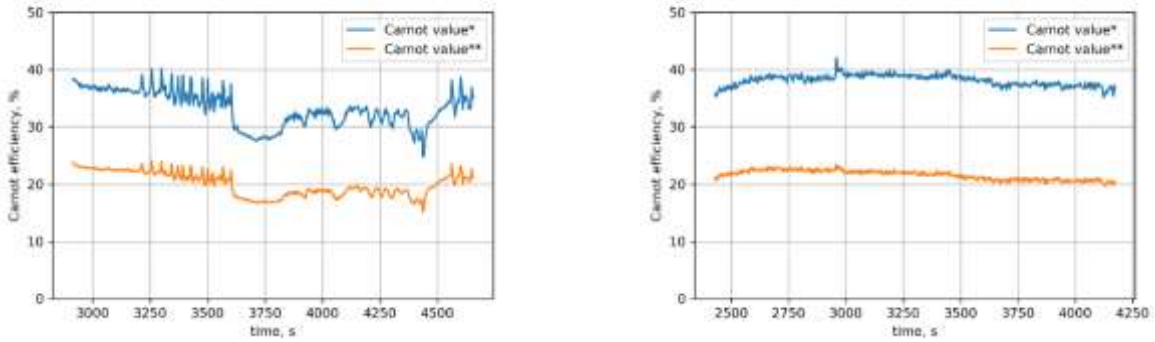

Figure 10. Carnot efficiency
(without regenerator – left side, with regenerator – right side)
** according to evaporation/condensing temperature*
*** according to heat sources temperatures*

Figure 10 presents the efficiency results in relation to the Carnot cycle. This parameter is often used to compare different circuits. Here, too, the comparison is presented in two ways.

4. CONCLUSIONS

As part of experimental research, it was possible to obtain the results of the operation of the ORC device with isobutane working medium for a system with a very low temperature of the upper source. The boiling point was in the range of 60 to 80 ºC. It has been proven that this solution has great potential for using this device in commercial solutions. In the ORC system without the regenerator, efficiency was achieved at the level of 3-4%, and with the regenerator at the level of 4.5%, which confirms that the use of regenerators can increase the efficiency of the device by 28% (for the upper source temperature at level 85 ºC). The use of the regenerator did not reduce the amount of heat in the upper heat source, but it increased the efficiency of the expander and allowed for higher power output on the expander.

The disadvantages of the tested device include the efficiency of the expander - a value of 40-50% was achieved, however, this is caused not so much by the construction of the expander, but by too low rotational speed that was achieved in the experiment. At higher speeds, the results should improve the results of the entire system.

Acknowledgment

The study was financed by the National Centre for Research and Development (Poland) in the framework of the grant No MAZOWSZE/0181/19.

References

[1] Rusowicz, A, Laskowski, R, Grzebielec, A. The numerical and experimental study of two passes power plant condenser, Therma Science 2017, 21, 1, 353-362, https://doi.org/10.2298/TSCI150917011R
[2] Kajurek J, Rusowicz A, Grzebielec A, Bujalski W, Fuktyma K, Rudowicz, Z. Selection of Refrigerants for a Modified Organic Rankine Cycle. Energy 168 (2019) 1-8, https://doi.org/10.1016/j.energy.2018.11.024
[3] Xu W, Qi Y,Yang Y, Ge Y, Lu Y, Liu Y, Zhao W. PVTx properties of the R600a/R245fa for low temperature organic rankine cycle. The Journal of Chemical Thermodynamics 176 (2023) 106904, https://doi.org/10.1016/j.jct.2022.106904
[4] Braimakis K, Mikelis A, Charalampidis A, Karellas S. Exergetic performance of CO2 and ultra-low GWP refrigerant mixtures as working fluids in ORC for waste heat recovery. Energy 203 (2020) 117801, https://doi.org/10.1016/j.energy.2020.117801.
[5] Longo G. A, Mancin S, Righetti G, Zilio C, Brown J. S. Assessment of the low-GWP refrigerants R600a, R1234ze(Z) and R1233zd(E) for heat pump and organic Rankine cycle applications. Applied Thermal Engineering 167 (2020), 114804, https://doi.org/10.1016/j.applthermaleng.2019.114804
[6] Rusowicz, A, Grzebielec, A, Łapka, P. Influence of the temperature difference between the heat source and the evaporation temperature in ORC systems working with natural refrigerants. Inżynieria Bezpieczeństwa Obiektów Antropogenicznych 2022, 1, 46-57. https://doi.org/10.37105/iboa.130
[7] Sun Z, Wang Y. Comprehensive performance analysis of cascade refrigeration system with two-stage compression for industrial refrigeration, Case Studies in Thermal Engineering 39 (2022) 102400, https://doi.org/10.1016/j.csite.2022.102400.
[8] Sobieraj M. Development of novel wet sublimation cascade refrigeration system with binary mixtures of R744/R32 and R744/R290. Applied Thermal Engineering 196 (2021) 117336, https://doi.org/10.1016/j.applthermaleng.2021.117336.
[9] Liu Y, Yu J. Performance evaluation of an ejector subcooling refrigeration cycle with zeotropic mixture R290/R170 for low-temperature freezer applications. Applied Thermal Engineering 161 (2019) 114128, https://doi.org/10.1016/j.applthermaleng.2019.114128.
[10] Rolka, P, Karwacki, J, Jaworski, M. Compatibility Tests between Three Commercially Available Organic PCMs and Metals Typically Used in Fin-and-Tube Heat Exchangers. Materials 14 (2021) 5172. https://doi.org/ 10.3390/ma14185172
[11] Jaworski, M, Bednarczyk, M, Czachor, M. Experimental investigation of thermoelectric generator (TEG) with PCM module, Applied Thermal Engineering 2016, 96, 527-533, doi: 10.1016/j.applthermaleng.2015.12.005
[12] Jaworski, M. Thermal performance of building element containing phase change material (PCM) integrated with ventilation system – An experimental study, Applied Thermal Engineering 2014, 70, 665-674, doi:10.1016/ j.applthermaleng.2014.05.093

RIGA 2023

About DC parameters of PV Panels

Nugzar Gomidze
Batumi Shota Rustaveli State University, Batumi, Georgia, gomidze@bsu.edu.ge, ORCID: 0000-0003-1750-6959

Lali Kalandadze
Batumi Shota Rustaveli State University, Batumi, Georgia, lali.kalandadze@bsu.edu.ge ORCID: 0000-0003-0633-9729

Omar Nakashide
Batumi Shota Rustaveli State University, Batumi, Georgia, omar.nakashidze@bsu.edu.ge, ORCID: 0000-0002-6310-6588

Izolda Jabnidze
Batumi Shota Rustaveli State University, Batumi, Georgia, izolda.jabnidze@bsu.edu.ge, ORCID: 0000-0002-4471-4027

Miranda Khajishvili
Batumi Shota Rustaveli State University, Batumi, Georgia, miranda.khajishvili@bsu.edu.ge, ORCID: 0000-0002-2827-7058

Jaba Shainidze
Batumi Shota Rustaveli State University, Batumi, Georgia, jabashainidze@gmail.com, ORCID: 0000-0002-9813-0641

Cite this paper as: *Gomidze, N., Kalandadze, L, Nakashidze, O., Jabnidze, I., Khajishvili M., Shainidze J. About DC parameters of PV panels Article title. 11. Eur. Conf. Ren. Energy Sys. 18-20 May 2023, Riga, Latvia*

Abstract: As solar energy has become increasingly popular around the world, high-quality PV panels have been developed. Modeling and identification of solar cell parameters must be accurate. The use of renewable energy is a major factor in increasing energy potential and protecting the environment in many countries. Solar energy accounts for a significant share of renewable energy. In order to avoid an increase in production costs, the issue of increasing the efficiency of photocells was on the agenda. It is crucial to correctly evaluate solar cells' parameters to determine their efficiency. Experimental data on polycrystalline silicon solar cells are presented in this paper. The results of the simulation experiment of individual solar cells and polycrystalline cells via the NI Multisim simulator are presented.

Keywords: *Solar sell, photovoltaic, Fill Factor, Current - Voltage characteristics*

1. INTRODUCTION

In recent years, there has been increasing scientific interest in the efficient use of solar energy to prevent the cost of manufacturing photovoltaic converters from increasing. To this end, new silicon-based structures have been introduced to reduce optical and recombination losses [1–3]. In the production of photovoltaics, it is crucial to accurately calculate the parameters that characterize the solar cell. One of the most important parameters that determine the efficiency of a photoelectric converter is its current-voltage characteristic. It is therefore essential to study solar photovoltaic parameters such as short-circuit current (SC), no-load voltage (VOC), fill factor (FF), and the efficiency of converting solar energy into electricity [5].

Silicon is the most commonly used semiconductor material in solar cells due to its high efficiency, low cost, and long service life. Manufacturers of silicon solar cells offer warranties of more than 25 years if the cells produce an average of more than 80% of their maximum power [6]. However, other semiconductor materials such as cadmium

telluride (CdTe) are also widely used in solar cells. While CdTe solar cells are less efficient than silicon solar cells, they can still be effective under certain conditions [8]. Additionally, thin-film solar cells are commonly used in practice, and they are made by depositing one or more thin layers of photovoltaic material onto a substrate material, which is often glass, plastic, or metal.

Recent research has found that one way to increase the efficiency of photovoltaic cells is by stacking multilayer semiconductors, similar to how solar cells are made. Each layer has its own frequency band, which enables it to absorb a different part of the solar spectrum and make more efficient use of solar energy. For instance, III-layer solar cells can achieve efficiencies of approximately 40% [5]. While the manufacturing technology for these cells can be challenging and expensive, photovoltaic materials become more efficient as light becomes more concentrated. Therefore, higher overall efficiency can be achieved with concentrated photovoltaic (CPV) cells and modules [4,7].

A recent study published in the journal Energy & Environmental Science found that the use of nanowires in photovoltaic cells could significantly improve their efficiency [8]. Nanowires are tiny, wire-like structures made of semiconductor materials that can be used to capture and transport electrons in a photovoltaic cell more efficiently than traditional solar cell materials. While nanowire-based photovoltaic cells are still in the experimental stage, they show promise for improving solar energy conversion efficiency.

2. THEORY

Short-circuit current (SC) is the maximum current that a solar cell can produce under short-circuit conditions, meaning that the positive and negative terminals of the cell are directly connected without any load. The short-circuit current is directly proportional to the intensity of the incident light and the active area of the solar cell.

No-load voltage (VOC) is the maximum voltage that a solar cell can produce when there is no current flowing through it, or in other words when it is operating in an open-circuit condition. The no-load voltage is directly proportional to the energy of the incident light and the type of semiconductor material used in the solar cell.

Fill factor (FF) is a measure of how effectively a solar cell can convert sunlight into electrical power. It is defined as the ratio of the maximum power output of a solar cell to the product of the short-circuit current and the open-circuit voltage. The fill factor is affected by factors such as the electrical resistance of the cell, the presence of defects in the semiconductor material, and the uniformity of the cell.

The efficiency of converting solar energy into electricity is the most important parameter of a solar cell. It is the ratio of the electrical power output of a solar cell to the energy of the incident light. The efficiency is affected by several factors, including the spectral response of the cell, the thickness and quality of the semiconductor material, and the design of the cell. Increasing the efficiency of solar cells is essential to reduce the cost of solar energy and make it a more competitive alternative to fossil fuels.

The p-n junction, which is formed by placing p- and n-type semiconductors in close contact with each other, is a crucial component of a photovoltaic cell. The electric field created at the border of the p-n junction accelerates minor charge carriers, which generate drift currents, while the main charge carriers create diffusion currents [4].

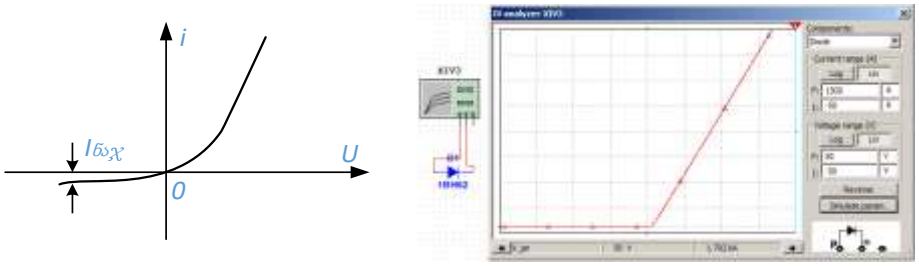

a) b)

Figure 1. a) current-voltage characteristic of a semiconductor diode at a p-n junction, b) current-voltage characteristic of a diode manufactured by Toshiba (1BH62), taken in the National Electronics company's Multisim simulator

In the theory of semiconductors, it is stated that the current-voltage characteristic of an ideal $p-n$ junction is described by the Shockley equation [4]:

$$i(u) = i_{max}\left[exp\left(\frac{qu}{k_BT}\right) - 1\right], \quad (1)$$

where e is the electron charge, k_B is the Boltzmann constant, T is the absolute temperature. Since at room temperature, the thermal voltage is: $\frac{k_BT}{q} = 0.026$, therefore, at positive voltages greater than 0.1 V, in equation (1) the right side in brackets can be neglected compared to the exponential term 1. In the case of non-polarity, on the contrary, the exponential term can be neglected, comparing it with 1. We conclude that with reverse polarity, the tail current, which is created by minority charge carriers, is practically independent of the voltage change and is equal to the saturation current. The expression "p-n junction open at the direct current" is derived because a relatively large current flows through it. On the other hand, with reverse bias, the current is small, and the p-n junction is said to be closed. The value of the reverse voltage at which the reverse voltage is zero is called the cutoff voltage.

At a certain value of the reverse voltage, an electrical breakdown of the $p-n$ junction is possible. fig.1. a) the current-voltage characteristic of the p-n junction is shown. which is non-linear. The nonlinearity of the light source is such that the direct and reverse are significantly different from each other. This means that the properties of the p-n junction change dramatically when the polarity of the external voltage changes. In other words, the p-n junction has unidirectional conduction.

Table 1. Dependence the open circuit voltage to temperature

N	I_0, A	I, μA	n	T, K	u_{oc}, V
1	e^{-10}	34.8	1	300	0.27
2				400	0.36
3				500	0.451
4				600	0.541
5				700	0.631
6				800	0.721
7				900	0.811
8				1000	0.901

Short circuit current and open circuit voltage is the maximum current and voltage of the solar cell. At this time, the power of the solar battery is zero. One of the important parameters is the "fill factor" - "FF", which is defined as the ratio of the maximum power of the solar cell to the product of u_{oc} and I_{sc} [6]:

$$FF = \frac{P_{MP}}{u_{oc}I_{sc}}, \quad (2)$$

u_{oc} – is open circuit voltage. It is maximum and at this stage solar cell current is zero. An equation for u_{oc} is found by setting the net current equal to zero in the solar cell equation to give:

$$u_{oc} = \frac{nk_BT}{q} ln\left(\frac{I}{I_0} + 1\right), \quad (3)$$

I – is Light Generated Current, I_0 - Dark Saturation Current, n - Ideality Factor. So, if we consider that $I_0 = e^{-10}$ A, $I = 34.8$ μA, $n = 1$, we can easily calculate u_{oc} for different temperatures (table 1). It can be seen from the data in the table that the open circuit voltage u_{oc} depends on the saturation current of the solar cell and the light generation current. In turn, the value of saturation current I_0 depends on the recombination factor of the semiconductor material of the solar cell.

Theoretical calculations were made based on standard parameters of crystalline silicon. I_{sc}= 350 μA, u_{oc}=0.67 V. If we consider that the solar cell likes as an ideal diode, the fill factor can be calculated as a function of open circuit voltage u_{oc} [7]:

$$FF = \frac{V_{oc} - \ln(V_{oc} + 0{,}72)}{V_{oc} + 1} = 0.84$$

where

$$V_{oc} = \frac{qu_{oc}}{k_B T} = \frac{0{,}67\ V}{0{,}0258\ V} = 26.8$$

is normalized voltage.

The efficiency of converting solar energy into electrical energy can be calculated by the formula: The conversion efficiency is calculated as the ratio between the maximum generated power and incident power:

$$\eta = \frac{P_{max}}{P_{inc}} = \frac{I_{SC} \cdot FF\ V_{oc}}{I_{irrad}} = 19{,}7\% \qquad (4)$$

where $P_{max} = I_{SC} \cdot FF\ V_{oc}$ - the maximum generated power, $P_{inc} = I_{irrad}$ - is irradiance of incident light.

3. EXPERIMENT

Experiments were performed on the regular solar cell, found on the market, with the following characteristics: sample manufacturer – NUZAMAS, dimensions - 90x60x2mm, with area $A = 54$ cm^2, $u_{max} = 6$ V, $P_{max} = 0.6$ W. Using the multimeter, we measured u_{OC}, I_{SC}, I_{mpp} (current at maximum power point), u_{mpp} (voltage at maximum power point) and by changing resistance measured current voltage at different values of external resistance.

As a result: $I_{SC} = 49.9$ μA, $u_{OC} = 5.1$ V, I_{mpp}=34,8 μA, u_{mpp}=3,9 V. Using these results fill factor and conversion efficiency (η) were calculated:

$$FF = \frac{u_{mpp} \cdot I_{mpp}}{I_{SC} \cdot u_{OC}} = \frac{3.9 \cdot 34.8}{49.9 \cdot 5.3} = 0.51,$$

$$\eta = \frac{I_{SC} \cdot u_{OC} \cdot FF}{I_{in}} = \frac{49.9 \cdot 5.3 \cdot 0.51}{1000} = 0.13 = 13\%.$$

Volt-ampere characteristics of the solar cell are shown on Fig.2 a):

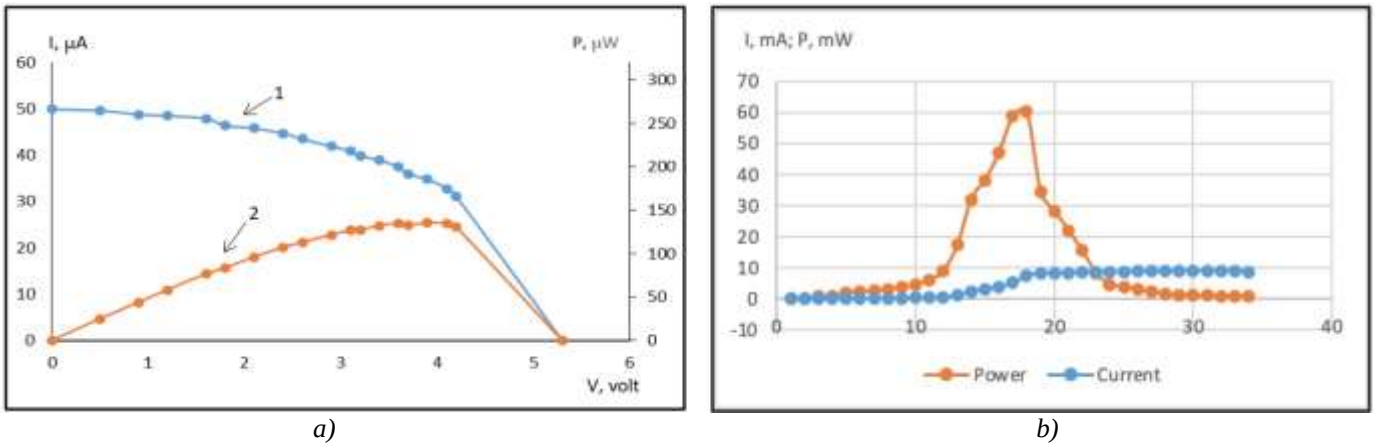

a) b)

Figure 2. a) characteristics of solar cell manufactured with NURZAMAS: I-V (1) and P-V (2) $I_{SC} = 49.9$ μA, $u_{OC} = 5.1$ V, I_{mpp}=34,8 μA, u_{mpp}=3,9 V; b) characteristics of solar module with the specification of the PV module at STC (1000 W/m 2 and 250C): P_{max} = 50 W, u_{mpp} = 18.2 V, I_{mpp} = 2.7 A, u_{OC} = 22.7 V, I_{SC} = 3.1 A

We conducted a comparison experiment on the solar module with the specification of the PV module at STC (1000 W/m^2 and 25^{0}C): P_{max} = 50 W, u_{mpp}= 18.2 V, I_{mpp} = 2.7 A, u_{OC} = 22.7 V, I_{SC} = 3.1 A, Minimum Bypass diode = 12 A, Maximum series due = 10 A, Power tolerance = 0-3% (fig.2 b). To calculate the surface area of the solar cell, we can use the formula:

$$FF = \frac{u_{mpp} \cdot I_{mpp}}{I_{SC} \cdot u_{OC}} = \frac{18.2 \cdot 2.7}{22.7 \cdot 3.1} = 0.72$$

next, we can calculate the surface area of the solar cell:

$$A = \frac{I_{SC} \cdot u_{OC} \cdot FF}{P_{max}} = \frac{3.1 \cdot 22.7 \cdot 0.72}{50} = 0.5028\, m^2$$

Finally, we can calculate efficiency:

$$\eta = \frac{P_{max}}{A \cdot 1000} 100\% = \frac{50}{0.5028 \cdot 1000} 100\% = 9.94\%.$$

Thus, to make a comparison between the solar cell with NURZAMAS parameters and the solar module with STC specifications, we need to consider the characteristics of both devices. The solar cell with NURZAMAS parameters has dimensions of 90x60x2mm and an area of 54 cm2. It has a maximum voltage of 6 V and a maximum power of 0.6 W. The solar module with STC specifications has an area of typically 1 square meter and is designed to operate at standard test conditions (STC) of 1000 W/m2 and 25°C. The module has a maximum power output, which is dependent on the specific model and manufacturer. Important conclusions that can be made based on this comparison are: 1. The solar cell with NURZAMAS parameters is a small-scale device, suitable for use in low-power applications or in small portable electronic devices; 2. The solar module with STC specifications is designed for use in larger-scale applications, such as residential or commercial solar power systems; 3. The efficiency of the solar module is less (9.94%) than that of the NURZAMAS solar cell (13%), as modules typically have better efficiency due to their optimized design; 4. Both devices have different characteristics and applications, and the choice between them will depend on the specific requirements and constraints of the application.

4. SIMULATION EXPERIMENTS

For comparison, here are three models of solar photovoltaic (PV) cells, on which a simulation experiment was carried out in the NI Multisim simulator. A solar cell is represented as an ideal current source with a semiconductor diode and load resistance connected in parallel.

Two DC power supplies are connected to the model: Virrad represents the illuminated level at which 1000 V = 1000 W/m^2, and Vbias allows you to change the offset point for measuring output Current – Voltage Characteristic. In a real application, Vbias will be replaced by a load (fig.3).

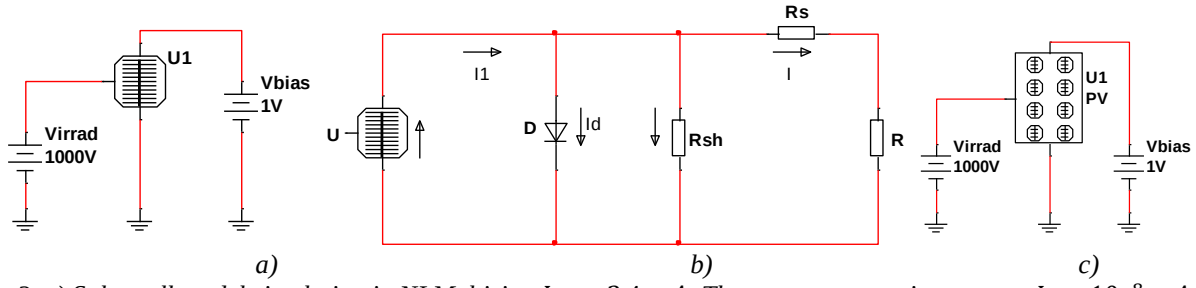

a) b) c)

Figure 3. a) Solar sell model simulation in NI Multisim. $I_{SC} = 3.4\ mA$, The reverse saturation current $I_0 = 10^{-8}\ mA$, solar cell area is $A = 1\ cm2$, b) PV cell circuit; c) Solar sell connected in series. Simulation model in NI Multisim. The short circuit current: $I_{SC} = 3.87\ A$, The series resistance $R_S = 0.47\ \Omega$, The shunt resistance: $R_{sh} = 1.365\ k\Omega$, The temperature coefficient of the power: $k_p = -0.5 \pm 0.05$, The number of solar cells in series: $n_s = 72$

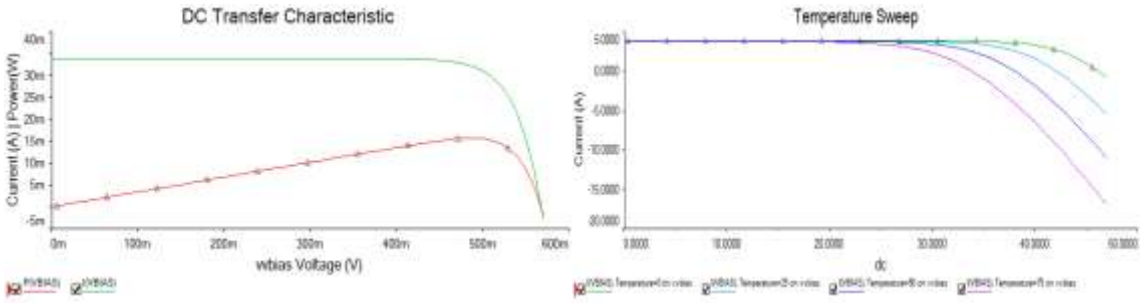

a) *b)*

Figure 4. a) Current – Voltage (1) and Power – Voltage (2) characteristics for the individual solar cell; b) Figure 7. The effect of temperature on the Current-Voltage characteristics of the solar cell

Solar cells, like semiconductor devices, are sensitive to temperature. An increase in temperature decreases the band gap of the semiconductor, so the electronic energy increases. The solar cell's temperature increase is most affected by the open circuit voltage. The effect of increasing temperature is shown in Fig. 4 b) and Fig. 5 a). In figure 5 b) presents Power – Voltage characteristics for different temperatures ($10 - 50^0C$).

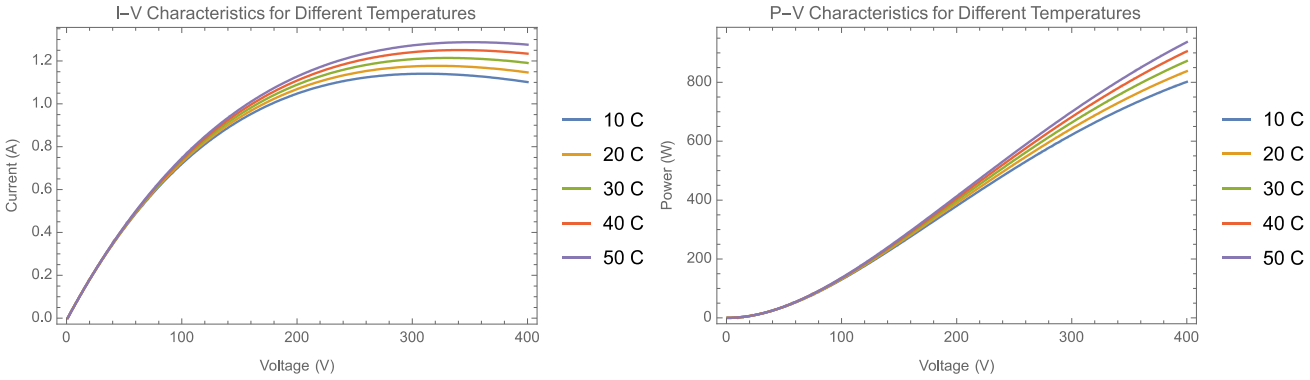

a) *b)*

Figure 5. Simulation modeling of the solar module: a) Current – Voltage characteristics for different temperatures; b) Power – Voltage characteristics for different temperatures

The fill factor is an important parameter that characterizes the performance of a solar cell (fig.6). It represents the efficiency of the solar cell in converting sunlight into electricity, and is defined as the ratio of the maximum power that can be obtained from the solar cell to the product of the open circuit voltage and short circuit current.

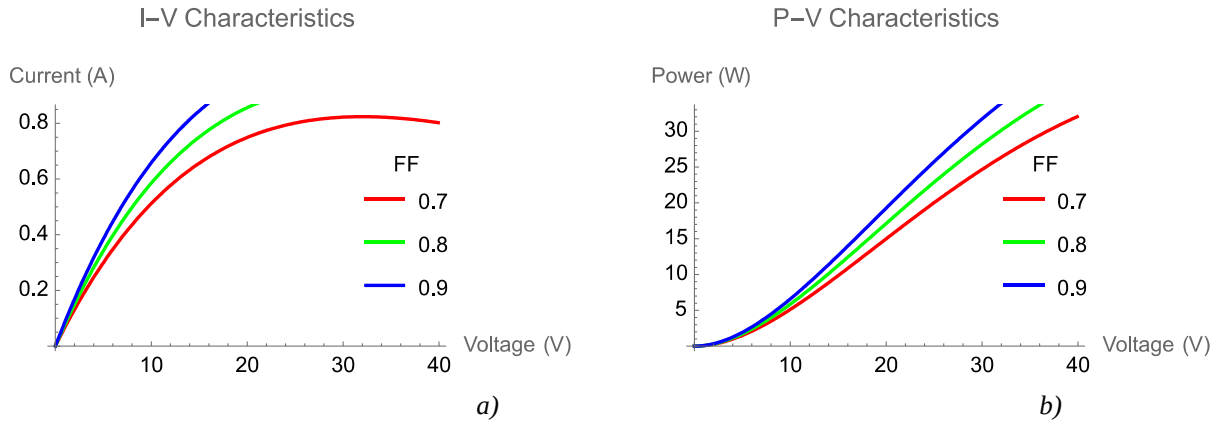

a) *b)*

Figure 6. Simulation modeling of solar module ($T = 25^0C$): a) Current – Voltage characteristics for different FF; b) Power – Voltage characteristics for different FF

5.CONCLUSIONS

Solar cell parameters' dependence on the photoelectric properties of semiconductors was studied. Using experimental results, the volt-ampere characteristic chart was created and from this chart short circuit current, open circuit voltage, fill factor and conversion efficiency were defined. Polycrystalline Silicon Solar Cell parameters were calculated theoretically. Theoretical and experimental results showed that ordinary solar cells, found on the market, have low fill factor and conversion efficiency and in most cases, they produce less electric current and voltage than according to the model description from the manufacturer datasheet. The manufacturer of a PV system usually provides information on open circuit voltage, short circuit current, and maximum power points. Though knowing specific parameters (fill factor (FF) or conversion efficiency) of PV cells is crucial for performance evaluation, control, efficiency computations, and maximum power point tracking of solar PV systems.

Simulation experiments were performed using NI Multisim. The volt-ampere characteristic is constructed for individual photovoltaics and for a solar panel model (polycrystalline photovoltaic) consisting of several individual photovoltaics. it is shown that under laboratory conditions the current-voltage characteristic of photovoltaics is similar to ideal.

Finally, it's worth noting that the performance of a solar cell can be improved by using various techniques, such as anti-reflection coatings, surface texturing, and material doping. These techniques can help increase light absorption, reduce reflection losses, and improve the collection of charge carriers.

Acknowledgment

The present work was funding by Batumi Shota Rustaveli State University and Ministry of Education, Sport and Culture of Ajara Autonomous Republic.

References

[1] Smets A., Jäger K., Isabella O., Swaaij R. V., Zeman M. Solar Energy. UIT Cambridge, 2016.
[2] Avsajanashvili G. Solar energy and Helioresources, TSU, Tbilisi, 2014.
[3] Shockley W. Electrons and holes in semiconductors with applications to transistor electronics, New York, 1950.
[4] Gomidze N., Gomidze Kh. Radiophysics. ISBN 978-9941-488-57-3. UDC (UAC) 621.39 (075.8) No.-796, 2022 (in Georgian). https://rustaveli.org.ge/geo/200916031925tsignebi/radiofizika
[5] Shainidze J., Kalandadze L., Nakashidze O., Gomidze N. Estimation of Parameters for a Model of Polycrystalline Solar Cells. Journal Nanotechnology Perceptions, 16, 52-55. DOI: 10.4024/N17SH19A.ntp.16.01, 2020. http://www.colbas.org/ntp/abstracts/N17SH19A-abs.pdf
[6] Cotfas D.T., Cotfas P.A., Kaplanis S. Methods to determine the dc parameters of solar cells. A critical review, Renewable and Sustainable Energy Reviews, vol. 28, pp. 588–596, 2013.
[7] Augusto A., Herasimenka S.Y., King R.R., Bowden S. G., Honsberg C. Analysis of the recombination mechanisms of a silicon solar cell with low bandgap-voltage offset, Journal of Applied Physics, vol. 121, no. 20, 205704, 2017.
[8] Zhang J., Yang P., & Wang Z. L. (2021). Nanowire-enabled high-efficiency solar energy conversion. Energy & Environmental Science, 14(4), 1966-1990.

RIGA 2023

Analysis of Energy Efficiency in Public Lighting Systems Friendly to the Environment and Protected Areas.

Carlos Velásquez
Dept. of Applied Mathematics University of Alicante, Alicante, Spain, cavf1@alu.ua.es, ORCID: 0000-0002-6779-4293
Universidad Central del Ecuador, Modalidad en Línea, Quito, Ecuador
Instituto de Investigación Geológico y Energético, Quito, Ecuador

Francisco Espín
Instituto de Investigación Geológico y Energético, Quito, Ecuador, francisco.espin@geoenergia.gob.ec, ORCID: 0000-0002-0945-6157
Departamento de Luminotecnia, Luz y Visión, Universidad Nacional de Tucumán, Tucumán, Argentina

Francisco Rodríguez
Dept. of Applied Mathematics University of Alicante, Alicante, Spain, f.rodriguez@ua.es, ORCID: 0000-0002-0753-7826

M. Ángeles Castro
Dept. of Applied Mathematics University of Alicante, Alicante, Spain, ma.castro@gcloud.ua.es, ORCID: 0000-0003-4331-4619

Cite this paper as: *Velásquez C., Espín F., Rodríguez F., Castro M.A. Analysis of energy efficiency in public lighting systems friendly to the environment and protected areas. 11. Eur. Conf. Ren. Energy Sys. 18-20 May 2023, Riga, Latvia*

Abstract: Solid-state lighting technology with LED equipment is the principal tool in the energy efficiency of public lighting systems. Particularly in Ecuador, state policies establish the exclusive purchase of LED systems from 2023, except for special projects. Ecuador has a large amount of biodiversity. National parks rich in flora, fauna, and natural wealth, are protected by international institutions and agreements such as UNESCO, CBD, CITES. However, the measure of energy efficiency, in general, is the reduction of electricity consumption. In this article, aspects such as the correlated color temperature in lighting in protected areas, light pollution, and reduction of energy quality due to harmonic distortion are considered, analyzed, and discussed in addition to energy consumption. It developed measurements of the electromagnetic spectrum of light sources. The high CCT can change some cycles of ecosystems. Additionally, the research found measurements of light pollution from the night skies and a considerable presence of harmonic distortion in the electrical network. The use of simulation in the prediction of the behavior of these variables presents an alternative to preserve protected environments and the quality of energy supply maintaining energy savings.

Keywords: *energy efficiency, harmonic distortion, light pollution, LED, environment*

1. INTRODUCTION

The energy efficiency of public lighting systems is a relatively new goal in some countries of the world [1–3]. Regions like the European community have seen this transition for some years ago. However, Central America and South America regions have recently started their changes [4]. Ecuador, for example, since 2023 has determined

that purchases for public street lighting will be exclusively with the use of LED technology except for specific projects [5].

Efficient lighting is a subject analyzed from the technological and design aspect. The first stage of analysis is from the point of view of the light sources. The SSL (solid-state lighting) technology with its greatest exponent, the LED (light-emitting diode), is today the most widely used technology for energy saving in lighting without affecting lighting levels. However, the second stage of analysis discusses the lighting design topic. The lighting design must be according to the activity and the users. In most cases, standards such as CIE 115 [6] promote recommendations on the levels that are required in street public lighting.

A great number of natural reserves in the world for its biodiversity are in various countries of South America [7]. Generally, some international treaties and organizations are responsible for protecting this natural wealth in different countries. Ecuador, for example, has 11 protected nature reserves (national parks) [8]. The most emblematic is the Galapagos National Park. It has national and international protection agreements such as the United Nations Educational, Scientific and Cultural Organization (UNESCO), Convention on Biological Diversity (CBD), Convention on International Trade in Endangered Species of Wild Fauna and Flora (CITES), among others.

Efficiently lighting in protected areas is a real challenge. Energy efficiency is usually associated with the reduction of electrical energy consumption. However, in protected areas, different parameters should be considered. There is a significant influence on night sky pollution, the electromagnetic spectrum of the lighting sources disturbs different ecosystems, and the harmonic distortion produces a poor quality of energy in the lighting dimming processes.

2. METHODOLOGY

The parameters of interest are analyzed through measurements in the Galapagos National Park of Ecuador. The brightness of the night sky was measured using a Sky Quality Meter SQM-LU-DL at 2 points with a lighting system, also having a measurement in an area far from lighting systems as a control group. The electromagnetic spectrum of the luminaires installed in these lighting systems was measured with a StelarNet UVIR spectrometer. Subsequently, using a mathematical approach, its correlated color temperature (CCT) was calculated. Total harmonic distortion was measured with a METREL 2892 power analyzer. In this case, an installed luminaire was isolated in the laboratory and powered with a LISUN LSP-15kVA adjustable source. The results were compared with the total harmonic distortion (THD) of the dimmed luminaire at 60% of its nominal luminous flux value. It is important to measure in the laboratory since THD measurements are sensitive to various parameters such as temperature [9]. Finally, through a simulation in Dialux, the analysis of the photometric behavior of the actual installation is carried out. A new installation is proposed that allows contributing to the solution of the problems of the parameters of interest, maintaining the lighting service with the required levels.

3. RESULTS AND DISCUSSIONS

Night sky quality

Values of night sky brightness S_b measured in $\frac{mag}{arcseg^2}$ were obtained during 13 days and nights. Temperatures vary approximately from 28 ℃ during the day to 16 ℃ degrees at night (see in Fig. 1). The measuring equipment is not affected by the environment in this temperature range.

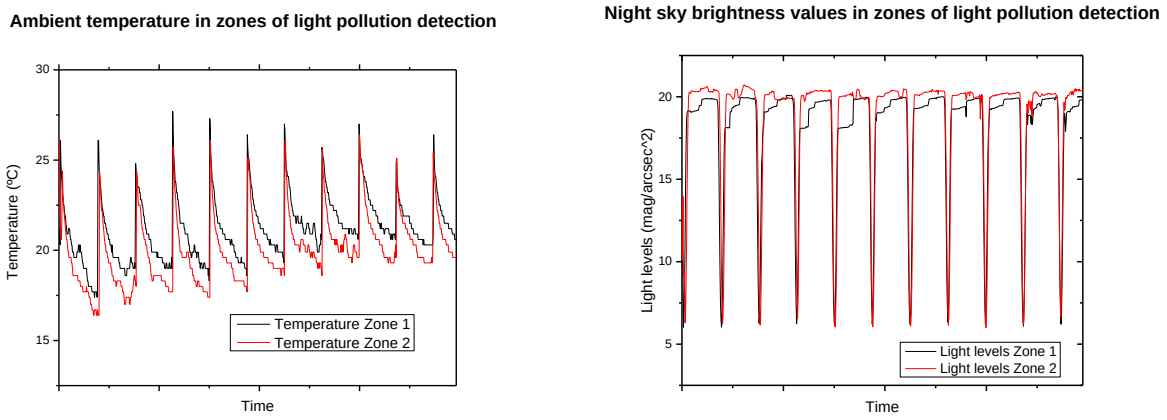

Figure 1. Behavior of the temperature in the measurement zones (left). Measured night sky brightness values (right).

Figure 1 shows that the same levels of sky darkness are reached every night. It is found that at the darkest point of the nights monitored in the two sampling areas, the highest value of S_b is 20.7 $\frac{mag}{arcseg^2}$. Which implies a 4.5 on the Bortle scale or a visibility of the Milky Way with lacks details. The reference measurement was carried out in a sector of the national park without lighting close to 3 km in all directions and an S_b value of 21.5 $\frac{mag}{arcseg^2}$ was observed, corresponding to a scale of 2 on the Bortle scale. That is a visibility of the milky way rich in detail.

Light pollution produced by uncontrolled lighting is affecting the sharpness of the night sky in a protected national park on 2 levels of the Bortle scale. One of the factors that can affect these measurements is the inclination of the luminaires in the system. At the moment they are with an angle of inclination of 15º. This angle is usually useful to meet street lighting levels both in luminance values and uniformities. However, it allows a certain amount of luminous flux to exit towards the sky, which can cause the measured behavior.

Electromagnetic spectrum and correlated color temperature

The electromagnetic spectrum of 11 installed luminaires was obtained (see in Fig. 2). It was found that qualitatively the spectra of the set of luminaires is very similar.

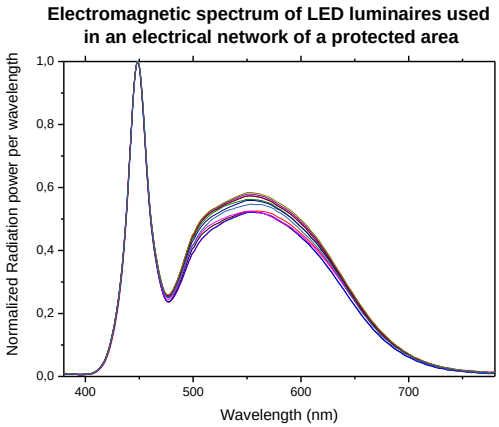

Figure 2. Electromagnetic spectrum of the installed LED luminaires, each color is a different luminaire.

To quantify the similarity obtained, the CCT is calculated. For this, given an electromagnetic spectrum $\Phi_\lambda(\lambda)$, were λ is wavelength, the parameters X, Y, and Z must be found according to Eqs. [1-3].

$$X = k\sum_{\lambda} \Phi_{\lambda}(\lambda)\bar{x}(\lambda)\Delta\lambda \quad (1)$$

$$Y = k\sum_{\lambda} \Phi_{\lambda}(\lambda)\bar{x}(\lambda)\Delta\lambda \quad (2)$$

$$Z = k\sum_{\lambda} \Phi_{\lambda}(\lambda)\bar{x}(\lambda)\Delta\lambda \quad (3)$$

Where, $\bar{x}(\lambda)$, $\bar{y}(\lambda)$, and $\bar{z}(\lambda)$ are defined in CIE 15 [10], and k is defined in Eq. [4].

$$k = \frac{100}{\sum_{\lambda} \Phi_{\lambda}(\lambda)\bar{y}(\lambda)\Delta\lambda} \quad (4)$$

Then, calculate the x and y parameters using Eqs. [5-6]

$$= \frac{X}{X+Y+Z} \quad (5)$$

$$y = \frac{Y}{X+Y+Z} \quad (6)$$

Finally, using equation Eq. [7] calculate the TCC.

$$TCC = a\left(\frac{x-x_e}{y-y_e}\right)^3 + b\left(\frac{x-x_e}{y-y_e}\right)^2 + c\left(\frac{x-x_e}{y-y_e}\right) + d \quad (7)$$

Where, $x_e = 0.3320$, $y_e = 0.1858$, $a = -437$, $b = 3601$, $c = -6861$, $d = 5514.31$. These values are suggested by [11].

It was obtained that the average CCT of the luminaires in nominal operation is 6051 K and when they are dimmed to 60% the CCT is 6218 K. According to NOM-031 [12], there are CCT intervals where the user can consider that the color is the same. In this case, $6532\ \text{K} \pm 510\ \text{K}$ is accepted. Therefore, there is no perceptible variation by the user in color temperature when the system has been dimmed.

Although for human users this color temperature does not have much influence since it is a transit street, ecosystems are seriously affected [13], [14]. Several species of invertebrates, bats, and turtles can be affected by the blue radiation of LED luminaires [14]–[17]. Figure 2 clearly shows an important load of blues represented in CCTs greater than 6000 K. This can significantly affect the natural functioning of ecosystems on national parks.

Power quality in dimming

Power quality is one of the main problems when using LED technology [18]. LED luminaires need to convert AC voltage to DC. The driver is the element that is in charge of this conversion, but it introduces harmonics in the network. One way of quantizing is called Total Voltage Distortion (THDv) and the other is Total Current Distortion (THDi). In the dimming process, the light emitted by the luminaire is reduced and, in general, its power is also reduced. This dimming can alter the energy quality in the electrical network.

From the measurements obtained, it is observed that at reduced power the amplitude and order of harmonics increase. Figure 4 shows the increases in THDv and THDi during the dimerization process. This causes a greater

deformation of the current wave, the reference were the signal of nominal power voltage and current meet in Figure 3.

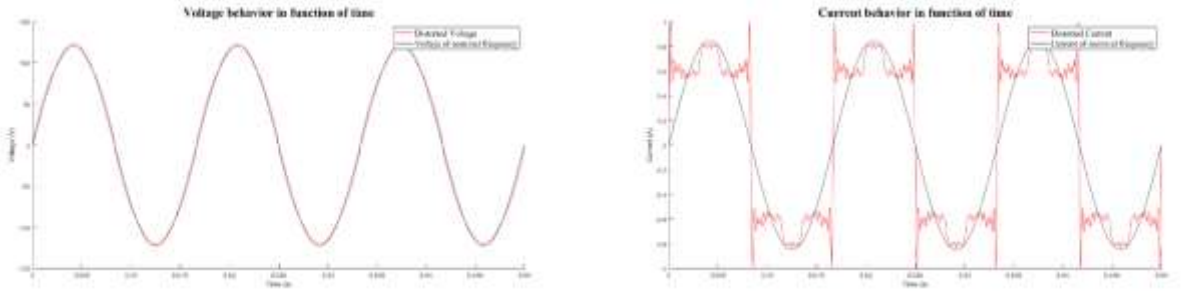

Figure 3. The red line is voltage signal (left) and current signal (right) with the harmonics in nominal power. The black signal is fundamental voltage (left) and current (right) at 60 Hz frequency.

A total harmonic distortion of voltage for nominal and reduced power is 4.69%. Both nominal and reduced power are complying with THDv according to IEEE 519 [19].

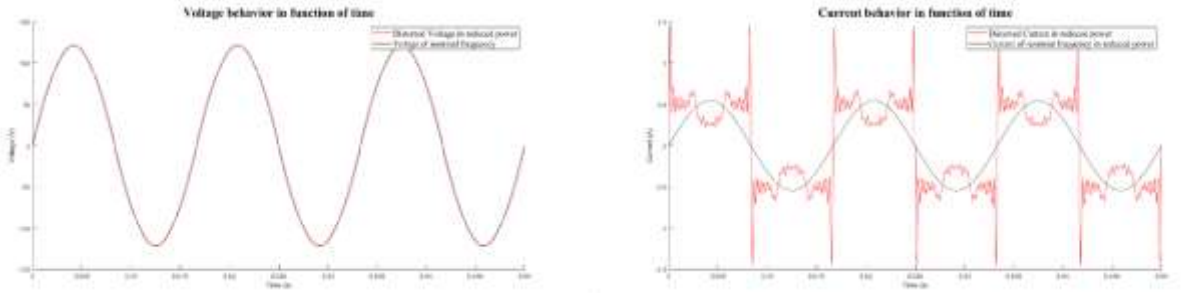

Figure 4. The red line is voltage signal (left) and current signal (right) with the harmonics in reduced power. The black signal is fundamental voltage (left) and current (right) at 60 Hz frequency.

The THDi of nominal power is 46.5% and 99.17% for reduced power. The luminaire at nominal power presents a distorted current wave (see in Fig. 1). However, when its power is reduced, its amplitude of the third harmonic increases by around twice, causing a greater distortion of its current (see in Fig. 2). It is known that the main effect of the third harmonic is increase the current in neutral line which results in higher current and losses in the distribution network. The organizations in charge of managing lighting systems must be aware of the number of luminaires installed per circuit to comply with the regulations, especially with dimmer or reduced power

Lighting design proposal

The street lighting class is M6, according to the criteria contained in the CIE 15 [6]. A roadway R3 is considered with a coefficient reflectance of q0=0.07, with two lanes of 7m each. According to Table 1, the two installations, the current one and the proposed one, comply with the requirements demanded in CIE for class M6. However, the proposed installation presents better efficiency in the LED luminaires. With the existing infrastructure, the luminous flux can be lowered with the proposed luminaires (2200 K) and at the same time meet the lighting quality criteria.

Table 1. Installation arrangement and lighting performance for each stage

	Street Arrangement								Lighting performance			
Stage	TCC [K]	Luminous flux (Luminaire) [lm]	Luminaire Wattage [W]	Efficiency [lm/W]	Height [m]	Overhang [m]	Boom Angle [°]	Boom Length [m]	L_{av} [cd/m²] ≥ 0.30	U0 ≥ 0.35	Ul ≥ 0.40	TI [%] ≤ 15
Actual	6000	4672	44.0	106.2	8.250	-0.650	15.0	0.5	0.38	0.37	0.4	8
Proposed	2200	2960	23.9	123.8	7.482	-0.650	0.0	0.5	0.3	0.47	0.43	10

4. CONCLUDING REMARKS

The results and the preliminary analysis show that the parameters of interest of the installation are a clear affectation on the ecosystem of the natural park and the quality of energy. The electromagnetic spectrum of the installed LED luminaires and the position of their installation affect the biological cycles of some species and also the pollution of the night sky. The dimming process reduces the power quality of the electrical network. The proposal presented shows that, by changing the CCT to values lower than 3000 K and the installation angle of the luminaire from 15º to 0º, the impact on the ecosystem and pollution of the night sky can be reduced. By controlling the THD at the time of dimerization, contamination of the electrical network would be avoided. It was done while maintaining the quality of the lighting system at the required lighting levels.

Acknowledgment

The authors thank TRANSELECTRIC CELEC EP for the use of their facilities.

References

[1] D. Radulovic, S. Skok, and V. Kirincic, "Energy efficiency public lighting management in the cities," *Energy*, vol. 36, no. 4, pp. 1908–1915, Apr. 2011, doi: 10.1016/J.ENERGY.2010.10.016.
[2] F. Pardo-Bosch, A. Blanco, E. Sesé, F. Ezcurra, and P. Pujadas, "Sustainable strategy for the implementation of energy efficient smart public lighting in urban areas: case study in San Sebastian," *Sustain. Cities Soc.*, vol. 76, p. 103454, Jan. 2022, doi: 10.1016/J.SCS.2021.103454.
[3] F. Sanchez-Sutil and A. Cano-Ortega, "Smart regulation and efficiency energy system for street lighting with LoRa LPWAN," *Sustain. Cities Soc.*, vol. 70, p. 102912, Jul. 2021, doi: 10.1016/J.SCS.2021.102912.
[4] United Nations Climate Change, "Replacement of Street Lighting with LED – Argentina | UNFCCC." https://unfccc.int/climate-action/momentum-for-change/activity-database/momentum-for-change-replacement-of-the-street-lighting-system-with-led-technology (accessed Feb. 14, 2023).
[5] Ministerio de Energía y Minas del Ecuador, "Especificaciones Técnicas de luminarias LED," *2022*. https://www.unidadespropiedad.com/index.php?option=com_content&view=article&id=579%3Aled&catid=18%3Apdfs&Itemid=744 (accessed Feb. 14, 2023).
[6] Commission Internationale de L'Eclairage, "Road Lighting Calculations," Vienna, 2000.
[7] J. Liu, Z. Ouyang, W. Yang, W. Xu, and S. Li, "Evaluation of Ecosystem Service Policies from Biophysical and Social Perspectives: The Case of China," *Encycl. Biodivers. Second Ed.*, pp. 372–384, Jan. 2013, doi: 10.1016/B978-0-12-384719-5.00335-X.
[8] A. y T. E. Ministerio del Ambiente, "Ecuador cuenta con 11 Parques Nacionales – Ministerio del Ambiente, Agua y Transición Ecológica." https://www.ambiente.gob.ec/ecuador-cuenta-con-11-parques-nacionales/ (accessed Feb. 15, 2023).
[9] C. Brusil, F. Espín, and C. Velásquez, "Effect of Temperature in Electrical Magnitudes of LED and HPS Luminaires," *Int. J. Electr. Comput. Eng. Syst.*, vol. 12, no. 4, pp. 225–234, Nov. 2021, doi: 10.32985/IJECES.12.4.6.
[10] Commission Internationale de L'Eclairage, "Colorimetry," Vienna, 2004.
[11] C. S. McCamy, "Correlated color temperature as an explicit function of chromaticity coordinates," *Color Res. Appl.*, vol. 17, no. 2, pp. 142–144, Apr. 1992, doi: 10.1002/COL.5080170211.
[12] Secretaría de Energía de México, "Eficiencia energética para luminarios con led para iluminación de vialidades y áreas exteriores públicas. Especificaciones y métodos de prueba.," 2019.
[13] M. Grubisic, R. H. A. van Grunsven, A. Manfrin, M. T. Monaghan, and F. Hölker, "A transition to white LED increases ecological impacts of nocturnal illumination on aquatic primary producers in a lowland agricultural drainage ditch," *Environ. Pollut.*, vol. 240, pp. 630–638, Sep. 2018, doi: 10.1016/J.ENVPOL.2018.04.146.
[14] T. W. Davies, J. Bennie, D. Cruse, D. Blumgart, R. Inger, and K. J. Gaston, "Multiple night-time light-emitting diode lighting strategies impact grassland invertebrate assemblages," *Glob. Chang. Biol.*, vol. 23, no. 7, pp. 2641–2648, Jul. 2017, doi: 10.1111/GCB.13615.
[15] L. M. Cruz, G. L. Shillinger, N. J. Robinson, P. S. Tomillo, and F. V. Paladino, "Effect of light intensity and wavelength on the in-water orientation of olive ridley turtle hatchlings," *J. Exp. Mar. Bio. Ecol.*, vol. 505, pp. 52–56, Aug. 2018, doi: 10.1016/J.JEMBE.2018.05.002.
[16] S. M. Pawson and M. K. F. Bader, "LED lighting increases the ecological impact of light pollution irrespective of color temperature," *Ecol. Appl.*, vol. 24, no. 7, pp. 1561–1568, Oct. 2014, doi: 10.1890/14-0468.1.
[17] E. L. Stone, G. Jones, and S. Harris, "Conserving energy at a cost to biodiversity? Impacts of LED lighting on bats," *Glob. Chang. Biol.*, vol. 18, no. 8, pp. 2458–2465, 2012, doi: 10.1111/J.1365-2486.2012.02705.X.
[18] C. Brusil, H. Arcos, F. Espin, and C. Velasquez, "Analysis of harmonic distortion of led luminaires connected to utility grid," *2020 IEEE ANDESCON, ANDESCON 2020*, Oct. 2020, doi: 10.1109/ANDESCON50619.2020.9272004.
[19] Institute of Electrical and Electronics Engineers, "Recommended Practice and Requirements for Harmonic Control in Electric Power Systems," 2014.

RIGA 2023

Will Industrial Green Total Factor Productivity be Affected By Digital Finance?

Luqi Miao
Shanghai University, Shanghai, 1041246598@shu.edu.cn, ORCID:0000-0002-4902-3436

Xiao Luo
Shanghai University, Shanghai, lorita_luo_2002@163.com, ORCID: 0000-0003-3950-7266

Jun Chen
Shanghai University, Shanghai, chenjun1@shu.edu.cn, ORCID:0000-0002-6781-600X

Cite this paper as: *Miao,L, Luo,X, Chen, J. Will Industrial Green Total Factor Productivity be Affected by Digital Finance?. 11. Eur. Conf. Ren. Energy Sys. 18-20 May 2023, Riga, Latvia*

Abstract: With the continuous advancement of digitalisation, digital finance has played an important role in the field of production and life. By collecting data and constructing a transmission mechanism, this article uses a two-way fixed-effects model to analyse the relationship between digital finance and industrial green total factor productivity, and further explores the reasons for the different results in different regions. Based on the findings, the paper offers constructive suggestions to the government in terms of accelerating the process of digital finance and improving industrial green total factor productivity.

Keywords: *Digital Finance; Industrial Green Total Factor Productivity; Influence Mechanism; Mediation Effect Model*

1.INTRODUCTION

Since the 21st century, with the rapid development of global industry, environmental issues are becoming increasingly prominent and pose a serious threat to public health [1]. Considering this background, sustainability mindset has attracted public attention; resources and environment are no longer simply endogenous variables affecting economic development [2], but have become the greatest rigid constraints on economic and social development. As one of the most industrialized countries in the world, China's environmental problems are a matter of great urgency [3]. In addition, China's long-standing path of sloppy growth that relies on consuming resources and polluting the environment has ended [3]. In 2015, China has brought together economic development and sustainable development, seeing them as driving forces for each other. It implies that the growth of total factor productivity will become the most significant driving force of China's economic growth in the future [4], while resources will be used more efficiently and the environment will be better protected, thus achieving sustainable economic development.

It is well known that finance is an important part of the economic system[3,5]. However, China's financial system still suffers from a number of problems and pitfalls, and there is severe scale discrimination and ownership discrimination in the allocation of financial resources. Considering China's current stage of slowing economic growth and economic structural transformation, improving the quality of China's financial system is an important part of meeting the needs of society. In recent years, thanks to the urgency of digital transformation, artificial intelligence, blockchain and other digitization skills, ***Digital Finance*** has emerged and become a powerful complement to the traditional financial system [6].

The possible innovations and contributions of this paper are as follows: first, based on the two-way fixed effect model, the impact of digital finance on industrial green total factor productivity is discussed from the perspective of real economy. Second, on the basis of theoretical mechanism analysis, we explore the intermediary channels of technological innovation, industrial structure and entrepreneurial vitality, and expand the depth of existing research.

2.THEORETICAL MECHANISM

2.1.Direct Action Mechanisms

Digital finance can accelerate the free flow and effective allocation of capital, information, digital and other factors. It provides more efficient and convenient financial services for economic agents, thus enhancing the industrial green total factor productivity. Based on the above analysis, hypothesis 1 is proposed in the following.

Hypothesis 1: The development of digital finance is conducive to enhancing industrial green total factor productivity.

2.2. Indirect Mechanism of Action

2.2.1 Technological Innovation

Technological innovation activities are characterized by high risks, long cycles and high investment. digital finance can also bridge the supply and consumer sides, providing direct feedback from consumers' product demand to producers, which in turn forces enterprises to increase technological innovation [8] and improve the efficiency of innovative products to the market. Based on the above analysis, hypothesis 2 is proposed in the following.

Hypothesis 2: Digital finance can improve industrial green total factor productivity by promoting technological innovation.

2.2.2 Industrial Structure

Digital finance can promote the development of high-tech industries which have high technological content and high added value, and their development will also contribute to industrial total factor productivity improvement. Based on the above analysis, hypothesis 3 is proposed in the following.

Hypothesis 3: Digital finance can enhance industrial green total factor productivity by promoting industrial structure upgrading.

2.2.3 Entrepreneurial Vitality.

The rapid development of digital finance provides fresh opportunities for startups to finance and promote entrepreneurship development. Based on the above analysis, hypothesis4 is proposed in the following.

Hypothesis 4: Digital finance can enhance industrial green total factor productivity by stimulating entrepreneurial dynamics.

3.MODELS AND VARIABLES

3.1.Model Construction

3.1.1.Green Total Factor Productivity Measurement Model

Traditional DEA or SBM models cannot handle the situation that both input and output variables have radial and non-radial characteristics, so the EBM (EBM-based metric) model proposed by Chen et al [7] is adopted. The model can consider the radial ratio of the target value and the actual value at the same time, and handle the radial and non-radial relaxation changes between the input and output elements at the same time, so as to improve the relative

comparability of DMUs. However, when there are multiple input and output indicators, the EBM model measures the result so that the efficiency value of multiple decision units is 1 at the same time, and vertical comparison cannot be made. In order to improve the comparability of dmu and consider the complexity of the relationship between industrial economy, energy and environment, EBM model is further constructed on the basis of EBM model, including the undesired output EBM model as follows.

$$\gamma = min \frac{\theta - \varepsilon_x \sum_{i=1}^{m} \frac{w_i^- s_i^-}{x_{ik}}}{\varphi + \varepsilon_y \sum_{r=1}^{s} \frac{w_r^+ s_r^+}{y_{rk}} + \varepsilon_b \sum_{p=1}^{q} \frac{w_p^{b-} s_p^{b-}}{b_{pk}}}$$

$$s.t. \begin{cases} \sum_{j=1}^{n} x_{ij} \lambda_j + s_i^- = \theta x_{ik} \ (i = 1, \ldots, m) \\ \sum_{j=1}^{n} y_{rj} \lambda_j - s_i^+ = \varphi y_{rk} \ (r = 1, \ldots, s) \\ \sum_{j=1}^{n} b_{pj} \lambda_j + s_p^{b-} = \varphi b_{pk} \ (p = 1, \ldots, q) \\ \lambda_j \geq 0, s_i^- \geq 0, s_i^+ \geq 0, s_p^{b-} \geq 0, k(k = 1, \ldots, n) \end{cases} \quad (1)$$

3.2.Variables Selection

All data are from China Statistical Yearbook, China Statistical Yearbook of Energy, China Statistical Yearbook of Industry, China Statistical Yearbook of Environment, China Statistical Yearbook of Science and Technology, Peking University Digital Comprehensive Finance Index (No.3 (2011-2020). Some missing data are completed through interpolation. Descriptive statistics of the data are shown in Table 1.

Table 1. Results of descriptive statistics of the data

Variable types	Variables	Symbol	Sample size	Average value	Standard deviation	Minimum	Maximum
Explained variable	Green total factor productivity	*gtfp*	300	1.3586	0.5763	0.7639	5.6340
Core explanatory variable	Digital finance	*dfi*	300	5.2193	0.6683	2.9085	6.0683
Mediators	Technological innovation	*tec*	300	0.1033	0.0527	0.0202	0.3516
	Industrial structure	*ins*	300	0.4055	0.8487	0.0167	7.9231
	Entrepreneurial dynamism	*ena*	300	8.1439	1.4250	3.7842	10.5976
	Level of industrialisation	*indl*	300	0.4097	0.0807	0.1597	0.6196
Control variables	Human capital	*hc*	300	9.2360	0.8940	6.7665	12.6811
	Infrastructure	*infra*	300	0.0651	0.0559	0.0198	0.2901
	Foreign trade	*open*	300	0.2743	0.2898	0.0076	1.4638
	Environmental regulation	*reg*	300	12.1034	12.3761	0.0855	110.3387
	Urbanisation	*urb*	300	0.5901	0.1222	0.3504	0.8958

4.EMPIRICAL RESULTS AND ANALYSIS

In order to ensure the scientific and credibility of the regression estimation results, the panel regression model is selected by using Hausmann test. The results show that the null hypothesis of the fixed effect model. Therefore, we choose the fixed effects model. Panel fixed effect model 1 tests the impact of digital finance on industrial green

total factor productivity. In order to avoid multicollinearity of explanatory variables, step-up regression method was adopted for variable selection and regression analysis, and the estimated results were shown in Table 2.

As shown in column (1) of Table 2, under the condition of controlling time and individual fixed effect, only the influence of digital finance on the total industrial green factor productivity is considered, and the influence coefficient is significantly positive at the 1% level. After gradually adding control variables, the benchmark regression test results as shown in column (7) are finally obtained. Comparing the regression results in column (1) with those in column (7), there is at least a positive significance level of 10% except for column (4), although there is a specific change in the effect of the size of the digital finance coefficient. In addition, after the introduction of control variables, the significance level is improved, which indicates that the total green factor productivity of digital finance industry has a significant impact, and preliminarily verifies hypothesis 1.

Table 2 Results of the benchmark regression

Variable	(1)	(2)	(3)	(4)	(5)	(6)	(7)
dfi	0.4435*	0.3980*	0.4454*	0.2150	0.5167**	0.5160**	0.6091**
	(1.7987)	(1.6970)	(1.9104)	(0.9459)	(2.0114)	(2.0056)	(2.3425)
indl		7.1522***	6.9360***	6.1887***	6.0105***	5.9725***	6.2349***
		(5.3602)	(5.2361)	(4.8572)	(4.7546)	(4.7046)	(4.9134)
hc			0.4104**	0.3860**	0.3491**	0.3477**	0.3306**
			(2.4436)	(2.4044)	(2.1857)	(2.1730)	(2.0756)
infra				6.5791***	6.9832***	6.8676***	8.0403***
				(5.0650)	(5.3833)	(5.1680)	(5.5604)
open					-0.9678**	-0.9748**	-0.3297
					(-2.4400)	(-2.4515)	(-0.6456)
reg						-0.0014	-0.0015
						(-0.4146)	(-0.4616)
urb							-5.3477**
							(-1.9955)
_cons	-0.4980	-3.6388***	-7.3727***	-6.1651***	-6.5248***	-6.4707***	-4.1850**
	(-0.5561)	(-3.5209)	(-4.0085)	(-3.4766)	(-3.7017)	(-3.6551)	(-1.9929)
Ind	Yes	Yes	Yes	Yes	Yes	Yes	Yes
Year	Yes	Yes	Yes	Yes	Yes	Yes	Yes
N	300	300	300	300	300	300	300
R^2	0.1496	0.2345	0.2518	0.3197	0.3352	0.3356	0.3459
F	4.5732	7.2128	7.2363	9.2913	9.2192	8.5882	8.3945

Note: *, * *, and * * * indicate the significance levels of 10%, 5%, and 1%, respectively, and the values in parentheses are t-values, the same as in the tables below.

5.CONCLUSIONS And POLICY RECOMMENDATIONS

To promote the development of digital finance and green total factor productivity, this paper proposes the following policy recommendations:

First, accelerate digital finance while preventing financial risks. On one side, the construction of financial data centres and cloud computing centres should be further improved, and the technological applications of emerging financial industries in different scenarios should be promoted to provide guarantees for digital financial services to the real economy. On the other hand, while vigorously developing digital finance, it is also necessary to guard

against possible market risks in digital finance, build a digital financial risk prevention and control system with digital technology, strengthen big data risk control, real-time risk control and intelligent risk control, strictly guard the risk bottom line and maintain the sustainable and stable development of digital finance.

Second, deepen financial market reform and unblock channels for disseminating the impact of digital finance on industrial green total factor productivity. First, give full play to the advantages of digital finance such as low cost, high precision and convenience, actively provide financial support for enterprises' innovation activities, and promote regional technological innovation; Second, we will build a financial service platform for the digital industry, actively distribute new industries and advanced manufacturing, and optimize and upgrade the industrial structure. Third, local governments can encourage and stimulate entrepreneurship through a series of policies such as fiscal subsidies, tax cuts and support for entrepreneurship.

Third, identify priorities and implement differentiated digital finance development strategies based on local conditions. On the one hand, the breadth and depth of digital finance are more important to use in improving the total factor productivity of green industry than the degree of digital, so the focus of development should be to increase the coverage of the breadth and depth of digital finance. On the other hand, the eastern region should give full play to its role as a model and leader, pay attention to “quality” improvement, radiate and promote the development of digital finance in the central and western regions; The central and western regions should consolidate the foundation of digital finance development, focus on industrial application, and narrow the gap with the eastern regions.

References

[1] Cui L, Li XM, Yao RX. Analysis on the coupling coordination degree of digital logistics, ecological environment governance and regional economic growth. *Statistics and decision*, 2023; 01: 29-33 <http://10.13546 / j.carol carroll nki tjyjc. 2023.01.005.>

[2] Qiu Y, Yan CJ, Zhang LG. Research on Security System Construction and Countermeasures of Chinese Industrial Chain in Digital Economy Era. *International trade*, 2022; 12: 32-43 <http://10.14114 / j.carol carroll nki itrade. 2022.12.004.>

[3] Li YL, Shen Y. Pratt &whitney financial and unbalanced regional economy. *Journal of economics (quarterly)*, 2022; 22 (5) : 1805-1828. <http://10.13821 / j.carol carroll nki ceq. 2022.05.17.>

[4] Liu C, Hua JG. The effects of financial development to the transformation of enterprise digital Numbers. *Journal of finance and economy*, 2022; 10 : 61-68. <http://10.19622 / j.carol carroll nki cn36-1005 / f 2022.10.006.>

[5] Gao K, He PM, Chen Y. How to promote urban and rural prosperity by digital inclusive Finance: Evidence from the Yangtze River Economic Belt. *Financial development research*, 2022; 10: 10-19. <http://10.19647 / j.carol carroll nki. 37-1462 / f 2022.10.002.>

[6] Zhang ML, Tong T, Chen ZJ. Does socialized agricultural Service help improve agricultural green Productivity? *Journal of southern economy*, 2023; 01 : 135-152. http://The DOI: 10.19592 / j.carol carroll nki scje. 400099.

[7] Chen BH, Feng W, Sun K, Zhang CH, Sun B. Cold hot electric installations, diversified energy storage system and isolated operation optimization scheduling method. *Journal of electrical engineering technology*, 2019; 15: 3231-3243. <http://The DOI: 10.19595 / j.carol carroll nki. 1000-6753.>

[8] Li CM, Li DM, Zhang ZY. Digital infrastructure, family multidimensional poverty reduction and common prosperity. *Journal of hebei university of economy and trade, the lancet*, 2022; 6: 61-72. <http://10.14178 / j.carol carroll nki issn1007-2101.20221107.003.>

[9] Li LH, Han MX, Hou YW. The Impact of Digital financial Inclusion on Real Economy: An Empirical analysis based on System GMM and panel threshold Model. *East China economic management*, 2022; 4 (12) : 14-25. <http://10.19629 / j.carol carroll nki. 34-1014 / f, 211026002.>

[10] Pan XQ. Pratt &whitney financial support logic mechanism and realization mechanism of low-income groups. *Regional economic review*, 2019; 4: 143-149. <http://10.14017 / j.carol carroll nki. 2095-5766.20190715.005.>

RIGA 2023

Applying Explainable AI for Heating Control in Low Power IoT Devices

Algirdas Dobrovolskis
Kaunas University of Technology, Kaunas, Lithuania, Algirdas.Dobrovolskis@ktu.lt, ORCID: 0000-0001-8143-238X

Egidijus Kazanavičius
Kaunas University of Technology, Kaunas, Lithuania, Egidijus.Kazanavicius@ktu.lt

Cite this paper as: *Dobrovolskis, A., Kazanavičius, E. Applying Explainable AI For Smart House Control in Low Power IoT Devices. 11. Eur. Conf. Ren. Energy Sys. 18-20 May 2023, Riga, Latvia*

Abstract: In this paper we explore viability to use expert knowledge driven Explainable AI for heating control using low power IoT device with limited computational resource. By incorporating XAI we aim to provide understanding the decision made by the model and make it more trustworthy for the end user. The Arduino platform was chosen for IoT development due to its widespread use and low cost. Model of heating control was implemented using temperature and presence sensors. Working prototype was benchmarked measuring time between input data and decision making with explanation, to determine if there is a bottleneck obstructing functioning of microcontroller.

Keywords: *Explainable AI, Expert knowledge, Internet of Things, Arduino*

1. INTRODUCTION

Power efficiency is a critical factor[1-8] in the Internet of Things (IoT) due to the widespread deployment of IoT devices and their limited battery life. IoT devices are often small, battery-powered, and deployed in remote locations, making it challenging to replace or recharge their batteries. This requires the devices to be designed to be as power-efficient as possible to ensure their longevity and reduce the costs associated with battery replacement or maintenance.

Moreover, IoT devices typically communicate wirelessly over long distances, which requires significant power for transmitting data. A power efficient IoT device will consume less energy when transmitting data, which prolongs its battery life and reduces the impact of IoT devices on the environment.

In addition to extending the life of IoT devices, power efficiency also plays an important role in the scalability of IoT networks. As the number of IoT devices increases, the overall energy consumption of the network also increases, leading to higher energy costs and increased carbon emissions. Power-efficient IoT devices can help to mitigate these negative impacts and make IoT networks more environmentally sustainable. Power efficiency is a crucial aspect of IoT design, as it impacts the longevity, scalability, and sustainability of IoT networks.

Deep learning algorithms require specialized hardware and significant computational resources to function effectively. This is because deep learning algorithms use complex mathematical models - neural networks which can contain millions of parameters and require intensive computation to train[2]. This computation requires large amounts of memory and processing power, which can be difficult to achieve with traditional computer hardware. In order to overcome this challenge, specialized hardware, such as Graphics Processing Units (GPUs) or Tensor Processing Units (TPUs), are often used to accelerate the computation required for deep learning algorithms.

In addition to hardware, deep learning algorithms also require access to large amounts of data for training. This data is used to "teach" the neural network to recognize patterns and make predictions. The volume of data used in deep learning algorithms can also be a challenge, as it requires large storage capacities and time to gather required amounts to train algorithms properly.

On the other hand, Fuzzy Expert Maps utilizes any hardware capable of running C++ code, does not require advanced processing power, data collection is not needed[5], because expert knowledge[3][4] is used in the process, system functioning is described using rules based on IF – THEN sentences which is a lot less time consuming than training algorithms with raw data and easily explainable[4][5][6][7] using computing with words.

2. MODEL

A fuzzy heating model shown in figure 1 was made with the MATLAB Fuzzy Toolbox package that provides a set of tools for building and simulating fuzzy models in MATLAB. It includes functions for defining fuzzy sets, creating membership functions, and building fuzzy inference systems.

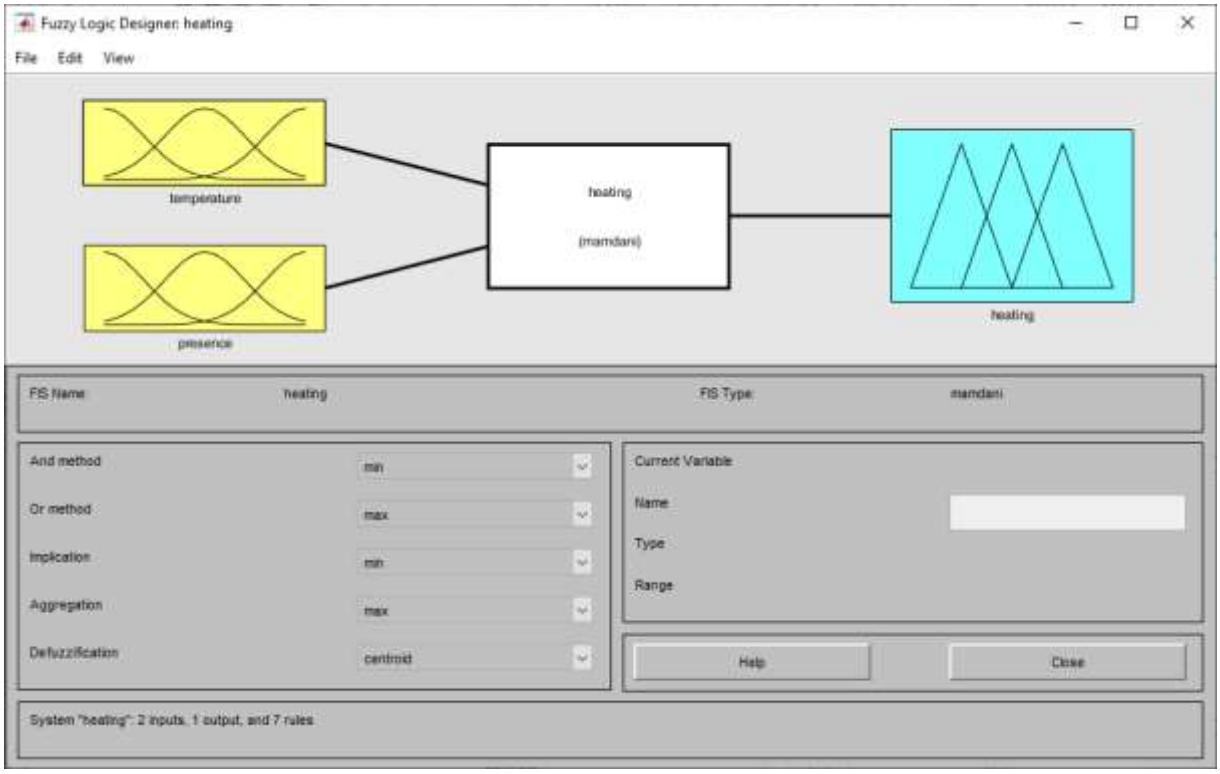

Figure 1. Heating system model in Matlab Fuzzy Toolbox

A fuzzy input function for temperature is a mathematical representation of the membership of a temperature value to a fuzzy set. In the case of temperature, a fuzzy input function represents the different degrees of membership of a temperature value to fuzzy sets such as "very cold", " cold", "warm", and "hot" as shown in figure 2.

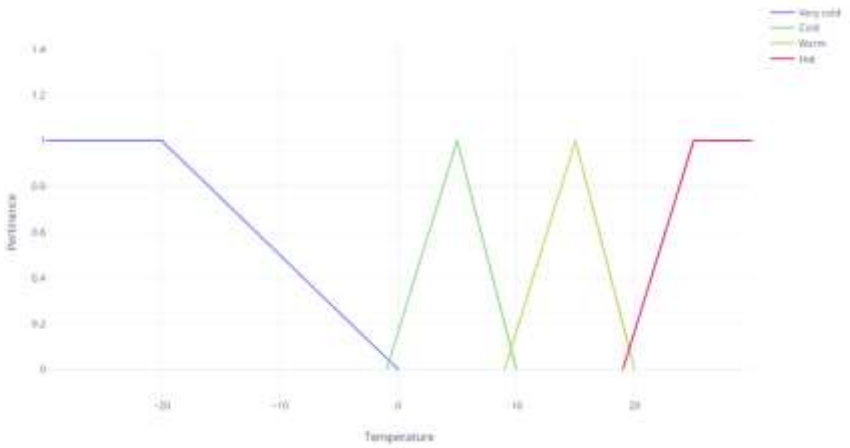

Figure 2. Input function for temperature

A fuzzy input function for presence is representation of a presence value to a fuzzy set. In the case of presence, a fuzzy input function represents if person is “present” or “not present” in the observed room as shown in figure 3.

Figure 3. Input function for presence

A fuzzy output function for heating shown in figure 4 is a mathematical representation of the relationship between the inputs of a fuzzy model and the desired output, in this case, the heating level. In a output function for heating, the inputs to the fuzzy model - temperature and presence, are combined using a set of rules that describe how the inputs affect the desired heating level. These rules can be defined using a human-readable syntax, such as "If the temperature is cold, then the heating level should be high".

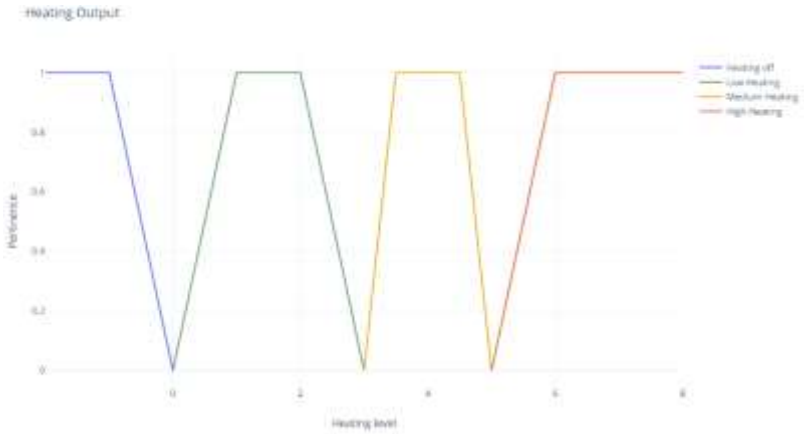

Figure 4. Output function for heating levels

Once the rules have been defined, the fuzzy model can be simulated to evaluate the outputs for a given set of inputs. The fuzzy output function then maps the inputs to the outputs, using a process known as defuzzification. The defuzzification process converts the fuzzy outputs into a value, which can be used to control the heating system.

3. RESULTS AND DISCUSSIONS

eFLL (A Fuzzy Library for Arduino) - a software library that was used for the implementation of fuzzy logic in Arduino. It is designed to be easy to use and provides a simple, high-level interface for building and running fuzzy models on an Arduino microcontroller.

To use eFLL for a fuzzy model, the first step was to define the inputs and outputs of the model, as well as the fuzzy sets and membership functions for each input. This information is then used to define the rules that describe the relationship between the inputs and outputs.

Next, the fuzzy model is implemented in the Arduino environment using the eFLL library. This involved writing code that integrates the inputs and outputs, defines the rules, and performs the fuzzy inference process. The eFLL library provides functions for this process, allowing the programmer to focus on the implementation of the model itself.

Once the fuzzy model is implemented, it can be run on the Arduino microcontroller and its outputs can be used to control the system. In the case of heating control, the outputs of the fuzzy model are used to adjust the heating level based on the inputs of temperature and presence. Multiple iterations of reading inputs and producing outputs, as well as generating verbal explanations were made, with benchmarks how much time it takes to complete one iteration of control cycle. Results are provided in figure 5, in graph describing the time for each iteration.

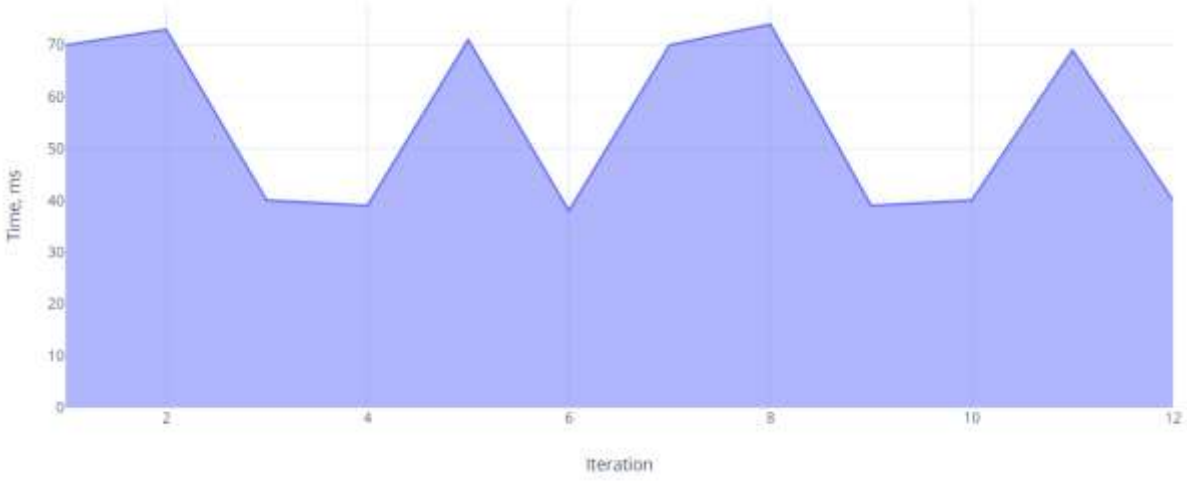

Figure 5. Time measurements of iterations for control cycle

A total of nine rules were checked during the experiment. Each rule triggered different explanations for the user to understand why current decision was made.

Twelve iterations were recorded, and time measured. Minimal iteration ran for 39 milliseconds and maximum iteration took 74 milliseconds to complete. Considering the experiment was running on Arduino Uno, with 8Mhz clock results are satisfactory, considering that reaction time is lower than 1 second, so response to user is instantaneous.

Even in a case of more complex scenarios, microcontrollers with similar architecture can be used for example ESP32, which runs at ten times higher clock speeds than Arduino, while eFLL software library and explanation interface code is fully compatible Arduino family.

References

[1] Milan Zdravković, Ivan Ćirić, Marko Ignjatović, Explainable heat demand forecasting for the novel control strategies of district heating systems, Annual Reviews in Control, Volume 53, 2022, Pages 405-413, ISSN 1367-5788, https://doi.org/10.1016/j.arcontrol.2022.03.009

[2] A. B. Arrieta, N. Díaz-Rodríguez, J. Del Ser, A. Bennetot, S.Tabik, et. al., "Explainable Artificial Intelligence (XAI): Concepts, taxonomies, opportunities and challenges toward responsible AI Information Fusion, Volume 58, 2020, Pages 82-115.

[3] Meskauskas, Z. (2019). CWW enhanced fuzzy SWOT evaluation for risk analysis and decision making under uncertainty. IVUS.

[4] Petrauskas, V. (2006). Dynamic SWOT Analysis as a Tool for System Experts. The Engineering Economics, 50.

[5] Ojha, V.K., Abraham, A., & Snášel, V. (2019). Heuristic design of fuzzy inference systems: A review of three decades of research. ArXiv, abs/1908.10122.

[6] U. Pawar, D. O'Shea, S. Rea and R. O'Reilly, "Explainable AI in Healthcare," 2020 International Conference on Cyber Situational Awareness, Data Analytics and Assessment (CyberSA), 2020, pp. 1-2, doi: 10.1109/CyberSA49311.2020.9139655.

[7] Shane T. Mueller, Robert R. Hoffman, William Clancey, Abigail Emrey, Gary Klein, Explanation in Human-AI Systems: A Literature Meta-Review Synopsis of Key Ideas and Publications and Bibliography for Explainable AI, DARPA XAI Program February 2019, 204 p.p.

[8] Milan Zdravković, Ivan Ćirić, Marko Ignjatović., Towards explainable AI-assisted operations in District Heating Systems, IFAC-PapersOnLine, Volume 54, Issue 1, 2021, Pages 390-395, ISSN 2405-8963, https://doi.org/10.1016/j.ifacol.2021.08.044.

RIGA 2023

Analysis OF Geothermal power Plant Process Design for Lahendong Expansion Area with Comparison of Flash Steam and Binary Cycle Systems

Juwari
Institute Technology Sepuluh Nopember, Surabaya, Indonesia, jueari@chem-teng.its.ac.id, ORCID: 0000-0001-5157-4248

Alhafiz Taufiqul Hakim
Institute Technology Sepuluh Nopember, Surabaya, Indonesia, hafizhamim3884@gmail.com, ORCID: 0000-0001-8009-1130

Aisyah Putri Prameswari Jasmine
Institute Technology Sepuluh Nopember, Surabaya, Indonesia,aisyahputrirme@gmail.com, ORCID: 0000-0003-4468-0477

Renanto
Institute Technology Sepuluh Nopember, Surabaya, Indonesia, renanto@chem-eng.its.ac.id, ORCID: 0000-0001-9172-6912

Cite this paper as: *Juwari, Hakim, AF, Jasmine, AP, Renanto. Analysis of Geothermal Power Plant Process Design ForLahendong Expansion Area With Comparation of Flash Steam and Binary Cycle. 11. Eur. Conf. Ren. Energy Sys. 18-20 May 2023, Riga, Latvia*

Abstract: Indonesia has a geothermal energy resource potential of 40% of the world's potential and only 8.9% of Indonesia's geothermal potential has just been utilized. The spread of various geothermal locations in Indonesia will affect the characteristics of Geothermal Power Plants with different process types, so an analysis is needed to compare geothermal process technology and the conditions of the power generation system between flash steam and binary cycle to find out the technology. geothermal process and suitable system conditions at the Lahendong area expansion location. In this research, simulation of double flash steam and binary cycle with regeneration were carried out and the results were then analyzed based on the highest power output and efficiency. It was found that the double flash steam system produces a power of 3125 kW with a thermal efficiency of 89.8%. Meanwhile, the binary cycle system with generation produces a power of 5433.25 kW with a thermal efficiency of 8.68%. Based on the simulation results that have been carried out, the suitability of the process for the expansion of the Lahendong Area Geothermal Power Plant location uses binary cycle technology with a binary cycle with generation system.

Keywords: *Binary Cycle, Power, Efficiency, Flash Steam, Geothermal Power Plant*

1.INTRODUCTION

The need for energy use in Indonesia continues to increase in line with the pace of industrial growth and population growth. Under these conditions, relying solely on fossil fuels whose reserves are depleting, will not be able to meet national energy needs [1]. Geothermal energy resources in Indonesia have a huge potential of around 40% of the potential worldwide with an estimated reach of 28.5 *Giga watt electrical* (GWe). However, until 2019 based on data from the Directorate of Geothermal, only 8.9% of Indonesia's geothermal potential has only been utilized or around 1,130.6 MW. As one of the most potential renewable energy sources, the Government continues to encourage the increase in the use of geothermal in Indonesia. The government itself targets an increase in geothermal utilization to 7,241.5 MW or 16.8% in 2025. Efforts to increase the utilization of potential geothermal energy sources by the Government of Indonesia are carried out by establishing Geothermal Power Plants through state-owned companies or by granting Geothermal Working Area (WKP) management permits granted to *Independent Power Producers* (IPPs).

One of the companies that received direction from the Indonesian government to run a geothermal processing and project business is located in the eastern part of Indonesia, Tomohon City, North Sulawesi Province since 2001. It has a total capacity of Geothermal Power Plants currently operated 120 MW consisting of a total of six units with a capacity of 20 MW each unit and currently plans to expand the Geothermal Power Plants unit seven located in Lahendong and unit eight located in Tompaso to maintain the availability of energy supplies as well as renewable energy. The characteristics of the steam produced from the *well* consists of 70% water and 30% steam, which has been directly injecting hot water from the cooling pool into the earth. The scheme of Lahendong PLTP Unit 3 is given in Fig. 1.

2.STUDY OVERVIEW

In this study, the data on the operating conditions of brine in Table 1 came from brine *wellhead cluster* 5 which is in Unit-3 Lahendong

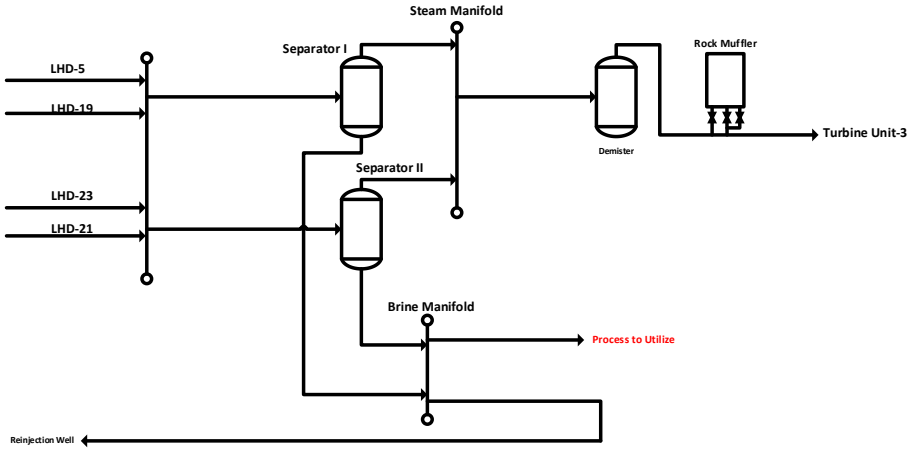

Figure 1. Lahendong PLTP Unit 3 Scheme

Table 1. Operating conditions on a cluster 5 reservoir [2]

Parameters	Value
Brine Temperature	180.8ºC
Brine Pressure	10.23 bar
Mass Flow Rate	624.82 tons/hour

Through this expansion plan, the residual heat in the brine can be utilized to generate electricity before being injected into the injection well. In unit 3, *non-condensable gases* on *the brine* will be removed using *a scrubber* before entering the turbine. Thus, the brine that will be used in the expansion unit only contains chemicals dissolved in liquid *waste brine.*

In this study, it was analyzed the use of the type of Geothermal Power Plant , *flash steam* or *binary cycle* to determine the selection of geothermal generation process technology in the expansion of the Lahendong Area

3.METHODOLOGY

This research method was carried out by collecting data from geothermal power plants in lahendong unit and from journal reference data , given in **Table 1** . This data was used as *feed* in the Lahendong expansion area.

In simulating geothermal power plant models, *double flash steam* and *binary cycle with generation technology,* Aspen HYSYS V. 11 software was used. The results were then used to calculate the thermal efficiency and power generated in each technology.

In addition to calculating the thermal efficiency and power output produced in each simulated PLTP model, silica *scaling* were also considered as one of the criteria in designing geothermal plants, since silica (SiO_2) is one of the causes of *scaling* in geothermal plants. In the analysis of the potential for silica formation, two relevant forms are used, namely quartz and amorphous silica. The concentration of silica in the geofluid produced from the reservoir can be correlated with the geofluid temperature using quartz solubility as a temperature function so that the calculation of quartz concentration using Qc (*quartz concentration)* based on reservoir temperature with the following equation:

$$Q_c = 41.598 + (0.23932)t_{brine} - (0.011172)t_{brine}^2 + (1.1713)10^{-4}t_{brine}^3 - (1.9708)10^{-7}t_{brine}^4 \quad (1)$$

Where, x = the quality of the geothermal fluid on the *main separator*

T_{brine} = temperature brine (180°C)

x_1 = quality of geothermal fluid entering *flash vessels* (*second separator*)

At lower temperatures encountered in *waste brine* after use in power generation, the solubility is controlled by an amorphous form of silica. With the equations of Fournier and Marshall, the solubility of amorphous silica [2] :

$$log_{10}s = -6.116 + 0.01625T - 1.758 \times 10^{-5}T^2 + 5.257 \times 10^{-9}T^3 \quad (2)$$

Where, T = brine *outlet* temperature (K)

S = silica solubility

Saturated silica concentrations can be analyzed using the *Silica Saturation Index* (SSI) as an empirical approach. SSI index is the ratio of silica concentration on *brine* and amorphous silica solubility [2]. The equation of SSI, namely:

Flash system:

$$SSI = \frac{S_{ii}}{s} \quad (3)$$

Binary system:

$$SSI = \frac{S_i}{s} \quad (4)$$

Where, S_i = silica *brine* concentration in *the main separator*

S_{ii} = silica *brine* concentration in *flash vessel*

For the calculation of S_i and S_{ii} are as follows :

$$S_i = \frac{Q_c(t)}{1-x} \quad (5)$$

$$S_{ii} = \frac{S_i}{1-x_1} \quad (6)$$

4.RESULT AND DISCUSSION

The liquid that is separated from the Geothermal Power Plant unit-3 of the lahendong area still has a high temperature to be reused. Data were obtained that the temperature of *waste brine* was 180.8°C, with a pressure of 10.23 bar, a mass flow rate of 624.82 tons/hour. There are several types of PLTP process systems that can be used in the use of *waste brine*, including *double flash steam* and *binary cycle with regeneration*. Therefore, a simulation

of PLTP modeling was carried out using these two technologies to compare the corresponding PLTP technology in the Lahendong area PLTP expansion.

Double Flash Steam

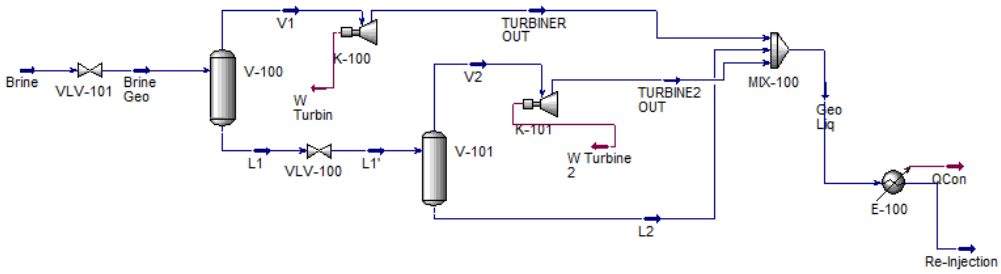

Figure 2. PLTP Scheme with Double Flash Steam Technology on Aspen HYSYS

Figure 2 is a simulation of Double Flash Steam technology on Aspen HYSYS. Based on the simulation that has been carried out, data based on **table 2** is obtained with the variable operating pressure of the flash separator that gives the optimal pressure to produce greater power.

Table 2. Operating Conditions PLTP Double Flash Steam Technology with Aspen HYSYS with the first Pflashing of 6 bars and the second Pflashing of 2 bars

Flowsheet	P(bar)	T (C)	Mass Rate (Tons/hour)
Brine	10.23	180.8	624.8
Brine Geo	6	158.9	624.8
V1	6	158.9	30.46
L1	6	158.9	594.3
L1'	2	120.2	594.3
TURBINE OUT	1	99.59	30.46
V2	2	120.2	46.94
L2	2	120.2	547.4
TURBINE2 OUT	1	99.59	46.94

In **table 2**, turbine power 1 *(*High Pressure turbine) is 1963 kW and turbine power 2 (*Low Pressure Turbine*) is 1162 kW so that the total power produced is 3125 kW. Therefore, *double flash steam* technology obtained *thermal* efficiency of 89.96%. As for the *Carnot cycle* efficiency in the *double flash steam* system itself is 21.06%.

Binary Cycle with Regeneration

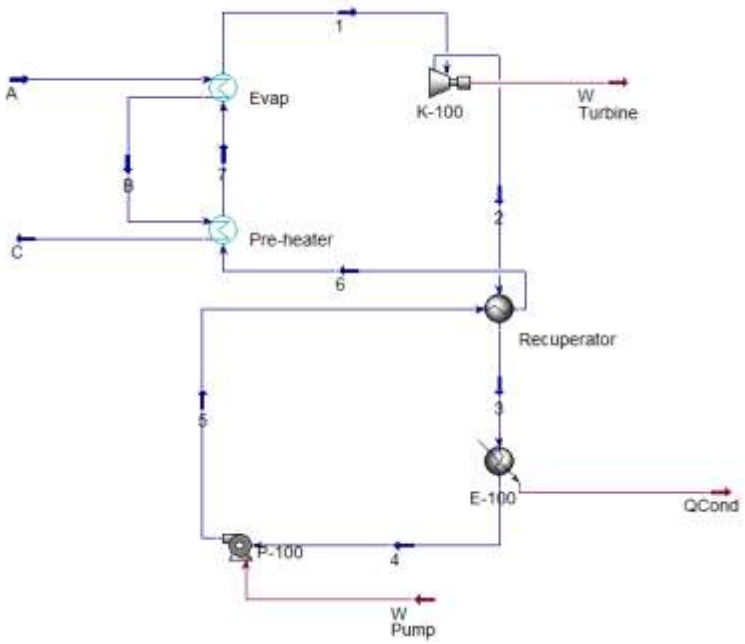

Figure 3. PLTP Scheme with Binary Cycle with Regeneration Technology on Aspen HYSYS

Figure 3 shows a simulation in *ASPEN HYSYS* using *binary cycle with generation* technology using n-pentane as the working fluid. The mass of the n-pentane in this cycle is 600 tons/hour (166.67 kg/s). Based on the simulation that has been conducted, data is obtained based on **table 3**.

Table 3. Simulation Results of PLTP Binary Cycle with Regeneration Technology on Aspen HYSYS

Flow	P(bar)	T (C)	Mass Rate (Tons/hour)
A	10.23	180.8	624.8
B	10.23	180.8	624.8
C	10.23	85.2	624.8
1	4	90	600
2	1	64.89	600
3	1	64.89	600
4	1	36.1	600
5	4	36.25	600
6	4	36.29	600
7	4	90	600

In table 3, the turbine power is obtained to produce 5526 kW, while for the pump it requires 92.75 kW of power. Therefore, this binary cycle with generation technology produces 5433.25kW of clean electrical power with a *Carnot* cycle efficiency in the *binary cycle with generation* system itself of 21.06% and for its thermal cycle efficiency of 8.7 %. This is in accordance with the literature which shows that *thermal* efficiency in binary cycles is in the range of 8-12%. [3]

5.RESULTS ANALYSIS

Table 4. Comparison of Electric Power, Efficiency, and SSI Index on Each Geothermal Power Plant Technology

Process System	Power output (kW)		Thermal Efficiency	SSI
	$W_{turbine}$	W_{net}		
Double Flash Steam	3125	3125	89.96 %	1.265
Binary Cycle with Regeneration	5526	5433.25	8.68 %	1.260

By modeling and simulating *Double Flash Steam* and *Binary Cycle with Regeneration* technologies using Aspen HYSYS V.11, the largest electrical power is obtained in *binary cycle with regeneration* technology. This is because the use of *Binary Cycle* is intended for *brine* heat sources that have low and medium temperatures with a temperature of < 200^{o}C. *Binary Cycle* itself uses a working fluid that has a lower boiling point and has a higher vapor pressure than water [4].

In addition, saturated silica needs to be analysed using the Silica Saturation Index (SSI) as an empirical approach considering that the brine used in geothermal power plants contains silica (SiO2) which can cause scaling. Based on the **table 4**, it was found that the SSI values in the double flash system and binary system were 1,265 and 1,260 respectively. The design of process conditions in the simulation of geothermal power plant research on binary cycle with generation technology and in double flash steam technology can still be operated without scaling from silica since from the experience of some developments in Geothermal Powerplant, it is possible to operate with SSI values greater than one where in double flash systems ≤ 1.30 and in binary systems SSI ≤ 2.0 [5].

6.CONCLUSION

Based on simulation data that has been obtained using ASPEN HYSYS V.11 software, the calculation results were obtained that in the double flash steam system using different variables of first flashing pressure and second flashing, it was found that in producing the greatest power in the conditions of the first flashing pressure and the second flashing successively by 6 bar and 2 bar by producing power of 3125 kW and thermal efficiency of 89.96% and SSI value of 1,265. Meanwhile, in the binary cycle with generation system using variable temperatures on the evaporator, power of 5433.25 kW was obtained with a thermal efficiency of 8,678% and an SSI value of 1,260.

Based on the results of simulations and calculations that have been conducted, the suitability of the process at the Lahendong Area Geothermal Power Plant expansion site is to use binary cycle technology with a binary cycle with generation system because it produces more power than double flash steam technology.

References

[1] DiPippo R. Geothermal energy technology and current status: an overview. In Renewable and Sustainable Energy Reviews. Massachusetts, USA: Elsevier Inc, 2016

[2] Nugroho, A. J. EVALUATION OF WASTE BRINE UTILIZATION FROM LHD UNIT III FOR ELECTRICITY GENERATION IN LAHENDONG GEOTHERMAL FIELD, INDONESIA. *orkustofnun* 2007. < https://orkustofnun.is/gogn/unu-gtp-report/UNU-GTP-2007-17.pdf

[3] Mines, G. Binary geothermal energy conversion systems: Basic Rankine, dual-pressure, and dual-fluid cycles. *Elsevier Inc* 2016. < https://doi.org/10.1016/B978-0-08-100337-4.00013-9>

[4] Fernando Monroy Parada, A., Tecla, S., & Salvador, L. el. GEOTHERMAL BINARY CYCLE POWER PLANT PRINCIPLES, OPERATION AND MAINTENANCE. *Orkustofnun 2013*.

[5] Zarrouk, S. J., Woodhurst, B. C., & Morris, C. GEOTHERMAL 101: THE BASICS AND APPLICATIONS OF GEOTHERMAL ENERGY Geothermal 101 The Basics and Applications of Geothermal Energy. *Dovetail Partners Inc* 2011. < http://www1.eere.energy.gov/geothermal/history.html >

RIGA 2023

What is Energy Informatics? An Inclusive View

Carlos Cuenca-Enrique
UPM, Spain, carlos.cuenca@upm.es

Laura del Rio Carazo
UPM, Spain, laura.delrio@upm.es

Santiago Iglesias-Pradas
UPM, Spain, s.iglesias@upm.es

Marta Gallego-Fernández
UPM, Spain, marta.gallego.fernandez@alumnos.upm.es

Cite this paper as: *Cuenca-Enrique, C, Rio Carazo, L, Iglesias-Pradas, S, Gallego-Fernández, M. What is Energy Informatics? An inclusive view. 11. Eur. Conf. Ren. Energy Sys. 18-20 May 2023, Latvia, Riga*

Abstract: As global energy consumption steadily increases, research and development of technologies to address energy challenges flourishes in developed countries. However, this situation does not acknowledge the reality of the most remote areas of the world, and little is known about the problems they face, or even if their energy challenges are the same as those of the rest of the world. Energy Informatics, a subfield of information systems that focuses on the analysis, design and implementation of information systems to reduce energy consumption, emerges as a fundamental concept in energy challenges. Nonetheless, the term energy informatics itself is still unclear and must be adapted to include all existing contexts. This paper investigates energy informatics through a scoping review to provide a comprehensive definition and analyze to what extent the term includes the particularities of energy challenges in developing countries.

Keywords: *Energy Informatics, Information Systems, Climate change, Developing countries, Sustainability*

1. INTRODUCTION

In recent decades, the widespread introduction of technologies in people's lives has placed access to energy as a fundamental part of what is considered decent living. According to the World Bank, around 13% of the population, or 940 millions of people, do not have access to electricity yet [1]. Meanwhile, the continued electrification of the world, driven by growing global energy consumption, is putting pressure on the global system, and the energy sector faces many challenges, conditioned by political and environmental drivers. The traditional structure of generation, transmission and distribution is also changing rapidly, and events in recent years, such as the pandemic caused by COVID-19, have stressed the global energy landscape, with unprecedented increases in energy demand worldwide, and where fossil fuels accounted for almost 70% of the growth [2]. Today, this demand is more than double the measured rate of growth since 2010. As a result, global energy-related CO2 emissions increased by 1.7% to 33 gigatons (Gt) in 2018 [3], [4].

Our society's inevitable dependence on a reliable energy supply has made the energy problem a top priority across the board. Therefore, by 2030, the seventh Sustainable Development Goal (SDG7) establishes the need to ensure universal access to energy in an affordable, secure, sustainable and modern way. At the same time, the European Union has set the long-term goal of reducing greenhouse gas emissions by 80-95% from 1990 levels by 2050 [5],

under the "The European Green Deal" to achieve carbon neutrality, an economy with zero net greenhouse gas emissions. This creates the need for decarbonizing the energy system while ensuring security of energy supply.

The various challenges described above can only be addressed in one way: a multidisciplinary approach, based on digitalization to ensure that tomorrow's energy systems are at least as reliable as today's. Energy Informatics (EI) emerges as the main precursor driving all other elements of digitalization. EI includes different fields of application that will play a key role in tomorrow's energy system and will be essential in developing countries to advance in the global energy challenge. Initially defined in the US by [6], as a field "concerned with analyzing, designing, and implementing systems to increase the efficiency of energy demand and supply system" (p. 24), it originates from the need to address climate crisis. The initial proposal states that there are different ways in which information systems could help solve the problem. Since that initial definition, multiple authors have proposed different theories and approaches to the term, although it does not appear that these approaches have included the context of developing countries.

The main objective of this research is to contextualize EI and define its role in the energy challenge, in both developed and developing countries. The remainder of this study is organized as follows. Section 2 details the methodology followed to prepare the scoping review and summarizes the main results of the study and Section 3 presents the main conclusion and provides some guidance on the role of Energy Informatics in energy access.

2. METHODOLOGY

Scoping reviews are an ideal tool to determining the scope or coverage of a the literature on a given topic and giving clear indications of the volume of literature and studies available and an overview of its focus, which is exactly what we intend. We follow the guidelines in [7] for conducting the scoping review: (1) identifying appropriate research questions, (2) identifying relevant studies, (3) study selection, (4) data charting, and (5) collation, summary and report of results.

Initial research questions

The main objective of this research is to understand IE and analyze its use in developing countries. Consequently, the study proposes the following research questions:

RQ1: What is Energy Informatics (EI)?

RQ2: In which fields and contexts is the term used?

RQ3: Is the concept of EI applicable to the reality of developing countries?

Identification of relevant studies

The identification of relevant studies has been performed by searching the *Web of Science* and the *Scopus* databases, using the term "*Energy Informatics"* as keyword.

Study selection

The criteria used for the screening are: publications from Web of Science or Scopus, published from 2010 (date of the first mention of EI) to 2022, in English or Spanish, that include definitions of the term EI or the aspects related to it. The screening process was carried out starting with a total of 220 publications. After removal of duplicates, the number of items was 175. These publications were subject to a preliminary review of abstracts and subsequent in-depth analysis, after which the set of valid publications was reduced to 15. The main reasons for screening were that no aspects related to Energy Informatics were addressed (79 items removed for this reason), and that the definition of EI was not included in the document (which led to the removal of 77 items). The selection of articles follows the PRISMA Statement [8] and is graphically illustrated in Figure 1.

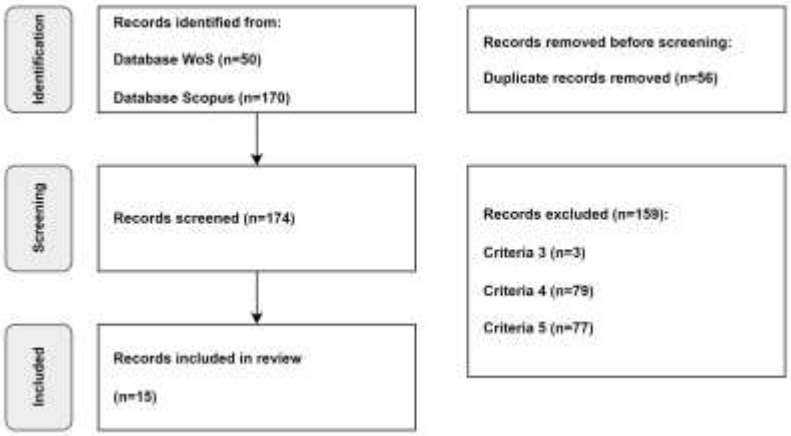

Figure 1.PRISMA flow diagram for article selection.

Data Charting

To analyze the fifteen publications resulting from the previous phase, a bibliographic analysis and a content analysis were performed. For the bibliographic analysis, we considered the type of publication, the date of publication and the country/countries of origin of the authors. For the content analysis, two descriptive aspects of the publication were considered: whether the study is of theoretical or empirical nature, and whether the study mentions developing countries, developed countries or the scope of application is not mentioned. The analysis categorizes the various definitions by differentiating the technologies covered by EI (Information Systems, Energy Systems, Intelligence Systems, Information and Communication Technology Systems). In our review, we also captured what was the purpose and main objectives set for EI, with a cumulative view (this is further detailed in the content analysis). Table 1 summarizes the results of the analysis, identified by author, year, type of research, scope, definition, and objectives of EI.

Table 1. Data Charting articles

Author(s)	Year	T/E	Scope	Definition				Objective				
				IS	ES	IntS	ICTS	1	2	3	4	5
Watson et al. [9]	2010	E	-	x				x				
Watson et al. [6]	2010	T	-	x					x			
Califf et al. [10]	2012	T	-	x					x		x	
Watson et al. [11]	2012	T	-	x				x				
Brocke et al. [12]	2013	T	-		x				x			
Goebel et al. [13]	2014	T	-			x			x			
Jørgensen et al. [14]	2015	T	-				x		x	x		
Kozlovskiy et al. [15]	2016	E	DEV	x				x	x			
Zhou et al. [16]	2016	T	-							x		x
Huang et al. [17]	2017	T	-				x		x			x
Liu et al. [18]	2017	T	-				x		x			
Heghedus et al. [19]	2018	T	-				x	x	x			
Bordin et al. [20]	2020	T	-				x		x			x
Bordin et al. [21]	2021	T	-				x					
Schmeck et al. [22]	2022	T	-				x		x			

T/E → T: Theoretical; E: Empirical; **Scope**→ DEV: Developed country; -: non specified; **Definition**→ SI: Information Systems; ES: Energetic Systems; IntS: Intelligence Systems; ICTS: Information Communication Technologies Systems; **Objective**→ 1: To reduce consumption; 2: To increase demand and supply efficiency; 3: To improve the use of renewable sources; 4: To achieve sustainability; 5: SDG7

Collation, summary, and report of results

Firstly, upon the bibliographic analysis, we observe that the publications are distributed homogeneously from the first definition of the term in 2010 to the present. No increase in publications has been observed in recent years; however, the term is still recent, so an increase in its use might likely happen in the coming years. Regarding the type of publications, there are journal articles (8; 53.3%), book chapters (1; 6.66%) and conference publications (7; 46.66%). Finally, there is a predominance of publications with origin in developed countries (12; 80%), with only 3 articles (20%) from developing countries; noteworthy, all these 3 are from China, the richest country of all developing countries in 2021.

The content analysis focuses on the analysis of the more theoretical aspects of the selected articles. First, aspects related to their definition are addressed. The definition by [6] has its origins in the need to address the problem of the climate crisis. Watson raises the potential that Information Systems could bring to address the problem and presents EI as a subfield of Information Systems [6]. Since then, the term has undergone numerous relevant variations. Only two years after the first definition of the term, [10] argued that the initial definition was too focused on Green IS ("refers to the use of Information Systems to achieve environmental objectives") and expands the definition by keeping information systems, but with a broader objective: to improve an energy supply and demand process to promote a sustainable outcome. The authors state that EI involves multiple aspects: environmental, individual, organizational and/or societal. As of 2013, EI is no longer considered a subfield of Information Systems, but rather a discipline related to electronic and/or intelligent systems [12], [13]; later, it is defined as an orchestrator of different systems carried out through the use of ICT [17], [19]–[22]. In these publications, the objectives pursued by EI focus on the energy challenges of increasing supply and demand efficiency and reducing consumption [6], [17], [18], [23], [24]. More recently, we observe the emergence of other aspects related to the correct management of renewable sources [14] and (from 2015 onwards) to the Sustainable Development Goals [16], [17], [20].

Finally, when analyzing the scope of application, most publications do not distinguish between developed and developing countries. However, and especially after observing the challenges defined and the technologies mentioned, it is reasonable to assume that the energy context of developing countries has not been considered in the definition of EI. The main challenge facing developing countries at the energy level is to democratize energy access and reduce energy costs to make access affordable for households. EIs can play a key role in increasing energy access rates in remote areas by facilitating the management of less conventional supply topologies, such as microgrids and isolated systems. Moreover, thanks to the increased connectivity that is occurring in developing countries, it is becoming easier to sensor energy devices to optimize domestic consumption and, above all, reduce monthly household costs. The approach that we propose after conducting this research is a broader work objective that includes global energy challenges, both in developed and developing countries, designing and implementing solutions that take into account the contexts of action, both when setting the objectives and when designing the technology, since the characteristics of the place of action will significantly condition the success or failure of the projects.

As a result of this analysis, we propose the following definition of EI: "Energy Informatics is the use of information and communication technologies (ICT) as enablers in the management of energy systems to meet the energy challenges set out in Sustainable Development Goal 7". To achieve these objectives, a multidisciplinary approach combining engineering, informatics and energy profiles should be used.

3. CONCLUSION

This study addresses the concept of EI initially proposed in 2010 by [6], as a subfield of information systems that should work together from different areas of knowledge to meet the energy challenges of the planet. After analyzing the existing literature on the term, several relevant conclusions have been obtained.

First, EI is still in its infancy. For the time being, EI has been mostly studied in developed countries, despite its great potential to address the energy challenges of developing countries. This is because most approaches to EI have been based on energy challenges in areas with close to access to energy by almost all the population.

Regarding the definition of EI, our proposed inclusive definition views the use of ICTs as enablers of global energy challenges. The role they play within energy systems is to act as a link between the different devices and

technologies to make the most of the information generated and to be able to design and implement solutions adapted to the needs of each area and user.

Finally, it is essential that the formulation of energy challenges be done with a global perspective that leaves no one behind; otherwise, EI will only be able to solve the problems of developed areas, leaving out the majority of the world's population.

REFERENCES

[1] "Ritchie Hannah," M. 'Roser, and P. 'Rosado, "Energy," Published online at OurWorldInData.org, 2022. https://ourworldindata.org/energy (accessed Dec. 12, 2022).

[2] S. 'Bhattacharjee and C. 'Nardi, "Implementation of industrial internet of things in the renewable energy sector. In: The intenet of things in the industrial sector.," Springer, pp. 223–259, 2019.

[3] I. Energy Agency, "The IEA examines the full spectrum of energy issues including oil," 2018. [Online]. Available: www.iea.org/t&c/.

[4] BP, "Statistical Review of World Energy." bp.com/statsreview (accessed Jan. 12, 2023).

[5] Eruopean Environmental Agency, "European Union (2050) Long term strategy.," 2020. [Online]. Available: https://ec.europa.eu/clima/policies/strategies/2050_en.

[6] R. T. Watson, M.-C. Boudreau, and A. J. Chen, "Information Systems and Environmentally Sustainable Development: Energy Informatics and New Directions for the IS Community," MIS Q., vol. 34, no. 1, pp. 23–38, 2010.

[7] H. Malley, "Theory & Practice This is an electronic version of an article published in Arksey," 2005. [Online]. Available: http://journalsonline.tandf.co.uk/OpenURLinktothearticle:http://www.journalsonline.tandf.co.uk/openurl.asp?genre=article&eissn=1464-5300&volume=8&issue=1&spage=19.

[8] M. J. Page et al., "The PRISMA 2020 statement: An updated guideline for reporting systematic reviews," J. Clin. Epidemiol., vol. 134, pp. 178–189, Jun. 2021, doi: 10.1016/j.jclinepi.2021.03.001.

[9] R. T. Watson, M.-C. Boudreau, S. Li, and J. Levis, "Telematics at UPS: en route to energy informatics," MIS Q., vol. 7, no. 3, pp. 113–122, 2010.

[10] C. B. Califf, X. Lin, and S. Sarker, "Understanding energy informatics: A gestalt-fit perspective," 18th Am. Conf. Inf. Syst. 2012, AMCIS 2012, vol. 6, pp. 4353–4365, 2012.

[11] R. T. Watson, J. Howells, and M. C. Boudreau, "Energy informatics: Initial thoughts on data and process management," Green Bus. Process Manag. Towar. Sustain. Enterp., vol. 9783642274, no. 2012, pp. 147–159, 2012, doi: 10.1007/978-3-642-27488-6_9.

[12] J. Brocke, H. Hasan, G. Fridgen, W. Ketter, and R. T. Watson, "Energy informatics : designing a discipline (and possible lessons for the is community)," in Thirty Fourth International Conference on Information Systems, Milano 2013, 2013, no. 3, pp. 1–6.

[13] C. Goebel et al., "Energy informatics: Current and future research directions," Bus. Inf. Syst. Eng., vol. 6, no. 1, pp. 25–31, 2014, doi: 10.1007/s12599-013-0304-2.

[14] B. N. Jørgensen, M. B. Kjærgaard, S. Lazarova-Molnar, H. R. Shaker, and C. T. Veje, "Challenge: Advancing energy informatics to enable assessable improvements of energy performance in buildings," in e-Energy 2015 - Proceedings of the 2015 ACM 6th International Conference on Future Energy Systems, 2015, pp. 77–81, doi: 10.1145/2768510.2770935.

[15] I. Kozlovskiy, M. Sodenkamp, K. Hopf, and T. Staake, "Energy informatics for environmental, economic and societal sustainability: A case of the large-scale detection of households with old heating systems," 2016.

[16] K. Zhou and S. Yang, "Understanding household energy consumption behavior: The contribution of energy big data analytics," Renew. Sustain. Energy Rev., vol. 56, pp. 810–819, 2016, doi: 10.1016/j.rser.2015.12.001.

[17] B. Huang, X. Bai, Z. Zhou, Q. Cui, D. Zhu, and R. Hu, "Energy informatics: Fundamentals and standardization," ICT Express, vol. 3, no. 2, pp. 76–80, 2017, doi: 10.1016/j.icte.2017.05.006.

[18] K. Liu and X. Zhang, "Energy informatics and fractional calculus," in Proceedings of the ASME 2017 International Design Engineering Technical Conferences and Computers and Information in Engineering Conference, 2017, pp. 1–11.

[19] C. Heghedus, A. Chakravorty, and C. Rong, "Energy informatics applicability; Machine learning and deep learning," Proc. - 2018 IEEE/ACIS 3rd Int. Conf. Big Data, Cloud Comput. Data Sci. Eng. BCD 2018, pp. 97–101, 2018, doi: 10.1109/BCD2018.2018.00023.

[20] C. Bordin, A. Håkansson, and S. Mishra, "Smart Energy and power systems modelling: An IoT and Cyber-Physical Systems perspective, in the context of Energy Informatics," Procedia Comput. Sci., vol. 176, pp. 2254–2263, 2020, doi: 10.1016/j.procs.2020.09.275.

[21] C. Bordin, S. Mishra, A. Safari, and F. Eliassen, "Educating the energy informatics specialist: opportunities and challenges in light of research and industrial trends," SN Appl. Sci., vol. 3, no. 6, Jun. 2021, doi: 10.1007/s42452-021-04610-8.

[22] H. Schmeck, A. Monti, and V. Hagenmeyer, "Energy informatics," Commun. ACM, vol. 65, no. 4, pp. 58–63, Mar. 2022, doi: 10.1145/3511666.

[23] C. Goebel et al., "Energy informatics: Current and future research directions," Bus. Inf. Syst. Eng., vol. 6, no. 1, pp. 25–31, 2014, doi: 10.1007/s12599-013-0304-2.

[24] I. Kozlovskiy, M. Sodenkamp, K. Hopf, and T. Staake, "Energy informatics for environmental, economic and societal sustainability: A case of the large-scale detection of households with old heating systems," 24th Eur. Conf. Inf. Syst. ECIS 2016, no. May, 2016.

RIGA 2023

The Chance for RESC in Italy: Study for a Sizing Model

Roberto Bosco
Università della Campania Luigi Vanvitelli, Aversa, Italy, roberto.bosco@unicampania.it, ORCID: 0000-0002-1585-0599

Savino Giacobbe
Engineer, Caserta, Italy, ingsavinogiacobbe@gmail.com, ORCID: 0000-0001-6376-7290

Renata Valente
Università della Campania Luigi Vanvitelli, Aversa, Italy, renata.valente@unicampania.it, ORCID: 0000-0001-8155-9583

Cite this paper as: *Bosco, R, Giacobbe, S., Valente, R., The chance for RESC in Italy: study for a sizing model. 11. Eur. Conf. Ren. Energy Sys. 18-20 May 2023, Riga, Latvia*

Abstract: n Italy, the establishment of Renewable Energy Communities (RECs) around photovoltaic systems built on public buildings represents an optimal solution to counter energy poverty, ensuring that all stakeholders have access to cheap, reliable, sustainable, and modern energy systems. In this study, we hypothesize a methodology for defining RESCs that considers dimensional, morphological, and social factors to maximize induced community benefits. To this end, within a processual efficiency program for building energy communities, the first studies of a calculation for their sizing in different urban settings are presented. Identifying the RESCs with criteria that are not exclusively technical opens the way to regaining good social practices, largely lost in the aftermath of the Pandemic, which in many cities has exacerbated the economic differences between the different strata of the population. The elaborated study can provide guidance to local administrators to implement sustainable technologies by preparing a map of potential energy communities.

Keywords: *Urban morphology, energy requirements, housing density, energy production suitability, community services.*

Nomenclature	
REC	Renewable Energy Communities
RESC	Renewable Energy Solidarity Communities
FTT	third-party financing
ENEA	Agenzia nazionale per le nuove tecnologie, l'energia e lo sviluppo economico sostenibile
ESCo	Energy Service Company

1. THEORY

An energy community is an organization where a group of citizens produces renewable energy, in sufficient quantities to sustain its self-consumption [1]. In Italy, the establishment of RECs around photovoltaic systems built on public buildings represents an optimal solution to counter energy poverty in organizational terms, ensuring that all stakeholders have access to cheap, reliable, sustainable and modern energy systems [2]. The new regulations on RECs encourage the association of public and private entities through the use of third-party financing (FTT) instruments. In this way, the relevant projects no longer have to be supported by non-repayable public grants or traditional credit but can simply be founded by private capital, to guarantee the investor an adequate return, in line with market rules [3].

This emerging pattern suggests that the experience can be replicated by implementing the photovoltaic systems serving Renewable and Solidary Energy Communities on the roofs of educational institutions and by supporting projects that can join the two goals of social and climate justice (countering energy poverty and education) [4]. In fact, the establishment of RESCs involving citizens' associations, businesses and public administrations can bring benefits not only on the energetic and economic level, but also on the social and sustainable development of the area through mutual exchange actions. In this study we hypothesize a methodology for defining RESCs that takes into account dimensional, morphological and social factors in order to maximize induced community benefits. To this end, within a processual efficiency program for building energy communities, the first studies of a calculation for their sizing in different urban settings are presented.

2. METHODOLOGY

From a technical and technological point of view, in Italy the possibility of creating RECs in urban areas is subject to both the availability of solar radiation on the building hosting the system and the energy potential of the plant. It is possible to identify certain factors to consider in the design phase of an urban photovoltaic installation, such as: conformation and orientation of roads, study of shading, ratio between the height of buildings and the width of the roadway (Urban Aspect Ratio), morphology of the built environment, and albedo of surfaces. According to the considered elements, it is possible to assume that some public buildings, particularly higher education plexuses, could be the reference for the construction of photovoltaic systems that power RESCs. In fact, they can already be considered by destination and spatial scope as aggregative elements, and their size and geometry would often allow the installation of appropriate PV systems to transform them into hubs of the communities. The Metropolitan City of Naples[1] manages 292 school buildings for higher education in an area of 1171 Sq. km that encompasses 92 municipalities. As part of the collaborative research work between the Authority and the team of the Department of Engineering of Luigi Vanvitelli University[2], we studied the intrinsic characteristics of the compounds from the 'interpretation of data in their database, to plan strategies for energy efficiency. Contextually, we study the morphological-environmental characteristics of urban fabrics to assess the efficiency of the RECs that can be constituted around the different high schools. Some typical case studies have been extrapolated from the variety that characterizes the urban landscape of the Metropolitan City of Naples, considering the implementability of plus-value services in comparable realities.

For this purpose, three school buildings located in different municipalities of the Metropolitan City of Naples were identified. The characteristics of each one were analyzed in four domains: the local spatial and climatic context; the settlement and urban morphology; the building envelope, analysing morphological and construction characteristics; energy requirements, analysing consumption and needs at the settlement scale [5]. At the urban tissue level, we analyzed the characteristics of one square kilometer of land area around each plex assumed to be an energy community hub. Within these areas, the destinations of existing buildings and their height, housing density declined in the average number of occupied dwellings[3], and the orography of the area were identified.

The three considered areas differ from each other in building density and land use. Building density varies from medium-low (Municipality of Melito di Napoli) to medium (Municipality of Giugliano in Campania) to high (Vomero District of Naples) (Fig. 1).

In the first density range falls the "Emmanuel Kant" institute in Melito, housed in a building with a reinforced concrete load-bearing structure that dates to 1999. It stands in a plain area on the border between a low-density industrial zone (warehouses, sheds) and a residential one characterized by the widespread presence of detached/ semi-detached villas and a few isolated apartment buildings between 6 and 10 stories high.

The area around the "Minzoni" Institute (reinforced concrete,1991), in the municipality of Giugliano in Campania, is an urban expansion zone with predominantly residential use with several public services (hospital, municipal offices); the number of floors of the buildings is constant around 4 above ground. Finally, the area in which the

[1] The Metropolitan City is the local entity that replaces the province of large Italian cities and comprises both the city and all the municipalities of the province itself.
[2] Coordinated by Prof. Arch. Renata Valente.
[3] Istat 2022 figure of the average number of housing units per building in each municipality.

"Mazzini" Institute is located (r.c., 1969) is a central area of a hilly district of the city of Naples. It is in a regular urban layout, built at the end of the 19th century that has undergone a strong urbanization as a result of the building speculation after World War II. This context can therefore be defined as one of high building density.

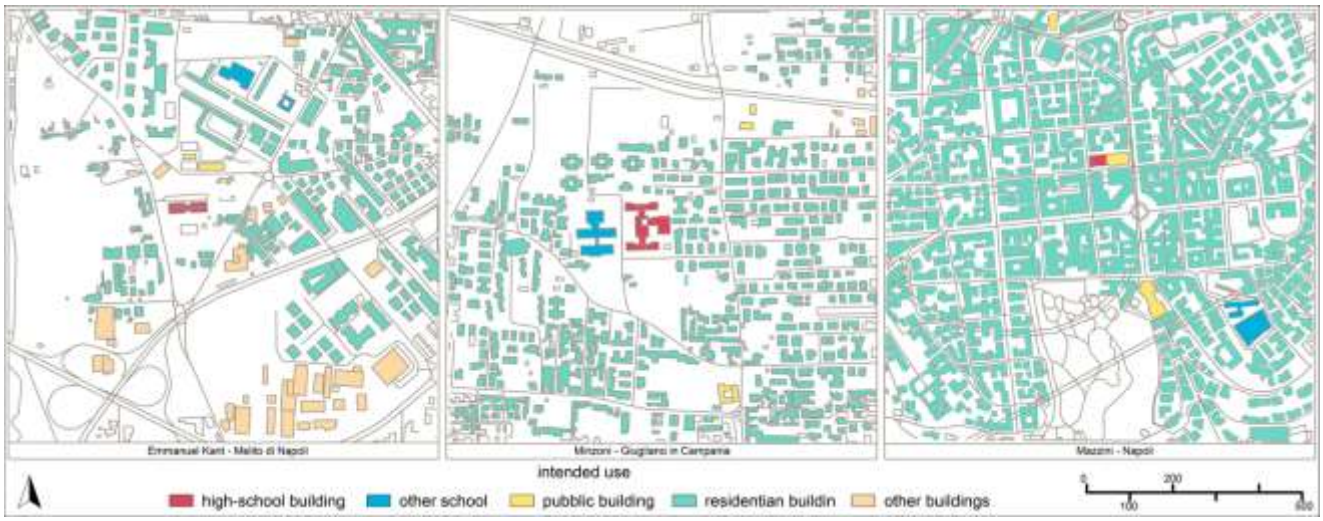

Figure 1. Use maps of the areas considered.

From the technological and environmental point of view, the three considered areas are characterized by the prevalence of reinforced concrete buildings of a few stories, except for the Vomero district, where the buildings are on average tall (5 to 10 stories above ground). The first two school buildings, located in areas of the respective municipalities characterized by low/medium building density, are distinguished by the large extent of covered area free of obstructions (taller buildings), which could decrease the uptake of PV panels. The situation of the Neapolitan institute is different. Being embedded in a context of high urban density, it is affected by the shadows generated by contiguous buildings. The result is a significant decrease in available area for the installation of properly exposed PV panels.

3. MODEL

A model integrating morphological-urban assessments, such as those previously outlined has been studied, including the socio-territorial characteristics of the sites on which the schools insist. The analysis is validly supported by software simulations performed using ENVI-Met and GSI data (study of shading, UAR, irradiance parameters), which complement the plant-electrical and technological-building ones, so far representing the conceptual standard for defining the benefits of a REC. Within this technical dialectic, it is appropriate to bring in an additional variable, which considers the further benefits from the association of individuals and public and commercial activities in RESCs. In these, the environmental returns are complemented by the benefits from increased social interaction (condominiums, technicians, public agencies). In fact, if plant and technology assessments represent the main investigative factor for implementing self-consumption within small and/or isolated communities (residential parks, villages), in urban and peri-urban situations such as considered, social interactions are often residual. Those may represent a decisive additional element compared to the mere economic benefit of saved energy, which may also be less than in typical configurations. By extending the reach of REC to the neighborhood scale, as the economic savings in electricity bills decrease, the potential human capital that the community could draw on will increase.

Therefore, the proposed model integrates morphological-urban assessments through the graphical construction of maps, identifying built and environmental features useful for an informed design of energy communities. To this end, a computational methodology for the dimensioning of these communities was designed. Starting with the achievable power installed on the analyzed school buildings, it is possible to estimate the perimeter of the RESC based on the expected bill savings for individual households. Effective ways of perimetering can be assumed for balancing community benefits, proportionate to their size, considering in the variables the commercial activities and public and private spaces that can provide a surplus-value service to the community.

There are several tools available online by public and private entities to estimate the achievable bill savings, by indicating the number of building units that will make up the REC. ENEA offers the *Recon* tool[4], the *GSE* ESCo has developed a simplified model useful for calculating even the payback of system installation and maintenance costs. These calculation models refer to the individual building, thus being insufficient to set up a holistic neighborhood-scale approach. In fact, two diriment factors are not considered for the purpose of calculation: the morphological and technological characteristics of the place and the potential arising from the existence of strong social ties among stakeholders. The first step in constructing an appropriate assessment method remains to properly demarcate the perimeter of the REC. For this reason, an attempt was made to identify a balancing equation between the self-consumption of the individual building and the perimeter of the REC with respect to the amount of installed power that is shared.

The basic assumption is that the school hosting the PV system is able to achieve the self-consumption. Given:

- S_c = School roof area expressed in square meters;
- S_{imp}(T) = Useful surface area for a photovoltaic system depending on the type of roofing, expressed in mq/kWh;
- η = % of surface area occupied by the panels, amounting to 80;
- n = the peak operating hours of a photovoltaic system within a day, i.e. 3.5 h.

With this data, it is possible to derive the energy E produced by a photovoltaic system, expressed in kWh/Year:

$$E = \frac{\eta \cdot S_c}{S_{imp}(T)} \cdot n \cdot 365$$

Given:

- C_S = Average annual electricity consumption in a school [kWh/year];
- $C_{U.I.}$ = Average annual electricity consumption in a building unit [kWh/year];
- c = unit cost of electricity [€/kWh];

through them it is possible to derive:

$$R_T = c \cdot E \quad (1.2)$$

$$R_S = c \cdot C_S \quad (1.3)$$

$$R_A = \frac{R_T - R_S}{A} \quad (1.4)$$

Where:

- (1.2) R_T shows the total bill savings [€];
- (1.3) R_S indicates the school's annual bill savings [€];
- (1.4) R_A indicates the annual bill savings of the building unit [€];
- A is the number of building units served by the CER.

Given the annual electricity bill saving of a building unit and the annual electricity consumption in a building unit, the annual electricity cost of a single building unit can be derived:

$$C_A = c \cdot C_{U.I.} - R_A \quad (1.5)$$

Replacing (1.5) with (1.2), (1.3), (1.4), we obtain:

$$A = \frac{c \cdot E - c \cdot C_S}{c \cdot C_{U.I.} - C_A} \quad (1.6)$$

[4] Web application developed by ENEA and aimed at supporting preliminary energy, economic and financial assessments for the establishment of renewable energy communities (https://recon.smartenergycommunity.enea.it).

The relation (1.6) is always true as long as $C_A \neq c \cdot C_{U.I.}$. As $C_{U.I.}$ changes, it is possible to derive the building units served in the CER. Similarly, it is possible to derive A, as a function of the annual bill savings, by substituting in (1.4) le (1.2) e (1.3):

$$A = \frac{c \cdot E - c \cdot C_S}{R_A} \tag{1.7}$$

The graphical representation of equations (1.6) and (1.7), in which the x-axis shows respectively the average cost and the average saving of each individual U.I. and the y-axis the U.I., defines a diagram that can be compared with the supply-demand diagram (Fig. 2). The calculation of the building units was carried out starting from the ISTAT data of the density of residents per residential building in the Metropolitan City of Naples, equal to 23.44 inhabitants.

Table 1.Number of building units for each municipality.

Municipality	Inhabitants/apartments	Dwellings per building
Melito di Napoli	3,40	6,90
Giugliano in Campania	2,40	9,80
Napoli	3,12	7,50

Tab

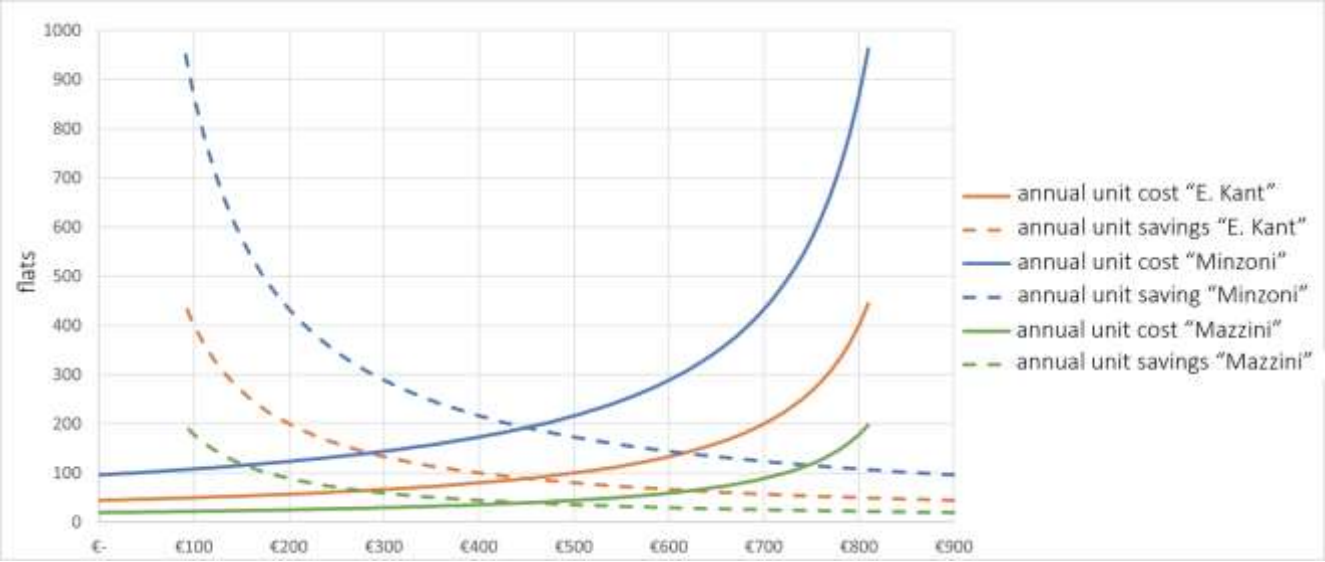

Figure 2. – Demand-supply diagram of a Renewable Energy Solidarity Community at the Minzoni Institute: cost and average annual bill savings.

4. RESULTS AND DISCUSSIONS

With the data obtained from relations (1.6) and (1.7) for each school, we defined the Map of the potential extensions of the RESC (Fig.3) present in the 1sq. km area considered in the case study. This allows to estimate, albeit approximate, the extent of the RESC based on the number of housing units potentially served by it (Fig. 3).

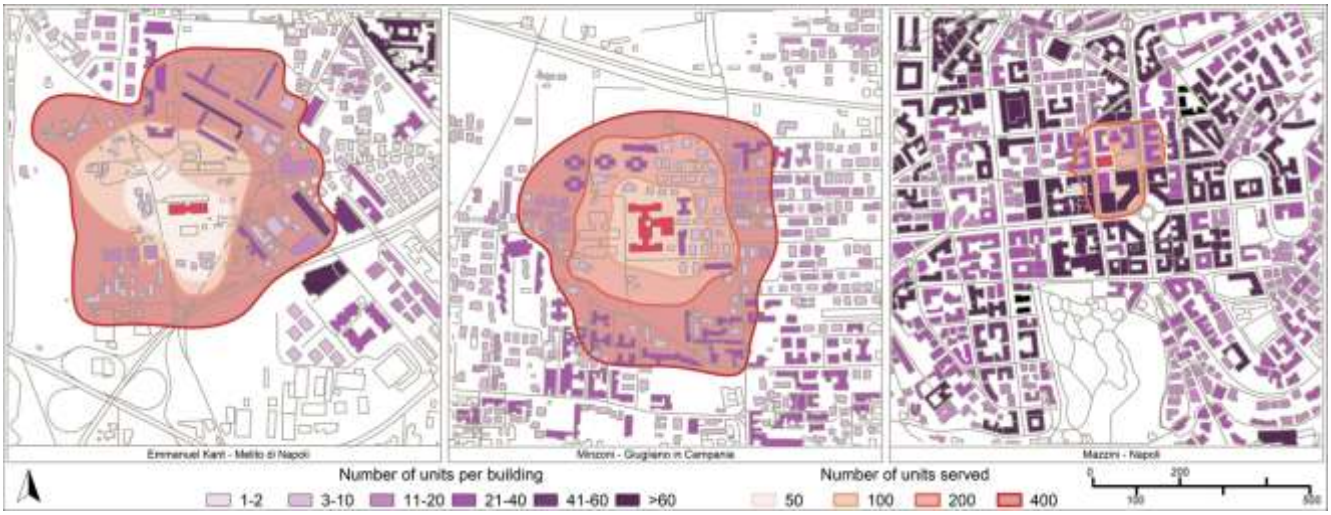

Figure 3 – Mapping of possible REC perimeters according to the units served.

According to the analysed case studies, the total savings in terms of electricity costs (net of system costs) are realised in communities of between 20 and 100 households. Depending on the power that can be installed, this can potentially invest the economic savings to satisfy other needs, not necessarily related to comfort or energy saving. On the other hand, in communities that are both territorially and numerically larger (more than 250 households), the lower economic savings may be more easily balanced by indirect returns inherent to community activities, such as time banks, family services, individual benefits like discounts in business and personal services.

Enhancing the concept of Community within these associations means overcoming the dichotomy between 'prosumer' and 'consumer' by not limiting the possibility of sharing goods and services but also expanding it to the capabilities of individuals or their time and the possibilities of associated small entrepreneurs. Identifying the RESC with criteria that are not exclusively technical or immediately economic opens the way to regaining ancient good social practices, largely lost also in the aftermath of the Pandemic, which in many cities has exacerbated the economic differences between the different strata of the population. In particular, the establishment of appropriately sized RECs can significantly improve the living conditions of those socially disadvantaged urban enclaves characterized by high population density, low financial resilience and difficult access to essential services.

5. CONCLUSIONS

Installing photovoltaic systems in schools helps reducing their energy costs, which are often among the main operating costs for public institutions. In addition, these systems can be used as an educational tool for students, representing a teaching resource and tangible example in the learning path of science and technology subjects. The presence of solar installations in public schools can also help develop local energy communities, extending benefits to different areas and sectors, such as health, safety, environment, culture and economic activities. The environmental designer has the skills to coordinate these instances. The careful study of the processes triggered for land transformation helps to imagine and implement interventions integrating economic, social and environmental needs. It also helps to preserve and enhance the environmental and landscape heritage, contributing to its quality and attractiveness. There is a need for good design practices to be acquired within the administrative processes of redevelopment, especially with a focus on an ecological transition already envisaged in national and international regulations, through the establishment of RECs. This will be possible by effectively implementing energy efficiency solutions within an integrated redevelopment process which often cannot get underway due to the age of building stock in need of extraordinary and urgent maintenance. This inevitably affects the availability of funds for innovative projects. In this scenario, it is desirable to implement the proposed method within an integrated program, that is capable of holistically consider the several aspects related to the management and retrofitting of the building stock, such as safety (structural, seismic, fire, etc...) and the well-being of users (environmental comfort, accessibility, etc...). This represents the next step in the research work, which, also due to the amount of data that can be obtained for the different purposes, will allow to improve the identification of areas and define in greater detail the characters of the social samples involved. The case studies selected and analyzed represent typical recurring settlements in Italy, particularly in the southern part of the country. This would allow the study to be

extended to more related contexts to verify its replicability. The study can provide valuable guidance to local technicians and administrators to implement sustainable technologies by preparing a map of potential energy communities. Furthermore, the proposed calculation parameters can provide a basis for defining strategies to facilitate administrations in the process of integrated environmental redevelopment.

Acknowledgment

We would like to thank the architects of the technical office of the Metropolitan City of Naples for their constant support and the data kindly provided during the working meetings. Architects Marianna Pedalino, Annarita Marciano, Daniela D'esposito, and Paolo Parravicini are mentioned with particular gratitude.

References

[1] ENEA. Glossario. *Comunità energetiche* 2019; <https://www.efficienzaenergetica.enea.it/glossario-efficienza-energetica/lettera-c/comunita-energetiche.html>
[2] UN General Assembly, *Transforming our world : the 2030 Agenda for Sustainable Development*, 21 October 2015, A/RES/70/1, available at: https://www.refworld.org/docid/57b6e3e44.html [accessed 10 February 2023]
[3] Valentini, G. Il ricorso al finanziamento tramite terzi. Roma, ITALY: ENEA Dipartimento Energia, Divisione promozione degli usi efficienti dell'energia e delle energie rinnovabili, 1997.
[4] Legambiente. *Scuole e università a zero emissioni: la sfida delle Comunità energetiche rinnovabili e solidali* 2022; <https://www.legambiente.it/comunicati-stampa/scuole-e-universita-a-zero-emissioni-la-sfida-delle-comunita-energetiche-rinnovabili-e-solidali/>
[5] Bosco, A., Scognamiglio, A. (A cura di). Fotovoltaico e riqualificazione edilizia. Roma, ITALY: ENEA, 2005.
.

RIGA 2023

Exploring the Green Transformation Path of Enterprises under the "Carbon Peaking and Carbon Neutrality" Target

Luqi Miao
Shanghai University, Shanghai, 1041246598@shu.edu.cn, ORCID:0000-0002-4902-3436

Xiao Luo
Shanghai University, Shanghai, lorita_luo_2002@163.com, ORCID: 0000-0003-3950-7266

Jun Chen
Shanghai University, Shanghai, chenjun1@shu.edu.cn, ORCID:0000-0002-6781-600X

Marja-Liisa Tenhunen
Dimitrie Cantemir Christian University, Bucharest, Romania, marja-liisa.tenhunen@anvianet.fi ORCID:0000-0002-4952-955X

Cite this paper as: *Miao, L, Luo, X, Chen, J, Tenhunen, ML. Exploring the Green Transformation Path of Enterprises under the "Carbon Peaking and Carbon Neutrality" Target. 11. Eur. Conf. Ren. Energy Sys. 18-20 May 2023, Riga, Latvia*

Abstract: The "carbon peaking and carbon neutrality" target is a solemn commitment made by China to address global climate change and an essential guarantee for China to achieve the second-century goal. As a market player in economical development, the green transformation of enterprises is of great significance to the realization of the "carbon peaking and carbon neutrality" target in China. Based on a systematic review of relevant literature, this paper identifies the main challenges faced by enterprises in China's green transformation: the task of optimizing their energy structure and improving energy efficiency is still arduous, the supply of green technologies is insufficient, and the cost of innovation is high, the carbon pricing mechanism is inadequate, and a carbon tax has not yet been imposed, and enterprises lack the incentive to adopt statistical standards and disclose information on carbon emissions. To this end, the new development stage should promote the green transformation of enterprises, accelerate the green transformation of enterprises' energy, promote the green technology innovation of enterprises, and better form the promotion strategy for the green transformation of enterprises' development.

Keywords: carbon peaking and carbon neutrality, corporate green transformation, theoretical mechanisms

1.INTRODUCTION

Climate change is a common challenge for all humankind, and the well-being of future generations is at stake. On 22 September 2020, President Xi Jinping, in his speech at the general debate of the 75th session of the United Nations General Assembly, proposed a "carbon peaking and carbon neutrality" goal of great significance to the world and China. To this end, the Party Central Committee and the State Council have issued a series of policy measures and implementation plans, such as the "Opinions of the CPC Central Committee and the State Council on the Complete and Accurate Implementation of the New Development Concept and Good Work on Carbon Neutrality" and the "Notice of the State Council on the Issuance of the Action Plan on Carbon Neutrality by 2030", which have formed a "1+N" policy to promote the "carbon peaking and carbon neutrality" work [1]. As explained earlier, the leading cause of climate change lies in the carbon dioxide generated by human activities, especially China's coal-based energy structure, which determines the enormity and long-term nature of the task of reducing carbon dioxide emissions. As the leading market player in China's economic development, enterprises have achieved rapid development in recent years. By the end of 2021, the number of enterprises in China reached 48.42 million, covering 20 industries such as agriculture, forestry, animal husbandry and fishery, mining, manufacturing, electricity, heat, gas and water

production and supply, and construction, which has become an essential support for the rapid development of China's economy. At the same time, enterprises are also the main contributors to China's CO_2 emissions, especially those in high energy-consuming and high-emission industries such as coal power, iron and steel, and building materials[2].

Promoting the green transformation of enterprises is the primary choice to achieve the goal of "carbon peaking and carbon neutrality" and is the necessary way to achieve high-quality development of China's economy in the 14th Five-Year Plan and even in the longer term, as well as an inevitable requirement to achieve Chinese modernization. It can be said that China's enterprises have made much exploration in green transformation development and achieved specific results. However, against the target of "carbon peaking and carbon neutrality," the green transformation of enterprises still faces many problems, the task is still arduous, and the road is still long and winding[3]. Based on the above considerations, it is of great theoretical significance and practical value to analyze the main challenges facing the green transformation development of enterprises and propose strategies to promote the green transformation development of enterprises in the new development stage.

2.GREEN TRANSFORMATION OF ENTERPRISES

The green transformation of enterprises requires significant and stable financial resources, which undoubtedly poses a considerable challenge to them. Fiscal policy is a critical institution in the public policy system. To address climate change, the existing fiscal policy should be reformed from a holistic, systematic, and forward-looking perspective, and the coordination between fiscal policy and other public policies should be strengthened to highlight the effectiveness of fiscal policy in the "governance" of climate change. Improve the incentive mechanism for green credit by strengthening the exploration of green credit policies, innovating green credit products and services, and increasing environmental subsidies[4]. Establish a long-term mechanism to support the green development of enterprises by deepening the structural reform of the financial supply side and building a credit guarantee and credit granting mechanism for green credit. Improve the government-based green subsidy and tax concession mechanisms, and develop market-oriented green credit and other mechanisms to effectively provide necessary financial guarantees for enterprises' green transformation and development.

Some scholars have also studied the relationship between green financial reform and innovation, inclusive digital finance and corporate outward direct investment, and corporate green transformation development. In 2017, the State Council approved the establishment of green financial reform and innovation pilot zones in five provinces (autonomous regions), including Zhejiang Province, to accelerate the utility of green finance for environmental improvement. The study found that compared to non-trial zones, the financing constraints of manufacturing enterprises in the green finance reform and innovation trial zones were alleviated and promoted green technological innovation among enterprises. The study also shows that green credit has a catalytic effect on the overall innovation and transformation of enterprises. Therefore, the experience of the Pilot Green Finance Reform and Innovation Zone can be precisely promoted in the future, and green financial products and tools can be continuously enriched and improved to promote enterprises' green transformation more quickly[5]. The green transformation of enterprises in China is vital to facilitate production and life and has grown considerably, especially during the New Crown Pneumonia epidemic. The outward investment activities of Chinese enterprises have gradually shifted from passive participation to an active search for markets, efficiency, technology, resources, etc. As a result, the outward direct investment of Chinese enterprises has become a driving force to boost green development and is beneficial to improve the level of green transformation of enterprises.

After the "carbon peaking and carbon neutrality" target was proposed, a series of policy measures have been introduced at the national level around the green transformation development of enterprises, but an indisputable fact is: why do enterprises stumble in the green transformation development? Why is there not a strong sense of self-innovation and self-innovation in the green transformation development of enterprises? What are the challenges faced by enterprises in green transformation development? What strategies should be adopted to promote the green transformation development of enterprises in the new development stage to help achieve the goal of "carbon peaking and carbon neutrality"? The studies above provide important theoretical references and practical lessons for answering these questions. At the same time, there is still some room for

expansion in the existing literature: firstly, most of the existing studies have focused on a particular aspect of the green transformation development of enterprises, and there is little literature that systematically studies the green transformation of enterprises at a macro level; secondly, there is still a lack of research that systematically analyses the challenges faced by the green transformation development of enterprises, especially around the issues of carbon emission statistical accounting system and carbon tax, which is also the critical starting point of this paper[6].

Enterprises are the main contributors to China's carbon dioxide emissions, and their green transformation is an essential strategy for achieving China's "carbon peaking and carbon neutrality" target. However, the green transformation of enterprises still faces a series of bottlenecks that need to be broken through, mainly reflected in the task of optimizing the energy structure and improving the energy efficiency of enterprises, the insufficient supply of green technologies, and high innovation costs of enterprises, the inadequate carbon pricing mechanism and the lack of carbon tax, and the lack of carbon emission statistical standards and information disclosure motivation of enterprises.

3.THEORETICAL MECHANISMS

3.1.A Mechanism for Pushing Back Restraint

Enterprises' degree of green transformation is closely related to the intensity of carbon emissions. It is governed by several factors, the most important of which is the guiding role of the government, especially the local government, as this guiding role can directly change the cost-benefit structure and thus have a decisive impact on the allocation of resources. In an institutional environment characterized by centralized governmental authority and economic decentralization, the ability to exert practical constraints on local governments directly determines the intensity of their efforts. Once the central government takes the "carbon peaking and carbon neutrality target" as an essential basis for assessing the performance of local governments, an invisible incentive mechanism will be formed among local governments, which will not only ensure that the “carbon peaking and carbon neutrality target” is successfully achieved or even completed ahead of schedule, but will also serve as an incentive for local governments to develop their regional economies and bring in external capital[7]. This incentive will not only ensure that the “carbon peaking and carbon neutrality target” is successfully achieved or even completed ahead of schedule but will also become an essential constraint for local governments to develop the regional economy and bring in external capital, thus fundamentally changing the cost-benefit structure of regional production and consumption, and thus accelerating the green transformation of enterprises. The green transformation of enterprises' production and lifestyle through a push-back constraint mechanism can be improved by “carbon peaking and carbon neutrality goal” .

3.2.International Monitoring Mechanisms

China’s “carbon peaking and carbon neutrality” target at international conferences such as the UN Biodiversity Summit, the Climate Ambition Summit, and the Davos Agenda Dialogue at the World Economic Forum[8]. This goal is also widely seen as the most critical climate change commitment in many years, which means that the international community, especially international organizations, will be an essential driving force behind the green transformation of Chinese companies as external witnesses and monitors of China's achievement of the “carbon peaking and carbon neutrality goal.” Under the leadership of the"carbon peaking and carbon neutrality target,” the green transformation of enterprises will also become more important for China to improve the international environment and reflect the role of great power. In particular, given the current fundamental changes in the domestic and international situation and the rise of the “cold war” mentality, China’s ability to fulfill its commitment to the “carbon peaking and carbon neutrality target” on schedule and to achieve the green transformation of its enterprises as soon as possible will have a direct bearing on China’s international status and international image[9]. Therefore, the “carbon peaking and carbon neutrality target” will further strengthen the internal mechanism of pushing back and restraining and linking supply and demand through the external international monitoring mechanism, thus accelerating the green transformation of enterprises.

4.SUMMARY

To enhance economic and social benefits, enterprises must grasp the opportunity of low-carbon green development, respond to the national call, and follow the relevant policies of "carbon peaking and carbon neutrality" through improving relevant laws and regulations, innovating low-carbon production technology, raising awareness of low-carbon production and strengthening the training of logistics management personnel, to bring legal, technical and human resources to the green development of enterprises[10]. By improving relevant laws and regulations, innovating low-carbon production technologies, raising awareness of low-carbon production, and strengthening the training of logistics management personnel, they will bring legal, technical, and human resources protection to the development of enterprises and they are beneficial for enterprises to achieve the goal of "carbon peaking and carbon neutrality."

References

[1] Wang G, et al. Can low carbon transformation enhance corporate environmental, social, and governance performa nce? --A quasi-natural experiment based on a "low carbon city pilot." Financial Theory and Practice, 2023, 44(01) :139-145. DOI:10.16339/j.cnki.hdxbcjb.2023.01.018.

[2] Lin YJ, Yang C, Cai XY. Digital transformation of enterprises and green innovation capability upgrading--an anal ysis based on network effects. Modern Finance and Economics (Journal of Tianjin University of Finance and Econ omics), 2023,43(02):3-19. DOI:10.19559/j.cnki.12-1387.2023.02.001.

[3] Han Q, Zhu H. Import trade, technology effects and green transformation of enterprises - Evidence from key equip ment import policies. Shanghai Economic Research, 2022, (12):63-74. DOI:10.19626/j.cnki.cn31-1163/f.2022.12. 005.

[4] Wang JX, Sun MN. The "Porter's hypothesis puzzle" of green development and governance transition - Evidence of corporate deleveraging under carbon risk. Economic Management, 2021,43(12):41-61. DOI:10.19616/j.cnki.bm j.2021.12.003.

[5] Cui F., et al. "Green Credit of China's Coal Power Enterprises during Green Transformation: A Tripartite Evolutio nary Game Analysis." Energies, 2022,15(16).

[6] Feng H. et al. "Digital Transformation on Enterprise Green Innovation: Effect and Transmission Mechanism." Inte rnational Journal of Environmental Research and Public Health, 2022,19(17).

[7] Hu J, et al. How corporate digital transformation affects corporate ESG performance - Evidence from Chinese liste d companies. Industrial Economics Revie, 2022, 1-20. DOI:10.19313/j.cnki.cn10-1223/f.20221104.001.

[8] Liang X., et al. "Green mergers and acquisitions and green innovation: an empirical study on heavily polluting ent erprises." Environmental Science and Pollution Research, 2022, 29(32): 48937-48952.

[9] Ren Y, Li B. Digital Transformation, "Green Technology Innovation and Enterprise Financial Performance: Empi rical Evidence from the Textual Analysis of the Annual Reports of Listed Renewable Energy Enterprises in China. " Sustainability, 2023,15:(1).

[10] Xue L, et al. "Can Digital Transformation Promote Green Technology Innovation?" Sustainability 2022 2, 14:(12).

[11] Li H. et al. "Impact of enterprise digitalization on green innovation performance under the perspective of producti on and operation." Frontiers in Public Health. 2022,10.

[12] Liu YW, et al. Research on the impact of green credit policy on corporate environmental information disclosure. S tatistical Research,2022,39(11):73-87. DOI:10.19343/j.cnki.11-1302/c.2022.11.006.

[13] Xie XMi, Han YH. How can local manufacturing enterprises achieve "magnificent transformation" in green innov ation? --A multi-case study based on an attention-based view. Management World, 2022,38(03):76-106. DOI:10.1 9744/j.cnki.11-1235/f.2022.0043.

.

RIGA 2023

Allocation of Photovoltaic Distributed Generations in a Radial Distribution System

Samson Ayanlade
Lead City University, samson.ayanlade@lcu.edu.ng

Funso K. Ariyo
Tennessee Technological University, funsoariyo@yahoo.com

Abdulrasaq Jimoh
Obafemi Awolowo University, jimohabdulrasaq@gmail.com

Adetunji Adeleye
Osun State University, tunjiat17@gmail.com

Emmanuel Ogunwole
Cape Peninsula University of Technology, emmanuelidowu18@gmail.com

Dolapo Owolabi
Ladoke Akintola University of Technology, owolabidolapo343@gmail.com

Cite this paper as: *Ayanlade, S, Ariyo, FK, Jimoh,A, Adeleye, A, Ogunwole, E, Owolabi, D. Allocation of photovoltaic distributed generations in a radial distribution system. 11. Eur. Conf. Ren. Energy Sys. 18-20 May 2023, Riga, Latvia*

Abstract: Among Distributed Generation (DG), the Photovoltaic Distributed Generation (PVDG) is one of the DG types that produces no greenhouse gases and require little maintenance. Consequently, PVDG found numerous applications in distribution networks, one of which is to boost the network's performance. This research article utilized the Dingo Optimization Algorithm (DOA) for optimizing the allocation of PVDG so as to elevate the distribution network performance. A single objective function for the distribution network was formulated and solved using DOA. The Newton-Raphson power flow solution approach was applied to solve the power flow problems in the network. The effectiveness of DOA in allocating PVDG was assessed using the voltage profile and overall active power loss as performance metrics. The approach was developed in MATLAB and applied on the IEEE 33-bus system. The results revealed that buses 13, 25, and 33 were the optimal buses for PVDG locations, while 833, 532, and 866 kW were appropriate PVDG sizes. The network performance was remarkably improved as the least voltage value was elevated to 0.966 p.u. and the overall active power was reduced by 61.21%. Therefore, DOA successfully optimized PVDG for distribution network performance enhancement.

Keywords: *Distributed Generation, PVDG, Dingo Optimization Algorithm, Voltage Profile, Active Power Loss*

Nomenclature	
PVDG	Photovoltaic Distributed Generation
DOA	Dingo Optimization Algorithm
GHG	Greenhouse Gas
DG	Distributed Generation
PSO	Particle Swarm Optimization
SPV	Solar Photovoltaic
ALOA	Ant Lion Optimization Algorithm

1. INTRODUCTION

The power system has proven to be the driving force of any nation's economy. It is so significant that it determines the classification of nations around the globe as low-income, lower-middle-income, upper-middle-income, and high-income economies based on their levels of income. The power system was divided into the generation, transmission, and distribution systems as a result of deregulation [1]. One of the key components of the entire power system is the distribution system, which is plagued by a number of technical issues, including a terrible voltage profile, extremely poor efficiency due to huge power loss, voltage collapse, etc. Power system engineers and academics have developed a wide range of strategies to address these issues to date. Many attempts are still being made to develop new methods to address these issues in order to enhance the effectiveness of the distribution networks. The intent is to significantly lower the overall active power loss as a consequence, leading to more effective distribution networks. Distribution Generation (DG) deployment is one of the most popular and successful techniques. There are four different varieties of DGs: type 1, type 2, type 3, and type 4 [2]. These four distinct DG types have a significant effect on reducing the overall active power loss in distribution networks. However, because of the push for green energy, type 1 DG, or photovoltaic distributed generation (PVDG), is the most often utilized because of its lack of greenhouse gas (GHG) emissions into the environment. It is capable of injecting active power into the distribution network to enhance network performance and active power delivery capability [3]. Similarly, it lessens the burden posed by the load demands on the distribution network, thus enhancing the network's reliability. In general, the deployment of DGs on distribution networks necessitates the proper allocation of DG in order to meet the set objectives. Scholars have authored literature on the best deployment of DG, particularly PVDG, on distribution networks to optimize operational performance. In order to reduce network dependency and GHG emissions as much as possible, [4] determined the best locations and sizes for solar photovoltaic (SPV) systems in distribution systems using the Archimedes optimization algorithm (AOA), which was inspired by physical principles. In order to reduce reliance on the grid and GHG emissions from traditional power plants, the search space for sites was predefined using loss sensitivity parameters, and SPV system locations and sizes were identified using AOA. Albadi et al. [5] investigated the best placement of photovoltaic (PV) systems in the distribution system. Particle swarm optimization (PSO) and genetic algorithms (GA) were used in a case study. The problem's objective was to reduce transmission loss while enhancing the voltage profile. The network of Masirah Island, Oman, was used as a case study system in the study. Khenissi et al. [6] found the best size and allocation of a photovoltaic distributed generation (PVDG) system to decrease overall power loss and improve the voltage and frequency profiles of the IEEE 14-bus network. In this study, an objective function was utilized to decrease network losses, and two optimization techniques were employed to tackle this function: the PSO and the GA. Furthermore, two scenarios were described in the research to examine the effect of a changeable PV integration level, an hourly load consumption profile fluctuation, and an atmospheric condition variation on size optimization resolution. Albadi et al. [7] provided a case study that used PSO to find the ideal position and capacity of solar systems in a distribution system, resulting in a better network voltage profile and reduced losses. The Masirah Island distribution network in Oman was chosen as a case study. The Ant Lion Optimization Algorithm (ALOA) was suggested by [8] for optimal allocation and scaling of DG-based renewable sources for distribution networks. First, utilizing loss sensitivity parameters, the most likely candidates for implementing DG were identified. The suggested ALOA was then used to determine the positions and capacities of DGs on the selected buses. On a 69-bus network, the suggested method was tested. Ahmed et al. [9] investigated the distribution network performance when single and multiple PV-based DG were incorporated in distribution systems. To decrease overall power losses and enhance the system voltage profile, the appropriate location and size of DG in the distribution system were found. The Augmented Grey Wolf Optimizer and Loss Sensitivity Factor were proposed to attain this objective. The suggested approach was tested using an IEEE 69-bus distribution network. The acquired results demonstrate the efficacy of the suggested approach. According to the literature examined thus far, the optimal allocation of PVDG has been addressed using existing metaheuristic methods. The effectiveness of these metaheuristic algorithms in allocating PVDG has been demonstrated. However, to further improve the distribution network's performance and drastically minimize total active power loss, it is necessary to employ a novel optimization algorithm and compare its performance in optimally allocating PVDG with other existing optimization algorithms, which is the main contribution of this research. The innovative aspect of this study is the use of a hitherto novel Dingo Optimization Algorithm (DOA) to tackle the problem of PVDG allocation on distribution networks. A MATLAB program was developed to implement the method and tested on the IEEE 33-node system.

2. PROBLEM FORMULATION

Objective Function

The primary goal of PVDG deployment on distribution networks is to minimize overall active power loss. The overall active power loss is the overall active power loss across all network branches. Hence, in this study, the objective function (OF) to be minimized is the overall active power loss, which is expressed by Eq. [1]:

$$OF_{min} = \sum_{i}^{n_b} |I_i|^2 R_i \quad (1)$$

where, n_b = total network branches, R_i = line resistance and $|I_i|$ = i^{th} line current.

Constraints

These are the equality and inequality constraints which the OF is subject expressed as Eqs. [2-5]:

$$P_{Gi} = P_{Di} + \sum_{j=1}^{n_b} |V_i| \, |V_j| \left[G_{ij} \cos\theta_{ij} + B_{ij} \sin\theta_{ij} \right] \quad (2)$$

$$Q_{Gi} = Q_{Di} + \sum_{j=1}^{n_b} |V_i| \, |V_j| \left[G_{ij} \sin\theta_{ij} - B_{ij} \cos\theta_{ij} \right] \quad (3)$$

$$V_{min} \leq V_i \leq V_{max} \quad (4)$$

$$PVDG_{(min)} \leq PVDG \leq PVDG_{(max)} \quad (5)$$

where V_i and V_j = voltage magnitudes, P_{Gi} and P_{Di} = active power generated and demanded, Q_{Gi} and Q_{Di} = reactive power generated and demanded, and G_{ij} and B_{ij} = line conductance and susceptance, respectively.

Dingo Optimization Algorithm

Dingoes are social creatures that live in packs of 12 to 15 and are very clever. All other members of the pack submit to the Alpha, who is the pack's most powerful and dominant member [10]. A dingo is regarded as a subordinate if it is neither an alpha nor a beta. Scouts are responsible for keeping an eye on the areas and alerting the group to any hazards or situations that may arise. Dingoes hunt in packs and exhibit a peculiar social behavior that involves pursuing, pestering, surrounding, and attacking prey. Dingo social organization and hunting behavior are utilized by DOA.

Mathematical Modeling of Dingo Optimization Algorithm

A mathematical model of the circling and attacking of prey is used to execute the DOA [9].

Encircling

The mathematical Eqs. [6–10] are used to model the dingoes' encircling behavior [11].

$$\vec{D}_c = \left| \vec{A} \cdot \vec{P}_p(x) - \vec{P}(x) \right| \quad (6)$$

$$\vec{P}(i+1) = \vec{P}_p(i) - \vec{B} \cdot \vec{D}(d) \quad (7)$$

$$\vec{A} = 2 \cdot \vec{a}_1 \quad (8)$$

$$\vec{B} = 2\vec{b} \cdot \vec{a}_2 - \vec{b} \quad (9)$$

$$\vec{b} = 3 - \left(I * \left(\frac{3}{I_{max}} \right) \right) \quad (10)$$

where, $\vec{D}_c$= separation between the prey and dingo, $\vec{P}_P$, $\vec{P}$= prey and dingo position vectors, $\vec{A}$, $\vec{B}$ = coefficient vectors, $\vec{a}_1$ = random vector, $\vec{a}_2$ = random vector, $\vec{b}$ = at each iteration, it decreases linearly from 3 to 0, I = 1,2,3,..., I_{max}.

Hunting

The dingoes' hunting behaviour are modelled mathematically by Eqs. [11–16].

$$\vec{D}_\propto = \left| \vec{A}_1 \cdot \vec{P}_\propto - \vec{P} \right| \quad (11)$$

$$\vec{D}_\beta = \left| \vec{A}_2 \cdot \vec{P}_\beta - \vec{P} \right| \quad (12)$$

$$\overrightarrow{D_o} = \left| \vec{A}_3 \cdot \vec{P}_o - \vec{P} \right| \quad (13)$$

$$\vec{P}_1 = \left| \vec{P}_\alpha - \vec{B} \cdot \vec{D}_\alpha \right| \quad (14)$$

$$\vec{P}_2 = \left| \vec{P}_\beta - \vec{B} \cdot \vec{D}_\beta \right| \quad (15)$$

$$\vec{P}_3 = \left| \vec{P}_o - \vec{B} \cdot \vec{D}_o \right| \quad (16)$$

Individual dingo intensity is calculated by Eqs. [17-19]:

$$\vec{I}_\propto = \log\left(\frac{1}{F_\propto - (1E - 100)} + 1 \right) \quad (17)$$

$$\vec{I}_\beta = \log\left(\frac{1}{F_\beta - (1E - 100)} + 1 \right) \quad (18)$$

$$\vec{I}_o = \log\left(\frac{1}{F_o - (1E - 100)} + 1\right) \quad (19)$$

where, F_α and F_β = α and β-dingo fitness values, respectively, and F_o = other dingo fitness value.

Attacking prey

If there is no update on the victim's position, dingo has concluded the search by attacking the target. In order to mathematically design the technique, $\vec{b}$'s value must decrease linearly. It should be noted that $\vec{b}$ also reduces the changing range of $\vec{D}_\alpha$.

Searching

As a result, $\vec{B}$ is used for random variables, where a number less than -1 implies fleeing the hunter and a value greater than 1 suggests being chased by the pack. Using this technology, the DOA can scan targets globally. $\vec{A}$ is another aspect of DOA that presents the potential for exploration. The flowchart is depicted in Fig. 1.

3. RESULTS AND DISCUSSION

The proposed DOA technique was implemented utilizing MATLAB software, and its effectiveness in handling numerous PVDG locations was evaluated using the IEEE 33-bus system. Line and load data for the network were sourced online. According to Fig. 2, the IEEE 33-bus network consists of 33 buses and 32 branches. In this study, the network three PVDGs were deployed on the distribution network in order to enhance its performance. The DOA variables utilized in this study were the population (D_n = 1000) and the maximum number of iterations ($iter_{max}$ = 200). The simulation converges after three iterations and the simulation results are shown in Table 1. Following PVDG optimization, buses 13, 25, and 33 were the appropriate locations for the PVDG units, and Table 1 reveals that the best PVDG unit sizes for these buses were 833, 532, and 866 kW, respectively. The allocation of the various PVDG units and its effects on the network voltage profile, as well as active and reactive power losses, are covered in the following subsections.

Table 1. Optimal PVDG allocations

PVDG size (kW)	Location
532	25
866	33
833	13

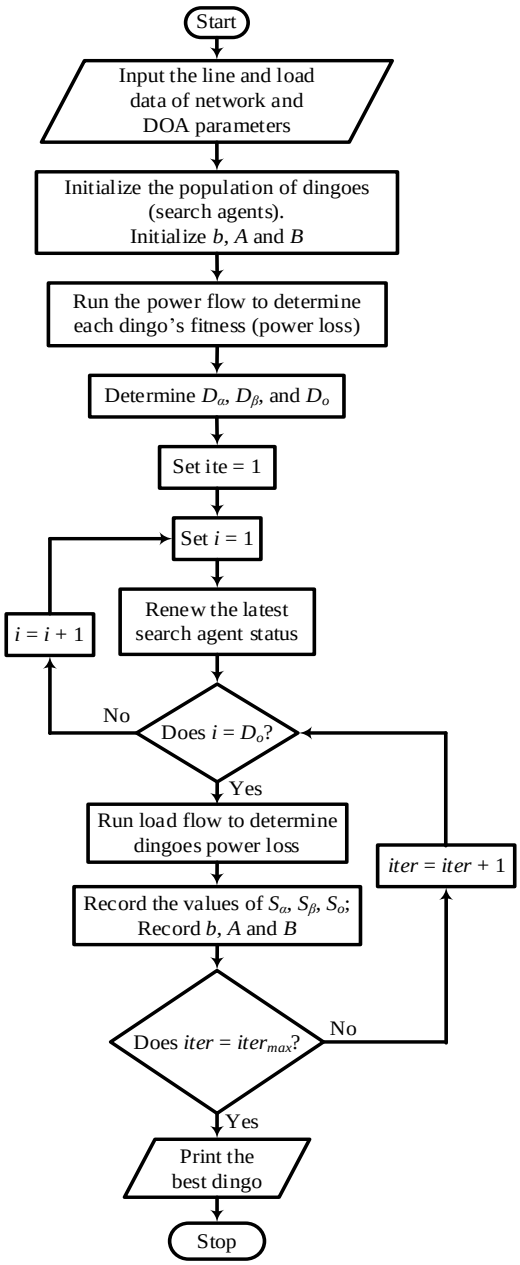

Figure 1. Implementation of the DOA PVDG allocation

Voltage Profile

The test network's voltage profile is depicted in Fig. 2 both with and without the deployment of PVDG units. Prior to the deployment of PVDG units, the voltage profile was insufficient since the majority of the bus voltage magnitudes violated the permitted voltage limits. According to Fig. 2, all of the voltage magnitudes at bus 7 and up until bus 18 were below the permitted 0.95 p.u. minimum voltage requirement, with bus 18 having the lowest voltage magnitude at 0.913 p.u. As indicated in Fig. 2, the voltage magnitudes of the buses whose voltage magnitudes had previously violated the allowable voltage limits dramatically improved, with bus 30 having the minimum voltage magnitude at 0.966 p.u. The voltage profile of the entire network increased significantly as a result of this. The performance of the test network was enhanced by employing DOA to optimize a number of PVDG units, as illustrated in Fig. 2.

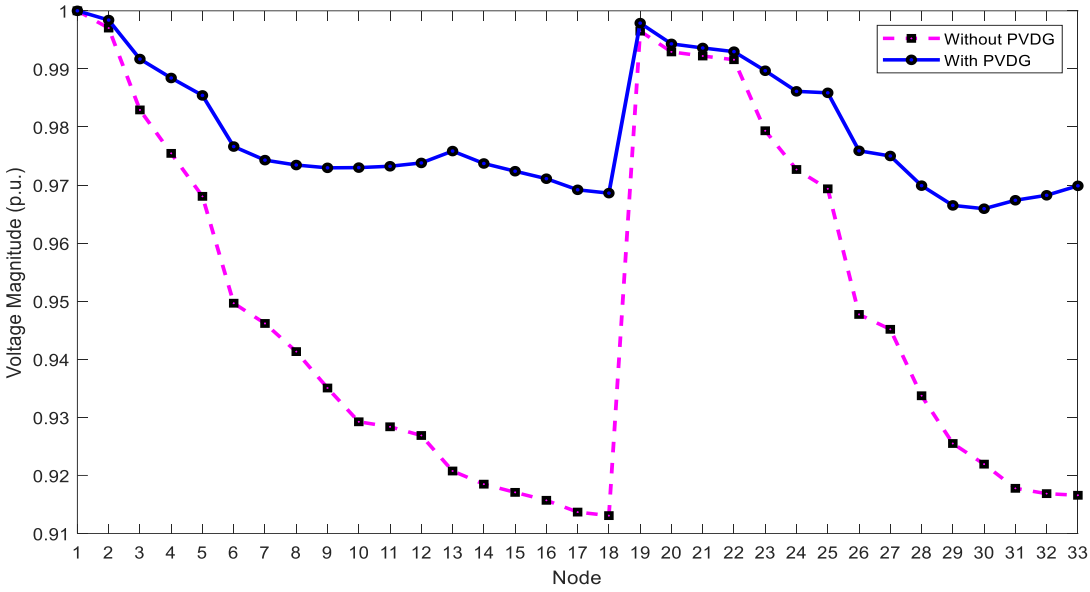

Figure 2. Voltage profile without and with PVDG placement

Active Power Loss

Before the placement of PVDG units, the total active power loss was 202.71 kW. When the DOA optimization algorithm was used to optimally allocate PVDG units, a remarkable 61.21% reduction in total active power, or 78.62 kW, was achieved. The maximum active power loss of 0.05 MW, which occurred in branch 2-3 of the test network without the deployment of PVDG units, was reduced to 0.02 MW (or a 60% reduction) following the optimal deployment of PVDG units. Similarly, there was a tremendous decrease in the active power losses in all the branches of the test network, which resulted in an overall improvement in the network's efficiency.

4. CONCLUSION

The use of DOA to optimize PVDG units to increase distribution network performance was proven in this study. The suggested optimization approach was effective since it distributed PVDG units as efficiently as was feasible on the tested distribution network. Therefore, DOA is advised to address the optimization problem of incorporating PVDG units to enhance the effectiveness of the distribution networks.

References

[1] Ayanlade, SO, Komolafe, OA. Distribution system voltage profile improvement based on network structural characteristics. In: OAUTEKCONF 2019. OAU Faculty of Technology Conference; September 2019: pp. 75-80.

[2] Adepoju, GA, Aderinko, HA, Salimon, SA, Ogunade, FO, Ayanlade, SO, Adepoju, TM. Optimal placement and sizing of distributed generation based on cost-savings using a two-stage method of sensitivity factor and firefly algorithm. In: 1st ICEECE & AMF, 1(1), 2021, pp. 52-58.

[3] Reddy, GH, Koundinya, AN, Gope, S, Singh, KM. Optimal sizing and allocation of DG and FACTS device in the distribution system using fractional Lévy flight bat algorithm. IFAC-PapersOnLine 2022; 55(1): 168-173.

[4] Janamala, V, Radha Rani, K. Optimal allocation of solar photovoltaic distributed generation in electrical distribution networks using Archimedes optimization algorithm. Clean Energy 2022, 6(2): 271-287.

[5] Albadi, M, Soliman, H, Thani, MA, Al-Alawi, A, Al-Ismaili, S, Al-Nabhani, A, Baalawi, H. Optimal allocation of PV systems to minimize losses in distribution networks using GA and PSO: Masirah island case study. Journal of Electrical Systems 2017, 13(4).

[6] Khenissi, I, Sellami, R, Fakhfakh, MA, and Neji, R. Power loss minimization using optimal placement and sizing of photovoltaic distributed generation under daily load consumption profile with PSO and GA algorithms. Journal of Control, Automation and Electrical Systems 2021, 32(5): 1317-1331.

[7] Albadi, MH, Soliman, HM, El-Saadany, EF, Thani, MA, Al-Alawi, A, Al-Ismaili, S, Baalawi, H. Optimal allocation of PV systems in distribution networks using PSO. In: 2017 7th International Conference on Modeling, Simulation, and Applied Optimization (ICMSAO) 2017 (pp. 1-5). IEEE.

[8] Ali, ES, Abd Elazim, SM, Abdelaziz, AY. Optimal allocation and sizing of renewable distributed generation using ant lion optimization algorithm. Electrical Engineering 2018, 100: 99-109.

[9] Ahmed, IM, Kamel, S, Abdel-Mawgoud, H, Yu, J. Optimal allocation of PV based DG in distribution networks at different load levels. In: 2018 Twentieth International Middle East Power Systems Conference (MEPCON) (pp. 649-654) 2018. IEEE.

[10] Bairwa, AK, Joshi, S, Singh, D. Dingo optimizer: A nature-inspired metaheuristic approach for engineering problems. Mathematical Problems in Engineering 2021, 2021, 1–12. DOI: https://doi.org/10.1155/2021/2571863

[11] Ayanlade, SO, Jimoh, A, Ogunwole, EI, Aremu, A, Jimoh, AB, Owolabi, DE. Simultaneous network reconfiguration and capacitor allocations using a novel dingo optimization algorithm. International Journal of Electrical and Computer Engineering (IJECE) 2023, 13(3): 2384-2395 DOI: 10.11591/ijece.v13i3.pp2384-2395.

RIGA 2023

A Process Mapping Study of End-Of-Life Electric Vehicle Battery Repurposing for Renewable Energy Storage

Melissa Venegas Vallejos
Aston University, Birmingham, UK, venegasm@aston.ac.uk, ORCID: 0000-0001-8238-6004

Andrew Greasley
Aston University, Birmingham, UK, a.greasley@aston.ac.uk, ORCID: 0000-0001-6413-3978

Aristides Matopoulos
Cranfield University, Cranfield, UK, aris.matopoulos@cranfield.ac.uk, ORCID: 0000-0002-5083-0534

Cite this paper as: *Venegas Vallejos, M, Greasley, A, Matopoulos, A. A study of EOL EV battery repurposing for renewable energy storage. 11. Eur. Conf. Ren. Energy Sys.18-20 May 2023, Riga,, Latvia*

Abstract: The aim of this article is to provide a detailed process map description of the reverse supply chain for electric vehicle batteries. In particular the main processing options of remanufacturing, repurposing and recycling. This will be achieved by a qualitative approach in which the main stakeholders are interviewed in order to provide a detailed picture at the operational level of the main processes and decisions involved in the end-of-life reverse supply chain for electric vehicle batteries. The focus of this study is on the repurposing end-of-life option which extends the lifetime of the battery pack in a different industry or application such as storage for intermittent renewable energy sources. Along with an estimation of future electric vehicle end-of-life capacity this will enable estimates of the amount and timing of battery capacity that will be available for repurposing for renewable energy applications.

Keywords: *Electric vehicles, end-of-life batteries, process mapping, renewable energy storage*

1.INTRODUCTION

Global EV sales are expected to increase steadily in the coming years, increasing from 3.1 million in 2020 to 14 million in 2025 [1]. Electric vehicle (EV) batteries are the most critical component of electric vehicles because they account for a significant part of the vehicle's cost and are highly relevant for EV development and adoption. Since EV batteries typically last between 8 to 10 years, the end-of-life (EOL) supply chain of this component needs to be prepared to handle the increasing volumes of batteries that are going to reach their end-of-life in the following decades.

The EV battery industry is a developing industry that needs to ensure its sustainability. Some of the drivers that are encouraging the development of reverse supply chains for EV batteries are the finite critical raw material supply [2,3], the negative environmental impact of EV battery production and disposal [4,5] and governmental regulations associated with used EV batteries [4,5]. Several barriers that affect the EV reverse supply chain implementation have also been identified, such as the early development stage of suppliers, capacity, a major investment for EOL management facilities, and the labour-intensive nature of activities. Therefore, EV manufacturers need to build sustainable EOL reverse supply chains on time to address future industry challenges.

Al-Alawi [6] found that there is significant potential for EOL EV batteries to deliver energy for alternative applications such as storing surplus energy. Specifically, batteries of electric vehicles obtained at their end-of-life can be repurposed as storage systems to integrate with renewable energies such as intermittent wind power [7]. Volan et al. [8] state that for the most optimistic scenario, EOL batteries will account for 86% of energy storage for

wind and 36% for solar PV in 2040.The decision about the best EOL alternative for processing batteries depends on the battery's design characteristics, quality of the EOL product and state of health (SOH) of the battery and cells. Previous studies have attempted to provide predictions of EOL battery availability at a strategic level [8], characterising the value proposition of the use of EV batteries in stationary battery energy storage systems (BESS) [9], the technical viability of repurposing retired EV batteries (REVB) [6] and the sustainability of the use of repurposing EV batteries [7].

The aim of this article is to provide a process description of the reverse supply chain (RSC) for EV batteries. In particular the main processing options of remanufacturing, repurposing and recycling. This will be achieved by a qualitative approach in which the main stakeholders are interviewed in order to provide a detailed picture at the operational level of the main processes and decisions involved in the EOL RSC for EV batteries. Along with future estimation of EV EOL capacity this will enable estimates of future amount and timing of battery capacity that will be available for repurposing in renewable energy applications. The article is structured as follows. A literature review of the main options for EOL EV batteries of remanufacturing, recycling and repurposing leads to identification of the processes and actors in the EOL RSC for EV batteries. Then a qualitative study will provide operational details of the activities involved in these processes. The aim of this analysis is to provide the basis for the construction of a predictive simulation model that can be used to estimate the future amount and timing of battery capacity for repurposing use for renewable energy applications.

2.LITERATURE REVIEW

The capacity of electric vehicle batteries reduces with the passing of the years due to the cells' degradation and growth of the internal resistance [10]. After reaching the end of their first life, electric vehicle batteries still have enough energy to be used in a second life that demands less capacity [10]. The decision about the best EOL alternative depends on the battery's design characteristics, quality of the EOL product and state of health (SOH) of the battery and cells. Remanufacturing and repurposing are the prefered options to maximise the recovered value from EV batteries and minimise the energy consumption after first-life treatment [11,12]. However, remanufacturing is the most exigent alternative in terms of quality and SOH requirements. The second desirable option after remanufacturing is repurposing of EV batteries for second life in a different industry such as intermittent renewable energy sources such as wind and solar. Recycling is the least favoured option from a circular economy perspective because of the reduced benefits, loss of material and energy consumption of the recycling processes. Nevertheless, recycling is still better than EOL EV batteries' disposal. Through recycling the valuable material of batteries can return to the EV battery supply chain reducing the extraction of raw material [12]. The three options are now outlined in more detail.

Remanufacturing

Remanufacturing is the process by which a product can be rebuilt and its components repaired and replaced to use the whole battery pack in its original automotive application [12]. The remanufacturing strategy includes diagnosing the battery modules and cells, replacing or repairing damaged cells and modules, and reassembling all the components into a new battery pack [12]. Remanufacturing is the preferred EOL alternative for battery packs when their SOH is sufficient for EV use. According to the US Advanced Battery Consortium (USABC) standard only batteries with a higher capacity than 80% can be used in an EV. EV batteries with a lower SOH than 80% do not have enough energy and capacity to be used for automotive applications [13]. A study made by Foster *et al.* [14] suggested that using remanufacturing batteries saves approximately 40% of the cost of producing a new Li-ion battery. However, remanufacturing also poses challenges. There is a wide variety of battery pack designs with different sizes, chemistries and formats (cylindric, prismatic and pouch), which adds complexity to the remanufacturing process due to the lack of standardisation [15]. By 2015 nearly 250 new EV models will be introduced to the market, produced with batteries from more than 15 manufacturers [15].

Repurposing

Repurposing is the second prefered EOL option for EV batteries after remanufacturing. It extends the lifetime of the battery pack in a different industry or application, e.g. energy storage. This alternative is recommended for EV batteries that are in good condition and still have high capacity left, but it is not enough to continue using them for

EV applications that normally require a capacity above 80% [13]. Repurposing EV batteries does not involve only replacing and repairing battery cells and modules. Repurposing also involves reconfiguring such elements into new modules and packs and a new battery management system to adapt them to the new applications needs. In contrast to remanufacturing, repurposing EV batteries poses different challenges. Some of the challenges are the accuracy of the quality grading of the repurposed battery pack, difficulty to disassembly battery packs with different designs, reconfiguration costs that should compete with new batteries and transfer of liability [12]. Finally, EV batteries were created for and to be used in EVs. Moreover, EV manufacturers are responsible for collecting and treating these batteries at their EOL. For this reason, the risks and legal responsibilities of using these batteries in a different application are not clearly defined [13].

The decision to repurpose EV batteries should pass through careful economic analysis. Repurposing batteries involve testing, grading and repacking, which are significantly expensive and could make the decision to repurpose not economically viable [12]. As Chen *et al.* [12] suggest these costs may be reduced by using more advanced technology to measure the batteries' SOH and grading. Repurposed batteries can be used for different applications such as peak shaving, backup energy storage, renewable energy storage, and EV charging [11,16]. For one of the repurposing applications, General Motors (GM) work with Empower Energies, a renewable energy services platform. They use the used Chevrolet batteries, solar arrays, and wind turbines to provide energy to the GM enterprise data centre in Michigan [17].

Recycling

Recycling is the third and last EOL option that can be used for EV batteries. The recycling option can accept batteries with all SOH levels. However, recycling is more expensive than remanufacturing and repurposing, and it is the process that loses the most valuable battery material. Sending EOL EV battery packs directly for recycling would imply the loss of their remaining energy when they could still be remanufactured and repurposed if they have enough capacity [18].

Figure 1 shows the main processes and actors involved in the EOL RSC for EV batteries in the UK which includes vehicle Dealer Service Centres and a specialised Authorised Treatment Facility (ATF) network. These companies are key players in the EOL supply chain for EV batteries since they are responsible for collecting the EV batteries from EV users. The batteries then progress to the three types of companies offering recovery options of remanufacturer, repurposer and recycler.

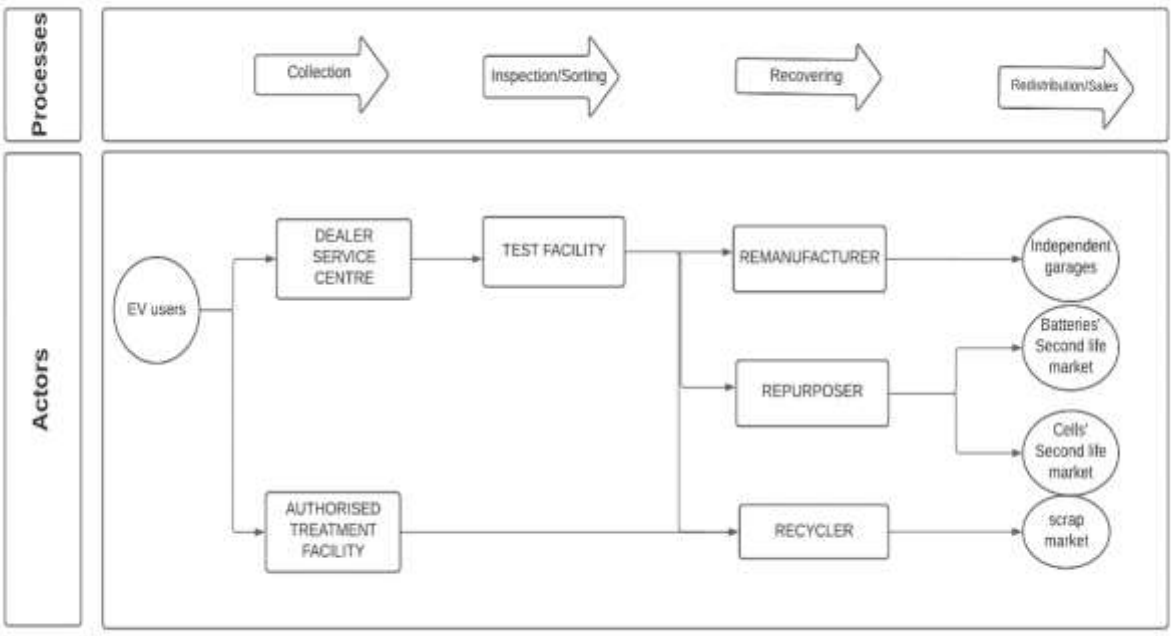

Figure 1. Processes and actors in the EOL RSC for EV batteries.

3.DISCUSSION

This study uses selected companies that offer different recovery alternatives to extend the life of EV batteries, components, and materials. All the companies involved in this research are UK-based. The UK was chosen for this research since it is one of the most influential electric vehicle markets in Europe; however, its RSC is developing and requires supporting tools to establish its long-term plans. Even though this study focuses on the UK context, the methodology can be used to study other contexts.

The real names of the companies are not presented to keep the confidentiality of the participant companies.

(1) Remanufacturer_A has undertaken refurbishing work and has experience working in some refurbishing and remanufacturing pilot projects with electric vehicle batteries.
(2) Repurposing_A was chosen for this study since it is developing projects to build Lithium-ion batteries for storage applications using used EV battery cells.
(3) Recycler_A is a UK-based material recycling company that offers lithium-ion battery recycling services with a dedicated factory area and specialised personnel.

Current process - Remanufacturing company

When Remanufacturing_A receives batteries from their clients, one of the first steps to follow is the discharge of the batteries if required. Then, the battery needs to be isolated by checking if the cooler pipes have come loose or split within the pack because they could cause a shortcut. The next step is the diagnosis. The diagnosis of EV batteries is a key step to identify what the faults are, and based on that information, decide where to send the batteries. The diagnosis of the battery involves the measurement of the state of health of a battery (SOH). To measure the SOH of the battery it is necessary to have either a reference from a new battery to benchmark against or have information about how exactly the battery was meant to perform. This process requires developing multiple tests that need to be designed to be flexible enough to check batteries from different manufacturers and EV models.

Remanufacturing_A has identified three possible routes with three separate lines for the batteries. The first line is for the batteries that are not good to use. In this first case, batteries should be dismantled to a module level and prepared for recycling. The parts that still can be reused would be kept at the facility. The second option for batteries is harvesting. Harvesting in this context refers to gathering the useful parts of products to store them and use them later for remanufacturing. For instance, if there is a battery with 18 modules and one string of 6 modules is fine, and the other two strings are broken, the good string with six modules combined with other useful parts could be used to build a full battery again. Finally, the third route would be for good functional batteries that can be either refurbished or remanufactured. The diagnosis for the third route is challenging since it would have multiple needs. For instance, measuring the state of health of a battery is not a straightforward process, and it will vary depending on the brand, model and technology of the batteries. Figure 2 shows a simplified map that includes the activities performed by the Remanufacturer.

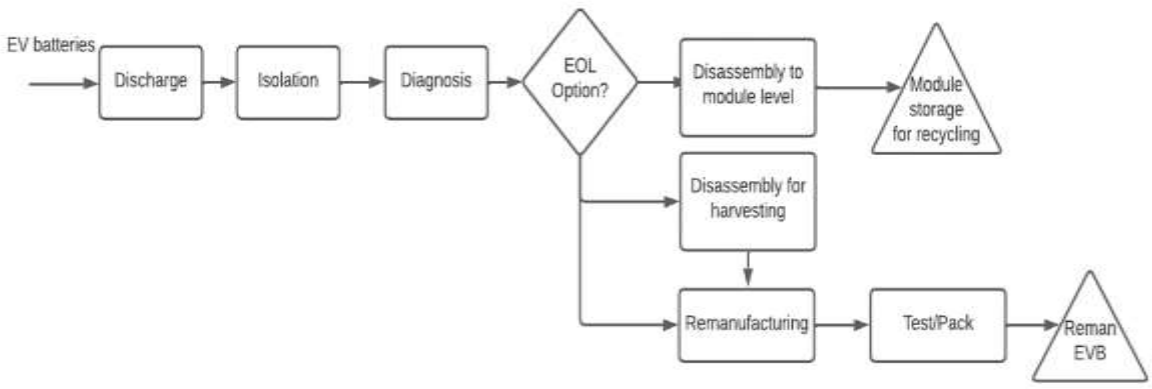

Figure 2. Process map Remanufacturing company.

Current process - Repurposing company

The process starts when Repurposing_A receives the waste battery cells from suppliers. Then, the cells pass through a visual inspection to identify which cells are in good condition. Next, the cells are labelled and loaded on to the testing machine. Then, the testing machine measures the SOH of the cells and establishes their grading category. When the battery cells performance is too low, these cannot be recovered. The cells that can be recovered, depending on their performance they can be used to build new batteries for different applications, for example home energy storage or turn them into a battery that goes into a boat or for power supply services. After the cells testing, the new battery assembly takes place. Afterwards, the whole battery pack needs to pass through a final testing. If the battery doesn't pass the final test the battery pack is disassembled and the cells are sent to the assembly step again. Figure 3 shows a simplified map that includes the activities performed by the Repurposing company.

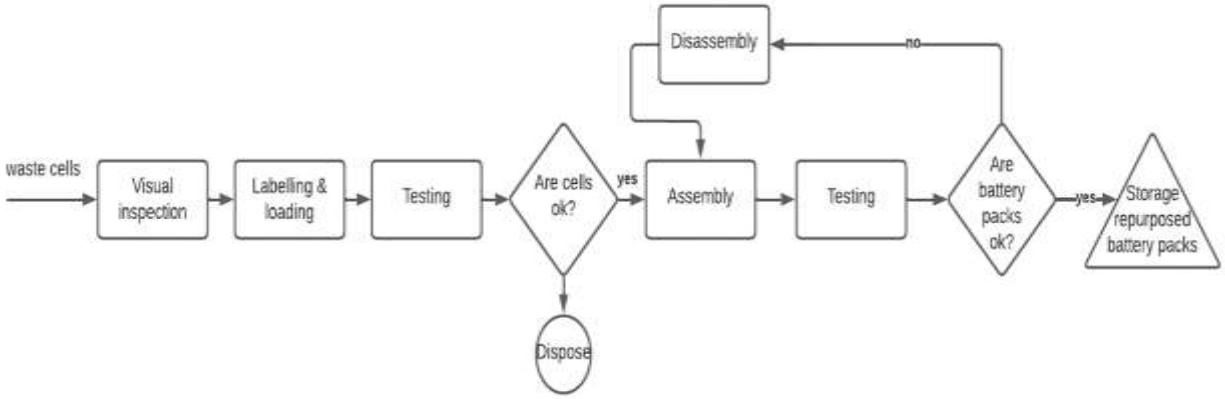

Figure 3. Process map repurposing company

Current process - Recycling company

The process begins when Recycler_A receive the EV battery packs. Then, the operators make sure that the batteries are discharged. The next step is the dismantling process which is done by hand and with the help of specific tools. First, the batteries have to be dismantled to a module level. Then, the cells are taken out from the modules, and then these are sent to the recycling plant where the recycling machines are set up. In the recycling plant, the cells are split up to pass through various mechanical and chemical processes to separate copper, plastic and cathode powder. On average, Recycler_ A expects to recover 80% of the total weight of the batteries. Figure 4 shows a simplified map that includes the activities performed by the Recycling company.

The manager from Recycler_A suggest that "the most complex processes are the batteries and cells dismantling and discharging because the diversity of batteries configurations add complexity to the activities. When working with different types of batteries, the operation staff have to follow different procedures and use different tools for each type of battery, extending the total processing time".

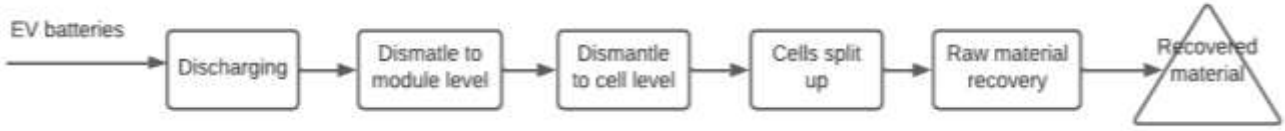

Figure 4. Process map Recycling company

4.CONCLUSION

The aim of this article has been to provide a process description of the reverse supply chain for EV batteries from the result of interviews with industry participants. In particular the main processing options of remanufacturing, repurposing and recycling are detailed. Further work is proposed in developing this work at an operational level to providing a discrete-event simulation of individual EOL battery flows. The purpose of this being to provide an estimation of the future amount and timing of EOL battery capacity. This can then assist in planning repurposing applications for renewable energy storage.

References

[1] BloombergNEF (2021) Electric Vehicle Outlook 2021. Available at: https://about.bnef.com/electric-vehicle-outlook/.
[2] International Energy Agency (2018) Global EV Outlook 2018. Available at: https://www.iea.org/reports/global-ev-outlook-2018.
[3] Moores, S. (2018) Energy storage technologies: the supply chain risks and opportunities. Oxford.
[4] Winslow, K. M., Laux, S. J. and Townsend, T. G. (2018) 'A review on the growing concern and potential management strategies of waste lithium-ion batteries', Resources, Conservation and Recycling, 129(October 2017), pp. 263–277. doi: 10.1016/j.resconrec.2017.11.001.
[5] International Energy Agency (2019) Global EV Outlook 2019. Available at: https://www.iea.org/reports/global-ev-outlook-2019.
[6] Al-Alawi, M.K., Cugley, J., Hassanin, H. (2022) Techno-economic feasibility of retired electric-vehicle batteries repurpose/reuse on second-life applications: A systematic review, Energy and Climate Change, 3, 100086. doi: 10.1016/j.egycc.2022.100086
[7] Shokrzadeh, S. and Bibeau, E. (2016) 'Sustainable integration of intermittent renewable energy and electrified light-duty transportation through repurposing batteries of plug-in electric vehicles', Energy, 106, pp. 701-711. doi: 10.1016/j.energy.2016.03.016
[8] Volan, T., Rodrigues Vaz, C., Uriona-Maldonado, M. (2021) 'Scenarios for end-of-life (EOL) electric vehicles in China', Revista de Gestão, 28(4), pp. 335-357. doi: 10.1108/REGE-12-2020-0143
[9] Schulz-Mönninghoff, M. and Evans, S. (2023) 'Key tasks for ensuring economic viability of circular projects: Learning from a real-world project on repurposing electric vehicle batteries', Sustainable Production and Consumption, 35, pp. 559-575. doi: 10.1016/j.spc.2022.11.025
[10] Klör, B., Bräuer, S. and Beverungen, D. (2014) 'A business process model for the reverse logistics of used electric vehicle batteries', Lecture Notes in Informatics (LNI), Proceedings - Series of the Gesellschaft fur Informatik (GI), P-232(January 2014), pp. 1631–1643.
[11] Canals Casals, L., Amante García, B. and Cremades, L. V. (2017) 'Electric vehicle battery reuse: Preparing for a second life', Journal of Industrial Engineering and Management, 10(2Special Issue), pp. 266–285. doi: 10.3926/jiem.2009.
[12] Chen, M. et al. (2019) 'Recycling End-of-Life Electric Vehicle Lithium-Ion Batteries', Joule, 3(11), pp. 2622–2646. doi: 10.1016/j.joule.2019.09.014.
[13] DeRousseau, M. et al. (2017) 'Repurposing Used Electric Car Batteries: A Review of Options', The Journal of The Minerals, Metals & Materials Society, 69(9), pp. 1575–1582. doi: 10.1007/s11837-017-2368-9.
[14] Foster, M. et al. (2014) 'Feasibility assessment of remanufacturing, repurposing, and recycling of end of vehicle application lithium-ion batteries', Journal of Industrial Engineering and Management, 7(3), pp. 698–715. doi: 10.3926/jiem.939.
[15] Engel, H., Hertzke, P. and Siccardo, G. (2019) 'Second-life EV batteries: The newest value pool in energy storage', McKinsey & Company, (April). Available at: https://www.febiac.be/public/statistics.aspx?FID=23.
[16] Olsson, L. et al. (2018) 'Circular business models for extended EV battery life', Batteries, 4(4). doi: 10.3390/batteries4040057.
[17] General Motors (2015) Used Chevrolet Volt Batteries Help Power New IT Building. Available at: https://news.gm.com/newsroom.detail.html/Pages/news/us/en/2015/jun/0616-volt-battery.html.
[18] Ramoni, M. O. and Zhang, H. C. (2013) 'End-of-life (EOL) issues and options for electric vehicle batteries', Clean Technologies and Environmental Policy, 15(6), pp. 881–891. doi: 10.1007/s10098-013-0588-4.

RIGA 2023

Solar PV Recycling Strategies

Zita Ngagoum Ndalloka
University of Massachusetts, Lowell, USA, zita_ngagoumndalloka@student.uml.edu, ORCID: 0000-0002-6693-0978

Harigovind Vijayakumar Nair
University of Massachusetts, Lowell, USA, harigovind_vijayakumarnair@student.uml.edu, ORCID: 0000-0002-1868-555X

Samuel Alpert
University of Massachusetts, Lowell, USA, samuel_alpert@student.uml.edu, ORCID: 0000-0003-4987-107X

Cordula Schmid
University of Massachusetts, Lowell, USA, Cordula_Schmid@uml, ORCID: 0000-0003-4753-6278

Cite this paper as: *Ndalloka, ZN., Nair, HV, Alpert, S, Schmid, C. Solar PV recycling strategies. 11. Eur. Conf. Ren. Energy Sys. 18-20 May 2023, Riga, Latvia*

Abstract: Solar PV is one of the most used and prominent renewable energy sources in meeting the world's increasing energy needs because of its advantages. As a result, there is an increase in solar panel installations worldwide. Considering its average lifetime of about 25 years and installation capacity, solar panels may become a source of waste in the next decades. Environmentally friendly and proper disposal of these panels is of the utmost importance. This paper reviews and summarizes the different recycling strategies of different solar panels such as crystalline solar panels, thin film, Organic solar cells, Gallium Arsenide (GaAs), Perovskite and Dye Sensitized Solar Cells (DSSC). Findings from the review show that though some recycling methods exist at the commercial level, a lot of research is underway. Crystalline PV recycling methods are advanced, followed by thin film technology. Solar PV recycling is an evolving field that requires more research to make the processes efficient, less complex, economically feasible and energy saving. PV recycling can reduce waste and possibly CO_2 emissions. This review informs companies and researchers who are active in solar PV recycling.

Keywords: Solar panel, solar PV recycling, waste management

1.INTRODUCTION

Solar photovoltaic is one of the most used and mature renewable energy sources worldwide because of the various advantages it has [1, 2]. It is a clean and environmentally friendly source of energy, reliable, safe, and the cost of installation keeps decreasing over the years [3]. Because of these advantages, it is considered a prominent source of generating and meeting the world's increasing energy demand. As a result, there has been a continuous increase in its installation and market and commitment in terms of research in order to increase its efficiency. The global PV installed capacity in 2017 was about 400GW and is expected to attain about 4500GW by 2050 [1, 4]. The continuous production and installation of solar PV worldwide will be a source of hazardous waste due to some metals used in its production. Solar PV panels are known to last for an average time of 25 years, after which they could be considered waste and therefore need to be discarded. Considering the continuous increase in solar PV installations and their lifetime, solar PV waste is forecasted to be between 4% and 14% of its total installation by 2030 and to further increase to about 80% by 2050, evaluated to about 78 million Tonnes of waste [1, 4, 5]. Land filling has been one of the methods used in disposing of this waste and due to the possibility of land destruction and pollution and hazards from the metals used in PV manufacturing and the increase scarcity of semiconductor materials in their manufacturing [2], an environmentally friendly option such as PV recycling is being considered [6]. Apart from the end-of-life modules, other modules like those with defects during production, damaged ones during transportation

and installation and malfunctioned ones during operation will equally need to be recycled [3]. Therefore, appropriate solar PV recycling technologies and waste management are of utmost significance [1, 2, 3]. The figure below shows the estimated cumulative worldwide solar PV module waste (Tonnes) 2016–2050 [1].

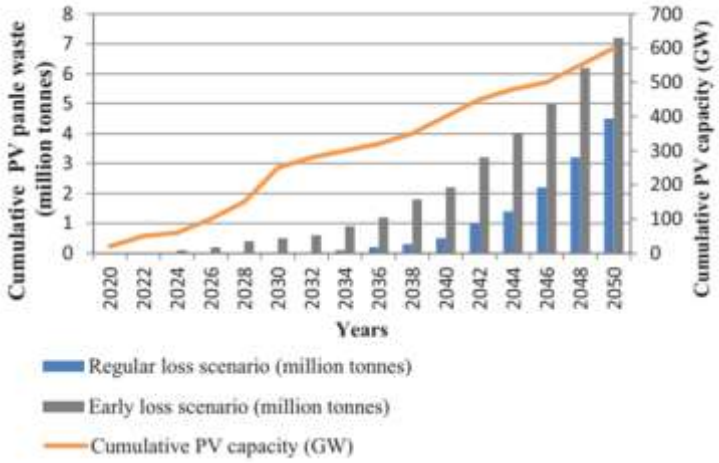

Figure 1. The estimated cumulative worldwide solar PV module waste (Tonnes) 2016–2050 Source:[1].

The aim of this review is to outline the various solar PV recycling strategies for different PV panels. It highlights the importance of recycling solar panels, gives an overview of the level of engagement of different countries in solar PV recycling. A review and summary of the different recycling strategies for the different types of solar PV technologies, and a conclusion and recommendation are provided. The review will be useful to companies and researchers interested in solar PV recycling to make informed decisions.

2.RECYCLING PROCESSES

Solar panel waste can be generated during any of its production phases, including panel production, transportation, installation and during its service life [1]. The recycling strategy depends on the type of solar technology because of the difference in their manufacturing processes. While two solar PV recycling strategies have been established at the industrial level, some are still under research. Several crystalline PV recycling strategies exist, followed by the thin film technology. The life cycle of a PV module and the possible stages of waste generation is shown below [3].

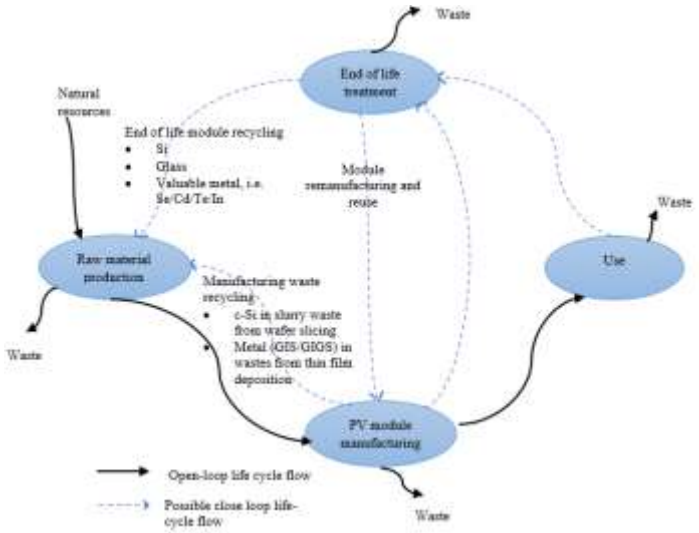

Figure 2. Typical life cycle of a PV module. Source: [3]

Based on the structure of PV modules, three basic processes can be applied for complete recycling. These are delamination, separation, and purification of the different elements [3]. These processes can be accomplished either physically, thermally, or chemically [7], as explained below.

- Physically: The panels are dismantled to remove the Aluminum frames, junction boxes and cables. The junction boxes and cables are then inspected for disposal, while the panels are then crushed for the next process.
- Thermally: The crushed panels are heated in furnaces. In one of such methods, the crushed panels are put in a high temperature furnace and heated up to a temperature of about (500°C) [7, 9] for one hour, and at 450°C/h heating rate. In another method by [9], the heat of the furnace is gradually increased at a rate of 10°C/min until it reaches 650 °C, and it's then held at this temperature for about an hour. 91% of glass is recovered by this method.
- Chemically: Different solvents and solutions are used to recover the different metals and materials found in the solar panels. The desired materials determine the solutions. In a study, [10] used phosphoric acid paste to recover solar wafers. In another study, [11] soaked crystalline silicon solar panels in trichloroethylene for 10 days at 80 degrees Celsius to completely remove Ethylene Vinyl Acetate (EVA) and recover Si cells. The panels obtained were successfully used. [12] recorded a high recovery rate of 90% by separating Cd and Te using chemicals such as Sulphuric acid solution, sodium carbonate and sodium sulphide. Kim and Lee [13] tested and used different organic solvents such as trichloroethylene, O-dichlorobenzene, benzene, and toluene at different temperatures to chemically enhance the dissolution of EVA. EVA fully dissolved in Toluene after 1 hour at 70 degrees.

Figure 3 below shows the different types of solar PV recycling processes by [1].

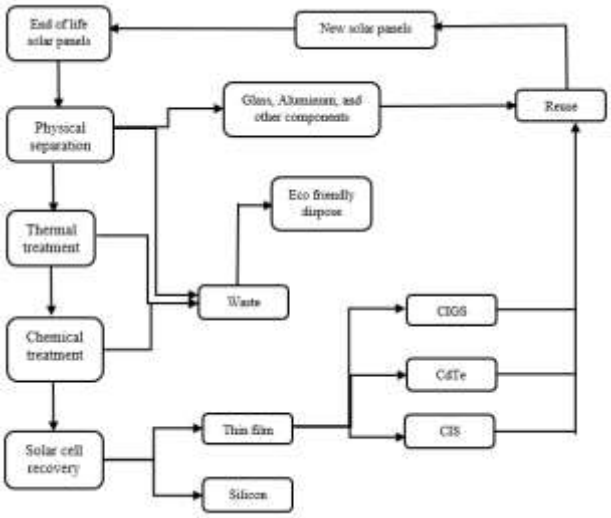

Figure 3. Different types of Solar PV recycling processes.Source: [1]

3.DIFFERENT COUNTRY DEVELOPMENTS/STATUS REGARDING PV RECYCLING

Different countries have initiated discussion and research about solar PV recycling. Most countries in Europe have adopted the EU Waste from Electrical and Electronic Equipment (WEEE)'s directives, which is an important first step towards their engagement in PV recycling. The EU rules on WEEE aim at treating electrical and electronic waste while contributing to sustainable development. In 2012, EU WEEE's directives pioneered the PV electric waste regulations including targets for end-of-life PV collection, recovery, and recycling. The cost is expected to be financed by all producers supplying PV panels to Europe [1, 5, 7]. Some other countries like Japan and the US have undergoing research regarding solar PV recycling. Developing countries are still lagging and are yet to initiate discussions regarding solar PV recycling. Table I below shows the developments/engagement of various countries in Solar PV recycling.

Table 1. The engagements of different countries in Solar PV recycling.

Country	Status on PV recycling
UK	- First European country to adopt EU Waste from Electrical and Electronic Equipment (WEEE) directives that relate to disposal and recycling of solar PV in the UK [1][5].
USA	- The state of California Department of Toxic Substances Control (DTSC) offered to take responsibility for solar waste treatment [1]. - First Solar, a USA-based solar panel manufacturing company has established factories in the United States, Germany, and Malaysia, and employs recycling methods with recovery rates of 95% for Cd and 90% for glass [1,4,6,8]. - Washington state passed a senate bill that modifies state renewable energy system tax incentives to include take back and recycling programs for end-of-life PV. The senate bill also urges PV module producers who want to sell their products to provide recycling plans for their products by January 1, 2021. - In North Carolina, PV modules are subjected to Toxicity Characteristics Leaching Procedure (TCLP) test before disposal for appropriate waste management. PV waste is treated as hazardous waste if indicated by the waste generator to be hazardous. Otherwise, they are treated as Universal waste. Rules making must be done to add PV modules as Universal waste [19]
Germany	- Second country to adopt the EU WEEE's directives [1]. - Also, a German based company called Solar World recycles crystalline PV panels. - A branch of First Solar in Frankfurt an der Oder, Germany recycles PV panels.
Czech Republic	- Entered a joined venture with EU for the recovery and recycling of End-of-Life (EoL) PV panels [1].
Italy	- A Legislative Decree No. 49 of 14 March 2014 was passed, that implements the Directive on WEEE (Directive 2012/19/EU) [1,5].
South Korea.	- Has adopted and initiated the discussion on PV waste. The industrial wastes in Annex Table 4 of Article 4.2 of South Korea's Enforcement Rule of Wastes Control Act (Act No. 14783) includes PV panels [1].
Japan	- The Japanese environment ministry and solar panel manufacturers participate with local companies in research on recycling technology [1]. - NPC.Int, a solar panel and equipment manufacturer, has entered a joint venture with Hamada (an industrial waste-processing company), to recycle solar panels.
Switzerland	- SENS and SWISCO RECYCLING, major recycling industries in Switzerland (recycling ovens, washing machines, fridges, etc.) adhered to the WEEE directives in 2014 [5].
Korea	- There are existing funded research projects on PV recycling. Also, other projects in non-R&D exist for the formation of a PV recycling center [5].

4.PV RECYCLING STRATEGIES

Crystalline solar cells

Crystalline solar cells are known as the first generation of solar cells, and are those cells manufactured using silicon. They are one of the oldest solar cells technologies and equally the most common ones with a greater share of the solar PV market. There are different methods used to recycle crystalline solar cells. Some of these methods are used commercially in some companies while others are research based. Table II (in the appendix section) gives a summary of some of the existing recycling methods for crystalline solar cells.

Thin film

These solar panels are known as the second generation of solar panels and are made by depositing thin films of semiconductor material on glass. Depending on the semiconductor used, there are different types of thin films solar panels such as amorphous, Cadmium Tellurium and Copper Gallium Indium Diselenide. Materials for thin film production using Cadmium Tellurium and Copper Indium Disulphide/ Diselenide are on increasing demand [2]. In addition, Indium and Tellurium are scarce materials whose prices continue to increase. As a result, recycling end of life thin film solar panels helps to recover these elements, which can be used to produce new panels. Table III (in the appendix section) summarizes some of the existing thin film recycling technologies.

Organic solar cells

Organic solar cells are known as the third generation of solar cells technology. In this type of solar cell, the absorbing layer is based on organic semiconductors. It used carbon-based materials and organic electronics, rather than silicon as used in crystalline solar PV. They are sometimes referred to as "plastic" or "polymer" solar cells. Organic solar cells are more flexible and cheaper than the conventional crystalline solar PV, though their efficiency is still low. Due to their flexibility, they are an appropriate option for integrated building PV.

Even though it's a new technology and research is still ongoing to improve its efficiency and lifetime, some recycling technologies already exist. Y. Zhou et al.,[17] reported a study in which they recycled organic solar cells fabricated on Cellulose Nanocrystal substrate (CNC). They separated and recycled the solar cell components using low energy processes at room temperature. The CNC substrate was observed to disintegrate completely within 30 minutes after they were immersed in distilled water, leaving solid residues which were separated by a filter paper. The photoactive layers were then separated from the electrodes (made with Ag and Molybdenum oxide (MoO_3)) by rinsing the solid residues in chlorobenzene on filter paper.

In another study, [18] recovered silver (Ag) from roll to roll processed organic solar cells. In their study, the organic solar cells were incinerated (combusted in heat) at 800 to 1000 degrees Celsius and later treated with diluted nitric acid. They realized a complete and high silver (Ag) recovery from the ashes of about 101.3 +- 3.8%. From the recycling methods above, it can be deduced that the final material of interest determines the recycling process used.

Gallium Arsenide (GaAs)

GaAs solar cells are a type of direct bandgap crystalline PV material based solar cells with a band gap of 1.42 eV at room temperature. With studies indicating efficiencies up to 28.8% on single junction cells [20] and efficiencies reaching up to 42.3% on triple junction cells [21], GaAs based PV technology is one of the most efficient in the current market. GaAs solar cells are mostly used in outer space power generation and concentrated PV power generation due to its high resistance to radiation damage and insensitiveness to overheating [22]. The global availability of gallium is moderate, being not naturally existing in its purest state, gallium is often found in combined form with Aluminum and Zinc [23]. Almost 85% of GaAs is wasted as scrap during production [23]. With the increase in demand for gallium due to its applications in semiconductor industry, the need for recycling strategies has increased in the past years.

Materials like glass, gallium and other useful organic components can be successfully recycled from solar cells by using methods like nitrogen pyrolysis and vacuum decomposition. Manual separation of cathode, anode and the anti-reflective layer is also still being widely practiced now. An experiment conducted by Shanghai Key Lab assessing the feasibility of recycling gallium and Arsenic from e-wastes using pyrolysis and vacuum metallurgy shows a stable gallium and arsenic recovery rate at 1273 K [24]. Other processes of recycling such as sulfurizing thermal treatment, leaching-selective precipitation and vacuum thermal reduction are also being researched on [25, 26, 27]. Vacuum metallurgy separation of solid gallium under optimized experimental conditions provides a recovery efficiency of 93.48% [28]. A reliability analysis on III-V GaAs solar cells grown on recycled GaAs substrate shows degradation in performance due to uneven surface morphology affecting the cell's V_{oc} and fill factor. Even though considerably old methods like pyrolysis and vacuum decomposition are still being used the most for GaAs solar cell recycling, the development in new methods appear promising.

Perovskite

Perovskites are crystal materials that generally have a chemical formula of XYZ_3 where the first two (X and Y) are cations and Z being a bonding anion. Halide perovskites are showing great progress in research making it potentially the face of third generation solar cells of the future [29]. In the last two years, the progress made in perovskite solar technology is impressive with efficiencies reaching up to 25% in experimental conditions [30]. Being cost efficient, perovskites have the potential to compete with Si based technologies to become the most used PV technology in the future. Commercialization of perovskites is however going to inevitably increase the presence of toxic wastes such as lead. Thus, development in waste management and recycling technologies is crucial for perovskites to develop a commercial market.

A cost analysis study [31] analyzing the feasibility of recycling toxic lead and other valuable conductor materials shows impressive results. Out of the total material cost of perovskite module which was $\$24.8/m^2$, the value of recycled materials was $\$12/m^2$ making the results considerably promising. Weakly acidic cation exchange resin was used to separate lead from the test module with a recycling efficiency of 99.2%. Another life cycle assessment study [32] of perovskite recycling strategies shows results of energy payback time reduction up to 72.6% and greenhouse gas emission factor reduction of 71.2%. Under a best-case recycling scenario, the energy payback time for a recycled perovskite module is 0.09 years and a greenhouse gas emission factor of 13.4 g CO_2/ kWh, which is lower than the respective values of silicon solar modules. Closed loop recycling and recrystallization using butylamine of perovskite solar cells is also an efficient recycling method with a recovery efficiency of 98.9%. A solar cell produced by recrystallization shows a similar performance as that of a fresh solar cell [33]. Common methods like stripping down layers of perovskite cells is also feasible as the collected materials can be reused with little or almost no reduction in performance. The PbI_2 which is recycled using this method can be recrystallized, and reused and has a power conversion efficiency of 13.5% [34]. With perovskite PV technology making fast progress, future developments in perovskite recycling are crucial to make the technology commercially viable.

Dye-sensitized solar cells (DSSC)

DSSC (dye-sensitized solar cell) is a solar cell type that is a type of thin-film solar cell. The typical components of a DSSC solar cell include these materials: two layers of glass, two layers of TCO (transparent conducting oxide), TiO_2 (anode), platinum (cathode) and an electrolyte (liquid conductor).

[35]. Since DSSC is a growing market N. Jamalullail, I. S. Mohamad, M. N. Norizan, N. A. Baharum, and N. Mahmed, “Short review: Natural pigments photosensitizer for dye-sensitized solar cell (DSSC),” *IEEE Student Conf. Res. Dev. Inspiring Technol. Humanit. SCOReD 2017 - Proc.*, vol. 2018-January, pp. 344–349, Feb. 2018, doi: 10.1109/SCORED.2017.8305367.

[36] and is expected to at least double in revenues by 2030, the amount of DSSC solar that will need to be recycled in the future decades will increase substantially in 10-20 years from now (2023). Recycling DSSC solar cells is a complicated task due to the thin film and compact nature of the cells.

The first step in lowering the amounts of raw materials required in the DSSC lifecycle is on reducing the raw materials used through building DSSC with recycled materials. Extending the lifetime of a solar cell is also being researched.

[38] Methods of reducing the environmental impact of DSSC’s include lowering the amount of rate and toxic materials in the solar cells (i.e., ruthenium, cobalt, silver, and platinum). However, the negatives of using other options are lower power conversion efficiencies and/or lower cell lifetime.

Recovering TiO_2 glass from old decommissioned DSSC solar cells is an option that is available to recycle a valuable and rare component which can be reused for new cells. The recycled TiO_2 can be gathered from Perovskite cells and reapplied with $CsPbIBr_2$ and carbon layers.

All these methods to recycle DSSC solar cells require more research and development, as alternative materials to be used which can be more easily recycled than conventional DSSC materials are not yet commercially available or efficient enough.

[39] Mechanical processing and separation of the components is expensive, especially if there is a module frame involved. Crushing DSSC’s can be done which is a mechanical process involved in making it easier to separate the components. Pyrometallurgical processes could be an alternative approach to the shredding and crushing method, however it is difficult to extract more than one type of metal easily through this process.

Figure 4. Diagram Flow Chart of Recycling[39

5.SUMMARY OF END-OF-LIFE PV RECYCLING STATREGIES

Table 4. A summary of end-of-life PV recycling technologies

Technology	**Methods used**	**Status**	**Module type**
Delamination	Physical disintegration [3, 9,10,15]	Research/commercial	C-Si /Thin film
	Thermal [3,9,10,15]	Research	C-Si
	Milling/ shredding [3,15]	Commercial	Thin film
Material separation	Manually [3,9]	commercial	C-Si
	Classifier [3]	Commercial	Thin film
	Sieving [9,10]	Research	C-Si
	Mechanical milling [9]	Research	C-Si
	Vibrating screen [16]	Commercial	Thin film
	Etching [3]	Research/Commercial	C-Si
	Precipitation [3,16]	commercial	Thin/film
	Leaching [3]	Research/Commercial	C-Si
	Mechanical attrition [15]	Research	Thin film
	Floatation [9]	Research	Thin film
	Vacuum blasting [9,16]	Research	Thin film
	Electrowinning [15]	Research	C-Si
	Chemical solutions (organic solvents, acids, chlorine etc.) [3, 9,10,15]	Research	C-Si
	Filtration [4]	Research	Thin film
Purification	Acidic oxidation [16]	Research	Thin film
	Precipitation [16]	Research	Thin film
	Hydrometallurgical process [9]	Research	C-Si

6.CONCLUSION

Solar PV recycling is an evolving field that requires further research. This will reduce waste, and CO_2 emissions, while contributing to a sustainable environment. This review gives an overview of PV recycling activities by country and elaborates the different recycling strategies for different end of life solar cells. Some of the challenges discovered during this review are, given the continuous variation in PV panel composition introduced in the different manufacturing technologies, the existing Solar PV recycling strategies are known to be complex. In addition, some proposed recycling methods are not economically viable, while some use materials which might be

dangerous. Energy is required for recycling, and the collection networks of the end-of-life PV panels are not efficient. Furthermore, there is a need for policies to encourage producer responsibilities. While a few countries have initiated the discussions and are working towards PV recycling, most developing countries are yet to initialize such discussions. While recycling strategies for recent solar technologies like organic solar and perovskites are still under research, there already exist recycling strategies for crystalline solar and thin film technologies at the commercial level. It is expected that the research for efficient PV recycling strategies will accelerate as the PV industry grows and as many more organizations and government are working towards a sustainable future.

References

[1] M. S. Chowdhury et al., "An overview of solar photovoltaic panels' end-of-life material recycling," Energy Strateg. Rev., vol. 27, p. 100431, 2020, doi: 10.1016/j.esr.2019.100431.

[2] W. Berger, F. G. Simon, K. Weimann, and E. A. Alsema, "A novel approach for the recycling of thin film photovoltaic modules," Resour. Conserv. Recycl., vol. 54, no. 10, pp. 711–718, 2010, doi: 10.1016/j.resconrec.2009.12.001.

[3] J. Tao and S. Yu, "Review on feasible recycling pathways and technologies of solar photovoltaic modules," Sol. Energy Mater. Sol. Cells, vol. 141, pp. 108–124, 2015, doi: 10.1016/j.solmat.2015.05.005.

[4] A. Wade, V. W. Gmbh, G. Heath, K. Wambach, P. Sinha, and F. Solar, IRENA andIEA PVPS (2016) - End-of-Life Management : Solar Photovoltaic Panels, no. June. 2016.

[5] A. Sharma, S. Pandey, and M. Kolhe, "Global review of policies & guidelines for recycling of solar pv modules," Int. J. Smart Grid Clean Energy, vol. 8, no. 5, pp. 597–610, 2019, doi: 10.12720/sgce.8.5.597-610.

[6] N. Rathore and N. L. Panwar, "Strategic overview of management of future solar photovoltaic panel waste generation in the Indian context," Waste Manag. Res., vol. 40, no. 5, pp. 504–518, 2022, doi: 10.1177/0734242X211003977.

[7] I. D'Adamo, M. Miliacca, and P. Rosa, "Economic Feasibility for Recycling of Waste Crystalline Silicon Photovoltaic Modules," Int. J. Photoenergy, vol. 2017, pp. 1–6, 2017, doi: 10.1155/2017/4184676.

[8] "Leading global provider of comprehensive PV solar solutions | First Solar." https://www.firstsolar.com/ (accessed Feb. 05, 2023).

[9] F. Pagnanelli et al., "Physical and chemical treatment of end of life panels: An integrated automatic approach viable for different photovoltaic technologies," Waste Manag., vol. 59, pp. 422–431, 2017, doi: 10.1016/j.wasman.2016.11.011.

[10] J. Shin, J. Park, and N. Park, "A method to recycle silicon wafer from end-of-life photovoltaic module and solar panels by using recycled silicon wafers," Sol. Energy Mater. Sol. Cells, vol. 162, no. December 2016, pp. 1–6, 2017, doi: 10.1016/j.solmat.2016.12.038.

[11] T. Doi, I. Tsuda, H. Unagida, A. Murata, K. Sakuta, and K. Kurokawa, "Experimental study on PV module recycling with organic solvent method," Sol. Energy Mater. Sol. Cells, vol. 67, no. 1–4, pp. 397–403, 2001, doi: 10.1016/S0927-0248(00)00308-1.

[12] W. Wang and V. Fthenakis, "Kinetics study on separation of cadmium from tellurium in acidic solution media using ion-exchange resins," J. Hazard. Mater., vol. 125, no. 1–3, pp. 80–88, 2005, doi: 10.1016/j.jhazmat.2005.02.013.

[13] Y. Kim and J. Lee, "Dissolution of ethylene vinyl acetate in crystalline silicon PV modules using ultrasonic irradiation and organic solvent," Sol. Energy Mater. Sol. Cells, vol. 98, no. x, pp. 317–322, 2012, doi: 10.1016/j.solmat.2011.11.022.

[14] W. H. Huang, W. J. Shin, L. Wang, W. C. Sun, and M. Tao, "Strategy and technology to recycle wafer-silicon solar modules," Sol. Energy, vol. 144, pp. 22–31, 2017, doi: 10.1016/j.solener.2017.01.001.

[15] M. Held, "Life cycle assessment of CdTe module recycling," Eur. Photovolt. Sol. Energy Conf., no. September, pp. 21–25, 2009.

[16] V. Fiandra, L. Sannino, C. Andreozzi, F. Corcelli, and G. Graditi, "Silicon photovoltaic modules at end-of-life: Removal of polymeric layers and separation of materials," Waste Manag., vol. 87, pp. 97–107, 2019, doi: 10.1016/j.wasman.2019.02.004.

[17] Y. Zhou et al., "Recyclable organic solar cells on cellulose nanocrystal substrates," 2013. doi: 10.1038/srep01536.

[18] R. R. Søndergaard, Y. S. Zimmermann, N. Espinosa, M. Lenz, and F. Krebs, "Incineration of organic solar cells: Efficient end of life management by quantitative silver recovery," Energy Environ. Sci., vol. 9, no. 3, pp. 857–861, 2016, doi: 10.1039/c6ee00021e.

[19] C. G. Assembly, "Final Report on the Activities Conducted to Establish a Regulatory Program for the Management and Decommissioning of Renewable Energy Equipment," 2021.

[20] Deshpande, Rashmi A. "Advances in Solar Cell Technology: An Overview." J. Sci. Res 65.02 (2021): 72-75.

[21] Li, Sheng S. Semiconductor physical electronics. Springer Science & Business Media, 2012.

[22] T. Takamoto, H. Washio and H. Juso, "Application of InGaP/GaAs/InGaAs triple junction solar cells to space use and concentrator photovoltaic," 2014 IEEE 40th Photovoltaic Specialist Conference (PVSC), Denver, CO, USA, 2014, pp. 0001-0005, doi: 10.1109/PVSC.2014.6924936.

[23] Dehnavi, Pouya Yarahmadi. "Global cycle of gallium production, use and potential recycling." L. Water Resour. Eng(2013).

[24] Zhan, L., Xia, F., Xia, Y., & Xie, B. (2018). Recycle gallium and arsenic from gaas-based E-wastes via pyrolysis–vacuum metallurgy separation: theory and feasibility. ACS Sustainable Chemistry & Engineering, 6(1), 1336-1342.Zhan, Lu, et

al. "Recycling arsenic from gallium arsenide scraps through sulfurizing thermal treatment." ACS Sustainable Chemistry & Engineering 5.4 (2017): 3179-3185.
[25] Ji, W., Xie, K., Yan, S., Huang, H., & Chen, H. (2020). "A new method of recycling gallium from yellow phosphorus flue dust by vacuum thermal reduction process". Journal of Hazardous Materials, 400, 123234.
[26] Hu, Shao-Hua, et al. "Resource recycling of gallium arsenide scrap using leaching-selective precipitation." Environmental Progress & Sustainable Energy 34.2 (2015): 471-475.
[27] Zhan, Lu, et al. "Novel recycle technology for recovering rare metals (Ga, In) from waste light-emitting diodes." Journal of Hazardous Materials 299 (2015): 388-394.
[28] Horng, Ray-Hua, Ming-Chun Tseng, and Shui-Yang Lien. "Reliability analysis of III-V solar cells grown on recycled GaAs substrates and an electroplated nickel substrate." International Journal of Photoenergy 2013 (2013).
[29] Liu, F. W., Biesold, G., Zhang, M., Lawless, R., Correa-Baena, J. P., Chueh, Y. L., & Lin, Z. (2021). Recycling and recovery of perovskite solar cells. Materials Today, 43, 185-197.
[30] Zhang, Zhihao, Lu Qiao, Ke Meng, Run Long, Gang Chen, and Peng Gao. "Rationalization of passivation strategies toward high-performance perovskite solar cells." Chemical Society Reviews (2023).
[31] Chen, Bo, Chengbin Fei, Shangshang Chen, Hangyu Gu, Xun Xiao, and Jinsong Huang. "Recycling lead and transparent conductors from perovskite solar modules." Nature communications 12, no. 1 (2021): 5859.
[32] Tian, X., Stranks, S. D., & You, F. (2021). Life cycle assessment of recycling strategies for perovskite photovoltaic modules. Nature Sustainability, 4(9), 821-829.
[33] Feng, X., Guo, Q., Xiu, J., Ying, Z., Ng, K. W., Huang, L., ... & He, Z. (2021). Close-loop recycling of perovskite solar cells through dissolution-recrystallization of perovskite by butylamine. Cell Reports Physical Science, 2(2), 100341.
[34] Binek, A., Petrus, M. L., Huber, N., Bristow, H., Hu, Y., Bein, T., & Docampo, P. (2016). Recycling perovskite solar cells to avoid lead waste. ACS applied materials & interfaces, 8(20), 12881-12886.
[35] N. Jamalullail, I. S. Mohamad, M. N. Norizan, N. A. Baharum, and N. Mahmed, "Short review: Natural pigments photosensitizer for dye-sensitized solar cell (DSSC)," IEEE Student Conf. Res. Dev. Inspiring Technol. Humanit. SCOReD 2017 - Proc., vol. 2018-January, pp. 344–349, Feb. 2018, doi: 10.1109/SCORED.2017.8305367.
[36] "Dye Sensitized Solar Cell Market is Anticipated to Grow US$ 244.8 Million By 2030 | AltEnergyMag." https://www.altenergymag.com/content.php?post=38323 (accessed Feb. 11, 2023).
[37] N. Jamalullail, I. S. Mohamad, M. N. Norizan, N. A. Baharum, and N. Mahmed, "Short review: Natural pigments photosensitizer for dye-sensitized solar cell (DSSC)," IEEE Student Conf. Res. Dev. Inspiring Technol. Humanit. SCOReD 2017 - Proc., vol. 2018-Janua, no. July 2019, pp. 344–349, 2018, doi: 10.1109/SCORED.2017.8305367.
[38] D. Wei, "Dye sensitized solar cells," Int. J. Mol. Sci., vol. 11, no. 3, pp. 1103–1113, 2010, doi: 10.3390/ijms11031103.
[39] K. Miettunen and A. Santasalo-Aarnio, "Eco-design for dye solar cells: From hazardous waste to profitable recovery," J. Clean. Prod., vol. 320, no. April, p. 128743, 2021, doi: 10.1016/j.jclepro.2021.128743.

APPENDIX

1.

Table 2. A review of Crystalline solar PV recycling

Company/ Researcher	Technology/processes	Solutions/ methods	Output/Results	Process efficiency	Advantage(s)	Disadvantage(s)	Reference(s)
Huang et al., 2017)	- Mechanical /Physical -Thermal (furnace heating) -Chemical (leaching, electrowinning)	-Leaching solution: HNO_3 -Etching solutions: (HF) and (NaOH)	-Thermal process: glass from cells -Leaching: Ag, Pb, Cu and Sn - Electrowinning: separates each metal from the others (Ag, Pb, Cu, Sn) -(HF): SiN_x layer and Al back electrode - (NaOH): emitters and back-surface field	-N/A	-waste handing is efficient -Full elimination of EVA -Process is Simple and effective -Recovery of high purity materials.	-Solar cells can be damaged -Other materials mix with EVA -Consumes High energy -Dangerous emissions	[14]
Solar World	-Thermal decomposition -Manual Material separation -Chemical (etching)	-Heating at 600 degrees	-Heating: solar cells, glass, metals -Etching on solar cells: wafers	-more than 90% of glass -95% of semiconductor materials (Si) -Up to 97% of intact wafer (4200 μm)	-High recovery rate of valuable materials -High purity of the recovered material -Possible direct reuse of wafers	-Thin wafer defects and degradation due to high temperature -Inefficient manual separation -Potential harmful emissions	[3]
Fiandra et al., 2019	-Manual material separation - Mechanical treatment -Thermal treatment	- Mechanical milling	-Mechanical milling: Flouropolymers, Tedlar material - Thermal: Silicon, glass, metals	-N/A	-Reduction in pollutants emission -Reduction in energy used	-N/A	[16]
Shin et al., 2017	-Chemical treatment	-Nitric acid -Potassium hydroxide - Phosphoric acid	- Nitric acid: Ag -Potassium hydroxide: Al -Phosphoric acid: wafer	-N/A	-N/A	-N/A	[10]
Pagnanelli et al., 2017	-Manual -Physical/ Thermal treatment -Chemical treatment	-Acid leaching	-Manual dismantling: Al frame -Acid leaching: metals (Al, Cu, Te, etc.) and glass	-91%	-N/A	-N/A	[9]
Doi et al., 2001	-Chemical	-Organic solvents	- Trichloroethylene: EVA	-N/A	-N/A	-Cracking of PV cells	[11]

2.

Table 3. A review of thin film solar PV recycling

Company/ Researcher	Technology/processes	Solutions used	Outputs/results	Process efficiency	Advantages	disadvantages	References
First solar	-Physical disintegration (shredding+ hammer milling) -Leaching -Solid-liquid separation -Vibrating screening -Precipitation	- leaching: Acid and hydrogen peroxide.	-Leaching, sold-liquid separation: Glass and laminate material -Screening: Glass from Laminate -Precipitation: metal rich liquid (Tellurium and Cadmium)	- 90% of glass -95% of semiconductor materials (Cd, Te) -More than 80% of Te of 99.7% purity	-Capable of mixed waste treatment -High recovery rate of glass and semiconductor materials -very automated process	-Breakage of solar cells -not possible to reuse -wafer reproduction required -High energy demand -Complicated process, Use of chemicals, Expensive equipment	[14]
ANTEC Solar GmbH	-Physical Disintegration -Pyrolysis treatment -Dry etching -Precipitation	-Oxygen at 300 degrees - Etching: Chlorine and atmospheric gas at 400 degrees	- Oxygen at 300 degrees: EVA -Etching: $CdCl_2$ and $TeCl_4$	-N/A	-Capable of mixed waste treatment -High recovery rate of glass and semiconductor material -Less use of chemicals -less complicated process	-High energy demand -Breakage of solar cells, not possible to reuse -Wafer reproduction required -High effort required for purification	[3]
Held, 2009	-Physical disintegration (shredding+ hammer milling) -Leaching -Solid-liquid separation -Precipitation	-Leaching solution: Sulphuric acid, Hydrogen peroxide	-After leaching: Glass separated from solution -Solution precipitated and filtered. Metals can then be obtained	-N/A	-N/A	-N/A	[15]
The EU-LIFE project RESOLVED (Recovery of Solar Valuable materials, Enrichment and Decontamination), coordinated by the Federal Institute for Materials, Research and Testing [2]	**Broken modules:** -Crushing/ milling -wet mechanical attrition -wet mechanical floatation -chemical treatment	-acidic oxidizing solution	- wet mechanical attrition process: semiconductor layers are separated. -Floatation: CdTe and CIGS products -acid oxidizing solution: Cd and Te	-99.99%	-Requires less amount of chemicals	-N/A	[2]
	End-of-life modules: -Crushing -Thermal dismantling (furnace at 500 degrees Celsius) -Vacuum blasting		-Furnace: EVA destroyed -Vacuum blasting: semiconductor materials				

RIGA 2023

Using FMEA Technique to Improve Steam Boiler Energy Efficiency

Ceyda Kocabaş
Bilecik Şeyh Edebali University, Bilecik, Türkiye, ceyda.pak@bilecik.edu.tr, ORCID: 0000-0001-8459-1650

Ahmet Fevzi Savaş
Bilecik Şeyh Edebali University, Bilecik, Türkiye, ahmetfevzi.savas@bilecik.edu.tr, ORCID: 0000-0001-8376-9234

Cite this paper as: *Kocabaş, C, Şavaş, AF. Using FMEA Technique to Improve Steam Boiler Energy Efficiency. 11. Eur. Conf. Ren. Energy Sys. 18-20 May 2023, Riga, Latvia*

Abstract: The steam boiler used in the distillation process in a company was investigated. The heat losses that occur during the production, distribution, and re-transmission processes are discussed in detail. The FMEA (Failure Modes and Effects Analysis) technique which is one of the quality improvement tools, was used to reduce losses and increase boiler system efficiency. By determining the risks that cause energy losses, various improvement suggestions are presented taking into account today's technological possibilities. The PRN (Risk Priority Number) scores before and after the implementation of the improvements are calculated and shown in the FMEA table. The mass and energy flow diagrams of the steam boiler system for the current situation and after the implementation of the recommendations are presented. When the proposed systems are implemented, energy losses will decrease. Also, water savings of around 21% will be realized, and the net steam production capacity sent to the process will increase by 9.2%. It is thought that this study will set an example for other industrial organizations that use industrial boilers.

Keywords: *Steam Boiler, Boiler Heat Losses, FMEA, Energy Efficiency*

1. INTRODUCTION

Energy should be used as effectively as possible to protect natural resources. It is estimated that natural gas reserves have a life span of 60 years, oil reserves 47, and coal reserves approximately 119 years in the world [1]. Energy resources should also be used efficiently in industrial organizations. For this purpose, the amount of energy consumed at all stages of production should be reduced. The steam system takes its first place in energy recovery studies. Steam has been one of the greatest forces in the service of humanity for nearly 250 years. The main reasons for the widespread use of water vapor until today are as follows [2]:

- Steam has the highest amount of energy that can be transferred per unit mass (in the form of latent heat).
- Steam flows inside the system without assistance from external energy sources such as pumps. Thus, the electrical energy consumed by the electric motors driving these machines is saved.
- The system temperature can be controlled very precisely by changing the steam pressure going to the end uses.

Boiler systems are widely used in industries and power plants to produce steam [3]. Steam boilers are devices that produce steam at the desired pressure, temperature, and amount. For this, the heat energy obtained in any way is given to the water in a closed container and evaporated. The thermal energy of the steam is used in steam turbines, steam engines, and processes like heating, drying, sterilization, cooking, etc. While a few kilograms of steam per hour can be produced in processes such as laundry and dyeing, steam production capacities of hundreds of tons per hour can be reached in thermal power plants. The pressure of the steam produced can exceed 370 bar and 650 ºC [4].

Significant energy savings can be achieved by optimizing the operation of steam boilers. For this purpose, it is necessary to identify the main sources of energy losses and to recover the wasted energy [5]. In this study, the steam boiler system is considered holistically. The FMEA technique is used to evaluate the energy loss during the steam production process. The risks that may lead to energy loss throughout the process flow have been examined. These risks were shown by preparing the Energy FMEA table. The effects of the failures on production and energy efficiency were investigated. Possibilities of the occurrence of risks and measures to prevent them are presented. RPN (Risk Priority Numbers) for each risk has been determined. Those with an RPN score below 40 falls into the insignificant risk category and are shown in green. Those between 40 and 100 are shown in yellow, and those over 100 are shown in red. Red areas with high RPN scores are priority areas for starting improvement work. For high-priority energy risks, improvement suggestions have been made following today's technological possibilities. The RPN scores are recalculated and shown in the FMEA table [6].

There are many studies on energy management in steam boilers so far. Some of them are as follows: Özer (2004) explained the energy recovery applications in a steam boiler used in a factory [4]. Karakurt (2006) examined the steam boiler in a leather processing factory and compared the current state of the factory with the new state where energy-saving methods were applied. He stated that 14.5% of energy savings can be achieved [7]. Çınar (2008) selected six textile factories operating in the textile sector. He listed the findings regarding the energy savings detected in their boiler rooms [8]. Ünlü (2009) examined the energy-saving studies in the industry and explained the losses that occur during the generation, distribution, and consumption of energy in boiler systems [9]. Kanoğlu (2010) presented some important energy-saving methods for industrial facilities [10]. Ostrowski et al. (2020) found that energy losses decreased from 15.33% to 0.98% by modernizing a steam boiler room [11]. Dhanre et al. (2014) prepared a review on energy auditing in boilers used in thermal power plants [12]. Saidur et al. (2010) analyzed the energy flow in a boiler. They stated that there are various methods to reduce the energy use of boilers (5).

2. METHODOLOGY

Failure Mode Effects Analysis (FMEA)

FMEA is a failure prevention tool that, can be used to improve production quality by reducing failures. In cases where it is difficult to obtain data, this method, which incorporates team experience, can also be used to improve the existing system. In this method, the risk priority coefficients of all failures are calculated, and then the necessary precautions are determined for all risks, starting from the potential failure with the highest risk priority coefficient. After the implementation of the measures taken, the risk priority coefficients are recalculated. FMEA study can also be used as a tool for improvements in the field of energy. Detailed information on the use of the FMEA technique can be found in previous studies [6,13]

Steam Boiler Heat Losses

The steam generated in the boiler is transported to the places of use. After the steam is used in the process, it condenses and completes its cycle by sending it back to the boiler. Naturally, as soon as the steam leaves the boiler, it will start losing its heat. Condensate water should be collected appropriately from the processes and sent to the boiler with minimum losses. The losses that occur during the production, distribution, and consumption of steam are shown in Figure 1 [7,9]. By performing the operations in this cycle efficiently, the total efficiency of the system increases. It is possible to minimize these energy losses in the boiler system with the measures to be taken. A highly efficient steam boiler operation can be achieved with the necessary heat recovery devices and modern automation systems [14].

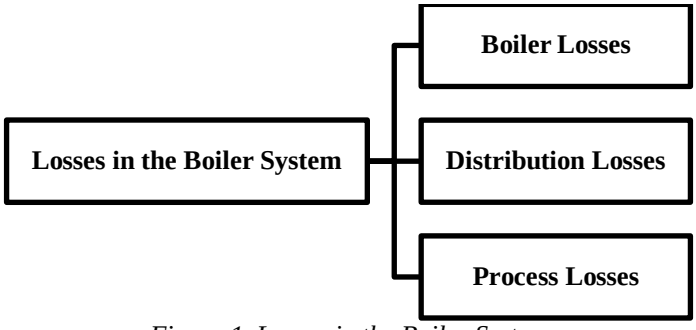

Figure 1. Losses in the Boiler System

Reducing Heat Losses of Steam Boiler System

Doğuş Faux Leather Factory, which has been operating in the textile industry since 1991, was chosen to analyze the heat losses in a boiler system in detail. The facility has a steam boiler with a steam capacity of 5000 kg/h producing steam at 10 bar operating pressure. The boiler is operated for an average of 5760 hours per year in the distillation process of coagulation production.

Currently Boiler System Mass and Energy Balance

The steam boiler in the facility produces 5000 kg/h of steam at a full load. However, some of the total steam produced is used for deaerator heating. Net steam production is 4540 kg/h. Currently, the mass and energy flow diagram in the deaerator is given in Figure 2 [6].

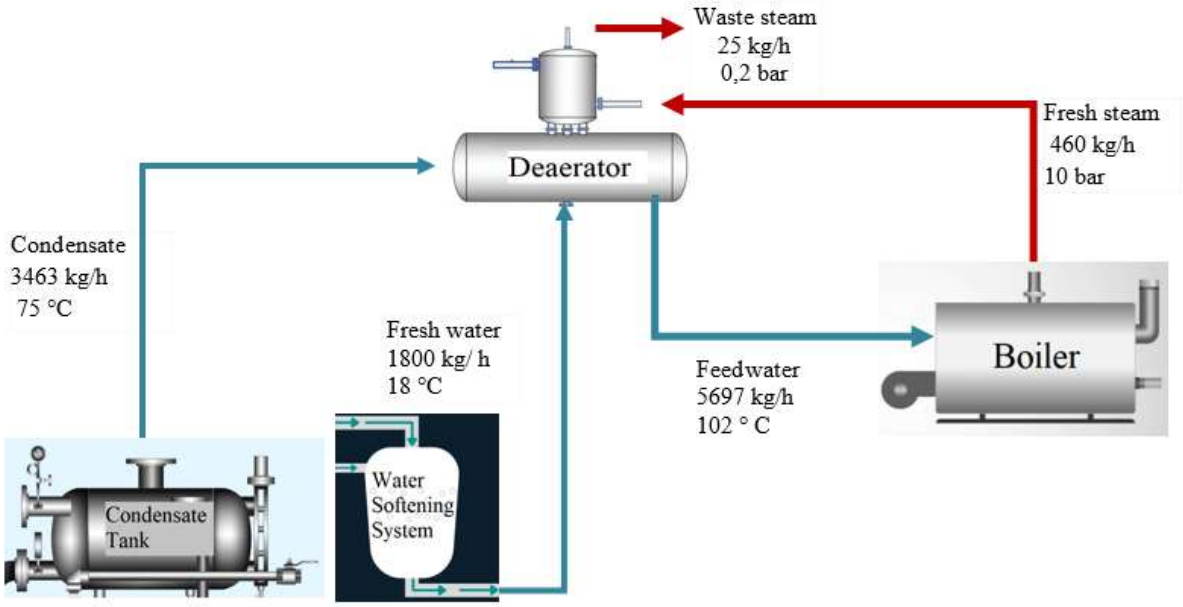

Figure 2. Mass and Energy Flow Diagram for the Current Situation

Energy FMEA Study After Improvements

FMEA study was conducted to assess the risks leading to energy loss in the steam boiler system. Improvement suggestions have been developed for risks with an RPN score above 100. After the proposed improvements, the new RPN scores are recalculated and given in Table 1. In this way, there is no risk in the red-risk group [6].

Boiler System After Improvements

Table 1. Boiler System After Improvements Energy FMEA Study

	Energy Failure Mode and Effects Analysis (FMEA)												
Process	**Potential Failure mode for Energy**	**Potential Failure Causes**	**Potential Failure Effects**	**Precaution, Current controls**	**Severity**	**Occurrence**	**Detection**	**RPN**	**Suggestion for Improvement**	**Severity**	**Occurrence**	**Detection**	**RPN (After improvements)**
Steam Production	High flue gas temperature	Excessive excess air	The excess air coefficient increases	Temperature control with indicators and flue gas analyzes performed every 6 months	8	4	4	128	Fuel/air ratio controlled O_2 Trim control system should be installed	8	2	1	16
		Boiler overload	A lot of energy is thrown into the atmosphere from the chimney										
	Lack of excess air , λ<1	Improper O_2/fuel ratio	The energy produced decreases	Flue gas analysis every 6 months	7	3	6	126	Fuel/air ratio controlled O_2 Trim control system should be installed, condensing economizer should be added to the system	7	2	1	14
		Low chimney draft											
	Too much excess air, λ>1	Improper O_2/fuel ratio	The air that does not participate in the combustion is heated in the furnace and expelled from the chimney		7	4	6	168		7	2	1	14
		Insufficient fuel supply											
		Excessive chimney draft											
	Formation of water vapor in the flue gas	Emission of water vapor as a result of combustion	It causes some of the useful energy in the boiler to be discharged from the chimney in the form of water vapor	-	8	5	4	**160**	Condensing economizer should be included in the system	8	1	4	32
	Surface heat loss	Temperature difference	The amount of heat transferred to the fluid and the boiler efficiency decrease	Increase in boiler outer surface temperature, surface being hot	6	5	4	120	Insulation jacket, tracking with thermal camera	6	2	2	24
	Performing more blowdown than it is necessary	Improper blowdown setting, high conductivity of feedwater	Over-blowdown leads to high energy losses. Fuel and chemical consumption increase	An automatic blowdown system is available. Water softening system is used. Some of the heat has been recovering by a heat exchanger.	8	5	4	160	Reverse Osmosis, Heat recovery with flash steam	8	1	4	32
	Loss of energy in the deaerator due to waste steam	Loss of steam with corrosive gases separated from the feed water	Boiler efficiency decreases, energy loss occurs	-	6	4	5	120	Recovery of waste heat using a heat exchanger	6	1	5	**30**
	Energy loss due to the use of fresh steam in the deaerator	Using the fresh steam produced in the system to separate the gases from the feedwater	Kazan verimi düşer	-	7	6	5	210	Use of flash steam from condensate instead of fresh steam	7	1	5	**35**
	Flash steam loss from the condensate tank	Flash steam formation by removing the pressure on the condensate at the point where it is discharged into the tank	The flash steam escapes from the air pipe of the condensate tank. 5- 15% of the condensate is lost	Visible	4	5	6	120	Flash steam unit usage	4	1	6	24
	Heat loss in Valves and Flanges	Leaving the valves uninsulated	Heat losses occur	-	6	6	4	144	Valve jacket, Thermal camera application	6	2	3	36

Boiler System After Improvements

The new view of the system after the implementation of the recommendations is shown in Figure 3. By the flash steam system and heat exchanger placed at the blowdown outlet, the fresh feed water temperature can be increased

from 18 °C to 20 °C first. When the condensing economizer is included in the system, the recovered heat can be used for second-stage heating of the fresh feed water. Thus, the feed water temperature can be increased from 20 °C to 90 °C. Third-stage heating of fresh feed water entering the system can be realized by placing a copper tube heat exchanger at the deaerator outlet, which is another improvement suggestion. According to the energy balance, the temperature of the fresh water can be increased from 90 °C to 97 °C. After the implementation of the Reverse Osmosis system, the new boiler feed water flow rate will be 5100 kg/h instead of 5697 kg/h. Since the flash steam of the condensate is used, the steam that needs to be sent to the deaerator will be met with flash steam instead of fresh steam. By using the mass and energy balances, the amount of steam to be sent to the deaerator was calculated as 210 kg/h. The amount of flash steam obtained from the condensate is 401 kg/h and all the steam needed by the deaerator can be provided from the flash steam. While the net steam production was 4540 kg/h in the previous case, it will be 5000 kg/h in the new case. In addition, the need for fresh feed water will be reduced from 1800 kg/h to 1418 kg/h, thus saving 382 kg/h of water. Detailed information can be reached in the previous study [6]. The mass and energy flow amounts in the new state are shown in Figure 3.

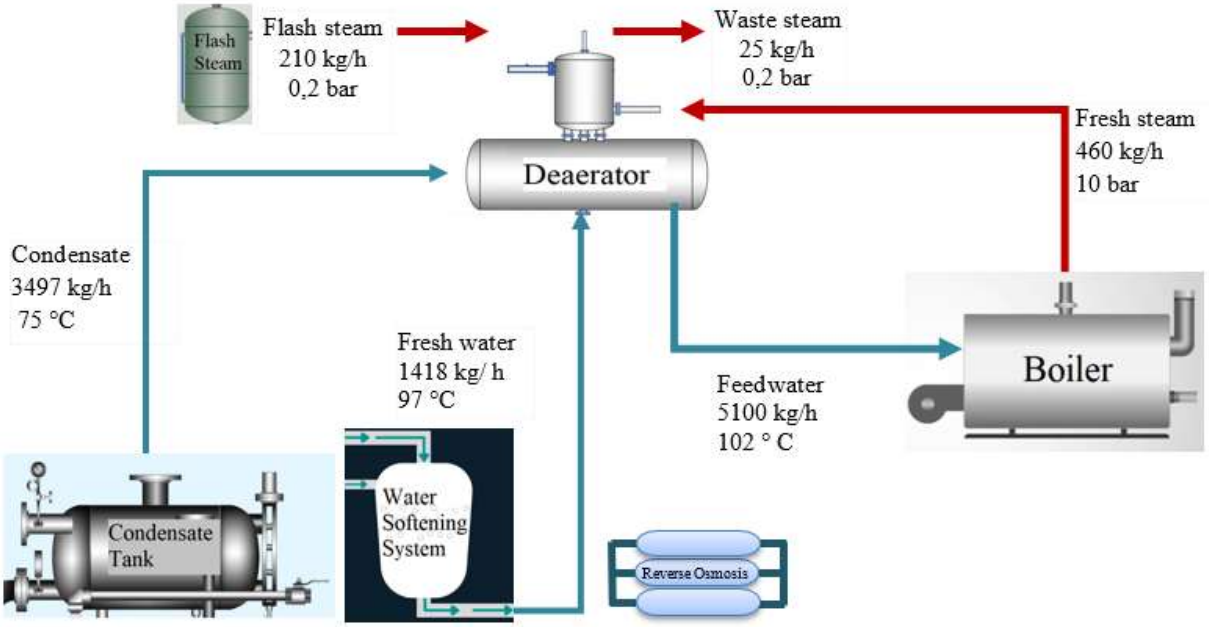

Figure 3. Mass and energy flow diagram in new condition

3. RESULTS AND DISCUSSIONS

Fossil fuels are rapidly depleting, and greenhouse gas emissions threaten our future. A significant part of the world's energy consumption is used in boilers. For this reason, it is of great importance to reduce energy consumptions by minimizing losses. A minor improvement in boiler efficiency will help save large amounts of fossil fuels and reduce environmental pollution. Energy saving is an energy source that can be obtained very quickly and cheaply, and it will contribute undeniably to the solution of energy supply problems of countries.

In this study, the steam system in a textile factory was investigated. The FMEA technique, one of the quality improvement tools, was used to determine the situations that may cause inefficient use of energy and the solution proposals for them. Some waste heat recovery options and today's cutting-edge technologies that can be used to increase energy efficiency have been revealed in FMEA. When the proposed systems are implemented, it is predicted that energy losses will decrease and around 382 kg/h (21%) of water will be saved and the net steam production capacity sent to the process will increase by 460 kg/h (9.2%).

It has been demonstrated that FMEA technique, which is used as a risk analysis and failure prevention method within the scope of preventive process improvement studies, can also be used easily in increasing boiler energy efficiency. FMEA is never-ending work. As existing technologies and possibilities evolve, they should be incorporated into the system and the FMEA study should be updated accordingly. Also, the research method

described here can be applied to other energy-using processes and equipment. In future studies, other energy losses in the company can be investigated with the FMEA technique. Today, the limited energy resources will encourage the execution of these studies not only in the textile sector but also in all industrial organizations. Such studies will increase the awareness of the industrial energy users.

Acknowledgment

This work was supported by the Scientific Research Projects (BAP) Commission of Bilecik Şeyh Edebali University (Project No: 201 -01. BŞEÜ.0 -01, 2019). https://bapoto.bilecik.edu.tr/index.php?act=guest&act2=projeler&durum=tamam

References

[1] General Directorate of Turkish Coal Enterprises (TKİ). Coal (Lignite) Sector Report, 2017; 94.
[2] YEGM [Yenilenebilir Enerji Genel Müdürlüğü - General Directorate of Renewable Energy], Endüstriyel Sistemlerde Optimizasyon Buhar Sistemleri [Optimization in Industrial Systems, Steam Systems], 2017, Türkiye.
[3] Barma, M. C., Saidur, R., Rahman, S. M. A., Allouhi, A., Akash, B. A., & Sait, S. M. A Review on Boilers Energy Use, Energy Savings, and Emissions Reductions. Renewable and Sustainable Energy Reviews 2017; 79, 970-983. https://doi.org/10.1016/j.rser.2017.05.187
[4] Özer, S., Buhar Sistemlerinde Kondenstop, Flaş Buhar ve Kazan Blöf Sistemi ile Enerji Geri Kazanımı [Energy Recovery with Steam Trap, Flash Steam and Boiler Blow Down in Steam Systems]. MSc. Trakya University, Çorlu, Türkiye, 2004.
[5] Saidur, R., Ahamed, J. U., & Masjuki, H. H. Energy, Exergy and Economic Analysis of İndustrial Boilers. Energy Policy, 2010; 38(5), 2188-2197. https://doi.org/10.1016/j.enpol.2009.11.087
[6] Kocabaş C. Enerji Veriminin Artırılmasında Süreç İyileştirme Tekniklerinin Endüstriyel Uygulaması. [Use of Process Improvement Techniques in Increasing Energy Efficiency and Practical Applications in Industry]. PhD, Bilecik Şeyh Edebali University, Türkiye, 2021.
[7] Karakurt, M. D., Deri Endüstrisinde Enerji Tasarrufu Uygulaması [Energy Saving Applications in Leather Industry]. MSc. Kocaeli University, Kocaeli, Türkiye, 2006.
[8] Çınar T. Tekstil Sanayisinde Enerji Yönetimi ve Enerji Verimlilik Analizi [Energy Management and Energy Efficiency Analysis for Textile Industry]. MSc. Pamukkale University, Denizli, Türkiye, 2008.
[9] Ünlü, O. Sanayide Enerji Tasarrufu Çalışmalarının Önemi ve Buhar Sistemleri ile İlgili Uygulama Örnekleri [Importance of Energy Saving Studies in Industry and Application Examples Related to Steam Systems]. IX. HVAC & Sanitary Congress and Exhibition (TESKON 2009), 6-9 May 2009, İzmir, 67-80.
[10] Kanoğlu, M. Enerji Verimliliği Örnek Projeleri [Energy Efficiency Sample Projects]. Gaziantep University Mechanical Engineering Department. 2010. [Available: 24.04.2019, http://www.tskb.com.tr/i/content/486_1_mehmet-kanoglu-enerji-verimliligi-ornek-projeleri.pdf].
[11] Ostrowski, P., Szelejewski, F., & Zymelka, Assessment of Improvement in the Energy and Exergy Efficiency of the Gas Heat Plant after the Exhaust Gas Cooled Down Below the Dew Point and the Use of Recovered Heat. Energy 2020; 190, 116179. https://doi.org/10.1016/j.energy.2019.116179
[12] Dhanre, G. T., Dhanre, U. T., Mudafale, K., & Mtech Scholar, K. I. T. S. (2014). Review Paper on Energy Audit of a Boiler in Thermal Power Plant. International Journal of Engineering Research and General Science 2014; 2 (6), 283-288.
[13] Savaş A. F. & Kocabaş C. (2022). Reducing Deaerator- Related Energy Losses in Steam Boilers. Thermal Science 2022; https://doi.org/10.2298/TSCI220616128S
[14] Durukafa, D. Buhar Üretim Merkezlerinde, Enerji Verimliliğinin Artırılması ve Bir Endüstriyel Tesisin Analizi [Increasing Energy Efficiency in Steam Production Centers and Analysis of an Industrial Facility]. MSc. Kocaeli, Yıldız Technical University, Istanbul, Türkiye, 2010.

RIGA 2023

Hybrid Photovoltaic Thermal (PV/T) Heat Pump Application in the National Stone Centre in UK

Tugba Gurler
University of Derby,Derby, UK, t.gurler@derby.ac.uk, ORCID:0000-0003-3255-5521

Zaharaddeen Hussaini
University of Derby,Derby, UK, z.hussaini@derby.ac.uk, ORCID: 0000-0003-1172-5886

Christopher Sansom
University of Derby,Derby, UK, c.sansom@derby.ac.uk, 0000-0003-1021-3133

Cite this paper as: *Gurler, T, Hussaini, Z.and Sansom, C, A novel Photovoltaic thermal (PV/T) system assisted heat pump utilization for National Stone Centre in UK. 11. Eur. Conf. Ren. Energy Sys. 18-20 May 2023, Riga, Latvia*

Abstract: In this study, a hybrid heat pump system, supported by a photovoltaic/thermal (PVT) panel, has been installed for heating National Stone Centre (NSC) in the UK. The building has a total useful area of 3,000 m2 and its projected annual electric power consumption is 145,000 kWh. The internal floor area considered in this paper is 810 m², requiring an annual fuel input of 321,318 kWh/year for heating. The system is designed to provide heating to NSC during winter months and consists of a 15-kW heat pump with an S-type Capillary heat exchanger that is supported by a photovoltaic/thermal PVT panel. The study shows that the PVT hybrid heat pump results in a higher COP of between 5.32 and 7.25 compared to independent air source heat pump system thus resulting in a more efficient and cheaper system. For a heating supply of 15KW, the COP of the system can be improved by 10% in 18◦ C ambient temperature conditions. For a full-sized hybrid system in NSC, the electrical heating load would be 54,624 kWh/year. This equates to an energy saving of 266,694 kWh/annum by using PVT hybrid heating system instead of gas boiler heating. The payback period is determined as 2.95 years. The PV system, covering an area of 514 m2 is designed to meet 75% of the annual electricity demands of the Centre and estimated to cost £184,226 resulting in a Levelized Cost of Energy (LCOE) of 12.42 p/kWh over a 30-year period and a payback period of 2.6 years.

Keywords: *National Stone Centre, Air source heat pump, PVT assisted Heat Pump, S-type Capillary heat exchanger*

Nomenclature	
ASHP	Air Source Heat Pump
COP	Coefficient of performance
GHG	Green House Gasses
LCOE	Levelized Cost of Energy
NSC	National Stone Centre
PVT	Photovoltaic/Thermal
RHI	Renewable Heat Incentive
LCOE	Levelized Cost of Energy

1. INTRODUCTION

The goal of reaching net-zero greenhouse gas emissions requires extensive national changes. Since 1990, the UK has made substantial progress by reducing its greenhouse gas emissions by almost half [1]. In 2019, the UK became

the first major economy to legislate a binding target to reach net zero emissions by 2050 [2]. As a front-runner in addressing climate change, the UK's 2008 Climate Change Action strategy has already resulted in estimated savings of £100 billion from early actions [3]. The main source of emissions from the residential and public sectors is the use of natural gas for heating [4]. The COVID-19 pandemic and subsequent restrictions in the UK led to a significant impact on greenhouse gas emissions during 2020 and 2021 period. In 2021, the primary drivers of the increase in GHG emissions were fossil fuels used in private road transportation and emissions from the residential sector, which rose due to quarantine measures [5]

Businesses contribute significantly to GHG emissions. The government must therefore ensure that firms have enough help to accomplish this transformation. It would be challenging to get to a position where we produce no greenhouse gas emissions. The term "net zero" rather than "absolute zero" refers to the commitment to eliminating sufficient emissions from the atmosphere to counteract those produced [6]. By doing this, emissions produced and removed are balanced. In recent years, the green energy movement has gained momentum as a direct result of the clear and catastrophic consequences of the fuel-based economy. Several areas of research have been developed to reduce CO2 emissions and make systems more sustainable. he UK government announced a new 'Energy Price Guarantee,' which superseded the 'Renewable Heat Incentive (RHI)' in October 2022. The Government has also outlined plans to help cut energy bills for businesses. This is called the "Energy Bill Relief Scheme: help for businesses and other non-domestic customers". Businesses, including schools, hospitals, and charities, will also get support through this plan. The scheme will provide discounts for energy usage to businesses between the 1st of October 2022 and the 31st of March 2023 [7-8], thereby helping reduce the impact of the cost increases.

A hybrid PV system is proposed a solution in this study. A hybrid photovoltaic system is capable of producing both electricity and heat at the same time, and by utilizing the waste heat, an overall efficiency of around 70% [9] can be achieved. A Solar Air Composite Heat Source Heat Pump System (SACHP) integrated with a fin tube and a tube heat exchanger was examined by Liu et al. [10] The dual heat source mode showed 62% higher heat capacity and 59% higher COP than a single heat source mode in the condition of -15°C ambient temperature. Moreover, the dual heat source mode showed 51% higher heat capacity and 49% higher COP than the single heat source mode in the heat transfer difference of 5°C [10]. A novel ground-coupled heat pump combined with solar collectors was assessed in order to find out the main operating conditions affecting the system's performance by Gurler et al [11-12].. The daily average COP was between 2.05 and 5.17. Short term [11] and long term [12] investigation of dynamic tests was allocated with the brine/water heat pump. It was observed that when the source temperature rises constantly, it causes considerable increase in the COP [11-12]. A large scale solar-heat pump system has been investigated under real weather conditions by Zhang et al. They observed that the average coefficient of performance (COP) of the system was achieved to 4.96 for the heating of 1500 L water tank from 5.5 °C to 45 °C on a sunny day.[13]. A Solar Air Composite Heat Source Heat Pump System that integrates compound parabolic concentrator-capillary tube solar collectors for domestic heating in the UK was examined by Yang et al. (2022) The results show that the required concentrated solar collector size is 12 m^2 while the it is 18 m^2 for flat plate solar collector under the same seasonal performance factor condition [14]. The combination systems of a PVT system and a heat pump look to improve a PV panel's efficiency, and subsequently to provide space heating with cost-effective environmental control systems. Potential use of PVT hybrid heat pump system has been assessed at the National Stone Centre's new site, including an assessment of the site's solar and air resources in the area.

2. SYSTEM DESIGN AND DESCRIPTION

The National Stone Centre (NSC)

The National Stone Centre (NSC) is in the middle of the Derbyshire Dales at Wirksworth, near Matlock Bath in Derbyshire. The most important and initial step is the determination of the building's thermal loads to size the required air conditioning systems. These figures below show images taken from 'The Institute of Quarrying' (Figure 1).

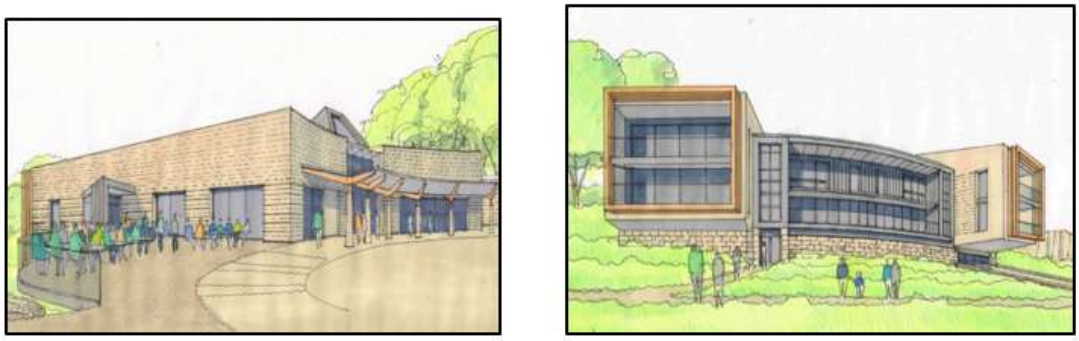

Figure 1. The National Stone Centre (NSC)

The design loads were only evaluated on block basis. The teaching spaces, coffee, shop, classroom, and office spaces within the building were heated by using convectors. Weather and location data parameters must be defined in Design Builder at site level before progressing onto the CAD stage as well as the type of analysis. Design Builder, supported by ASHREA, offer an array of location templates which define geographical location and weather data for all buildings on site. The 'East Midlands' location template was selected in addition to the 'Energy Plus' analysis type, The selected internal floor area for all Block units of 810 m², the annual fuel input is 321,318 kWh/year.

The total useful area of the new building is 3,000 m^2, resulting in a projected annual consumption of 145,000 kWh.The monthly distribution of this consumption is based on data from the number of visitors currently utilizing the building. Due to the low solar radiation during some months, particularly during winter, the establishment would still require electricity from the grid. Figure 2 compares the electricity usage with and without the PV system. The PV system, covering an area of 514 m^2 is designed to meet 75% of the annual electricity demands of the Centre. It is estimated to cost £184,226 resulting in a Levelized Cost of Energy (LCOE) of 12.42 p/kWh over a 30-year period. The payback period of the PV system is 2.6 years.

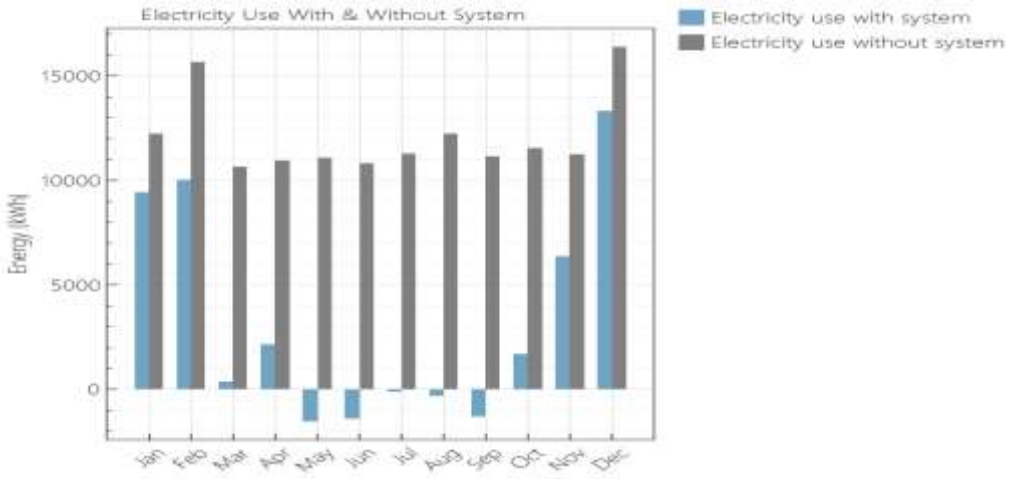

Figure 2. Electricity usage with the PV system and without the system

PVT hybrid heat-pump system

The diagram of the innovative PVT heat pump system is depicted in Figure 3. This efficient hybrid design enables the PV cell to function optimally at elevated temperatures. The heat absorbed by the S-type Capillary heat exchanger is utilized to meet the heating needs in the evaporative section of the heat pump for space heating in the National Stone Centre. The hot water in the buffer tank is then routed to the convector units. The convector thermostat is adjusted based on the desired indoor temperature of the building.

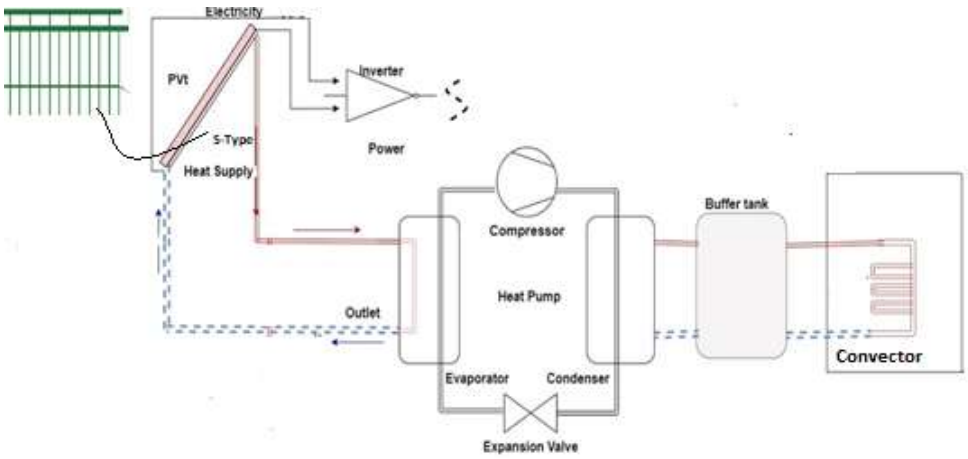

Figure 3. PVT-GSHP integrated S-type Capillary heat exchanger Heating system

PVT Model: S-type Capillary heat exchanger:

A 107 kWp photovoltaic (PV) generation installation has been proposed for the NSC. This installation will require approximately 514 m2 of available roof and field space, and will utilize standard 450 W PV modules. The installation of a 107 kW photovoltaic (PV) system is expected to generate an excess of 3,361 kWh of electricity per year during peak solar radiation months, which can be exported to the grid. MATLAB software is used to perform the PVT thermal simulation.

PV top surface energy balance equations:

$$M_g C_g \frac{dT_g}{dt} = G\alpha_g + h_{wind} A_{ag}(T_{am} - T_g) + h_{ag} A_{ag}(T_{sky} - T_g) + h_{gp} A_{gp}(T_p - T_g) \quad (1)$$

Where T_g, M_g and C_g are the top glass surface's temperature, mass and specific heat, respectively. G is the irradiation in the solar glass. α_g is absorptance of glass. h_{ag} is the heat transfer between ambient air and glass top surface, respectively.

PV back surface energy balance equations:

$$M_b C_b \frac{dT_b}{dt} = h_{pb} A_{pb}(T_p - T_b) + h_{mb} A_{mb}(T_m - T_b) + h_{br} A_{br}(T_r - T_b) \quad (2)$$

S-Type S-type Capillary heat exchanger energy balance equatios:

$$M_m C_m \frac{dT_m}{dt} = h_{pm} A_{pm}(T_p - T_m) + h_{rm} A_{rm}(T_r - T_m) + h_{mw} A_{mw}(T_w - T_m) \quad (3)$$

Where M_b, C_b and T_b are back sheet's mass, specific heat and temperature, respectively. the heat transfer coefficient between back sheet and S-type Capillary heat exchanger is h_{mb} ; and the heat transfer coefficient between roof sheet and back sheet is h_{rm} .

Heat pump

A 15 kW hybrid heat pump and a heat pump equipped with an S-type Capillary heat exchanger were installed behind commercial PV panels to provide partial heating to the NSCduring heating months, depending on the necessary temperature. The surplus thermal energy produced by the heat pump during the day is channeled into a 300-liter buffer tank and then utilized during periods of insufficient thermal input. This commercial buffer tank is linked to the Convector units in the NSC

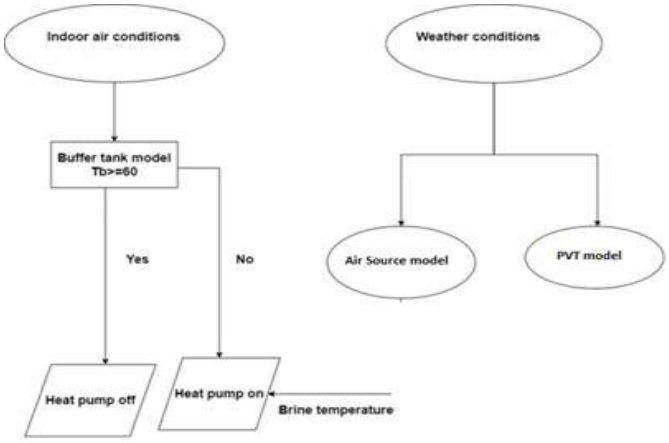

Figure 4. Flowchart of air source and solar assisted heat pump

The analysis using the basic operating condition presented in Figure 4 has been conducted for selected temperatures, from heating season. Convector delivery temperatures are designed to a set temperature of 55 ^{o}C in the system. When temperature reaches the set temperature, 55^{o}C, the heat pump is switched off. The system is not switched on until the temperature at the top of the buffer vessel falls below 55 ^{o}C. Queasy steady state assessment is identified in this section

COP can be calculated by the electrical energy consumed during working and the difference between heat sink and heat source, as shown in the following equations.

$$COP = \frac{Q_b}{W_{hp} + W_{cp}} \tag{4}$$

Based on total selected internal floor area for all Block units of 810 m², the annual fuel input is 321,318 kWh/year. The potential annual fuel usage will be 67 kWh/year/m². loads. The heat pump is sized as 16 kW to provide part load in winter (considering the parameters affecting heat pump efficiency, including return temperature, heat sink, and source temperature) A simplified thermodynamic/physical approach has been taken to characterize the operation of the air source and the PVT heat pump. The model has a good match with performance data described by the manufacturer of the air source heat pump (Table 1). When the average ambient temperature is -7 °C and 2 °C, it is assumed that the PVT collector cannot deliver enough heat as a heat source for the heat pump

Table 1. COP comparison between PVT heat pump and air-source heat pump manufactured

T out [°C]	COP of S-Type PVT heat pump	Air source heat pump
7 °C	5.32	5.01
10 °C	6.01	5,85
14 °C	6.50	6.31
18 °C	7.25	6.55

For a full-sized hybrid system in NSC, the electrical heating load would be 54,624 kWh/year. This equates to an energy saving of 266,694 kWh/annum by using PVT hybrid heating system instead of gas boiler heating.

4. CONCLUSION

The work presents detailed investigations of a hybrid heat pump heating system for the National Stone Centre in the UK, focusing on PVT to heat pump systems. The following points summarize the essential findings of the simulations:

• The total functional area of the new building is 3,000 m2, resulting in a projected annual consumption of 145,000 kWh, including the café. The selected internal floor area for all Block units of 810 m², and the yearly fuel input is 321,318 kWh/year.

• The air source heat pump COP fluctuates from 5.01 to 6.55 during the selected temperatures under queasy steady-state conditions. The PVT hybrid heat pump results in a higher COP of between 5.32 and 7.25 compared to the air source heat pump, resulting in a more efficient system. The COP of the air source heat pump can be improved by 10 % by this hybrid design under 18 ◦C ambient temperature for a heating supply of 15 kW.

• For a full-sized hybrid system in NSC, the energy saving is determined as 266,694 kWh/annum by using a PVT hybrid heating system instead of gas boiler heating resulting in a payback period of 2.95 years.

• The PV system is capable of meeting 75% of the annual electricity demands of the Centre and is estimated to cost £184,226, resulting in a payback period of 2.6 years.

Acknowledgment

This study is supported by National Stone Centre project in University of Derby. The authors would like to acknowledge the effort of Mr. Harry George.

References

1] Department for Business Energy & Industrial Strategy (BEIS), “2020 UK greenhouse gas emissions, provisional figures,” 2021.
[2] Department for Business Energy and Industrial Strategy, “Net Zero Strategy: Build Back Greener,” 2021. [Online]. Available: https://www.gov.uk/government/publications/net-zero-strategy
[3] British Chamber of Commerce, “What is net zero and why is it important?” https://www.britishchambers.org.uk/page/net-zero-hub/what-is-net-zero-and-why-is-it-important (accessed Sep. 19, 2022).
[4] Department for Business Energy & Strategy Industrial, “2021 UK greenhouse gas emissions, provisional figures 31,” Natl. Stat., no. March, 2022.
[5] BEIS, “Government Response to the Climate Change Committee,” HH Associates Ltd. on, 2021.
[6] British Chamber of Commerce, “What is net zero and why is it important?” https://www.britishchambers.org.uk/page/net-zero-hub/what-is-net-zero-and-why-is-it-important (accessed Sep. 19, 2022).
[7] R. Mullis, “UK business action on net zero and historical energy use,” Off. Natl. Stat., pp. 1–23, 2021.
[8] Department for Business Energy & Strategy Industrial, “Energy Bill Relief Scheme: help for businesses and other non-domestic customers,” UK Goverment, 2022.
[9] Zhang, Xingxing, Xudong Zhao, Jihuan Xu, and Xiaotong Yu. 2013. “Characterization of a Solar Photovoltaic/loop-Heat-Pipe Heat Pump Water Heating System.” Applied Energy 102. Elsevier Ltd: 1229–45. doi:10.1016/j.apenergy.2012.06.039.
[10] Liu, Yin, Jing Ma, Guanghui Zhou, Chao Zhang, and Wenlei Wan. 2016. “Performance of a Solar Air Composite Heat Source Heat Pump System.” Renewable Energy 87. Elsevier Ltd: 1053–58. doi:10.1016/j.renene.2015.09.001.
[11] Gurler, T., Elmer, T., Cui, Y., Omer, S., & Riffat, S. (2018). Experimental investigation of a novel PVt/heat pump system for energy-efficient poultry houses. International Journal of Low-Carbon Technologies, 13, 404–413. https://doi.org/10.1093/IJLCT/
CTY049
[12] Gurler, T., Elmer, T., Cui, Y., Omer, S., & Riffat, S. (2021). Performance evaluation of a novel PVT-GSHP heating system on energy-efficient poultry houses: long-term monitoring. International Journal of Low-Carbon Technologies 2021;16:393–406.
[13] Zhang, S., He, W., Fan, Y., Wang, K., Hu, Z., Chu, W. and Yu, H., 2022. Field experimental investigation on electricity and thermal performances of a large scale photovoltaic solar-thermal direct expansion heat pump system. Energy Conversion and Management, 267, p.115941.
[14] Yang, L.W., Xu, R.J., Zhou, W.B., Li, Y., Yang, T. and Wang, H.S., 2023. Investigation of solar assisted air source heat pump heating system integrating compound parabolic concentrator-capillary tube solar collectors. Energy Conversion and Management, 277, p.116607.

RIGA 2023

Study of the Use of Agrovoltaics in the Canary Islands. Issues to Consider

Antonio Pulido Alonso
Las Palmas de Gran Canaria University, Spain, antonio.pulido@ulpgc.es, ORCID: 0000-0002-3406-5086

Gabriel Winter Althaus
Las Palmas de Gran Canaria University, Spain, gwinter@iusiani.ulpgc.es , ORCID: 0000-0003-0890-7267

Néstor Rubén Florido Suárez
Las Palmas de Gran Canaria University, Spain, nestor.florido@ulpgc.es , ORCID: 0000-0002-1824-6792

Yasmina Afonso Mosteiro
CO2 Innova, Spain, info@co2innova.com , ORCID: 0000-0001-5992-0838

Rina Sainani Vega
Self-employed, Spain, rina.sainani101@hotmail.com,ORCID: 0000-0003-343-3980

Cite this paper as: *Pulido,A.et al. Study of the use of agrovoltaics in the Canary Islands. Issues to consider. 11. Eur. Conf. Ren. Energy Sys. 18-20 May 2023, Riga, Latvia*

Abstract: The effects and particularities that the implementation of agrovoltaics in the Canary Islands will be analyzed, aspects that should be considered as they will affect these facilities, and weaknesses that could be reinforced by the realization of this type of installation are analyzed. The implementation of two installations of equal power in two different arrangements is compared: vertical E-W, and with the optimal angle, each option has advantages and disadvantages, it is difficult to find an objective way to bet on one or the other. Due to the proximity of the islands to the Sahara desert, the presence of dust-haze is frequent, together with the lack of rain on the islands, this dirt effect is worse the more horizontal the panel is. On the other hand, an effect of deformation of the demand curve due to the use of solar energy, known as Duck Curve, is taking place in Spain and throughout the world. The vertical arrangement helps to alleviate those effects.

Keywords: *Agrovoltaic. Vertical E-W, bifacial*

1.- INTRODUCTION

Agrovoltaics is the simultaneous use of the soil, for agricultural or livestock production, and electricity, it is a symbiosis in which both win. If you have 1 ha, it could be dedicated to 100% photovoltaics or 100% to agricultural production. If agrovoltaics were applied, it would be possible to obtain 103% of agricultural production, and 83% of solar electricity in just 1 ha [1].

In any case, it is a matter of ensuring that the installation does not hinder agricultural tasks and occupies as little land as possible, and that sufficient light reaches both the panels and the plants. All of this may require a higher structure and a lower FV density than if there were no crops. Another possibility is the proposal in this work, based on the placement of the panels vertically, oriented East-West, these being bifacial.

Although agrovoltaics are more expensive installations than conventional photovoltaics on the ground, they are cheaper than small rooftop installations, in addition to the large contributions they produce, mainly food, jobs and soil conservation.

In addition, it provides extra income to the farmer, and/or allows reducing energy costs on their farm. Providing energy for desalination, pumping water for irrigation, and other local energy needs.

Despite the multiple articles that have been produced on crops under this type of facility in different parts of the world [2], more research and experimentation are needed.

Although it has been used for more than a decade, its interest has skyrocketed, in a world with a growing population, trying to decarbonize its activities. It is especially interesting in island systems, where the territory is limited.

We are going to talk about a case in the Canary Islands, where more than 40% of the territory is under conservation, with a population density of 291 inhabitants/km2, in 2019 it was visited by more than 15.11 million tourists, figures that have declined sharply after the pandemic. With a high population density, great scarcity of water, total dependence on energy 96% and food 92% on basic products, more than 66% of agricultural land has been abandoned. With a high unemployment rate above 14%, it is necessary to find a way to compensate the farmer to return to his job, agrovoltaics appearing as an additional force, to respond to all these problems.

2.- CHARACTERISTICS THAT COULD BENEFIT FROM AGROVOLTAICS

- *Food dependency*

The food dependency of the Canary Islands is 92% on basic consumer products [3]. This reality has been going on for many years, and it has not been solved [4].

- *Abandonment of agricultural land*

66% of agricultural land in the Canary Islands is out of exploitation, without any use.

- *Desertification of the soil*

Desertification is a global, national problem and affects the entire island of Fuerteventura, resuming agricultural work could partially alleviate this problem, avoiding erosion and taking soil fertility back.

- *External energy dependence, exclusively on oil. Null diversity*

It is observed in [5] that of the primary energy consumed in the Canary Islands in 2020, 96% was oil. In addition, there is the bunkering service that is carried out from the archipelago, like a service petrol station in the middle of the Atlantic Ocean. The amount for this concept is 2.16 million toe.

Agrovoltaics arises as a way to partially alleviate the enormous dependence on foreign energy, doubly polluting, since it contaminates its local use, and its transport to the islands.

- *Shortages of freshwater*

100% of the water used in Fuerteventura [6] comes from desalination, in Gran Canaria it is 86%. The desalination plants are supplied directly from the grid, exchanging oil for water, since it is the majority of energy on the islands for the production of electricity [5].

3.- CHARACTERISTICS TO CONSIDER WHEN APPLYING AGROVOLTAICS IN CANARY ISLANDS

Figure 1. Cultivation terraces on the island of La Gomera

There are three peculiarities in the Canary Islands, which agrivoltaics will not be able to cope with, but must be taken into account when implementing this technology in this territory.

- *Complicated orography*

Las The Canary Islands are volcanic peaks that rise out of the sea from the ocean floor, as the islands rise outside of the African continental shelf. Its orography is very abrupt, cultivation on terraces is very common on the islands, Fig.1 shows some cultivation terraces. This would make it difficult to implement photovoltaic panels on a massive scale, due to the large number of hours that many areas would be in shadow. Therefore, in the case of the Canary Islands, it is essential to carry out a complete shadow study for the location and installation that is intended to be carried out.

- The haze is a meteorological phenomenon that consists of the abundant presence of sand and dust suspended in the atmosphere. Between 2004 and 2014, an average of 101 hazy days per year were recorded in the Canary Islands.

Figure 2. Haze in Canary Islands

Figure 3. Donkey belly in Canary islands

Due to its proximity to the Sahara desert, quite frequently, the Canary Islands receives the visit of "Calimas" Fig.2, which are dust hazes caused by dust storms stirred up by high winds in the Sahara, which are driven over the Canary Islands by south easterly winds. In Canary Islands, the maximum annual electricity production obtained with a photovoltaic panel is with zero azimuth, and 20º inclination, but it is true that the panel will remain more immune to the effect of haze the more vertical it is, and the almost non-existent rains will not clean dust panels.

- Donkey belly, is how we know the low clouds that the trade winds bring to the Canary Islands, and given the altitude of the islands, they are trapped to the north of them, the solar resource being much greater in the south of the islands, observe Fig3. A photovoltaic installation can obtain a production of 1,800 h/year in the south, and a few kilometers to the north 1,300 h/year, due to cloudiness.

4. PRACTICAL CASE CARRIED OUT

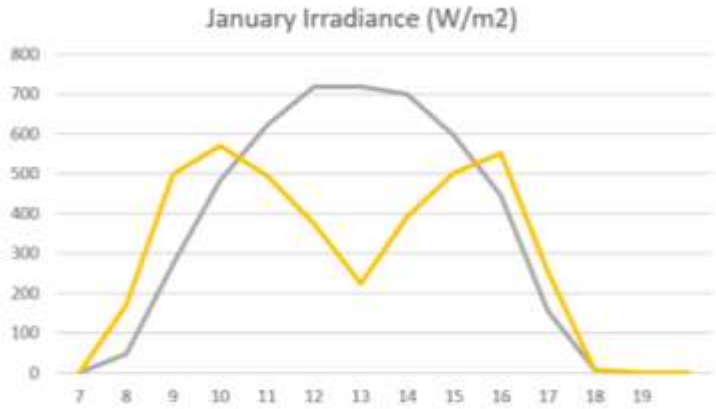

Figure 4. Irradiance tilted 20º (grey) and vertical E-W (orange)

Agricultural land in the south of the island of Fuerteventura has been selected to analyze a practical case, a surface area of 375 ha. In the following coordinates lat 28º10'59.24" N and lon 14º12'19.40" O, being at an elevation of 30 m, with a distance of 830 m from the coast. Placing vertically, with E-W orientation. Considering occupying the limits of the plot to the east and west, a power of 204.8 kWp has been obtained.

A comparison will be made at equal power, with respect to the vertical bifacial panels looking E-W, with respect to monofacial panels to the south, and inclined at an optimal angle. For this, the European PVGIS software [7] will be used.

The incident radiation will be reflected in each case, shown in Fig.4 for the month of January, it is observed that in the case of the vertical arrangement the radiation captured in the first and last solar hours increases, with the total count being less than the arrangement at optimum angle. The vertical E-W system generates 8.37% less energy per year with respect to an installation of the same power facing south, inclined at the optimum angle, which in the Canary Islands is 20º.

In the case of the E-W vertical bifacial panels, vertical panels oriented to the West (Fig.5) and vertical panels oriented to the East (Fig.6) have been considered, and both productions have been added.

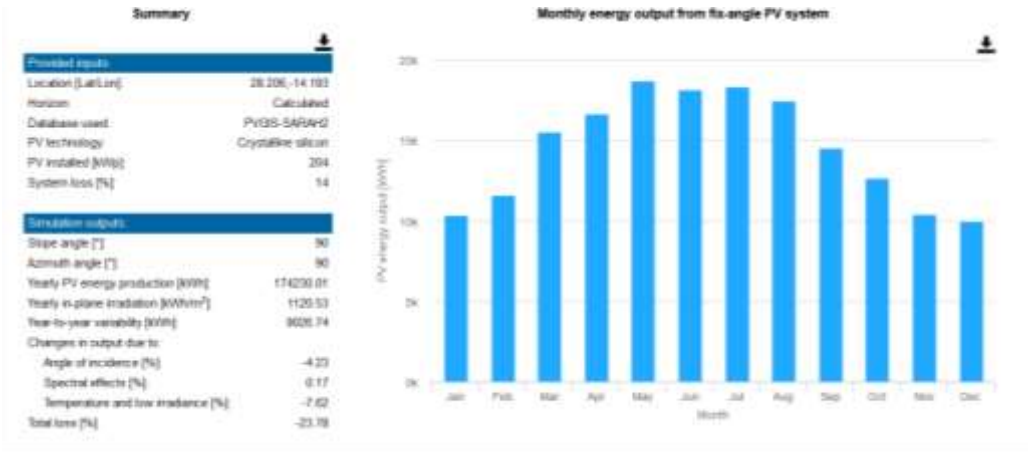

Figure 5. West vertical panel

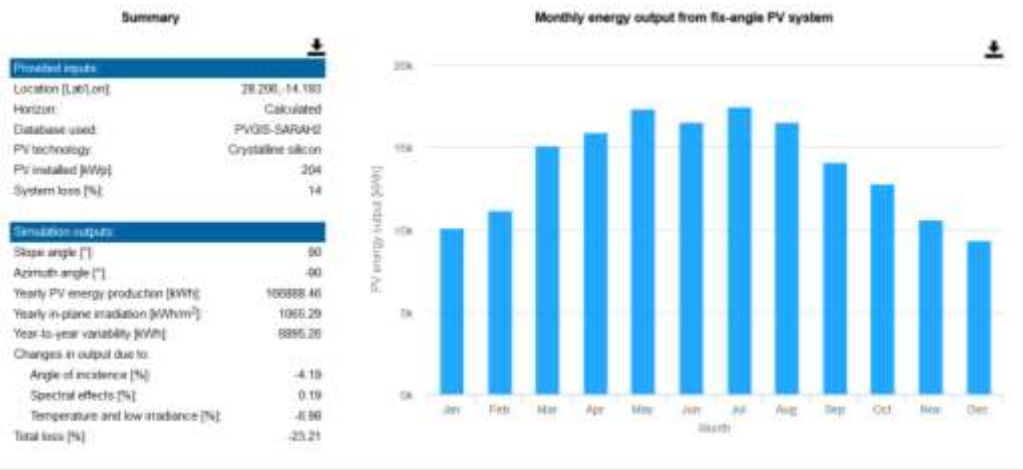

Figure 6. East vertical panel

5.- CONCLUSIONS

As seen in the previous sections, the vertical layout compared to the optimal inclination will present:

- Null land occupation, avoiding the cost of tall structures, which allows the transit of agricultural vehicles

- Zero affectation due to the recurring episodes of haze, aggravated by the lack of rain to clean the modules.

- By not providing any shade on the crop at central hours, it hardly reduces the need for irrigation.

- It does not affect the creation of a strip of local bushes, which encourages the presence of pollinators, which favor crops and local biodiversity.

- Does not protect the crop from extreme weather conditions.

- Because it changes the generation curve with respect to conventional photovoltaics, it does not contribute to accentuating the duck curve [8].

- Productive soils are maintained, helping their profitability due to the added economic contribution

- Promoting local employment and increasing food autonomy

- It produces only 8.37% less energy per year compared to an installation with an optimal angle, but the economic income obtained will be very similar, since generation increases during extreme hours, which are the most expensive, and income may be higher at as the installed photovoltaic power increases, and the hourly price difference accentuates.

- The use that will be made of the electricity produced is not contemplated, and it can be injected directly into the grid, or part of it can be used in the desalination of seawater to be used in cultivation, with the advantage of desalinating more water on sunnier days.

- Much remains to be analyzed in this field, given that each location will have its own peculiarities, as those of the Canary Islands have been described here, we are sure that agrovoltaics can greatly improve the current energy and food situation of these islands.

REFERENCES

[1] Trommsdorff, Max et al. 'Agrivoltaics: Opportunities for Agriculture and the Energy Transition. A Guideline for Germany'.[Internet], Fraunhofer Institute for Solar Energy Systems ISE. <https://www.ise.fraunhofer.de/content/dam/ise/en/documents/publications/studies/APV-Guideline.pdf> 2022. (accessed on 05.02.23)

[2] Chalgynbayeva, A. et al. 'Worldwide Research Trends in Agrivoltaic Systems—A Bibliometric Review', Energies (19961073), 16(2), p. 611. 2023. doi:10.3390/en16020611.

[3] Canarias Semanal 'Canarias: El incierto futuro de una dependencia alimentaria suicida' Canarias Semanal. [Internet], <https://kaosenlared.net/canarias-el-incierto-futuro-de-una-dependencia-alimentaria-suicida/> 2019. (accessed on 05.02.23)

[4] La Vanguardia 'Cabildo de Gran Canaria fomentará alimentos locales para reducir dependencia', La Vanguardia. [Internet], <https://www.lavanguardia.com/local/canarias/20150717/54433462733/cabildo-de-gran-canaria-fomentara-alimentos-locales-para-reducir-dependencia.html> 2015. (accessed on 05.02.23)

[5] Gobierno de Canarias 'Anuario Energético de Canarias 2020' [Internet], <https://www.itccanarias.org/web/images/actualidad/Publicaciones/ITC_Memoria_2020_DIGITAL.pdf > 2022. (accessed on 05.02.23)

[6] Palacios, C.J. 'Fuerteventura logra la cuadratura del círculo con la gestión integral del agua' 20 minutos [Internet], <https://blogs.20minutos.es/cronicaverde/2016/02/23/fuerteventura-logra-la-cuadratura-del-circulo-con-la-gestion-integral-del-agua/> 2023. (accessed on 05.02.23)

[7] European Commission 'PHOTOVOLTAIC GEOGRAPHICAL INFORMATION SYSTEM' https://re.jrc.ec.europa.eu/pvg_tools/en/ [Internet], (accessed: 05.02.23).

[8] Becca Jones-Albertus 'Confronting the Duck Curve: How to Address Over-Generation of Solar Energy' Office of Energy Efficiency & Renewable Energy. USA. [Internet], <https://www.energy.gov/eere/articles/confronting-duck-curve-how-address-over-generation-solar-energy> 2017. (accessed on 05.02.23)

RIGA 2023

Bioclimatic Design Strategies in Social Housing for Cold Weather-Tacna - Peru 2022

Doris Esenarro Vargas
Ricardo Palma University, Lima, Perú, doris.esenarro@urp.edu.pe, ORCID: 0000-0002-7186-9614

Vanessa Oshin Raymundo Martinez
Ricardo Palma University, Lima, Perú, 202112586@urp.edu.pe, ORCID: 0000-0001-9264-0176

Jhonny Fernando Flores Rojas
Ricardo Palma University, Lima, Perú, jhonny.flores@urp.edu.pe, ORCID: 0000-0000-0000-0000

Jesús Manuel Prado Meza
Ricardo Palma University, Lima, Perú, jesus.prado@urp.edu.pe, ORCID: 0000-0002-8166-6044

Rosa Elvira Ruiz Reyes
San Luis Gonzaga National University, Ica, Perú, rruiz@unica.edu.pe, ORCID: 0000-0001-5026-1362

Cite this paper as: *Esenarro, D, Raymundo, VO, Flores, JF, Prado, JM, Ruiz, RE. Bioclimatic design strategies in social housing for cold weather-Tacna - Peru 2022. 11. Eur. Conf. Ren. Energy Sys. 18-20 May 2023, Riga, Latvia*

Abstract: The extreme weather in the town of Tarata in Tacna, brings as a consequence many problems among the residents. Therefore, the objective of this research is to evaluate the climatic characteristics of the town, as a methodology bioclimatic design strategies were applied in housing modules, supported by digital tools (AutoCad, Sketch Up, Revit and Insight). As results in natural lighting, illuminated spaces were obtained from 5:45 a.m. to 6 p.m. Especially thanks to the greenhouse for its transparency capacity against sunlight, the greenhouse gives an optimal thermal transfer which will be distributed in the environments) the separation of the floor of the house with the natural soil, of 80cm. the location and adequate dimensions of the openings, a greenhouse patio that would capture the temperature and distribute it through a system of perforations towards the different internal environments and separation between the slab and the natural soil in order to avoid contact of the house with the frost that could cause the desired internal temperature to be lost. In conclusion, the strategies apply to the SDGs; 6, 7, 9, 11 and 13.

Keywords: *Thermal comfort, bioclimatic strategies, greenhouse patio and temperature*

1. INTRODUCTION

In foreign countries such as Denmark, passive heating measures have been applied in the design of new buildings. They successfully reduced the energy demand for heating.[1]

The environmental crisis that we are currently facing has no setback, and is not exclusive to a particular society, but the product of a scenario that is presented as a context of global order, which is spread through the industrial and technological revolution in greater extent. In this way, it is inadmissible not to question what happens around us, especially when we know that Mother Nature is a grand plot that provides life in a subtle and dynamic way, capable of converting the molecules of the primitive earth into the complex forms of life we know today. In this case, reason is given regarding environmental change, its consequences and the lack of knowledge and interest on the part of people.[2] In Peru, a total of 3 million 713 thousand inhabitants, who live in more than 931 thousand rural adobe houses (according to the 2007 national census), are subjected to extreme climatic conditions in the

departments of Arequipa, Ayacucho, Cajamarca, Ancash, Apurímac , Cusco, Huancavelica, Huánuco, Junín, La Libertad, Moquegua, Pasco, Puno and Tacna (all above 3000 meters above sea level). Between January and October 2009, 665 people have already died, including children under 5 years of age and the elderly, as a result of acute respiratory diseases (pneumonia), according to the national health ministry. [3]

In our country, 28 of the 32 types of climates in the world develop [1] And the impact caused by frosts and friajes are causing serious damage to the population. For which policies and regulations have been developed to implement actions such as the development of specific plans for each type of disaster. [4]. For example, Imata is a town located at more than 4,457 meters above sea level, and registers temperatures below zero. In towns like Imata, the HDI or human development index is below optimal; Due to the fact that the greatest number of Iras or acute respiratory infections are registered, being school-age children the most affected, which are spread in schools that are not adequate to protect them from the weather, this affects the performance and development of students. There is also little labor supply, and many families migrate to urban areas, to seek a better quality of life. [5] The cold hits the inhabitants of the Peruvian Andes. The frosts claim hundreds of human lives and thousands of camelid cattle characteristic of these regions of the country. From the north to the south, temperatures in the sierra oscillate between 5 degrees and minus 16.7 degrees [6].

The need to face the growing housing demands, within a critical national economic panorama, has required the implementation of alternative solutions to the traditional ones. One of them is directed self-construction, in which families are involved in all phases of the project, which includes, in addition to housing construction, other processes aimed at promoting the personal and group growth of the participants, added to the lack of knowledge environment and the rush to have a place to live, generates problems represented mainly inside the home and therefore for the members of the families.[7] . Inadequate constructions in high Andean areas and how these influence the lives of people and the population in general, putting their lives and their livestock at risk, they do not have adequate openings or characteristics in the infrastructure of their homes that help to generate the internal comfort of the house. Various strategies are proposed in order to achieve solutions to the problems posed by cold weather in these areas.[8]

The presence of extreme weather in Tarata and in other parts of Peru cause many deaths annually, these due to respiratory diseases, and the animals are not exempt from this problem, the lack of adequate space for them, where they are free from having to resist extreme weather, cause their death.[9] Recent research has shown that bioclimatic architecture, with its application of passive measures, can be an efficient cooling strategy and can reduce the need for conventional heating in winter periods. At present, in the high Andean areas, houses are built based on adobe and local vegetation since many of these materials maintain the internal heat of the house, however, the construction of houses with the same materials does not provide the same thermal comfort since it varies according to the composition of the material, as is the case of Chuapalca. Its physical precariousness does not comply with the canons of habitability and quality of life that are established in cities. However, the socio-cultural dimension must be considered to obtain an emic approach and understand its behavior and architecture. [10] Currently, adobe is considered one of the oldest materials in construction that is still used, since its application represents a low cost and easy to acquire, mostly these types of materials are applied in self-construction because it does not require a lot of effort when using it and in turn, these techniques are passed from generation to generation. This type of construction tries to use local materials, and they are more represented in rural areas in different parts of the world; however, unconventional constructions are being replaced by new construction systems based on brick, cement, metal, among others. others.[11] These houses have walls that can be made of adobe, mud or stone, which guarantees a wall of no less than 40 cm with a high degree of thermal inertia, very good for conserving heat, however, they have holes that allow the entry of Cold air. The roofs frequently have a gabled wooden structure, covered with ichu or tiles that provide an insulating layer protecting them from the cold, rain and hail. Most are replaced by galvanized calamine sheets, which, although waterproof, have practically no heat resistance, making them the worst option for combating frost. [12] In the mountains, measures are taken to combat the cold, such as heating systems that require electricity. This problem has been dragging on since previous years, which is why the need to implement heating systems without the direct need for energy sources and low cost arises. It is intended to take advantage of the energy resources (renewable energies) available to implement a prototype solar thermal with flat collectors to improve the quality of life of the inhabitants of high Andean areas, especially in frosty seasons.[13]

The south of the country registers the lowest temperatures. In the district of San Antonio de Chuca, in Caylloma, Arequipa, the cold reaches -8.4 degrees. In Palca, Tacna, at -9 degrees. The areas with the most severe frosts are in the Capazo district, in El Collao, Puno with -16 degrees and in Chuapalca, Tarata district in Tacna with -16.7 degrees. In the center of the country, Aija in Áncash and the district of Junín, in the region of the same name, temperatures register peaks of -0.8 degrees. And in Marcapomacocha, Yauli (Junín) reaches -1 degree. In the North, the coldest areas are located in Cajamarca, with 2.9 degrees in La Encañada and 2.2 degrees in the Porcón farm.

A report released on July 10 by the Ombudsman's Office revealed that so far this year 182 people have died in 9 regions due to frost [14].

In many regions of our country, high Andean areas, there is a great impact due to cold weather and frost. In this case, speaking of Tarata in Tacna, there are multiple deaths due to respiratory diseases, all of this caused mainly by the weather and its consequences [15] this problem is being reinforced and increased by the poor design of the houses in these places, the which do not have characteristics that help cope with extreme climates. Some solutions could be mentioned within the architectural design, such as correct orientation with a prior analysis of the area, in order to correctly locate the openings, thus taking advantage of the hours of sun and generating retention and heat management within the homes, generating thermal comfort [16] , this to mention something, in addition to the problem with the population, you can also visualize problems with their cattle, they do not support the extreme weather in some seasons and when they are outdoors or in places that are not suitable for them they die. Therefore, it would also be appropriate to create suitable spaces for them, thus improving the experience within these areas. In this research, we also want to have a method to take advantage of energy resources, renewable energies available to create a solar thermal bath taking advantage of the hours of sun to improve the quality of life of the inhabitants in this area. [17] In addition, the precariousness index of the houses located in Tarata is quite high, this thanks to multiple aspects such as the self-construction of houses in vulnerable areas and urban planning is not correct, they use materials that do not belong to the area or It provides that thermal comfort that is required in the place. Therefore, a housing system with thermal treatment will be proposed, to provide a better quality of life, through the appropriate construction system and materials. [18]. The bioclimatic adaptation consists of using an infiltration strategy, use of materials with high thermal resistance, shutters, slab height and optimal orientation. [19]

The objective of the research project is to apply bioclimatic strategies in social housing for cold climates in the City of Tarata in Tacna. Provide alternative solutions to the problems generated by intense cold inside the home. In addition to analyzing how bioclimatic design influences thermal comfort in a cold climate home. Likewise, we will be able to evaluate the existing materials in the area and their impact on the costs for the social housing to be proposed. [20]

2. METHODOLOGY

Section titles can be Theory, Experimental Setup, Methodology, Model, Simulation, Results and Discussions, Experimental Findings, Analytical Study, etc. But other titles are also welcome. Uppercase letters should be used in all section headings.

Place of study:

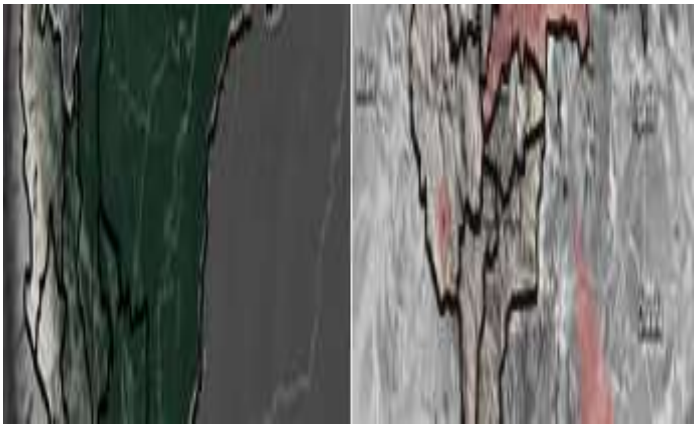

Figure 1. Place of study.

Figure 1 shows the location map which has an average altitude: 3,070 m.s.n.m. Topography and Type of Soil: It presents a 50% to 70% rugged terrain and the type of soil is Clay Loam.

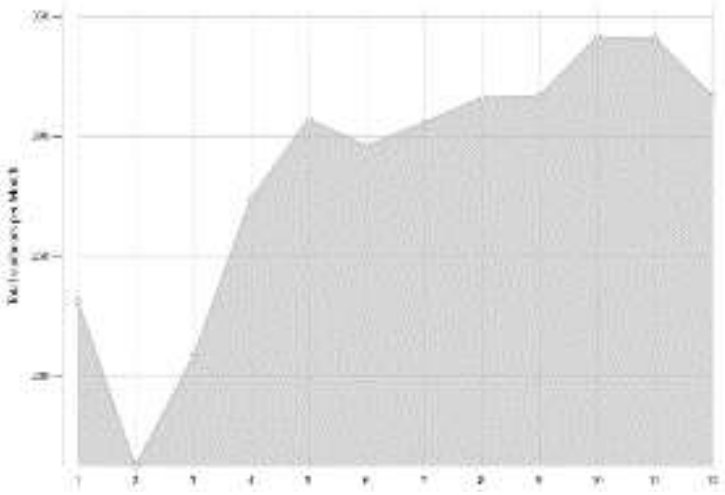

Figure 2. Sun hours.

Figure 2 shows that, in Tarata, the month with the most daily hours of sunshine is November with an average of 11.02 hours of sunshine. In total there are 341.59 hours of sunshine throughout November. The month with the fewest daily hours of sunshine in Tarata is January with an average of 10.23 hours of sunshine per day. In total there are 317.01 hours of sunshine in January.

In Tarata there are around 3418.72 hours of sunshine throughout the year. On average, there are 112.16 hours of sunshine per month. [22]

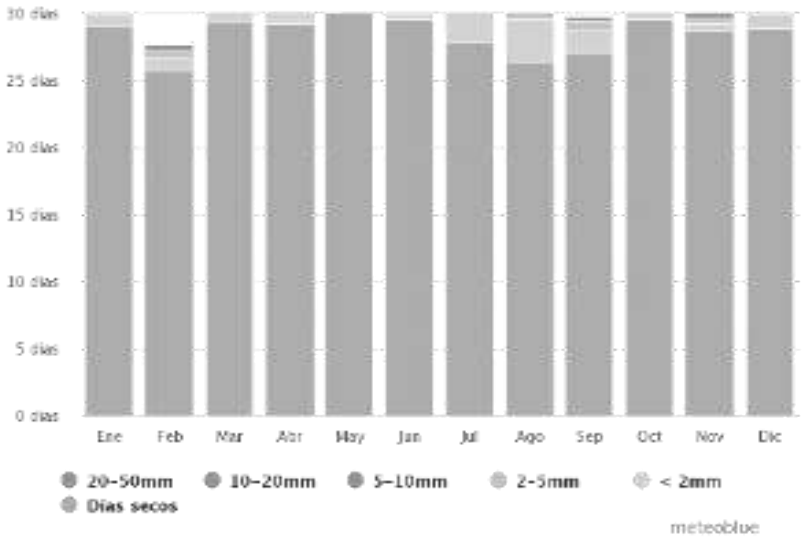

Figure 3. precipitation.

In figure 3 the variation in precipitation between the driest and wettest months is 176 mm. During the year, average temperatures vary by 2.2 °C [23]

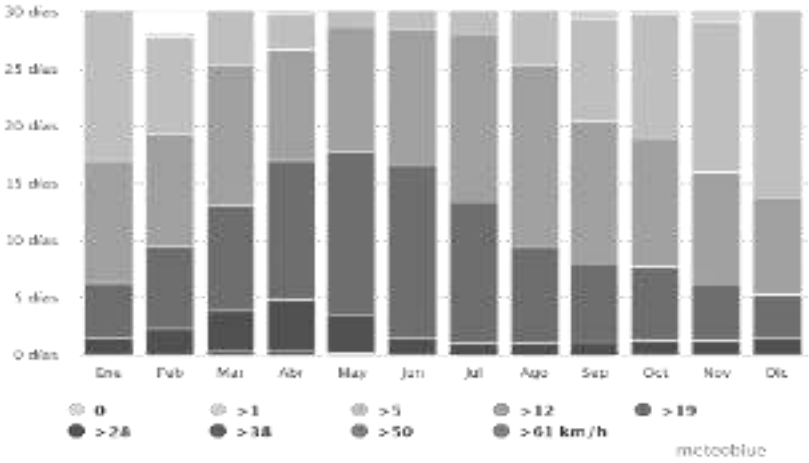

Figure 4. wind

Figure 4 deals with the wide area hourly average wind vector (speed and direction) at 10 meters above the ground. The wind of a certain location is highly dependent on local topography and other factors; and instantaneous wind speed and direction vary more widely than hourly averages. [24]

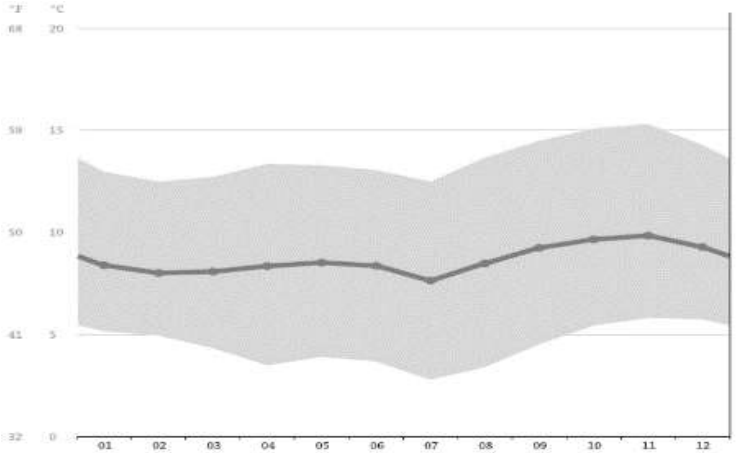

Figure 5. Temperature.

Figure 5 shows that temperatures are higher on average in November, around 9.8 °C. July has the lowest average temperature of the year. It is 7.6°C. [22]

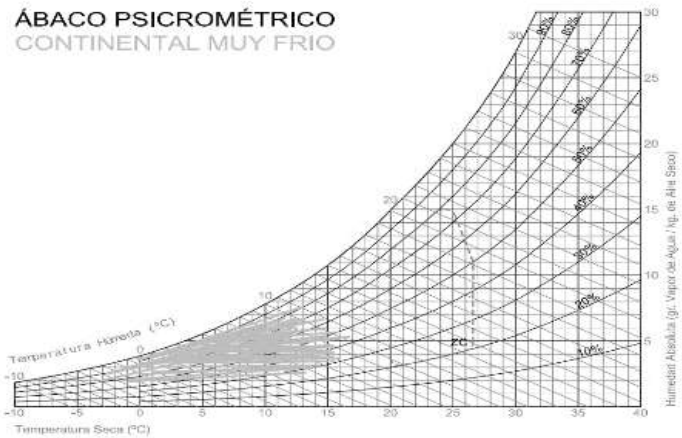

Figure 6. Pisocometric Abacus.

In figure 6 we can see that the project is located in a very cold continental zone and does not reach the comfort zone, so passive gain strategies must be applied in order to reach the ZC. [24]

Figure 7. Flora

In figure 7 we see that in terms of flora, one of the most representative trees of this bioclimatic zone is the Willow [Figure 7a], which can measure up to 10 meters in height, has a thick trunk and abundant elongated, lanceolate leaves. and slightly toothed with abundant pendulous branches; Another tree that stands out is the Molle [Figure 7b], it is an arborescent woody tree, with evergreen leaves, being one of the most abundant species of Schinus in the Americas; finally, the Alder [Figure 7c], which is a wild and cultivated tree. This tree has a white and soft wood, being highly appreciated for the manufacture of rustic furniture. [25]

Figure 8. Fauna

In figure 8 we see that regarding the Fauna, we find three animals that are representative of the area, in the first place the Puma [Figure 8d], being the second largest feline in the American continent, after the jaguar, and the fourth largest of the world, after the tiger, and the lion; secondly, the guanaco [Figure 8e], this is an artiodactyl mammal of the Camelidae family typical of South America, it is a wild animal, as opposed to the llama (Lama glama) which is domestic; finally, the vicuña [Figure 8f], an artiodactyl mammal of the camelid or auquénido family and the group of South American camelids that lives in the Andean highlands, mainly in the Andean heights of Peru. [25]

3. RESULTS

Location:

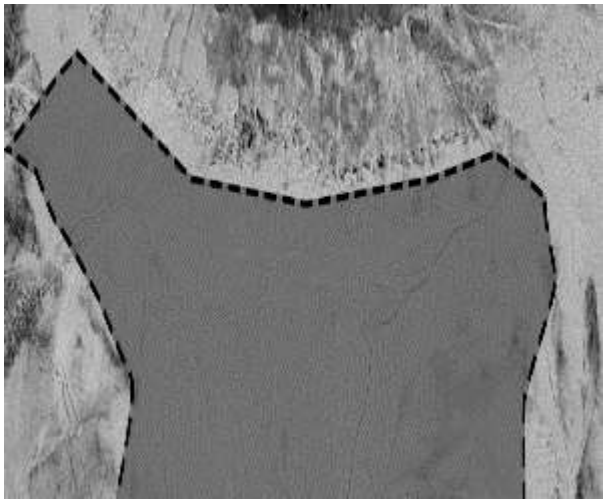

Figure 9. Altitude of the study sites.

Figure 9 shows an Altitude of 4 500 masl Latitude -17.432° and Longitude of -69.945°.

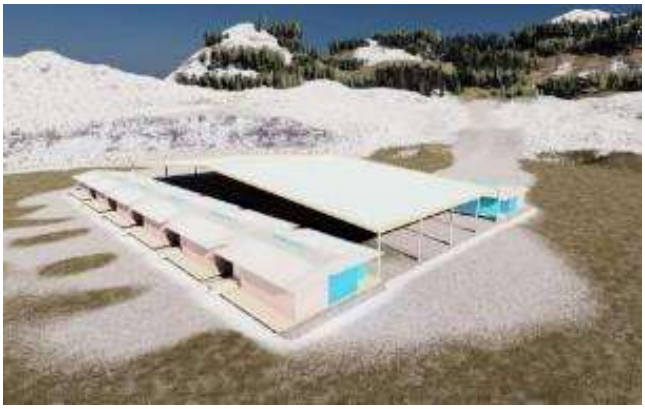

Figure 10. volumetric set.

Figure 10 shows the set formed by the housing modules.

Figure 11. Planimetry.

In figure 11, we see the distribution and composition of the dwelling. Essentially the greenhouse patio that will have the important role of capturing solar radiation and distributing it internally to its environments.

Figure 12. Materiality.

Figure 12 shows the materials used for the modules, the use of wood for the main floor and the false ceiling thanks to its thermal processing, polycarbonate for the greenhouse cover, thanks to its ability to transmit and let light through. radiation to favor the objective of the greenhouse patio, adobe for the walls due to its thermal mass, the stone that will be used on the floor of the greenhouse for its heat retention and covered with a plastic compound that will help keep the heat inside the house and reach the desired thermal comfort.

Figure 13. Strategies in the project.

Figures 13 show the first strategy applied in the proposal, this is the separation of the housing module with respect to the floor, with the aim of avoiding the cooling of the interior by frost, which is generated in this location.

Figure 14. Proposed materials.

Figures 14 show the materials used for the floors. Wood is being used outside, since, being a local material, it is easily accessible and generates less investment. In the interior, wood is used in the same way, this with the aim of maintaining the desired internal temperature. Stone is used in the greenhouse patio, with the aim of retaining the temperature to later be distributed to the different environments.

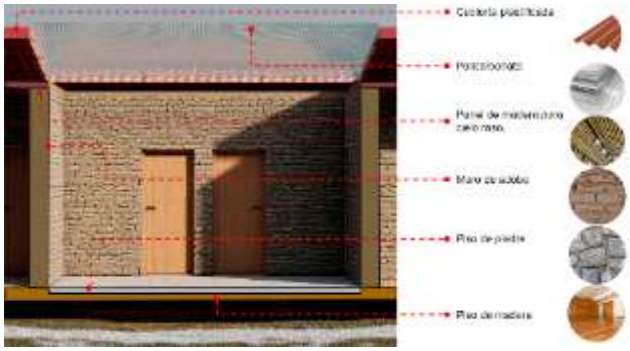

Figure 15. Materials in the greenhouse.

In figure 15 we can see the materials used for the greenhouse patio, adobe was used, due to its thermal mass, stone on the ground to retain the temperature.

Figure 16. Temperature distributors.

Figure 16 shows the perforations in the perimeter walls of the greenhouse patio, which will fulfill the function of distributors of the temperature assimilated by the greenhouse patio, towards the other environments.

Figure 17. Gable roof.

Figure 17 shows the separation between the gabled roof and the wooden platform, this will fulfill the function of retaining heat and creating a space for hot air, which will later be distributed inwards.

Figure 18. Construction system.

Figure 18 shows the components of the construction system and how they would be distributed to achieve the bioclimatic treatment that is intended.

Figure 19. Strategy in the project.

Figure 19 shows an exterior module, which is being placed on a wooden platform, which generates a separation between the interior floor and the ground floor, this as a strategy to separate the so-called "Frost" from the house, and thus be able to maintain the desired internal temperature.

Figure 20. Strategy in the project.

In figure 20 we can see the final composition of the proposal, applying strategies such as the separation of the module from the house and the natural soil, the drainage of rainwater and the materials used to generate the internal thermal comfort of the house.

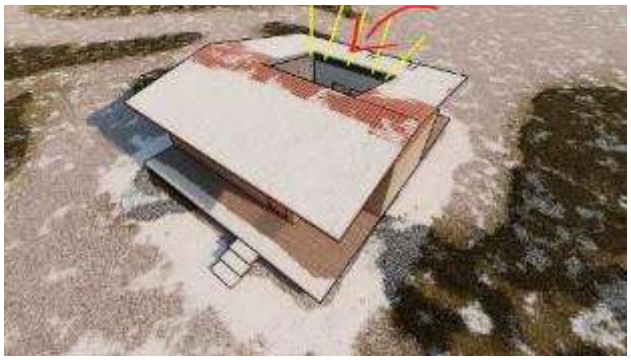

Figure 21. Lighting input.

Figure 21 shows the lighting input that is generated thanks to the greenhouse patio proposed for the housing module.

Insight:

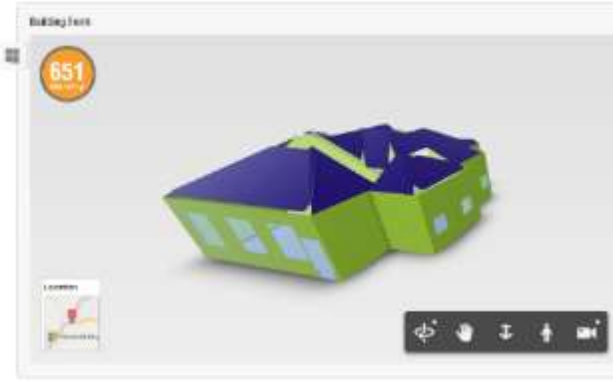

Figure 22. Modulation in the house

Figure 22 shows the modulation applied in the INSIGHT program to be able to analyze the thermal conditions used by the house, located in the location for the proposal.

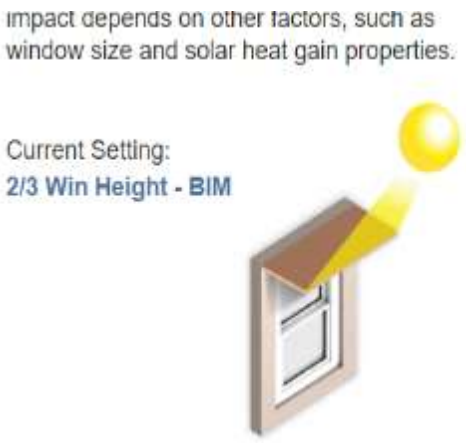

Figure 23. Window features.

The impact depends on other factors such as window dimensions and solar heat gain properties.

Figure 24. Glass properties.

The properties of the glass control the amount of heat transfer from daylight and solar heat gain into the building along with other factors.

Figure 25. Sizing of the span and the proportion.

The window to wall ratio (glazing area/gross wall area) interacts with window properties to affect daylighting, heating, and cooling.

Figure 26. Glass properties.

It represents the overall ability of roof constructions to resist heat gain and loss.

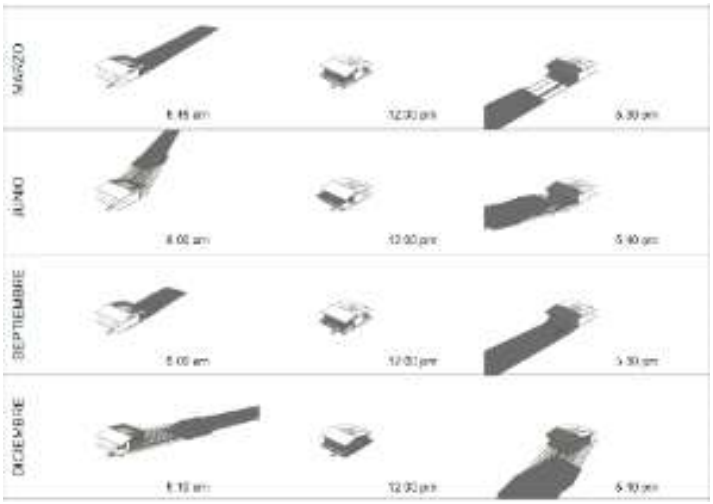

Figure 27. Solar path analysis.

Figure 27 shows the solar path analysis applied to the housing module, this in order to correctly locate the openings and make the most of the strategies applied to generate the desired thermal comfort.

4. DISCUSION

Passive air conditioning strategies through natural systems are the most appropriate option to improve the thermal conditions of habitability in adobe houses. This thanks to the easy acceptance that can be implemented in new homes as well as existing ones, without modifying the traditional characteristics of the home. [11]

Applying adobe as a base material in a high Andean construction, which is thermally conditioned, is adequate to present optimal thermal comfort conditions in the face of temperature changes. [31]

In the design of homes in high Andean areas, where frost occurs, it would be appropriate to use internal heat sources, such as the use of a study, with intermediate technologies, to give an example. These increase the internal temperature gain by 32%. These could be generated through alternative energies to electricity and fuel, such as the use of biomass and derivatives of the transformation of fecal and vegetable residues. [29]

The constructions through the adobe construction system, it is appropriate to take into account and apply the E. 080 standard design and construction with reinforced earth and through these indications, obtain safe buildings, with the correct use of materials, proper location and orientation of openings, etc. [9]

5. CONCLUSION

The contribution of this research is to propose bioclimatic strategies to solve the main problem of the town of Tarata in Tacna. Which would be the extreme weather.

For which, air conditioning and thermal gain strategies were taken through materials and characteristics applied to the house, such as a greenhouse patio and a separation space between the slab and the natural soil in order to avoid direct contact with frost.

In conclusion, it can be affirmed that the strategies applied for the house are the most appropriate to improve the internal temperature of the houses in the town of Tarata in Tacna, since, thanks to the materials used such as adobe, due to its thermal mass and its ability to retain internal temperature and not allow cold temperatures to enter, and the use of rock for greater retention of internal temperature in the composition of the greenhouse patio.

The houses made with adobe in the area are mostly self-built thanks to the ease of access of the material, however, this is done empirically, so there are no climatic considerations or strategies that help generate thermal comfort. . The houses also do not have any finishing time, more than adobe, so the use of wood, for example, would help to better retain temperature in their environments.

Acknowledgment

We want to express our special thanks and gratitude to the colleagues who gave us the golden opportunity to carry out this wonderful project on the subject of Bioclimatic Design Strategies in social housing for cold climates. We also thank the Ricardo Palma University (URP) for everything we have learned.

References

[1] Bugenings, L.A.; Kamari, A. (2022) Bioclimatic Architecture Strategies in Denmark: A Review of Current and Future Directions. Buildings 2022, 12, 224. ttps://doi.org/10.3390/buildings 12020224
[2] Cantú Martínez, P. C. (2012). Sustentabilidad ecológica; Crisis ambiental: desconocimiento del conocimiento. Ciencia UANL, 15(58), 20-27.
[3] Espinoza Paredes, R. L., Saavedra, G., Huaylla, F., Gutarra, A., Molina Fuertes, J. O., Barrionuevo, R., & Lau, L. (2009). Evaluación experimental de cambios constructivos para lograr confort térmico en una vivienda Altoandina del Perú. Avances en Energías Renovables y Medio Ambiente, 13.
[4] Universidad Católica de Santa María. (2018, mayo 11). En el territorio nacional se desarrollan 28 de los 32 tipos de climas existentes en el mundo - Universidad Católica de Santa María. Universidad Católica de Santa María. https://www.ucsm.edu.pe/en-el-territorio-nacional-se-desarrolla-28-de-los-32-tipos-de-climas-existentes-en-el-mundo/
[5] Poma Garcia, J. L., Garay, L., & Romero, K. (2019). Estudio climático en la región alto-andina y el análisis de indicadores bioclimáticos de aplicación potencial en el diseño arquitectónico. In XIII CTV 2019 Proceedings: XIII International Conference on Virtual Cityand Territory:"Challenges and paradigms of the contemporary city": UPC, Barcelona, October 2-4, 2019. Centre de Política de Sol i Valoracions, CPSV/Universitat Politècnica de Catalunya, UPC.
[6] Barreda Fuentes, D. D., & Castro Bustamante, M. Modelo de Infrastructures Educativa para Zonas Alto Andinas a 4000 msnm, Imata–Arequipa.
[7] Clima de Tarata. (2021). SENAMHI. https://www.senamhi.gob.pe/?p=pronostico-detalle&dp=23&localidad=0163
[8] Wiesenfeld, E. (2011). La autoconstrucción: Un estudio psicosocial del significado de la vivienda. Fondo Editorial Humanidades.
[9] Nonajulca Lopez, C. D. (2019). El confort arquitectónico de la vivienda rural altoandina de la meseta andina, como herramienta para una arquitectura bioclimática (caso de estudio comunidad campesina de arenales, meseta andina, Frias-Ayabaca-Piura), 2019. *
[10] RPP. (2018, julio 23). Habitantes de sur peruano soporta hasta 16.7 grados bajo cero por las heladas. RPP. https://rpp.pe/peru/actualidad/habitantes-de-sur-peruano-soportan-hasta-167-grados-bajo-cero-por-las-heladas-noticia-1138616?ref=rpp
[11] Umán Juarez, S. J. (2019). Estrategias de climatización pasiva y confort térmico en la vivienda de adobe en la zona rural

de Anta-Cusco, 2017.
[12] Atalaya Tafur, B. D. (2021). Aplicación de sistemas de acondicionamiento ambiental en la construcción no convencional de adobe en las zonas rurales andinas de Ancash.
[13] E. D. O. Patricio Cevallos, Jorge Ramón, Francisco Trigueros, Arquitectura de tierra. Patrimonio y sustentabilidad en regiones sísmicas. 2014.
[14] C. Moncloa, "Confort Térmico: Un sistema aislante para la vivienda alto andina fabricado con materiales reciclados," Modul. Arquit., vol. 18, no. 1, pp. 73–90, 2017, doi: 10.17981/mod.arq.cuc.18.1.2017.04
[15] Indeci (2018)
[16] S. A. EDITORA PERÚ, E. P. (s/f). Temperatura llega a -19 grados Celsius en distritos de Arequipa y Tarata. Andina.pe. Recuperado el 9 de mayo de 2022, de https://andina.pe/Agencia/noticia-temperatura-llega-a-19-grados-celsius-distritos-arequipa-y-tarata-723897.aspx
[17] Wieser, M., Rodríguez-Larraín, S., & Onnis, S. (2021). Estrategias bioclimáticas para clima frío tropical de altura. Validación de prototipo en Orduña, Puno, Perú. Estoa. Revista de la Facultad de Arquitectura y Urbanismo de la Universidad de Cuenca, 10(19), 10-21.
[18] Catunta Mamani, R. N. (2016). Diseño de un complejo turístico termal–recreacional y de descanso, para incrementar el flujo turístico en los baños terminales de Putina–Ticaco, provincia de Tarata, Tacna.
[19] CORDOVA, A. I. M., & MENDOZA, R. R. R. PROPUESTA DE UN SISTEMA CONSTRUCTIVO EN BASE A PANELES ESTRUCTURALES NO CONVENCIONALES PARA VIVIENDAS UNIFAMILIARES EN EL CASERÍO DE CHUAPALCA, DISTRITO DE TARATA, PROVINCIA DE TARATA EN LA REGIÓN DE TACNA–PERÚ.
[20] Carrazco Cota, C., & Morillón Gálvez, D. (2004). Adecuación bioclimática de la vivienda de interés social del noroeste de México con base al análisis térmico de la arquitectura vernácula. Avances en Energías Renovables y Medio Ambiente, 8.
[21] Paredes, R. E. L. (2020). Evaluación experimental de cambios constructivos para lograr confort térmico en una vivienda altoandina del Perú. REPOSITORIO INSTITUCIONAL DE LA UNLP. http://sedici.unlp.edu.ar/handle/10915/97335
[22] El clima en Tarata, el tiempo por mes, temperatura promedio (Perú) - Weather Spark. (s/f). Weatherspark.com. Recuperado el 18 de mayo de 2022, de https://es.weatherspark.com/y/26555/Clima-promedio-en-Tarata-Per%C3%BA-durante-todo-el-a%C3%B1o
[23] Michaelaschludecker. (2022, mayo 12). Tiempo Tarata. meteoblue. https://www.meteoblue.com/es/tiempo/semana/tarata_per%C3%BA_3927774
[24] Caso Peruano Martín, E., Rey, W., Ledgard, R., & Ruiz, I. (s/f). Edu.pe. Recuperado el 18 de mayo de 2022, de https://repositorio.pucp.edu.pe/index/bitstream/handle/123456789/28699/CUADERNOS-14-digi.pdf?sequence=1
[25] Excellent group. (s/f). Municipalidad Distrital de Palca - Tacna. Gob.pe. Recuperado el 18 de mayo de 2022, de https://www.munipalca.gob.pe/web/distrito.php?id=3
[26] (Tarata · 23200, Peru. (s/f). Tarata · 23200, Peru. Recuperado el 18 de mayo de 2022, de https://www.google.com/maps/place/Tarata+23200/@-17.4280525,-69.948683,2134m/data=!3m1!1e3!4m5!3m4!1s0x915b15e21679a3e9:0x92aed6187f2e7f40!8m2!3d-17.4776078!4d-70.0339387
[27] Análisis de sensibilidad de estrategias de diseño pasivo para edificios residenciales en climas semiáridos fríos
[28] Facebook. (s/f). Facebook.com. Recuperado el 11 de junio de 2022, de https://www.facebook.com/arquitecturaciclica/photos/a.1425336294432784/2501980586768344/?type=3&theater
[29] Cuéllar Cajahuaringa, J. N. (2017). Estudio para el acondicionamiento térmico de viviendas sometidas a heladas. caso: centro poblado de Santa Rosa (Puno).
[30] Saavedra Salazar, G. G. (2014). Diseño, construcción y evaluación térmica de un módulo de vivienda rural en la localidad de Vilcallamas Arriba, distrito de Pisacoma, provincia Chucuito, región Puno (Doctoral dissertation, Universidad Nacional de Ingeniería).
[31] Flores Cervantes, N. R. (2018). Acondicionamiento térmico en viviendas de adobe Ubicados a más de 3800 msnm en la Región Puno.
[32] Parque Chura, E. R. (2022). Modelamiento de viviendas rurales bioclimatizadas para optimizar el confort térmico a más de 4000 msnm Picotani-Puno 2022.

RIGA 2023

Design of the Tubercle Leading Edge Blade for Small-Scale Wind Turbines

Chung-Neng Huang
National University of Tainan, Tainan, Taiwan, kosono@mail.nutn.edu.tw, ORCID: 0000-0001-9556-2791

Yi-Lun Tsai
National University of Tainan, Tainan, Taiwan, diauson.service@gmail.com, ORCID: 0000-0002-6349-9123

Jenn-Kun Kuo
National Sun Yat-Sen University, Kaohsiung, Taiwan, jenn.kun@mail.nsysu.edu.tw, ORCID:0000-0001-7134-1230

Cite this paper as: *Huang, CN, Tsai, Y, Kuo, JK. Design of the Tubercle Leading Edge Blade for small-scale wind turbines. 11. Eur. Conf. Ren. Energy Sys. 18-20 May 2023, Riga, Latvia*

Abstract: The limit of blade length and poor operation condition block the development of small-scale wind turbines (SSWTs). In order to improve the wind-capturing capacity for SSWTs, first, the concept of Tubercle Leading Edge (TLE) is adopted in this study to conduct the blade design. Next, for edge of a TLE blade is not smooth and undulating, the Blade Element Momentum Theory (BEMT) is used to calculate the generating torque of a blade. Third, the Taguchi's method involved in ANSYS simulation is used to find the optimal TLE parameters. Here, the wing features form three species of birds are chosen to be the control factors in the Taguchi's optimization. Through the Taguchi's optimization, it found that about 10.74% of the torque increasement can be achieved, and the coverage of TLE is the most important design factor. Finally, the simulation platform is setup to conduct tests for evaluating the performance of the TLE blade. The computational fluid dynamic (CFD) results proved that the optimal design on the TLE blade is feasible and reproduceable.

Keywords: *small-scale wind turbines (SSWTs), Tubercle Leading Edge (TLE), wind-capturing capacity, Taguchi's method, computational fluid dynamic (CFD).*

1. INTRODUCTION

With the economic development of each country and the exponential growth of the world population every year, the global demand for energy is increasing. In order to generate more energy, countries rely on fossil fuels. However, the use of fossil fuels increases the environmental pollution, especially carbon dioxide [1]. Therefore, how to achieve a balance between economic development and environmental protection, such as developing low-carbon economy, renewable energy or improving energy conversion efficiency, has become a common topic of all countries in the world. As the carbon emission of wind power generation is far lower than other renewable energy sources, wind power is the most competitive among renewable energy sources. In recent years, various large-scale wind farms have been newly built or expanded on land or offshore in various countries. However, the cost and price of new construction or maintenance of large-scale wind farms are high, and some key components are difficult to obtain, so some countries turn to develop small-scale wind turbines (SSWTs), attracting more and more attention in recent years [2].

According to the wind energy formula $P_w = 1/2\rho\pi R^2V^3$, when setting up SSWTs, there generally tend to consider in two directions: first, set SSWTs on the roof of buildings to increase the height to intercept the larger wind speed V [4]. The other is to increase the swept area of the fan at low wind speed to improve its wind capture capability [3], such as increasing the number of blades B and the size of blades R to improve the wind capture capability. However, in this process, the number, material, length and weight of fan blades will directly affect the efficiency

of power generation and the cost of setting. Pourrajabian, A. et al. [5] discussed the optimization of wind turbine start-up time through numerical simulation, and found that increasing the number of blades can reduce the start-up time of SSWTs and also increase the power coefficient. However, the authors also proposes that the increase in the number of blades will increase the overall energy consumption of the system, while also increasing the overall cost of the system. Bukała, J. et al. [3] proposed that increasing the number of blades may slightly improve the aerodynamic efficiency, but greatly increase the quality and material cost. Under the trade-off between the two (improving aerodynamic efficiency and process cost), the authors think that it exceeds the gains obtained. The more blades there are, though the more power they generate. However, due to the interference between blades, a large number of blades will reduce the efficiency of the fan [6]. Ahmadi Asl, H., R., et al. [7] believe that increasing the blade number will reduce the lift force and speed on each blade, while the rotation speed and torque are important parameters, and the authors suggested that the blade number should be selected with good torque and acceptable speed. Verma et al. [8] proposed that increasing the blade length increases the energy output per unit of sweep area of the blade. From the perspective of efficiency output, this would be the best choice. However, as the blade size becomes longer and larger, the blade weight and gravity load also increase [9], which poses major challenges and concerns for the blade material and the life cycle of the fan, including structural design, manufacturing, and installation stages. In terms of material properties, the stronger blades will not bend too much when rotating and make the blades heavier, which means that more lifting force is required to drive the turbine [10].

Due to the existence of terrain and obstacles in the suburban areas where are easy to cause intermittent and low-speed winds. Therefore, it is necessary to improve the energy capturing capacity of SSWTs at low-speed wind to achieve high torque performance. In order to achieve this target, it usually needs to be done through the blade design. Although the main target in designing a wind blade is to maximize its power coefficient [11], power output is not the only consideration in the design of SSWTs. The factors such as start-up time (cut-in speed), reliability and cost-effectiveness etc. that also must be put into the consideration [12]. In the view of abovementioned, this study will use the Blade Element Momentum Theory (BEMT) combined with bionic technology and Taguchi's method to redesign and optimize the standard blade to improve its aerodynamic performance while maintaining the minimum change in blade weight.

The excellent flying ability of birds is not only related to the skeleton structure that can have a wide range of wing changes, but also closely related to the wing structure composed of many feathers [13]. First, it is observed that the feather size arrangement of birds' wings is gradually shrinking from the outer edge of wings to the body and in different shapes. Feather Size is selected as the first design variable. Secondly, the feather density arrangement of birds varies with species, and it is selected as the design variable; in the end, the coverage of the feathers that are with more prominent shape is used as the third design variable to discuss their respective effect on windmill performance.

Due to the complex geometric design of the blades and involving many non-linear mathematical models, although the optimization parameters can be obtained by simulation calculations to improve the aerodynamic performance of the blades, for the excessively complex structure, the manufacturing is too costly to implement. However, there is no such a problem in small horizontal-axis windmill. Therefore, this study will use the Taguchi's method to statistically analyze the optimal TLE parameters to maximize the blade performance, and use 3D printing to mold the optimized TLE blades and assembly them to be the windmill. A lot of physical tests will be conducted through the test platform to verify the feasibility and reproductivity of this design.

2. BLADE ELEMENT MOMENTUM THEORY (BEMT)

The BEMT was proposed by Glauert in 1935. It combines the momentum theory and the blade element theory. It is widely used in the analysis and design of wind turbines. It provides hydrodynamic design of blades and evaluates the performance of wind turbines. In this method, the blade R is divided into several segments along the direction of the blade tip. As shown in Fig. 1, where r_i is the blade radius of the i-th section, C_i is the blade chord length of the i-th section, and dr is the section length. These segments are called elements, and assumed that there is no aerodynamic interaction between these elements. By adding the force and moment, which are acting on each element, then the total force and torque, acting on the wind turbine, can be found.

The definition of the blade section is shown in Fig. 2. Chord Length C is the straight line connecting the leading edge and the trailing edge; U_{rel} is the relative wind speed; Vs is the wind speed; ω is the angular rotation speed of the wind turbine; φ is the angle relative to the wind speed; α is the angle of attack (AOA) between the chord length and U_{rel}; θ is the pitch angle between the chord length and the blade rotation plane; C_{mol} is Lift Coefficient perpendicular to U_{rel}; C_D is drag Coefficient parallel to U_{rel}; dF_N is normal force called thrust; dF_T is tangential force of torque dQ.

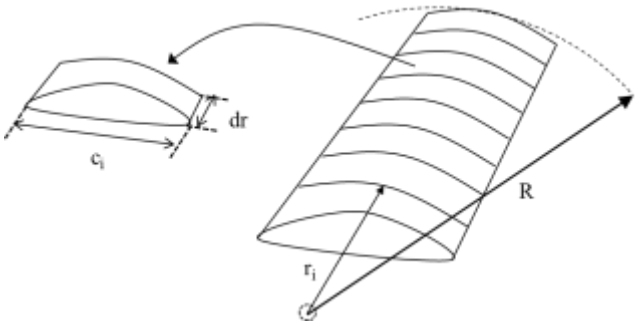

Figure 1. Schematic diagram of blade elements

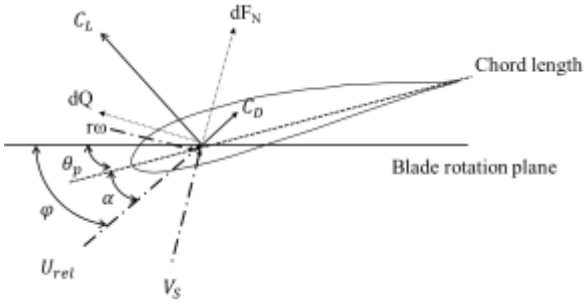

Figure 2. Definition of blade section

Airfoil selection and characteristics:

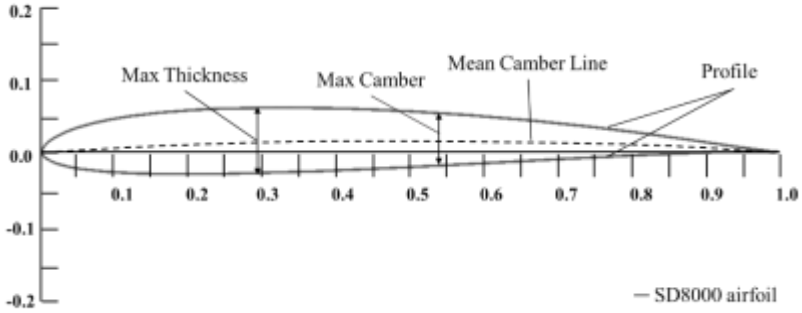

Figure 3. SD8000 airfoil

The numerator of the Reynolds number (*Re*) is the inertial force of the fluid, and the denominator is its viscous force. Since airfoils are characterized with a specific *Re* range and inherent in different performances [14]. Among them, the SD8000 airfoil has a maximum thickness and a maximum curvature at 29.4% and 54% chord length, respectively (Fig. 3). Through Xfoil simulation shows that the SD8000 has excellent lift drag ratio natures in low-*Re*, can produce higher power coefficient. In addition, the thin-style feature of SD8000 makes it lighter to be suitable for horizontal SSWTs. Therefore, the SD8000 airfoil is selected for design planning and research in this study.

Geometrical calculations of blade:

In this study, the BEMT is applied to the design of wind turbine blades. The design procedure is as follows;

First, the blade length (R) must be determined before blade design, which can be found by the following equation;

$$R = \sqrt{\frac{2 \cdot p_{rat}}{\rho \cdot {v_{rat}}^3 \cdot \pi \cdot c_p}} \qquad (1)$$

where, in this study, the parameters of Eq.(1) are given as; the air density ρ is 1.225 (kg / m3), and the rated wind speed V_{rat} is 4 (m / s). According to the Betz limit, the maximum power coefficient *Cp* is 0.593, and which can be expressed as;

$$C_P = \frac{blade\ power}{wind\ energy} = \frac{torque \times \omega}{\frac{1}{2}\rho\pi R^2 {v_s}^3} \quad (2)$$

However, wind turbines are generally with some energy consumption and wake effects, cannot achieve the maximum *Cp*. In general, the power coefficient is often between 0.3-0.4[15, 16]. *Cp* is set to 0.34. Under the condition of the maximum power P_{max} is 480W and by substituting the above setting into Eq. (1), R = 0.42m is obtained.

The windmill radius is composed of blade length R and hub length H. As shown in Fig.1, the blade rotational radius r_i of the ith section can be defined as;

$$r_i = \frac{R-h}{9} \times (i-1) + h \quad (3)$$

where, the blade length R is divided into 10 elements and the hub length H is set to 0.08m in this study.

Tip Speed Ratio (TSR), λ, is the ratio of tip speed to wind speed, and it is one of the important reference parameters for evaluating the performance of wind turbines. TSR is defined as;

$$\lambda = \frac{R\omega}{V_s} = \frac{2\pi R\, {}^{N}/_{60}}{V_s} \quad (4)$$

where ω is the rotational angular velocity of the wind turbine in rad / s and *N* is the rotational speed in rpm. In this study, λ is set at 4. The TSR of each blade section, λr, is defined as;

$$\lambda_{ri} = \lambda\left(\frac{r_i}{R}\right) \quad (5)$$

Regarding the angle of relative wind φ, the following geometric relationship can be considered from Fig 2.

$$tan\,\varphi = \frac{V_s(1-a)}{\omega r(1+a')} = \frac{1-a}{(1+a')\lambda_r} \quad (6)$$

where under the condition of a '= 0 in no wake rotation and a = 1/3 with the Betz optimum rotor [17, 18], can obtain;

$$tan\,\varphi = \frac{2}{3\lambda_r} \quad (7)$$

Therefore, the angle of relative wind speed angle φi of each blade section can be expressed as;

$$\varphi_i = tan^{-1}\left(\frac{2}{3 \cdot \lambda_{ri}}\right) \quad (8)$$

According to Fig. 2, the angle of relative wind speed φ is the sum of the pitch angle θp and the angle of attack α. After conversion, the pitch angle (θpi) of each blade section can be calculated as

$$\theta_{pi} = \varphi_i - \alpha \quad (9)$$

In order to obtain a better-than-average blade performance, the XFOIL software was used to simulate the SD8000 airfoil for the maximum lift-drag ratio, which could be achieved when the angle of attack is 5 °. Then, substituting the values of λ_{ri} and φ_i obtained above into the following equation, the corresponding chord length C_i can be obtained.

$$c_i = \frac{8\pi r_i sin\varphi_i}{3BC_L\lambda_{ri}} \quad (10)$$

where, B is the blade number, and generally the blade number of a windmill is 3. This study takes this as the parameter value and the total lift coefficient of blade C_l is fixed at 1[15, 16].

The geometric parameters of each blade section can be obtained through above equations and shown in Table1.

Table 1. Geometrical characteristics of each blade section

Section	Radius r_i [m]	Chord length C_i [m]	Pitch angle θpi [degree]
1	0.080	0.0663	0.0000
2	0.118	0.0801	22.0000
3	0.156	0.1003	18.0000
4	0.193	0.0998	14.9000
5	0.231	0.0850	11.8508
6	0.269	0.0739	9.5920
7	0.307	0.0653	7.8581
8	0.344	0.0584	6.4875
9	0.382	0.0528	5.3781
10	0.420	0.0482	4.4623

Based on the above geometrical parameters, the total torque Q, which is generated and accumulated by each blade section can be calculated by follows;

$$Q = \sum_{i=1}^{10} \frac{1}{2} B\rho\ U_{rel}^2 r_i \left(C_L^{(i)}\ sin\ \varphi_i - C_D^{(i)}\ cos\ \varphi_i\right)\ C_i dr \quad (11)$$

where, φ_i is the relative wind speed angle, and c_i is the chord length of the i-th dr, respectively. Besides, the relative wind velocity U_{rel} can be expressed as

$$U_{rel}^2 = (r\omega)^2 + \left(\frac{2}{3}V_s\right)^2 \quad (12)$$

and $C_L^{(i)}$ and $C_D^{(i)}$ are the lift and drag coefficients as follows;

$$C_L^{(i)} = \frac{\frac{L}{s}}{\frac{1}{2}U\ Re\ \mu} \quad (13)$$

$$C_D^{(i)} = \frac{\frac{D}{s}}{\frac{1}{2}\ U\ Re\ \mu} \quad (14)$$

where, L and D is lift and drag forces respectively, s is airfoil span, U is free stream velocity, μ is dynamic viscosity, and Re is the Reynolds number which can be expressed as;

$$Re = \frac{\rho\, U\, D_C}{\mu} \tag{15}$$

where, D_c is the diameter of cylindrical flow field.

3. BIONIC DESIGN AND TAGUCHI'S OPTIMIZATION

TLE parameters based on the nature of birds' wings:

In order to improve the wind capture capacity for blades at low-wind speed, the bionic design by using TLE concept is proposed. As shown in Fig. 4, the key parameters of the TLE including amplitude, wavelength and coverage are considered. According to previous studies [11, 13], above parameters that do affect the blades' performance.

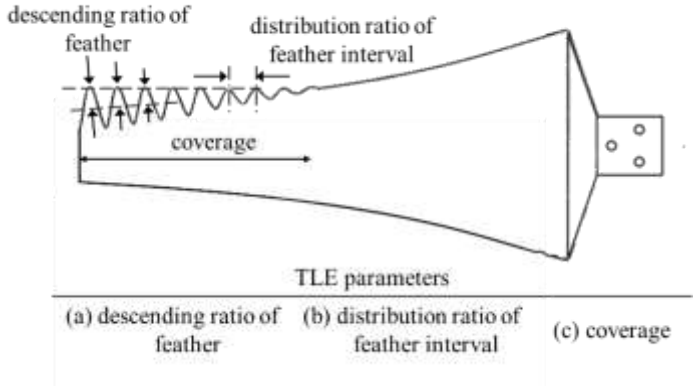

Figure 4. Bionic blade with the TLE of imitating bird's wing and important factors

The feather length of the bird's wings is gradually shortening from the outer edge of the wings to the body. Therefore, this study imitated this nature to arrange the parameters of the TLE from the tip to the end of the blade. As shown in Fig. 4, the important factors of the TLE, including the descending ratio of feather, the distribution ratio of feather interval and the coverage ratio.

Determination of the optimal TLE parameters based on the Taguchi's method:

The orthogonal Array (OA) of the Taguchi's method is constructed based on the statistical principles. Through OA the optimal combination of TLE parameters can be found with the least number of experiments. It is helpful to the Taguchi's method to identify what degree of each TLE parameter is influent on the fitness function. In order to find out the optimal combination of TLE parameters which can generate the-larger-the-better value of fitness function such as the output torque and the signal-to-noise ratio (S/N) as follows;

$$S/N = -10\log\frac{S}{n} \tag{16}$$

$$\bar{y} = \frac{\sum_{i=1}^{n} y_i}{n} \tag{17}$$

$$S = \sqrt{\frac{\sum_{i=1}^{n}(y_i - \bar{y})^2}{n-1}} \tag{18}$$

where, n is the total number of experiments, S is the standard deviation of n measurements, y_i is the i-th quality measurement, and $\bar{y}$ is the average of n measurement. The larger the S/N ratio is, the smaller the variance of quality characteristics is and the closer to the optimal target is.

The design procedure of the Taguchi's method is set as follows;

step1: problem formulation, determine the TLE parameters such as the control factors and their alternative levels to approach the-larger-the-better output.

step2: experimental design, select the orthogonal array and conduct experiment subject to the fitness function.

step3: analysis of variance (ANOVA), analyze variances of outputs and predict the optimal levels for the control factors.

Step4: criterion validity, if the output performances achieved the criterion validity then end the experiment, if not, revise the level ranges and go the step 2.

In order to match the size of the SD-8000 airfoil, the wing features of three species of birds such as the barn owl, the rock pigeon and the Eurasian sparrow hawk (in Fig. 5) were adopted to design the TLE blade.

Among them, the barn owl has a wing length of 0.45 m, which is similar to the blade length R = 0.42 m calculated above. The rock pigeon, whose wing length is 0.29 m less than the barn owl, and the Eurasian sparrow hawk has the shortest wings of 20.8cm.

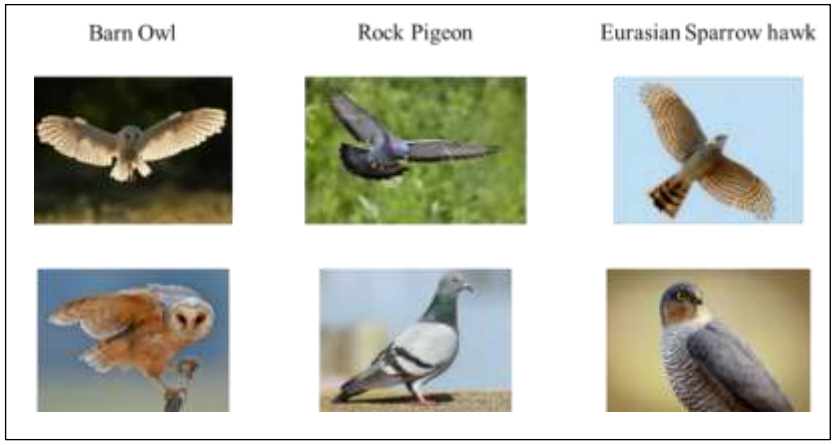

Figure 5. Three species of birds

(Barn Owl: Marko König, https://www.featherbase.info/; Rock Pigeon: Laitche, https://commons.wikimedia.org/; Eurasian Sparrow Hawk: Klaus-Dieter Franzke, https://www.featherbase.info/)

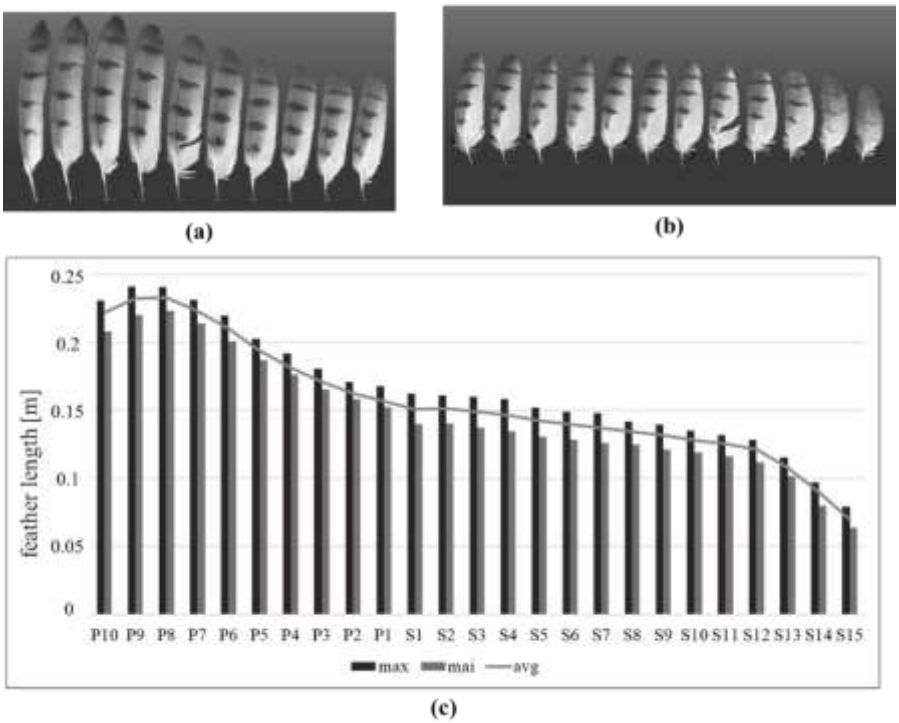

Figure 6. wing feathers of a barn owl（a） primary feathers（b）secondary feathers（c）bar and curve chart

Although the number and size of feathers of birds depends on the species and even if they are in the same species, will be different. Fig. 6 (a) to (c) show the feathers on the lower edges of the wings and their arrangements of a barn owl. In the figures, (a) and (b) show the arrangements of primary and secondary feathers, respectively. In (c), they are bar and curve charts of feather length and arrangement respected to (a) and (b). Where, the vertical axis represents the feather length and the horizontal axis shows the feather arrangement in number sequence from P10 to P1 and S1 to S15. Table 2 shows the feature parameters respect to the three birds, including number of feathers, wing length, length of maximum and minimum feathers.

By using the features in Table II, three control factors as (a) descending ratio of feather length; (b) distribution ratio of feather interval; (c) coverage were set as follows and illustrated in Fig. 7.

Table 2. feature parameters of three birds

parameters	barn owl	rock pigeon	Eurasian sparrow hawk
number of feathers n	22	24	21
wing length w [m]	0.45	0.290	0.208
the maximum feather f_{max} [m]	0.2324	0.1826	0.1835
the minimum feather f_{min} [m]	0.0701	0.0625	0.0403

Through the definitions to the three control factors, the three levels respect to the three factors based on the three birds were calculated and summarized in Table 3.

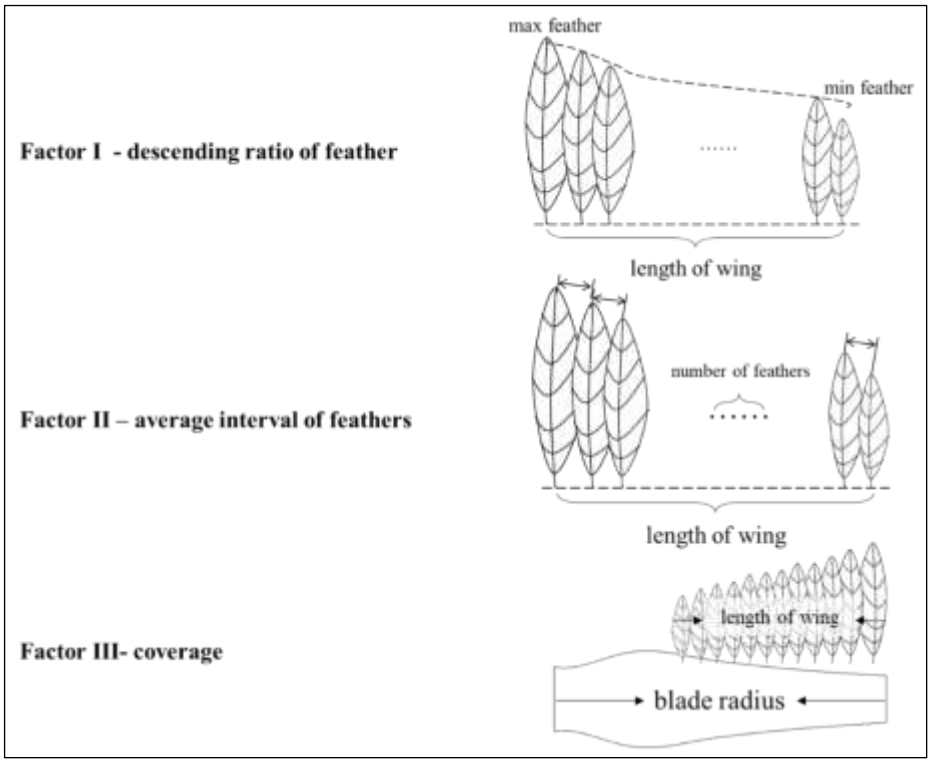

Figure 7. three controllable factors

Table 3. Three levels subject to three control factors

control factors		barn owl	rock pigeon	Eurasian sparrow hawk
		level 1	level 2	level 3
I	*drf*	0.361	0.414	0.688
II	*aif* [m]	0.0191	0.0121	0.0099
III	*tcr* [%]	100	69	49.5

Table 4. experiment sets, results, mean, MSD, and S/N

trial number	factor			TSR changes and results									$\bar{y}$	MSD	S/N
	A	B	C	1.5	2	2.5	3	3.5	4	4.5	5	5.5			
1	1	1	1	0.1010	0.1246	0.1447	0.1677	0.1882	0.1897	0.1785	0.1598	0.1505	0.1488	56.148	-17.493
2	1	2	2	0.0969	0.1169	0.1388	0.1599	0.1766	0.1772	0.1651	0.1462	0.1336	0.1393	62.385	-17.951
3	1	3	3	0.0901	0.1206	0.1491	0.1823	0.2097	0.2116	0.1962	0.1737	0.1537	0.1560	59.863	-17.772
4	2	1	2	0.0880	0.1198	0.1453	0.1721	0.1963	0.2034	0.1918	0.1714	0.1614	0.1526	59.972	-17.780
5	2	2	3	0.0942	0.1298	0.1579	0.1880	0.2158	0.2213	0.1980	0.1731	0.1591	0.1612	55.896	-17.474
6	2	3	1	0.1023	0.1332	0.1354	0.1436	0.1511	0.1437	0.1279	0.1110	0.0893	0.1208	81.377	-19.105
7	3	1	3	0.1149	0.1306	0.1630	0.1998	0.2303	0.2338	0.2184	0.1964	0.1710	0.1742	45.776	-16.606
8	3	2	1	0.0951	0.1114	0.1177	0.1237	0.1330	0.1305	0.1183	0.1062	0.1030	0.1123	83.872	-19.236
9	3	3	2	0.0913	0.1150	0.1320	0.1507	0.1682	0.1706	0.1579	0.1367	0.1196	0.1315	71.960	-18.571

It is known that a total of 9 experiments were done based on the experiment design in Table IV. Then according to the experimented data, the response tables and graphs were made to carry out the ANOVA and evaluate the influence of each factor.

4. SIMULATION AND ANALYSIS

In this study, ANSYS fluent 14.5 was used to simulate the CFD (computational fluid dynamic) analysis. In ANSYS fluent, RANS (Reynolds Averaged Navier-Stokes Equation) is used to be the governing equation. Since the RANS turbulence model is one of the most popular methods which can illustrate the aerodynamic properties for predicting the air fluidity around the wind turbine [19]. Moreover, the SST k-ω has high accuracy in three-dimensional wind turbine performance simulation [20]. Therefore, the SST k-ω turbulence model is used to solve the RANS equation, the SIMPLE (Semi Implicit Method for Pressure Linked Equations) is selected to solve the pressure and velocity coupling, and the second-order upwind method is used to discretize, until the computation converged.

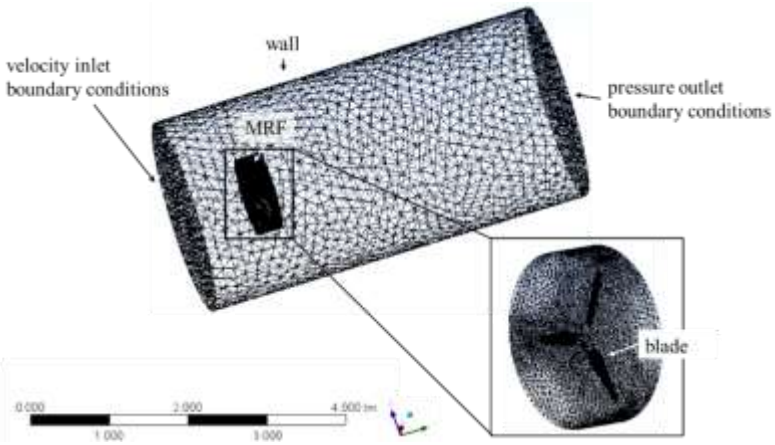

Figure 8. Tet mesh scheme

As shown in Fig. 8, the CFD computational field of this study is consisted by two cylinders. Where, the small one is the rotating fluid space in which a moving reference frame (MRF)will be built and connected to the blade to simulate rotation. Its area radius is the length of the blade. In addition, the Boolean algebra computation is used to cut the blade entity and leave the virtual boundary only with the MRF area for simulation. The large one is the surrounding space and its radius, upstream and downstream lengths are set at 4 times, 5 times, and 10 times of the blade length, respectively [19-20]. In addition, the boundary conditions are set as; the wind velocity of inlet (upstream) is 4m/s, wind pressure of outlet (downstream) is 0 pa (same as the atmospheric pressure), external wall is the translational wall motion with slip condition, blade is the rotational wall motion with no-slip condition, and the rotational velocity of MRF is between 150~600 rpm.

Taguchi's experiments:

The purpose of this experiment is to find the optimal parameters to design the TLE blades so that the windmill can get the maximum torque under low wind speed conditions. According to the relative wind speed U_{rel} in the blade torque formula (12), it is calculated based on a rotational angular speed ω of a windmill under a wind speed. In this study, under the rated wind speed is set at 4m/s, since each value of the rotation angular velocity ω corresponds to a blade TSR λ (4), so this study changes the blade TSR λ to conduct simulation experiments. Since the TSR values used in designing SSWT is generally set in the testing range from 1.5 to 5.5 [21],[22], where taking 0.5 as a changing interval, 8 sets of experiments have been done. The average mean, MSD, and S/N ratio values of all levels are also calculated and tabulated in Table IV.

The larger S/N ratio and average mean correspond to better robustness and quality characteristics, respectively, the largest values of them are employed in this study. According to the average mean and S/N ratio values of all levels calculated in Table V and VI, the optimal level setting is $A_1B_1C_3$.

Table 5. response table for S/N

	A	B	C
LEVEL1	-17.739	-17.293	-18.612
LEVEL2	-18.119	-18.220	-18.100
LEVEL3	-18.138	-18.482	-17.284
$E^{1\rightarrow2}$	-0.381	-0.927	0.511
$E^{2\rightarrow3}$	-0.018	-0.262	0.817
Range	0.399	1.189	1.328
Rank	3	2	1

Table 6. response table for means

	A	B	C
LEVEL1	0.1480	0.1585	0.1273
LEVEL2	0.1449	0.1376	0.1411
LEVEL3	0.1393	0.1361	0.1638
$E^{1\rightarrow2}$	-0.0032	-0.0209	0.0138
$E^{2\rightarrow3}$	-0.0056	-0.0015	0.0227
Range	0.0087	0.0224	0.0365
Rank	3	2	1

The aim of ANOVA in this study is to evaluate the importance of TLE parameters on generating the blade torque. It gives a clear graph to manifest how far the TLE parameters affect the response and the level of significance of the factor considered. The results from ANOVA are shown in Table VII which is based on Table V and VI. Statistically, the verification value *F* indicates which design parameter is with more significant effect on the quality characteristic. In this study, the TLE coverage and the average interval of feathers are highly significant factors which play the dominate roles in generating torque by a TLE blade.

Table 7. ANOVA

Factor	DOF	SS	Var	F	Confidence
A	2	0.3048	0.152	0.965	5.7%
B	2	2.3431	1.172	7.422	43.9%
C	2	2.6904	1.345	8.522	50.4%
Error	2	0.3157	0.158		
Total	8	5.6541		16.909	100.0%

In order to confirm the accurateness of the optimal design in abovementioned, the ANSYS simulation was conducted again based on the optimal parameters A1, B1, and C3. The results were calculated and compared with the one based on the standard blade (without TLE) and the one subject to the trail no. 7 in the Taguchi's experiment (in Table IV) which performs higher characteristics as shown in Table VIII. It can find that the optimal design with better performance than the other two. Moreover, the S/N ratio resulted from the optimal parameters was -15.799 and to compare with the predicted value -16.318 though MINITAB calculation, a 3.18% of the prediction error was known. That is, this optimal parameter set is feasible.

Table 8. the comparisons of torque, mean, MSD, and S/N based on the trail no. 7 in the Taguchi's experiment, standard blade, and optimal TLE parameters

compariso n	factor			TSR changes and results									$\bar{y}$	MSD	S/N
	A	B	C	1.5	2	2.5	3	3.5	4	4.5	5	5.5			
no. 7	3	1	3	0.1149	0.1306	0.1630	0.1998	0.2303	0.2338	0.2184	0.1964	0.1710	0.1742	45.776	-16.606
standard	0	0	0	0.1098	0.1266	0.1509	0.1869	0.2177	0.2266	0.2133	0.1931	0.1654	0.1676	47.9503	-16.808
optimum	1	1	3	0.1220	0.1463	0.1738	0.2105	0.2409	0.2446	0.2280	0.2083	0.1842	0.1856	38.0075	-15.799

5. CONCLUSIONS

This study explores how to improve the wind-capturing efficiency for a horizontal-axis SSWT under the limitation of low-speed wind speed and constant blade length. In order to well fit the size of the SSWTs and the wind field conditions where they operate, the wing size and feather characteristics adopted from the three species of birds were involved into the blade design in this study. In addition, in order to obtain the optimal design parameters which can mold the TLE blade to generate the maximum torque, the Taguchi's method is used. Through the Taguchi's optimization, it found that there about 10.74% of the torque increasement is performing, and the coverage of TLE is the most important design factor affecting the wind-capturing capability of the TLE blades, followed by the average feather interval.

Acknowledgment

This study is financially supported by the National Science and Technology Council of Taiwan under Grant No.111-2221-E-024 -005 -MY3.

References

[1] Administration, U.S.E.I., International Energy Outlook, 2019.
[2] Ko, D.H., S.T. Jeong, and Y.C. Kim, Assessment of wind energy for small-scale wind power in Chuuk State, Micronesia. Renewable and Sustainable Energy Reviews 2015, 52: 613-622. <https://doi.org/10.1016/j.rser.2015.07.160>
[3] Bukala, J., Damaziak, K., Kroszczynski, K., Malachowski, J., Szafranski, T., Tomaszewski, M., Karimi, H. R., Jozwik, K., Karczewski, M., and Sobczak, K.: Small Wind Turbines: Specification, Design, and Economic Evaluation, in: Wind Turbines – Design, Control and Applications, edited by: Aissaoui, A. G. and Tahour, A., InTechOpen London, 2016.
[4] Ohya, Y., T. Karasudani, T. Nagai, and K. Watanabe, Wind lens technology and its application to wind and water turbine and beyond. Renewable Energy and Environmental Sustainability 2017, 2: 2. <https://doi.org/10.1051/rees/2016022>
[5] Pourrajabian, A., P.A. Nazmi Afshar, M. Ahmadizadeh, and D. Wood, Aero-structural design and optimization of a small wind turbine blade. Renewable Energy 2016, 87: 837-848. <https://doi.org/10.1016/j.renene.2015.09.002>
[6] Kosasih, B., and H. Saleh Hudin, Influence of inflow turbulence intensity on the performance of bare and diffuser-augmented micro wind turbine model. Renewable Energy 2016, 87: 154-167. <https://doi.org/10.1016/j.renene.2015.10.013>
[7] Ahmadi Asl, H., R. Kamali Monfared, and M. Rad, Experimental investigation of blade number and design effects for a ducted wind turbine. Renewable Energy 2017, 105: 334-343. <https://doi.org/10.1016/j.renene.2016.12.078>
[8] Verma, A.S., N.P. Vedvik, P.U. Haselbach, Z. Gao, and Z. Jiang, Comparison of numerical modelling techniques for impact investigation on a wind turbine blade, Composite Structures 2019, 209: 856-878. <https://doi.org/10.1016/j.compstruct.2018.11.001>
[9] Scappatici, L., N. Bartolini, F. Castellani, D. Astolfi, A. Garinei, and M. Pennicchi, Optimizing the design of horizontal-axis small wind turbines: From the laboratory to market. Journal of Wind Engineering and Industrial Aerodynamics 2016, 154: 58-68. <https://doi.org/10.1016/j.jweia.2016.04.006>
[10] Vaz, J.R.P., D.H. Wood, D. Bhattacharjee, and E.F. Lins, Drivetrain resistance and starting performance of a small wind turbine. Renewable Energy 2018, 117: 509-519. <https://doi.org/10.1016/j.renene.2017.10.071>
[11] Wei, Z., T.H. New, and Y.D. Cui, An experimental study on flow separation control of hydrofoils with leading-edge tubercles at low Reynolds number. Ocean Engineering 2015, 108: 336-349.

<https://doi.org/10.1016/j.oceaneng.2015.08.004>
[12] Öztürk, N., A. Dalcalı, E. Çelik, and S. Sakar, Cogging torque reduction by optimal design of PM synchronous generator for wind turbines. International Journal of Hydrogen Energy 2017, 42: 17593-17600. <https://doi.org/10.1016/j.ijhydene.2017.02.093>
[13] Hui, Z., Y. Zhang, and G. Chen, Aerodynamic performance investigation on a morphing unmanned aerial vehicle with bio-inspired discrete wing structures. Aerospace Science and Technology 2019, 95: 105419.< https://doi.org/10.1016/j.ast.2019.105419>
[14] Kishore, R.A., T. Coudron, and S. Priya, Small-scale wind energy portable turbine (SWEPT). Journal of Wind Engineering and Industrial Aerodynamics, May. 2013, 116: 21-31. < https://doi.org/10.1016/j.jweia.2013.01.010>
[15] J. F. Manwell, J.G.M.a.A.L.R., Wind Energy Explained: Theory, Design and Application. John Wiley & Sons, Inc. Sep. 2010.
[16] T. Burton, D.S., N. Jenkins, and E. Bossanyi, WIND ENERGY HANDBOOK. John Wiley & Sons, Inc. Dec. 2001.
[17] Chu, Y.-J., and W.-T. Chong, A biomimetic wind turbine inspired by Dryobalanops aromatica seed: Numerical prediction of rigid rotor blade performance with OpenFOAM®. Computers & Fluids 2017,159: 295-315. <https://doi.org/10.1016/j.compfluid.2017.10.012>
[18] Khaled, M., M.M. Ibrahim, H.E. Abdel Hamed, and A.F. AbdelGwad, Investigation of a small Horizontal–Axis wind turbine performance with and without winglet. Energy 2019, 187: 115921. < https://doi.org/10.1016/j.energy.2019.115921>
[19] Yang, M., and Z. Xiao, Distributed roughness induced transition on wind-turbine airfoils simulated by four-equation k-ω-γ-Ar transition model. Renewable Energy, May. 2019, 135: 1166-1177. < https://doi.org/10.1016/j.renene.2018.12.091>
[20] Rezaeiha, A., H. Montazeri, and B. Blocken, Towards accurate CFD simulations of vertical axis wind turbines at different tip speed ratios and solidities: Guidelines for azimuthal increment, domain size and convergence. Energy Conversion and Management, Jan. 2018, 156: 301-316. < https://doi.org/10.1016/j.enconman.2017.11.026>
[21] Fatchurrohman, N., and S. Chia, Performance of hybrid nano-micro reinforced mg metal matrix composites brake calliper: simulation approach. 4th International Conference on Mechanical Engineering Research (ICMER2017) 1–2 August 2017,Oct. 2017, IOP Conference Series: Materials Science and Engineering, 257: pp. 012060.
[22] Wang Z., and M. Zhuang, Leading-edge serrations for performance improvement on a vertical-axis wind turbine at low tip-speed-ratios. Applied Energy, Dec. 2017, 208: pp. 1184-1197. < https://doi.org/10.1016/j.apenergy.2017.09.034>

RIGA 2023

Parameter Estimation of PV System Towards Self-Consumption of Electric Energy for Dormitory

Piotr Hylla
Silesian University of Technology, Gliwice, Poland, piotr.hylla@polsl.pl, ORCID: 0000-0001-5195-5374

Arkadiusz Mężyk
Silesian University of Technology, Gliwice, Poland, arkadiusz.mezyk@polsl.pl, ORCID: 0000-0001-9746-2030

Tomasz Trawiński
Silesian University of Technology, Gliwice, Poland, tomasz.trawinski@polsl.pl, ORCID: 0000-0002-0246-2343

Bartosz Polnik
KOMAG Institute of Mining Technology, Gliwice, Poland, bpolnik@komag.eu, ORCID: 0000-0002-6803-3090

Cite this paper as: *Hylla, P., Mężyk, A., Trawiński, T., Polnik, B., Parameter estimation of PV system towards self-consumption of electric energy for dormitory. 11. Eur. Conf. Ren. Energy Sys. 18-20 May 2023, Riga - Latvia*

Abstract: The article presents the results of calculations of the parameters of the photovoltaic installation and the energy storage increasing the level of energy self-consumption in the selected student's dormitory. It also presents the actual annual consumption of electricity in this dormitory where an online system for monitoring electricity consumption has been operating for over one year. The average daily electricity consumption was calculated for each calendar month. In this way, the standard average daily electricity consumption was defined, characterizing a given month, with a resolution of one hour within 24 hours. Electricity generation curves specific for PV installations of various capacities have been plotted on the average daily energy consumption. A procedure algorithm was developed, operating on the above-mentioned consumption and production curves, allowing for the calculation of the PV installation power and the size of the energy storage to ensure the highest possible level of electricity self-consumption in the widest possible range of months.

Keywords: *photovoltaic systems, energy self-consumption, energy storage, algorithm*

1.INTRODUCTION

The events of the early 2020s, such as the Covid-19 pandemic, armed conflicts in Europe, the interruption of energy supply chains, and the gradual decarbonization of the energy industry made it necessary to change the existing power system, e.g. Poland to reduce the threat of the so-called 'Blackout' as a serious failure of the electricity production and distribution system. The solution may be to increase the share of renewable energy sources (RES) in total electricity production. According to the data provided by the Energy Market Agency (in Polish: Agencja Rynku Energii SA - ARE) RES, the following systems can be distinguished: photovoltaics [1], wind turbines [2], hydropower plants [3], biogas power plants [4] and biomass power plants [5]. The most popular RES sources in terms of installed capacity in Poland, according to data from December 2022, are photovoltaics (12189.1 MW) and wind farms (8255.9 MW) [6]. Electricity generators using solar or wind energy are highly dependent on weather conditions which may cause instability and unpredictability in the operation of these systems [7]. Increasing the number of renewable energy sources, e.g. photovoltaics, in a given area might result in the need to increase the capacity of transmission lines??? to enable the discharge of surplus of produced energy [8]. Therefore, it is most beneficial to use energy for current energy needs, preferably within the smallest possible installation to reduce losses in energy transmission [9]. The parameter determining the degree of current use of energy E_{RES} from RES is self-consumption determined by the Eqn. (1), as follows:

$$\text{selfconsumption} = \frac{E_c}{E_{RES}}\ 100\% \quad (1)$$

where E_c – consumed energy from RES, E_{RES} – energy generated by RES.

In the case of PV installations connected via an inverter to the facility's power grid, it is practically impossible to use the energy obtained for current needs to the maximum extent due to the shifted periods of production and demand E_D for electricity. The parameter determining the degree of use of energy obtained from RES to the total energy consumption of the installation is the degree of energy independence of the facility, expressed by the Eqn. (2), as follows:

$$\text{independence} = \frac{E_c}{E_D} 100\% \quad (2)$$

where E_D – energy demand within 24 hours (whole day).

The degree of complete energy independence of the facility from the external power supply means that the total energy consumption is covered by renewable energy sources. Due to the limited possibilities of controlling the production of energy from RES, it becomes necessary to attach an energy storage device to the installation to increase self-consumption. It can be obtained thanks to charging the storage device during the production of energy from RES and increasing the energy independence of the building by supplying it in periods outside the operation of RES. A fully energy-balanced building can be defined by Eqn. (3), as follows:

$$E_{RES} - E_c = 0 \quad (3)$$

This article presents an algorithm for selecting the parameters of a PV installation for a dormitory building based on electricity consumption characteristics and estimated characteristics of energy production from a photovoltaic installation for a given location. Next, an algorithm for selecting the energy storage parameters will be presented to achieve a high degree of self-consumption and energy independence in the dormitory.

2.CHARACTERISTICS OF THE FACILITY AND THE ELECTRICITY CONSUMPTION MEASUREMENT SYSTEM.

The analysis of electricity consumption and, consequently, the selection of the size of the photovoltaic installation and the suggested energy storage to increase the self-consumption of energy was carried out for an example student's dormitory located on the campus of the Silesian University of Technology in Gliwice city in Poland. It is a five-story building with 80 single and double guest rooms. This dormitory is equipped with the IPOE electricity consumption measurement and monitoring system (manufacturer APA Ltd. .) [10]. This system enables ongoing monitoring of electricity consumption, and its parameters such as active, reactive, and apparent power, RMS voltage, RMS current, power factors, voltage, and current harmonic content, as well as it enables their archiving. In addition, this system offers the possibility of integrating information from the consumption of other utilities, such as water and gas, and photovoltaic systems, and above all, it enables energy consumption management. Figure 1 shows the example voltage waveforms at the main dormitory connection, recorded throughout the whole day on February 17, 2023. RMS voltage values practically oscillate around the nominal value by +/- 3 V during the day. The lowest voltage values can be observed in the morning, noon, and afternoon, and the highest in the evening and at night time of the day. The waveforms of the current drawn from the grid by the entire dormitory on the same day are shown in Figure 2. The values of the currents drawn from the grid are the lowest at night and in the morning, they oscillate below the value of 10 A for each phase, occasionally exceeding it, sometimes reaching values up to 15 A. The highest current surges and a very large differentiation in a load of individual phases can be observed in the afternoon, the load values reach 32 A, with the most heavily loaded phases L1 and L2. Visually, the waveforms of the currents are similar to the waveforms of the active power consumed by the dormitory, and they are presented in Figure 3. The highest power consumption takes place in the afternoon and evening and occurs in phases L1 and L2, while moderate power consumption takes place in phase L3. Consumption in this phase increases in the evening and at night but is characterized by a balanced and stable increase. High active power consumption from the L1

phase suggests that a significant part of loads, such as cookers, microwave ovens, etc. are powered from this phase, computers are powered from the L3 phase and the L2 phase, e.g. cordless kettles, refrigerators.

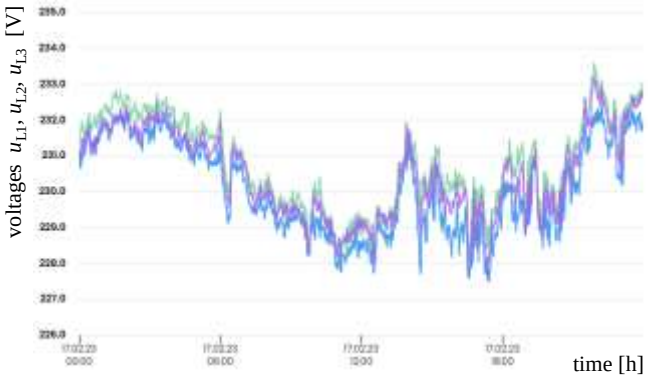

Figure 1. Time plot of phase RMS value of voltages at power connection (u_{L1} – blue line, u_{L2} – green line, u_{L3} – magenta line)

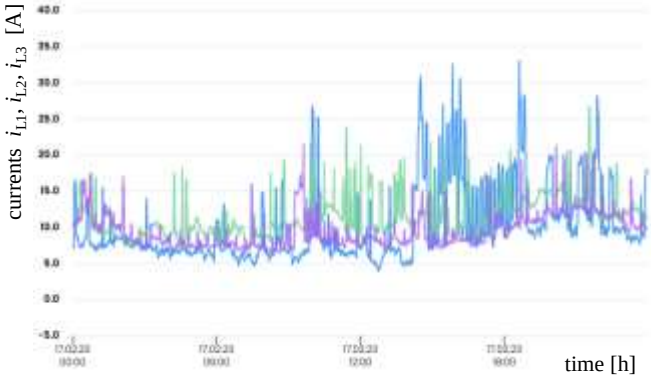

Figure 9. Plot of phase RMS value of currents at power connection (i_{L1} – blue line, i_{L2} – green line, i_{L3} – magenta line)

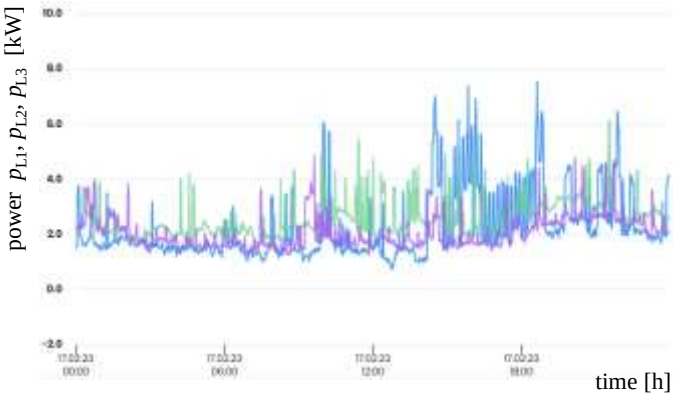

Figure 3. Plot of phase power at power connection (p_{L1} – blue line, p_{L2} – green line, p_{L3} – magenta line)

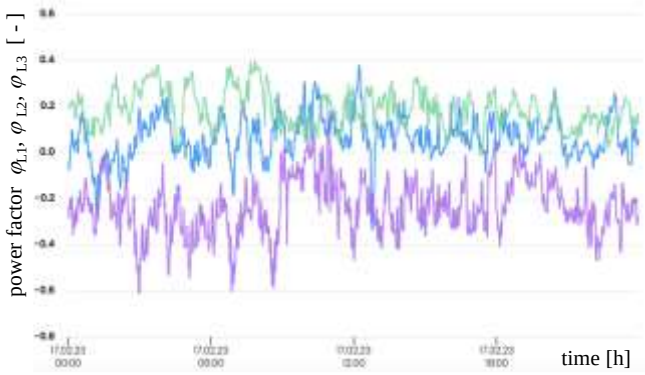

Figure 4. Plot of phase power factor value at power connection terminals (φ_{L1} – blue line, φ_{L2} – green line, φ_{L3} – magenta line)

This estimation is confirmed by the nature of the load, which is reflected in the power factor $\tan\varphi$ in individual phases. The waveforms of the power factor in individual phases are shown in Fig. 4. Negative - capacitive power factor in the L3 phase proves a large number of installed receivers in the form of switching power supplies and LED lighting. A power factor oscillating close to zero and slightly higher values indicates a load that consumes only active power, such as cordless kettles. A positive power factor in the L2 phase proves that electric motors are powered from a given phase, i.e. refrigerators and washing machines are powered from this phase. Figure 5 shows the current waveforms drawn by a refrigerator in one of the temporarily unoccupied guest rooms.

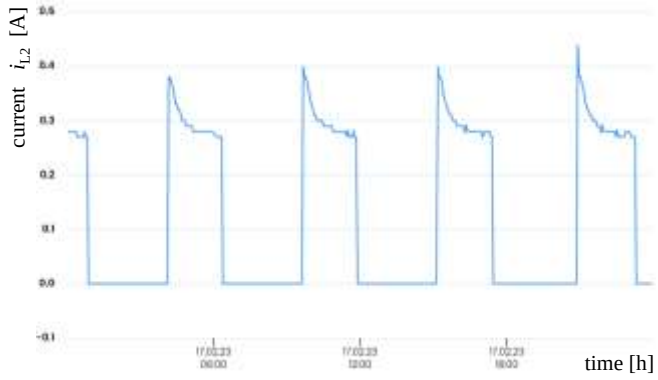

Figure 5. Plot of L2 phase current value by selected room. Curve typical for refrigerator current consumption

Throughout the year, the entire dormitory, counting from the beginning of September 2021 to the end of September 2022, consumed 70.1 MWh of electricity, the average daily electricity consumption was 192.1 kWh and the average hourly electricity consumption was 8 kWh. In this dormitory, in the above mentioned period , the maximum daily energy consumption of 282 kWh and the maximum daily energy consumption of 19 kWh were observed. Figure 6 shows the average monthly electricity consumption in the dormitory in a slightly larger time period i.e. until the end of 2022.. The maximum value was observed in November 2021, which was 7.8 MWh. A year later, there was observed a significant decrease in consumption in the corresponding month of 5.8 MWh, this decrease was 25.6%.

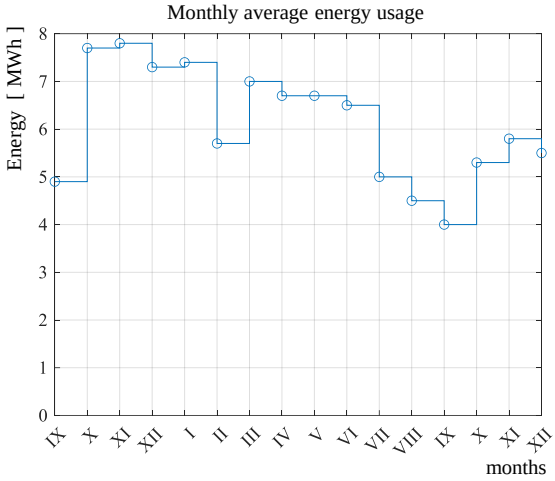

Figure 6. Monthly average electric energy usage in the designated dormitory

Figure 7 shows the average daily electricity consumption in the dormitory. The maximum value was also observed in November 2021, which was 258.3 kWh, and a year later 192.6 kWh, the decrease was 25.4%. Similar decreases were observed in the average hourly energy consumption, and they are presented in Figure 8.

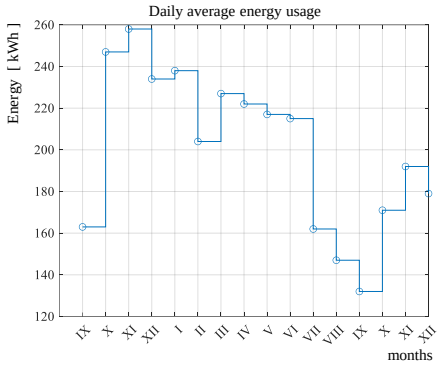

Figure 7. Daily average electric energy usage in the designated dormitory

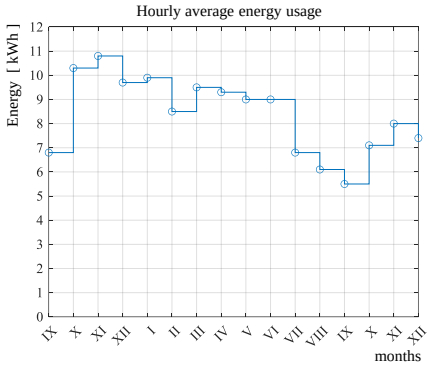

Figure 8. Hourly average electric energy usage in the designated dormitory

3.ESTIMATION Of PARAMETERS OF A PHOTOVOLTAIC INSTALLATION

For the construction of a stationary photovoltaic installation, the most important parameters are the amount of available space, the load-bearing capacity of the substrate, and the ability to ensure the appropriate inclination and position of the panels. For the designated dormitory, whose geographical location is a width of 50.286 degrees and a length of 8.680 degrees, the most favorable inclination of the panels of the stationary photovoltaic installation is 39 degrees and the azimuth is -2 degrees. Based on the data [11] on the location, the maximum values of the average monthly solar energy were determined for a given location, and they are shown in Figure 9, for the installation with a capacity of 50 kWp. The average monthly produced energy by the 50 kWp installation (curve

marked "1") was compared with the average monthly consumed energy by the dormitory (curve "2"). Similarly in Figure 10 and 11 photovoltaic systems of higher power are presented.

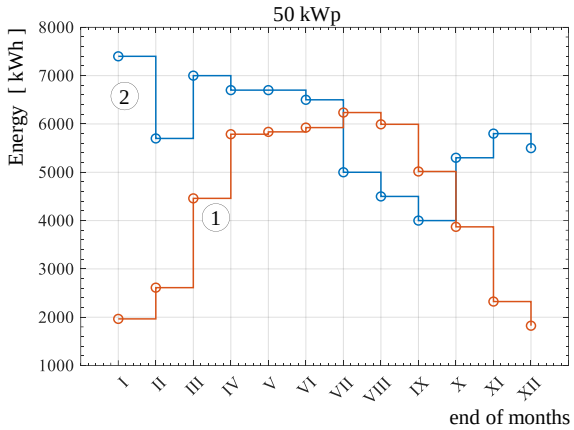

Figure 9. Monthly average electric energy assumed to be produced by 50 kWp PV – (1) and consumed – (2) in the designated dormitory

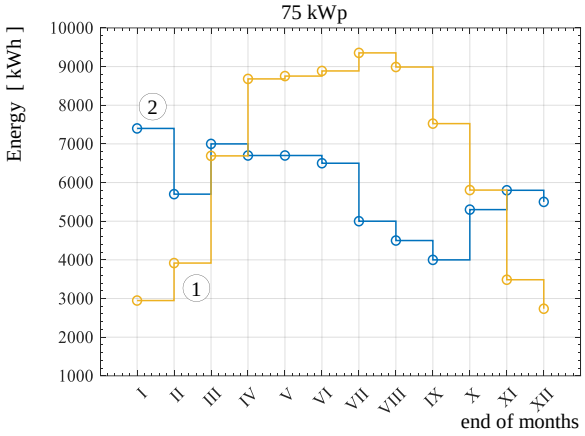

Figure 10. Monthly average electric energy assumed to be produced by 75 kWp PV – (1) and consumed – (2) in the designated dormitory

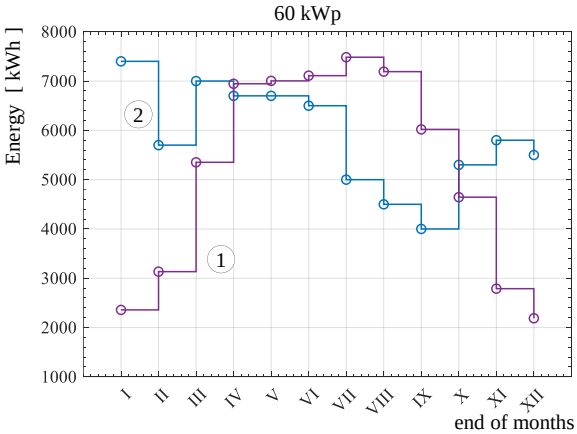

Figure11. Monthly average electric energy assumed to be produced by 60 kWp PV – (1) and consumed – (2) in the designated dormitory

4.ALGORITHM FOR SELECTING INSTALLATION PARAMETERS

As part of the analyzes and tests, the parameters of the PV installation and energy storage units were selected to ensure the highest possible degree of energy independence of the facility along with the possibility of maximum use of energy obtained from RES. To determine the individual parameters, the actual data of energy consumption in the student's dormitory and the average hourly parameters of energy production for the considered location were used. One of the basic parameters is the self-consumption calculated on the basis of Eqn.(1). The self-consumption parameter determines the degree of current use of energy from the PV installation, while the energy independence of the facility determines the degree of use of the obtained energy to the energy consumption. Eqn. (2) was used to determine this parameter. The value of energy consumed for current needs directly from RES installations is determined on the basis of Eqn. (4).

$$E_c = \begin{cases} E_{RES} & if \quad E_{RES} < E_d \\ E_d & if \quad E_{RES} > E_d \end{cases} \tag{4}$$

where E_d - current electricity demand.

Due to the average hourly parameters of energy consumption and production, the energy independence of the facility and self-consumption were determined for the proposed PV installations with a capacity of 10-100kWp. The obtained data are presented in Figure 12. The best parameters were obtained for installations with a capacity of 80kWp and 90kWp with the small difference between the degree of independence and self-consumption amounting to only about 2%.

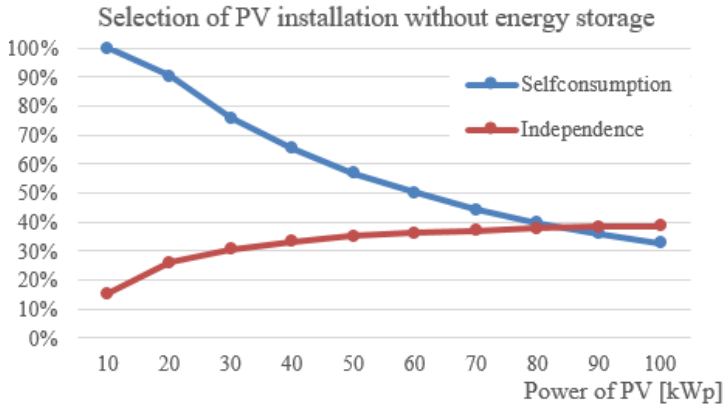

Figure 12. PV installation selection chart

To increase the energy independence of the facility, there was madean attempt to select a short-term energy storage that could allow energy balancing within one day. The energy balance is the difference between the surplus of energy from RES and the deficit of energy, taking into account the efficiency of the energy storage Eqn. (5).

$$balance = surplus - \frac{deficiency}{storage\ efficiency} \tag{5}$$

Surplus energy is the energy obtained from the PV installation that is not used for the current energy demand of the facility, while energy deficiency is the energy consumption of the facility not balanced with current RES production. Energy storage efficiency was assumed at 80%. A prerequisite for achieving full energy independence is a zero or positive energy balance. The degree of energy independence of the facility equipped with a daily storage tank, based on the determined data, was estimated (Figure 13).

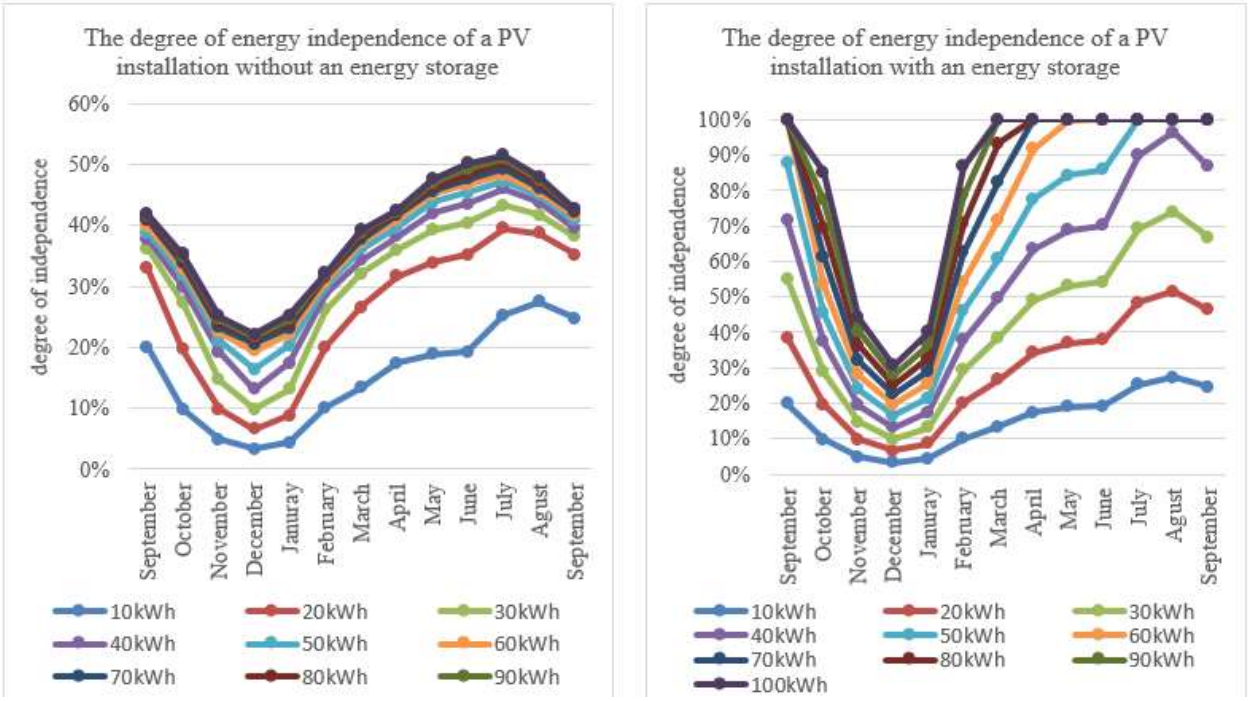

Figure 13. Degree of energy independence of the installation

According to the obtained data it is not possible to achieve full energy independence only by using a daily energy storage. In the next stage, the data of the actual energy consumption and the estimated energy production by the photovoltaic installation were analyzed for the whole year. In order to balance the energy of the facility within one year, it is necessary to supply it partially from the grid or to use long-term energy storage to accumulate energy for the period of reduced production of photovoltaics. Drawing upon the data obtained in the previous stage, the surplus energy for the PV installation on a monthly basis was calculated on the basis of the Eqn. (6).

$$E_{\mathrm{Nm}} = (1 - selfconsumption)E_{\mathrm{PVm}} \tag{6}$$

where E_{Nm} – surplus energy from PV on a monthly basis, E_{PVm} – total PV energy production per month.

To determine the energy balance for the dormitory facility on a monthly and annual basis, it is necessary to calculate the surplus and deficit parameters of energy, taking into account the operation of the daily energy storage. Energy shortage on a monthly basis means that the energy balance determined by the Eqn. (5) has a negative value of Eqn. (7).

$$deficiency = \frac{(1 - E_{\mathrm{Nze}})E_{\mathrm{Zm}}}{\mu_{\mathrm{ze}}} \tag{7}$$

where E_{Nze} – degree of energy independence of the facility with a PV installation and daily energy storage, E_{Zm} – actual monthly electricity consumption, μ_{ze} – efficiency of the seasonal energy storage was assumed at 80%. The monthly surplus of energy resulting from the operation of the PV installation connected to the daily energy storage means that the balance determined by the Eqn. (5) has a positive value. The monthly energy surplus was determined using the Eqn. (8).

$$surplus = |1 - E_{\mathrm{Nze}}|E_{\mathrm{Zm}} \tag{8}$$

To assess the possibility of achieving full energy independence, thanks to the use of an additional long-term energy storage device, it is necessary to determine the annual energy balance consisting of the difference between the sum of all energy surpluses and the sum of all energy shortages for a period of one year. The condition for achieving full energy independence of the facility is a zero or positive value of the annual energy balance. The annual energy independence of the facility is calculated using the Eqn. (9).

$$E_{\mathrm{Nr}} = \frac{\sum_1^{12}(E_{\mathrm{Nze}}\, E_{\mathrm{Zm}}) - E_{\mathrm{Szs}}}{E_{\mathrm{Zr}}} \tag{9}$$

where E_{Szs} – the energy of losses resulting from the operation of the seasonal energy storage, E_{Zr} – the actual annual energy consumption.

Figure 14 shows the annual degree of energy independence of the dormitory. Complete energy independence of the facility can be achieved by using only PV installations with a capacity of 100kWp and 90kWp connected to a hybrid energy storage consisting of a short-term storage tank with a capacity of 200kWh and seasonal energy storage with a proposed capacity of 17.5MWh for 100kWh and 19.5MWp for 90kWp. In addition, it is noted that the use of a seasonal energy storage allows to increase the energy independence of the facility only in the case of PV with a capacity of 80kWp and 70kWp. In other cases, the use of a long-term energy storage device is associated with a reduction in energy independence from the energy supplier. The operation of a seasonal storage tank for a 10kWp PV installation results in full use of the energy obtained from photovoltaic panels, resulting in a negative energy independence index.

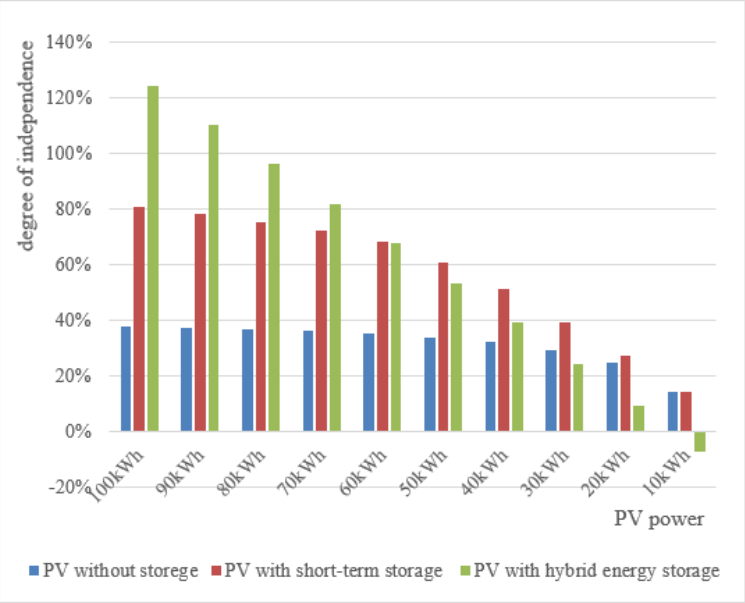

Figure14. The annual indicator of the facility's energy independence

5.SUMMARY

This article presents the method of selecting the parameters of the PV installation along with the selection of energy storage to obtain the highest degree of energy independence. Full energy independence is possible only through the use of a 100kWp or 90kWp PV installation connected to hybrid energy storage. It is proposed to use photovoltaics with a capacity of 90kWp due to the lower values of surplus energy returned to the power grid and the costs of purchasing and mounting the installation. There were presented possibilities of increasing the energy independence of the building were presented as well the use of short- and long-term energy storage and the usage of energy obtained from RES. The proposed power supply system for the dormitory has the form of a microgrid because through the use of appropriate power electronics, it can operate on-grid, i.e. in cooperation with an external network, and off-grid (island operation).

The decarbonization of the power industry along with the growing popularity of RES makes it necessary to move away from the conventional power system in favor of distributed power generation consisting of microgrids. The advantage of using a microgrid is the ability to balance the energy obtained from RES directly in the facility or the immediate vicinity, additionally reducing the risk of interruptions in energy supplies.

References

1. Woszczyński M,. Rogala-Rojek, J. Bartoszek S., Gaiceanu, M., Filipowicz, K., Kotwica K., (2021). In Situ Tests of the Monitoring and Diagnostic System for Individual Photovoltaic Panels. Energies. 14. 1770. 10.3390/en14061770.
2. Manwell, J.F., McGowan, J.G., Rogers, A.L. Wind Energy Explained: Theory, Design and Application (2010) ISBN: 978-047001500-1 doi: 10.1002/9781119994367
3. Ioannis Kougias, George Aggidis, François Avellan, Sabri Deniz, Urban Lundin, Alberto Moro, Sebastian Muntean, Daniele Novara, Juan Ignacio Pérez-Díaz, Emanuele Quaranta, Philippe Schild, Nicolaos Theodossiou, Analysis of emerging technologies in the hydropower sector, Renewable and Sustainable Energy Reviews, Volume 113, 2019, ISSN 1364-0321, https://doi.org/10.1016/j.rser.2019.109257.
4. Scarlat, N., Dallemand, J.-F., Fahl, F. Biogas: Developments and perspectives in Europe (2018) Renewable Energy, Part A 129, doi: 10.1016/j.renene.2018.03.006
5. Pang, S. Advances in thermochemical conversion of woody biomass to energy, fuels and chemicals (2019) Biotechnology Advances, 37 (4), pp. 589-597
6. https://www.are.waw.pl/ (access at 02.2023)
7. Biskup T., Cieniuch A,, Kołodziej H., Paluszczak D., Sontowski J., Przekształtnik typu dab w systemie magazynowania energii z akumulatorem niskonapięciowym, Maszyny Elektryczne - Zeszyty Problemowe Nr 1/2022 (127) (in polish)
8. H. Wang, N. Good and P. Mancarella, Modelling and valuing multi-energy flexibility from community energy systems, 2017 Australasian Universities Power Engineering Conference (AUPEC), Melbourne, VIC, Australia, 2017, pp. 1-6, doi: 10.1109/AUPEC.2017.8282399.
9. Widén, Joakim. Improved Photovoltaic Self-Consumption with Appliance Scheduling in 200 Single-Family Buildings. Applied Energy, t. 126, Agust 2014, s. 199–212. https://doi.org/10.1016/ j.apenergy.2014.04.008.
10. https://www.apagroup.pl/monitoring-mediow-w-akademiku-zobacz-film (access at 19.02.2023)
11. https://re.jrc.ec.europa.eu/pvg_tools/en/ (access at 19.02.2023)

RIGA 2023

Cost Models of Single-Phase and Three-Phase Cable Underground Lines

Alexander Bronshtein
ELTA, Beer Sheva, Israel, alik.bronshtein@gmail.com, ORCID: 0009-0000-5909-2286

Dmitry Baimel
SCE, Beer Sheva, Israel, dmitrba@sce.ac.il, ORCID: 0000-0001-6384-3900

Svetlana Bronshtein
SCE, Beer Sheva, Israel, svetlanab@sce.ac.il, ORCID: 0009-0004-9740-215X

Cite this paper as: *A.Bronshtein, D.Baimel, S.Bronshtein. Cost Models of Single-Phase and Three-Phase Cable Underground Lines. 11. Eur. Conf. Ren. Energy Sys. 18-20 May 2023, Riga, Latvia*

Abstract: With the increasing use of underground power delivery, the issue of the optimal planning of cable power distribution lines becomes very important. While transmission and distribution lines are commonly three-phased, under certain conditions, the power delivery can be more cost-effective by utilizing a single-phase cable line rather than a three-phase one. The primary goal of this study was to develop cost models of single-phase and three-phase underground power lines for comparison between the cost of power delivery, and to provide suggestions for the cost-effective planning of cable lines. Two types of cost models for underground cable were developed: a unitized cost model based on catalogues' cable parameters, and a cost model based on the rated power of the cables. The comparison results show the boundaries of superior selection of single-phase lines for power delivery.

Keywords: *cost model, single-phase and three-phase, underground cable power line, breakeven power*

1. INTRODUCTION

Recently, power delivery in developed countries transferred to underground cable lines. This transaction is highly expensive which is why the issue of optimal planning of power delivery networks becomes very relevant.

Transmission and distribution lines are three-phased and the transition to single-phase lines is carried out only at the stage of low voltage distribution of the power between customers. Meanwhile, under certain conditions, the delivery of electricity by a single-phase high voltage cable line can be more cost-effective than by a three-phase one.

Underwater power lines, the number of which is constantly growing, are also transporting power by three-phase cable lines which are tremendously expensive and not because of a cable cost only but also because of the high cost of an associated equipment (connectors, compensators, transformers, etc.) and a very high installation cost.

Very little attention has been paid so far to the building of an economic model of the transmission/distribution line whereas such a model can help to prepare recommendations for a practical choice between three-phase or single-phase lines for power delivery.

A very small amount of published works is dedicated to the utilizing or creating a financial model of the overhead or cable power lines during design process and only a few considered a single-phase transmission line for high voltage power delivery.

One approach to the cost estimation model is unitized cost model which is widely used in economic prognoses. Its definition and explanation can be easily found in internet sites [1]. With this model, the unknown cost of a certain cable can be estimated using a known price and parameters of a similar cable type. This approach can be very useful for the estimation of the cable line cost because there is very little available information about electrical equipment prices which can be found elsewhere.

Additional study [2] presents very accurate and detailed cost analysis of the distribution network in the building by studying AC or/and DC network types for power supply. The report proposes standard formulas for calculating costs for each of the categories and discusses sources of cost modeling data. This work provides a framework for comparison of AC, DC, and hybrid distribution system design alternatives, but it does not provide quantitative cost comparisons or draw conclusions about whether AC or DC distribution systems are more cost-effective, and analysis is carried out for the low voltage network. Similar study [3] compared DC low voltage distribution system with 230V AC. A simple cost model was utilized in this study for choosing an optimal conductor cross section for minimal power losses. Another work [4] presents useful and accurate financial analysis of rural electrification projects but three-phase distribution lines are overhead, and the proposed approach does not use any mathematic models of the equipment. W. Hatem and K. Erzaij [5] propose a cost model for electrical projects of the overhead high voltage transmission lines. This model can assist in determining the cost of establishing electric power transmission lines and implementing future projects; model can also promote the economic development of electric power and energy industry. In Stefan Lundberg's report [6] the author presented cost models of the wind farm equipment including models of transmission lines, transformers, etc., all of which are three-phase.

R. A. Baig [7] analyzing Pakistan three-phase overhead distribution system concluded that a single-phase distribution system instead of three-phase should be considered for power supply in rural and urban areas. It can provide up to 30% cost reduction. This conclusion supported authors ideas that a single-phase power transmission and distribution may be more efficient than three-phase. To verify this idea, mathematical cost models of the single-phase and three-phase power line should be built.

This work is dedicated to the development of a cost model of an underground cable power line. The study employs the commonly used three-phase (three core) cable line models based on the rated power [6] as a base for developing the cost model of a single-phase (two core) cable line. Conversely, cable parameters in catalogs usually contain the information about rated voltage and conductor cross section. In this regard, another cost model which uses available cable parameters were created for both, single-phase and three-phase cable lines.

By employing proposed models, this study shows the results of the comparison between single-phase and three-phase cable lines for supplying the same amount of power at the same voltage level and gives the recommendations for the cost-effective selection of cable lines.

2. COST MODELS OF CABLES

In this study we developed two types of cost models for a cable line:

- Unitized cost model
- Cost model based on the rated power of cable.

Cost models for single-phase cables were developed using available cables information and cost models of three-phase cable lines [6], [8]-[10].

Unitized Cost Model

For the unitized cost model, a base case is required. Let the reference cable be the 35mm^2/20kV (cooper conductor). This cable will have an installed utilized cost of 1 (or 100%) and all other cables will be presented as a multiple of this. The cable price $C_r(V, A)$ relatively to the reference cable obtained from the several known prices [8]-[10] as a function of conductor area and rated voltage (cable environment assumed to be the same, so the relative price is not affected by the type of installation, it may be in duct, ground, or air) by using fitting algorithm that is applicable for power cables with cross section up to 35mm^2:

$$C_r(V, A) = (aV + b)A + cV + d \quad (1)$$

Where:

A	conductor area of the cable [mm^2]
V	cable rated voltage [kV]
a, b, c, d	cost constants

Parameters a, b, c, and d were defined as: a=0.0032; b=1.3293; c=0.6373; d=3235.

The results of unitized cost calculation for different cable sizes transmitting different powers are presented in tables 1 (20kV line) and 2 (35kV line).

Table 1. Unitized cost of 20kV cable transmission line.

Transmitted Power [MVA]	A [mm^2]		Unitized cost per cable [%]		Total unitized cost [%]	
	3-phase	1-phase	3-phase	1-phase	3-phase	1-phase
2	4	16	54	71.8	162	143.6
3	10	30	62.9	92.6	188.72	185.17
4	16	50	71.8	122.25	215.4	244.5

Table 2. Unitized cost of 35kV cable transmission line.

Transmitted Power [MVA]	A [mm^2]		Unitized cost per cable [%]		Total unitized cost [%]	
	3-phase	1-phase	3-phase	1-phase	3-phase	1-phase
2	2.5	10	57.6	68.4	172.8	136.8
3	4	16	59.7	77	179.3	154
4	6	35	62.6	89.9	187.9	179.9

It can be noticed from these results that for transmission of the electric power up to 4MVA the cost-effective way is to use a single-phase line 35kV.

Similar analysis and proper cable selection can be made for other operating voltages and conductor material.

Since different manufacturers use different production technologies and materials, the cable's price may fluctuate. Therefore, the proposed unitized model is rather qualitative analysis than quantitative. However, relative price behavior is adequately reflected in the proposed cost model. This approach is suitable for rural areas where transmitting power is low.

Cost Model Based on the Cables' Rated Power

The cost model of the three-core AC cable is based on the rated power of the cable. It was developed in [6] from the known cable data. The cost model is described as:

$$C_{AC}^{3ph} = a + b \cdot exp\left(\frac{c \cdot S}{100}\right) \quad (2)$$

Where:

C_{AC}^{3ph}	cost of three-core AC cable [k$/km]
S	rated power of the cable [MVA]
a, b, c	cost constants.

Cost constants are presented in Table 3 for different rated voltages. As can be noticed from equation (2) and table 3, the cost of three-phase AC cables increases exponentially with the rated power of the cable.

Table 3. Cost constants.

Rated Voltage [KV]	a	b	c
22	33.46	68.68	6.15
33	48.42	70.217	4.1
45	60.79	72.10	3.0
66	81.06	73.63	2.05
132	232.21	24.62	1.66
220	374.76	12.96	1.16

To transmit the same power as in the case of three-core cable through the single-phase system (two wires) the rating power of each cable should be 3 times higher, but the cost of each cable will be one third of the three-phase cable. The cost model for this case is:

$$C_{AC}^{1ph} = \frac{2}{3}\left[a + b \cdot exp\left(3 \cdot \frac{c \cdot S}{100}\right)\right] \quad (3)$$

Let the breakeven power (BEP) be the power at which the cost of the cables is equal for different operating voltages. The values of BEP for different rated voltages and different combinations of wire cores in the underground cable are presented in Table 4.

Table 4. Breakeven cost power.

Rated Voltage [KV]		22	33	45	66	132	220
BEP [MVA]	3/2	4.25	6.85	10	15.58	40.35	82.28

The meaning of BEP values presented in the table 4 is that up to certain level of the power a three-phase transmission line (3 wires) is more expensive than a single-phase (2 wires). For example, 22kV single-phase cable transmission line is cheaper than three-phase up to 4.25MVA power, whilst 33kV single-phase line is cheaper than three-phase up to 6.85MVA power delivered by the line.

Figs 1, a-d present cable cost per kilometer of high-power underground line as a function of a cable rated power for three-phase and single-phase lines for different rated voltages calculated using equations (2)-(3). BEP points are circled. Observing these plots, the conclusion can be made that the cost-advantage power range of the single-phase two wire cables is wider for higher operating voltages. This can be used for selecting cables with optimal parameters for achieving less expansive power delivery systems.

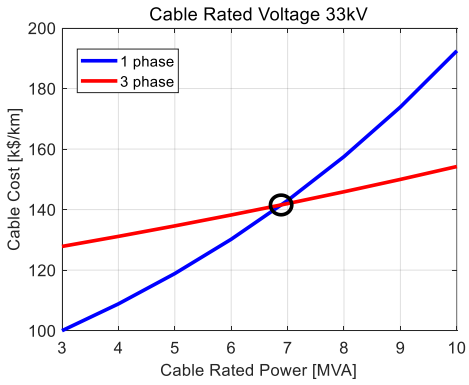

(a)

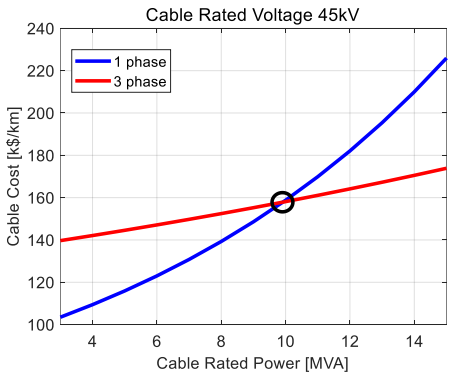

(b)

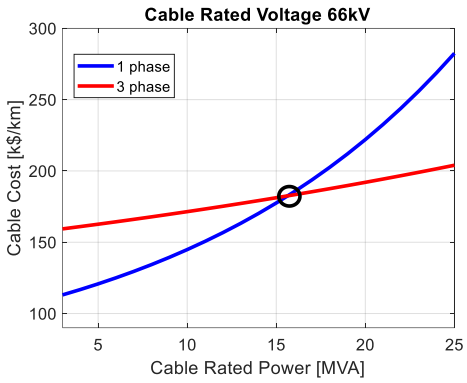

(c)

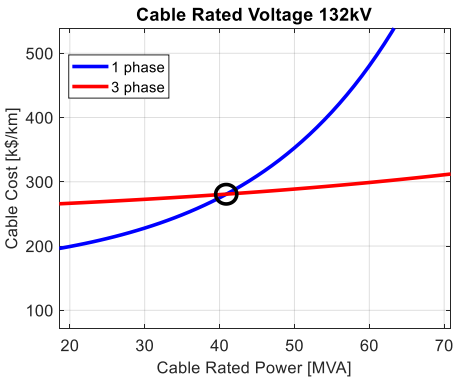

(d)

Figure 1. Cable cost per kilometer of a cable line as a function of a rated power for three-phase and single-phase lines for different rated voltages.

2. COST MODELS OF TRANSFORMER

The model developed for the cost of transformers is based on the rated power. The cost model was developed in [6] from information available for three-phase transformers with a rated power in the range 6.3 to 150 MVA and a high voltage side in the range 47 to 140 kV and low voltage side in the range 10.5 to 77 kV The model is described as:

$$C_{Tr}^{3ph} = A + B \cdot S^{\beta} \tag{4}$$

Where:

C_{Tr}^{3ph}	is the cost of three-phase transformer [k$]
S	is the rated power [MVA]
A= -141.73	is the offset constant [k$]
B=121.4	is the slope constant [k$]
β =0.4473	is the exponent.

Cost estimation for a single-phase transformer operating at the same rated power and the same rated voltage as a three-phase transformer is based on a fact that the cost of three single-phase transformers with rated power S are about 15% higher than a single three-phase transformer with rated power 3S:

$$C_{Tr}^{1ph} = \frac{1.15}{3}\left[A + B \cdot (3 \cdot S)^{\beta}\right] \tag{5}$$

Fig. 2 shows single-phase and three-phase transformers' costs as a function of the rated power. As it can be seen from figure 2, single-phase transformer is cheaper than three-phase for all high-power ratings. It should be noted that the cost in dollars is changing with currency rate, however the general behavior remains the same.

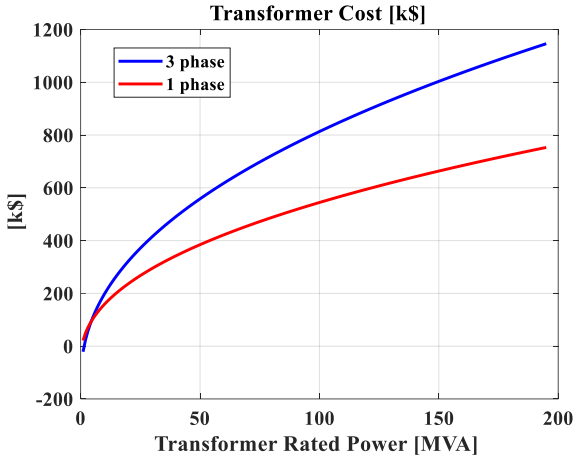

Figure. 2. Transformer cost as a function of a rated power for three-phase and single-phase transformers.

4. CONCLUSIONS

A cost models of an underground cable power line and transformer were proposed and analyzed in this study. Two types of cost models for underground cable were developed: a unitized cost model utilizing catalogues cable parameters and a cost model based on the rated power of the cables. This study shows the results of the comparison between single-phase and three-phase cable lines for supplying the same amount of power at the same voltage level and gives the recommendations for the cost-effective selection of cable lines. It should be noted that the cost in dollars presented in this study is changing with currency rate, however the general behavior remains the same.

The analysis shows that conditions exist for high power underground transmission line when a single-phase power line can provide sufficient cost advantage. This analysis did not include possible savings on substations with simplified equipment used for single-phase compared to three-phase transmission. Additional economical advantage of single-phase network could be achieved using renewable energy sources (wind farms, PV, etc.) because single-phase converter/inverter is cheaper and simpler.

A complete economic analysis of the single-phase line, including the transfer from three phase to single and related equipment, is planned to continue this study.

References

[1]https://corporate.findlaw.com/law-library/unitization-a-mathematical-formula-to-calculate-redeterminations.html#_ednref2
[2] S. Reese, S. Frank, B. Ball, and V. Vossos. (2021) "Cost Analysis Framework for Comparing AC and DC Design Alternatives for Building Electrical Distribution Systems." Technical Report, National Renewable Energy Laboratory, Lawrence Berkeley National Laboratory. www.nrel.gov/publications
[3] M. Amin, Y. Arafat, S. Lundberg, and S. Mangold. (2011) " Low voltage DC distribution system compared with 230 V AC." IEEE Electrical Power and Energy Conference, DOI: 10.1109/EPEC.2011.6070222
[4] https://www.nrecainternational.coop/wp-content/uploads/2016/11/Module8FinancialAnalysisofRuralElectrificationProjects.pdf
[5] W. A. Hatem, K. R. Erzaij. (2020) "Estimation and Analysis of Costs for Electrical Power Transmission Lines in Iraqi Projects." 3rd International Conference on Sustainable Engineering Techniques (ICSET 2020, doi:10.1088/1757-899X/881/1/012044
[6] Stefan Lundberg. (2003) "Performance Comparison of wind park configurations." Technical report, Department of Electric Power Engineering, Chalmers University of Technology, Sweden 2003, https://research.chalmers.se/en/publication/2691
[7] R. A. Baig. "Introducing Single-Phase Distribution System."
https://www.barqaab.com/mainwebsite/Technical%20Papers/Introducing%20Single-phase%20Distribution%20system.pdf
[8] https://rpgcables.com/
[9] https://hdc-cables.com/medium-voltage-abc-cable/
[10] https://www.nexans.no/en/products.html

RIGA 2023

The Exploration of the Influence of a Magnetic Field on a Fuel-cell System

Mustafa Melih Kale
Gazi University, Graduate School of Natural and Applied Sciences, Branch of Electrical and Electronic Engineering, Ankara, Türkiye, melihkale.58@gmail.com, ORCID: 0000-0001-8979-9805

Erol Kurt
Gazi University, Technology Faculty, Department of Electrical and Electronic Engineering, Ankara, Türkiye, ekurt52tr@yahoo.com, ORCID: 0000-0002-3615-6926

Cite this paper as: *Kale, M.M., Kurt, E ,. The Exploration of the Influence of a Magnetic Field on a Fuel-cell System, 11. Eur. Conf. Ren. Energy Sys. 18-20 May 2023, Riga, Latvia*

Abstract: Fuel cell systems convert the chemical energy to the electrical energy. Although there are many types of fuel cell systems, the most preferable one is so-called polymer electrolyte membrane (PEM) type. Since PEM has many advantageous on the other types, there are many applications for the energy requirements. In Ref. [1], Bizon, et. al., recommended a new energy control strategy for an energy efficient hybrid power system. This energy control strategy mainly uses an optimization scheme for the control of fuel economy by seeking a global extremum in a relevant algorithm, so that the dc power requirement on the load is considered for the flowing charge amount and applied to the air velocity used in the stack. In the present work, the effect of magnetic field *B* applied externally to the PEM fuel-cell stack in the hybrid power system is explored. Using the MatLab/Simulink code, *B* is varied to some extend from very low to the higher values in an arbitrary unit and the conversion output is examined versus the field strength. *B* gives a positive effect to the flowing current along the cell stack and contributes to the efficiency of the system. There exists an optimum field value, where the cell current flow maximizes. Besides, there are certain fluctuations in the current, where an optimization work is still required.

Keywords: *Fuel-cell, magnetic field, PEM, current fluctuation*

1. INTRODUCTION

Recent years have seen a growth in the utilization of renewable energy sources. Especially the use of solar and wind energy is important for microgrids. Since renewable energy sources are environmentally friendly, their usages in micro and smart grids around the world have become more important [1,2].

In addition to the renewable energy sources such as solar and wind, backup sources such as fuel cells are also used. Fuel cells are electrochemical systems converting chemical energy into the electrical energy. It has advantages on good mechanical properties, high selectivity, high power density and high efficiency in energy production. Although there are many different types of fuel cells, PEM is the most preferred fuel cell. Compared to other fuel cells, they can operate at lower temperatures, take up less volume, are lightweight and easy to operate. For these reasons, research and development activities on fuel cells today are performed in PEM fuel cells [3,4,5]. By using fuel cells as a backup source, the variability of the power flow in renewable energy sources is reduced. Therefore, the optimum operation of the hybrid power system and the energy storage system (ESS) design should be ensured. There are many algorithms in the literature for Hybrid Power System (HPS) optimization. Since there are two or more energy sources and loads in the HPS topology, the ESS must be properly designed. For this reason, many types of fuel cells can be used as backup energy sources in the HPS topology. However, in renewable energy sources, estimation is difficult as load flow (P_{Res}) and load demand (P_{load}) are variable. The boost converter is also

analyzed with LF control to reduce the uncertainty of the available power from renewable energy sources and to eliminate the variability in load demand [1].

Because fuel cells are electrochemical energy systems by applying a magnetic field to the fuel cells by increasing electron transfer rates. The increase in the electron transfer rate also affects the system [3]. In this work, the effect of *B* applied externally to the PEM fuel-cell stack in a hybrid power system is explored. For this process, *B* gives a positive effect to the flowing current along the cell stack and contributes to the efficiency of the system. There exists an optimum field value, where the cell current flow maximizes. Besides, there exist certain fluctuations in the current where an optimization work is still required.

2. MATERIALS AND METHODS

The HPS topology is simulated in Matlab-Simulink tool. The HPS topology considered in this study is reduced to a DC bus by modeling the other parts of the HPS with an equivalent DC load as shown in Fig. 1. Thus, an inverter system is modeled on the DC bus as it actually is. This energy control strategy mainly uses an optimization scheme for the control of fuel economy by seeking a global extremum in a relevant algorithm, so that the dc power requirement on the load is considered for the flowing charge amount and applied to the air velocity used in the stack [1,4]. The 6 kW / 45 V PEMFC model in the Matlab-Simulink library is used as a fuel cell in the design. The sketch of the magnetic field applied PEM fuel cell is shown in Fig. 1(a). The modeled HPS topology is illustrated in Fig. 1(b).

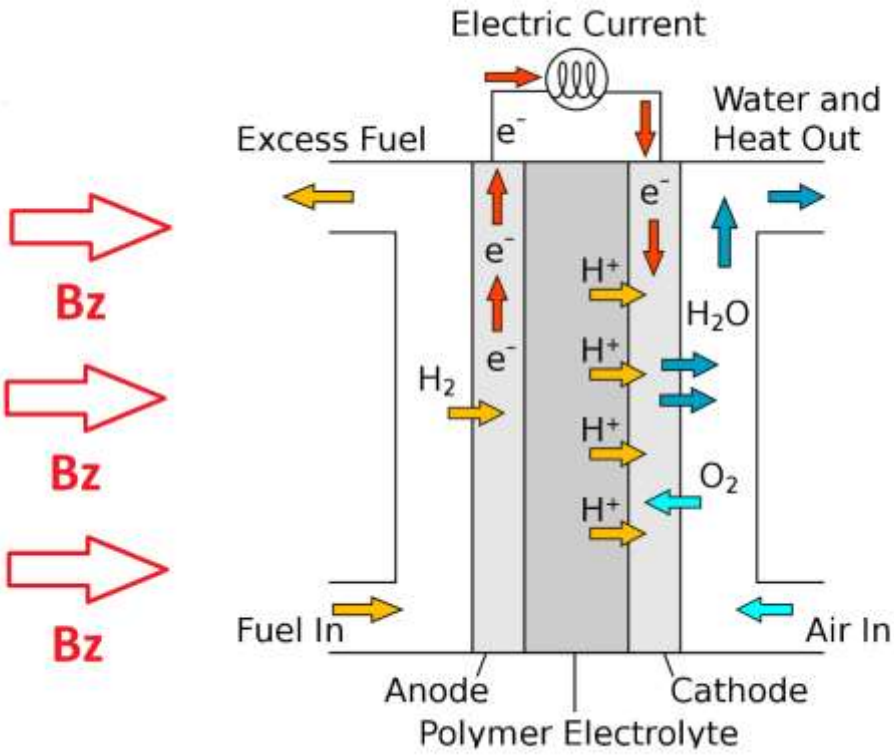

(a)

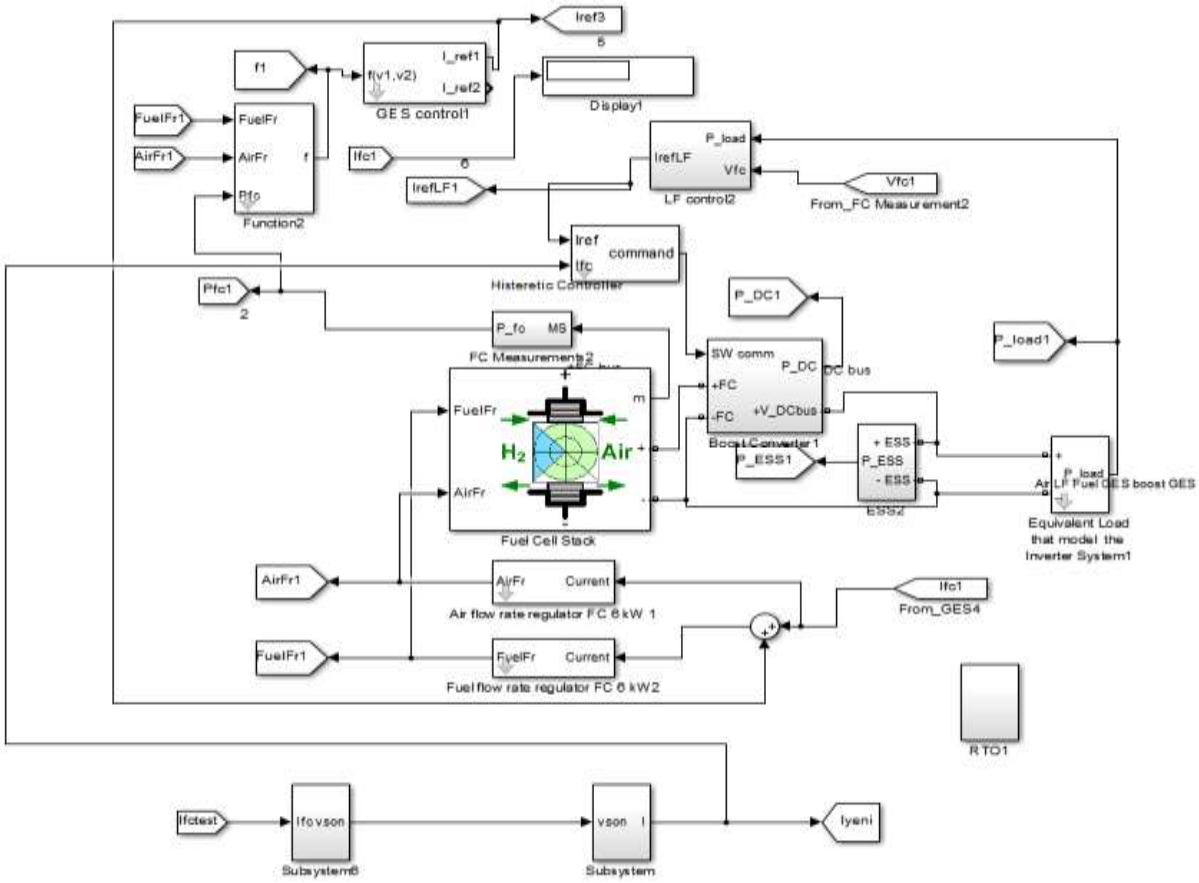

(b)

Figure 1 (a) The sketch of the magnetic field applied PEM fuel cell. (b)The HPS topology of the system.

In the designed model, the magnetic field to the fuel cell is performed over the I_{FC} current. I_{FC} current is the current measured from the fuel cell. The magnetic field is applied to this current through Eqs. 1-7.

$$\frac{dq}{dt} = I \tag{1}$$

$$\frac{dv_x}{dt} = a_x \tag{2}$$

$$\frac{dv_y}{dt} = a_y \tag{3}$$

$$\frac{dv_z}{dt} = a_z \tag{4}$$

$$\frac{da_x}{dt} = \frac{1}{m} I\, v_y\, B_z + \frac{q}{m} a_y\, B_z \tag{5}$$

$$\frac{da_y}{dt} = -\frac{1}{m} I\, v_x\, B_z - \frac{q}{m} a_x\, B_z \tag{6}$$

$$\frac{da_z}{dt} = 0 \tag{7}$$

The B_z value in these equations represents the magnetic field, which we apply to the system. By giving different B_z values, v_x and v_y values are obtained as the numerical solution of these equations. With these obtained velocity values, the new speed values in the system are calculated by,

$$V = \sqrt{v_x^2 + v_y^2 + v_z^2} \tag{8}$$

The new velocity value obtained from Eq. 8 is used in Eq. 9 to obtain the new electrical current of the system.

$$I = n\,q\,v\,S \qquad (9)$$

In Eq. 9, n represents the number of carriers per unit volume, q represents the electrical charge, v represents the averaged magnitude of velocity of charges in stack, and S represents the area, which is the cross-sectional area of the fuel cell, obtained by using the dimensions of the model specified in the Matlab-Simulink tool. Both n and q values are taken as constant. As a result of Eq. 9, new I_{FC} current is obtained and transferred to the system after each iteration.

3. RESULTS AND DISCUSSION

The maximum value of new current obtained as a result of the applied magnetic field values is given in Fig. 2. The maximum value of the current does not vary much, when the applied magnetic field value is small. However, as it continues to increase, the maximum value of the current increases. Even if the magnetic field continues to increase after reaching the optimum value, the maximum value of the current tends to decrease. In some magnetic field values, however, optimization work is required as the maximum value of the current fluctuates.

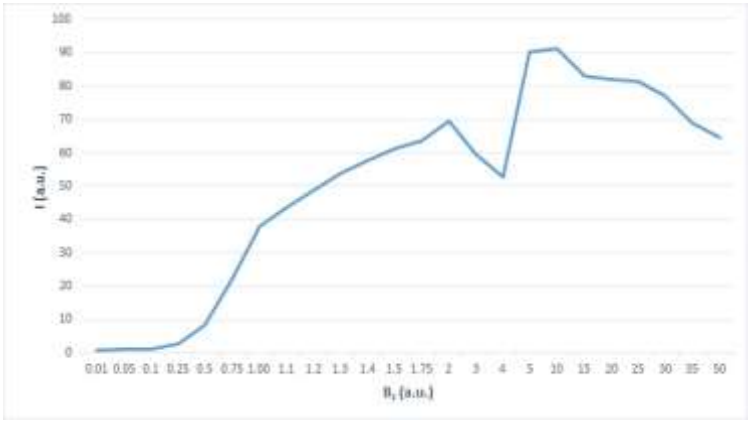

Figure 2. Maximum value of current.

Another value obtained by applying a magnetic field is the air flow rate (AirFr) of the fuel cell. The maximum value of AirFr also exhibited the behavior at the maximum value of the same current. The variation of the AirFr maximum value with respect to the magnetic field is given in Fig. 3

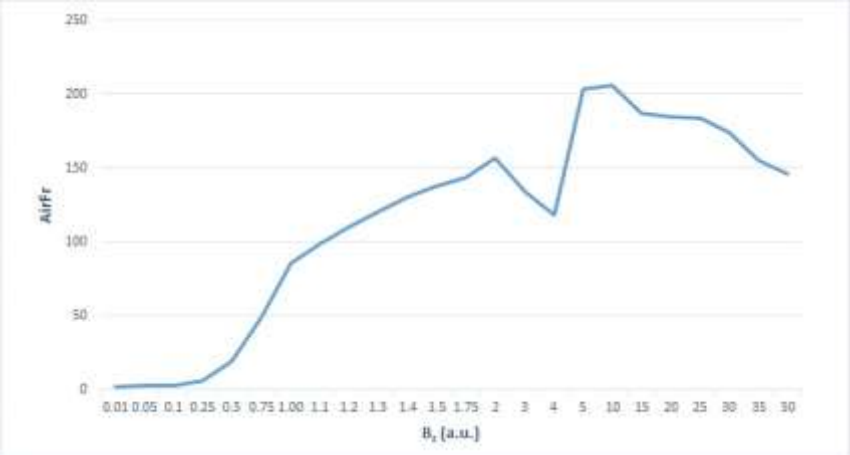

Figure 3. Maximum value of AirFr.

Another value obtained by applying a magnetic field is the fuel flow rate (FuelFr) of the fuel cell. The maximum value of FuelFr also exhibits the behavior at the maximum value of the same current. The variation of FuelFr maximum value with respect to magnetic field is given in Fig. 4.

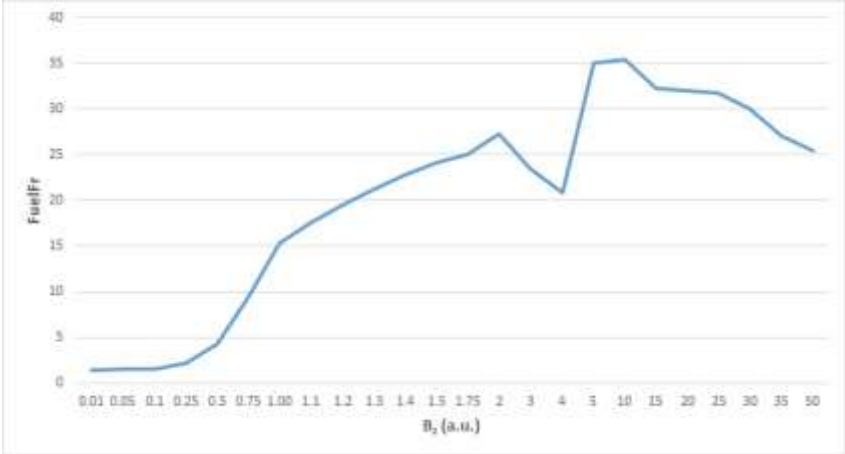

Figure 4. Maximum value of FuelFr.

Another value obtained by applying a magnetic field is the net power of the fuel cell (P_{fcnet}). The maximum value of P_{fcnet} also exhibits the similar behavior of the current at its maximum value. The variation of the P_{fcnet} maximum value according to the magnetic field is given in Fig. 5.

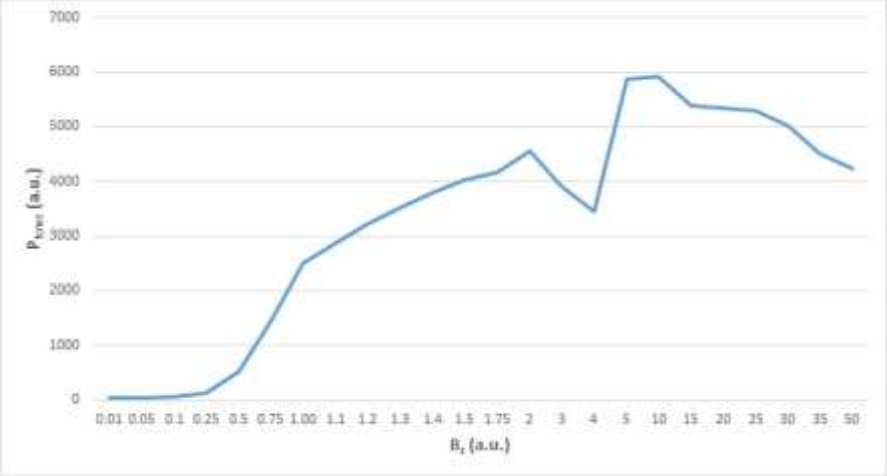

Figure 5. Maximum value of Pfcnet.

Another value obtained by applying a magnetic field is the efficiency of the fuel cell (Fig. 5).

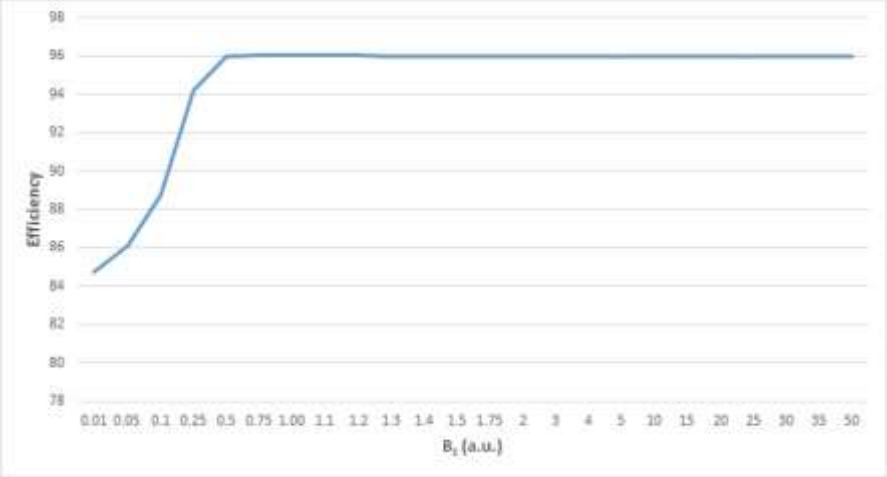

Figure 6. The efficiency variation with respect to the applied magnetic field B_z.

When low magnetic field values are applied, the efficiency obtained is less than about 90%, while the maximum value of the efficiency increases as the magnetic field increases. However, as the external magnetic field is increased, the maximum value of the efficiency stays constant.

4. CONCLUSIONS

In this study, the effect on the hybrid power system is simulated by applying a magnetic field to the PEM fuel cell. 24 different magnetic field values from 0.01 to 50 are adjusted to the system in theoretical manner. The magnetic field value applied to the fuel cell has a certain positive effect up to 15 a.u. Indeed, it contributes to an increase in fuel-cell current and hence it gives an increasing trend in net power in a.u. All these positive effects indicate better system efficiency up to 96 %. However, as the magnetic field value is increased above 15 a.u., it leads to a decrease in current. This proves that there exists a certain range in magnetic field giving better fuel cell results. To conclude, the application of an optimum level of magnetic field increases the performance of the system. In our future works, the optimization will be performed in detail for the stabilization problem in some magnetic field values so that the fluctuations may decay.

References

[1] Bizon N, Lopez-Guede JM, Kurt E, Thounthong P, Mazare AG, Ionescu LM, et al. Hydrogen economy of the fuel cell hybrid power system optimized by air flow control to mitigate the effect of the uncertainty about available renewable power and load dynamics. Energy Convers Manage;2019; 179:152-65.

[2] Olatomiwa L, Mekhilef S, Ismail MS, Moghavvemi M. 2016. Energy management strategies in hybrid renewable energy systems: areview. Renew Sustain Energy Rev; 2016; 62:821-35.

[3] Ahmed A. Abdel-Rehim. The influence of electromagnetic field on the performance and operation of a PEM fuel cell stack subjected to a relatively low electromagnetic field intensity. Energy Convers Manage;2019; 198:111906.

[4] Bizon N. Energy optimization of Fuel Cell System by using Global Extremum Seeking algorithm. Appl Energ; 2017; 206:458–74.

[5] Matsushima H, Iida T, Fukunaka Y, Bund A. PEMFC performance in a magnetic field. Fuel cells; 2008; 08(1):33–6

RIGA 2023

Adsorbed Gas Storage Digital Twin

Georg Klepp
Institute for Energyreserch (IFE), Technical University of Applied Science Ostwestfalen Lippe (TH OWL), Lemgo, Germany, georg.klepp@th-owl.de, ORCID: 0000-0003-1435-7468

Cite this paper as: *Klepp, Georg: Adsorbed Gas Storage Digital Twin, 11. Eur. Conf. Ren. Energy Sys. 19-20 May 2023, Riga, Latvia*

Abstract: One possibility for energy storage are fuels. With gaseous fuels like hydrogen or methane significant efforts are necessary for a feasible storage in terms of compression or liquefaction. This is of particular importance in the mobility sector. An alternative to high pressure or cryogenic gas storage is the storage by adsorption in porous media using nano carbons, metal-organic frameworks or metal hydrides as adsorbents. In order to assess the performance of the charging and discharging of adsorption tanks the mass and energy balance as well as the phase equilibrium (adsorption isotherm) and if present the spatial distribution of properties has to be considered. In order to simplify the analysis and prediction of these models an attempt is made to develop digital twins based on machine learning. Neural networks and Gaussian process regression are applied to replace the system of coupled nonlinear and differential equations. The data basis used is generated by simulations. Thus it is possible to easily predict the performance of a storage tank for different gases or to determine an optimum storage device (material and tank design).

Keywords: *adsorbtion, gas storage, machine learning*

1. INTRODUCTION

Energy storage in the form of gaseous fuels like methane and lately hydrogen is of increased importance. For a high volumetric storage capacity the gases have to be compressed to very high pressures (up to 100 bar for methane and up to 700 bar for hydrogen) or cooled to very low temperatures (-160 °C for methane (LNG) and -250°C for hydrogen (LH2)).

A less expensive alternative is adsorption storage, using the adhesion of the gas particles on the wall of a porous material like nano-carbons, metal-organic frameworks (MOF) or metal hydrides [1-4]. Thus in a tank with fixed volume at a given pressure and temperature level more gas can be stored together with the porous adsorbent material.

Due to the heat of adsorption the temperature changes during charging and discharging. Thus the ability of quickly charging or discharging the tank may be diminished. An optimization of the charging and discharging process includes the sizing of the tanks, the shape of the adsorbent, additional cooling/heating of the tanks, adaption of pressure level and mass flow rates for single tank and tank bundles.

Adsorption gas storage is of particular interest for use as fuel tanks in vehicles. Thus some experience is already available concerning the storage of methane (natural gas) and hydrogen (for fuel-cells) [3-5]. For the investigation lumped parameter models and CFD models [6-8] are used. For simple geometries and cooling by natural convection only, the temperature and pressure distribution is roughly uniform. With regard to the storage of gas mixtures there is less data available.

2. PHYSICAL MODEL

The adsorption of gases is described by the mass balance and the energy balance. The adsorption equilibrium is described by the Dubinin-Astakhov equation. The system of coupled non-linear algebraic and differential equation is solved by a Euler-forward numerical scheme. This model is described in detail in [9], some results for the charging of methane and hydrogen are shown in Figures 1-3.

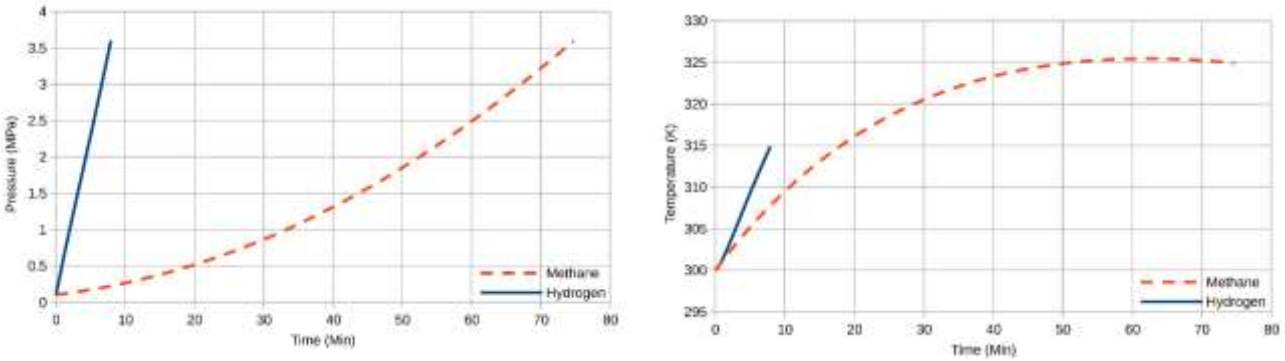

Figure 1. Charging of cylindrical tank filled with nano-carbon tank with gas. Temperature and pressure distribution for methane and hydrogen.

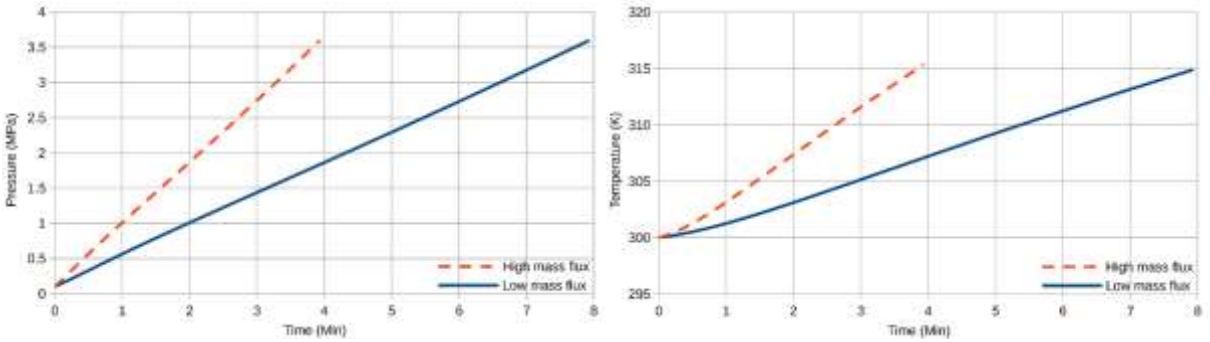

Figure 2. Charging of cylindrical tank filled with nano-carbon tank with hydrogen. Temperature and pressure distribution for different mass fluxes.

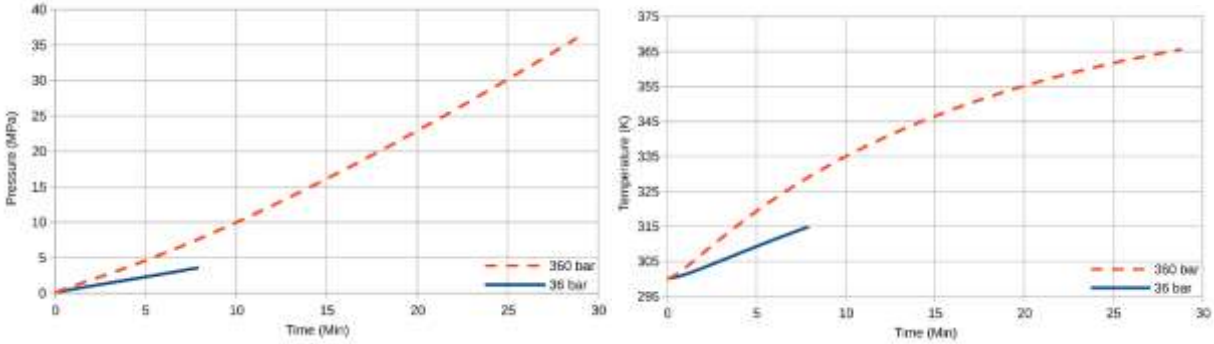

Figure 3. Charging of cylindrical tank filled with nano-carbon tank with hydrogen. Temperature and pressure distribution for different storage pressure.

The computational costs are relative high: The step size is restricted due the explicit computation (of particular importance with high storage pressures as for hydrogen) and the adsorption equilibrium is solved by iteration. Thus an alternative formulation, which is computationally significantly less expensive, is desirable. One possibility is to use a data driven machine learning model.

3. MACHINE LEARNING MODEL

The final target is to develop a machine learning model which can act as a digital twin of the adsorption gas storage system. The significant amount of varied data may be computed by physical models validated by experimental results. As a first step here the feasibility of this approach is investigated and appropriate methods are identified.

We will investigate the prediction of the charging process of hydrogen in nano-carbons in a cylindrical tank. Temperature, pressure and concentration of adsorbed hydrogen is computed as a function of time, mass flow rate, maximum storage pressure and mass flow, cylinder height and diameter or the hydrogen concentration in a methane-hydrogen mixture (enriched methane). Using the concentration as a variable the dependency of the model on material properties is described by one variable only. (The description in terms of material and adsorption properties requires significantly more variables.) The data sets used for training, validation and testing were generated with the method described in [9], the parameter range is shown in Table 1. The ambient conditions are 300 K and 100 kPa. Due to this approach the number of data points in the time range is of several orders of magnitudes higher than for the other variable ranges.

The methods used for machine learning are artificial neural networks (NN) and Gauss Process Regression (GPR). These models are used as implemented in Matlab [10]. A similar approach was used successfully in the modelling of heat transfer for impinging jets and the prediction of characteristics of double cambered profiles [11].

Table 1. Parameter range of design variables for machine learning

Variable	Range
Maximum storage pressure	36 bar – 700 bar
Hydrogen concentration	0 – 1
Tank diameter	0.11 m – 0.46 m
Tank height	0.6 m – 2.4 m
Mass flux	0.16 g/s – 0.62 g/s

4. RESULTS

For the modelling of the dependence on the operating conditions and on the hydrogen concentration respectively data sets of 14032 x 9 points for teaching and validation and a data sets of 3508 x 9 points for testing was computed. Input variables are time, maximum storage pressure, mass flow, tank diameter and height and hydrogen concentration. Output variables are pressure, temperature and adsorbed hydrogen concentration in the tank. In order to assess the number of data points needed some computations were performed with subsets of the original full datasets. Fivefold cross validation is used for the teaching and validation data sets.

Table 2. Correlation results machine learning pressure distribution

Method	GPR exp.	GPR square exp.	GPR Matern 5/2	NN 30/30	NN 30/30/30
Computation time	56	38	30	30	48
Validation R^2	1	1	1	1	1
Test R^2	0.47	-0.29	0.80	-0.03	-0.034

Table 3. Correlation results machine leaning different output variables

Variable	Pressure	Temperature	Adsorbed concentration
Computation time	39	33	66
Validation R^2	1	1	1
Test R^2	-2.4	0.99	-11

Some results of the machine learning and testing are shown in Table 2 and Table 3. The training and validation data is predicted with very good accuracy, the prediction of the test data is significantly worse. One reason for this effect is the uneven distribution of the data points. For the results shown, there are only 3 data points in the range of concentration, mass flow, diameter and height. Here the difference in the results are most pronounced The best results are for the GPR method with a Matern 5/2 covariance function. The NN with 2 layers of 30 neurons performs best of all NN, but still predicts significantly worse than the GPR model, see Table 2. Thus the GPR with 5/2 is chosen.

The temperature variation is predicted best, the greatest deviation between test values and predicted values are for the concentration of adsorbed species.

Decreasing the number of data sets in then time range and significantly increasing the number of data points in the other parameter ranges increases the quality of the predictions. The prediction of the pressure distribution is improved when the temperature is considered as an additional input variable.

5. OUTLOOK

The generated machine learning models may be used to predict the charging process of hydrogen and hydrogen-methane mixtures in cylindrical tanks filled with nano-carbon. As a next step more dimensions may be included in the machine learning model. In addition to mass flow, maximum storage pressure, tank dimensions and hydrogen concentration for hydrogen-methane mixtures other parameters may be taken into account in a similar way, i.e. tank shape or tank heat transfer characteristics. Most challenging will be the modelling of the adsorption characteristics and properties.

References

[1] R.W. Judd, D.T.M. Gladding, R.C. Hodrien, D. R. Bates, J.P. Ingram, M. Allen, “The Use of Adsorbed Natural Gas Technology for Large Scale Storage”, ACS Division of Fuel Chemistry, Preprints. 43, 1998
[2] H. Li, K. Wang, Y. Sun, C. T. Lollar, J. Li, H.-C. Zhou, “Recent advances in gas storage and separation using metal–organic frameworks”, Materials Today, Vol. 21 Number 2, 2018
[3] D. DeSantis, J. A. Mason, B. D. James, C. Houchins, J. R. Long, M. Veenstra, “Techno-economic Analysis of Metal−Organic Frameworks for Hydrogen and Natural Gas Storage”, Energy & Fuels, Vol. 31 Issue 2, pp. 2024-2032, 2017
[4] .C. Santos, F. Marcondes, J.M. Gurgel, “Performance analysis of a new tank configuration applied to the natural gas storage systems by adsorption”, Applied Thermal Engineering, Vol. 29 Issue 11-12, pp. 2365-2372, 2009
[5] P. Pfeifer, R. Little, T. Rash, J. Romanos, B. Maland, “Advanced Natural Gas Fuel Tank Project”, California Energy Commission, 2017
[6] S. Sahoo, M. Ramgopal, “A New Tank Configuration for Large Scale Storage of Natural Gas in Adsorbed Form”, International Journal of Petrochemical Science & Engineering, Vol. 2 Issue 7, 2017
[7] P. K. Sahoo, M. John, B. L. Newalkar, N. V. Choudhary, K. G. Ayappa, “Filling Characteristics for an Activated Carbon Based Adsorbed Natural Gas Storage System”, Ind. Eng. Chem. Res., Vol. 50 Issue 23, pp. 13000-13011, 2011
[8] P. K. Sahoo, B. P. Prajwal, S. K. Dasetty, M. John, B. L. Newalkar, N. V. Choudary, K. G. Ayappa, “Influence of exhaust gas heating and L/D ratios on the discharge efficiencies for an activated carbon natural gas storage system”, Applied Energy, Vol. 119, pp. 190-203, 2014
[9] Klepp G.: Adsorbed Renewable Gas Energy Storage. International Renewable Energy Storage (IRES) Conference. Düsseldorf 2020
[10] The Math Works, Inc. MATLAB. Version 2021b
[11] Klepp G.: Überführen von CFD-Ergebnissen in ML-Modelle, Seminar "Machine Learning und Artificial Intelligence in der Strömungsmechanik und der Strukturanalyse" NAFEMS Seminar 16.-17. Mai 2022 in Wiesbaden, NAFEMS CAE Online Magazin 62

RIGA 2023

Production and Consumption Load Profile Characterization in Energy Communities

Wolfram Rozas
Universidad Nacional De Educación A Distancia, ETS Ingeniería Informática, Madrid, Spain,
wrozas@scc.uned.es, [0000−0003−3036−1803]

Rafael Pastor
Universidad Nacional De Educación A Distancia, ETS Ingeniería Informática, Madrid, Spain,
rpastor@scc.uned.es, [0000−0002−4089−9538]

José Carpio
Universidad Nacional De Educación A Distancia, ETS Ingenieros Industriales, Madrid, Spain,
jcarpio@ieec.uned.es, [0000−0001−6397−1734]

Cite this paper as: *Rozas, W., Pastor, R., Carpio, J. Production and consumption load profile characterization in Energy Communities. 11. Eur. Conf. Ren. Energy Sys. 18-20 May 2023 Riga, Latvia*

Abstract: Energy Transition is changing the renewable energy participation in current generation systems. Due to its inherent intermittent and variable nature, forecasting production and consumption load profile will be more challenging and demand more complex predictive models. In this paper, the production and consumption load profile of the Cornwall Local Energy Market Energy Community were analyzed with statistical time series methods to improve their accuracy in identifying the opportunity market provided by the storage units. With this more accurate and detailed knowledge, all units will benefit more from their installation by optimizing their energy consumption, production, and storage and will make the Local Energy Market more fluid and safer to state a flexibility system that will guarantee the technical quality of the product in the whole system. The research has trained several SARIMA, and Granger Causality model combinations to fit the time series observations with a low forecast error rate, outperforming the equipment vendor estimations and setting the path for more advanced predictive methods, which will automatically make accurate decisions to produce better performance in every unit belonging to the Energy Community.

Keywords: *Uncertainty, Flexibility, Time Series, Granger Causality*

1. INTRODUCTION

The Energy Transition is boosting the integration and development of distributed energy resources (DER) in the power grid, resulting in demand and prices becoming more unstable and less predictable than ever. The technical quality of this new electricity generation system will face the challenge of coping with the massive entrance of new renewable energy generation assets. The reason is renewable energy's inherent intermittent nature, which depends on variable meteorological conditions. Under this new complexity, a load and renewable generation forecasting model is critical to avoid ramp rates and grid instability. These forecasts will benefit all agents (from system operators to new generators like Energy Communities) since it optimizes energy costs and minimizes system management uncertainties by adopting Flexibility Systems that utilize all available resources optimally.

Our research is based on the Cornwall Local Energy Market [1], which has established 100 dwellings identified with owner-occupiers. Some of these sites were AC-coupled, with existing Solar PV array + Inverter; others were DC-coupled, with new solar PV array. This Local Energy Market trial published a dataset [2] about the sites, including energy and Battery Energy Storage System State of Charge measurements from the equipment and an

independent management system. The dataset also includes consumption and production forecast along with weather forecast measurements. The dataset has a properly documented dictionary [3]. All energy flows are depicted in Fig. 1. Trilemma Consulting produced several reports analyzing the Sites Metadata [4], the Fleet Self-Consumption [5], and the BESS Utilisation [6].

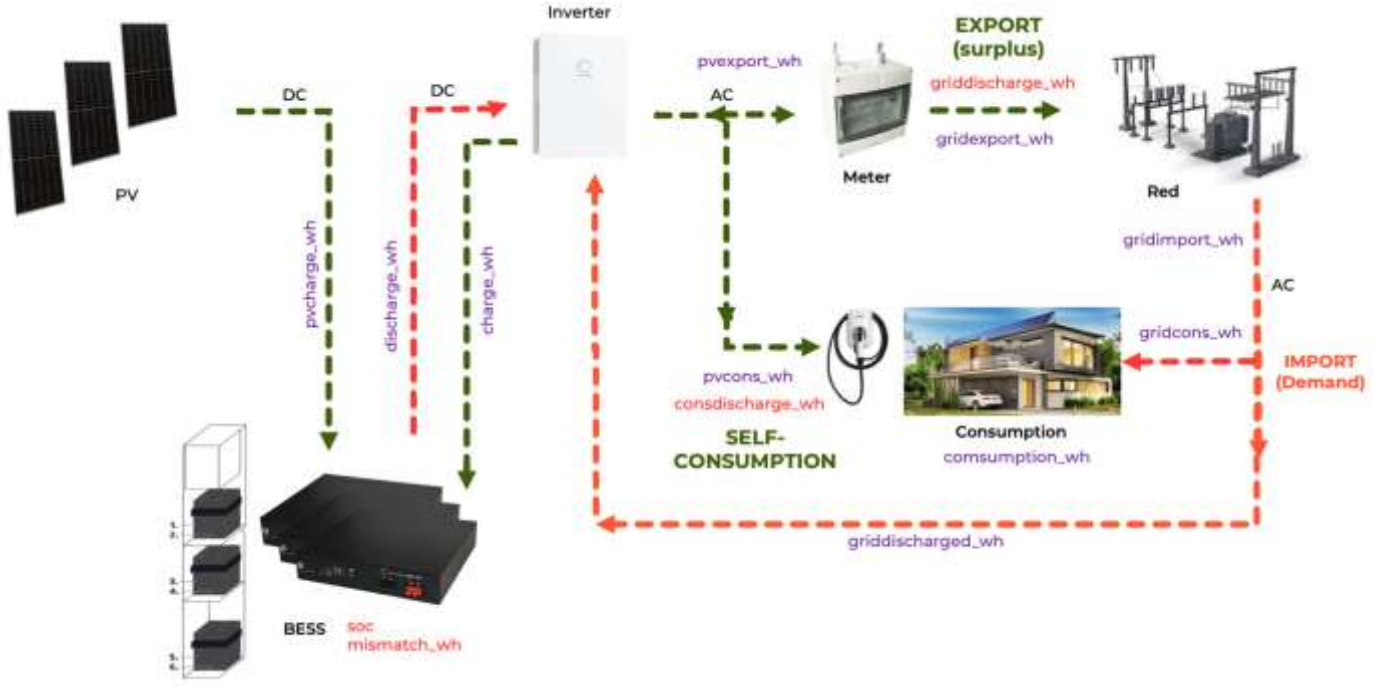

Figure 1. Cornwall LEM Dataset: Energy and BESS State of Charge Measurements

2. METHODS

We propose to develop accurate predictive models that guide the dwellings in purchasing energy inexpensively by consuming or charging BESS (downward flexibility) and selling it when it is expensive by discharging BESS (upward flexibility). This research aims to build predictive sequence models that forecast Consumption and Production time series for a certain site and compare results with Consumption and Production equipment-based forecasts.

Today researchers are applying multiple regression techniques for Renewable Energy Forecasting in solar, wind, hydro-power, geothermal, and biomass domains. Algorithm categories include advanced statistical methods, machine learning techniques, deep machine learning techniques, and new exotic hybrid models. At this point, we develop our analysis with statistical methods. Today's advanced statistical methods include Multivariate Regression, Multiple linear regression (MLR), Forward Regression, Quantile regression, Exponential smoothing model, Autorregresive

Integrated Moving Average (ARIMA), Nonlinear autoregressive exogenous model (NARX), Autoregressive Fractionally Integrated Moving Average (ARFIMA), Generalized autoregressive conditional heteroskedasticity (GARCH), Maximum likelihood, Bayesian approach, Kernel density estimation (KDE) among others[7], [8], [9], [10], [11]. The methods chosen for this analysis are SARIMA and Granger Causality methods. SARIMA methods based on correlation are selected because they accurately capture sequences of stationary time series. Granger Causality method was selected to verify the cause-effect relationship between the time series to be predicted and its predictor variables.

2.1. Sequence Models: ARIMA models

Time Series forecasting uses a statistical model to predict future time series values based on past results. SARIMA (Seasonal Autorregresive Integrated Moving Average) models is a particular type of ARIMA (Autorregresive Integrated Moving Average). These models explain a given time series based on its past values -i.e., its lags and the lagged forecast errors, both stationary and non-stationary. The equation can be used to forecast future values. Any time series exhibiting patterns and not a random white noise can be modeled with SARIMA models. SARIMA models suit stationary time series like electricity load or renewable generation. SARIMA Models are specified by six order parameters: (p, d, q) x (P, D, Q). The first three parameters represent the non-seasonal part of the model is the second three parameters the seasonal part. p represents the order of the AR term, q the order of the MA term, and d the number of differences required to make the time series stationary; all of them refer to the nonseasonal part of the model. P, D, Q represent the same in the seasonal part of the model. AR(p) Autoregression – a regression model that utilizes the dependent relationship between a current observation and observations over a previous period. An autoregressive (AR(p)) component refers to using past values in the regression equation for the time series. I(d) Integration – uses differences of observations (subtracting an observation from observation at the previous time step) to make the time series stationary, a necessary condition using SARIMA models. Differencing involves subtracting the current values of a series with its previous values d number of times. MA(q) Moving Average – a model that uses the dependency between an observation and a residual error from a moving average model applied to lagged observations. A moving average component depicts the model's error as a combination of previous error terms. The order q represents the number of terms included in the model.

$$Y_t = \alpha + \beta_1 Y_1 + \cdots + \beta_p Y_p + \cdots + \phi_1 \varepsilon_1 + \cdots + \phi_q \varepsilon_q$$

To identify the AR parameter (p), the Total Autocorrelation Function (ACF) is used, and to identify the MA parameter (q), the Partial Autocorrelation Function (PACF) is used. These functions draw correlograms that help to identify lags where total or partial autocorrelation is meaningful. The Integration (d) parameter represents the number of differences to be taken in the series to make it stationary. Finally, to check if the identified SARIMA model has captured the data process, the Ljung- Box Q test is used. This test contrasts the null hypothesis that the autocorrelations of a time series are random. If residual errors are not random, that implies there is a structure in the observed series that the model does not explain. The more random the errors, the more likely it is a good model. If p-values are bigger than 5%, we cannot reject the null hypothesis reinforcing the evidence our model is capturing the data process.

2.2. Time-causal Models: Granger Causality

Time-causal modeling (TCM) is a method that attempts to discover key temporal relationships in time series data. It is a method to discover temporal relationships using a combination of Granger Causality [12] and regression algorithms for variable selection. Introduced by Clive Granger, Granger causality in time series is based on the intuition that a cause should necessarily precede its effect and that if time series causally affects time series, then past values should be useful in predicting future values. More specifically, time series is said to be a "Granger cause" time series if the accuracy of regressing in terms of past values of both is statistically significantly better than regressing just with past values.

An essential feature of a Time Causal Model algorithm is that it measures the influence of independent variables on the dependent variable and the influence of the dependent variable on the independent variables. The model tests the significance of this cause-effect relationship between the production, consumption load profile, and the predictors variables.

3. EXPERIMENTATION AND RESULTS

3.1. SARIMA and Granger Causality models

SARIMA and Granger Causality models for Consumption and Production have been developed for sites with different profiles (#28 and #37). A prior site clustering obtained 4 groups: ORDINARY FAMILIES, BIG FAMILIES, SMALL COMMERCIAL, and MEDIUM-SIZE COMMERCIAL. Site #28 belongs to the first profile,

and Site #37 belongs to the second profile. Consumption time series needs to be differentiated once to be stationary. Production is a stationary time series.

SARIMA models are specified with and without predictor variables (inputs). Selected predictor variables included the following: discharge, energy discharged from the battery (measured in kWh); charge, energy used to charge the battery (measured in kWh); consumption, energy consumption on the site (measured in kWh); grid export, energy exported to the grid (measured in kWh); PV charge, energy from Solar PV system that is diverted instantaneously.

to BESS charge (measured in kWh); PV consumption, energy from Solar PV system that is used instantaneously for Consumption (measured in kWh); PV export, energy from Solar PV system that is spilled instantaneously to Grid Export (measured in kWh); grid discharge, energy from BESS discharge that is spilled instantaneously to Grid Export (measured in kWh); grid charge, energy for BESS discharge that is supplied instantaneously by Grid Import (measured in kWh); grid consumption, energy from Grid Import that is used instantaneously for Consumption (measured in kWh); grid consumption discharge, energy from BESS Discharge that is used instantaneously for Consumption (measured in kWh); BESS State of Charge (SOC), customer state of charge compared to an absolute state of charge (measured as a percentage); precipitation (measured in mm); precipitation probability %; wind direction (wind direction in degrees. 0 is north, 90 is east, 270 is west); wind speed (measured in knots); solar radiation (measured in J/cm2); and sunshine duration (measured in minutes).

Fig. 2 presents different ARIMA, and Granger Causality models have been assessed using the Q-test Ljung box for testing the absence of serial autocorrelation; Mean Error or average of errors across all records (it indicates whether there is a systematic bias in the model); Mean Absolute Error or an average of the absolute values of the errors across all records (it indicates the average magnitude of error, independent of the direction); Standard Deviation of the errors; Linear Correlation between the predicted and actual values.

Function	Site		Model	Q-test	Mean Error	Mean Absolute Error	Standard Deviation	Linear Correlation	Most important Predictors
Production kWh	Site 28	w/o Inputs	SARIMA (0,1,3)x(1,0,1)	0.3	-0.093	3.040	3.921	0.844	
			SARIMA (6,1,6)x(0,0,0)	0.4	-0.027	3.019	3.903	0.845	
		w/Inputs	Exponential Smoothing	0.0	-1.510	5.136	7.722	0.914	
			SARIMA(0,1,1)X(0,0,0)	0.5	0.000	0.000	0.001	1.000	PV Export kWh, PV Charge kWh, PV Consumption kWh
			SARIMA (3,1,3) x (2,0,2)	0.6	-0.059	2.266	2.941	0.909	Grid Import kWh, Consumption kWh
			Granger Causality	N/A	0.000	3.058	3.948	0.830	Solar radiation, wind direction, PV Consumption kWh, Wind Speed
	Site 37	w/o Inputs	Exponential Smoothing	0.0	0.053	4.410	5.495	0.726	
			SARIMA(3,0,4)X(0,0,0)	0.5	-0.082	4.321	5.405	0.735	
		w/Inputs	Exponential Smoothing	0.0	-1.791	4.952	6.158	0.676	
			SARIMA(0,1,1)X(1,0,1)	0.3	0.000	0.000	0.001	1.000	PV Charge kWh, PV Consumption kWh, PV Export kWh
			SARIMA (1,1,1)x(0,0,0)	0.1	-0.006	3.367	4.290	0.857	kWh
			Granger Causality	N/A	0.000	3.925	5.037	0.762	Grid Discharge kWh, Wind Direction, PV Export kWh, Solar Radiation
Consumption kWh	Site 28	w/o Inputs	SARIMA(0,1,2)x(0,0,0)	0.8	-0.015	3.762	4.815	0.965	
		w/Inputs	Exponential Smoothing	0.0	-1.510	5.136	7.722	0.914	
			SARIMA(0,1,2)X(0,0,0)	0.1	0.016	0.842	1.163	0.998	Grid Consumption kWh, Discharge kWh
			SARIMA (7,1,7)x(0,0,0)	0.2	0.069	3.617	4.829	0.965	Discharge kWh, Consumption Discharge kWh
			Granger Causality	N/A	0.000	4.446	6.506	0.935	Grid Export kWh, PV Charge kWh, Grid Charge kWh, precipitation
	Site 37	w/o Inputs	SARIMA(2,0,1)x(0,0,0)	0.3	0.140	3.054	4.182	0.948	
		w/Inputs	Exponential Smoothing	0.2	-0.309	3.762	5.880	0.894	
			SARIMA(0,1,1)X(0,0,0)	0.0	0.004	0.082	0.127	1.000	Grid Import kWh, Discharge kWh, PV Consumption kWh
			SARIMA (13,1,13)x(0,0,0)	0.63	0.006	2.882	3.789	0.958	Solar irradiance, PV Consumptoion kWh, Charge kWh, Discharge kWh, Grid Import kWh, Sunshine duration, Production kWh, SOC%
			Granger Causality	N/A	0.000	3.655	5.374	0.911	Precipitation probability, Wind direction, PV Export kWh, Wind speed

(*) SARIMA (p,d,q) x (P,D,Q)

Figure 2. Production and Consumption SARIMA and Granger Causality with and without predictor variables model accuracy comparison for sites 28 and 37

3.2. ARIMA and Granger Causality model vs. forecast performance comparison with Equipment Forecast

ARIMA and Granger Causality estimation models for the Production and Consumption load profiles fit the time series properly and outperform the Equipment forecasts. The results for Production kWh are depicted in Fig. 3 for Site 28 for one year (April 2019 to March 2020).

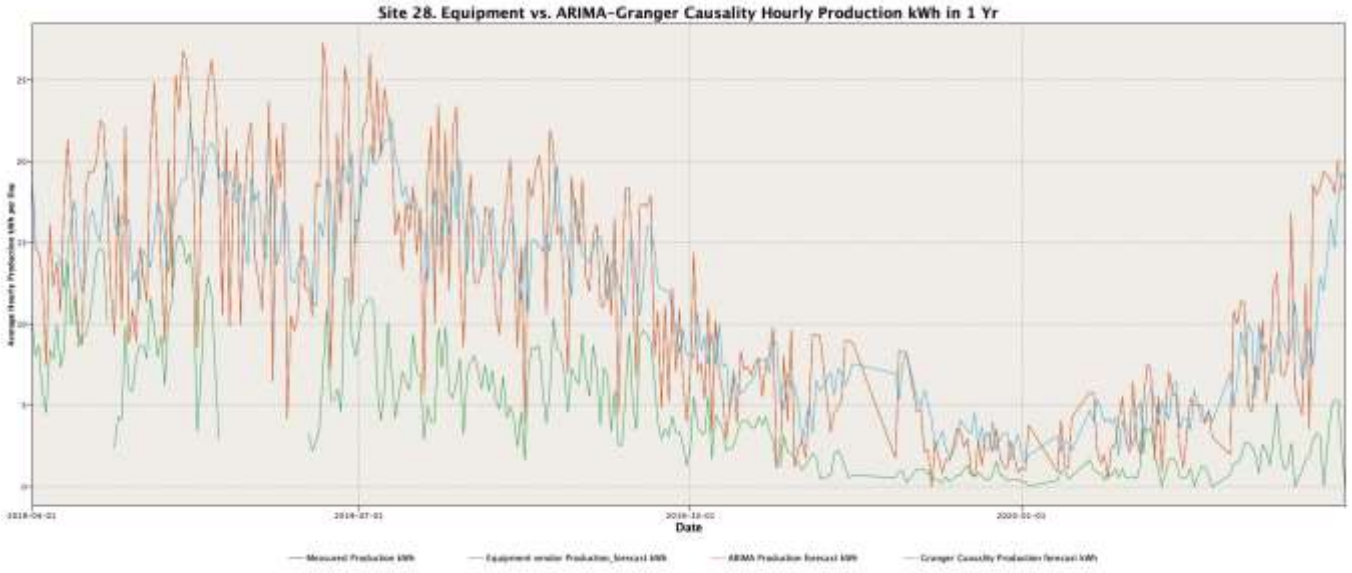

Figure 3. Site 28. Equipment vs. SARIMA-Granger Causality Average Hourly Production kWh per Day in 1 Yr

The best SARIMA models and Granger Causality present high fitness rates with real observed time series. This annual time series (April 2019 to March 2020) shows the better performance of time series models confronted to the forecasts produced by the equipment vendor. A clear annual profile in the average hourly production shown by the model indicates the highest production at the end of spring and summer. The lowest average hourly production is generated at the end of the autumn and during the winter.

4. CONCLUSIONS & FUTURE RESEARCH

In the paper, the Cornwall Local Energy Market dataset is analyzed for Consumption and Production in their 100-dwelling energy community with two time series algorithms, SARIMA and Granger Causality models. These two relevant sequence predictive methods and the results are suitable and present a significant improvement in their forecasting error rate compared with the forecast produced by the equipment vendor in this community.

Further research is needed to improve accuracy and stability with new sequence deep learning methods like recurrent neural networks, LSTM neural networks, bayesian neural networks, or 1D transformers [13], [14], [15], [16], [17], [18]. Analyzing ultra-frequency data with these non-linear methods will help all players in the system to react optimally to ordinary life situations.

Acknowledgment

The authors want to thank UNED for its support. Also, we thank D. Nicholls from Centrica PLC and D. Kane from Trilemma Consulting Limited for sharing the Cornwall LEM dataset [2].

References

[1] Dr David Kane, Dr Andrew Peacock DPM. Cornwall Local Energy Market Residential Project A Whistle stop Tour; 2020.
[2] Dan Nicholls, Dr David Kane. Cornwall LEM Residential Electricity Dataset with Solar Production and Battery Storage, 2018 2020. UK Data Service; 2021.
[3] Dr David Kane, Dr Andrew Peacock DPM. LEM Residential Data Dictionary PUBLIC; 2020.
[4] Dr David Kane*, Dr Andrew Peacock DPM. LEM Residential Metadata Summary Report; 2020.
[5] Dr David Kane, Dr Andrew Peacock DPM. LEM Residential Fleet Self-Consumption Summary Report; 2020.

[6] Dr David Kane, Dr Andrew Peacock DPM. LEM Residential BESS Utilisation Summary Report; 2020.
[7] Zendehboudi A, Baseer MA, Saidur R. Application of support vector machine models for forecasting solar and wind energy resources: A review. Journal of Cleaner Production. 2018;199:272-85. Available from https://doi.org/10.1016/j.jclepro.2018.07.164.
[8] Das UK, Tey KS, Seyedmahmoudian M, Mekhilef S, Idris MYI, Van Deventer W, et al. Forecasting of photovoltaic power generation and model optimization: A review. Renewable and Sustainable Energy Reviews. 2018;81(June 2017):912-28. Available from: http://dx.doi.org/10.1016/j.rser.2017.08.017.
[9] Wang H, Lei Z, Zhang X, Zhou B, Peng J. A review of deep learning for renewable energy forecasting; 2019.
[10] Lai JP, Chang YM, Chen CH, Pai PF. A survey of machine learning models in renewable energy predictions. Applied Sciences (Switzerland). 2020;10(17).
[11] Voyant C, Notton G, Kalogirou S, Nivet ML, Paoli C, Motte F, et al. Machine learning methods for solar radiation forecasting: A review; 2017.
[12] Song X., Taamouti A. A Better Understanding of Granger Causality Analysis: A Big Data Environment. Oxford Bulletin of Economics and Statistics. 2019;81(4):911-36.
[13] Pin Lai J. et al. “A survey of machine learning models in renewable energy predictions”. In: Applied Sciences (Switzerland) 10.17 (2020). issn: 20763417. doi: 10.3390/app10175975
[14] Mellit A. et al. “Advanced methods for photovoltaic output power forecasting: A review”. In: Applied Sciences (Switzerland) 10.2 (2020). issn: 20763417. doi: 10.3390/app10020487.
[15] Mosavi A. et al. “State of the art of machine learning models in energy systems, a systematic review”. In: Energies 12.7 (2019). issn: 19961073. doi: 10.3390/en12071301.
[16] Pérez-Ortiz M. et al. “A review of classification problems and algorithms in renewable energy applications”. In: Energies 9.8 (2016). issn: 19961073. doi: 10.3390/en9080607.
[17] Ferrero Bermejo J. et al. “A review of the use of artificial neural network models for energy and reliability prediction. A study of the solar PV, hydraulic and wind energy sources”. In: Applied Sciences (Switzerland) 9.9 (2019). issn: 20763417. doi: 10.3390/app9091844.
[18] Kumar Das U. et al. “Forecasting of photovoltaic power generation and model optimization: A review”. In: Renewable and Sustainable Energy Reviews 81.June 2017 (2018), pp. 912–928. issn: 18790690. doi: 10.1016/j.rser.2017.08.017. url: http://dx.doi.org/10.1016/j.rser.2017.08.017.

RIGA 2023

The Use of Renewable Energy Sources and Radiant Capillary Heat Exchangers to Increase the Energy Efficiency of an Existing Apartment

Staņislavs Gendelis
University of Latvia, Rīga, Latvia, stanislavs.gendelis@lu.lv, ORCID: 0000-0003-3699-2526

Oskars Puļķis
Hydrokapillar Tech, Ltd., Rīga, Latvia, oskars.pulkis@gmail.com, ORCID: 0009-0001-9328-4043

Andris Jakovičs
University of Latvia, Rīga, Latvia, andris.jakovics@lu.lv, ORCID: 0000-0003-3410-5081

Indulis Bukans
Hydrokapillar Tech, Ltd., Rīga, Latvia, inismail@gmail.com

Cite this paper as: *Gendelis, S., Puļķis, O., Jakovičs, A., Bukans, I. The use of renewable energy sources and radiant capillary heat exchangers to increase the energy efficiency of an existing apartment. 11th Eur. Conf. Ren. Energy Sys. 18-20 May 2023, Riga, Latvia*

Abstract: The use of capillary heat exchangers with large area means the lowest heat carrier temperature – typically less than 30°C for the heating. This determines the very efficient use of the installed heat pump due to increasing of coefficient of performance (COP) with decreasing of provided water temperature. The aim of the study was to find out whether renewable energy sources and radiant capillary heat exchangers increases energy efficiency. In order to achieve the maximum energy efficiency during the renovation of the existing apartment, a combination of two green approaches was used. One of them is the replacement of the existing high-temperature radiator heating system with radiant capillary mats. The same system is also used for cooling, which was not possible with the existing system. The necessary energy is provided from renewable aerothermal energy by installing a heat pump together with PV panels to ensure the electricity consumption.

The measurements were made in the apartment to determine the thermal transmission properties of all boundary structures, and an air exchange rate using long-term monitoring. Experimental data was used to create the heat balance, to estimate the heating and cooling powers as well as the seasonal energy need. The amount of capillary heat exchangers and the size of the heat pump were chosen accordingly.

The very first energy consumption data allow to conclude that the planned improvement of the energy efficiency has been successfully achieved by using technology combination described, without improvement of the thermal properties.

Keywords: *Radiant heat exchanger, heat pump, energy efficiency, renewable energy source*

1.INTRODUCTION

Because of the recent increase in the energy prices, the issue of usage of renewable energy sources has become highly important. It is critical not only to alter energy sources, but also to minimize end-user energy requirements by enhancing building energy efficiency and utilizing highly efficient heating and cooling systems.

Heat pumps are the most widely used renewable and very efficient energy source for heating, with costs equivalent to natural gas and district heating systems [1]. Their efficiency described as coefficient of performance (COP) increases when the temperature difference between the energy source and the heat exchanger in the room decreases [2, 3]. Traditional convectors have heat carriers with temperatures above 50°C, the use of an underfloor water-based heating system reduces the temperature to 40°C due to the larger area. However, radiant capillary heat exchangers (RCHE) [4] with the biggest surface areas are the most effective heat exchanger options, allowing decrease the water temperature down to 26-30°C with the same amount of power. Another advantage of RCHE is that it may be used in both heating and cooling modes. Therefore, the most effective way to reduce the heating costs without doing anything with the boundary structures is a combination of the efficient heat pump with as low as possible heat carrier temperature.

The aim of the study is to experimentally show the possibility to reduce to minimum or even to avoid the externally supplied energy by installation of combination of modern technical systems and technologies (Fig. 1), with the focus on efficiency and renewable energy sources. It is important to note that the study is carried out in an old non-insulated building from without improvement of their boundary structures.

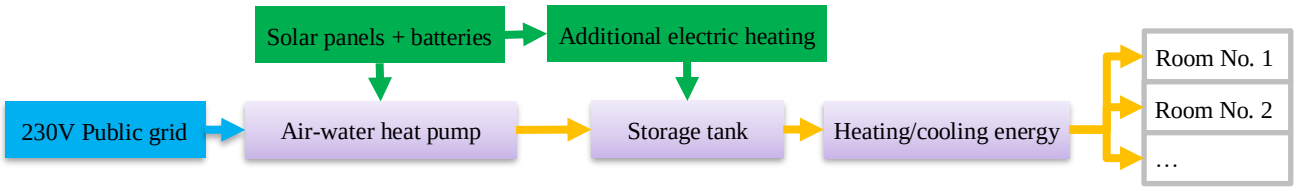

Figure 1. Planned energy flows in a studied apartment.

2.MATERIALS AND METHODS

In order to achieve the maximum energy efficiency during the renovation of the heating system only in an existing apartment with four rooms and heated floor area of 47 m^2 (Fig. 2), a combination of three modern and energy effective approaches was used. One of them is the replacement of the existing high-temperature radiator heating system with radiant capillary mats (Fig. 3, left); the same system is also used for cooling, which was not possible with the existing system. The other is to use of air-water heat pump technology for needed energy production (Fig. 3, center). And the third component is solar panel system with batteries for production of electricity, which is necessary to operate the heat pump (Fig. 3, right). A comprehensive scheme showing all installed components is shown on Fig. 4.

Before starting the experiment, the required power and annual energy demand and for the apartment was determined to select the most appropriate heat pump, the number of solar panels and the necessary number of capillary mats to be installed. Two calculation methods - a complex and precise approach based on the ISO 52016-1 standard [5, 6] and a simplified calculation tool with capillary mats plugin [7] developed at the Institute of Numerical Modelling of University of Latvia were used.

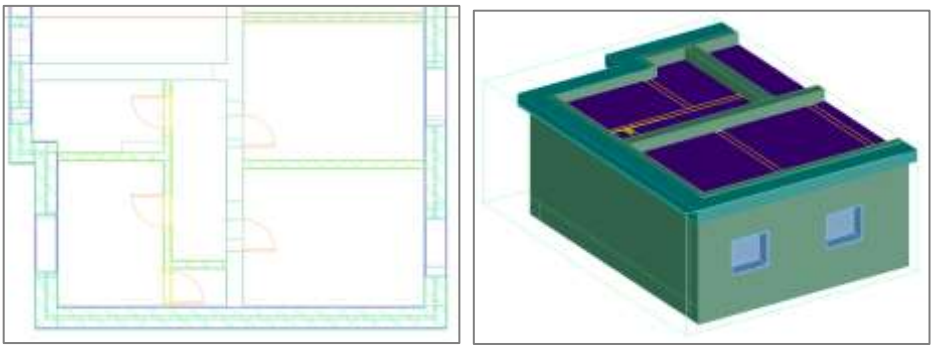

Figure 2. Plan (left) and 3D model (right) of the apartment with installed components.

Figure 3. Components used in a studied apartment – capillary mats, heat pump and solar panels (see also Fig. 4).

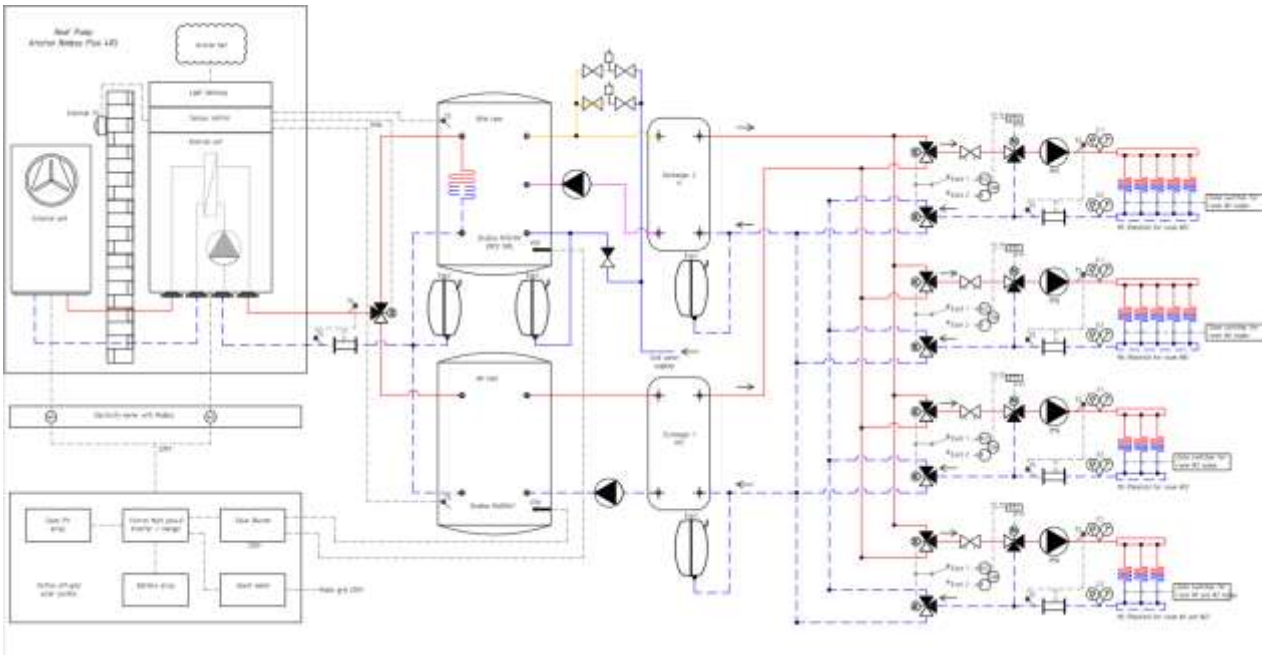

Figure 4. Overview of the installed combination of technical systems and technologies (see Figs. 2, 3).

The main parameters who determine the heat losses from the apartment – thermal transmission (*U*-values) of all boundary structures incl. walls, ceiling and floor, as well as air exchange rate, who determine the convective heat losses – were determined experimentally using long-term measurements (Fig. 5). Get results are used in above mentioned simplified and detailed calculation heat balance models – resulting energy demand for both approached produces very similar results (9200 kWh per year), but the estimated heating power value differs by more than 20%, therefore 4 kW value is taken from the standard-based (as the most detailed and verified) model.

Figure 5. Measurements of thermal transmittance and air change rate.

In the next step, the power of the heat pump and the appropriate model *Ariston Nimbus Plus 40 S* was matched to provide full heating needs and potential domestic hot water demand. Its maximum heat output for water temperature regime in a capillary mats 35/30°C is 5.7 kW at air temperature of 7°C; rated COP at this temperature reaches 5.1 (in accordance with EN 14511), which is typical for modern air-water heat pumps [8].

The parameters of installed solar system are selected in such a way as to maximally cover the electricity need of the heat pump compressor throughout the 24-hour cycle. The following parameters were obtained as a result of the modelling [9]: 3.75 kWp total installed peak power (10 modules); 6kWh LFP-type battery; 2kW additional electric water heating device.

Radiant capillary heat exchangers are installed in four rooms using different installation methods (Fig. 6): on the ceiling using *KNAUF D112* gypsum board suspended ceiling system [10], on the walls – using wood wool panels [11] and on the floor made of the dry expanded clay – with self-leveling floor mix.

Figure 6. Capillary heat exchangers installed in ceiling, walls and floor.

Installed capillary heat exchangers system (Fig. 4) allows to provide the set temperature in each room independently, regardless of the heating or cooling need and heat sources like different solar intensity of the opposite facades and variable occupancy. This type of solution is especially useful in cases of temperature fluctuations during the spring/autumn seasons. For this purpose, two water tanks are installed in the system (Figs. 4 and 7). Hot water is prepared in one of them (incl. also domestic hot water for shower and kitchen), and cold water in the other. Three-way valve is used for switching between heating/cooling and domestic hot water preparation. Accordingly, two heat exchangers (see Fig. 4) are also installed in the system, which can optionally be connected to the manifold of any room with the help of a motorized 3-way switch valve. Dozens of temperature, air humidity and pressure sensors are installed for monitoring, control and management of the heating/cooling modes. For cooling mode very critical are dew point sensors. Ultrasonic heat energy meters are installed on the water pipes in each room; the different energy loops (incl. heat pump and solar system) are equipped with the electric energy meters.

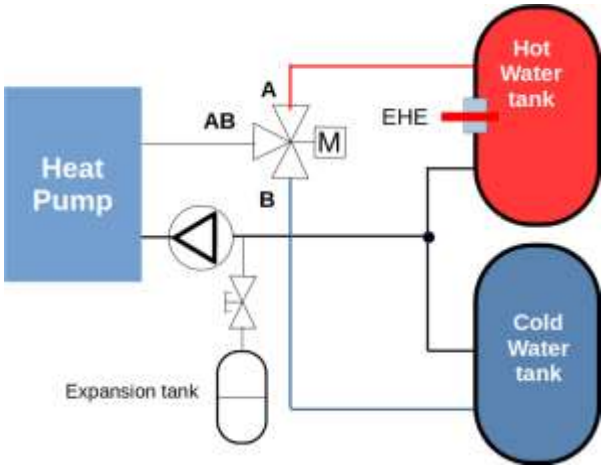

Figure 7. Connection of hot and cold-water tanks to simultaneous heating and cooling in different rooms.

3.RESULTS AND DISCUSSIONS

Since the installation of the systems components in the experimental apartment was completed in the spring of 2023, the quantitative measurements data of the overall system will be available only after one full year of operation. However, it is possible to approximately estimate the expected minimum (guaranteed) reduction in the energy consumption under real operating conditions determined by the use of two renewable resources (air-water heat pump and solar panels) in combination with low temperature heat exchanger (capillary mats).

As mentioned above, the manufacturer declares the coefficient of performance of the installed heat pump as 5.1 if the temperature of a used heat carrier does not exceed 35°C at the external temperature or 7°C. However, it should be considered that the average outdoor temperature in Rīga, Latvia during the heating season is 1.1°C [12], which means he lower efficiency of the heat pump. The practical long-term operation experience from 2014 of more than 100 of various air-to-water heat pump systems installed in Latvia [13] shows that the experimentally measured seasonal COP (SCOP) value is approximately 30% lower than widely used default values [14] – depending on the installation type, heat pump power and heat carrier temperature, varies between 3 and 4. According to statistics [13], typically, at outdoor temperature within -5…0 °C, COP for air-to-water heat pumps is experimentally estimated as 2.9 (Fig. 8), but with the temperature increase up to +7°C, the measured real efficiency reaches the value of 4.2 (within 0…7 °C) [13]. Therefore, during the heating season, it can be guaranteed that the consumption of primary energy (electricity) using an air-water heat pump in combination with low-temperature heating system will decrease by at least three times.

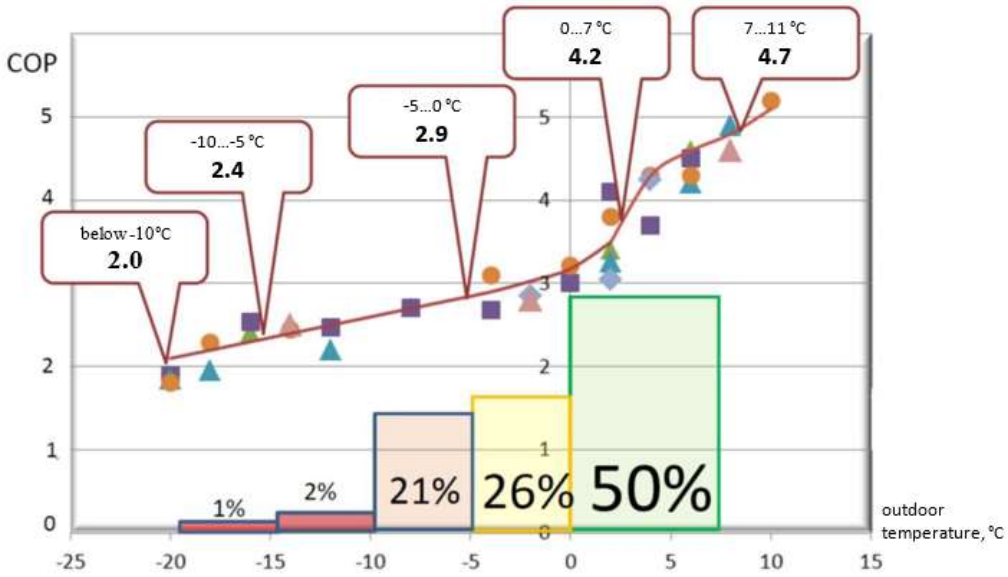

Figure 8. Distribution of experimentally estimated COP of installed air-water heat pumps [13].

The cooling demand of buildings in the climatic condition of Latvia [12] (especially with massive external walls and relatively small glazing part) is significantly smaller than heating need, therefore the use of installed heat pump is not analyzed in detail. It is important to highlight, that the power of PV modules with a maximum power of 3.8 kWp installed together with 6 kWh energy storage is sufficient to provide more than 75% of the necessary heating energy and all the energy needed for shorter cooling periods during the summer. Energy production from the installed solar system in combination with hot water tank and additional electric heater (see Fig. 7) can also fully ensure the supply of domestic hot water needs. The energy production from the installed solar panels during from October to February [15] is relatively small (Fig. 9) and approx. 25% of needed energy must be bought from the public grid, but it is fully compensated by the energy produced during the summer months.

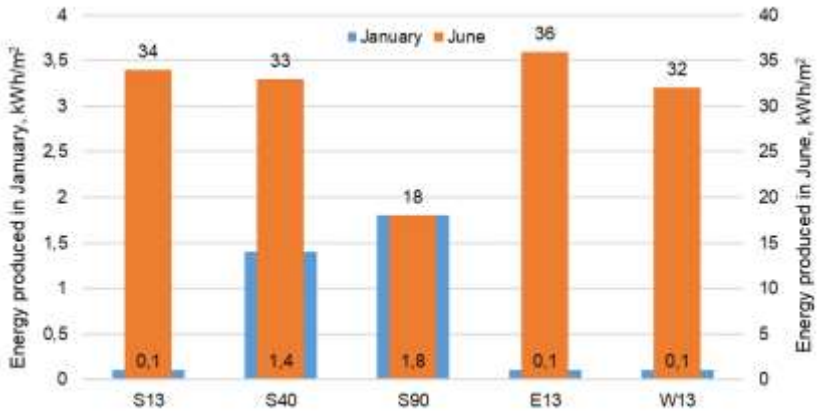

Figure 9. Monthly energy produced by different oriented PV panels in winter and summer (2019-2022)..

4.CONCLUSIONS

The first actual heat energy consumption data will be available until the end of 2023, but the already registered electricity production form the solar panel system (which is in good agreement with the theoretical values) allow to conclude that the planned energy efficiency improvement can be successfully achieved using a combination of heat pump with low temperature heat exchanger and solar panels with battery systems, without changing the thermal properties of the boundary structures.

Acknowledgment

This work is supported by the by the European Regional Development Fund project "Development and approbation of complex solutions for optimal inclusion of capillary heat exchangers in nearly zero energy building systems and reduction of primary energy consumption for heating and cooling" (1.1.1.1./19/A/102).

The project is co-financed by REACT-EU funding for mitigating the consequences of the pandemic crisis.

References

[1] Song, J., Li, H., Wallin, F. Cost Comparison Between District Heating and Alternatives During the Price Model Restructuring Process. Energy Procedia 105 (2017) 3922 – 3927. DOI: 10.1016/j.egypro.2017.03.813.
[2] Goldschmidt, VW., Heat pumps: Basics, Types, and Performance Characteristics. Ann. Rev. Energy (1984) 9: 447-72.
[3] C. Arpagaus, F. Bless, M. Uhlmann, J. Schiffmann, S.S. Bertsch, High temperature heat pumps: market overview, state of the art, research status, refrigerants, and application potentials, Energy 152 (2018) 985–1010, DOI:10.1016/j.energy.2018.03.166.
[4] Nemethova, E., Krajcik M., Petras D., Performance of the Building with Three Different Radiant Systems, IOP Conf. Series: Materials Science and Engineering 471 (2019) 062013. DOI: 10.1088/1757-899X/471/6/062013.
[5] International Organization of Standards. ISO 52016-1:2017. Energy performance of buildings — Energy needs for heating and cooling, internal temperatures and sensible and latent heat loads — Part 1: Calculation procedures. 2017.
[6] HeatMod.lv - application for calculating of the building's energy performance in accordance with LVS EN ISO 52000 series standards. [Accessed 01.03.2023]. Available: http://www.heatmod.lv
[7] Gendelis, S., Teličko, J., Jakovičs, A., Bukans, I. Radiant capillary heat exchangers – power calculation for optimal heating and cooling. Journal of Physics: Conference Series (2023) 2423 (1), art. no. 012011. DOI: 10.1088/1742-6596/2423/1/012011.
[8] O'Hegarty, R., Kinnane, O., Lennon, D., Colclough, S. Air-to-water heat pumps: Review and analysis of the performance gap between in-use and product rated performance, Renewable and Sustainable Energy Reviews, Volume 155 (2022) 111887. DOI:10.1016/j.rser.2021.111887.
[9] Gendelis, S. Experimental studies of a long-term operation of different batteries used in PV system. International Multidisciplinary Scientific GeoConference Surveying Geology and Mining Ecology Management, SGEM (2022) 22 (4.1), pp. 89 – 96, DOI: 10.5593/sgem2022/4.1/s17.12.
[10] KNAUF ceiling systems. [Accessed 01.04.2023]. Available: http://knauf.iq/en/systems/ceiling/
[11] CEWOOD wood wool panels. [Accessed 01.04.2023]. Available: https://www.cewood.com
[12] Latvian Cabinet of Ministers, Regulations regarding the Latvian Building Code LBN 003-19 "Construction Climatology",

Riga, 2019.
[13] RIKON AC – heat pump operation statistics in Latvia [Accessed 01.04.2023]. Available: http://www.gaiss-udens.lv/lv/siltumsuknu-eksplutacijas-statistika
[14] Zirngibl, J. Heat pump standard EN 15316-4-2 – From compliance to real consumption, REHVA Journal (2022), pp. 5–9.
[15] Gendelis, S., Heincis, D., Telicko, J. Measurements of the actual efficiency of PV panels depending on their orientation and environmental temperature, International Multidisciplinary Scientific GeoConference Surveying Geology and Mining Ecology Management, SGEM (2021), 21 (6.2), pp. 75-82. DOI: 10.5593/sgem2021V/6.2/s26.13.

RIGA 2023

Simulation Model of A Parabolic Trough Concentrated Solar Power Plant in Khobar city, Saudi Arabia

Nidal Abu-Libdeh
Prince Mohammad Bin Fahd University, Al-Khobar, Saudi Arabia, nabulibdeh@hotmail.com, ORCID: 0000-0002-0272-9255

Huda Mohammed Alotaibi
Prince Mohammad Bin Fahd University, Al-Khobar, Saudi Arabia, Huda_m_alotaibi@hotmail.com, ORCID: 0009-0007-2142-3482

Saleh Mahmoud
American University of the Middle East, Egaila, Kuwait, Saleh.Mahmoud@aum.edu.kw, ORCID: 0000-0002-3244-4146

Wael Al-Kouz
American University of the Middle East, Egaila, Kuwait, wael.kouz@aum.edu.kw, ORCID: 0000-0002-2116-7673

Cite this paper as: *Abu-Libdeh, N, Alotaibi, H, Mahmoud, S, AL-Kous, W. Simulation model of a parabolic trough concentrated solar power plant in Khobar city, Saudi Arabia. 11. Eur. Conf. Ren. Energy Sys. 18-20 May 2023, Riga, Latvia*

Abstract: Climate change, along with undesirable power plant outcomes such as greenhouse gas emissions and air pollution have raised the awareness to the implementation of renewable energy. One major sustainable source is the sun which represents an infinite source of energy supply. In Saudi Arabia, the eastern city of Khobar city is an area that receives a great amount of direct solar radiation. This paper proposes a design and performance study of a 100 MW parabolic trough concentrated solar power plant (CSP) with thermal energy storage in Khobar city. The power plant performance is analysed through System Advisor Model (SAM). The study reveals the proposed CSP produces an annual energy of 369,592,896 kWh with a capacity factor of 42.2%. The optimum design for this plant is achieved by altering the size of the solar field as well as the full load hours of thermal energy storage (TES). Results show that the proposed design of the parabolic trough is optimal at a solar field size of 1,150,000 m2 and a thermal energy storage of 6 hours, which in turn yields the lowermost Levelized Cost of Energy (LCOE) with a maximum production of annual electricity. This study contributes to the implementation of sustainable energies and the reduction of fossil fuel dependency in this region..

Keywords: *Concentrated Solar Power, Solar Energy, SAM, Thermal Energy Storage, Saudi Arabia*

1.INTRODUCTION

The sun is an infinite source of energy which provides an effective and sustainable energy supply [1]. For example; the emitted solar energy the earth receives in 45 minutes is more than what the world consumes in one year [2], as Earth receives every day around 1366 W of sunlight per square meter. The essential benefit of solar power over the conventional power from fossil fuels that it is free, relatively clean, and reachable with large quantities compared to the oil and fossil fuel [3]. The usage of solar energy helps in creating new economic opportunities and providing energy for numerous people nowadays without access to a steady and proper energy supply. Concentrated solar power (CSP) is an energy system that absorbs solar heat and later transforms it to electricity. This technology is used to produce energy in different applications such as; manufacturing, and electro-mobility. Unlike the photovoltaic (PV) technology, CSP has the capacity to for energy storage and conversion into electricity even after sunset or in cloudy weather conditions. One mirror in the solar field can produce around 400kWh of electricity in one year, cutting down the discharge of CO_2 by 12 tons and fossil fuels by 2.5 tons throughout a 25-years lifetime [4].

Variant CSP techniques are developed with a focus on Thermal Energy Storage (TES). One CSP technology is the solar tower, which focuses sunlight on a receiver at the top of a tower, hence needing support for a rigid structure with a large amount of mirrors. Linear Fresnel Reflector is a different CSP technology, where mirrors are spaced in a large area in order to avoid shading, which in turn means more land and higher cost. Parabolic trough is also another CSP technique, which is less complex compared to the solar tower with a higher capacity factor [5]. This technology allows solar energy to be stored through TES. The low cost and high efficiency of parabolic trough as compared to other technologies are the best advantages of parabolic trough [6]. A parabolic trough with (TES) achieves a higher capacity factor and compensates for the absence of energy production at night and in clouded weather, unlike the case for solar tower and photovoltaic technologies [7].

A study on the financial and technical regulations that are needed to build up CSP in the developing countries was conducted by the World Bank in 2012 [8]. This study revealed that most of the Middle East with the exception of the northern regions is appropriate for CSP plants installation. States like Saudi Arabia and Yemen have the highest exposed area in the region followed by the United Arab Emirates, Oman, Syria, and Jordan [9]. In Saudi Arabia, electricity consumption is increasing annually by about 8%, the highest in the region [10]. The main electricity consumption in Saudi Arabia is from air conditioning systems, which represents 70% of the total consumption, followed by water desalination. However, Saudi Arabia has plans of shifting to alternative energy sources that are more sustainable and contribute to the reduction of carbon emissions [11]. Geographically, Saudi Arabia is located strategically with an extensive desert landscape. It receives a large amount of solar irradiation, with an average solar irradiation ranging from a 4.48 kWh/m^2/day in Tabuk to 7.0 kWh/m^2/day in Bisha. In the eastern city of Khobar, the average solar radiation is 5.16 kWh/m^2/day, which, besides other parameters, makes it ideal for a CSP plant installation.

In light of the points discussed above, this paper aims to present a simulation model of a parabolic trough CSP in Khobar city in Saudi Arabia. This paper focuses on a design and performance analysis of 100 MW parabolic trough power plant, thermal energy storage included, in Khobar city. It starts with a brief description of System Advisor Model (SAM) software. Then, the reasons for choosing Saudi Arabia & evaluation of some solar parameters are discussed. A mathematical model based on the solar field thermal output, energy equations, and energy analysis is later presented. This is followed by the CSP plant discussion based on the full load hours of TES together with the size of the solar field, which can affect the capacity factor, capital cost, and Levelized Cost of Energy (LCOE) as well. Finally, discussion of the results and conclusions based on our findings are presented.

2.METHODOLOGY

System Advisor Model (SAM)

SAM is a simulation computer program made by the National Renewable Energy Laboratory (NREL). Validation of SAM simulation results vs experimental results was found to be excellent, making SAM suitable to model many renewable energy systems [12, 13]. NREL generated a Microsoft Excel spreadsheet for the performance and economic model of a parabolic trough. This model features the cost of operation and maintenance (O&M), capital cost, and financial calculations, in order to allow for a smoother plant design. The model also allows for a detailed project design where the cost and performance are both analysed. The model requires input data to calculate the system performance and the related cost, while SAM requires weather and location data to be included in the model [14]. It was found that the performance and capacity factor of the plant can be enhanced by using two molten salt tanks for thermal storage, particularly at night. A system of a heat exchanger with log mean temperature differences (LMTD) ranging from 2°C to 15°C was developed for each thermal storage size. The design of the heat exchanger and the size of the solar field were found to yield energy at lower cost for each Thermal Energy Storage (TES) size [15].

Components & Solar Parameters Evaluation

The principal factor for a CSP plant design is the solar field, where various devices of solar radiation like the collector and the absorber are installed [16]. Parabolic trough plant comprises subsystems such as a solar collector, a receiver with heat transfer fluid (HTF) system and a power cycle block. Sunlight is focused on a parabolic-shaped collector and is then reflected to the receiver with the HTF pipe. The fluid absorbs the heat which is then transferred

to water through a heat exchanger, where the fluid becomes sufficiently hot for steam generation. Afterwards, steam is cooled down, condensed and recycled. Also in the absence of sunlight, the HTF warms up the thermal storage system which allows for electricity generation [17].

The solar field of a CSP comprises solar collector assemblies (SCA's) loops, as solar multiples, while each solar collector assembly is calculated as an independent node [18]. The receiver used is Schott PTR80 from SAM library. The inner diameter of this receiver is 0.076 m and the outer diameter is 0.12 m for the glass envelope, while the annular pressure is 0.0001Torr. The HTF used, Therminol VP-1, warms and circulates through the receiver's inner diameter, and operates with a minimum and maximum temperatures of 12 ^{o}C and 400 ^{o}C, respectively. Therminol VP-1 is an appropriate choice because of its low viscosity, high density and high specific heat, making it ideal for a steady and effectual operation [18]. Sky Fuel Sky Trough, with a receiver of 80-mm OD, was the collector chosen from SAM library. The collector has an apparatus area of 656 m^2, width of 6 m, length of 115 m and the piping distance is 1 m. The solar tracking error, defined as the collector's incapability to perfectly orientate along the tracking angle is set to 0.988. The power block's inlet and outlet temperatures are 391 ^{o}C and of 293 ^{o}C respectively, and the conversion efficiency is 0.356. Thermal storage for HTF used is Hitec Solar Salt is less expensive compared to thermal oil and has working temperatures ranging from 238 ^{o}C to 593 ^{o}C. Through changing the TES full load hours, the quantity and cost of energy varies consequently.

In order to obtain the best parabolic trough design, different trials are attempted based on changing the size of the solar field and the Thermal Energy Storage (TES) for the minimum (LCOE), which is the financial model employed in this paper. Detailed analysis regarding parabolic trough cost is presented by Kurup and Turchi [19]. The formula used to calculate LCOE is given by:

$$LCOE = \frac{FCR \cdot TCC + FOC}{AEP} + VOC \qquad (1)$$

where VOC is the variable operating cost, FOC is the fixed annual operating cost, TCC is the total capital cost, FCR is the fixed charge rate, and AEP is the annual electricity production (kWh).

3.MATHEMATICAL MODEL

Useful Heat Gain

Duffie and Beckman [20] presented a model for the useful heat gain Q_u for a single collector as:

$$Q_u = F_R\, A_a [\frac{S - A_r}{A_a\, U_L\, (T_i - T_a)}] \qquad (2)$$

where F_r and A_a are the heat removal factor and the aperture area of the collector, respectively. A_r is area of the receiver, S is the absorbed solar radiation, U_L is heat loss coefficient, and T_a and T_i are the ambient and fluid inlet temperatures, respectively.

Collector Output Temperature and Number of Loops

Collector output temperature is given by [17]

$$T_o = T_i + \frac{Q_u}{m\, C_p} \qquad (3)$$

where C_p is the specific heat capacity and m is the mass flow rate of HTF [17]. The number of loops required (NL) can be defined in eq. (4)

$$NL = \frac{(\frac{P_{th}}{collector\ output\ power})}{No\ of\ collector\ per\ loop} \qquad (4)$$

Solar Multiple

Solar Multiple (SM) is the ratio of thermal energy collected at the design point of the solar field to that needed by the power block at given conditions [21]:

$$SM = \frac{Power\ cycle\ capacity}{Solar\ field\ capacity} \quad (5)$$

Solar Field Thermal Output

The thermal output of the solar field is the thermal energy that is released at a specific solar multiple. The value of the solar field output is measured at the interface of power block and receiver; the equation for the solar field output is expressed as [17]:

$$Q_{sf,des} = SM\ (\frac{W_{pb,des}}{\eta_{des}}) \quad (6)$$

where $Q_{sf,des}$ is the heat output of the solar field, $W_{pb,des}$ is the designated work out from the power block and η_{des} is the design efficiency.

Full Load Hours of TES

TES full load hours is measured as the stored thermal energy capacity in energy hours of the TES system, released at power block design [22], and is given by the following equation:

$$H_{tes} = \frac{P_{des}\, h_{tes}}{\eta_{des\ cycle}} \quad (7)$$

where H_{tes} is the storage capacity of thermal energy, measured in power block capacity hours (kWht).

Energy Equations

Each SCA contains several parabolic collectors and receivers in series sharing a single tracking drive. Each SCA is considered an independent node within the loop. Therefore, the absorbed energy, pressure drop, temperature, losses and few other performance values are measured for each SCA independently. The nodal approach is shown in Figure (1) [23].

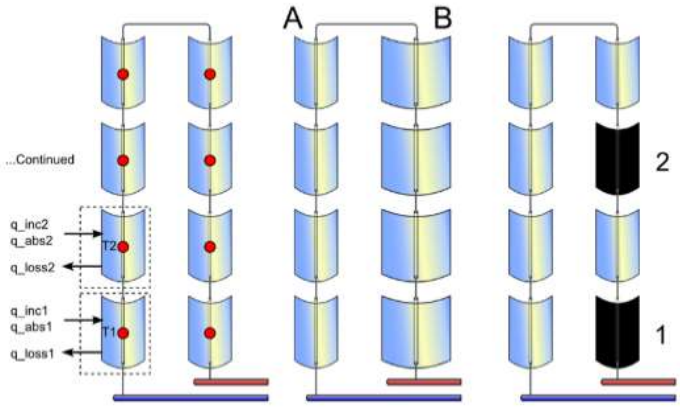

Figure 1. The nodal structure of each SCA in the loop [23].

The solution of equation of energy balance for a single node is shown in Eq. (8), where $\dot{m}_{htf}$ is the HTF mass flow rate, $\dot{q}_{abs}$ is the absorbed thermal energy, C_{htf} is the HTF specific heat, m is the mass of HTF in the node, T_{in} is the HTF incoming temperature, T is the node temperature at time t, and Δt is the time step duration [23].

$$T = \frac{\dot{q}_{abs}}{\dot{m}_{htf} \cdot c_{htf}} + C_1 e^{-\frac{\dot{m}_{htf}}{m}\Delta t} + T_{in} \quad (8)$$

Collectors and Feld Optics

The collector is used to reflect incoming irradiation onto the receiver. The incidence angle α is determined using the orientation information and tracking angle. The collector model is largely borrowed from the SAM empirical collector model [23].

$$\theta = cos^{-1}\sqrt{1 - [\cos(\theta_e - \theta_{col}) - \cos(\theta_{col})\ \cos(\theta_e)(1 - \cos(\gamma_s - \gamma_{col}))]^2} \quad (9)$$

Receivers

Figure (2) shows a cross-section of one-quarter of the receiver. The receiver geometry is designed by the user with radii R1 to R4 [23].

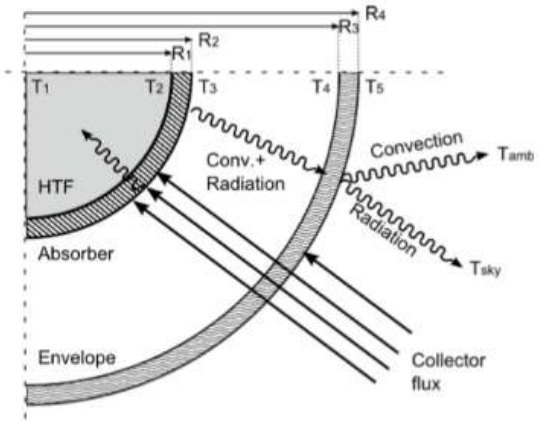

Figure 2. Heat balance for the receiver model [23].

Plant Control

The plant controller links the requirements of the power block with the user's input and the production from the thermal storage, solar field, and auxiliary heater. SAM uses four main modes in operation including (1) the solar field total energy output is less than the usable minimum, (2) the total energy output is between the minimum and the design-point power block load, (3) more energy is produced than can be used in storage or in the power block and (4) more energy is produced than the power block needs, where all of the remaining energy can be diverted to storage. The inlet temperature solar field is deduced by a weighted average of the TES charge mass flow and the power block mass flow [22].

Energy Analysis

The total solar incident energy collected at the solar field is [23]:

$$E_i = A\ cos\theta\ \cdot\ DNI \quad (10)$$

The total useful energy produced by the solar field is given by:

$$E_u = m_f \cdot (H_{sfo} - H_{sfi}) \quad (11)$$

Therefore, the thermal efficiency of the solar field is given by:

$$\eta_{Esf} = \frac{E_u}{E_i} \quad (12)$$

The power block thermal efficiency is found by:

$$\eta_{EPB} = \frac{P_{net}}{E_{in}} \quad (13)$$

The overall plant energy efficiency is then deduced by:

$$\eta_{Eo} = \frac{P_{net}}{E_i} \quad (14)$$

Estimated Net Output (MWe)

The capacity of the power cycle is measured as the estimated gross to net conversion factor (EG) multiplied by the design gross (DG) output in MWe [17]:

$$Estimated\ Net\ Output\ (MWe) = EG\ \cdot DG \quad (15)$$

Finally, the 100 MWe CSP plant net capacity factor is found by [22]:

$$CF = \frac{P_{net}}{No.of\ days.\left(24\frac{h}{day}\right).plant\ power\ capacity} \quad (16)$$

4.RESULTS

The CSP Plant Design Analysis Based On The Size Of The Solar Field

The input thermal power depends on the turbine, while the net electrical output is a subject to the incident irradiation. SAM simulation shows that the input thermal power peaks at approximately 310 MW in August, while the peak incident thermal power for solar plant in Khobar city is around 750 MW in June. The simulation also reveals that the cycle efficiency for the plant peaks at about 0.36 in June. In July and August, the dry bulb temperature reaches the peak value of 42 ºC at noon. Because of the higher sun radiation in the warm season, particularly from June through August, there is additional storage of energy in the molten salt tank, and this energy usage peaks in the aforementioned months. On SAM, after choosing the location of Khobar city, the parameters are varied in order to obtain the optimal design. These variations are in regards to the solar field size (m^2) and the consequent changes in significant parameters as the net capital cost, the capacity factor (CF), and the (LCOE), and the full load TES.

Capacity Factor, Capital Cost and LCOE Based On Different Solar Field Size and TES

Figures (3), (4), and (5), show the relationships among the size of the solar field and each of the capacity factor, capital cost and (LCOE), respectively. The capacity factor measures the actual energy the plant produces divided by its full output potential during the same time. Figures (3) and (4) shows a direct correlation among the capacity factor and the size of the solar field, and a linear correlation between the capital cost and the size of the solar field, respectively. It is also seen that the LCOE is lowest at 12.29$/kwh, at a solar field size of 1,150,000 m^2 where the capacity factor is 42.20% and the capital cost is $688,081,536. If the solar field size is increased past this value, LCOE will further rise as shown in figure (5). The effect of thermal energy storage in the aforementioned solar field size based on LCOE is presented in Figure (6), which shows that the lowest value of LCOE is acquired at 6h

of TES. A summary of SAM simulation results for the design with a 6h full load of thermal energy storage (TES) is presented in Table (1). This plant produces energy at 369,592,896 kWh annually, in strong agreement with an earlier simulation in the city of Abu Dhabi city that has similar weather conditions to Al Khobar city [20].

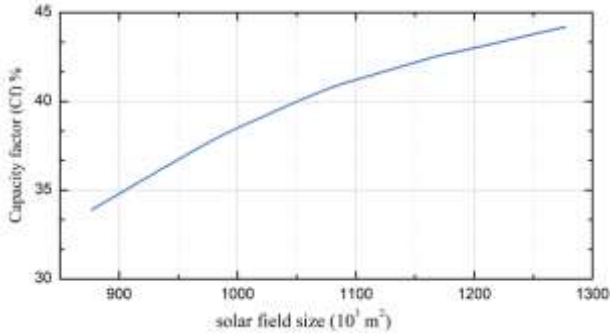

Figure 3. Correlation of the capacity factor and the size of the solar field.

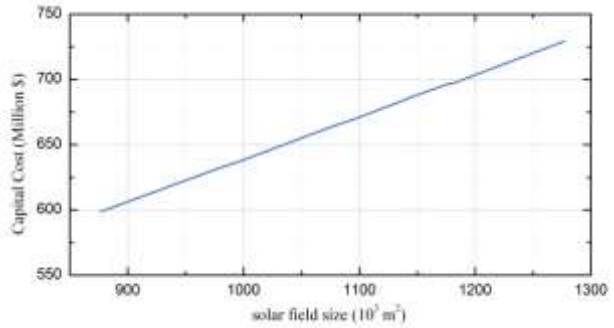

Figure 4. Correlation of the capital cost and the size of the solar field.

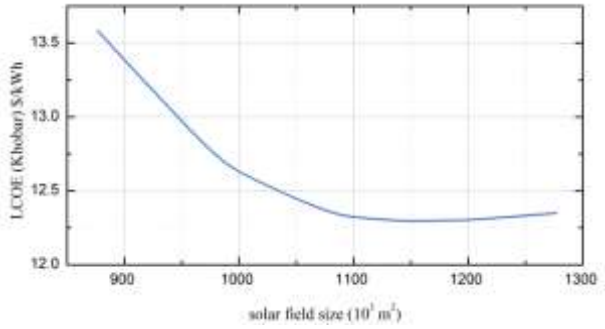

Figure 5. Correlation of the LCOE and the size of the solar field.

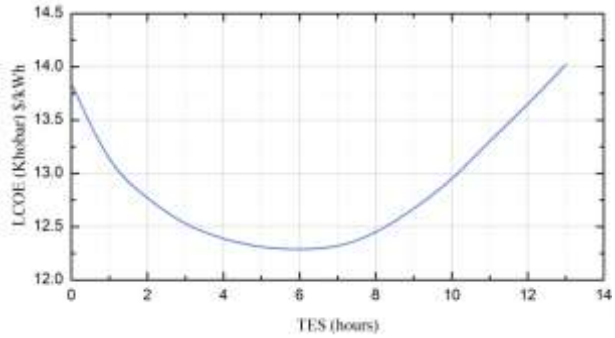

Figure 6. Correlation between the LCOE and the TES

Table 1. SAM after simulation at a solar field size of 1,150,000 m^2.

Metric	Value
Annual energy (year 1)	369,592,896 kWh
Gross-to-net conversion	90.8%
Capacity factor (year 1)	42.2%
Annual Water Usage	92,180 m^3
PPA price (year 1)	11.80 €/kWh
PPA price escalation	1.00%/year
Levelized PPA price (nominal)	16.68 €/kWh
Levelized PPA price (real)	13.24 €/kWh
Levelized COE (nominal)	15.48 €/kWh
Levelized COE (real)	12.29 €/kWh
Net present value	$43,393,880
Internal rate of return (IRR)	11.00%
Year IRR is achieved	20
IRR at end of project	12.75%
Net capital cost	$688,081,536
Equity	$319,574,080
Size of debt	$368,507,456

5.CONCLUSIONS

A comprehensive design analysis of a 100 MWe Solar Power plant with parabolic trough design and a thermal energy storage is made for Khobar city. NREL provides a significant tool for the design of such model and the corresponding plant performance, economic analysis and system capital cost, helping researchers to optimize the plant design with less time and effort. The performance was assessed by SAM software. The CSP plant performance is improved by parameters variation such as size of the solar field as well as the full load hours of TES. The optimal values for the size of the solar field size and the TES full load hours for Khobar are deduced to be 1,150,000 m^2 and 6h respectively. The configuration using Therminol VP-1 as HTF, shows an LCOE value of 12.29 $/kwh and a capacity factor of 42.20%. The plant generates 369,592,896 kWh of energy annually while the capital cost is found to be $688,081,536. This design is conducted without taking sand and dust and effects in consideration. As per these results, TES system of a 100 MWe Solar Power of parabolic trough design is perfectly suitable for Saudi Arabia's eastern region, contributing in turn to sustainable energy future in this area of the world.

Refrences

[1] Kassem, A, Al-Haddad, K, Komljenovic, D. Concentrated solar thermal power in Saudi Arabia: Definition and simulation of alternative scenarios. *Renewable and Sustainable Energy Reviews* 2017, 80, 75-91. DOI: https://doi.org/10.1016/j.rser.2017.05.157

[2] Von Reeken, F, Arbes, S, Weinrebe, G, Wöhrbach, M, Finkbeiner, J. CSP Parabolic Trough Technology for Brazil A comprehensive documentation on the current state of the art of parabolic trough collector technology Seite. Bonn, GERMANY: Deutsche Gesellschaft für Internationale Zusammenarbeit (GIZ) GmbH, 2014.

[3] Shaikh, M, Waghmare, S, Labade, S, Fuke, P, Tekale, A. A Review Paper on Electricity Generation from Solar Energy. *International Journal for Research in Applied Science and Engineering Technology*, 2017, 5 (IX), 1884 – 1889. DOI:10.22214/IJRASET.2017.9272

[4] Răboacă, M, Badea, G, Enache, A, Filote, C, Răsoi, G, Rata, M, Lavric, A, Felseghi, RA. Concentrating Solar Power Technologies. *Energies* 2019. 12, 1048. DOI: https://doi.org/10.3390/en12061048

[5] Boretti, A. Concentrated Solar Power Plants Capacity Factors: A Review. In L Dai, RN Jazar (Eds.) Nonlinear Approaches in Engineering Applications: Energy, Vibrations, and Modern Applications, Gewerbestrasse, Cham, Switzerland: Springer International Publishing AG, 2018, 41-62.

[6] Islam, MT, Huda, N, Abdullah, AB, Saidur, R. A comprehensive review of state-of-the-art concentrating solar power (CSP) technologies: Current status and research trends. *Renewable and Sustainable Energy Reviews* 2018, 91, 987-1018. DOI: https://doi.org/10.1016/j.rser.2018.04.097

[7] Renewables Global Status Report. Paris: REN21 (Renewable Energy Policy Network for the 21st Century); 2015

[8] N. Kulichenko, J. Wirth, World Bank (2012)

[9] CSP Prospects in Saudi Arabia. CSP Today; 2014.

[10] Furman, HKH. Dust Storms in the Middle East: Sources of origin and their temporal characteristics. *Indoor and Built Environment* 2003, 12(6), 419-426. DOI:10.1177/1420326X03037110

[11] Alyahya, S, MA Irfan, MA. Analysis from the new solar radiation Atlas for Saudi Arabia. *Solar Energy* 2016, 130, 116 -127. DOI: https://doi.org/10.1016/j.solener.2016.01.053

[12] Boretti, A, Nayfeh, J, Al-Kouz, W. Validation of SAM Modeling of Concentrated Solar Power Plants. *Energies* 2020, 3, 1949. DOI: doi:10.3390/en13081949

[13] Al-Kouz, W, Almuhtady, A, Abu-Libdeh, N, Nayfeh, N, Boretti, A. A 140 MW Solar Thermal Plant in Jordan. *Processes* 2020, 8 (6), 668. DOI: https://doi.org/10.3390/pr8060668

[14] Bishoyi, D, Sudhakar, K. Modeling and performance simulation of 100 MW PTC based solar thermal power plant in Udaipur India. *Case Studies in Thermal Engineering* 2017, 10, 216-226. DOI: https://doi.org/10.1016/j.csite.2017.05.005

[15] H. Price, National Renewable Energy Laboratory (2003).

[16] Average Weather in Khobar, Saudi Arabia, Year Round - Weather Spark. (2020). Retrieved 29 February 2021, from https://weatherspark.com/y/104952/Average-Weather-in-Khobar-Saudi-Arabia-Year-Round

[17] Liaqat, K, Anss, M, Ali, A, Mengal AN. Modeling and Simulation of a 100 MW Concentrated Solar Thermal Power Plant Using Parabolic Trough Collectors in Pakistan. *IOP Conf. Ser.: Mater. Sci. Eng.* 2018, IOP Publishing 414, 12032,

[18] Wagner, MJ, Gilman, P. Technical manual for the SAM physical trough model (No. NREL/TP-5500-51825). National Renewable Energy Lab. (NREL), Golden, CO, USA. 2011.

[19] Kurup, P, Turchi, CS. Parabolic Trough Collector Cost Update for the System Advisor Model (SAM) Parabolic Trough Collector Cost Update for the System Advisor Model (SAM) (2015)

[20] Duffie, JA, Beckman, WA. Solar Engineering of Thermal Processes, New Jersey: Wiley, 2013.

[21] Montes, MJ, Abánades, A, Martínez-Val, J M. Performance of a direct steam generation solar thermal power plant for electricity production as a function of the solar multiple. *Solar Energy* 2009, 83, 679-689. DOI: https://doi.org/10.1016/j.solener.2008.10.015

[22] Parveen, RP, Baseer, MA, Awan, AB. Zubair, M, Performance Analysis and Optimization of a Parabolic Trough Solar Power Plant in the Middle East Region, *Energies* 2018, 11(4), 741. DOI: https://doi.org/10.3390/en11040741

[23] Wagner, MJ, Blair, N, Dobos, A. Detailed Physical Trough Model for NREL's Solar Advisor Model (No. NREL/CP-5500-49368). National Renewable Energy Lab.(NREL), Golden, CO, USA. 2010.

RIGA 2023

Determination of Structural Parameters of Boilers Loading Devices on a Small Biomass to Reduce the Air Excess Coefficient in the Boiler Chamber

Yuliia Shyshko
Ukrainian State University of Science and Technologies, Dnipro, Ukraine, juliashishko2014@gmail.com, ORCID: 0000-0003-4919-6297

Anatolii Cherniavskyi
National Technical University of Ukraine «Igor Sikorsky Kyiv Polytechnic Institute», Kyiv, Ukraine, canatoliy1976@gmail.com, ORCID: 0000-0003-2858-8224

Daria Shyshko
Oles Honchar Dnipro National University, Dnipro, Ukraine, dshishko44@gmail.com, ORCID: 0009-0001-3603-9172

Olena Borichenko
National Technical University of Ukraine «Igor Sikorsky Kyiv Polytechnic Institute», Kyiv, Ukraine, borichenko_olena@ukr.net, ORCID: 0000-0002-6127-2945

Cite this paper as: *Shyshko, Y., Cherniavskyi, A., Shyshko, D., Borichenko, O. Determination of structural parameters of boilers loading devices on a small biomass to reduce the air excess coefficient in the boiler chamber. 11. Eur. Conf. Ren. Energy Sys. 18-20 May 2023, Riga, Latvia*

Abstract: This article discusses the process of loading sunflower husks into the boiler with a screw feeder with ensuring the gas tightness of the working chamber due to the "cork" from biomass. The "cork" is formed due to friction forces when the biomass moves along the cylindrical channel in the tail part of the screw. The aim of this paper was to determine the parameters of these boilers loading devices to reduce the air excess coefficient in the boiler chamber. The following research methods were used in this article: experimental methods to determine the properties of biomass as a bulk material, the compaction force of the biomass layer and the geometric dimensions of the biomass "cork"; numerical methods to obtain the dependence of the compaction force of the biomass layer on the coefficient of excess air in the boiler furnace. As a result of experimental studies, the dependence of the compaction of the biomass waste layer on the pressure value was obtained. It has been determined that for the specified operating conditions of the feeder, the relative increase in the density of sunflower husk "cork" exceeds the bulk density of the non-compacted layer by no more than 11.5%.

Keywords: *air excess coefficient, biomass boiler, gas tightness, sunflower husk "cork"*

1. INTRODUCTION

Today's difficult situation in the global energy market requires continuous development of technologies of the usage of renewable fuels, the main requirements for which are energy, environmental and economic efficiency. One of the available renewable energy sources is biomass, both in the form of primary wood and in the form of wood and agriculture processing waste (chips, sawdust, straw, sunflower and buckwheat husks, walnut shells, etc.).

Biomass as a fuel has the following advantages: it is widely distributed and in significant volumes, has large energy potential, can be renewed relatively quickly, can be used in its original form with existing energy equipment, and it is also easily recyclable in other fuels. In addition, the harmful effects of biomass are minimal –the amount of greenhouse gases released while burning this fuel, is equal to the amount of CO_2 absorbed during its growth. Since

there is no increase in the concentration of greenhouse gases in the atmosphere, biomass is considered CO_2-neutral fuel. Furthermore, finely dispersed biomass in the form of waste is a by-product of the main production, and therefore has a relatively low cost. The main disadvantages of such biomass include low bulk density, a large number of volatile, uneven in size and shape particles. The properties of various types of biomass waste have been investigated by many scientists as in Ukraine [1,2] and abroad [3,4], but due to the large number of types of biomass, suitable for energy use, and the development of new technologies, projects are being carried out with the aim to improve the research area.

There is a large number of technologies for the energy efficient use of biomass: combustion, gasification, pyrolysis, anaerobic fermentation, etc. The most common method is the direct combustion of biomass and its wastes in the boiler furnaces for heat and electricity [5]. For example, currently in Ukraine there are up to 20 CHPs and thermal power plants that function on wood chips and sunflower husks; projects of another 30 power plants are at different stages of development, from the idea to the project design [6]. Depending on the type of boiler, it is possible to burn biomass of various sizes (firewood, briquettes, pellets, sawdust, agricultural waste) and in different ways (burning in a dense layer, boiling layer, ingrown burning, etc.).

A necessary requirement for the work of a fine dispersed biomass solid fuel boiler is the sealing of the boiler working space, which prevents air suction when working under discharge, so the device for loading fuel into the boiler is one of the main components that determines both the efficiency of the entire boiler installation and its safety. In this regard, improving the work of the feeder for finely dispersed biomass is relevant not only for Ukraine, but also for many countries in the world [3,4,7-10].

It is known from previous studies that when loading into the working chamber of the boiler unit of finely dispersed material, a consequent installation of two feeders was previously traditional: drum and screw [4,11,12]. Another option was the installation of intermediate tanks – bunkers. Such a solution regarding biomass waste, with low bulk density and a tendency to suspend the layer, requires the installation of additional mechanical devices (vibrators, screws, etc.), which increase capital costs and complicate the operation of the entire energy complex [11].

According to studies [13], another property of small biomass is it's ability to compact when being pushed through a channel. Such a method is widely used, for example, in the briquetting of waste. This property lays in the basis for the work of screw feeders with an elongated tail channel (sometimes narrowing), in which a layer of material compacted due to friction forces is formed [7]. The disadvantage of such a device is that for each individual technological unit and type of fuel it is necessary to perform separate calculations.

In this work, the method of loading is considered, which ensures the gas density of the working chamber of the unit by the formation of a "plug" of finely dispersed biomass, formed as a result of the movement of biomass along the cylindrical channel. The purpose of the work is to obtain data in the form of tables and graphic dependencies to determine the parameters of compaction of the layer of small biomass from the level of suction cups in the furnace of the boiler unit for screw feeders with different geometric characteristics.

2. METHODS AND RESULTS

Compaction and movement of finely dispersed biomass (agricultural waste) is carried out by a screw, which feeds with the material from the hopper. The feeder scheme proposed for consideration is shown in Fig. 1.

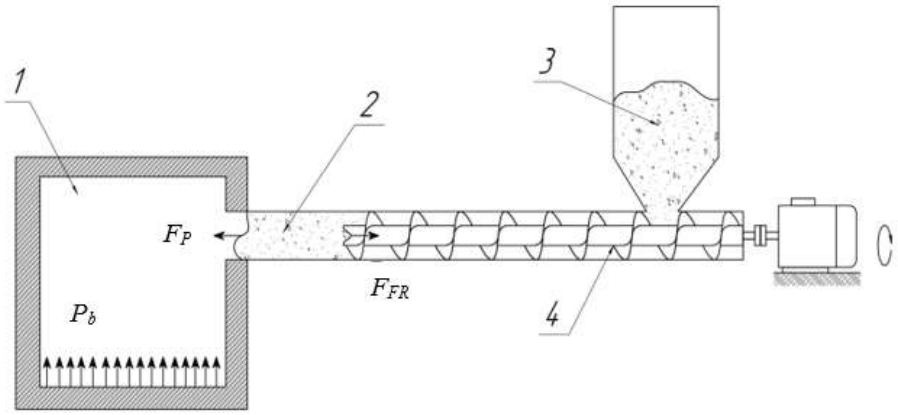

Figure 1. Scheme of the screw feeder with a gas-sealing "plug" of biomass:
1 – the boiler furnace; 2 – "cork" of biomass; 3 – loading hopper; 4 – screw feeder.

To check the possibility of applying the proposed method of loading, the following data is required:

- properties of biomass as a bulk material;
- patterns of compaction of the material as it moves through the channel;
- conditions of the movement of compacted material.

All these data will allow us to determine the structural ratios (channel diameter, length of the sealing cylindrical area from screw to furnace boiler) and technological parameters (sealing forces, drive power), providing specified conditions for the tightness of the screw feeder.

Determination of the angle of internal friction of biomass

For bulk materials, the angle of internal friction φ is equal to the angle of natural slope α_0 [1].

During the experiment, the angle of internal friction for three types of biomass was determined: sunflower husks, sawdust and walnut shells. The values of the angle of internal friction for three types of biomass are given in Table 1.

Table 1. Angle of internal friction for sunflower husks, sawdust and walnut shells

№	Weight, kg			tg α_0			φ		
	sunflower husks	sawdust	walnut shells	sunflower husks	sawdust	walnut shells	sunflower husks	sawdust	walnut shells
1	0,365	0,158	0,438	0,005445	0,01036	0,00826	18,5	38,7	29,3
2	0,360	0,161	0,445	0,006463	0,00924	0,007508	22,2	33,5	26,3
3	0,368	0,177	0,422	0,007192	0,01044	0,008155	25,0	39,0	28,9
4	0,382	0,177	0,416	0,00738	0,01062	0,007875	25,8	39,9	27,8
5	0,392	0,170	0,434	0,008125	0,007878	0,007508	28,8	27,8	26,3

Based on the results of experimental studies, it can be concluded that the considered types of biomass belong to well-loose materials. Thus, according to this indicator, the use of the proposed method of loading biomass with a screw feeder with the formation of a gas-sealing "plug" at the outlet and its subsequent scattering in the boiler furnace is possible.

Study of efforts required for biomass layer compaction

The study of the efforts, required for the compaction of the biomass layer was carried out on an experimental installation, consisting of hydraulic press with adjustable pressure in the range of 0.039 ÷ 24.5 MPa, container, which is a pipe with a diameter of d = 146×10 mm, height 500 mm and piston with base diameter dP = 140 mm.

Sunflower husks were used as the studied material. Three series of experiments were conducted to hang weighing 0.4, 0.5 and 0.6 kg. During the pressing process, the height of the waste layer and the oil pressure in the working cylinder were monitored. The pressure size was determined by the indications of the exemplary pressure gauge.

In the course of previous experiments, it turned out that when compressing the material with the pressure of the seal (on the surface of the biomass layer), more than 500 kPa, a dense briquette is formed. The density of it practically does not increase with further increase of compression force. Therefore, the experiments were stopped when the pressure of the specified value was reached. The experimental data allowed to determine the density of the layer of material ρ_L and its porous E.

Fig. 2 shows the graphic dependence of the density of the biomass layer on the seal pressure, which showed that in the studied range of parameters, the effect of the hanging mass on the density of the layer is insignificant. Mathematical processing of experimental data was carried out by regression analysis using the Microsoft Excel package of programs.

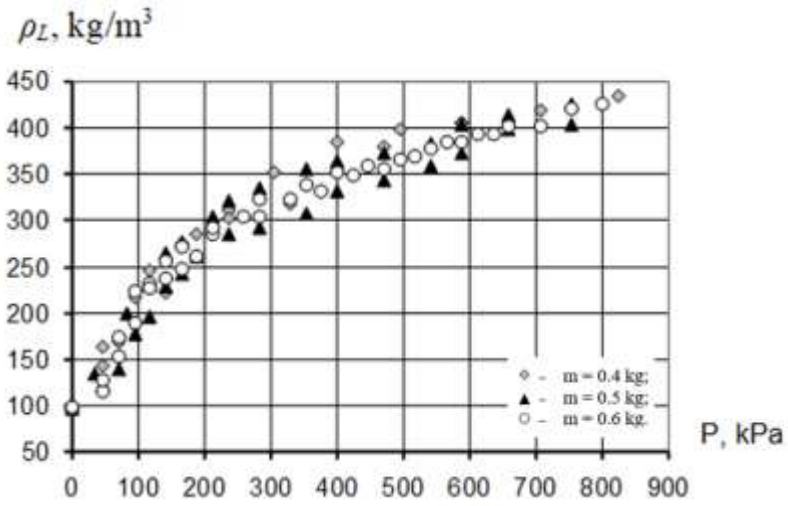

Figure 2. Dependence of the density of the biomass layer on the sealing force.

As a result, we acquired an empirical dependence of the density of the biomass layer on the pressure of the compaction P, acting on the surface of the sunflower husk layer in the form of:

$$\rho_L = x \cdot \sqrt{P} + y, kg/m^3 \qquad (1)$$

where x = 0,4 is empirical coefficients and y = 87,3 kg/m^3 is average value of bulk density of sunflower husks [2].

Determination of the parameters of the screw feeder for loading with sunflower husks

The process of loading biomass waste into the boiler furnace must meet the following requirements:

- ensure continuous and uniform supply of material;
- ensure that the level of suction in the furnace is not higher than acceptable in accordance with safety conditions.

Dependence that determines the ratio of the size of the biomass "cork" and the conditions of its movement by the channel is determined by the formula:

$$\frac{d}{L} = 4 \cdot \mu \cdot \varepsilon, \qquad (2)$$

where:

d – the diameter of the screw channel, m;
L – the height of the "cork" of biomass waste, m.

The value of the product of μ and ε coefficients for sunflower husks is experimentally determined. For research, a container was used – a pipe with a diameter of Ø218×10 mm, 500 mm high, which was filled with sunflower husks (the weight of the backfill was 3 kg). On a vertical press, the material was consistently pushed from one end of the container to the other until the height of the waste plug stopped changing.

A total of three experiments were conducted, as a result of which the final height of the sunflower husk stopper was determined, which amounted to 230 ± 5 mm. This value was applied to determine the numerical value of the product value of the coefficients from the Eq. [2]: $\mu \cdot \varepsilon = 0{,}22$.

Thus, the height of the "cork" of biomass, that is, the length of the channel from the end of the screw to the space of the boiler furnace should be:

$$L = 1{,}136 \cdot d, \text{ m.} \qquad (3)$$

Determination of the choice of parameters of the process, providing a given level of gas leaks or air suction, was carried out by joint numerical solution of the system of the Eq. [2] and Eq. [3].

The following range of parameters was investigated in the work:

- pressure drop between the furnace of the boiler unit and the environment ΔP = 0,05 ÷ 0,3 kPa;
- the permissible level of suckers in the boiler furnace Q = 0,01 ÷ 0,1 m^3/h;
- screw channel diameter d = 0,1 ÷ 0,25 m.

Statistical processing of the results of numerous studies in the specified range of parameters made it possible to obtain a generalized regressive dependence of the effort of compaction of the biomass waste layer on the diameter of the channel, the pressure difference in the boiler and the surrounding space and the permissible level of suckers [14]:

$$P = 120 \cdot Q^{-0{,}85} \cdot \Delta P \cdot d + 90 \cdot Q^{-0{,}4} \cdot d + 345 \cdot Q^{0{,}35} \cdot \Delta P + \\ +7795 \cdot Q^2 - 1486 \cdot Q + 32, Pa \qquad (4)$$

Dependence Eq. [4] was used for calculated studies of the dependence of the effort of compaction of the biomass waste layer on the level of suction cups in the boiler furnace, subject to controlled pressure drops between the boiler furnace and the environment for feeders with different diameters of auger. The results of calculations are given in the form of graphic dependencies in Fig. 3.

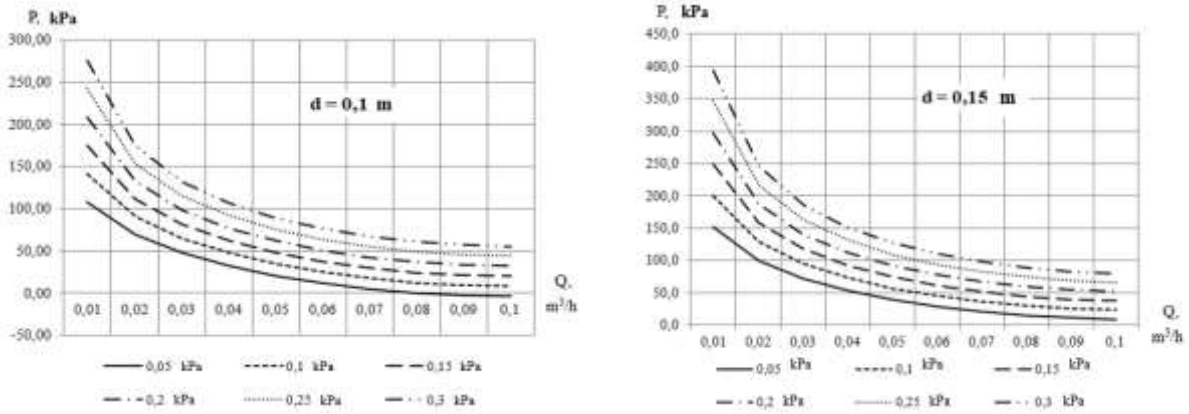

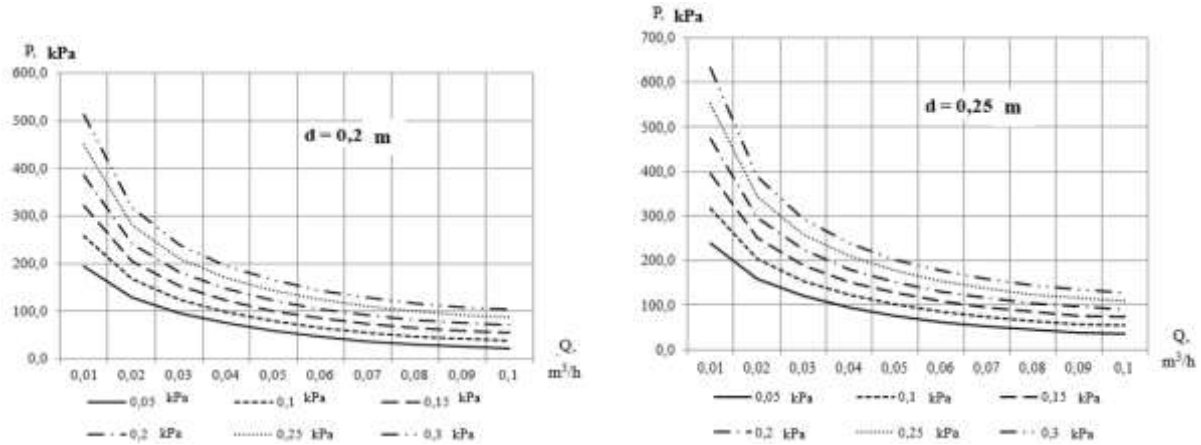

Figure 3. Dependence of the operating parameters of the screw feeder with different diameter of the screw on the permissible level of suckers in the boiler furnace.

The joint solution of the Eq. [1] and Eq. [4] made it possible to determine the value of the compaction of the layer, which corresponds to the forces of compaction of the sunflower husk layer, depending on the levels of suckers in the furnace of the boiler unit, subject to controlled pressure drops between the furnace of the boiler unit and the environment for feeders with different diameters of auger. As an example of the results of the calculation of the dependence of the sunflower husk layer density on seal pressure in the screw feeder for the diameter of the screw d = 0.15 m is shown in Table 2.

Table 2. Dependence of sunflower husk layer density on seal pressure in screw feeder with d = 0,15 m

Q, m³/h	Δp = 0.05 kPa		Δp = 0.1 kPa		Δp = 0.15 kPa		Δp = 0.2 kPa		Δp = 0.25 kPa		Δp = 0.3 kPa	
	P, kPa	ρ_L, kg/m³	P, kPa	ρ_L, kg/m³	P, kPa	ρ_L, kg/m³	P, kPa	ρ_L, kg/m³	P, kPa	ρ_L, kg/m³	P, kPa	ρ_L, kg/m³
0,01	151,6	92,23	200,2	92,96	248,7	93,61	297,3	94,20	345,8	94,74	394,4	95,24
0,02	99,4	91,29	128,8	91,84	158,2	92,33	187,6	92,78	217,0	93,19	246,4	93,58
0,03	72,1	90,70	94,9	91,20	117,7	91,64	140,5	92,04	163,2	92,41	186,0	92,76
0,04	53,4	90,22	72,9	90,72	92,4	91,14	111,9	91,53	131,3	91,88	150,8	92,21
0,05	39,5	89,81	57,0	90,32	74,5	90,75	92,1	91,14	109,6	91,49	127,1	91,81
0,06	28,8	89,45	45,1	89,99	61,3	90,43	77,6	90,82	93,9	91,18	110,2	91,50
0,07	20,7	89,12	36,1	89,70	51,6	90,17	67,0	90,57	82,4	90,93	97,9	91,26
0,08	14,9	88,84	29,7	89,48	44,6	89,97	59,4	90,38	74,2	90,75	89,1	91,07
0,09	11,2	88,64	25,6	89,32	40,0	89,83	54,3	90,25	68,7	90,62	83,1	90,95
0,1	9,3	88,52	23,4	89,24	37,5	89,75	51,6	90,17	65,6	90,54	79,7	90,87

According to the results of calculations of the dependence of the density of the sunflower husk layer on the seal pressure in screw feeder with different screw diameters, it can be concluded that for certain working conditions of the feeder, the relative increase in the density of the "cork" from the sunflower husk exceeds the bulk density of the non-compacted layer by no more than 11,5%.

3. CONCLUSIONS

The paper considers the method of loading sunflower husks into the boiler with a screw feeder, which ensures the gas density of the working chamber due to a compacted layer of biomass waste ("cork"), formed in a result of the movement of waste through the cylindrical channel in the tail of the screw (in front of the boiler furnace chamber). Such a method will help to avoid the installation of additional mechanical devices (cut-offs, latches, etc.), which increase capital expenditures and complicate the operation of the entire energy complex.

According to the results of the research, it was concluded that the considered types of biomasses (sunflower husks, sawdust and walnut shells) belong to well-loose materials.

It has been proven that for certain working conditions of the feeder, the relative increase in the density of the "cork" from the sunflower husk exceeds the bulk density of the non-compacted layer by no more than 11,5%.

References

[1] Artyukhov A.M., Orishaka O.V., Orishaka V.O., Malashenko Y.A., Research of physical and mechanical properties of fine-grained bulk materials. *Technology in agricultural production, branch engineering, automation. Issue 24, part II*, 2011, pages 72-76.

[2] Shevchenko G.L., Shyshko Y.V., Usenko A.Yu., Kremenova E.V. Study of the main characteristics of biomass waste as a fuel. Metallurgical heat engineering: Collection of scientific works of the National Metallurgical Academy of Ukraine. – Dnipropetrovsk: "PE Grek O.S.", 2007. pp. 305 - 313.

[3] Heping Cui, John R. Grace. Pneumatic conveying of biomass particles: a review. *China Particuology, Volume 4, Issues 3–4*, 2006, pages 183-188. DOI: https://doi.org/10.1016/S1672-2515(07)60259-0.

[4] Jianjun Dai, John R. Grace, Biomass granular screw feeding: An experimental investigation. *Biomass and Bioenergy, Volume 35, Issue 2*, 2011, pages 942-955. DOI: https://doi.org/10.1016/j.biombioe.2010.11.026.

[5] Perea-Moreno, M.-Á., Manzano-Agugliaro, F., Perea-Moreno, A.-J. Sustainable Energy Based on Sunflower Seed Husk Boiler for Residential Buildings. *Sustainability*, 2018. *10, 3407*. DOI:10.3390/su10103407.

[6] Road map of bioenergy development in Ukraine until 2050 and Action Plan until 2025. https://saf.org.ua/wp-content/uploads/2021/06/Dorozhnya-karta-rozvytku-bioenergetyky-v-Ukrayini-do-2050-roku-i-Plan-dij-do-2025.pdf.

[7] Jianjun Dai, Heping Cui, John R. Grace, Biomass feeding for thermochemical reactors. *Progress in Energy and Combustion Science, Volume 38, Issue 5*, 2012, pages 716-736. DOI: https://doi.org/10.1016/j.pecs.2012.04.002.

[8] Yalechko, V.I. Improving the efficiency of the energy-technological process of burning the healthy wood biomass. – Qualification of science practice as a manuscript. Dissertation for the degree of candidate of technical sciences for the specialty 05.14.06 – technical thermophysics of the heat and power industry. National University "Lviv Polytechnic", Lviv, Ukraine, 2021.

[9] Thais L.C. Gomes, Giovani A. Lourenço, Carlos H. Ataíde, Claudio R. Duarte. Biomass feeding in a dilute pneumatic conveying system. *Powder Technology, Volume 391*, 2021, pages 321-333. DOI: https://doi.org/10.1016/j.powtec.2021.06.020.

[10] Barroso, G., Hediger, L., Nussbaumer, T. Modelling and validation of biomass combustion in a screw burner. *Fuel, Volume 254*, 2019, 115672. DOI: https://doi.org/10.1016/j.fuel.2019.115672.

[11] Smuldyrev, A.E. Hydro- and pneumotransport in metallurgy. – M.: Metallurgy, 1985. – 280 p.

[12] Jianjun Dai, John R. Grace. A model for biomass screw feeding. *Powder Technology, Volume 186, Issue 1*, 2008, pages 40-55. DOI: https://doi.org/10.1016/j.powtec.2007.10.032.

[13] Bulinko, M.G., Petrovsky, E.E. Technology of peat-briquetting. – M.: Nedra, 1968. – 312 p.

[14] Gubinskiy, M.V., Shyshko, Y.V. Study of the hydraulic resistance of a dense layer of biomass waste. *Metallurgic heating, Volume 4*, 2001, pages 145-151.

RIGA 2023

Two-Element MIMO Antenna for UWB Wireless Communications

Erol Kurt
Department of Electrical and Electronics Engineering, Technology Faculty, Gazi University, Ankara, Türkiye, e-mail: ekurt52tr@yahoo.com, ekurt@gazi.edu.tr, ORCID: 0000-0002-3615-6926

Kayhan Çelik
Department of Electrical and Electronics Engineering, Technology Faculty, Gazi University, Ankara, Türkiye, e-mail: kayhancelik1923@gmail.com, kayhancelik@gazi.edu.tr, ORCID: 0000-0003-0371-0473

Emre Kaan Kaynar
Department of Electrical and Electronics Engineering, Technology Faculty, Gazi University, Ankara, Türkiye, e-mail: emrekaan.kaynar@gmail.com, emrekaan.kaynar@gazi.edu.tr, ORCID: 0000-0003-0145-7750

Cite this paper as: *Kurt, E, Çelik, K, Kaynar, EK. Two-Element MIMO Antenna for UWB Wireless Communications. 11. Eur. Conf. Ren. Energy Sys. 18-20 May 2023, Riga, Latvia*

Abstract: In this paper, the design and analyses of the two port MIMO antenna are presented. The antenna is a modified version of the rectangular monopole. It has a dimension of 35 x 20 x 1.6 mm^3. The stub and slot are used for improving antenna performance. The antenna works efficiently from 2.75 GHz to 12.3 GHz, covering the entire UWB band. It has a minimum efficiency value of 60%, an ECC value lower than 0.5 and minimum isolation nearly lower than -10 dB. As a result, the proposed antenna can be used in UWB wireless applications.

Keywords: *MIMO antenna, UWB antenna, Rectangular monopole antenna*

1. INTRODUCTION

Scientific research on UWB antenna design has increased and become a popular wireless communication area with the formal authorization of the 3.1–10.6 GHz spectrum for use in Ultra-wideband domain by the Federal Communications Commission in 2002 [1]. Since UWB systems need features such as low power consumption, complexity, cost and high data rates, hardware and software units must be designed to meet these requirements [2] [3]. Antennas, one of the essential elements of a wireless communication unit, must meet these needs [4] [5] [6]. However, single-element printed antennas suffer from multipath fading in the wireless communication channel [7] [8]. At this point, to solve the problem, multiple-input-multiple-output (MIMO) technologies emerge. In the modelling of the MIMO antennas with a spatial multiplexing and diversity property, the fading effect can be decreased [9] [10]. This concept reduces channel capacity losses, and as a result of this process, the data transmission and reception rate rises [11] [12]. Printed MIMO antennas have a property of low cost, profile, compact and ease of integration with microwave components, which makes them suitable for the UWB systems [13] [14].

When the literature is examined, it can be seen that many two-port UWB-MIMO antennas with different shapes were presented. For instance, the octagonal-shaped antenna [15], the semi-elliptical antenna with a modified Koch fractal-shaped boundary [16], the antenna consisting of a combination of semicircular and rectangular structure [17], the antenna with semi-arc shaped monopole [18], elliptical-shaped monopole antenna [19], F-shaped monopole antenna [20], classical patch antenna shaped antenna [21] can be given as a major tutorials.

In addition to this, many techniques for satisfying the higher isolation between each antenna are also presented. Using the neutralization line technique [17], using a Maple leaf fractal structure shorted with ground plane [16], placing parasitic elements between the antennas [19], using T-shaped junction [20], using the T-like stub extruding from the ground plane [22] can be given as examples of studies to increase isolation between the antenna elements.

In this paper, the novel dual-element MIMO antenna for the UWB systems is presented. In the next section, the design concept of the antenna is presented. In addition, the obtained results of the proposed structure such as S-parameters, efficiency, radiation patterns and ECC are presented. Lastly, the paper is finished with the conclusion section.

2. DUAL-ELEMENT STRUCTURE

The general structure of the dual-element MIMO antenna for the ultra-wideband communication systems is depicted in Figure 1. The FR4 substrate with Ɛr = 4.4, tan δ = 0.02 and thickness of 1.6 mm is used in antenna design. As seen from the figure that, the single-element of the antenna is a modified version of the rectangular monopole antenna. The S-parameters of MIMO system is given in Figure 2. According to the figure, the MIMO-antennas has an impedance bandwidth of nearly 9.55 GHz. The bandwidth starts at 2.75 GHz and ends at 12.3 GHz.

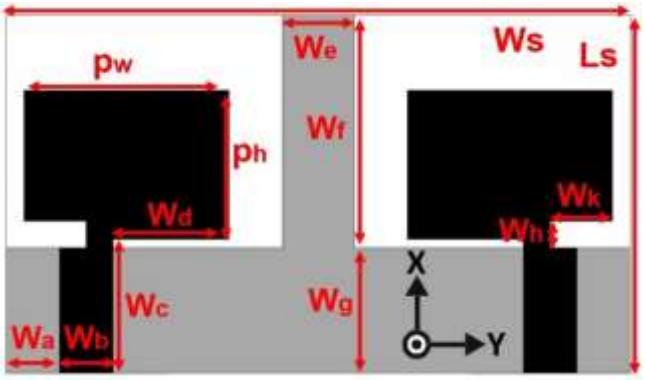

Figure 1. The designed dual-element MIMO antenna

Table 1. The parameters of the antenna

Parameter	Value (mm)
Ws	35
Ls	20
p_w	11.5
p_h	8.3
Wa	3
Wb	3
Wc	7.5
Wd	6.5
We	4
Wf	13
Wg	7
Wh	1.5
Wk	3.5

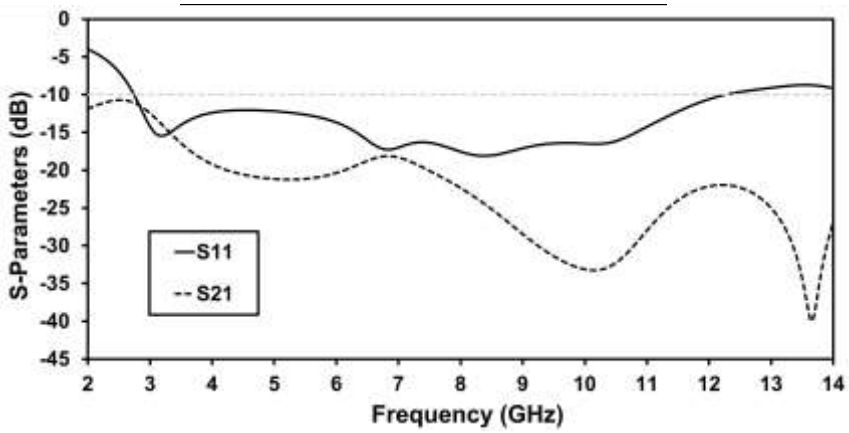

Figure 2. The S-parameters of the designed antenna.

The difference of the designed antenna from the normal rectangular monopole antenna is that the transmission lines used for the feeding of the antennas are shifted outward from MIMO center for increasing the impedance matching of the system. In addition to this, a slot is added at the point where the feeding line connects to the radiation element. The another change is made at the ground plane. A stub is placed between the two antennas on the ground plane. The effect of these modifications on the antenna S-parameters are given in Figure 3.

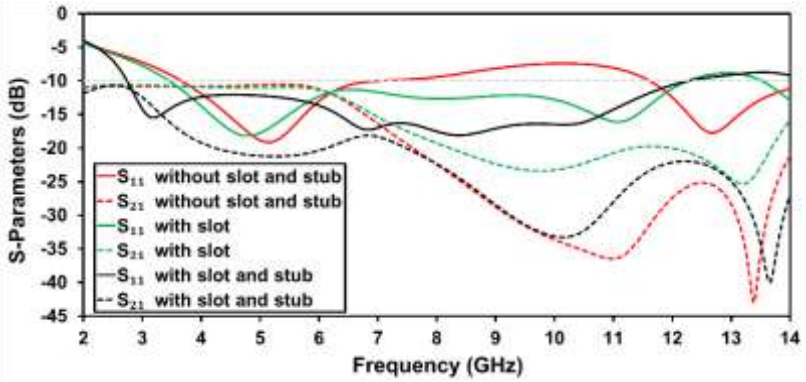

Figure 3. The S-parameters of the designed antenna.

According to the figure, impedance matching of the antenna (S_{11}) is not very good, especially between the 7-11 GHz range. With the addition of the slot, it is seen that the impedance matching in this frequency range improves and the values fall below -10 dB. In addition, the lower operating frequency of the antenna decreases from 3.66 GHz to 3.48 GHz with the help of the slot. When the stub is added in addition to the slot, the impedance of the antenna improves further and the lower operating frequency decreases from 3.48 GHz to 2.75 GHz. Finally, the addition of slot and stub improves the isolation between the ports, especially in the 3-7 GHz range.

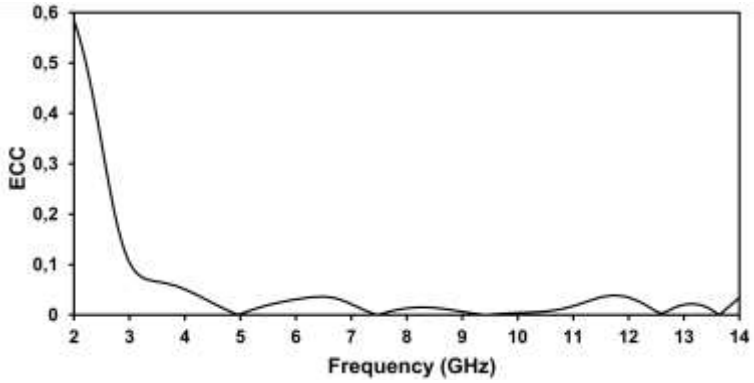

Figure 4. ECC graph of the designed antenna.

Envelope Correlation Coefficient (ECC) is one of important parameters for defining the performance of the MIMO antennas. The calculation of the ECC using S-Parameter of a two element MIMO antenna system is given as:

$$ECC = \frac{\left|S_{ii}^{*}S_{ij}+S_{ji}^{*}S_{jj}\right|^{2}}{\left(1-\left(|S_{ii}|^{2}+|S_{ji}|^{2}\right)\right)\left(1-\left(|S_{jj}|^{2}+|S_{ij}|^{2}\right)\right)} \quad (1)$$

The calculated ECC values of the designed antenna is given in Figure 4. In the operation bandwidth, the system has a values of lower than 0.5 which one is acceptance value. The variation of antenna efficiency with frequency is given in Figure 5. It is seen that the antenna has a minimum 60% and a maximum 90% efficiency in the operating band range.

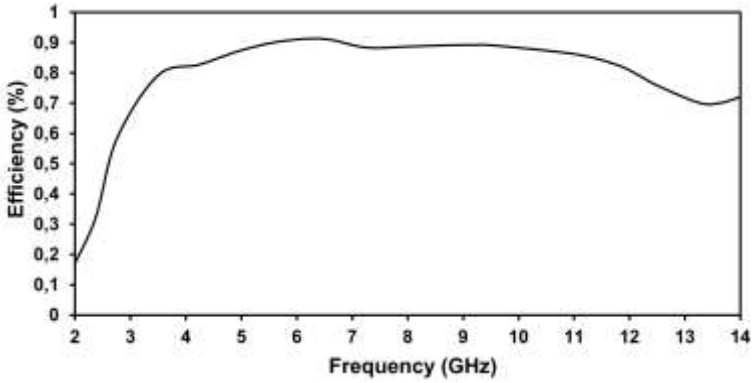

Figure 5. The efficiency graph of the designed antenna.

Examples of the radiation patterns of the antenna at different frequencies are presented in Figure 6. Due to the stub placed between the two antennas, it is seen that the designed antenna radiates mostly in the x-z (black line) and y-z (red line) planes and the least radiation occurs in the x-y (green line) plane as expected.

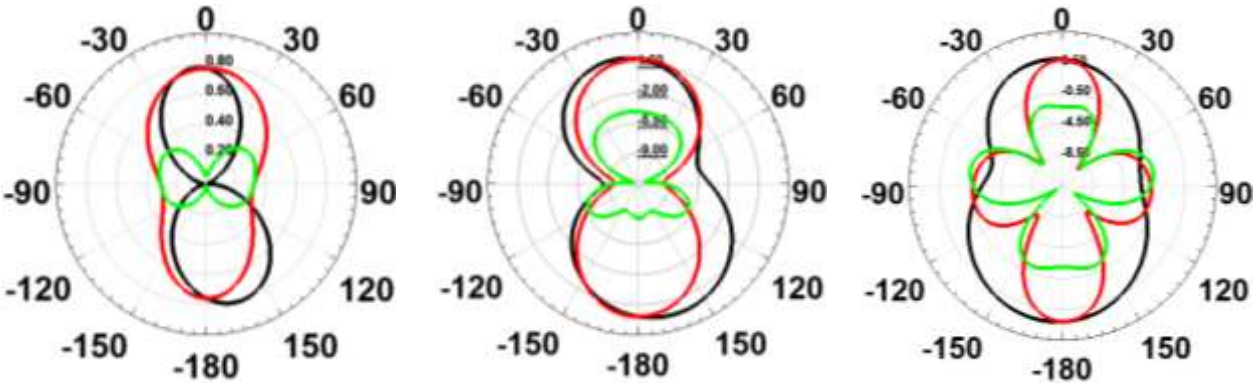

a) 4 GHz *b) 6.5 GHz* *c) 9 GHz*

Figure 6. The sample radiation patterns of the antenna (x-z, y-z, x-y)

3. CONCLUSION

This paper presents the design and analyses of the two-port MIMO antenna. The shape of the antenna is obtained from the rectangular monopole with the small modifications which one has a stub and slot are used for improving antenna performance. It has a dimension of 35 x 20 x 1.6 mm^3 and works efficiently from 2.75 GHz to 12.3 GHz, covering the entire UWB band. It has a minimum efficiency value of 60%, an ECC value lower than 0.5 and minimum isolation nearly lower than -10 dB. As a result, the proposed antenna can be used in UWB wireless applications.

References

[1] Breed, G. A summary of FCC rules for ultra wideband communications. High Frequency Electronics, 2005;4(1), 42-44.
[2] Oppermann, I., Stoica, L., Rabbachin, A., Shelby, Z., & Haapola, J. UWB wireless sensor networks: UWEN-a practical example. IEEE Communications Magazine, 2004;42(12), S27-S32.
[3] Gerrits, J. F., Farserotu, J. R., & Long, J. R. Low-complexity ultra-wide-band communications. IEEE Transactions on Circuits and Systems II: Express Briefs, 2008; 55(4), 329-333.
[4] Constantinescu, C. A., Pacurar, C., Giurgiuman, A., Munteanu, C., Dragan, F., Andreica, S., & Gliga, M. The Influence of Human Tissues on the Patch Antennas' Parameters. Transactions On Electromagnetic Spectrum,2023; 2(1), 1–11.
[5] Borel, T. T. S., & Priyadarshini, R.A Compact Microstrip Patch Antenna for X-Band Applications. Transactions On Electromagnetic Spectrum, 2022; 1(2), 24–30.
[6] Ambavaram, P. R., & Muthusamy, P. Bandwidth and Gain Enhancement of Parasitic Loaded Proximity Coupled Antenna for WLAN Applications. Transactions On Electromagnetic Spectrum,2022; 1(2), 31–37.

[7] See, C. H., Abd-Alhameed, R. A., Abidin, Z. Z., McEwan, N. J., & Excell, P. S. Wideband printed MIMO/diversity monopole antenna for WiFi/WiMAX applications. IEEE transactions on antennas and propagation,2012; 60(4), 2028-2035.
[8] Eltrass, A. S., & Elborae, N. A. New design of UWB-MIMO antenna with enhanced isolation and dual-band rejection for WiMAX and WLAN systems. IET microwaves, antennas & propagation, 2019;13(5), 683-691.
[9] Heath, R. W., & Paulraj, A. J. Switching between diversity and multiplexing in MIMO systems. IEEE Transactions on Communications, 2005; 53(6), 962-968.
[10] Heath, R. W., & Paulraj, A. Characterization of MIMO channels for spatial multiplexing systems. In ICC 2001. IEEE International Conference on Communications. Conference Record (Cat. No. 01CH37240) (2001, June. Vol. 2, pp. 591-595). IEEE.
[11] Fletcher, P. N., Dean, M., & Nix, A. R. Mutual coupling in multi-element array antennas and its influence on MIMO channel capacity. Electronics Letters,2003; 39(4), 342-344.
[12] Babu, K. V., & Anuradha, B. Design of multi-band minkowski MIMO antenna to reduce the mutual coupling. Journal of King Saud University-Engineering Sciences, 2020; 32(1), 51-57.
[13] Hussain, N., Jeong, M. J., Abbas, A., & Kim, N. Metasurface-based single-layer wideband circularly polarized MIMO antenna for 5G millimeter-wave systems. Ieee Access,2020; 8, 130293-130304.
[14] Zaidi, Abir, et al. A low profile ultra-wideband antenna with reconfigurable notch band characteristics for smart electronic systems. Micromachines, 2022, 13.11: 1803.
[15] Kumar, A., Ansari, A. Q., Kanaujia, B. K., Kishor, J., & Kumar, S. An ultra-compact two-port UWB-MIMO antenna with dual band-notched characteristics. AEU-international journal of electronics and communications,2020; 114, 152997.
[16] Gorai, A., & Ghatak, R. Utilization of shorted fractal resonator topology for high isolation and ELC resonator for band suppression in compact MIMO UWB antenna. AEU-International Journal of Electronics and Communications, 2020;113, 152978.
[17] Tiwari, R. N., Singh, P., Kanaujia, B. K., & Srivastava, K. Neutralization technique based two and four port high isolation MIMO antennas for UWB communication. AEU-International Journal of Electronics and Communications, 2019; 110, 152828.
[18] Agarwal, M., Dhanoa, J. K., & Khandelwal, M. K. Ultrawide band two-port MIMO diversity antenna with triple notch bands, stable gain and suppressed mutual coupling. AEU-International Journal of Electronics and Communications,2020; 120, 153225.
[19] Addepalli, T., & Anitha, V. R. Compact two-port MIMO antenna with high isolation using parasitic reflectors for UWB, X and Ku band applications. Progress In Electromagnetics Research C, 2020;102, 63-77.
[20] Dkiouak, A., Zakriti, A., El Ouahabi, M., & Mchbal, A. Design of two element Wi-MAX/WLAN MIMO antenna with improved isolation using a short stub-loaded resonator (SSLR). Journal of Electromagnetic Waves and Applications, 2020; 34(9), 1268-1282.
[21] Iqbal, A., A Saraereh, O., Bouazizi, A., & Basir, A. Metamaterial-based highly isolated MIMO antenna for portable wireless applications. Electronics,2018; 7(10), 267.
[22] Wu, L., Xia, Y., Cao, X., & Xu, Z. A miniaturized UWB-MIMO antenna with quadruple band-notched characteristics. International Journal of Microwave and Wireless Technologies, 2018;10(8), 948-955

RIGA 2023

Adaptive Mesh Refinement Criterion Comparison for DrivAer Model

Oscar Irigaray Pérez de San Román
Department of Nuclear and Fluid Dynamics University of the Basque Country (UPV/EHU), Nieves Cano 12, 01006 Vitoria-Gasteiz, Spain, oirigaray001@ikasle.ehu.eus, ORCID: 0000-0001-8737-4694

Zugatz Ansa Otxoa
Department of Nuclear and Fluid Dynamics University of the Basque Country (UPV/EHU), Nieves Cano 12, 01006 Vitoria-Gasteiz, Spain, zansa001@ikasle.ehu.eus, ORCID: 0000-0002-9918-0595

Ander Larrinaga Aguirre
Department of Nuclear and Fluid Dynamics University of the Basque Country (UPV/EHU), Nieves Cano 12, 01006 Vitoria-Gasteiz, Spain, alarrinaga032@ikasle.ehu.eus, ORCID: 0000-0002-2016-8412

Unai Fernandez Gámiz
Department of Nuclear and Fluid Dynamics University of the Basque Country (UPV/EHU), Nieves Cano 12, 01006 Vitoria-Gasteiz, Spain, unai.fernandez@ehu.eus, ORCID: 0000-0001-9194-963X

Koldo Portal-Porras
Department of Nuclear and Fluid Dynamics University of the Basque Country (UPV/EHU), Nieves Cano 12, 01006 Vitoria-Gasteiz, Spain, koldo.portal@ehu.eus, ORCID: 0000-0003-4747 -0595

Roberto Garcia Fernandez
Department of Nuclear and Fluid Dynamics University of the Basque Country (UPV/EHU), Nieves Cano 12, 01006 Vitoria-Gasteiz, Spain, Sunsundegui S.A., Poligono Ibarrea, s/n, 31800, Altsasu, Navarra, rgarcia@sunsundegui.com, ORCID: 0000-0002-9918-0595

Jose Manuel Lopez Guede
Automatic Control and System Engineering Department, University of the Basque Country (UPV/EHU), Nieves Cano, 12, 01006 Vitoria-Gasteiz, Spain, jm.lopez@ehu.eus, ORCID: 0000-0002-5310-1601

Ekaitz Zulueta Guerrero
Automatic Control and System Engineering Department, University of the Basque Country (UPV/EHU), Nieves Cano, 12, 01006 Vitoria-Gasteiz, Spain, ekaitz.zulueta@ehu.eus, ORCID: 0000-0001-6062-9343

Cite this paper as: *Lopez Guede, JM, et al. Adaptive Mesh Refinement Criterion Comparison for DrivAer Model. 11. Eur. Conf. Ren. Energy Sys. 7-9 May 2023, Riga, Latvia.*

Abstract: Aerodynamics is one of the main development areas of vehicle design, in part because in this day and age, fuel consumption and in consequence greenhouse gas emissions and electric vehicles' autonomy is a matter that is present in the scientific community, as aerodynamics optimization can be really beneficial to reduce emissions and enhance electric vehicles' range. The aim of this paper is to carry out a comparison of an AMR (Adaptive Mesh Refinement) based on different fluid dynamic criterions on a DrivAer car model, in order to compare the obtained results from the CFD (Computational Fluid Dynamics) with the experimental data available for this same exact model.

Keywords: *Aerodynamics, Adaptive Mesh Refinement (AMR), Computational Fluid Dynamics (CFD), DrivAer*

Nomenclature	
AMR	Adaptive Mesh Refinement
BR	Blockage Ratio
BL	Boundary-Layer

Cd	Drag Coefficient
CFD	Computational Fluid Dynamics
DDES	Delayed Detatched Eddy Simulation
DNS	Direct Numerical Simulation
FB	Fastback
RANS	Reynolds Averaged Navier-Stokes
Re	Reynolds Number
P_T	Total Pressure
CpT	Total Pressure Coefficient

1. INTRODUCTION

Due to the latest developments in computational fluid dynamics and due to the increase in the importance of milage and energy efficiency (especially since the uprise of the electric vehicle), aerodynamics has become one of the most important branches of vehicle design. The latest developments in aerodynamics have produced several models in order to accurately represent and analyze the phenomena surrounding private vehicles when passing through a mass of air. The main way to analyze and control wind energy by optimizing the vehicles geometry has been Computational Fluid Dynamics (CFD). These recently optimized methods allow us to accurately predict flow-fields and aerodynamic loads around complex geometries. The world of aerodynamics engineering has been constantly improving the CFD methodology and therefore the accuracy and efficiency of the simulations has been growing exponentially.

With respect to the field of private transport vehicles, one of the most widespread vehicle models that has been used is the DrivAer model. This model was developed by the Technical University of Munich in a joint project together with Audi and Volkswagen [1]. The aim of this model was to provide a generic geometry which has the main characteristics of modern privet vehicles, and provide variations of this model in order to more accurately understand and predict flow fields around a wide range of private vehicle variants. To be able to do so this model has been thoroughly tested using Wind Tunnel facilities as well as road test by several different investigators and institutions such as Cho et al. [2] who used the DrivAer model to test several drag reduction devices on passenger cars, specifically on the rear end of the vehicle, and Nabutola and Boetcher [3] who used CFD to develop and asses jet wheel deflectors on passenger cars.

Other researchers also used the DrivAer model for their studies, for example, in 2018 Avadirar et al. [4] experimentally investigated the time-averaged wake through wind-tunnel tests, using velocities maps, drag-force measurements and base pressure distributions to characterize and quantify the flow behind and around the vehicle. They concluded that the up-wash caused by flow exiting the smooth underbody diffuser dominated the near wake and base-pressure distribution. In 2016 Christopher Collin et al. [5] carried out an investigation in which they performed a CFD simulation of the DrivAer model, precisely an unsteady Delayed Detached Eddy Simulation (DDES), to evaluate wind tunnel interferences for open jet test sections. Furthermore, the experimental measurements of the 40% scaled wind tunnel DrivAer model, confirm the relevance of wind tunnel effects for different blockage ratios and test sections characteristics. In 2015, Lu Miao et al. [6] introduced a new wind tunnel setup for the DrivAer model, a new suspensions system that allowed to measure the drag and lift forces while the wheels were rolling on the moving ground. They later compared the obtained data with the numerical investigations, favorably concluding the correlation.

Authors like the aforementioned Collin [5] used Wind Tunnel testing and numerical computations analyzing the flow over the DrivAer model, creating therefore, a vast amount of both experimental and computational data which makes model validation more achievable when working on the DrivAer model. This is not a common thing in the field of aerodynamics due to the scarceness of experimental data for contrasting purposes.

As for the main goal of this study, one of the main development areas of CFD is computational resource optimization and overall efficiency of the simulations. Due to the large computational cost of obtaining accurate CFD representations, it is indispensable to optimize the available resources in the main areas of interest of the simulation. Optimizing the spatial discretization of the analyzed domain is one of the most effective ways of optimizing resources. By determining the areas of interest where the mesh density should be higher, we can reduce the number of cells needed elsewhere, greatly enhancing the computational efficiency of our simulation. It is

common to guess the areas of interest based on theoretical knowledge of aerodynamic flow fields and previous experience, but although this method is also effective, the latest advances in computational science allow us to produce more accurate discretization of the areas of interest using output-based mesh optimization also known as Adaptive Mesh Refinement (AMR). This method of mesh adaptation uses precomputed calculations to determining refinement areas based on previous results automatically for as many iterations as desired. This becomes an iterative process in which the variable of choice is analyzed in each cell determining whether the mesh should be refined or coarsened in that specific cell.

The use of AMR for CFD applications can vary a lot depending on the goal of the mesh refinement as well as the optimization parameters used. Different studies have use AMR for improving their simulations efficiency, such as Le Moigne [7], who studied unsteady Delta-wing aerodynamics using AMR, or Lee and Kwon [8] who used AMR to refine local vorticity maximum areas for multi-point aerodynamic optimization of rotor blades.

Taking into account that AMR is an iterative process, the accuracy of the results depends heavily on the initial mesh, which has to be fine enough to capture the phenomena going on in the flow-field but coarse enough so that the refinement does not result in an overproduction of cells.

2. METHODOLOGY

2.1 Geometry

For this study, as mentioned above, the analyzed geometry consists on the DrivAer model introduced by heft et al. [1], specifically its fastback (FB) variant with a simplified smooth underbody as shown in Figure 1. This version of the DrivAer model has been chosen over other variants due to it being the most commonly used DrivAer model in CFD simulations due to its simplified underbody geometry which reduces the complexity of the mesh generation and its fastback based rear-end shape which is very common among passenger vehicle manufacturers. The use of this geometry provides us with a wider set of experimental and computational data which can be used to validate the development of our model.

Figure 1. DrivAer FastBack model

As for the preparation of the geometry for CFD purposes, some minimal alterations have been included to ensure convergence of the simulation. One of the two main alterations is the elevating of the tires on cylindrical structures to model the contact patch. This ensures that no acute angle is formed between the tire and the road which could result in a floating-point exception error. The second alteration of the geometry has been the smoothing of the connection edge between the mirrors and the bodywork. These edges have been rounded and smoothed to allow for more accurate meshing and ensuring a low wall Y+ value in order to be able to calculate the boundary layer in that area.

2.2. Numerical set-up

2.2.1. Boundary Conditions

In terms of the boundary conditions for the simulations, every simulation has been carried out under a set of conditions defined to mimic and match the conditions defined by Heft et al.[9]. For the simulations the 1:1 FB DrivAer model has been used and the double precision Star CCM+ software has been used [10]. The simulations were conducted for a constant-density, time averaged steady-state solution. The simulations are run over 5000 iterations and the convergence criteria was set at 10^{-3} for all normalized residuals and a variance lower than 5N for the drag force over at least 100 iterations. Additionally, the drag force and drag coefficient (Cd) values are averaged over the last 100 iterations. The simulation has been run on an Intel Xeon Gold 5120CPU@2.2GHz with 28 cores and 56 threads and a RAM of 94GB.

For the domain dimensions a length of 20L has been defined to allow for the development and dissipation of the turbulent events in the wake of the vehicle. As for the width and height of the domain dimensions of 11L and 15L respectively. These dimensions allow for a low blockage-ratio ($BR < 1\%$) which ensures that the walls won't have a significant effect on the flow field around the model according to Choi C. and Kwon D. [11] who studied the effect of BR on the aerodynamic behavior of bluff bodies for a wide range of Reynolds numbers. Although this BR value can result in more realistic flow-field predictions, it is significantly lower than the experimental BR achieved at the wind tunnel A of the Institute of Aerodynamics and Fluid Mechanics at the Technische Universität München as shown by Heft et al. [1].

For the Reynolds conditions of the simulations, the conditions have been defined to ensure comparability of the results with both the experimental data and other CFD simulations performed by different authors such as those performed by John. et al. [12] and Peters et al. [13] and Collin et al [5]. For this study a Reynolds of $Re = 1.1 \times 10^7$ has been used as it has been proven by Collin et al. [5] to be high enough to have a sufficient Cd independency. This is equivalent to an inlet velocity of $V = 140\ km/h$ for the 1:1 DrivAer which is a common testing speed.

To mimic the conditions of the moving belt used in experimental tests, a moving ground conditions has been defined using a sliding mesh and, a rotating motion has been specified in all four tires matching the speed of the inlet. The effect of the rotating wheels on the flow-field around the DrivAer model was studied by Aultman et al. [14].

2.2.2. Turbulence Model

Private ground vehicles such as the ones the DrivAer model tries to mimic operate at relatively low Reynolds number and at which, the flow-field around them must be considered fully turbulent. This means that a turbulent model is needed to resolve the boundary-layer (BL) interactions.

Reynolds Averaged Navier-Stokes (RANS) are historically the most used models in the field of ground vehicle aerodynamics. These models, although slightly less accurate than other physical and empirical models such as the Large-Eddy Simulation (LES) models due to a slight loss of accuracy in the averaging process, are able to resolve the turbulence around the studied geometries with lower space discretization requirements resulting in a reduced computational cost. Additionally, Rodi [15] proved RANS models to be more accurate than the Direct Numerical Simulation (DNS) models for relatively higher Reynolds values ($Re > 10^4$).

For this study, the k-ω SST (Shear-Stress Transport) model developed by Menter [16], which comes from Wilcox's [17] original k-ω model is used. This is one of the most used two-equation models, due to its versatility and higher accuracy than other RANS models when resolving adverse pressure gradients: The k-ω SST model calculates the lower half of the BL using the original k-ω model, and instead, transitions to Jones-Launder's [18] k-ϵ model in the outer 50% of the BL for higher Reynolds numbers and free shear layers. One of this model's advantage with respect to other RANS models is the accounting for the shear stress transport in adverse pressure gradients, making it more accurate when predicting separation points and pressure recoveries.

Different studies such as the one carried out by Ashton N. and Revell A.[19], which compares different turbulent models for DrivAer geometry simulations, have concluded that the model developed by Menter can produce accurate results with much less computational power requirements such as those needed for Detached Eddy Simulations (DES) and Large Eddy Simulations (LES).

Menter's [16] k-ω SST model is defined by the following equations:

$$\frac{\partial \rho \kappa}{\partial t} + \frac{\partial u_j \kappa}{\partial x_j} = P_k - \beta^* \rho \omega \kappa + \frac{\partial}{\partial x_j}\left[(\mu + \sigma_\kappa \mu_t)\frac{\partial \kappa}{\partial x_j}\right] \quad (1)$$

$$\frac{\partial \rho \omega}{\partial t} + \frac{\partial u_j \omega}{\partial x_j} = \gamma P_\omega - \beta^* \rho \omega^2 + 2(1 - F_1)\sigma_{\omega 2}\frac{u_t}{\kappa}\frac{\partial \kappa}{\partial x_j}\frac{\partial \omega}{\partial x_j} + \frac{\partial}{\partial x_j}\left[(\mu + \sigma_\omega \mu_t)\frac{\partial \omega}{\partial x_j}\right] \quad (2)$$

where:

$$P_k = u_t \frac{\partial u_i}{\partial x_j}\left(\frac{\partial u_i}{\partial x_j} + \frac{\partial u_j}{\partial x_i}\right) - \frac{2}{3}\rho \kappa \delta_{ij}\frac{\partial u_i}{\partial x_j} \quad (3)$$

$$P_\omega = \rho \frac{\partial u_i}{\partial x_j}\left(\frac{\partial u_i}{\partial x_j} + \frac{\partial u_j}{\partial x_i}\right) - \frac{2}{3}\rho \omega \delta_{ij}\frac{\partial u_i}{\partial x_j} \quad (4)$$

The set of constants ϕ is interpolated from the constants $\phi_1$and ϕ_2 for k-ω SST and the k-ϵ models respectively as stated by Menter [16] using the following expression in which F_1 varies from 1 to 0 as it gets away from the wall and closer to the boundary layer edge:

$$\phi = F_1 \phi_1 + (1 - F_1)\phi_2 \quad (5)$$

Additionally, the eddy-viscosity is defined as:

$$\nu_t = \frac{a_1 \kappa}{\max(a_1 \omega; \Omega F_2)} \quad (6)$$

where $a_1 = 0.3$ and Ω is the absolute value of the vorticity. Additionally, F_2 is defined as:

$$F_2 = \tanh(\max\left(2\frac{\sqrt{\kappa}}{0.09\omega y}; \frac{400\nu}{y^2 \omega}\right)^2) \quad (7)$$

2.2.3. Spatial Discretization (AMR)

For the spatial discretization of the domain an initial hexahedral based coarser mesh has been defined so that all the governing phenomena going on in the flow-field are identified before the mesh optimization is carried on after the first convergence of the solution. Considering that the AMR is not configured to re-mesh the prism layers, these must be defined accurately for the coarser mesh. The prism layer configuration has been set to obtain a nondimensionalized wall height value of $Y+ < 1$ in every surface so that the turbulence model resolves the wall instead of modelling it. A total of 20 layers have been set over a thickness of 15mm and with a 1.5 stretching factor. The coarse mesh is made out of a total of 6M cells.

Once the initial mesh is developed, the simulation is run until convergence for around 500 iterations. After an initial convergence the AMR is triggered and the desired function is analyzed at each cell and compared over a threshold. If the value at the cell is above or below this threshold the hexahedral cells are divided or merged accordingly. On the first AMR iteration, the algorithm is not able to coarsen the original mesh, it can only refine it, but after that first refinement, the algorithm is able to coarsen a previously refined cell by merging it with the other refined mesh in case that cell is below the lower threshold value. In the case of hexahedral cells, these are divided into 8 cells by splitting the original sides in half.

For this AMR optimization, the refinement criterion has been defined base on previous knowledge of flows around ground vehicles similar to the DrivAer model and with special focus on accurately predicting the drag force and Cd of the model. Therefore, knowing the importance of the wake of the vehicle and how the geometry of the vehicle may affect it, the refinement criterion has been based on the total pressure (P_T). Since the wake of the vehicle is where the total pressure is lowest, the Laplacian of the P_T is appropriate. The Laplacian is defined as the divergence of a gradient of a scalar field. This value therefore will be greatest where the change of P_T increases as we move away from the cell we are evaluating, therefore, refining these areas will result in the refinement of the wake with

more levels of refinement deeper into the close field wake and it will fade out as it approaches the far-field and as we move outwards from the wake. In order to have an adapting field function that is updated after each refinement, said function must include the adaption cell size as a factor. This allows the user to control the minimum desired cell size as well as limiting the refinement and cell count with the threshold values. Additionally, some power factors must be included to prioritize and weigh the cell size over the refinement criteria. The refinement field function is defined as follows:

$$(\nabla \cdot \nabla P_T) \cdot s_{Cell\ Size}^2 = \left(\frac{\partial^2 P_T}{\partial x^2} + \frac{\partial^2 P_T}{\partial xy^2} + \frac{\partial^2 P_T}{\partial z^2}\right) \cdot s_{Cell\ Size}^2 \quad (8)$$

As for the threshold values, the upper limit has been defined at 10, so that every cell over this value is refined and the lower value has been set at 0.01, 3 orders of magnitude lower than the upper value so that only the smallest cells are re-coarsened. The AMR has been run 4 times until all cells are under the upper limit, resulting in a final mesh of 73M cells. The initial and final meshes with the number of refinement levels can be seen in Figure 2.

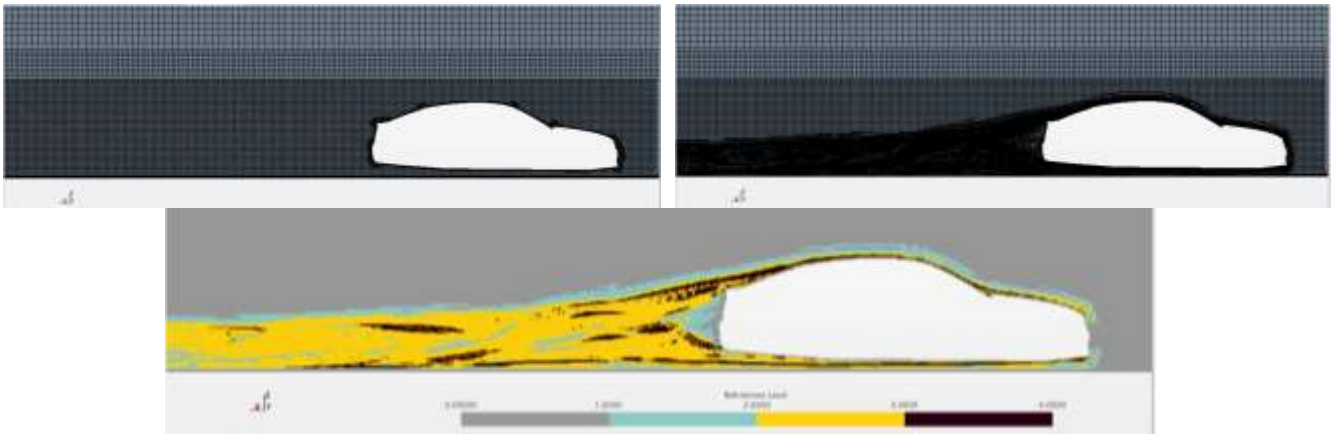

Figure 2. Initial mesh, AMR mesh and refinement levels.

3. RESULTS

After carrying out the mentioned simulations it is time to compare the results obtained. First of all, Table 1 compares the Cd obtained in the simulation with experimental data from three different sources. The correlation between the computational values and the experimental values differs slightly for the coarser base mesh but as the mesh is refined the Cd error is greatly reduced.

Table 1. Cd comparison.

3. Source	*4. Cd*	*5. AMR Error with respect to each Exp (%)*
6. Experimental data Collin et al. [5]	***7. 0.252***	***8. +0.4%***
9. Experimental data Peters et al. *[13]*	***10. 0.256***	***11. -1.2%***
12. Experimental data Heft et al. [9]	***13. 0.254***	***14. -0.4%***
15. CFD; Base mesh (6M cells)	***16. 0.258***	*17. -*
18. CFD; AMR (73M cells)	***19. 0.253***	*20. -*

Apart from the Cd figures, it is essential to compare more characteristics of the experiments. Figure 3 shows the pressure coefficient distribution on the central plane (Y=0m) over the upper surface of the DrivAer model for both the study carried out by Heft et al. [9] and the AMR based results. As shown in the chart, the red line shows the

experimental data obtained by Heft et al [9], the green line the CFD simulation of Heft et al [9] and finally, the dark line is the CFD simulation performed by ourselves. The stagnation point is clearly depicted in all the three curves, with that pressure peak. Later the flow accelerates as it flows over the hood and the pressure drops abruptly. Then the pressure constantly increases until the junction between the bonnet and the windshield. The pressure drops again as it is accelerated over the windshield and then it is stabilized over the top of the vehicle. The pressure is then recovered over the rear end of the FB model until it approaches atmospheric pressure in the near wake of the vehicle. All three curves show good correlation, with a couple of exceptions. The first pressure drop is overpredicted in the AMR CFD simulation. On the other hand, the AMR simulation shows better correlation with the experimental data in the vicinity of the bonnet and windshield junction, but again, overpredicts the pressure drops on the top of the vehicle. Both CFD simulations show great correlation between them over the length of the top of the vehicle, but they slightly underpredict the pressure recovery. This could be due to inefficient calculations of the adverse pressure gradient areas due to errors of the turbulence model. Nevertheless, the overall accordance between the carried simulation and the experimental data is good and shows the efficiency of the AMR method.

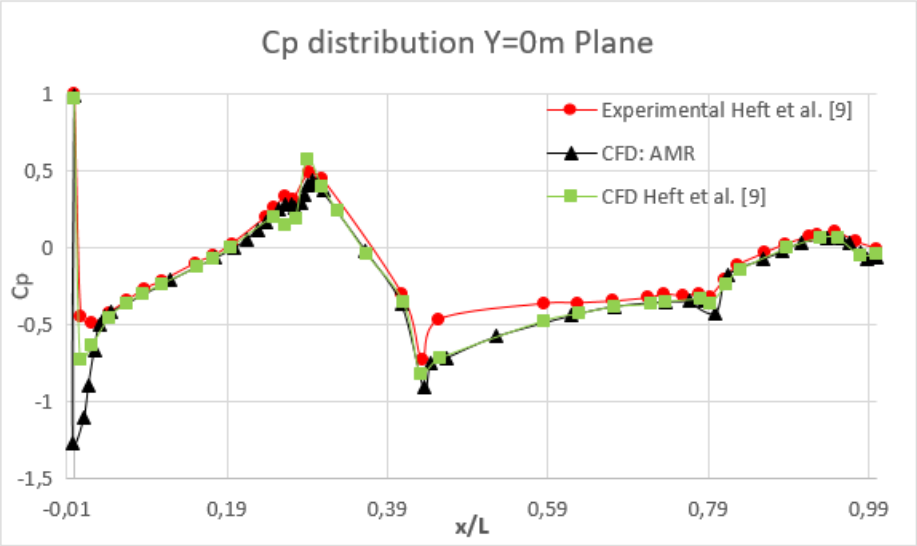

Figure 3. Cp distribution chart on plane Y=0m.

Since the selected criteria for the AMR focuses on the wake of the vehicle, it is indispensable to analyze this area. Figure 4 shows the prediction of the Total Pressure Coefficient (CpT) in the wake of the DrivAer model of the AMR based CFD simulation in different sections along the fluid direction (4m, 5.5, 7m and 8.5m from the front axle of the vehicle). As depicted, just behind the car the energy is, as expected, very low, but it approaches 1 (or free-stream CpT) as we move outward from the wake. As we move backward the low energy area is dissipated across the field and the wake becomes wider and lower. This suggests a downwash motion of the flow and gives us an idea of the lift being produced. Apart from that, the wake shows two sets of rounded areas, the bigger ones representing the inward rotating wake of the rear tires, and the smaller ones on the upper side of the wake represent the vortices generated by the mirrors.

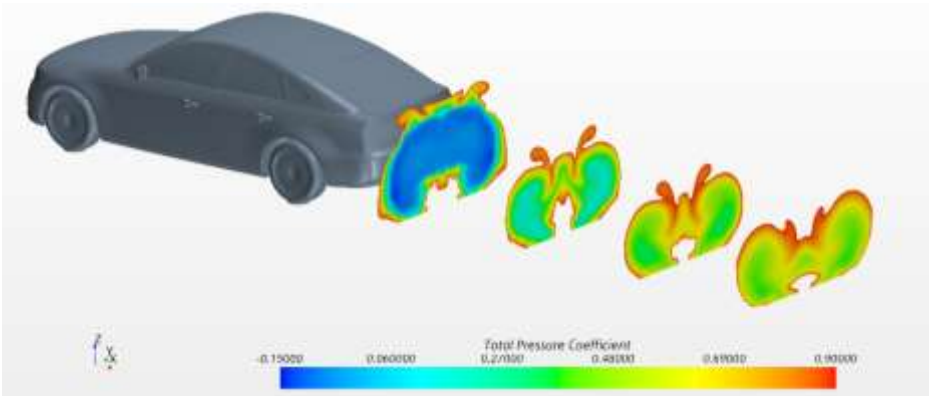

Figure 4. Total Pressure Coefficient prediction in the wake.

4. CONCLUSIONS

This study has developed a simulation for the DrivAer model in which an Adaptive Mesh Refinement method is implemented. The criterion for the refinement has been defined based on experience of ground vehicle aerodynamics and the well-known importance of the wake. To do so, the Laplacian of the total pressure or energy of the fluid has been coupled with the cell size squared. This method provides a more effective way of discretization and allocation of resources in order to obtain the most accurate results possible efficiently with the available computational resources.

The obtained results show great correlation with experimental data and have proven the effectiveness and efficiency of this method. This method can be used to analyze in an optimum way the effect of geometry alterations on the Cd of the vehicle, providing vehicle manufacturers with a great tool for vehicle design optimization and fuel consumption reduction.

Future studies will work on providing new optimization criteria and combinations of criteria for further improvement of this method along with studying the effectiveness of this method under different sets of conditions.

5. FUTURE WORK

This paper has shown a comparison between experimental data and two CFD simulations, one with a basic mesh and the other with an AMR mesh. Therefore, just one AMR criterion has been studied, Laplacian of the total pressure. A broader study with other criterions to perform the AMR should be carried out, other criterions will include the turbulent kinetic energy (TKE) which will also refine the wake of the DrivAer, Lambda2 and Q-Criterion for vorticity refinement, due to vorticity having a partial dominance of the flow-field around complex geometries such as those seen on ground vehicles and the curvature of the velocity components in order to refine the upwash region as well as the circulation region. These different refinement methods can also be combined using weighted functions in order to base the refinement on different areas of interest and not limiting it to a single one.

Another interesting approach would be that of adapted mesh refinement rather than adaptive mesh refinement. Although AMR is a really useful tool, it has its limitations, as it is not able to refine cells in an anisotropic manner. AMR can only divide previously computed cells by halving their edges. On the other hand, adapted meshing, although less automated than AMR and although it needs more user input, it can provide the designer with more efficient remeshing tools. Adapted meshing is also an output based remeshing technique in which the user creates refinement volumes based on the previously simulated results (using the desired criteria such as with the AMR), and then uses those volumes to completely re-mesh the whole domain. Doing this allows the user to completely alter the way a certain area of interest is meshed allowing for anisotropic mesh sizes or growths or even coarsening of the least relevant areas. The downside of this method apart from the obvious greater user intervention, is the additional computational requirements due to having to completely re-mesh the whole domain in each refinement iteration.

Other mesh refinement techniques are also being developed that although rougher, are great indications of what the future discretization optimization methods might look like. One of these methods, is the adjoint based mesh refinement. This method requires much more computational power than the previous ones especially in the form of RAM requirements. The procedure of this method consists on running the adjoint solution after an initial simulation is computed, to calculate the error contribution prediction of each cell to a certain parameter or combination of weighted parameters such as drag or lift forces so that the cells with the grater error can be refined using the AMR technique. This method is might be the most accurate one as it is able to predict where the error for one specific output might lay on the mesh and reduce that error by refining that area. Moreover, a more thorough study will dig into the behavior of different AMR meshes over a wider range of Re.

References

1. Heft, A.I.; Indinger, T.; Adams, N.A. Introduction of a New Realistic Generic Car Model for Aerodynamic Investigations.; SAE International: Detroit, MI, USA, 2012; p. 14.
2. Cho, J.; Park, J.; Yee, K.; Kim, H.-L. Comparison If Varius Drag Reduction Devices and Their Aerodynamic Effects on the DrivAer Model. SAE Int. J. Passeng. Cars - Mech. Syst 2018, 11, 225–238, doi:10.4271/06-11-03-0019.

3. Nabutola, K.L.; Boetcher, S.K. Assesment of Conventional Air-Jet Wheel Deflectors for Drag Reduction of the DrivAer Model. Advances in Aerodynamics 2021, 3, 29, doi:10.1186/s42774-021-00086-7.
4. Avadiar Characterisation of the Wake of the DrivAer Estate Vehicle. 2018.
5. Collin, C.; Mack, S.; Indinger, T. A Numerical and Experimental Evaluation of Open Jet Wind Tunnel Interferences Using the DrivAer Reference Model. SAE Int. J. Passeng. Cars - Mech. Syst 2016, 9, 23, doi:10.4271/2016-01-1597.
6. Miao, L. EXPERIMENTAL AND NUMERICAL INVESTIGATION OF AUTOMOTIVE AERODYNAMICS USING DRIVAER MODEL.; 2015.
7. Le Moigne, Y. Adaptive Mesh Refinement and Simulations of Unsteady Delta-Wing Aerodyamics, KTH Aeronautical and Vehicle Engineering (Royal Institute of Technolgy): SE-100 Stockholm, Sweeden, 2004.
8. Lee, S.W.; Kwon, O.J. Multi-Point Aerodynamic Shape Optimization of Rotor Blades Using Unstructured Meshes. KSAS International Journal 2007, Vol. 8, 13.
9. Heft, A.I.; Indinger, T.; Adams, N.A. EXPERIMENTAL AND NUMERICAL INVESTIGATION OF THE DRIVAER MODEL. In Proceedings of the Proceedings of the ASME 2012; ASME: Rio Grande, Puerto Rico, 2012; p. 11.
10. SIEMENS Siemens Star-CCM+.
11. Choi, C.-K.; Kwon, D.-K. Wind Tunnel Blockage Effects on Aerodynamic Behavior of a Bluff Body. Wind and Structures 1998, Vol. 1, 35–364.
12. John, M.; Buga, S.-D.; Monti, I.; Kuthada, T.; Wittmaier, F.; Gray, M.; Laurent, V. Experimental and Numerical Study of the DrivAer Model Aerodynamics.; SAE International: Detroit, MI, USA, 2018; p. 15.
13. Peters, B.C.; Udinn, M.; Bain, J.; Curley, A.; Henry, M. Simulating DrivAer with Structured Finite DIfference Overset Grids.; 2015; p. 9.
14. Aultman, M.; Auza-Gutierrez, R.; Disotell, K.; Duan, L. Effects of Wheel Rotation on Long Period Wake Dynamics of the DrivAer Fastback Model. Fluids 2022 2021, 7, 19, doi:10.3390/ fluids7010019.
15. Rodi, W. Comparison of LES and RANS Calculations of the Flow around Bluff Bodies. Journal of Wind Engineering and Industrial Aerodyamics Elsevier 1997, 55–75.
16. Menter, F.R. Inproved Two-Equation k-ω Turbulence Models for Aerdynamic Flows. NASA 1992, 38.
17. Wilcox, D.C. Reassesment Ofthe Scale-Determining Equation for Advanced Turbulence Models. AIAA Journal 1998, Vol. 26, 1299–1310.
18. Jones, W.P.; Launder, B.E. The Calculation of Low-Reynods-Number-Phenomena with a Two-Equation Model of Turbulence. International Journal of Heat Mass Transfer 1973, Vol. 16, 1119–1130.
19. Ashton, N.; Revell, A. Comparison of RANS and DES Methods for the DrivAer Automotive Body.; Detroit, MI, USA, 2015; p. 11.

RIGA 2023

Trends in Lithium-Ion Battery Optimization for Electric Vehicle Fleets

Felipe A. Nunez-Donoso
University of Bio Bio Chile, Department of Electrical Engineering, Concepcion, Chile, felipe.nunez@ayn.cl, ORCID: 0000-0001-7564-5522

Jose Manuel Lopez-Guede
University of the Basque Country (UPV/EHU), Vitoria-Gasteiz, Spain, jm.lopez@ehu.eus, ORCID: 0000-0002-5310-1601

Cite this paper as: *Nunez-Donoso, FA, Lopez-Guede, JM. Trends in Lithium-Ion Battery Optimization for Electric Vehicle Fleets. 11. Eur. Conf. Ren. Energy Sys. 18-20 May 2023, Riga, Latvia*

Abstract: This paper reviews the literature related to the optimization of lithium-ion batteries in electric vehicle (EV) fleets over the period of 2010-2020. The purpose of the study is to identify the current state of research in this area and to predict future trends. The methodology involved a comprehensive search of academic databases and a review of recent publications in relevant journals. The results indicate a growing trend towards the optimization of lithium-ion batteries in EVs, particularly in China. Recommendations for future research include a focus on renewable energy integration and a more collaborative and interdisciplinary approach to battery optimization.

Keywords: *Electromobility, battery optimization, electric vehicle fleets*

1. INTRODUCTION

Lithium-ion batteries are a critical component of electric vehicle (EV) fleets, providing the necessary energy storage for efficient and sustainable transportation. As the demand for EVs continues to grow, as shown in figure 1, the optimization of lithium-ion batteries becomes increasingly important to improve their performance, efficiency, and longevity. The purpose of this paper is to review the literature related to the optimization of lithium-ion batteries in EV fleets and identify current and future trends.

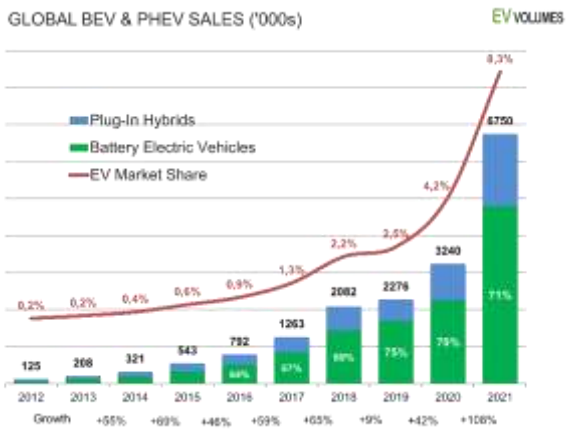

Figure 1. Global EV sales growth in last decade.

The text begins with an introduction to the importance of lithium-ion batteries in electric vehicle fleets and the need to optimize their performance. The literature review covers various topics related to the optimization of lithium-ion batteries in electric vehicles, including energy management, battery management, charging and discharging control,

and battery optimization. The methodology involves a comprehensive search of academic databases to identify relevant publications between 2010 and 2020. The results show a growing trend towards the optimization of lithium-ion batteries in electric vehicle fleets, with China leading the research in this area. The paper concludes with recommendations for future research, including a focus on renewable energy integration and a more collaborative approach to battery optimization.

2. LITERATURE REVIEW

The literature related to the optimization of lithium-ion batteries in EV fleets is vast and covers a range of topics, including energy management in EVs, lithium-ion battery management, charging and discharging control, and battery optimization [1]. The search strategy for this review involved a comprehensive search of academic databases, including Web of Science, Scopus, and IEEE Xplore, using relevant keywords and filters. The inclusion criteria for the review were publications that addressed the optimization of lithium-ion batteries in EV fleets between 2010 and 2020.

The literature review revealed a growing trend towards the optimization of lithium-ion batteries in EV fleets, with a focus on improving their energy density, power output, and thermal stability [2]. The optimization of lithium-ion batteries in EV fleets has been identified as a critical area of research due to its potential to improve the performance and efficiency of EVs, reduce their cost, and enhance their environmental sustainability.

3. METHODOLOGY

The methodology for this study involved a comprehensive search of academic databases, using relevant keywords and filters, to identify publications related to the optimization of lithium-ion batteries in EV fleets between 2010 and 2020. The search strategy used a funnel approach and included the following topics: energy management in EVs, lithium-ion battery management, charging and discharging control, and battery optimization [3]. The inclusion criteria for the review were publications that addressed the optimization of lithium-ion batteries in EV fleets.

4. RESULTS

The search strategy identified 5,415 publications related to the optimization of lithium-ion batteries in EV fleets between 2010 and 2020. Most of the publications (66.4%) were conference papers, followed by journal articles (22.9%) and book chapters (3.3%). The results shown in figure 2 reveal a clear trend towards the optimization of lithium-ion batteries in EV fleets, with a significant increase in the number of publications on this topic in recent years.

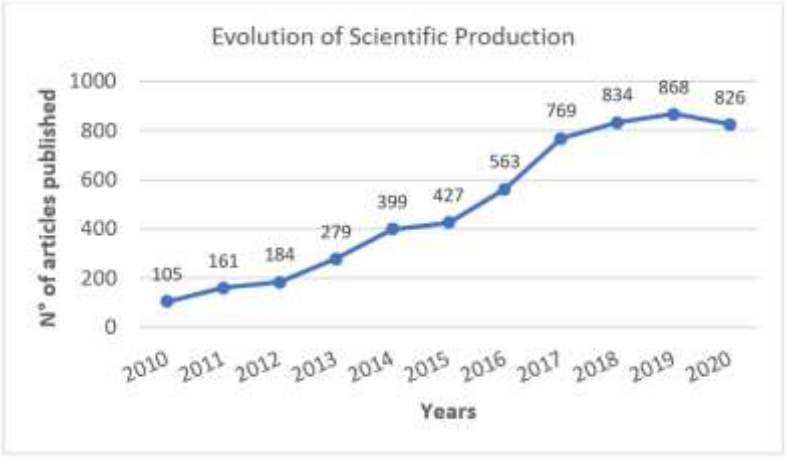

Figure 2. Evolution of scientific production, for the period 2010-2020.

The results also indicate that China is leading the way in research related to the optimization of lithium-ion batteries in EV fleets [4], with the highest number of publications and the most influential institutions in the field. However, institutions from the United States and the United Kingdom also have a significant presence in the field.

5. DISCUSSION

The findings of this literature review have important implications for the optimization of lithium-ion batteries in EV fleets. First, the results show a clear trend towards the optimization of lithium-ion batteries in EV fleets, indicating the importance of this area of research. Second, the dominance of Chinese institutions in the field suggests that the country is investing heavily in research related to the optimization of batteries.

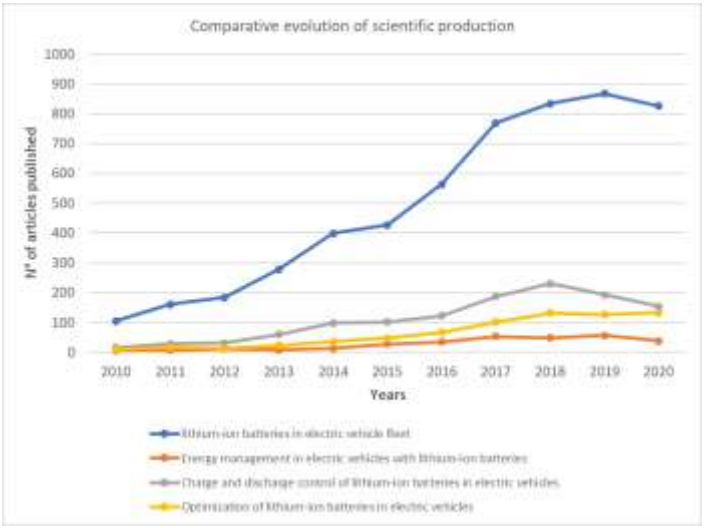

Figure 3. Evolution of scientific production, for the period 2010-2020.

The results of this study demonstrate the significant advancements made in the optimization of lithium-ion batteries in electric vehicle fleets over the past decade. There is a clear trend towards optimizing lithium-ion batteries in electric vehicles, as evidenced by the high percentage of publications focused on this area compared to other trends in the sector, as shown in figure 3.

Figure 4. Evolution of scientific production, for the period 2010-2020.

This study also reveals that China dominates the scientific development in this area, except for the University of Warwick (United Kingdom) and the University of Michigan (United States). It is worth noting in figure 4, that China has been a leader in the production of lithium-ion batteries for electric vehicles, making this finding unsurprising.

The integration of renewable energies into the electric vehicle industry has become increasingly important in recent years. While this study does not directly address the issue of renewable energy, it is essential to consider the role of renewable energy in the optimization of lithium-ion batteries in electric vehicles. Renewable energy sources such as wind and solar power can be used to charge electric vehicle batteries, which can help reduce the carbon footprint of the transportation sector.

6. CONCLUSIONS

This study evaluated the state of research on the optimization of lithium-ion batteries in electric vehicle fleets from 2010 to 2020. The results suggest that the trend towards optimizing lithium-ion batteries in electric vehicles will continue in the coming decade. This trend is significant given the rapid growth of the electric vehicle market and the importance of reducing the carbon footprint of the transportation sector.

The dominance of China in the scientific development of lithium-ion batteries in electric vehicles highlights the importance of international collaboration in this field. Furthermore, the integration of renewable energy sources into the electric vehicle industry should be a priority for future research to enhance the sustainability of this sector.

Overall, this study provides valuable insights into the current state of research on the optimization of lithium-ion batteries in electric vehicle fleets. However, future studies should expand on this research to include more diverse sources and data sets. Additionally, studies should focus on the integration of renewable energy sources into the electric vehicle industry to enhance its sustainability further.

References

[1] A. Zhai et al., "Design and operation optimization of electric vehicle battery charging station considering energy storage system," 2015 IEEE 11th International Conference on Power Electronics and Drive Systems (PEDS), Sydney, Australia, 2015, pp. 794-799.

[2] M. Razak, M. Shahzad and M. Hussain, "A review of energy management strategies for electric vehicles," 2015 IEEE Conference on Energy Conversion (CENCON), Johor Bahru, Malaysia, 2015, pp. 56-61.

[3] H. Alsuwaidi, Y. Abdel-Magid and M. El-Hagry, "Optimized Battery Size for Electric Vehicles Based on Driving Cycle Using Genetic Algorithm," 2018 IEEE 7th International Conference on Renewable Energy Research and Applications (ICRERA), Paris, France, 2018, pp. 7-12.

[4] L. Li, X. Li and Z. Li, "Optimization of Battery Size for Electric Vehicles with Particle Swarm Optimization," 2018 IEEE 8th Annual International Conference on CYBER Technology in Automation, Control, and Intelligent Systems (CYBER), Tianjin, China, 2018, pp. 1006-1011.

RIGA 2023

Computational Analysis of Variable Electrode Compression on the Performance of Vanadium Redox Flow Battery

Joseba Martinez-Lopez
Univ. Basque Country UPV/EHU, Nuclear Eng & Fluid Mechanics Dept, 01006 Vitoria-Gasteiz, Spain, ORCID: https://orcid.org/0000-0002-3268-1336

Unai Fernandez-Gamiz
Univ. Basque Country UPV/EHU, Nuclear Eng & Fluid Mechanics Dept, 01006 Vitoria-Gasteiz, Spain, ORCID: https://orcid.org/0000-0001-9194-2009

Iñigo Aramendia
Univ. Basque Country UPV/EHU, Nuclear Eng & Fluid Mechanics Dept, 01006 Vitoria-Gasteiz, Spain, ORCID: https://orcid.org/0000-0002-4960-2729

Aitor Beloki Arrondo
Centre for Cooperative Research on Alternative Energies (CIC energiGUNE), Basque Research and Technollogy Alliance (BRTA), Alava Technology Park, Albert Einstein 48, 01510 Vitoria-Gasteiz, Spain, ORCID: https://orcid.org/0009-0003-4815-4359

Eduardo Sanchez-Diez
Centre for Cooperative Research on Alternative Energies (CIC energiGUNE), Basque Research and Technollogy Alliance (BRTA), Alava Technology Park, Albert Einstein 48, 01510 Vitoria-Gasteiz, Spain, ORCID: https://orcid.org/0000-0001-7100-5181

Jose Manuel Lopez-Guede
Univ. Basque Country UPV/EHU, Syst Eng & Automat Control Dept, 01006 Vitoria-Gasteiz, Spain, ORCID: https://orcid.org/0000-0002-5310-1601

Cite this paper as: *Martínez, J., Fernández-Gamiz, U., Aramendia, I., Beloki, A., Sanchez, E., López-Guede, JM. Computational Analysis of Variable Electrode Compression on the Performance of Vanadium Redox Flow Battery. 10. Eur. Conf. Ren. Energy Sys. 7-9 May 2022, Istanbul, Türkiye*

Abstract: Batteries have been in the spotlight due to a combination of factors that have increased their importance in recent years. Some of these include the growing energy demand and the implementation of renewable energy sources. Vanadium redox flow batteries seem as a suitable option for stationary applications as they provide extended cycle life, high efficiency and safety. However, its low power density and high costs are set as major drawbacks for the commercial integration. Testing novel stack geometries and electrode configurations are ways to deal with the presented issues. This work aims to analyse the impact of applying variable electrode compression to the electrochemical performance of the VRFB. The study was performed by developing a 2D model, flow-through configuration with two electrodes and an ion exchange membrane.

Keywords: *Vanadium redox flow battery, computational model, variable compression, reaction rate*

Nomenclature	
VRFB	Vanadium Redox Flow Battery
CR	Compression Ratio

1. INTRODUCTION

With the transition from hydrocarbon-based energy to renewable sources, there has been a growing need to implement energy storage systems[1]. By smoothing out the intermittency of renewable energy sources, batteries can increase the reliability and stability of the power grid, making it possible to use more renewable energy and reduce reliance on fossil fuels. As a result, the development and implementation of batteries has become a critical component in the transition to a cleaner, more sustainable energy system[2–4]. Vanadium Redox Flow Battery (VRFB) is a type of rechargeable flow battery that has been gaining popularity in recent years as an energy storage solution[5]. One of the main advantages of VRFBs is their ability to be scaled up to very large sizes, making them suitable for use in grid-level energy storage[6, 7]. The vanadium redox flow battery (VRFB) consists of two electrolyte tanks, two sets of electrodes, and a membrane separator. The two electrolyte tanks contain different vanadium electrolytes. The two sets of electrodes, usually made of carbon felt, are placed in separate compartments of the battery and are used to convert the chemical energy of the electrolytes into electrical energy. The membrane separator is a permeable membrane that separates the two compartments, while allowing the flow of ions between them[8].

Electrode compression has been presented as a key factor in improving the cell performance. Increasing the electrode compression ratio to values near 30% has been proven to increase the ionic conductivity and species mass transfer [9]. Oh et al. [10] concluded that 20% CR achieved the highest energy efficiency and that species were better distributed with high compressions, due to convection. Other works suggest that 20 to 30% compression ratio shows the best achieved values of capacity, power and efficiency[11]. Gundlapalli [12] showed that 35% of CR was the optimal point for larger cells in terms of efficiency. Monteiro et al. [13] indicated that electrode compression had more effect on the reaction kinetics than on the ionic conductivity for CR values of 8 to 33%. This works aims to apply a variable electrode compression to study its effects on reaction kinetics and pressure drop.

2. NUMERICAL MODEL

Computational domain

This section provides a detailed description of a 2D vanadium redox flow battery model. The model represents a cell that is simulated using COMSOL Multiphysics®, a commercial software widely used for electrochemical applications. In Figure 1, the cell is depicted as being separated into three subdomains: a membrane, a positive electrode, and a negative electrode. The dimensions of the electrodes and membrane are listed in Table 1, with the electrode being modelled as a commercial Sigracell GFD 4.6 EA, and the membrane as Nafion material. To generate a structured mesh with 21420 elements, quadrilateral cells have been utilized. The mesh has been refined near the interfaces where steeper gradients are anticipated.

As one progresses from the inlet to the outlet, a gradual increase in the compression of the electrode can be observed, see Fig 1. The direction of the increase in compression is aligned with the direction of the electrolyte flow. The level of compression at the inlet is set at 10%, while at the outlet it is set at 30%. The values of porosity and conductivity were determined by their position along the y-axis.

Table 1. Dimensions of the 2D cell.

Parameter	Value	Unit
Electrode thickness (inlet)	$4.14 \cdot 10^{-4}$	m
Electrode thickness (outlet)	$3.22 \cdot 10^{-4}$	m
Membrane thickness	$2.03 \cdot 10^{-4}$	m
Cell height	$5.0 \cdot 10^{-2}$	m

The simulation model is based on the following assumptions:

- The model is steady-state.
- The cell is isothermal.
- Parasitic reactions are disregarded.
- The membrane and electrode possess isotropic properties.

- The fluid is incompressible.
- Electroneutrality and complete wettability of the membrane are assumed.

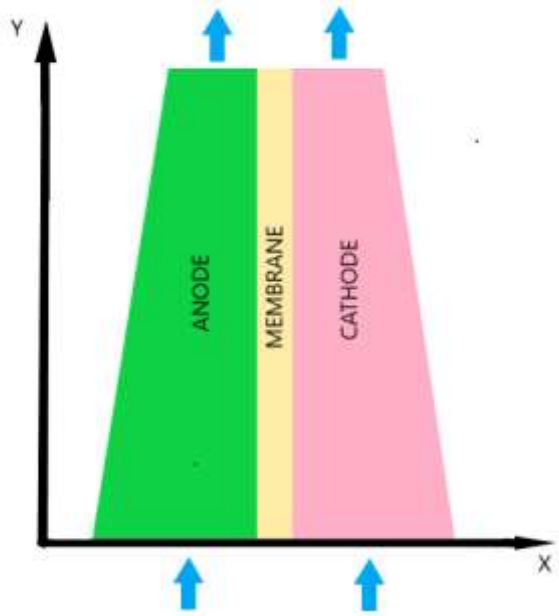

Figure 1. Scheme of the 2D computational model.

The Nernst-Planck equation is utilized to describe mass transport, encompassing molar flux arising from advection, migration, and diffusion. The Nernst-Einstein equation is utilized to represent the ionic mobility in the electrolyte, under the dilute solution approximation. Moreover, the Butler-Volmer kinetic model is applied, with a charge balance being considered between the solid and liquid phases. Cross contamination in the membrane is not neglected, transportation of all charged species is taken into consideration. For the modelling of fluidynamics, Darcy´s Law is applied to calculate the velocity term.

The positive and negative electrode reactions are described in Eqs, [1,2] respectively:

$$VO_2^+ + e^- + 2H^+ \leftrightarrow VO^{2+} + H_2O \quad (1)$$

$$V^{3+} + e^- \leftrightarrow V^{2+} \quad (2)$$

The main electrochemical properties and operating parameters are listed in Table 2 and Table 3 respectively:

Table 2. Electrochemical properties.

Parameter	Symbol	Value	Unit
V(II) diffusion coefficient	D_{V2}	$2.4 \cdot 10^{-10}$	$m^2 \cdot s^{-1}$
V(III) diffusion coefficient	D_{V3}	$2.4 \cdot 10^{-10}$	$m^2 \cdot s^{-1}$
V(V) diffusion coefficient	D_{V5}	$3.9 \cdot 10^{-10}$	$m^2 \cdot s^{-1}$
V(V) diffusion coefficient	D_{V5}	$3.9 \cdot 10^{-10}$	$m^2 \cdot s^{-1}$
HSO_4^- diffusion coefficient	$D_{HSO_4^-}$	$1.33 \cdot 10^{-9}$	$m^2 \cdot s^{-1}$
SO_4^{2-} diffusion coefficient	$D_{SO_4^{2-}}$	$1.065 \cdot 10^{-9}$	$m^2 \cdot s^{-1}$
H^+ diffusion coefficient	D_{H^+}	$9.312 \cdot 10^{-9}$	$m^2 \cdot s^{-1}$
Positive transfer coefficient	α_{pos}	0.55	–
Negative transfer coefficient	α_{neg}	0.45	–

Table 3. Operating parameters.

Parameter	Symbol	Value	Unit
State of Charge	SOC	15	–
Temperature	T	293	K
Flow Rate	Q	30	$ml \cdot \mathrm{min}^{-1}$
Outlet Pressure	P_{out}	0	Pa

Current Density	i	-100	$mA \cdot cm^2$

3. RESULTS

The numerical results were obtained under discharge conditions with a state of charge of 15% and a flow rate of 30 ml/min. Figure 2 depicts the distribution of the reaction rate in the cell. A comparison was conducted between a model without electrode compression and the model with variable compression to gain a deeper insight into how variable compression affects the cell's performance. The conventional model exhibits significant gradients, primarily along the x-axis, while the implementation of variable compression results in a more consistent profile of reaction rates. The reaction rates are also consistently higher over a larger area of the cell.

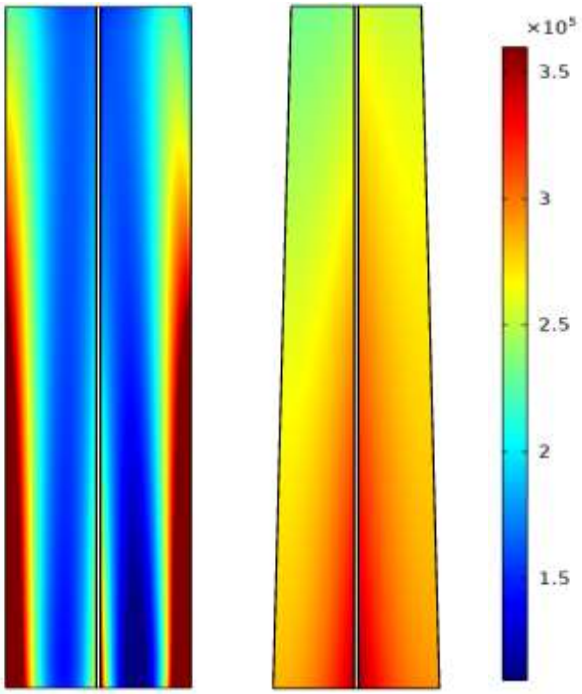

Figure 2. Reaction rate profiles (A/m3) for no compression case (left) and variable compression case (right).

The comparison of mean velocity and pressure drop between both cases is presented in Table 4. By implementing variable compression, higher velocity values can be achieved, resulting in increased convection effects on electrochemistry. As compared to the case without compression, the variable compression case showed a 25.9% increase. However, it was observed that compressing the electrode resulted in a noticeable impact on the pressure drop, as it reduced the permeability, consequently increasing the resistance to fluid movement.

Table 4. Comparison of mean velocity and pressure drop between both cases.

Case	Mean Velocity (m/s)	Pressure Drop (kPa)
No compression	0.0026923	3.577
Variable compression	0.0033903	20.397

4. CONCLUSION

This study presents a flow-through configuration of a vanadium redox flow battery, analyzing the impact of variable compression on fluid dynamics and reaction kinetics compared to no compression. It was set at discharge mode, with 30 ml/min and a state of charge of 15%. The application of variable compression resulted in a 25.9% increase in mean velocity, potentially improving the convection part of reaction kinetics, while also producing more stable reaction rate profiles with evenly distributed values. However, it is important to note that compressing the electrode increased resistance to fluid movement, resulting in a noticeable pressure drop, which should be taken into account.

Acknowledgment

The authors would like to express their gratitude to the government of the Basque Country for their support through research programs ELKARTEK CICe2022. They would also like to extend their appreciation to the Microfluidics Cluster UPV/EHU for the computational support provided.

References

[1] N. Kittner, F. Lill, and D. M. Kammen, 'Energy storage deployment and innovation for the clean energy transition', Nat Energy, vol. 2, no. 9, Art. no. 9, Jul. 2017, doi: 10.1038/nenergy.2017.125.
[2] A. R. Dehghani-Sanij, E. Tharumalingam, M. B. Dusseault, and R. Fraser, 'Study of energy storage systems and environmental challenges of batteries', Renewable and Sustainable Energy Reviews, vol. 104, pp. 192–208, Apr. 2019, doi: 10.1016/j.rser.2019.01.023.
[3] X. Fan et al., 'Battery Technologies for Grid-Level Large-Scale Electrical Energy Storage', Trans. Tianjin Univ., vol. 26, no. 2, pp. 92–103, Apr. 2020, doi: 10.1007/s12209-019-00231-w.
[4] A. G. Olabi, C. Onumaegbu, T. Wilberforce, M. Ramadan, M. A. Abdelkareem, and A. H. Al – Alami, 'Critical review of energy storage systems', Energy, vol. 214, p. 118987, Jan. 2021, doi: 10.1016/j.energy.2020.118987.
[5] I. Aramendia, U. Fernandez-Gamiz, A. Martinez-San-Vicente, E. Zulueta, and J. M. Lopez-Guede, 'Vanadium Redox Flow Batteries: A Review Oriented to Fluid-Dynamic Optimization', Energies, vol. 14, no. 1, p. 176, Dec. 2020, doi: 10.3390/en14010176.
[6] H. Wang, S. A. Pourmousavi, W. L. Soong, X. Zhang, and N. Ertugrul, 'Battery and energy management system for vanadium redox flow battery: A critical review and recommendations', Journal of Energy Storage, vol. 58, p. 106384, Feb. 2023, doi: 10.1016/j.est.2022.106384.
[7] A. Lucas and S. Chondrogiannis, 'Smart grid energy storage controller for frequency regulation and peak shaving, using a vanadium redox flow battery', International Journal of Electrical Power & Energy Systems, vol. 80, pp. 26–36, Sep. 2016, doi: 10.1016/j.ijepes.2016.01.025.
[8] J. H. Vinco, A. E. E. da C. Domingos, D. C. R. Espinosa, J. A. S. Tenório, and M. dos P. G. Baltazar, 'Unfolding the Vanadium Redox Flow Batteries: An indeep perspective on its components and current operation challenges', Journal of Energy Storage, vol. 43, p. 103180, Nov. 2021, doi: 10.1016/j.est.2021.103180.
[9] Q. Wang, Z. G. Qu, Z. Y. Jiang, and W. W. Yang, 'Experimental study on the performance of a vanadium redox flow battery with non-uniformly compressed carbon felt electrode', Applied Energy, vol. 213, pp. 293–305, Mar. 2018, doi: 10.1016/j.apenergy.2018.01.047.
[10] K. Oh, S. Won, and H. Ju, 'Numerical study of the effects of carbon felt electrode compression in all-vanadium redox flow batteries', Electrochimica Acta, vol. 181, pp. 13–23, Nov. 2015, doi: 10.1016/j.electacta.2015.02.212.
[11] S.-K. Park et al., 'The influence of compressed carbon felt electrodes on the performance of a vanadium redox flow battery', Electrochimica Acta, vol. 116, pp. 447–452, Jan. 2014, doi: 10.1016/j.electacta.2013.11.073.
[12] R. Gundlapalli and S. Jayanti, 'Effect of electrode compression and operating parameters on the performance of large vanadium redox flow battery cells', Journal of Power Sources, vol. 427, pp. 231–242, Jul. 2019, doi: 10.1016/j.jpowsour.2019.04.059.
[13] R. Monteiro, J. Leirós, M. Boaventura, and A. Mendes, 'Insights into all-vanadium redox flow battery: A case study on components and operational conditions', Electrochimica Acta, vol. 267, pp. 80–93, Mar. 2018, doi: 10.1016/j.electacta.2018.02.054.

RIGA 2023

NOx emissions modeling for a gas lean burn engine

Javier Del Valle
Guascor-Energy Engines R&D, Vitoria, Spain, javier.del_valle@guascor-energy.com, University of the Basque Country (UPV/EHU), Faculty of Engineering of Vitoria-Gasteiz, Department of Systems Engineering and Automatic Control,Vitoria-Gasteiz, Spain, javier.delvalle@ehu.eus, ORCID: https://orcid.org/0000-0001-8485-7148

Jose Manuel Lopez-Guede
University of the Basque Country (UPV/EHU), Faculty of Engineering of Vitoria-Gasteiz, Department of Systems Engineering and Automatic Control, 01006 Vitoria-Gasteiz, Spain, jm.lopez@ehu.es, ORCID: 0000-0002-5310-1601.

Cite this paper as: *Del Valle, J, Lopez-Guede, J. M. NOx emissions virtual sensor for a gas lean burn engine with active prechamber using a machine learning model. 11. Eur. Conf. Ren. Energy Sys. 18-20 May 2023, Riga, Latvia*

Abstract: In today gas gensets NOx emissions sensors are becoming a key element. NOx sensors have a limited time life of around 5,000 hours or less when some conditions are not met. It is common to find damaged sensors. The purpose of this paper is to analyze real engines, address the creation of a machine learning model and analyze if the obtained model is valid in order to create a good estimation of NOx vs real measurements. This could be useful to detect NOx sensors malfunction or have an estimated NOx measured in gas gensets that do not mount them or when that NOx sensors cannot be active.

Keywords: *NOx virtual sensor, Lean burn, Machine learning, Active prechamber*

Nomenclature	
ECU	Engine Control Unit
NOx	Nitric oxide and nitrogen dioxide gases

1. INTRODUCTION

Today, power generation gas engines (gensets) come with an extensive set of instrumentation sensors. These sensors are connected to the engine control unit (ECU) by means of communication protocols like CANopen, J1939, etc. Most of the sensors used today present a good life endurance and the same sensor can perform properly in the engine during more than twenty thousands of hours easily. Others more advanced instrumentation sensors have a reduced lifetime due to different considerations.

One of the newest sensors that comes with gas lean burn gensets since some years ago is the NOx measurement sensor. A sensor that measures the NOx emissions in the exhaust of the engine allows to monitor or control the suitable air fuel ratio. The price of this sensor is significative, and its life is estimated around 2,500 – 5,000 hours. This means that in an engine that runs 24h/day there is a need for changing the sensor each four months. If the ECU is using it for control, then it means that normally two sensors should be used. The NOx sensor uses ceramic materials that tend to be damaged in the presence of hot water. If the sensor is activated too early while the engine is not hot enough and the dew point is reached in the sensor, then activating (heating) the sensor could cause cracks in the sensor ceramic.

The objective of this paper is to analyze engines running with NOx sensors and create a machine learning model based on common instrumentation already present in the engine. One of the aims of the investigation is to get a model of NOx measurements during engine cranking time. The use of the NOx virtual sensor at those times could

improve the engine response for applications like emergency power generation, where engines should be at full power in less than 30 seconds.

This machine learning model should be compared against the real sensors in the future and some conclusions should be done regarding if the model could be good enough in order to replace one NOx sensor on the engine, or even add a NOx sensor to a digital twin of the engines that are not already mounting those sensors [1]. Using a model in the digital twin could allow to raise deviations or notifications to the customer based on a sensor which is not already in place and to provide extra services to the customers [2].

2. BACKGROUND

A genset, or a generator set, is a device that generates electrical power by converting mechanical energy into electrical energy. Gensets are often used in places where a reliable source of electricity is not available, such as in remote locations or during power outages.

Nitrogen oxides (NOx) emissions from gensets, especially diesel generators but also applicable to other gas fuels like hydrogen gensets, have been a significant concern for the environment due to their negative impact on air quality and human health. NOx emissions have been regulated by various agencies worldwide, such as the US Environmental Protection Agency (EPA), European Union (EU), and the International Maritime Organization (IMO) [4]. To comply with the NOx emission regulations, genset manufacturers have been incorporating NOx sensors in their products. However, conventional NOx sensors are often expensive, require frequent maintenance, and have a limited lifespan.

To overcome these challenges, a NOx virtual sensor could be developed for gensets. The NOx virtual sensor uses mathematical models and engine parameters to estimate NOx emissions. Machine learning has been used in the oil and gas industry in order to improve emissions [3].

How does a NOx Virtual Sensor Work in a Genset?

The NOx virtual sensor in a genset uses a model-based approach to estimate NOx emissions by using the engine's operating parameters. The model is developed based on the engine's physical and chemical characteristics, and it considers factors such as engine speed, load, fuel injection timing and air-fuel ratio. The sensor's output is a calculated value of NOx emissions, which is used to control the engine's combustion process to achieve optimal NOx emissions levels.

Advantages of NOx Virtual Sensor in Genset

The NOx virtual sensor has several advantages over traditional NOx sensors, including but not limited to:

1. Reduced Cost: The NOx virtual sensor is less expensive than traditional NOx sensors, as it does not require any additional hardware.

2. Improved Accuracy: The NOx virtual sensor provides accurate NOx emission estimates, which can be used to optimize the engine's combustion process.

3. Increased Lifespan: The NOx virtual sensor has a longer lifespan than traditional NOx sensors, as it does not require frequent maintenance.

4. Easy Integration: The NOx virtual sensor can be easily integrated into the genset's engine control system, making it easy to install and use.

Applications of NOx Virtual Sensor in Genset

The NOx virtual sensor has found several applications in gensets, including:

1. Emissions Monitoring: The NOx virtual sensor can be used to monitor NOx emissions in real-time, enabling genset operators to comply with NOx emission regulations.
2. Optimal Combustion: The NOx virtual sensor can be used to optimize the engine's combustion process, reducing NOx emissions while maintaining engine performance.
3. Diagnostic Tool: The NOx virtual sensor can be used as a diagnostic tool to detect and identify engine faults, enabling quick and efficient maintenance.

Most of the papers related to modeling NOx sensors are focused on diesel engines [5, 6], automotive engines [7] or even to lean burn engines, but based on systems that have capabilities like ion sensing [8]. In this case the concept is to create the model for an active prechamber gas genset lean burn engine, but trying to use standard instrumentation sensors already present in the engine.

For model creation different approaches and methods will be considered during the study.

3. SETUP TESTBENCH

On a Guascor-Energy 2Mw Gas Engine testbench equipped with different sensors and among them, also with NOx sensors data is going to be recorded at different conditions (power ramp, cranking, etc.). This data is going to be the basis for model creation. The new Guascor-energy 2MW engine is the engine with the highest efficiency on the market (both in the 50Hz market with the G-86EM and in the 60Hz market with the G-100EM engine), with the capacity to operate in a stable and continuous manner with very low emissions, maximum reliability and the lowest maintenance costs. Figure 1 and Figure 2 shown the real testbench and NOx sensor installation respectively.

Figure 1. © Guascor Energy – G-86EM Gas Engine

Figure 2. NOx Sensor install detail

4. METHODOLOGY

For better model creation NOx coming from different engines with active prechamber and lean burn with different gas fuels are going to be recorded. Here the pipeline is going to be described:

1. Define the problem: we want to develop a NOx machine learning model to optimize the combustion efficiency of an internal combustion engine.

2. Gather data: We need to collect data on the engine's performance and real NOx measurements to train our machine learning model. This data can be obtained from sensors installed on the engine.

3. Define inputs and outputs: The inputs to our machine learning model will be sensors or variables already present in the engine. The output will be the combustion NOx estimation.

4. Choose a machine learning paradigm: We can use a regression algorithm such as linear regression, decision tree regression or random forest regression to train our model.

5. Preprocess data: We need to preprocess the data by removing any missing or inconsistent data, scaling the features, and splitting the data into training and testing sets.

6. Train the model: We can train the model on the training set using one specific algorithm.

7. Evaluate the model: We can evaluate the model's performance on the testing set using metrics such as mean squared error or R-squared.

8. Optimize the model: We can further optimize the model by tuning the hyperparameters of the algorithm.

9. Deploy the model: Finally, we can deploy the model to the NOx virtual sensor

5. GATHERING DATA AND INPUTS AND OUTPUTS DEFINITION

Real data is available due to remote monitoring system already in use in Guascor-Energy (Spain) as show below. In this case a G-86EM 2Mw engine is used and several tags has been preselected as inputs for the model and can be seen in Figure 3. The rationale for being preselected is explained below:

- Lube Oil Temperature: It is the temperature of the oil. When the engine starts if it is cold the emissions could be affected.
- Main Circuit Temperature: It is the temperature of the coolant in the main circuit. When the engine starts if it is cold the emissions could be affected.
- Air Temperature: Ambient Air temperature that enters the engine.
- MAT (Manifold Air Temperature): It is the temperature of the mixture in the manifold. The temperature of this mixture affects the fuel density and could affect the emissions.
- Engine Speed: The speed of the engine in rpms.
- dP Prechamber: Delta pressure between the Manifold Air pressure and the prechamber gas pressure. This delta pressure affects the gas entering into the prechamber and affects the Air fuel ratio having a impact in the engine emissions.
- MAP1 (Manifold Air Pressure): It is the pressure in the manifold. It relates to the engine power.
- PTP1 (Prethrottle Air Pressure): It is the pressure that controls a bypass valve to avoid surge. Probably it is not going to affect the emissions.
- Global Timing: The engine ignition timing.
- Left Exhaust Temp After Turbo: Exhaust temperature in the left turbocharger. This exhaust temperature it is related to the engine emissions somehow.
- Right Exhaust Temp After Turbo: Exhaust temperature in the right turbocharger. This exhaust temperature it is related to the engine emissions somehow.
- NOx Sensor: The real NOx value coming from the sensor to be modeled and virtualized.

Figure 3. Real Gas Engine Data

One of the targets of the model will be to estimate a NOx measurement at cranking times when NOx sensors can not be active due to avoid damaging the sensor when their ceramic tip could we wet and the preheat is activated. The activation of the sensor when there is water in the tip can crack the ceramic part of the sensor.

In order to get the starting/cranking transient, data sensors are going to be active during the full start sequence although it could be damaged or reduced its lifetime.

6. FUTURE WORK

Nowadays the G-86EM engine has been instrumented with the suitable sensors. Further data is going to be recorded during cranking time in order to have a model based on machine learning that could estimate NOx sensor during cranking time for engine applications like emergency, etc. where the NOx sensors cannot be active in less than one minute due to lifetime limitation.

References

[1] Madni, A., Madni, C., Lucero, S. Leveraging Digital Twin Technology in Model-Based Systems Engineering. 2018.
[2] Fuller, A., Zong, F., Day, C., Barlow, C. Digital Twin: Enabling Technologies, Challenges and Open Research. 2020.
[3]. Machine Learning and Data Science in the oil and gas industry.
[4] Environmental Protection Agency. (2020). Control of Emissions of Air Pollution from Nonroad Diesel Engines and Fuel. Retrieved from https://www.epa.gov/regulations-emissions-vehicles-and-engines/control-emissions-air-pollution-nonroad-diesel-engines
[5] Wang, J., Huang, Z., Zou, X., Wu, Y., & Yang, J. (2016). A virtual NOx sensor for diesel engines based on a dynamic model and an optimized calibration method. Applied Energy, 175, 356.
[6]. K. I. Olowojolu, O. Folorunso, and J. N. Ayeni. Predicting NOx emissions from diesel engines using machine learning algorithms. Applied Thermal Engineering, vol. 116, pp. 328-337, 2017.
[7]. Y. K. Kim, H. C. Lee, and K. H. Kim. Development of a machine learning-based NOx sensor for automotive applications. Sensors and Actuators B: Chemical, vol. 215, pp. 571-577, 2015.
[8]. H. Li, Y. Li, and W. Li. Development of a machine learning-based NOx sensor for lean-burn natural gas engines. Fuel, vol. 279, pp. 118669-1-9, 2020.

RIGA 2023

Power System Equipment Mentoring using Web-Based Controller

Mustafa J.M Alhamdi
Automation and Robotics, Control Engineering Department, University of the Basque Country (UPV/EHU), Spain, Mustafa.AlHamedy@gmail.com , ORCID: 0000-0001-5723-6426

José Manuel Lopez-Guede
Automation and Robotics, Control Engineering Department, University of the Basque Country (UPV/EHU), Spain, jm.lopez@ehu.es, ORCID: 0000-0002-5310-1601

Javad Rahebi
Department of Software Engineering, Istanbul Ayvansaray University, Istanbul, Türkiye, javadrahebi@gmail.com, ORCID: 0000-0001-9875-4860

Ekaitz Zulueta
Automation and Robotics, Control Engineering Department, University of the Basque Country (UPV/EHU), Spain, ekaitz.zulueta@ehu.es, ORCID: 0000-0001-6062-9343

Unai Fernandez-Gamiz
Department of Nuclear and Fluid Dynamics University of the Basque Country (UPV/EHU), Spain, unai.fernandez@ehu.eus, ORCID: 0000-0001-9194-963X

Josean Ramon-Hernanz
Department of Electric Engineering, University of the Basque Country, (UPV/EHU), Spain,josean.ramos@ehu.es, ORCID: 0000-0001-9706-4016

Cite this paper as: *Alhamdi, M, Lopez, J, et al.. Power System Equipment Mentoring Using Web-Based Controller. 10. Eur. Conf. Ren. European Conference on Renewable Energy Systems. 18-20 May 2023, Riga, Latvia*

Abstract: Power system is playing vital role in man-kind life, it is integral part of the life by whole and totally depended by all industries, organizations and end users (residential). However, residential premises consist of essential components and devices that participate in power generation, transformation and distribution. Transformers are vital member in power plants complex which takes responsibilities to transfer the high potential power into low potential or vise-versa. Transformers are attributed by their high cost so that it has to be maintained properly. In this paper, we proposed a smart power monitoring system with microcontroller infrastructure. Webserver based PIC 18F microcontroller is used to implement this system. The outcomes of study emphasis the reliability and location independent service. System can update the maintenance engineer with real-time sensing information about the system in form of web information that is being shared through a computer network.

Keywords: *PIC, ADC, DAC, WLAN, Monitoring, Sensors.*

1. INTRODUCTION

A collection of technology has emerged in recent years that has become a barrier to human daily activity. Information systems have piqued the interest of large technological businesses, which now dominate the industry [1]. Information systems have been ingrained in practically everyone's life, owing to the various benefits they give, such as time and cost savings, as well as their status as a life-facilitating technology that people can't live without. Big engineering industries, on the other hand, aren't contributing to technological advancement. Transformers are used to transport energy from one level to the next in most power networks [2]. Power is transferred from a high to a low level in step-down conversion (transformation), whereas power is transferred from a low to a higher level in

step-up conversion (transformation). Protective systems, which were developed to support power systems, can be distinguished from more modern systems by the presence of protective switches and relays. The area of the power system that needs to be protected is where these devices are located [4]. One aspect of the new technology is the creation of secure, environmentally friendly protection systems that can be controlled remotely and enable autonomous protection of any component without the need for human input. The new security system comes with superior remote monitoring technology that can keep track of any electrical system in real time.

In this paper, the power equipment mentoring system is being designed using web based model through micro controller. The simulation has taken place in Porteus using a 18F4620 microcontroller, this device is entitled for its capability to be converted into web-server where computer network can be formed and this device can be part of it. This device is programmed and executed using micro-C language.

2. SYSTEM OVERVIEW

The current circuit must be built in a virtual form under specific power system parameters. According to the simulator, the current sensor can handle 30 A of current. The output of the power transformer must be decreased in order to comply with the tolerance of the current sensor. Three current circuit gates, each rated at 10 A, were designed to handle 30 A in the current circuit via hole. When the current reaches 30 A, there is an overcurrent. The underlying scenario is depicted in Figure 1.

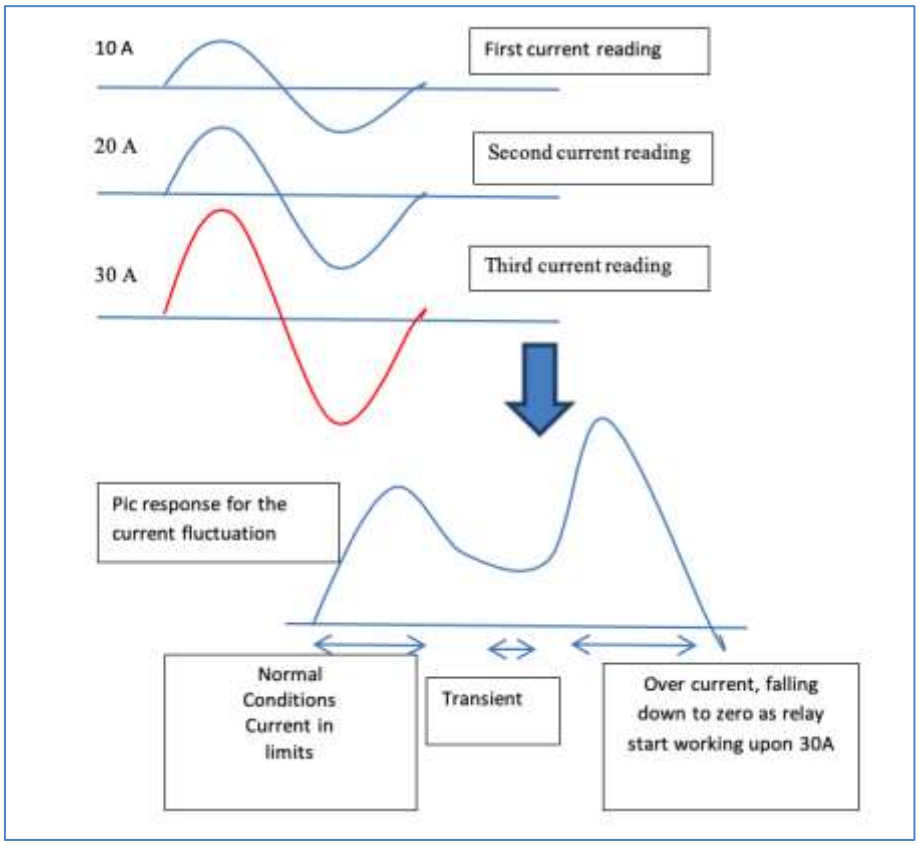

Figure 1. Response of the model to current fluctuation.

3. MICROCONTROLLER CHIP

The prototype of the control and monitoring unit was previously shown in this chapter. However, it does involve the presence of a processing unit capable of handling all sensor outputs and sending them over the network to the remote terminal unit. Pic type microcontrollers are employed to meet these needs [5].

Because of its attractive features, including low-watt technology, an effective fly mode, a variety of working modes, and an on-demand idle mode, the "18F4620" microcontroller family was chosen. It is possible to utilize the gadget,

with model number 18f4620, as a webserver to send data over the internet. The chip contains forty ports on both sides, according to the gadget. Device accelerators with the following features are useful for monitoring and controlling systems.

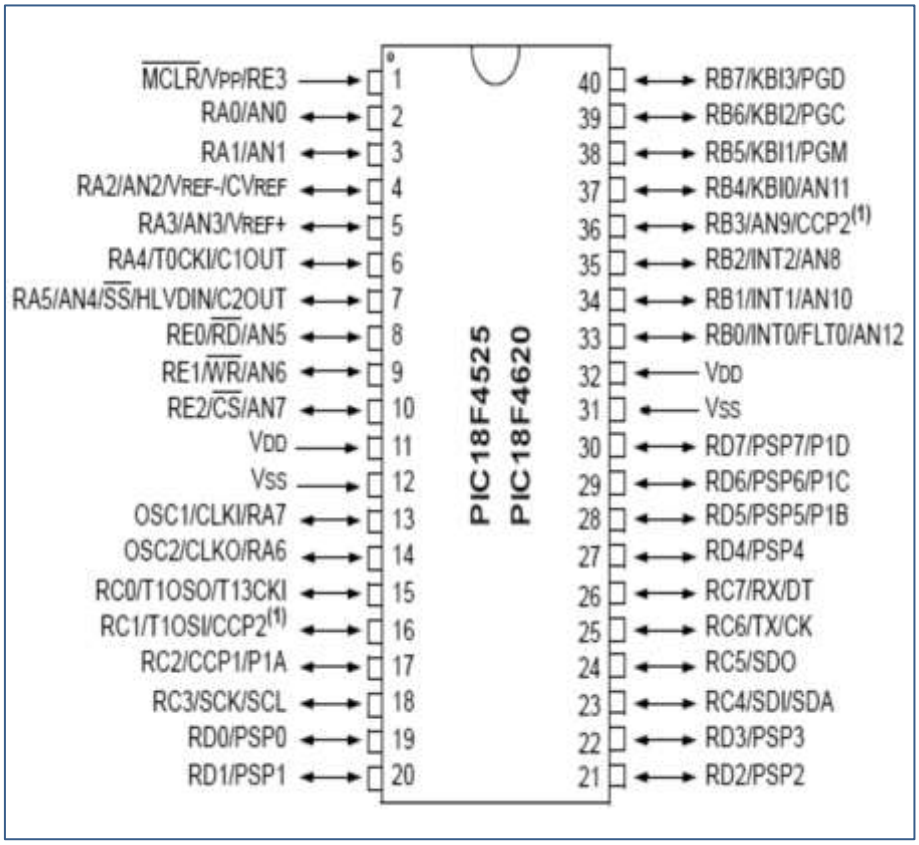

Figure 2. The input and output ports are shown in the 18F4620 Pin-out.

4. THERMAL INPUT

Temperature fluctuations in transformer windings must be observed because when high amounts of current are provided, the temperature of the windings rapidly rises. The LM 35 is a popular integrated circuit for detecting temperature changes in degrees Celsius without the need for external calibration. In both indoor and outdoor settings, it has a temperature detection accuracy of (88%) 0.25 and (99%) 0.75. In an outdoor scenario, the stated sensor accuracy must stay within an acceptable error range, which is normally between -55 and +150 degrees Celsius [6]. The temperature was converted into DC stable scaled voltage in this sensor's mode of operation, which ranged from zero to five volts. After receiving a Vcc voltage of 5 volts DC, the chip begins to function.

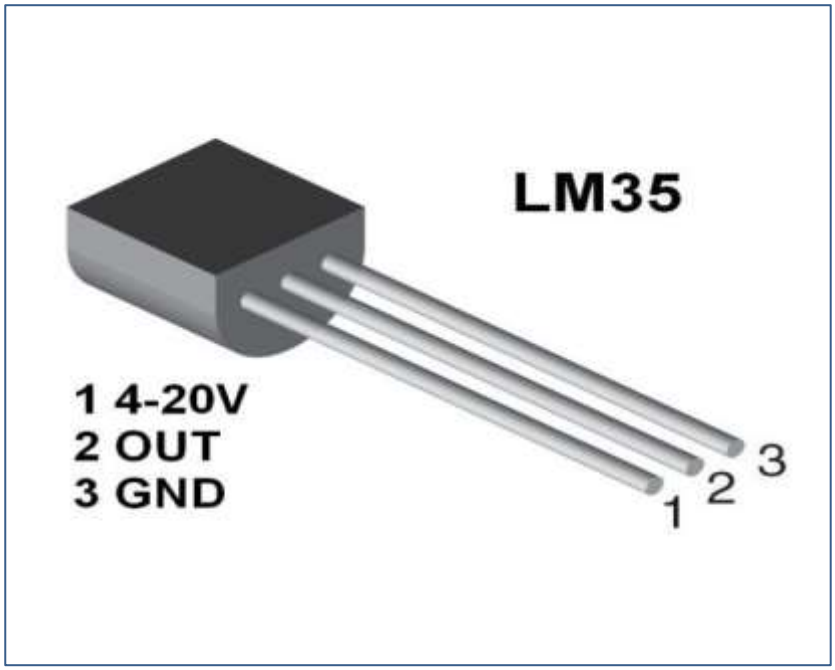

Figure 3. LM 35, thermal sensing unit that used in this study.

5. CURRENT INPUT

Current sensors can be used to monitor the current flowing through power connections due to potential variations. The current sensor utilised in this experiment is the ACS712. It was created by "Allegro" and is now on the market. This sensor is ideal for communications, current control in electric motors, and a variety of other industrial applications. The gadget distinguishes out for its simplicity when it comes to detecting DC or AC current [7].

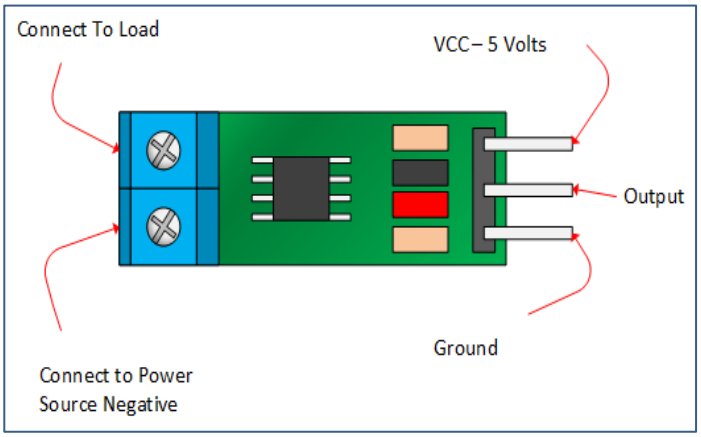

Figure 4. ACS712 chip with pinout of he so called current sensor.

6. MONITORING PARADIGM

A monitoring system, in essence, requires the observer to collect data on the monitored elements. The data from the sensors may be seen on-site using meters or displays, or it can be transmitted to the observer over the internet. The infrastructure for displaying sensor data on remote terminal devices like laptops and tablets is created by the remote monitoring system, which is utilized in power system monitoring and other industrial applications. You'll have greater authority and freedom on the job as a result of this. In this project, the microcontroller will function as a mini webserver, delivering web services such as data transfer through a computer network. This network is connected to a remote terminal device, and the information may be seen at any time via a web browser by the observer.

The HTML webpage is designed to display all sensor data and alarm signals to the viewer. Figure 5 shows the web page that was visible on the remote terminal device.

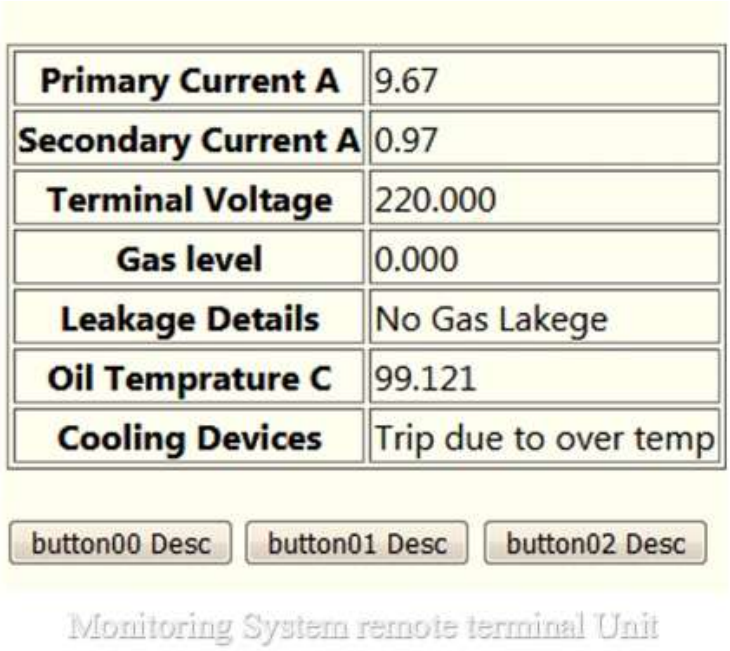

Figure 5. A webpage that displays the monitoring station's parameters

7. CONCLUSION

Microcontroller technique enables total web-based control over a power transformer in order to protect the power system equipments. This study looked at both the expense of a GSM-based monitoring system and the issue of coverage. If the network looks like a wireless router, it provides flexible monitoring and mobility (monitor and control the system). A microcontroller with web service capability keeps track of the terminal voltage, current, temperature, and gas leakage. Specific features, such as current and temperature, are extensively examined in this study since they are more likely to vary with load quantity and season (peak load, winter, and summer loads).

References

[1] W. Jiang and B. Fahimi, “Active current sharing and source manage-ment in hybrid power,” IEEE Trans. Ind. Electron.,vol.57,no.2,pp.752–761, Feb. 2010.

[2] S. M. J. ,. S. B. J. Ashok J. Naiknaware, "Protection of power transformer by using PIC microcontroller Fault Detection System," International Journal of Current Trends in Engineering & Research (IJCTER) e-ISSN 2455–1392, vol. 2, no. 4, 2016.

[3] J. S. A. D. Arpit Rana, "Simulation of Power Transformer Protection Using Microcontroller Relay," International Journal of Scientific Engineering and Technology, vol. 4, no. 6, 2017.

[4] V. K. v. K. Y. Mangesh .L. Kawale, "DESIGN AND IMPLEMENTATION OF LOW COST DISTRIBUTION TRANSFORMER MONITORING SYSTEM FOR REMOTE ELECTRIC POWER GRID," International Journal of Industrial Electronics and Electrical Engineering, ISSN: 2347-6982, vol. 1, no. 2016, 4.

[5] M. T. S. S. S. Y. M. V. S. Sunen Soni, "Home Automation System using Arduino," IOSR Journal of Computer Engineering (IOSR-JCE) e-ISSN: 2278-0661, vol. 3, no. 4, 2018.

[6] d. K. n. H. a. M. a. K. R.V. Patil, "Transformer Health Monitoring And Control Through Arduino," International Journal Of Electrical, Electronics And Data Communication, vol. 5, no. 1.

[7] M. L. X. P. P. K. M. Sripan, "Research and Thinking of Smart Home Technology," International Conference on Systems and Electronic Engineering (ICSEE'2012), 2012.

RIGA 2023

The Effect of Demagnetization Faults in Permanent-Magnet Synchronous Wind Generators

Adem Dalcalı
Department of Electrical and Electronic Engineering, Bandırma Onyedi Eylül University, Bandırma, Balıkesir, Türkiye, adalcali@bandirma.edu.tr, ORCID: 0000-0002-9940-0471

Erol Kurt
Department of Electrical and Electronic Engineering, Gazi University, Ankara, Türkiye, ekurt@gazi.edu.tr, ORCID: 0000-0002-3615-6926

Cite this paper as: *Dalcalı, A, Kurt, E. The effect of demagnetization faults in permanent-magnet synchronous wind generators. 10. Eur. Conf. Ren. Energy Sys. 7-9 May 2022, Istanbul, Türkiye*

Abstract: To prevent fossil resources from being depleted and protect the natural balance, renewable resources come to the forefront as an alternative to fossil resources. Wind energy resources, among the renewable energy resources, are important in terms of ensuring the reliability of energy and the use of own resources. Generators are the most important components of the wind energy system. Permanent magnet synchronous generators (PMSGs) are preferred in wind turbines since they have high efficiency and volume/torque density. In this study, the performance of PMSG when a magnet was demagnetized at different rates (33%, 50%, and 100%) was obtained by Finite Element Analysis (FEA) at rated conditions. The torque performances of the generator at rated load were determined, and the flux density distribution was revealed. The rated torque decreased when the demagnetization rate of the magnet increased.

Keywords: *permanent magnet synchronous generator, partial demagnetization, finite element analysis, wind energy*

1. INTRODUCTION

Ensuring the security of electrical energy supply is of critical importance. The destruction caused by fossil fuels in nature and the decrease in known reserves turn this situation into an even more difficult problem. Furthermore, increasing population and energy demand adversely affect the security of supply. Ensuring the security of energy supply is possible by diversifying resources. Renewable resources may be an important alternative both to meet the increasing energy demand and reduce the damage to nature in energy production. Renewable energy is known as the energy that renews itself over time. Renewable energy is a local solution and is an environmentally friendly and fuel-free energy. With the use of renewable resources, it is possible to reduce emissions caused by fossil fuels and ensure the effective use of countries' own resources. Solar, wind, hydroelectric, biomass, and geothermal resources can be indicated as the main renewable energy sources [1, 2].

Electricity generation from wind energy can be carried out on a wide power scale. Generators are among the most important components of wind turbines. Generators are used in many different structures in electricity generation from wind energy. Permanent magnet synchronous generators (PMSGs) are widely used in parallel with the developing material technology [3]. The rotor magnetic field of PMSGs is formed by permanent magnets. Permanent magnets can be grouped as Alnico, ceramic (or ferrite), and rare-earth magnets. Advancements in materials and production technologies have increased the use of rare-earth magnets. They are especially preferred in applications where high-power density is required [4, 5]. Operating environments and continuous long operating periods can cause various faults in machines. These faults can be classified as magnetic, mechanical, and electrical faults. Brush-collector assembly fault, short-circuit ring fault, rotor bar fault, and magnet breakage fault may occur in the rotor part, depending on the type of machine [6]. Faults that may occur will affect the machine’s performance and reliability.

In the study, analyses of a 14-pole internal rotor, surface-mounted permanent magnet synchronous generator with a rated power of 2.5 kW designed for wind turbines were conducted in the partial demagnetization status. Induced torque and voltage waveforms were obtained by demagnetizing a magnet selected in the rotor at different rates.

2. DESIGNED PMSG

Generators are among the most important components of wind turbine systems. Many generator models are used in different structures in wind turbines. Factors such as the presence of a gearbox, economic constraints, location selection, and power level affect the generator selection. Since direct-current generators have a brush-collector assembly, there is a disadvantage of difficulty in maintenance and frequent maintenance. In asynchronous generators, this disadvantageous situation is not in question. However, their low torque density and relatively low efficiency are their negative aspects, especially when compared to machines with magnets. Furthermore, the reactive power requirement of asynchronous generators and the need for a capacitor bank for this are important requirements. In synchronous generators, salient pole synchronous generators can be preferred especially in high pole applications, while permanent magnet synchronous generators can be preferred for high efficiency and power density requirements [7, 8]. Figure 1 shows the detailed structure of turbine systems.

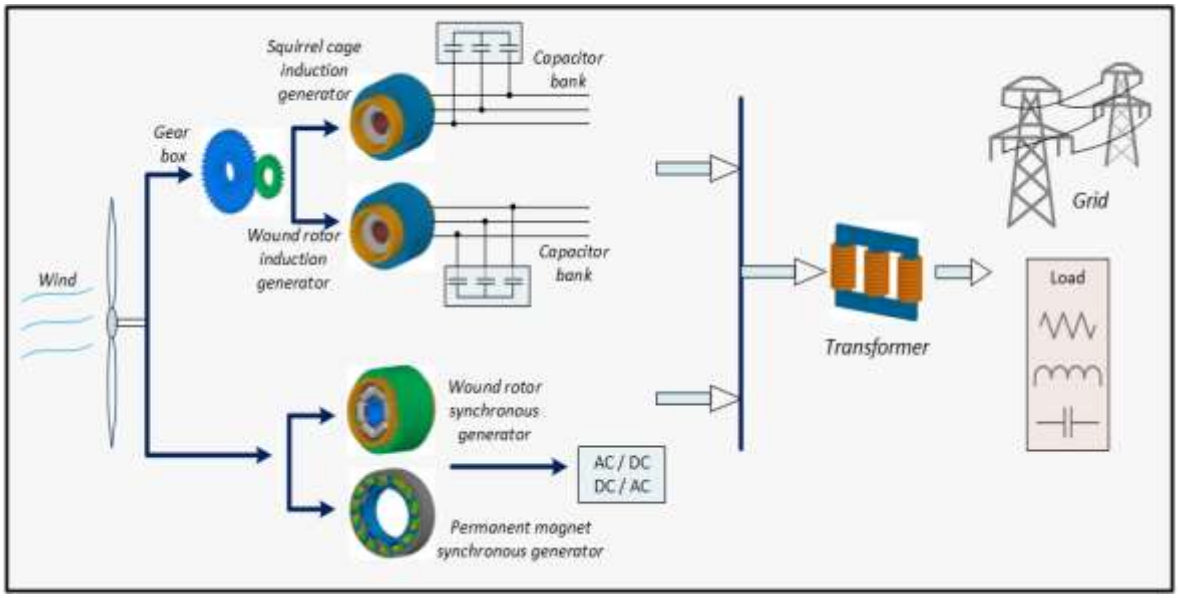

Figure 1. Generator systems used in wind turbines.

PMSGs have the capacity to produce at high efficiency, high power density, and low wind speeds without the need for a gearbox [9]. Table 1 contains the specifications of the generator subject to the study.

Table 1. Designed generator parameters

Parameter	Value	Parameter	Value
Stator / Rotor OD (mm)	280 / 198.4	Skew	0
Stator / Rotor Inner Diameter (mm)	202 / 164	Embrace	0.75
Axial Length (mm)	54	Offset (mm)	0
Magnet Thickness (mm)	5.4	Stator / Rotor Material	M470
Number of Poles / slots	14 / 84	Magnet Material	N35

Figure 2 shows the 3D model and mesh structure of the designed generator.

Figure 2. PMSG model with mesh structure.

3. DEMAGNETIZATION FAULT

Permanent magnets provide the magnetic energy that they store to the circuit continuously. Ideally, permanent magnets have a high demagnetizing force and permanent magnetism. Furthermore, permanent magnets are rigid magnetic materials with large hysteresis loops. Many different magnet materials are used in practice. Alnico, samarium-cobalt, neodymium-iron-boron, and ferrite alloys are currently commercially used [10]. Permanent magnet machines are frequently preferred in industrial applications due to their high efficiency, high power/weight ratio, and high flux density advantages [11]. For a comparison of magnets, BHmax, the product of permanent magnetism and coercive force, is often used. The magnetic field provided by the magnet becomes stronger with the increase in this value. Table 2 contains the magnetic and thermal properties of some commercially used magnets [10,12, 13].

Table 2. Magnetic properties of magnets

Material	B_r (T)	H_c (kA/m)	BH_{max} (kJ/m^3)	Maximum operating temperature (C°)	Curie temperature (C°)
Ferrit	0.4	240	27-35	300	450
Alnico	1.1	130	75-80	500	830
SmCo	0.97	750	130-190	250	720
NdFeB	1.20	870	200-290	140	310

In addition to the materials in the table, the process of producing different components and magnets and improving their performance continues with the help of developing magnet production technology. As is known, losses emerge in electric machinery during operation, and these losses occur in the form of heat. As stated in Table 2, there are certain thermal limits for the operation of magnets. This heat adversely affects the performance of permanent magnets. Additionally, magnets are very hard and brittle. Considering the operating conditions and these disadvantageous conditions of magnets, demagnetization may occur in magnets. Demagnetization faults that occur in permanent magnet machines take an important place in these machines. Demagnetization can occur in all or part of the magnet [14]. Demagnetization faults can be determined by many different methods [15]. They can be determined directly by a Hall sensor [16] or by examining signals such as output torque and current [17, 18].

4. FEM ANALYSIS of PMSG

In order for generators to provide the desired performance, mechanical, thermal, and material problems need to be evaluated together. Under the determined constraints, many different investigations are needed to reach a design with the desired cost and efficiency values. All these designs and analyses involve time-consuming processes. Mathematically based methods are used to solve such problems. Among these methods, the Finite Element Method (FEM) is used in a wide range of applications, including electric machinery [19], the healthcare sector [20], and the automotive industry [21]. FEM is used in the solution of quantities that can be expressed by partial differential equations in a certain region. The determined region is divided into a finite number of small regions. The contributions of the elements surrounding the region are chained together. The desired sizes are obtained by solving this chain equation set. By applying FEM to the generator, the performance parameters of the generator, such as flux distribution, losses, efficiency, and induced voltage waveform, can be obtained [22]. In the study, different

rates of breakage of the determined magnet are considered as magnet fault. Figure 3 displays the structures created. In the first model, there is no fault in the magnet (Figure 3a). In the model in Figure 3b, 1/3 of the magnet is broken, while 1/2 is broken in the structure in Figure 3c. In the structure in Figure 3d, the magnet was completely removed since it was assumed that the magnet was completely broken.

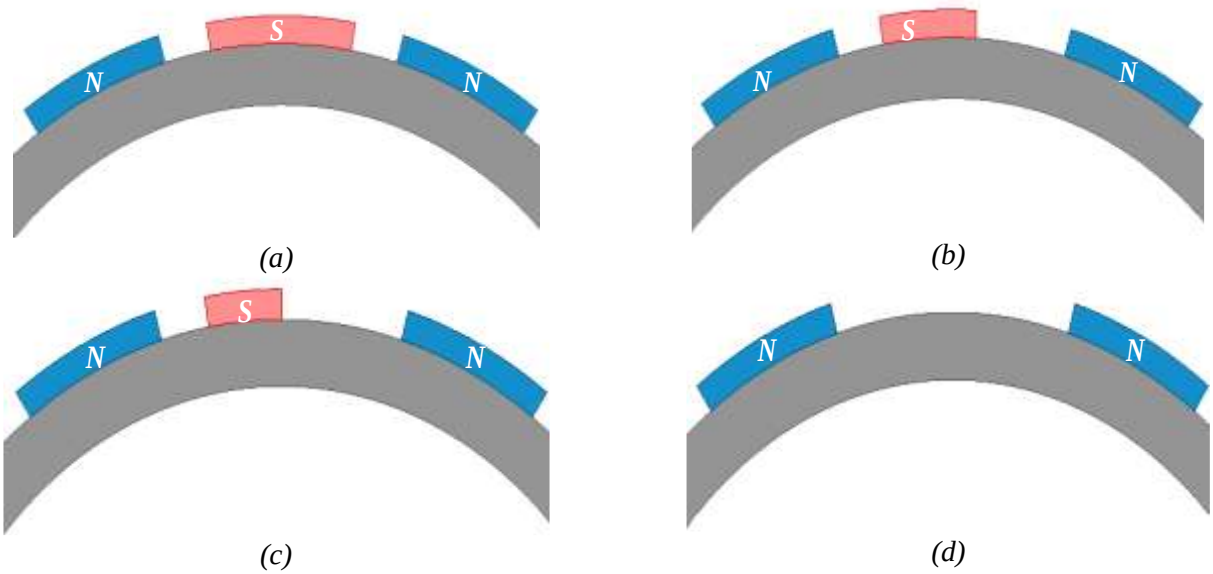

Figure 3. Magnet structures a) healthy model, b) 1/3 broken structure, c) 1/2 broken structure, and d) all broken.

Magnetic flux densities were acquired by applying FEA to these four different structures created. In Figure 4, the magnetic flux density distributions and the state of the magnetic flux lines are given at rated load in the cross-sectional area.

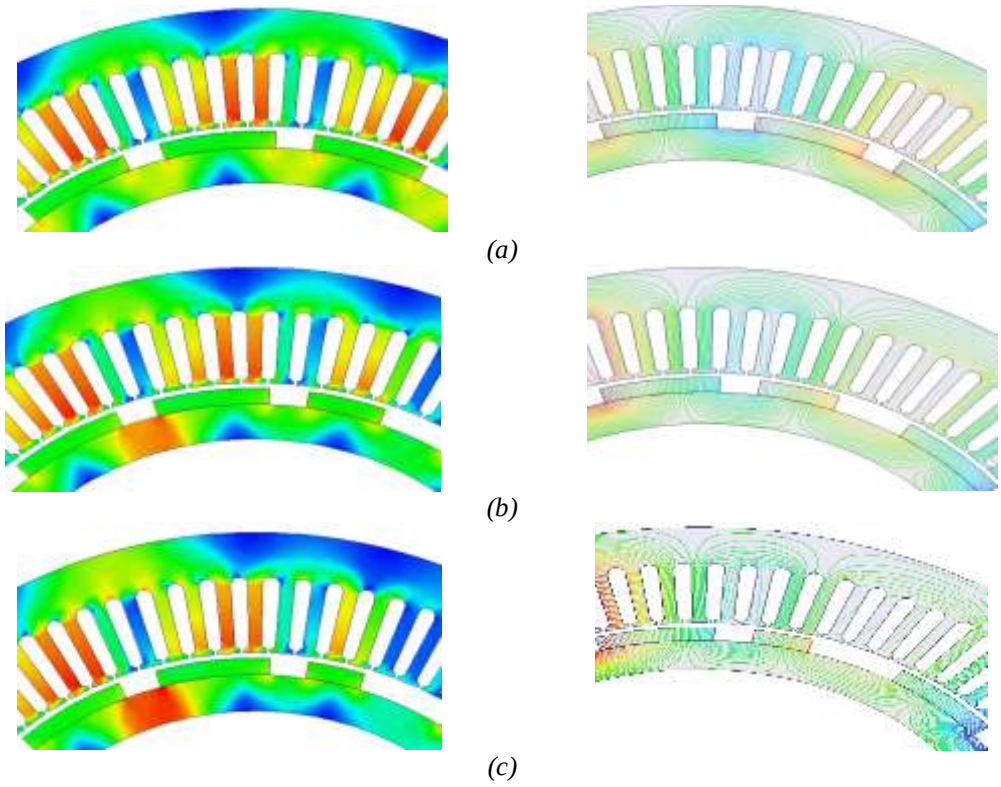

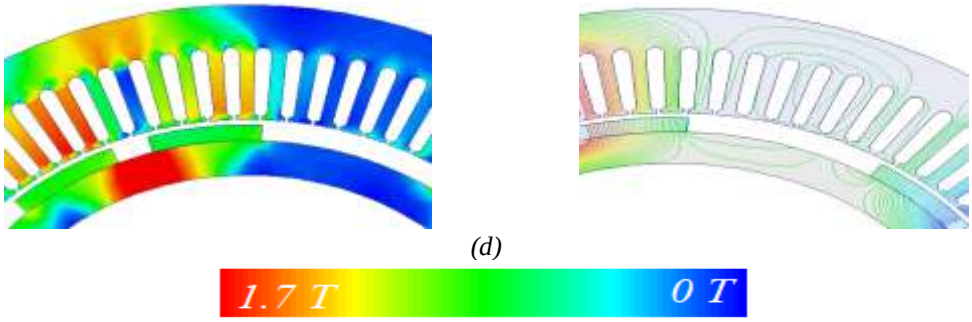

Figure 4. Magnetic flux density distribution a) healthy model, b) 1/3 broken structure, c) 1/2 broken structure, and d) all broken.

Considering the magnetic flux densities and flux paths, as expected, the fluxes in the stator teeth decreased in the regions where the magnet was broken. Since there was no flux source in the regions where the magnet was broken and reluctance increased, the flux was directed toward the other parts, and an operation close to partial saturation was observed. The torque values of the generator were obtained at rated load and are given in Table 3.

Table 3. Rated torque of design

Model	Torque (Nm)
Healthy	63.4167
1/3 demagnetization	59.7818
1/2 demagnetization	57.9554
1 pole demagnetization	53.2662

In permanent magnet machines, torque is formed by the interaction of the stator windings and magnets in the rotor. The magnet area and material affect the magnitude of this torque. When the amount of magnet used decreases, the torque value also decreases [15]. While the torque obtained in the healthy state was 62.5841 Nm, it was obtained as 53.2662 Nm when one magnet was completely demagnetized. The average torque decreased as the amount of breakage of the magnet increased. There is a 14.88% torque variation between the demagnetized state of a complete magnet and the healthy state. The average torque decreased as the magnetic flux weakened and the distance between the magnets increased. Demagnetization fault also disrupts the distribution of the air gap magnetic flux density. The air gap flux waveform obtained on the contour drawn in the air gap is given in Figure 5. Figure 5 clearly shows the healthy state of a magnet and its effect in the demagnetized state at different rates. The width of the flux waveform of the healthy magnet is equal at all poles in the contour covering the three poles. There is a narrower flux waveform in the structure with 33% breakage and an even narrower flux waveform in the structure with 50% breakage. As expected, the incomplete magnet also has low flux, supporting Figure 4.

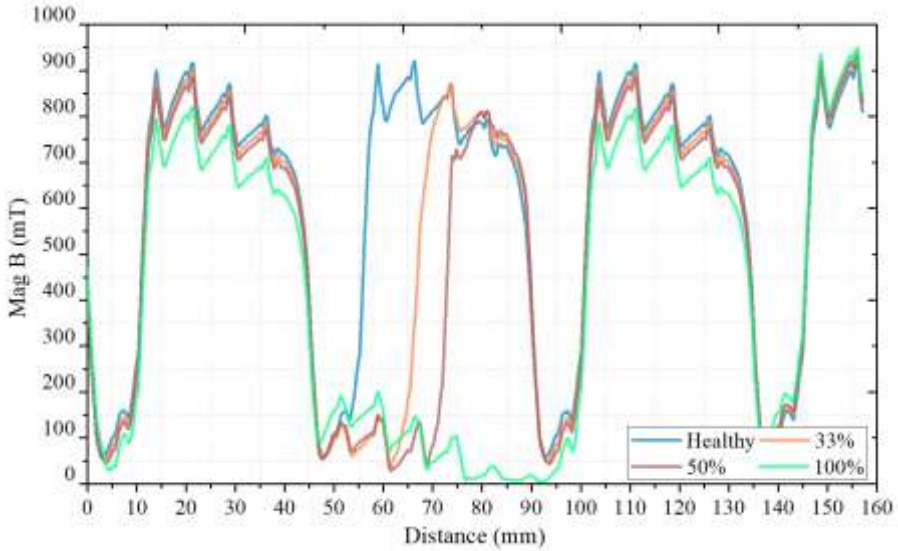

Figure 5. Air gap magnetic flux density waveform.

5. CONCLUSION

Different types of generators are used in wind turbines. Among these, permanent magnet generators offer the advantage of high torque density and high efficiency. In permanent magnet machines, the material and geometry of the magnet impact the machine's performance. The study investigated the performances of a magnet belonging to one pole of the PMSG for different demagnetization rates. Flux waveforms were acquired on the contour drawn in the air gap. When the amount of demagnetization increased, it was observed that the flux became narrower both on the contour and the stator teeth. When the demagnetization amount of the magnet increased, the rated torque value decreased.

References

[1] Olabi AG, Abdelkareem MA. Renewable energy and climate change. Renewable and Sustainable Energy Reviews, 2022, 158, 112111.
[2] Jiang Q, Zeng X, Li B, Wang S, Liu T, Chen Z, Wang T, Zhang M. Time-Sharing frequency coordinated control strategy for PMSG-Based wind turbine. IEEE Journal on Emerging and Selected Topics in Circuits and Systems, 2022, 12(1), 268-278.
[3] Huang S, Wang J, Huang C, Zhou L, Xiong L, Liu J, Li P. A fixed-time fractional-order sliding mode control strategy for power quality enhancement of PMSG wind turbine. International Journal of Electrical Power & Energy Systems, 2022, 134, 107354.
[4] Verma P, Misra H, Rajpurohit BS. Design and Analysis of Interior PMSM for Low Power EV Applications in Hilly Terrain. In: IEEE 10th Power India International Conference, 25-27 November 2022.
[5] Ruiz-Ponce G, Arjona MA, Hernandez C, Escarela-Perez R. A Review of Magnetic Gear Technologies Used in Mechanical Power Transmission. Energies, 2023, 16(4), 1721.
[6] Nath AG, Udmale SS, Singh SK. Role of artificial intelligence in rotor fault diagnosis: A comprehensive review. Artificial Intelligence Review, 2021, 54, 2609-2668.
[7] Tawfiq KB, Mansour AS, Ramadan HS, Becherif M, El-Kholy EE. Wind energy conversion system topologies and converters: Comparative review. Energy Procedia, 2019, 162, 38-47.
[8] Polinder H, Van der Pijl FF, De Vilder GJ, Tavner PJ. Comparison of direct-drive and geared generator concepts for wind turbines. IEEE Transactions on Energy Conversion, 2006, 21(3), 725-733.
[9] Metwally Mahmoud M, Salama HS, Aly MM, Abdel-Rahim AMM. Design and implementation of FLC system for fault ride-through capability enhancement in PMSG-wind systems. Wind Engineering, 2021, 45(5), 1361-1373.
[10] Strnat KJ. Modern permanent magnets for applications in electro-technology. In: Proceedings of the IEEE, 1990, 78(6), 923-946.
[11] Jeong CL, Hur J. Optimization design of PMSM with hybrid-type permanent magnet considering irreversible demagnetization. IEEE Transactions on Magnetics, 2017, 53(11), 1-4.
[12] Ma BM, Herchenroeder JW, Smith B, Suda M, Brown DN, Chen Z. Recent development in bonded NdFeB magnets. Journal of Magnetism and Magnetic Materials, 2002, 239(1-3), 418-423.
[13] Dalcalı A, Ocak C. Effect of Different Magnet Materials on The Performance of Surface Mounted Direct Drive PMSM. Journal of Awareness, 2018, 3, 217-224.
[14] Moosavi SS, Djerdir A, Amirat YA, Khaburi DA. Demagnetization fault diagnosis in permanent magnet synchronous motors: A review of the state-of-the-art. Journal of Magnetism and Magnetic Materials, 2015, 391, 203-212.
[15] Faiz J, Mazaheri-Tehrani E. Demagnetization modeling and fault diagnosing techniques in permanent magnet machines under stationary and nonstationary conditions: An overview. IEEE Transactions on Industry Applications, 2017, 53(3), 2772-2785.
[16] Park Y, Yang C, Lee SB, Lee DM, Fernandez D, Reigosa D, Briz F. Online detection and classification of rotor and load defects in PMSMs based on hall sensor measurements. IEEE Transactions on Industry Applications, 2019, 55(4), 3803-3812.
[17] Ebrahimi BM, Faiz J. Demagnetization fault diagnosis in surface mounted permanent magnet synchronous motors. IEEE Transactions on Magnetics, 2013, 49(3), 1185-1192.
[18] Espinosa AG, Rosero JA, Cusido J, Romeral L, Ortega JA. Fault detection by means of Hilbert–Huang transform of the stator current in a PMSM with demagnetization. IEEE Transactions on Energy Conversion, 2010, 25(2), 312-318.
[19] Qi J, Zhu Z, Yan L, Jewell GW, Gan C, Ren Y, Brockway S, Hilton, C. Influence of Armature Reaction on Electromagnetic Performance and Pole Shaping Effect in Consequent Pole Pm Machines. Energies, 2023, 16(4), 1982.
[20] Gongal D, Thakur S, Panse A, Shankarrao P, Stark JA, Hetling JR, Ozgen B, Foster CD. Thermal finite element analysis of localized hypothermia treatment of the human eye. Medical Engineering & Physics, 2023, 111, 103928.
[21] Moon J, Chang H, Lee J, Kim CW. Prediction of Internal Circuit and Mechanical-Electrical-Thermal Response of Lithium-Ion Battery Cell with Mechanical-Thermal Coupled Analysis. Energies, 2022, 15(3), 929.
[22] Dalcalı A, Akbaba M. Comparison of the performance of bridge and bridgeless shaded pole induction motors using FEM. International Journal of Applied Electromagnetics and Mechanics, 2017, 54(3), 341-350.

RIGA 2023

Breakdown Voltage of DC Capacitive Discharge Plasma

Bekir Dursun
Trakya University, Edirne Technical Sciences Vocational College, Department of Electrical and Energy, Edirne, Türkiye,
bekirdursun_@hotmail.com, https://orcid.org/0000-0002-7741-8873

Erol Kurt
Gazi University, Technology Faculty, Department of Electrical and Electronics Engineering, Ankara, Türkiye,
ekurt52tr@yahoo.com, https://orcid.org/0000-0002-3615-6926

Cite this paper as: *Dursun, B, Kurt, E. Breakdown Voltage of DC Capacitive Discharge Plasma. 11th Eur. Conf. Ren. Energy Sys. 18-20 May 2023, Riga / Latvia*

Abstract: In this paper, we present the results for voltage–pressure (V–P) correlations of dc low-pressure low to moderate discharges of hellium gas. We analyzed the effect of voltage rise time over the Paschen curves by using kinetic and fluid models, in that way we described the dependence of the breakdown voltage. We tried to obtain minimum values to correspond to optimal conditions for plasma generation according to Ubr on the product pd of gas pressure p and the characteristic length d between the electrodes. Paschen curve was the focus of our work . First of all, Experimental system has been set-up as the new plasma system in the laboratuary. The internal environment of the insulator vessel was filled with helium gas. The designed system has two electrodes. One of them is the 0 volt applied anode, the other is the -500, -1000, -1500 and -2000 Volt applied cathode. The relationship between voltage and pressure was analyzed experimentally. The Paschen curve obtained is in parallel with the literature.

Keywords: Particle Trajectories, Plasma, Electron Density, Potential Distribution

1. INTRODUCTION

Plasmas operating in liquids and the gas–liquid interface, have been of great attention in the last decade because of their wide usage areas in nanoparticle synthesis,organic compound decomposition, water treatment ,biomedical areas even medical procedures. The universal Paschen Curve is known to be able to characterize the electrical breakdown of planar gas-filled gaps. The dependence of the breakdown voltage, U*br* , on the product of gas pressure p and the cathode-anode gap d can be described with this curve. The Paschen curves shows the characteristic minimum, corresponding to optimal conditions for plasma formation for the gas we used. Paschen's curves also depends on the the shape of the electrode material[1-3].

Paschen's curve is an important tool in the study and application of gas discharges, and it is widely used in various fields of science, engineering, and technology.

$$U_B = f(p, d) \qquad (1)$$

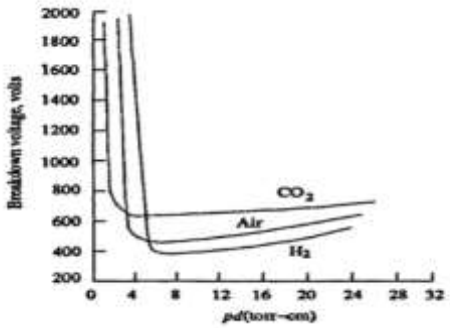

Figure 1. Paschen's law for breakdown voltages of H_2, Air, CO_2[7]

Since the breakdown voltage of each substance is different, spots on the Paschen curve occur and decrease inversely with the pressure until the value of P_{min} and U_{min}. After that value, it fives itself.

Gas Discharge is defined as a plasma type. Luminousity is a characteristic of plasma. Laminated structure of plasma results from colliding electrons within atoms. This collision also leads to generate visible light and photons. Direct continuous dc and radio frequency rf discharge are the two most common types of electric discharge. Above mentioned electric discharge types bear requirements and features for discharge applications. When a potential difference between the two gas filled electrodes at a limited pressure inside a chamber is applied, glow discharge is generated[4-5].

The process of gas discharge is affected by some parameters; the distance between electrodes, electrodes' shape, the type of material used for electrodes,pressure,and gas type. Electirical discharge of gases has a lot of application areas some of which are as follows; microelectronics production,surface treatment,nano materials, coating technology,integrated curcuit production.Furthermore flat plasma display units and fluorescence lamps need the light produced from excited atoms and some medical uses for example cutting tissue and sterilizations of medicaltools.In this paper we experimentally studied the dc discharge operation,and used helium gas and two electrodes.We calculated potential lines distributions between the electrodes using CST software[6].

2. EXPERIMENTAL SCHEMA

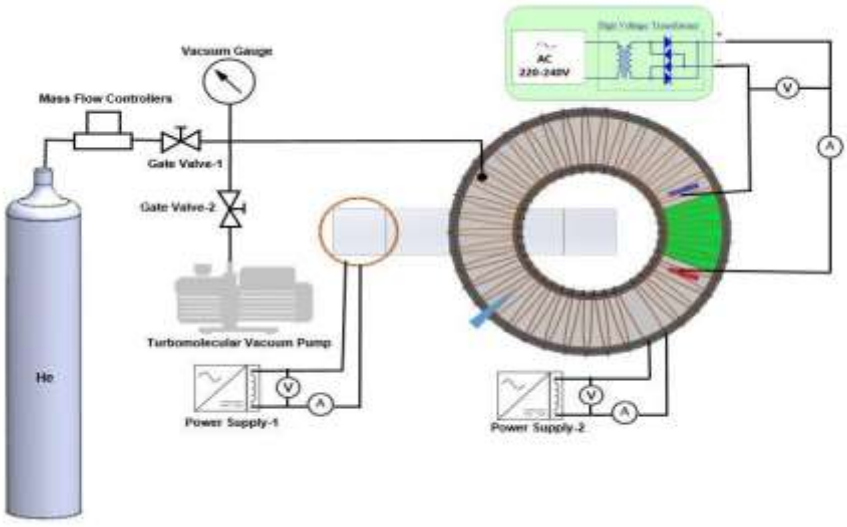

Figure 2. Experimental Schema we used in measurements

The experimantal schema shown in figure 2 is made up of 2 parts which are plasma reactor and electrical circuit. The structure of the discharging part in our experimantal curcuit: stainless steel toroidal cross, which has 270mm outer diameter,130mm inner diameter, 100mm height, and 9mm material tickness.In our study we used a Turbomolecular Vacuum Pump to be able to obtain the pressure of ~ 10^{-3},which we measured at a vacuum gauge,in

our discharge chamber.we used püre tungsten as the material of our cathode and anode electrodes.our cathode's shape was spherical and its diameter was 30mm and tickness was 1mm.Figure 3 shows real experimental setup with electrical circuit.

Figure 3. The experimental setup and the electrical circuit used in measurements

3. RESULT

Figure 4 shows the Pacshen's curve obtained from different pressure and voltage values when the poloidal and toroidal current is zero. The curve we have obtained is clearly similar to the Paschen curve associated with opposing plate electrodes. It is seen that breakdown voltage occurs at low voltage and low pressure. As we lower the pressure at high and increase the voltage, the system will start to feed itself at the breakdown voltage. This point is best seen on the Paschen's curve in fig.4.

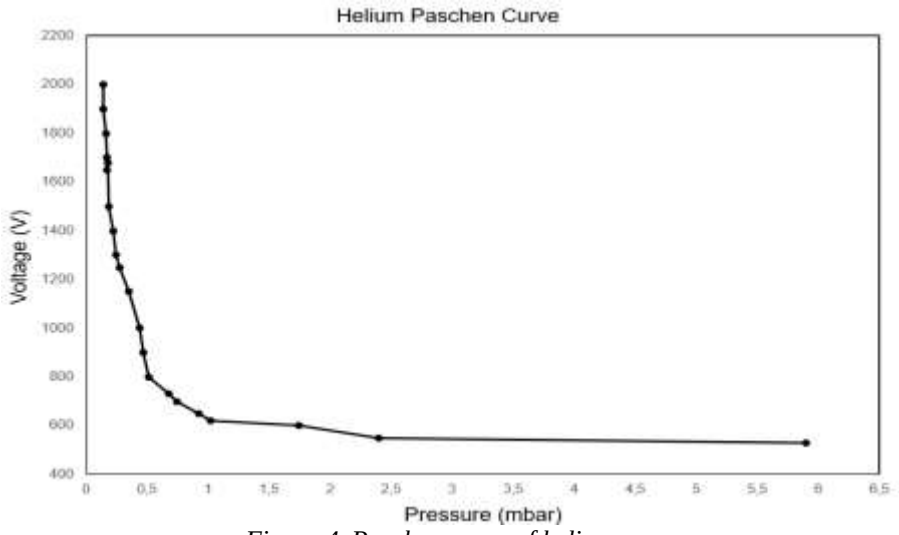

Figure 4. Paschen curve of helium gas

Figure 5 shows the system will be vacuumed and helium gas will be sent inside. The presence of the plasma can be understood from the reddish glow that occurs when the neutral helium gas is ionized by passing an electrical energy between the anode and cathode poles in the system. The glow, which can be seen in the figure, is obtained without current being applied to the poloidal and toroidal windings. Which means that glow is seen from cathode to anode only under the influence of pressure and voltage.

Figure 5. Gas glow in TOKAMAK device

4. CONCLUSIONS

In our study, the relationship between voltage and pressure for helium gas, as it should be in the literature, has been obtained. This relationship is expressed in the paschen's curve. Paschen's curve shows that voltage, pressure and distance between electrodes are important.

In this study, poloidal and toroidal currents were kept constant(I=0). The results we obtained are of great importance in terms of plasma as well as their compatibility. We plan to develop this study with different gases in the future.

Acknowledgement

This study was supported by Gazi University Scientific Research Projects Commission under the grant no: FDK-2022-7897, Türkiye.

Authors would like to thanks Trakya University for financial support, Türkiye.

References

[1] Marjanović, J., Marić, D., Malović G., Petrović Z. Lj, Voltage–current characteristics of lowpressure discharges in vapors of several alcohols. J. Appl. Phys. 2021; *129*: 143303. https://doi.org/10.1063/5.0044419

[2] P J Bruggeman, M J Kushner, B R Locke, J G E Gardeniers, W G Graham, D B Graves, R C H M Hofman-Caris, D Maric, J P Reid, E Ceriani, D Fernandez Rivas, J E Foster, S C Garrick, Y Gorbanev, S Hamaguchi, F Iza, H Jablonowski, E Klimova, J Kolb, F Krcma, P Lukes, Z Machala, I Marinov, D Mariotti, S Mededovic Thagard, D Minakata, E C Neyts, J Pawlat, Z Lj Petrovic, R Pflieger, S Reuter, D C Schram, S Schröter, M Shiraiwa, B Tarabová, P A Tsai, J R R Verlet, T von Woedtke, K R Wilson, K Yasui and G Zvereva. Plasma–liquid interactions: a review and roadmap. Plasma Sources Sci. Technol. 2016; *25*(5) 053002. DOI 10.1088/0963-0252/25/5/053002.

[3] G. Petitpas, J.-D. Rollier, A. Darmon, J. Gonzalez-Aguilar, R. Metkemeijer, L. Fulcheri. A comparative study of non-thermal plasma assisted reforming technologies. *International Journal of Hydrogen Energy* 2007; *32*(14): 2848-2867.

[4] Dmitry Levko, Robert R. Arslanbekov, and Vladimir I. Kolobov. Modified Paschen curves for pulsed breakdown. Phys. Plasmas 2019; *26*: 064502. https://doi.org/10.1063/1.5108732

[5] Leonid P Babich, T V Loĭko and V A Tsukerman, High-voltage nanosecond discharge in a dense gas at a high overvoltage with runaway electrons. *Soviet Physics Uspekhi* 1990; *33*(7): 521. DOI 10.1070/PU1990v033n07ABEH002606.

[6] Estbrq A Abd-Alwahed and Khalid A Yahya. Operational characteristics of disc and spherical cathode electrodes in dc plasma discharge. IOP Conf. Series: Materials Science and Engineering 2020; 871: 012059. doi:10.1088/1757-899X/871/1/012059.

[7] internet website: https://www.oocities.org/thana755/index6.html https://www.oocities.org/thana755/index6.html

RIGA 2023

RIGA 2023

COUNTRIES AND PRESENTERS LIST

ID	TITLE	COUNTRY	PRESENTER
Opening Session	The Welcome Messages	Türkiye	Erol Kurt
Keynotes	Hydrogen in Electricity's Future	UK	Ahmed F. Zobaa
	Building Integrated Photovoltaics: From Sufficiency to Sharing towards Carbon Neutral Cities	Greece	Dimitrios Karamanis
	Theoretical and Empirical Modeling	Spain	Jose Manuel Lopez-Guede
11	Capacity Factor of Wind Parks in Bosnia and Herzegovina	Bosnia and Herzegovina	Elvir Zlomušica
14	Experimental Study and Modeling of Solar Drying in a Ventilated Attic	Côte d'Ivoire	Zokagon Aristide Tieu
18	Benchmark of Electronic Controllers in a Biofuel Production Plant	Ecuador	Lenin Calero
23	Forecasting Electricity Consumption for Covid-19 Pandemic Period and Beyond	Brazil	Gabriel Nasser Doyle de Doile
25	Energy Efficiency in The Last Mile: from Conventional to Renewable Energy Transport	The Netherlands	Adriana Saraceni
28	Use of A Low-Cost Catalyst for The Production of Fuel Gas and Carbon Nanotubes From The Pyrolysis of Plastic Waste	Spain	Mónica Calero
29	Development of Sorbents for Carbon Capture to Achieve Carbon Neutrality	Latvia	Maris Klavins
32	The Analysis of Energy Efficiency Measures in Multiapartment Buildings in Latvia	Latvia	Aleksandra Cimbale
33	Investigation of Metal-Impregnated Zeolites as Catalysts in Pyrolysis of Mixed Plastic Wastes	Spain	Mª Ángeles Martín-Lara
34	The Expected Dynamics of Wind Energy in Baltic and North Seas	Romania	Eugen Rusu
35	An Evaluation of The Future Expected Wind and Wave Power in The Black Sea	Romania	Alina Beatrice Raileanu
36	A Compact Unit of Photovoltaic Solar Still Air Gap Membrane Distillation Process for Simultaneous Production of Water and Electricity	Kuwait	Adnan Alhathal Alanezi
37	PV based DC-DC Converter for Hybrid Storage System using Deadbeat Controller	India	Sukhi Y
38	Role of The Transport Sector in Hydrogen Energy System	Austria	Amela Ajanovic
39	Conditions for Sustainable and Democratic Electricity Systems	Austria	Reinhard Haas
40	Characterization of Bifacial Technology PV Systems	Sapin	Jorge Aguilera Tejero
41	Development of Skutterudite-Type Thermoelectric Materials LaxCo4Sb12 using High-Pressure Synthesis Method	Thailand	Yuttana Mona
42	Assessment of The Synergy between Marine Energy Resources in The West Iberian Coast	Romania	Liliana Rusu
43	Comparable Recovery of Metals from Waste Photovoltaic Panel using Microbial Media and Organic Acids	Taiwan	Hong Hocheng
44	Prediction of The Variability of Wave Energy Potential in An Offshore Point	Spain	Deivis Avila
46	Comparative Study of Cylindrical and Triple Concentric Tube Models for PCM-based Thermal Energy Storage	India	Abhinav Rajan
50	Decarbonizing a Thai Coal Power Plant: Effect of Flue Gas Loads on Carbon Capture Performance and Economics	Thailand	Nakorn Tippayawong
51	Design and Implementation of DC-DC Converter for PV based EV Battery Storage System	India	Sukhi Y
53	The Effect of Thin Strontium Titanate Films on The Raman spectrum: Ab Initio Calculations	Estonia	Veera Krasnenko
56	Ammonia Nitrogen Removal and Recovery using Bipolar Membrane Electrodialysis with A Membrane Contactor	South Korea	Kyo Sik Hwang
57	Ball mill pretreatment for improved bioavailability of biomass	Republic of Korea	Jin Hyung Lee
60	Challenges and Opportunities of Enhanced Biogas Production using Anaerobic Co-digestion with a Low Carbon Footprint	Taiwan	Shu-Yuan Pan
61	Characteristics of A Low Aspect Ratio Tokamak Fusion Reactor for Nuclear Transmutation with A Molten Salt Blanket	Republic of Korea	Bong Guen Hong
62	CO2 Capture by Mineralization and Utilization: Primary Assessment of Thai Ultramafic Rock Resource	Thailand	Waranya Thepsasku
63	Enhancing Breakdown of Microplastics by Hydrothermal Fenton Reaction	Republic of Korea	Chang Gyun Kim
65	Energy Utilization of Waste for The Production of Hydrogen	Czech Republic	Jan Najser, Jan Kielar
66	Performance Evaluation of Solar Aggregation Platform on The Cloud and Edge Device Integration	USA	Panitarn Chongfuangprinya

67	Educational Study on Performance Comparison of PID, Fuzzy Logic-PID, and Bode Editor Techniques for Series Wound DC Motor Speed Control	Türkiye	Gonca Çam
68	Design, Performance Testing and Optimization of A Forced Convection Indirect Solar Dryer	Cote D'ivoire	Yves Narcisse Droguy
72	Design and Control of Switched Reluctance Motors with Different Stator and Rotor Pole Numbers by Co-simulation: Comparatively Performance Analysis	Türkiye	Bekir Gecer
73	Activation to Elasticity in Electricity and Heat Consumption	Finland	Merja Mäkelä
74	Investigation of The Latest Developments in Battery Technology for Enhanced Performance and Increased Range in Electric Vehicles	Morocco	El Fakkak Omar
75	Technical Analysis of The Scale-Up and Implementation of A Membrane Contactor Plant for Biomethane Recovery in A Full-Scale Anaerobic Digestion Facility	Spain	Jesús M. Martín-Marroquín
76	Anaerobic Digestion of Kitchen Residue and its Biogas Production	Taiwan	Chihhao Fan
77	Anaerobic Digestion for Biogas Production using Wastewater from Polyhydroxyalkanoates Production Process	South Korea	Hyunook Kim
78	Estimating Energy Consumption of Battery Electric Vehicles using In-Vehicle Sensing and Machine Learning Approaches	Thailand	Pana Suttakul
79	A potential Reduction of Energy Consumption By The Flexible Working Hour Policy: An Experimental Study in Chiangmai, Thailand	Thailand	Witsarut Achariyaviriya
80	Performance of Microwave-Assisted Hydrolysis of Cattle Manure and the Effect of Food Wastewater as Chemical Catalyst	South Korea	Junghyeon Kim
84	Engineering Rumen Microbiome with Megasphaera Hexanoica for Mitigating Biogas Emission	South Korea	Pranav Sasidharan Nair
85	Machine Learning Approaches for Predicting Methane Production from Anaerobic Digestion of Thermally Pretreated Slaughter Waste	South Korea	Darsha Prabhaharan
86	Evaluation of The Microbial Methanation Process on The Pilot Scale with Enhanced Hydrogen Mass Transfer for The High-Purity Methane Production	Republic of Korea	Young-Wook Go
90	Saving Energy by Changing Lighting in a 24-Hour Store	Poland	Artur Rusowicz
91	State of charge estimation by online OCV Evaluation Using an Auxiliary Controlled Load	Algeria	Abdelaziz Zermout
92	Experimental Investigation of PCM Based Thermal Energy Storage Unit with Finned Tubes	Poland	Maciej Jaworski
93	Study of Thermodynamic Processes of Hydraulic Compression of Hydrogen By Numerical Simulation	Latvia	Bezrukovs V.
94	Grid-Connected and Grid-Islanded Energy Consumption Management	Algeria	Djillali Kaddour
98	Unsupervised Neural Network Optimized with Genetic Algorithm for MPPT Control of a Floating Wind Turbine	Spain	Eduardo Muñoz-Palomeque
100	Floating DC Nano Grid for Solar Charging of Recreational Boats	Netherlands	P.J. van Duijsen
106	LSTM and GRU Neural Networks for Prediction of Wind Turbine Active Power	Ecuador	Pablo Buestán-Andrade
107	Experimental Study of The ORC System with Isobutane (R600a) as A Working Fluid	Poland	Andrzej Grzebielec
108	Towards Li2S All Solid State Batteries	Germany	Zahilia Cabán Huertas
113	Design of a Shape Memory Alloy Heat Engine By Using Waste Heat	Taiwan	Chi Hsiang Pan
118	About DC Parameters of PV Panels	Georgia	Nugzar Gomidze
125	Comparing The Efficiency of Nano zero Valent Iron, Activated Carbon and Hydrochar as Additives on Biohydrogen Production By Dark Fermentation	Spain	Enrique PérezZapater
127	Analysis of Energy Efficiency in Public Lighting Systems Friendly to The Environment and Protected Areas	Ecuador	Carlos Velásquez
131	The Relation Between Top-Cell Bandgap and Silicon Bottom-Cell Thickness in Double-Junction 2-Terminal Silicon-Based Tandem Solar Cells	The Netherlands	Hesan Ziar
132	Characterization of Biocrude Oils from Hydrothermal Liquefaction of De-ashed Energy Grass	Thailand	Nakorn Tippayawong
133	Conceptual Design of An Aluminum-Air Battery System to Remove Hydrogen and By-Products	Republic of Korea	Jeong-Seog Oh
134	Iron-Chlorine Chemical Cycle for On-Demand Green Hydrogen Production Powered By Waste Heat	Slovenia	Matjaz Valant
137	Will Industrial Green Total Factor Productivity be Affected by Digital Finance?	China	Luqi Miao
141	Hydro-Energy Plants Modeling in Optimal Power Flow Problems	Spain	Rafael Zárate-Miñano
142	Optimization of the Iron Chloride Electrochemical Cycle as a long-term energy storage technology	Slovenia	Uroš Luin
143	Applying Explainable AI For Heating Control in Low Power IoT Devices	Lithuania	Algirdas Dobrovolskis
145	Analysis of Geothermal Power Plant Process Design for Lahendong Expansion Area With Comparison of Flash Steam and binary Cycle Systems	Indonesia	Juwari
146	What is Energy Informatics? An Inclusive View	Spain	Laura del Rio Carazo
158	The Chance for RESC in Italy: Study for a Sizing Model	Italy	Roberto Bosco

159	Enhancing the Performance of Human Motion Energy Harvesting through Optimal Smoothing Capacity in the Rectifier	Latvia	Ilgvars Gorņevs
160	Exploring the Green Transformation Path of Enterprises under the “Carbon Peaking and Carbon Neutrality” Target	China	Luqi Miao
162	The Influence of Recuperative Cooling Approach for Energy Harvesting on Efficiency of Thermoelectric Cooling	Latvia	Vilnis Jurķāns
165	Allocation of Photovoltaic Distributed Generations in A Radial Distribution System	Nigeria	Samson Ayanlade
166	A Process Mapping Study of End-Of-Life Electric Vehicle Battery Repurposing for Renewable Energy Storage	UK	Andrew Greasley
169	Solar PV Recycling Strategies	USA	Zita Ngagoum Ndalloka
170	Using FMEA Technique to Improve Steam Boiler Energy Efficiency	Türkiye	Ceyda Kocabaş
173	Hybrid Photovoltaic thermal (PV/T) Heat Pump Application in the National Stone Centre in UK	UK	Tugba Gurler
177	Study of the Use of Agrovoltaics in The Canary Islands. Issues to Consider	Spain	A. Pulido Alonso
180	Bioclimatic Strategies in Floating Houses and Quality of Life in The Lower Area of Belén, Iquitos 2022	Peru	Vanessa Raymundo Martínez
196	Groundbreaking Materials for Retrofitting Light Water Reactor Fuels	USA	Raul B. Rebak
200	Bioclimatic Design Strategies in Social Housing for Cold Weather-Tacna - Peru 2022	Peru	Vanessa Oshin Raymundo Martinez
208	Design of the Tubercle Leading Edge Blade for Small-Scale Wind Turbines	Taiwan	Chung-Neng Huang
209	The Reliability of The Forecast of Energy Yield, Case of Kitka Wind Farm	Republic of Kosovo	Bukurije Hoxha
216	Bacterial Cellulose - A Potential Biomaterial for Energy Storage and Energy Conversion Devices	Czech Republic	Nabanita Saha
218	Numerical Study on Indoor Air Purification and Heating Energy Consumption	Latvia	Andrejs Sabanskis
219	Sustainable Energy Strategies Applied to An Experimental Aquaponic Farming Production System	Spain	Luis Mazorra Aguiar
221	Parameter Estimation of PV System Towards Self-Consumption of Electric Energy for Dormitory	Poland	Tomasz Trawiński
223	Cost Models of Single-Phase and Three-Phase Cable Underground Lines	Israel	Svetlana Bronshtein
225	The Exploration of the Influence of a Magnetic Field on a Fuel-cell System	Türkiye	Mustafa Melih Kale
226	Adsorbed Gas Storage Digital Twin	Germany	Georg Klepp
228	Raising Awareness and Uncertainty Caused by Green Deal Targets within Companies Involved in Emission Trading Scheme in Latvia	Latvia	Iveta Steinberga
230	Production and consumption load profile characterization in Energy Communities	Spain	Wolfram Rozas, Rafael Pastor
231	The Use of Renewable Energy Sources and Radiant Capillary Heat Exchangers to Increase The Energy Efficiency of An Existing Apartment	Latvia	Stanislavs Gendelis
233	Simulation Model of a Parabolic Trough Concentrated Solar Power Plant in Khobar city, Saudi Arabia	Saudi Arabia	Nidal Abu-Libdeh
235	Determination of Structural Parameters of Boilers Loading Devices on a Small Biomass to Reduce The Air Excess Coefficient in The Boiler Chamber	Ukraine	Anatolii Cherniavskyi
236	Two-Element MIMO Antenna for UWB Wireless Communications	Türkiye	Emre Kaan Kaynar
237	Adaptive Mesh Refinement Criterion Comparison for DrivAer Model	Spain	Oscar Irigaray Pérez de San Román
238	Trends in Lithium-Ion Battery Optimization for Electric Vehicle Fleets	Spain	Felipe A. Nunez-Donoso
239	Computational Analysis of Variable Electrode Compression on The Performance of Vanadium Redox Flow Battery	Spain	Joseba Martinez-Lopez
240	NOx emissions modeling for A gas Lean Burn Engine	Spain	Javier Del Valle
241	Power System Equipment Mentoring using Web-Based Controller	Iraq	Mustafa Alhamdi
242	The Effect of Demagnetization Faults in Permanent-Magnet Synchronous Wind Generators	Türkiye	Adem Dalcalı
243	Efficiency Analysis of Fixed and Axis Tracking Options of Photovoltaic Systems to be Installed in A Marina	Türkiye	Hacı Mehmet Şahin
244	Breakdown Voltage of DC Capacitive Discharge Plasma	Türkiye	Bekir Dursun

HOPE TO SEE YOU IN OUR NEXT EVENT

www.icmece.org